



Chula
Chulalongkorn University



TSB 2025

Biotechnology in Action

Proceedings Book

The 37th Annual Meeting of the Thai Society
for Biotechnology and International Conference

29th – 31st October 2025

Mandarin Hotel Bangkok, Thailand



www.tsb2025.org

CONTENT

	Page
Committee	1
BS-O-002: Transcriptomics analysis of <i>Starmerella riodecensis</i> GT-SL1R under High carbon to nitrogen ratio Condition for Enhanced Sophorolipid Production <i>Sirawich Sapsirisuk and Nitnipa Soontorngun</i>	5
BS-P-008: Impact of heterologous <i>Beta Carotene Ketolase (bkt)</i> gene expression from <i>Hematococcus pluvialis</i> in <i>Synechocystis</i> sp. PCC 6803 on carotenoid production under salt stress <i>Benjamat Sukkokee and Saowarath Jantaro</i>	14
BS-P-014: Complete genome insights into a <i>bacillus cereus</i> group isolates from food <i>Sawanya Potirungsee, Phornphan Sornchuer and Kritsakorn Saninjuk</i>	22
BS-P-016: Microbiome biomarkers for colorectal cancer diagnosis via metagenomic analysis <i>Kasidet Taweapon, Tavan Janvilisri, Joy Scaria, Supeecha Kumkate and Phurt Harnvoravongchai</i>	30
MB-O-022: Functional analysis of aromatic amino acid transporter gene <i>aaaT</i> on antimicrobial resistance in <i>Pseudomonas aeruginosa</i> <i>Pacharapon Phoopanish, Jintana Duang-nkern, Saharit Wijitpittayanon and Adisak Romsang</i>	40
MB-O-024: Distribution of <i>Vibrio</i> spp. in relation to water quality in the Songkhla lake basin, Thailand <i>Jutamas Manit, Kurrotulayunee Kareeya and Rattanaruji Pomwised</i>	47
MB-P-005: Performance testing of a urine microalbumin dip test strips developed for preliminary kidney disease screening <i>Umaporn Pimpitak, Wanwisa Poonlapdecha Anumart Buakeaw, Sirirat Rengpipat and Kittinan Komolpis</i>	56
MB-P-010: ITS-based identification of common poaceae species found around bangkok <i>Lilian Haidvogel, Umaporn Siriwattanukul, Wanichaya Chaiwimol and Wisuwat Songnuan</i>	63
MB-P-012: Enhancing scoliosis detection using ai: integrating deep learning into the medical field <i>Pittayud Aursukitwattan and, Pakwalan Kiewwichai</i>	71
MB-P-015: Evaluation of chondrocyte culture formats for enhancing early cartilage matrix formation <i>Matthuros Sonthisathaporn, Nattanan T-Thienprasert and Chomdao Sinthuvanich</i>	77
MB-P-017: Optimizing a split lentiviral delivery system for CRISPR/Cas9-based gene knockout in mesenchymal stem cells <i>Lanlalit Pongsasakulchot, Kanok Keerati-Opasawat, Natcha Gahawong and Waracharee Srifa</i>	84
MB-P-025: OCT-4 activating compound 1 enhances developmental competence and pluripotency of porcine SCNT embryos <i>Thida Praeksamut, Phattarawadee Noita and Rangsun Parnpai</i>	93

	Page
MB-P-026: Assessment of the antioxidant and anti-inflammatory properties of human placental extract in human mesenchymal stem cells <i>Kanda Rungboon, Nipha Chaicharoenaudomrung, Natchadaporn Sorraksa, Phongsakorn Kunhorm, and Parinya Noisa</i>	104
MB-P-027: Novel insights into the role of vesicle- and monolayer-derived extracellular vesicles from bovine oviduct epithelial cells in enhancing embryo quality <i>in vitro</i> <i>Apisit Polrachom, Kamolchanok Tonekam, Worawalan Samruan, Traimat Boonthai and Rangsun Parnpai</i>	111
MB-P-029: Establishment of the glycoprotein CD147 knockout in a human leukemia cell line (K562) using lentivirus-based CRISPR/Cas9 system <i>Wannakan Jaikamlue, Kumpanat Pomlok, Suparat Lithanatudom, Jiraprapa Wipasa and Pathrapol Lithanatudom</i>	120
IE-O-005: Sorghum stem juice valorization to produce bioethanol: Process simulation and life cycle assessment <i>Jutima Tantrakool, Aye Myat Theint Kyaw, Penjit Srinophakun, Anusith Thanapimmetha, Maythee Saisriyoot, Khemmathin Lueangwattanapong and Nutchapon Chiarasumran</i>	126
IE-O-011: Enhancing biotransformation of cassava pulp to biomethane with liquid hot water and microbial pretreatments <i>Saengmany Phommakod, Suppanut Varongchayakul, Warinthorn Songkasiri and Pawinee Chaiprasert</i>	135
IE-O-022: Effects of Thai herbal extracts on mitigatingalachlor-induced oxidative stress in <i>Saccharomyces cerevisiae</i> <i>Pham Ngoc Nhi Huynh and Choowong Auesukaree</i>	146
IE-P-031: Sugarcane leaf derived-biochar acid catalyst for efficient isosorbide production from sorbitol <i>Chonthicha Nilapornkul, Pongtanawat Khemthong, Bunyarit Panyapinyopol, Wasawat Kraithong, Pawan Boonyoung, Saran Youngjan, Jakkapop Phanthasri and Kamonwat Nakason</i>	153
IE-P-041: Genetic improvement and chitinolytic enzyme production of <i>Stenotrophomonas maltophilia</i> Mc_E05 isolated from termite exoskeleton <i>Chinnaphat Meeto, Kittipong Chanworawit and Pinsurang Deevong</i>	163
IE-P-044: Reducing sugar extraction from over-roasted coffee beans and coffee silverskins <i>Sukon Tantipaibulvut, Patchanida Nuttipongpairroj, Areerat Khumpoln, Kanjanakorn Piyarat, Sukanya Yot-aon, Jirayut Euanorasetr and Sukanya Phuengjayaem</i>	170
IE-P-046: Characterization of UV-mutated <i>Kluyveromyces marxianus</i> : isobutanol tolerance and xylose utilization <i>Krittaporn Thungmuthaswade, Navaphorn Pinrenu, Thanyalak Vorawongsakul and Jirasin Koonthongkaew</i>	175
IE-P-048: Factors influencing on development of trehalose production by <i>Saccharomyces cerevisiae</i> <i>Warissara Chotiwanee, Sitanan Thitiprasert and Nuttha Thongchul</i>	183
IE-P-052: Nitrate reducing bacteria from oil sludge and their potential roles on metal corrosion inhibition <i>Luxnapol Marturunkakul, Chutima Rotchum and Ekawan Luepromchai</i>	190

	Page
IE-P-053: Effect of potentially pathogenic and plastic-degrading bacterial co-culture on polylactic acid microplastics <i>Nutthamon Boonlum, Chonchanok Muangnapoh and Ekawan Luepromchai</i>	199
BN-O-018: Investigation of the antioxidant activity of a selected compound derived from <i>Curcuma comosa</i> Roxb. in <i>Saccharomyces cerevisiae</i> <i>Trin Tangnararatchakit, Anyaporn Sangkaew, Apichart Suksamrarn and Chulee Yompakdee</i>	207
BN-P-012: <i>Cratogeomys formosum</i> extract attenuates inflammation in LPS-activated macrophages by reducing IL-6 expression <i>Tuangtong Vongpipatana, Talayboon Pooyoi and Kotchakorn Srikhong</i>	216
BN-P-016: Chitinase production by <i>Aeromonas caviae</i> EW02 newly isolated from giant mud crab pond and potential to degrade chironomid egg masses (<i>Chironomus plumosus</i>) <i>Chirath Pitakkhuamdee, Kittipong Chanworawit, Piyangkun Lueangjaroenkit and Pinsurang Deevong</i>	221
BN-P-023: <i>Phyllosticta capitalensis</i> , an endophytic fungus isolated from <i>Ocimum sanctum</i> with antibacterial activity <i>Pattaranan Ounjai, Khwanruedee Sangjan, Onchapron Jitkumkoon, Urarux Romruen and Eakaphun Bangyeekhun</i>	229
BN-P-026: Screening of potent flavor compounds produced by non- <i>Saccharomyces</i> yeast <i>Naphattarachon Thammpanyaphong, Thamonwan Tassanaset and Jirasin Koonthongkaew</i>	236
BN-P-027: Antimicrobial activity against <i>Cutibacterium acnes</i> of corn agro-residues extract as waste utilization for cosmetic application <i>Natthawut Thitipramote, Ranchana Samaniam, Prinyaporn Pradmeeteekul, Junniphaphorn Nimkamnerd, Thiyapan Noppakoon and Witayapan Nantitanon</i>	244
BN-P-030: Optimization of pectin yield from <i>Cyclea barbata</i> miers leaves using response surface methodology <i>Witayapan Nantitanon, Pimpailin Rodpradit and Natthawut Thitipramote</i>	255
AB-O-008: Biomass production of <i>in vitro</i> <i>Microchirita involucreta</i> roots and evaluation of biological activity of root culture extracts elicited with elicitors <i>Adsadayu Thonnondang, Onrut Inmano, Anupan Kongbangkerd and Apinun Limmongkon</i>	263
AB-O-021: Antifungal activity of <i>Priestia aryabhatai</i> ptku-123 crude extract against <i>Fusarium</i> spp. associated with durian die-back disease <i>James Konkov, Nisit Watthanasakphuban and Paiboon Tunsagool</i>	274
AB-O-024: Biological properties of alkali lignin extract from longan peel for cosmetic application <i>Kittiya Phiguntong and Jidapha Tinoi</i>	283
AB-P-003: SSR-based marker-trait associations for the selection of drought-tolerant maize S1 genotypes <i>Theerawut Wongwarat, Chaiyawat Nantachot and Suriphat Thaitad</i>	292

	Page
AB-P-012: Encapsulated freeze-dried lactic acid bacteria modulate gut microbiota, health, and growth of <i>Penaeus monodon</i> <i>Narongchai Chupoon, Nomchit Kaewthai Andrei, Sirinat Srionnual and Thanikan Thorasin</i>	302
AB-P-014: Expression of chitinase encoding gene from <i>Serratia marcescens</i> Mc_G07 and termiticidal activity against the wood-feeding termite <i>Microcerotermes</i> sp. <i>Kittipong Chanworawit, Torphan Vitoonpanyakij and Pinsurang Deevong</i>	312
AB-P-018: Genome-based discovery of novel cyanobacterial natural products derived from <i>Gloeocapsa</i> sp. strain BRSZ <i>Hari Winanda, Sasiprapa Samsri, Stephen B. Pointing, Hakuto Kageyama and Rungaroon Waditee-Sirisattha</i>	323
AB-P-019: Exploring cyanobacterial diversity from a neutral-alkaline hot spring in Thailand and their photoprotective compound productions <i>Chatchadarat Anantasophon, Pawat Wangthaphan, Tanawat Leknawin, Sasiprapa Samsri, Stephen B. Pointing, Hakuto Kageyama and Rungaroon Waditee-Sirisattha</i>	329
AB-P-020: Phenotypic variation and plasticity of root hair traits in Australian durum wheat (<i>Triticum turgidum</i> subsp. Durum) under phosphorus deficiency <i>Sukrita Majak, Samir Alahmad, Lee Thomas Hickey, Alexander Bucksch and Patompong Johns Saengwilai</i>	336
AB-P-026: Unveiling the quantitative landscape of gingerol and its derivatives in Thai ginger (<i>Zingiber officinale</i> Roscoe) <i>Kronsrinut Rothjanawan, Nattakanwadee Khumpirapang, Alisa Kongthong and Pimprapa Chaijak</i>	346
AB-P-030: Characterization of multi-stress tolerant PGPR from orchard soils in Chanthaburi province, Thailand <i>Jirapat Chanthamalee, Winyou Puckdee and Chewa Thassana</i>	354
AB-P-033: Effect of skim milk supplementation on the production of air-dried lactic acid bacterial starter culture immobilized on corn husk and its antagonistic activity against <i>Aspergillus flavus</i> <i>Possawee Boonyong and Cheewanun Dachoupan Sirisomboon</i>	362
AB-P-034: Bioelectricity from palm oil mill effluent: the role of the pentose phosphate pathway in <i>Choricystis parasitica</i> SW-03 <i>Alisa Kongthong, Thanopon Yooyen and Pimprapa Chaijak</i>	370
AB-P-035: Isolation and characterization of fungi from organic rice cultivation soil for enhancing rice seed germination <i>Anuruk Seeka, Gregorius Nico Adi Setiawan, Manato Nishikawa and Nuttapon Pombubpa</i>	378
AB-P-036: Identification and functional characterization of small heat shock proteins in shrimp immune responses to <i>Ecytonucleospora hepatopenaei</i> (EHP) infection <i>Pithiwat Maiket, Nutthapon Sangklai and Anchalee Tassanakajon</i>	387
AB-P-038: Identification of signaling pathways controlling antimicrobial peptide gene expression in black tiger shrimp <i>Penaeus monodon</i> <i>Chayanit Khunrit, Thapanan Jatuyosporn, Anchalee Tassanakajon and Kuakarun Krusong</i>	397

	Page
AB-P-040: The efficacy of in straw dilution method on survival rates of vitrified bovine embryos <i>Chanyada Angchuan, Traimat Boonthai and Rangsun Parnpai</i>	403
FB-O-008: Process optimization of liquefaction in enzymatic hydrolysis of waste bread using response surface methodology <i>Hsu Yadanar Htun, Natta Laohakunjit, Nattapon Kaisangsri, Apiradee Uthairatanakij, Punchira Vongsawasdi, Ratchadaporn Kaprasob and Orrapun Selamassakul</i>	408
FB-O-011: Development and characterization of cellulose acetate/chitosan films incorporated with piper betel extract for antimicrobial food packaging <i>Prapot Kumhang, Piyarat Khanthawaro and Nichapat Takiaw</i>	417
FB-O-012: Discrepancies of antimicrobial resistant genotypes and phenotypes in foodborne bacteria <i>Vibrio parahaemolyticus</i> from aquatic bird feces in Thailand <i>Wijitra Khaosoong, Yuki Matsumoto, Shota Nakamura, Tetsuya Iida, Carla N. Mavian and Chonchanok Muangnapoh</i>	426
FB-O-014: Impact of bacteriophage contamination from silage on yogurt fermentation <i>Noppakorn Thadasawate, Jeeranan Kamchai, Suratsa Nuansakun, Punyawee Dulyayangkul and Thanyaporn Srimahaeak</i>	436
FB-O-017: Characterization and screening of flavor-producing non-saccharomyces yeasts for fermentation applications <i>Manutsanun Boonyanuwat, Thamonwan Tassanaset and Jirasin Koonthongkaew</i>	445
FB-P-009: Isolation and characterization of <i>Chlorella</i> sp. AARLG049N mutants with high protein and low Chlorophyll content <i>Kitkarn Veeraphisitt and Niyom Kamlangdee</i>	452
FB-P-010: Isolation, morphological identification, and growth of thraustochytrid isolated from mangrove habitats in the gulf of Thailand <i>Sasiwimol Duangvichai, Niyom Kamlangdee and Kaliyamoorthy Kalidasan</i>	459
FB-P-019: Influence of ethanol desolvation ratio on lutein encapsulation in whey protein isolate particles <i>Peerapong Wongthahan, Araya Chaoruangrit and Panadda Nonthanum</i>	467

INTERNATIONAL SCIENTIFIC COMMITTEE

Prof. Dr. Kohsuke Honda <i>ICBiotech, The University of Osaka</i>	<i>Japan</i>
Prof. Dr. Hiroshi Shimizu <i>Graduate School of Information Science and Technology, The University of Osaka</i>	<i>Japan</i>
Prof. Dr. Randeep Rakwal <i>Institute of Health and Sport Sciences, University of Tsukuba</i>	<i>Japan</i>
Prof. Dr. Takeharu Tsuge <i>Department of Materials Science and Engineering, Major in Human Centered Science and Biomedical Engineering, Institute of Science Tokyo</i>	<i>Japan</i>
Prof. Dr. Beom Soo Kim <i>Department of Chemical Engineering, Chungbuk National University</i>	<i>Republic of Korea</i>
Assoc. Prof. Dr. Rietie Venter <i>UniSA Clinical and Health Sciences, Health and Biomedical Innovation, University of South Australia</i>	<i>Australia</i>
Assoc. Prof. Dr. Joy Scaria <i>Veterinary Pathobiology, Oklahoma State University</i>	<i>USA</i>
Prof. Dr. Stephen Brian Pointing <i>Yale-NUS College & Department of Biological Sciences, National University of Singapore</i>	<i>Singapore</i>
Prof. Dr. Sudesh Kumar <i>School of Biological Sciences, Universiti Sains Malaysia</i>	<i>Malaysia</i>
Prof. Dr. Tuck Seng Wong <i>Department of Chemical & Biological Engineering, The University of Sheffield</i>	<i>UK</i>
Assoc. Prof. Dr. Masaki Honda <i>Department of Chemistry, Meijo University</i>	<i>Japan</i>
Prof. Dr. Hakuto Kageyama <i>Graduate School of Environmental and Human Sciences, Meijo University</i>	<i>Japan</i>
Prof. Dr. Shinya Kodani <i>Shizuoka University</i>	<i>Japan</i>

Prof. Sheng-Fan Wang
Kaohsiung Medical University

Taiwan

LOCAL ORGANIZING COMMITTEE

Prof. Dr. Tanapat Palaga
Department of Microbiology, Faculty of Science, Chulalongkorn University, Thailand

Prof. Dr. Tavan Janvilisri
Department of Microbiology, Faculty of Science, Chulalongkorn University, Thailand

Prof. Dr. Wanchai Assavalapsakul
Department of Microbiology, Faculty of Science, Chulalongkorn University, Thailand

Prof. Dr. Chulee Yompakdee
Department of Microbiology, Faculty of Science, Chulalongkorn University, Thailand

Assoc. Prof. Dr. Panan Rerngsamran
Department of Microbiology, Faculty of Science, Chulalongkorn University, Thailand

Assoc. Prof. Dr. Rungaroon Waditee-Sirisattha
Department of Microbiology, Faculty of Science, Chulalongkorn University, Thailand

Assoc. Prof. Dr. Suchada Chanprateep Naphorn
Department of Microbiology, Faculty of Science, Chulalongkorn University, Thailand

Assoc. Prof. Dr. Ekawan Luepromchai
Department of Microbiology, Faculty of Science, Chulalongkorn University, Thailand

Assoc. Prof. Dr. Onruthai Pinyakong
Department of Microbiology, Faculty of Science, Chulalongkorn University, Thailand

Assoc. Prof. Dr. Cheewanun Dachoupan Sirisomboon
Department of Microbiology, Faculty of Science, Chulalongkorn University, Thailand

Assoc. Prof. Dr. Naraporn Somboonna
Department of Microbiology, Faculty of Science, Chulalongkorn University, Thailand

Asst. Prof. Dr. Kobchai Pattaragulwanit
Department of Microbiology, Faculty of Science, Chulalongkorn University, Thailand

Asst. Prof. Dr. Supat Chareonpornwattana
Department of Microbiology, Faculty of Science, Chulalongkorn University, Thailand

Asst. Prof. Dr. Chonchanok Muangnapoh
Department of Microbiology, Faculty of Science, Chulalongkorn University, Thailand

Asst. Prof. Dr. Chompoonik Kanchanabanca

Department of Microbiology, Faculty of Science, Chulalongkorn University, Thailand

Asst. Prof. Dr. Sita Virakul

Department of Microbiology, Faculty of Science, Chulalongkorn University, Thailand

Asst. Prof. Dr. Nuttapon Pombubpa

Department of Microbiology, Faculty of Science, Chulalongkorn University, Thailand

Dr. Jirasin Koonthongkaew

Department of Microbiology, Faculty of Science, Chulalongkorn University, Thailand

Dr. Tatpong Boontawon

Department of Microbiology, Faculty of Science, Chulalongkorn University, Thailand

Prof. Dr. Nuttha Thongchul

Institute of Biotechnology and Genetic Engineering, Chulalongkorn University, Thailand

Assoc. Prof. Dr. Kittinan Komolpis

Institute of Biotechnology and Genetic Engineering, Chulalongkorn University, Thailand

Assoc. Prof. Dr. Aphichart Karnchanatat

Institute of Biotechnology and Genetic Engineering, Chulalongkorn University, Thailand

Assoc. Prof. Dr. Chuenchit Boonchird

Mahidol University

Prof. Dr. Vilai Rungsardthong

King Mongkut's University of Technology North

Assoc. Prof. Dr. Prakrit Sukyai

Kasetsart University

Assoc. Prof. Dr. Ratchaneewan Aunpad

Thammasat University

Assoc. Prof. Dr. Sehanat Prasongsuk

Chulalongkorn University

Dr. Kuakoon Piyachomkwan

Poon Phol Company Limited

Dr. Korsak Towantakavanit

Mitr Phol Sugar Corp., Ltd.

Mr. Niwat Suriyakamon

Pharmafac plan technology Co.,Ltd.



Assoc. Prof. Dr. Tatsaporn Todhanakasem
King Mongkut's Institute of Technology Ladkrabang

Assoc. Prof. Dr. Theppanya Charoenrat
Thammasat University

Asst. Prof. Dr. Adisak Romsang
Mahidol University

Assoc. Prof. Dr. Apichart Karnchanatat
Chulalongkorn University

Assoc. Prof. Dr. Rujikan Nasanit
Silpakorn University



TRANSCRIPTOMICS ANALYSIS OF *Starmerella riodocensis* GT-SL1R UNDER HIGH CARBON TO NITROGEN RATIO CONDITION FOR ENHANCED SOPHOROLIPID PRODUCTION

Sirawich Sapsirisuk¹, Nitnipa Soontorngun^{1*}

¹Excellent Research Laboratory for Yeast Innovation, Biochemical Technology Division, School of Bioresources & Technology, King Mongkut's University of Technology Thonburi (KMUTT), Bangkok 10150, Thailand

*Correspondence to: Excellent Research Laboratory for Yeast Innovation, Biochemical Technology Division, School of Bioresources & Technology, King Mongkut's University of Technology Thonburi (KMUTT), Bangkok 10150, Thailand.

*e-mail: nitnipa.soo@kmutt.ac.th

Abstract:

Sophorolipid (SL) is a one of biosurfactant produced by the yeast strain *Starmerella bombicola*, a well-known SL-producing yeast. SLs have potential applications in various fields, including food preservation, cosmetics, antimicrobial agents, and bioremediation. In this study, we identified a new SL-producing yeast species, *Starmerella riodocensis* GT-SL1R, which was isolated from honey. This yeast strain demonstrates the potential to produce SLs, and its production performance was further evaluated under different cultivation conditions. Specifically, *S. riodocensis* GT-SL1R was cultivated under varying carbon-to-nitrogen (C/N) ratios to investigate its metabolic response and SL production capacity. At a high C/N ratio of 100, the yeast produced nearly 30 g/L of SL after 7 days, compared to 18 g/L at a low C/N ratio of 25, while biomass accumulation was significantly reduced. Transcriptomic profiling revealed a global metabolic shift under nitrogen-limited conditions, with approximately 500 genes upregulated and more than 500 downregulated. Genes involved in cell cycle regulation, DNA replication, ribosome biogenesis, and ergosterol synthesis were strongly repressed, suggesting growth arrest. In contrast, key SL biosynthetic genes (*CYP52M1*, *UgtA1*, *UgtB1*, *At*, and *Sble*) and the transporter *MDR* were highly induced, along with genes related to nitrogen uptake and recycling. These findings demonstrated that *S. riodocensis* reprogrammed its metabolism under nitrogen limitation, suppressing growth and redirecting resources toward SL biosynthesis. Thus, this transcriptomic data provided insights for optimizing glycolipid production at an industrial scale.

Keywords: Biosurfactant, C/N ratio, Sophorolipid production, *Starmerella riodocensis*, Transcriptomics



Introduction:

Microbial biosurfactants have attracted considerable attention as sustainable alternatives to chemically synthesized surfactants due to their biodegradability, low toxicity, and diverse industrial applications in pharmaceuticals, cosmetics, food processing, and bioremediation (Marchant & Banat, 2012; Varjani & Upasani, 2017). Among various biosurfactants, sophorolipids (SLs), glycolipid molecules mainly produced by yeasts of the genus *Starmerella*, are one of the most promising due to their high production yield and versatile biological activities, including antimicrobial, anticancer, and anti-inflammatory properties (Van Bogaert et al., 2011; Shah et al., 2021). The type strain *Starmerella bombicola* ATCC 22214 is the most extensively studied SL-producing yeast, capable of secreting over 300 g/L of sophorolipids under optimized conditions (Saerens et al., 2011). The biosynthesis of SL proceeds through a well-coordinated pathway involving both fatty acid metabolism and carbohydrate utilization. Initially, cytochrome P450 monooxygenase (*CYP52M1*) hydroxylates the fatty acid substrate, typically a long-chain fatty acid such as oleic acid, to produce ω - or ω -1-hydroxy fatty acids (Van Bogaert et al., 2013). These hydroxylated fatty acids are then sequentially glycosylated by UDP-glucosyltransferases (*UgtA1* and *UgtB1*), which transfer glucose moieties from UDP-glucose to generate the sophorose head group, resulting in acidic sophorolipids. Further structural modifications, such as acetylation by an acetyltransferase (*At*) and lactonization catalyzed by sophorolipid lactone esterase (*Sble*), diversify the SL molecules into lactonic forms, which display different physicochemical and biological properties (Ueda et al., 2019). This pathway highlights the interplay between primary metabolic routes and specialized enzymes, enabling *Starmerella* species to produce a broad spectrum of SL structures. Recently, novel yeast species such as *Starmerella riodocensis* have been isolated from natural environments and identified as potent SL producers with potentially unique metabolic traits (Alfian et al., 2022). Understanding the regulation of SL biosynthesis in these non-model strains is essential for broadening the biotechnological applications of SL. The biosynthesis of SL is influenced by nutritional and environmental factors, particularly the carbon-to-nitrogen (C/N) ratio, which plays a critical role in directing cellular metabolism toward biomass formation or secondary metabolite production (Konishi et al., 2015; Gautam & Tyagi, 2006). A high C/N ratio typically promotes lipid or glycolipid accumulation, while a low C/N ratio favors cell growth (Ribeiro et al., 2020). However, the molecular mechanisms underlying this metabolic shift in *Starmerella riodocensis* remain poorly understood.

Advances in high-throughput transcriptomics and quantitative real-time PCR (qRT-PCR) provide powerful tools to investigate global gene expression patterns and the regulation of key biosynthetic genes. In *Starmerella* spp., genes such as *CYP52M1* (cytochrome P450 monooxygenase), *UgtA1* and *UgtB1* (UDP-glucosyltransferases), *At* (acetyltransferase), and *Sble* (sophorolipid lactone esterase) are known to be central in SL biosynthesis and structural modification (Van Bogaert et al., 2013; Ueda et al., 2019). Profiling their transcriptional response under different C/N conditions provides insights into how nutrient availability regulates SL production. Therefore, this study aimed to investigate SL production by *S. riodocensis* GT-SL1R under varying C/N ratios, combined with gene expression and transcriptomic analyses. These findings will not only expand the current understanding of sophorolipid biosynthesis in non-model *Starmerella* species but also provide a foundation for metabolic engineering strategies to enhance SL production for industrial applications.

Methodology:

1. Yeast strain and maintenance

The yeast strain *Starmerella riodocensis* GT-SL1R was isolated from honey collected in Ratchaburi province, Thailand, and identified based on ITS1 and ITS2 regions as reported by Alfian et al. (2022). The strain was preserved in 70% glycerol (v/v) in YPD broth and stored at $-20\text{ }^{\circ}\text{C}$. For working cultures, the strain was re-streaked on YPD agar plates and incubated at $30\text{ }^{\circ}\text{C}$ for 48 h.

2. Seed preparation and sophorolipid production

An active colony of *S. riodocensis* GT-SL1R was inoculated into 50 mL of YPD broth and incubated at $30\text{ }^{\circ}\text{C}$ with shaking at 150 rpm for 24 h. The cells were harvested by centrifugation at $4,000 \times g$ for 10 min, washed twice with sterile deionized (DI) water, and resuspended in sterile DI water. Cell density was adjusted to OD_{600} for inoculation. A 10% (v/v) seed inoculum was transferred into 50 mL of sophorolipid (SL) production medium containing 10% (w/v) glucose (total carbon content 40% w/w), 10% (v/v) palm oil (Gaysorn brand™, Thailand; total carbon content 50% w/v), 0.1% (w/v) KH_2PO_4 , 0.1% (w/v) K_2HPO_4 , 0.05% (w/v) $\text{MgSO}_4 \cdot 7\text{H}_2\text{O}$, 0.01% (w/v) $\text{CaCl}_2 \cdot 2\text{H}_2\text{O}$, and 0.01% (w/v) NaCl, with an initial pH of 4.5. To adjust the carbon-to-nitrogen (C/N) ratio, yeast extract (Gibco™, USA; total nitrogen content 10% w/w) was supplemented at 3.6% (w/v) for a C/N ratio of 25, or at 0.9% (w/v) for a C/N ratio of 100. Cultivation was carried out at $30\text{ }^{\circ}\text{C}$ with shaking at 150 rpm for 7 days. For the adjusted C/N ratios, the carbon sources were fixed, and the nitrogen source was varied by modifying the yeast extract concentration, as shown in the formulation below:

$$\text{C to N ratio} = \frac{\text{Total carbon content}}{\text{Total nitrogen content}}$$

3. Sophorolipid extraction and analysis

At the end of cultivation, yeast cells were separated from the culture broth by centrifugation. The culture broth was then extracted twice with ethyl acetate at a 1:2 (v/v) ratio. The phases were separated using a separatory funnel, and the upper phase containing SL and ethyl acetate was collected. The solvent was evaporated to obtain crude SL, which were subsequently weighed. SL production was calculated as the total weight of crude SL (g) divided by the cultivation volume (L). For cell dry weight (CDW) measurement, yeast cells were washed twice with sterile DI water and dried overnight in a hot air oven. CDW was calculated as dried cell mass (g) divided by cultivation volume (L).

4. Gene expression analysis

The yeast strain *S. riodocensis* GT-SL1R was cultured in SL medium under two different C/N ratios (25 and 100) for 24 h. The optical density of the cells was measured and adjusted to 0.1 at OD_{600} nm for the initial inoculum. Total RNA was extracted using the chloroform–methanol method and purified with the RNeasy Mini Kit (QIAGEN, Hilden, Germany). cDNA was synthesized from purified RNA using the qPCRBIO cDNA Synthesis Kit (PCRBIO SYSTEMS, UK). qRT-PCR experiments were performed using a real-time PCR detection system with the corresponding analytical software. Reaction mixtures contained Universal qPCR Master Mix (NEB). The *ACT1N1* gene was used as the internal reference to analyze the relative fold change in the transcription of target genes in this yeast strain. Relative expression levels were determined using the $2^{-\Delta\Delta\text{Ct}}$ method with gene-specific oligonucleotides, including *CYP52M1*, *UgtA1*, *UgtB1*, *At*, and *Sble*.

5. Transcriptomics analysis

RNA from *S. riodocensis* GT-SL1R grown under different C/N ratios (25 and 100) was sent to Biomarker Technologies (Beijing, China) for transcriptomic analysis. cDNA libraries were prepared and sequenced on an Illumina NovaSeq 6000 platform (PE150). Clean reads were processed using FastQC and Trimmomatic, then aligned to the *S. bombicola* ATCC 22214T reference genome with HISAT2. Gene counts were obtained with featureCounts, and differential expression analysis was performed in R using DESeq2. Genes with $\text{padj} < 0.05$ and $|\log_2\text{FC}| > 1$ were considered differentially expressed. Functional enrichment of DEGs was assessed using Gene Ontology (GO) and KEGG pathway analysis with clusterProfiler.

6. Statistic analysis

Statistical analysis was performed using the SPSS statistical package version 25.0 (IBM SPSS Inc., New York, NY, USA). The data were analysed using a one-way analysis of variance (ANOVA) followed by Tukey's test to calculate significant differences in treatment means. The least significant difference ($p < 0.05$) was considered statistically significant.

Results and Discussion:

The cultivation of *S. riodocensis* GT-SL1R in SL production medium under different C/N ratios, namely 25 (low C/N ratio) and 100 (high C/N ratio), revealed clear differences in SL production after 7 days of fermentation. Yeast grown at a C/N ratio of 100 produced 26 g/L of SL, which was significantly higher than the 18 g/L obtained at a C/N ratio of 25. These results indicate that a higher C/N ratio promotes SL production (**Figure 1**). However, in terms of cell dry weight (CDW), yeast cultivated at the higher C/N ratio (100) exhibited a significantly lower CDW compared to those grown at the lower C/N ratio (25) (**Figure 2**).

This finding is consistent with the gene expression analysis performed under the same cultivation condition, where the transcription levels of five key SL biosynthetic genes *CYP52M1*, *UgtA1*, *UgtB1*, *At*, and *Sble* were markedly upregulated under the C/N ratio of 100 compared to the low C/N ratio condition (**Figure 3**). To better understand how *S. riodocensis* GT-SL1R produced SL, we performed a comparative transcriptomic analysis under two conditions: nitrogen-limited (high C/N ratio of 100, which promotes SL production) and nitrogen-sufficient (low C/N ratio of 25). The results showed a clear metabolic switch. In total, 500 genes were significantly upregulated, and 550 genes were downregulated under nitrogen-limited (High C/N ratio) conditions (**Figure 4**).

This indicates that the yeast reprogrammed its metabolism—reducing growth-related processes and instead redirecting energy and resources into SL production to store excess carbon. Many genes involved in the cell cycle, DNA replication, and chromosome segregation were downregulated. Key regulators of the cell cycle such as cyclins and kinases (*NIM1*, *CDC5*) also showed strong repression. Structural genes and septins protein (*CDC3*, *CDC10*) were suppressed, suggesting that cell division had nearly stopped. Ribosomal protein genes and glycolysis genes were also downregulated. Even ergosterol biosynthesis genes were reduced, likely redirecting acetyl-CoA away from membrane synthesis toward fatty acid production for SL biosynthesis. Key enzymes such as *CYP52M1*, *UgtA1*, *UgtB1*, and *At* were highly expressed. A lactone esterase (*SBLE*) was also upregulated, suggesting enhanced modification of fatty acid precursors.

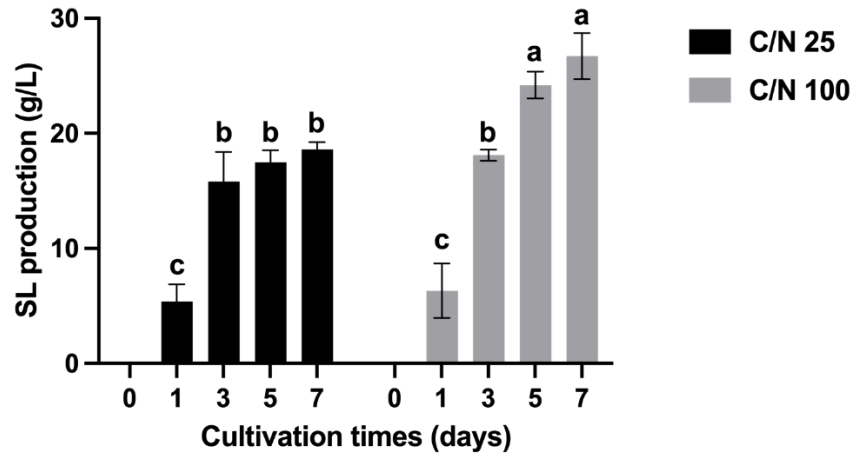


Figure 1.

Sophorolipid production by *S. riidocensis* GT-SL1R under different C/N ratios: 25 (black) and 100 (grey) for 7 days. The X-axis represents cultivation time (days), and the Y-axis represents SL production (g/L).

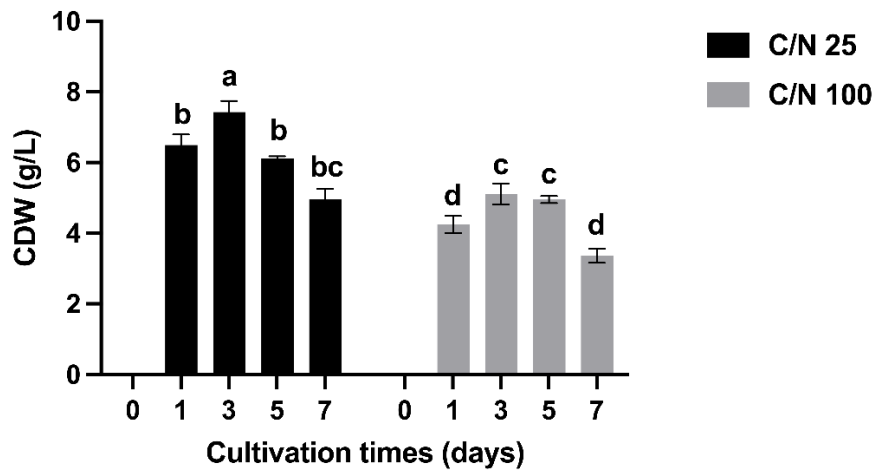


Figure 2.

Cell dried weight by *S. riidocensis* GT-SL1R under different C/N ratios: 25 (black) and 100 (grey) for 7 days. The X-axis represents cultivation time (days), and the Y-axis represents CDW (g/L).

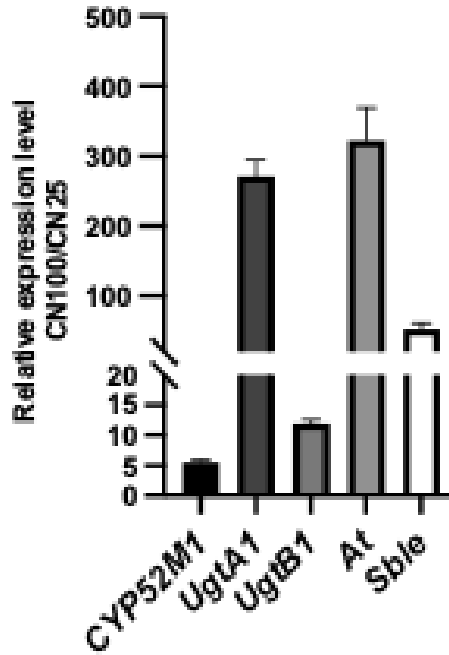


Figure 3.

The effect of C to N ratio on relative genes expression in SLs biosynthesis from *S. riodesensis* GT-SL1R of C to N 100/ C to N 25.

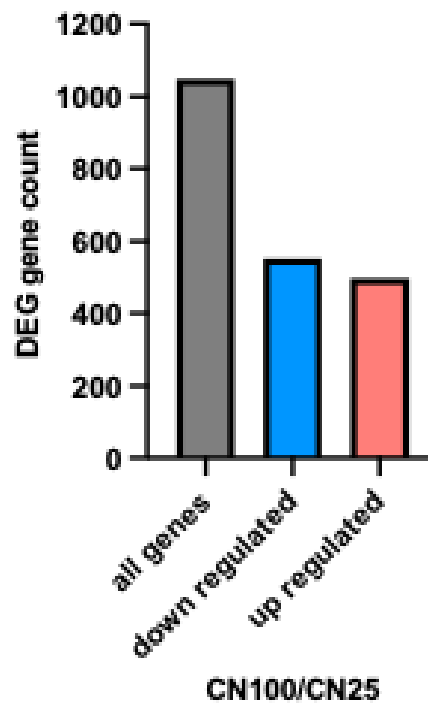


Figure 4.

Number of genes from DEGs analysis

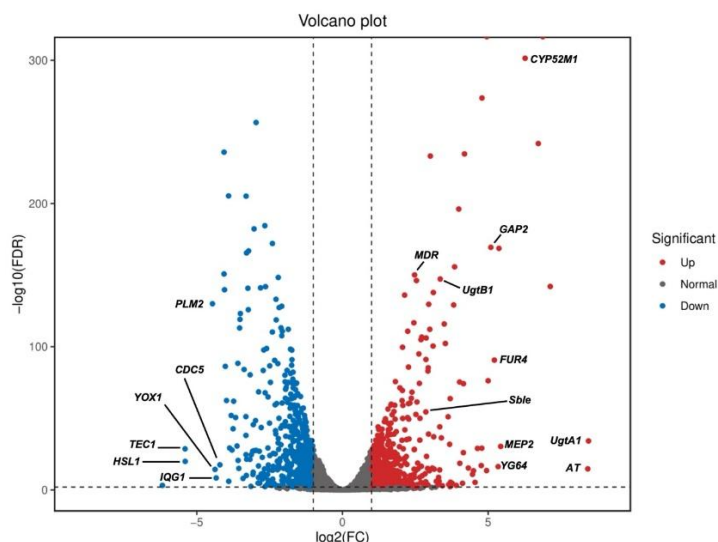


Figure 5.

Transcriptomic comparison between high C/N ratio (100) and low C/N ratio (25). Red, grey, and blue spots represent upregulated, unchanged, and downregulated genes, respectively.

Additionally, the SL transporter gene *SLMDR* (ABC transporter) showed higher expression, indicating active export of SLs from the cell. The yeast increased the expression of genes involved in nitrogen uptake and recycling, such as the ammonium transporter, amino acid permeases, and enzymes like amidase and arginase. Multiple transporters from the MFS and ABC families were also upregulated, likely to manage metabolic stress and export compounds. Genes related to energy production were upregulated, reflecting the high energy demand of SL synthesis (**Figure 5**).

These findings highlight a well-known trade-off in oleaginous yeasts: nutrient limitation, particularly nitrogen restriction, shifts metabolism away from growth and toward the biosynthesis of storage or secondary metabolites (Papanikolaou & Aggelis, 2011; Li et al., 2016). Our transcriptomic analysis further confirmed this metabolic switch. Under nitrogen-limited conditions (C/N = 100), genes associated with cell cycle progression, DNA replication, and ribosome biogenesis were markedly downregulated. This repression, including cyclins (*CCN1*, *PCL1*) and microtubule components (*TUB1*, *TUB2*), suggests that cell division was actively suppressed. Such downregulation is a typical response of yeasts under nutrient stress, where growth-related processes are curtailed to conserve energy (Brauer et al., 2008). Conversely, genes essential for SL biosynthesis were strongly upregulated, confirming that nitrogen limitation promotes the channeling of carbon flux into sophorolipid pathways. These results are in agreement with studies in *Starmerella bombicola*, where nitrogen-limited conditions triggered strong induction of SL biosynthetic genes and elevated SL titers (Van Bogaert et al., 2009; Roelants et al., 2016).

Furthermore, the upregulation of the SL transporter gene (*SLMDR*) suggests that enhanced efflux capacity may facilitate secretion and prevent intracellular accumulation, a mechanism similarly reported in *S. bombicola* (Van Bogaert et al., 2013). Interestingly, we also observed that ergosterol biosynthesis genes were suppressed under high C/N conditions, which may redirect acetyl-CoA from membrane sterol production toward fatty acid synthesis, thereby supporting SL biosynthesis. This metabolic rerouting of acetyl-CoA has also been described in lipid-accumulating yeasts such as *Yarrowia lipolytica* (Beopoulos et al., 2009). Additionally, upregulation of nitrogen uptake and recycling genes (e.g., *MEP2*, *GAP2*, *DUR3*) indicates an adaptive response to scavenge limited nitrogen sources, similar to nitrogen catabolite repression relief observed in *Saccharomyces cerevisiae* (Magasanik &



Kaiser, 2002). Taken together, our data demonstrated that *S. riodocensis* GT-SL1R undergoes a global metabolic reprogramming in response to nitrogen limitation, where growth is suppressed while carbon flux and energy are redirected toward sphingolipid biosynthesis. This strategy reflects an evolutionary adaptation of *Starmerella* species to nutrient-fluctuating environments and provides a foundation for metabolic engineering to further enhance SL productivity.

The observed increase in SL production at a high C/N ratio can be attributed to the metabolic reallocation that occurs under nitrogen deficiency. When nitrogen is abundant, yeast cells preferentially channel carbon flux into biomass accumulation, protein synthesis, and cell division. However, under nitrogen-limited conditions, these growth-related processes are repressed, as evidenced by the strong downregulation of genes involved in DNA replication, ribosome biogenesis, and cytoskeletal organization. This metabolic downshift frees up both carbon and reducing equivalents, which are then redirected into lipid-related pathways, including SL biosynthesis. In this way, the yeast effectively uses SL as a strategy to balance intracellular carbon overflow, converting excess carbon into extracellular glycolipids rather than continuing to proliferate. This shift explains why a high C/N ratio leads to nearly a two-fold increase in SL production despite reduced cell dry weight (Papanikolaou & Aggelis, 2011; Li et al., 2016).

Mechanistically, nitrogen deficiency also acts as a cellular stress signal that reprograms global gene expression to favor survival under nutrient limitation. Previous studies in model yeasts such as *Saccharomyces cerevisiae* have shown that nitrogen starvation activates stress-response transcription factors and signaling pathways, including TOR (Target of Rapamycin) downregulation, which suppresses growth-related processes and induces autophagy, amino acid recycling, and secondary metabolite synthesis (Brauer et al., 2008; Conrad et al., 2014). Consistent with this, our transcriptomic data revealed upregulation of genes involved in nitrogen scavenging (e.g., ammonium transporters and amino acid permeases) as well as transporters from the MFS and ABC families, which likely mitigate metabolic stress by exporting excess metabolites. At the same time, the strong induction of SL biosynthetic genes (*CYP52M1*, *UgtA1*, *UgtB1*, *At*, *Sble*) and the SL efflux transporter SLMDR suggests that nitrogen deficiency does not merely suppress growth but actively redirects metabolism toward SL synthesis and secretion (Van Bogaert et al., 2007; Roelants et al., 2019). Thus, the combination of metabolic rerouting, stress-responsive regulation, and enhanced transport capacity provides a mechanistic explanation for why a higher C/N ratio substantially enhances SL production in *S. riodocensis*.

Conclusion:

The results demonstrate that *S. riodocensis* GT-SL1R responded to nitrogen limitation (high C/N ratio) by markedly increasing SL production at the expense of cell growth. Cultivation at a C/N ratio of 100 yielded significantly higher SL levels compared to a C/N ratio of 25, despite reduced biomass. Transcriptomic analysis confirmed this metabolic shift, with strong repression of genes associated with cell cycle progression, ribosome biogenesis, and ergosterol synthesis, alongside pronounced upregulation of key SL biosynthetic genes, transporters, and nitrogen acquisition pathways. Collectively, these findings indicate that *S. riodocensis* undergoes a global reprogramming of cellular metabolism under nitrogen-limited conditions, redirecting resources from growth toward secondary metabolite production. This metabolic adaptation highlights the potential of nutrient manipulation as a strategy to enhance SL biosynthesis for industrial applications.



Acknowledgements:

This research project was supported by King Mongkut's University of Technology Thonburi (KMUTT), Thailand Science Research and Innovation (TSRI), and National Science, Research and Innovation Fund (NSRF) Fiscal year 2025 to N.S., Excellent Research Laboratory for Yeast Innovation of Fiscal Year 2023 (No. 6620864), KMUTT to N.S., as well as Petchre Pra Jom Klao Scholarship, King Mongkut's University of Technology Thonburi to S.S.

References:

1. Alfian, A. R., Watchaputi, K., Sooklim, C., & Soontorngun, N. (2022). Production of new antimicrobial palm oil-derived sophorolipids by the yeast *Starmerella riodocensis* sp. nov. against *Candida albicans* hyphal and biofilm formation. *Microbial Cell Factories*, 21(1), 163.
2. Beopoulos, A., Chardot, T., & Nicaud, J. M. (2009). *Yarrowia lipolytica*: A model and a tool to understand the mechanisms implicated in lipid accumulation. *Biochimie*, 91(6), 692-696.
3. Brauer, M. J., Huttenhower, C., Airoidi, E. M., Rosenstein, R., Matese, J. C., Gresham, D. & Botstein, D. (2008). Coordination of growth rate, cell cycle, stress response, and metabolic activity in yeast. *Molecular biology of the cell*, 19(1), 352-367.
4. Conrad, M., Schothorst, J., Kankipati, H. N., Van Zeebroeck, G., Rubio-Teixeira, M., & Thevelein, J. M. (2014). Nutrient sensing and signaling in the yeast *Saccharomyces cerevisiae*. *FEMS Microbiology Reviews*, 38(2), 254–299.
5. Intasit, R., & Soontorngun, N. (2023). Enhanced palm oil-derived sophorolipid production from yeast to generate biodegradable plastic precursors. *Industrial Crops and Products*, 192, 116091.
6. Kolouchová, I., Mařátková, O., Sigler, K., Masák, J., & Řezanka, T. (2016). Lipid accumulation by oleaginous and non-oleaginous yeast strains in nitrogen and phosphate limitation. *Folia microbiologica*, 61(5), 431-438.
7. Magasanik, B., & Kaiser, C. A. (2002). Nitrogen regulation in *Saccharomyces cerevisiae*. *Gene*, 290(1-2), 1-18.
8. Papanikolaou, S., & Aggelis, G. (2011). Lipids of oleaginous yeasts. Part I: Biochemistry of single cell oil production. *European Journal of Lipid Science and Technology*, 113(8), 1031-1051.
9. Roelants, S., Solaiman, D. K., Ashby, R. D., Lodens, S., Van Renterghem, L., & Soetaert, W. (2019). Production and applications of sophorolipids. *Biobased surfactants*, 65-119.
10. Taowkrue, E., Songdech, P., Maneerat, S., & Soontorngun, N. (2024). Enhanced production of yeast biosurfactant sophorolipids using yeast extract or the alternative nitrogen source soybean meal. *Industrial Crops and Products*, 210, 118089.
11. Van Bogaert, I. N., Saerens, K., De Muynck, C., Develter, D., Soetaert, W., & Vandamme, E. J. (2007). Microbial production and application of sophorolipids. *Applied microbiology and biotechnology*, 76(1), 23-34.

IMPACT OF HETEROLOGOUS *Beta Carotene Ketolase (bkt)* GENE EXPRESSION FROM *Haematococcus pluvialis* IN *Synechocystis* sp. PCC 6803 ON CAROTENOID PRODUCTION UNDER SALT STRESS

Benjamat Sukkokee,¹ Saowarath Jantaro,^{1*}

¹Laboratory of Cyanobacterial Biotechnology, Department of Biochemistry, Faculty of Science, Chulalongkorn University, Bangkok 10330, Thailand

* e-mail: saowarath.j@chula.ac.th

Abstract:

Synechocystis sp. PCC 6803 is a model cyanobacterium extensively studied for its photosynthetic capacity and potential in the sustainable bioproduction of high-value compounds, herein carotenoids. Among these, ketocarotenoids are particularly valuable due to their potent antioxidant properties. However, *Synechocystis* sp. PCC 6803 naturally produces only limited types of carotenoids and lacks an efficient pathway for the biosynthesis of high value ketocarotenoids. In this study, we explored strategies to improve carotenoid biosynthesis via heterologous expression of the β -carotene ketolase gene (*bkt*) from *Haematococcus pluvialis* (or OX_BKT) in *Synechocystis* sp. PCC 6803. All strains were cultured in BG₁₁ medium containing 0.25%, 1%, and 2% (w/v) NaCl. Unknown peaks that were undetectable in WTc were found in certain HPLC chromatograms of the OX_BKT strain at 1% and 2% NaCl. It is considered that the peaks are either new carotenoid species or free astaxanthin. In addition, exposure to high NaCl concentrations altered the carotenoid profile in both WTc and OX_BKT; myxoxanthophyll and zeaxanthin contents decreased, whereas β -carotene and chlorophyll *a* contents increased. These findings suggest that salt stress may change carotenoid metabolism and pigment composition and also induce the *bkt* gene expression to produce new carotenoid products in *Synechocystis* sp. PCC 6803.

Introduction:

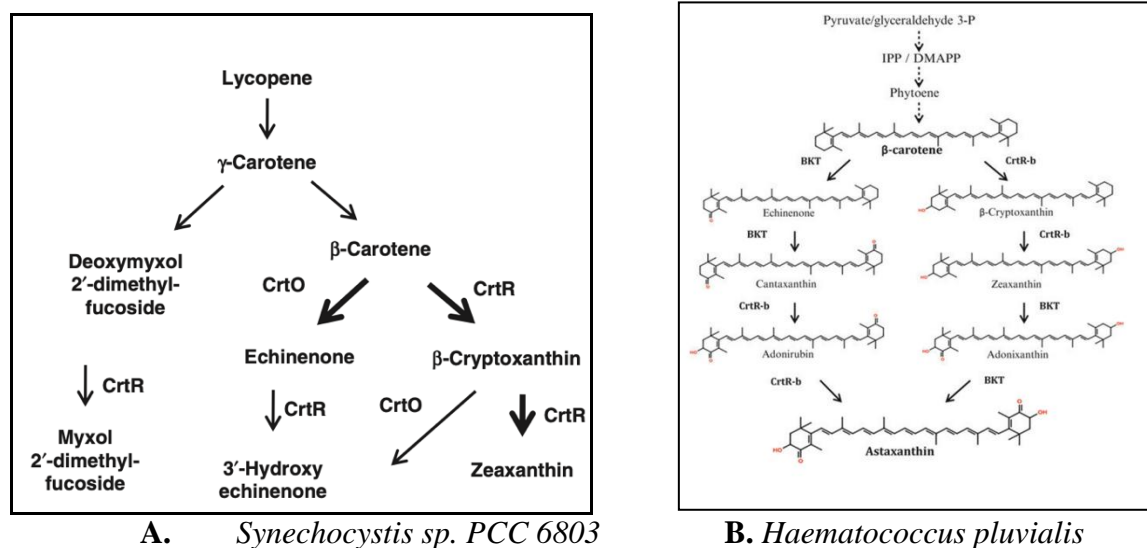


Figure 1.

Carotenoid biosynthetic pathway in (A) *Synechocystis* sp. PCC 6803 (Makino *et al.* (2008)) and (B) *Haematococcus pluvialis* (Henrriquez *et al.* (2016)).

Carotenoids are accessory pigments that play critical roles in photosynthesis and photoprotection, as well as serving as precursors for various bioactive compounds. Two classes of carotenoids including carotenes and xanthophylls are potentially applied in broader applications. Among these, ketocarotenoids, which contain a ketone group in the carotenoid molecule, like echinenone, canthaxanthin or astaxanthin, are particularly valuable carotenoids known for its potent antioxidant properties and wide-ranging applications in the food, cosmetic, and pharmaceutical industries.

In recent years, *Synechocystis* sp. PCC 6803, a model cyanobacterium, has gained attention as a potential alternative for the sustainable production of valuable bioproducts. This organism offers several advantages due to its rapid growth, ability to utilize CO₂, and established genetic manipulation techniques. The native carotenoid biosynthetic pathway in *Synechocystis* sp. PCC 6803 involves several key intermediates that can be further converted into various ketocarotenoids. However, *Synechocystis* sp. PCC 6803 naturally produces only a limited type of carotenoids and lacks an efficient pathway for the biosynthesis of high value ketocarotenoids. The native β -carotene ketolase (encoded by *crtO* gene) catalyzes the conversion of β -carotene to echinenone but shows limited activity toward further ketolation steps and produces the 3'-hydroxyechinenone as the final ketocarotenoid product via a conversion from echinenone by β -carotene hydroxylase (encoded by the *crtR* gene). In contrast, comparing carotenoid synthesis in *Haematococcus pluvialis*, the beta-carotene ketolase (*bkt*) can convert zeaxanthin into astaxanthin by adding keto groups. Additionally, it can catalyze the transformation of beta-carotene into canthaxanthin, which serves as an intermediate that can be further converted into astaxanthin through the action of beta-carotene hydroxylase (Figure 1). Therefore, to improve carotenoid synthesis, we created *Synechocystis* sp. PCC 6803 expressing the heterologous *bkt* gene from *Haematococcus pluvialis* (*OX_BKT*) in order to investigate the potential of this strain as a host.

Methodology:

1. Construction of the recombinant plasmid

For the heterologous *bkt* gene from *Haematococcus pluvialis*, the gene sequence was obtained from NCBI database (GU143690.1). Restriction enzyme recognition sequences were added to the 5' and 3' ends of the gene sequence and the *bkt* gene fragment was synthesized by a commercial gene synthesis service (U2Bio (Thailand) Co., Ltd., Bangkok, Thailand). Before ligation, the *bkt* gene fragment was amplified by PCR. Next, the amplified gene fragment and the pEERM vector were digested with specific restriction enzymes and ligated using T4 DNA ligase. The reaction mixture was incubated at 4°C for 16-18 hours. Following ligation, the recombinant plasmid was transformed into the competent *Escherichia coli* DH5 α cells using the heat shock method. Then, the transformants were spread on LB agar plates containing 30 μ g/mL chloramphenicol and incubated overnight at 37°C. After incubation, a single colony was selected from the LB agar plate and inoculated into 3 mL of LB medium for 16-18 hours at 37°C with shaking. Following incubation, the plasmid DNA was extracted using the Presto™ Mini Plasmid Kit (Geneaid Biotech Ltd., Taiwan). To determine the size of the recombinant plasmid, the samples were digested with restriction enzymes and analyzed by agarose gel electrophoresis.

2. Natural transformation into *Synechocystis* sp. PCC 6803 cells

Synechocystis sp. PCC 6803 cells were grown in BG₁₁ medium until the optical density (OD) at 730 nm of about 0.5. Then, the cell culture was harvested by centrifugation at 5,500 rpm, 25°C for 10 minutes, and the cell pellet was resuspended in fresh BG₁₁ medium before aliquoting into a new tube. Subsequently, 10 μ L of recombinant plasmid was mixed with *Synechocystis* cell suspension, followed by incubation under white light with an



intensity of 40-50 $\mu\text{mol photons m}^{-2} \text{ s}^{-1}$ for 16-18 hours at 27-30°C. After incubation, the mixture was spread on a BG₁₁ agar plate containing 10 $\mu\text{g/mL}$ chloramphenicol. The plates were incubated until single colonies appeared. The transformants were transferred to a BG₁₁ agar plate containing up to 30 $\mu\text{g/mL}$ chloramphenicol. The transformants were confirmed for gene size, location, and segregation by PCR using specific primers, and the results were verified by agarose gel electrophoresis.

3. Growth culture and measurement of pigment content

3.1 Culture condition

Synechocystis sp. PCC 6803 wild type control (WTc) and OX_BKT strains were cultured in BG₁₁ medium containing various NaCl concentrations. The conditions included normal BG₁₁ without NaCl as the control (0%, w/v), and BG₁₁ supplemented with NaCl at 42.8 mM (0.25%, w/v), 171 mM (1%, w/v), and 342 mM (2%, w/v). The cultures were maintained at 27–30°C under continuous white light illumination with an intensity of 40-50 $\mu\text{mol photons m}^{-2} \text{ s}^{-1}$. Culture flask, with an initial optical density (OD) of approximately 0.2 at 730 nm, was placed on a rotary shaker at 160 rpm for 14 days. Cell growth was monitored spectrophotometrically by measuring the OD₇₃₀ every two days to construct the growth curve. The representative growth rates were calculated regarding the logarithmic (log) phase and transition from the lag to the logarithmic phase.

3.2 Determination of intracellular pigment content

One mL of cell culture was extracted by N,N-dimethylformamide (DMF) and resuspended to dissolve cell pellet and incubated in the dark for 10 minutes. After centrifugation to remove debris, the absorbance of supernatant was measured at 461, 625 and 664 nm, respectively. The contents of chlorophyll *a* and carotenoids were calculated according to following equations;

Chlorophyll *a* content ($\mu\text{g}/\text{OD}_{730}$) = $[(12.1 \times A_{664}) - (0.17 \times A_{625})] / \text{OD}_{730}$ (Moran, 1982)

Carotenoid content ($\mu\text{g}/\text{OD}_{730}$) = $[(A_{461} - (0.046 \times A_{664})) \times 4] / \text{OD}_{730}$ (Chamovitz *et al.*, 1993)

4. Quantitative analysis of carotenoids by HPLC

The *Synechocystis* cell cultures of both wild type (WTc) and OX_BKT strains were harvested by centrifugation at 5,500 rpm for 10 minutes. Before starting solvent extraction, the cell suspension was concentrated to an OD₇₃₀ of approximately 1. Then cell culture 2 mL was centrifuged, after that supernatant was discarded, and the remaining pellets were extracted with 1 mL of absolute methanol for 10 minutes. Following centrifugation at 10,000 rpm for 5 minutes, the supernatant was collected and filtered through a 0.45 μm . polypropylene membrane filter

Pigment extracts were analyzed by high-performance liquid chromatography (HPLC) using a reverse-phase C18 column with the UV–vis detector at 440 nm. The solvent system consisted of a gradient of mobile phase A (acetonitrile:water = 9:1) to mobile phase B (ethyl acetate) at a flow rate of 1 mL/ minutes. After elution, the retention times and spectra were analyzed and confirmed the identity of all peaks (Liang *et al.*, 2023). Carotenoid content was calculated following equation from Lagarde and Vermaas (1999);

$$C_{\text{car}} = C_{\text{chl}} \times [(\epsilon_{\text{chl}} \times A_{\text{car}}) / (\epsilon_{\text{car}} \times A_{\text{chl}})]$$

Where C_{chl} = the chlorophyll concentration in the pigments extracts determined by the extinction coefficient of chlorophyll *a*, ϵ_{chl} , and ϵ_{car} = the specific extinction coefficients of the chlorophyll *a* and the carotenoids obtained from Mantoura and Llewellyn (1983).

Results and Discussion:

To evaluate the growth rate of wild type control (WTc) and the overexpressing strain (OX_BKT), *Synechocystis* cells were cultured in BG₁₁ medium containing various NaCl concentrations. During days 6 to 10 (log phase) in Figure 2A, the result revealed that under normal BG₁₁ condition (0% NaCl), OX_BKT showed a comparable growth rate (0.153 ± 0.005) to WTc (0.129 ± 0.010). However, when NaCl was added at 0.25% and 1% concentrations, the growth rate of OX_BKT was insignificantly higher than WTc by approximately 5% and 4%, respectively. Unexpectedly, at 2% NaCl condition, the growth rate of OX_BKT (0.148 ± 0.015) demonstrated the insignificant decrease, which became lower than WTc (0.160 ± 0.005).

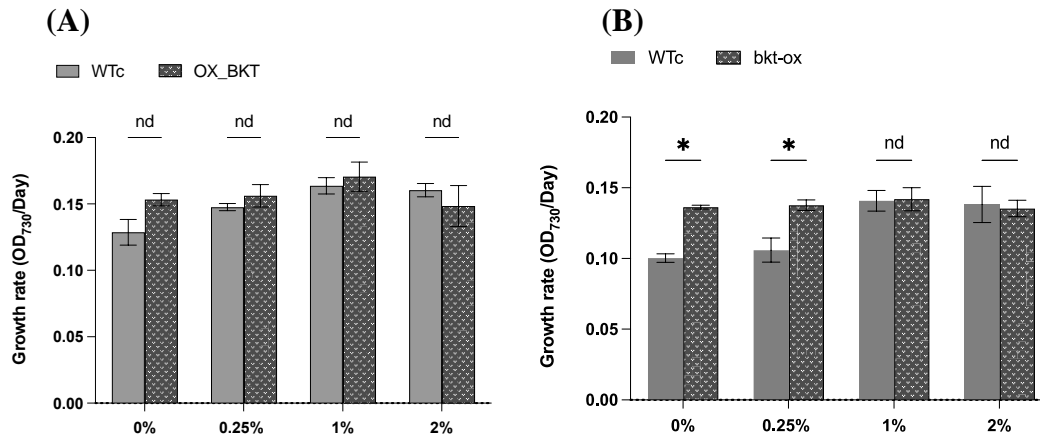


Figure 2.

Growth rates of WTc and OX_BKT strains during (A) log phase (day 6 to day 10) and (B) adaptation from lag to log phase (day 4 to day 8) under various NaCl conditions. Data represent mean \pm SD ($n=3$). Statistical analysis was performed using multiple t -test of the statistical difference of the data between the values of WTc and the engineered strain indicated by an asterisk at $*p < 0.05$, “nd” means no significant difference.

On the other hand, in Figure 2B, the growth rate from day 4 to day 8, representing the adaptation from lag to log phase, OX_BKT showed a higher growth rate than WTc under normal BG₁₁ (0%) and 0.25% NaCl conditions by 35.91% and 29.98%, respectively. However, at 1% and 2% NaCl conditions, the growth rate of OX_BKT was comparable with the WTc. These results indicate that the heterologous expression of beta-carotene ketolase gene from *Haematococcus pluvialis* apparently enhanced cell growth rate during the adaptation from the lag to the log phase under normal condition and salt stress, particularly at 0.25% NaCl condition. This may be considerably explained by the role of carotenoids in protecting cells from oxidative stress generated by salinity. Carotenoids can stabilize membranes and scavenge reactive oxygen species (Widomska et al., 2019), thereby supporting better growth performance. Consistent with studies in sweet potato, it has been demonstrated that the accumulation of carotenoids, particularly β -carotene, reduces reactive oxygen species (ROS) and H₂O₂ levels under salt stress and enhances stress tolerance (Kim et al., 2012).

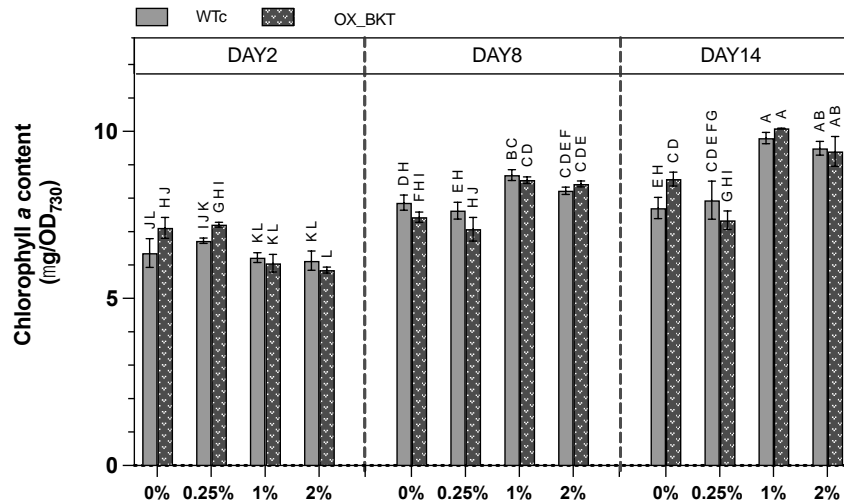


Figure 3.

Total chlorophyll *a* contents of WTc and OX_BKT strains under various NaCl conditions during the lag phase (Day 2), logarithmic phase (Day 8), and late logarithmic phase (Day 14). Data represent mean \pm SD ($n=3$). Statistical analysis was performed using two-way ANOVA followed by Tukey's multiple comparisons test of the statistical difference of the data across the various media. Bars labeled with different letters indicate statistically significant differences ($p < 0.05$) and sharing at least one letter are not significantly different.

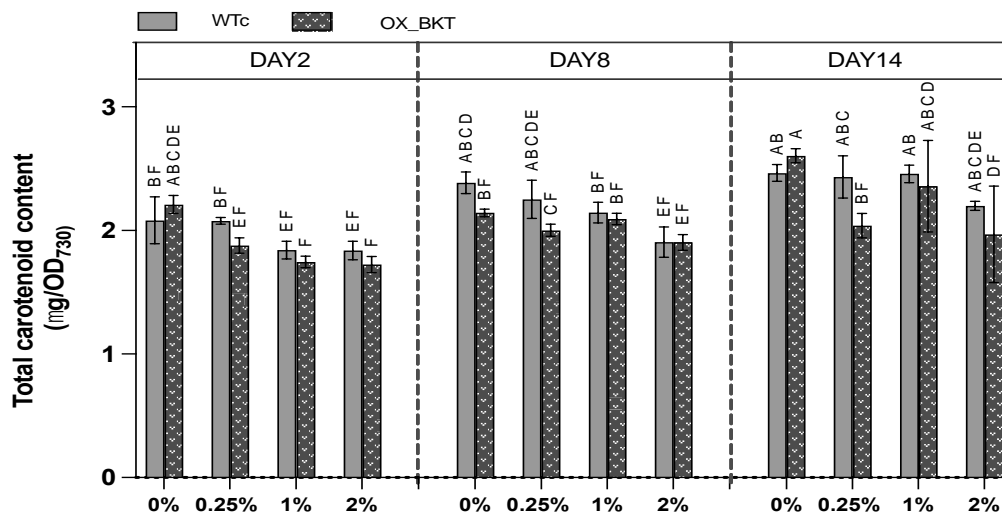


Figure 4.

Total carotenoid contents of WTc and OX_BKT strains under various NaCl conditions during the lag phase (Day 2), logarithmic phase (Day 8), and late logarithmic phase (Day 14). Data represent mean \pm SD ($n=3$). Statistical analysis was performed using two-way ANOVA followed by Tukey's multiple comparisons test of the statistical difference of the data across the various media. Bars labeled with different letters indicate statistically significant differences ($p < 0.05$) and sharing at least one letter are not significantly different.

For the total content of major pigments (Figures 3 and 4), during the lag phase (Day 2), both wild type (WTc) and the engineered strain (OX_BKT) showed similar levels of total carotenoids and chlorophyll *a* under all NaCl conditions. When the cultures entered the logarithmic phase (Day 8) and late logarithmic phase (Day 14), it was found that

chlorophyll *a* contents were increased under salt stress, particularly at 1–2% NaCl conditions in comparison with those at the lag phase (Day 2) (Figure 3). At 1% NaCl treatment, both strains had the highest chlorophyll *a* content, with WTc increasing by 27% and OX_BKT by 17%, compared to the normal medium BG₁₁ condition. In contrast, the total carotenoid content of OX_BKT was decreased with increasing NaCl concentration in the medium. For the wild type strain, carotenoid levels remained relatively stable under 0%, 0.25%, and 1% NaCl conditions but exhibited a decrease under the 2% NaCl condition (Figure 4). Moreover, under all NaCl conditions, OX_BKT consistently contained lower levels of total carotenoids than WTc, in particular at 0.25% NaCl condition. In contrast, previous studies have shown that overexpression of *bkt* gene in *Chlamydomonas reinhardtii* significantly increased total carotenoid content by 2.13–2.20 times (Chen et al., 2023).

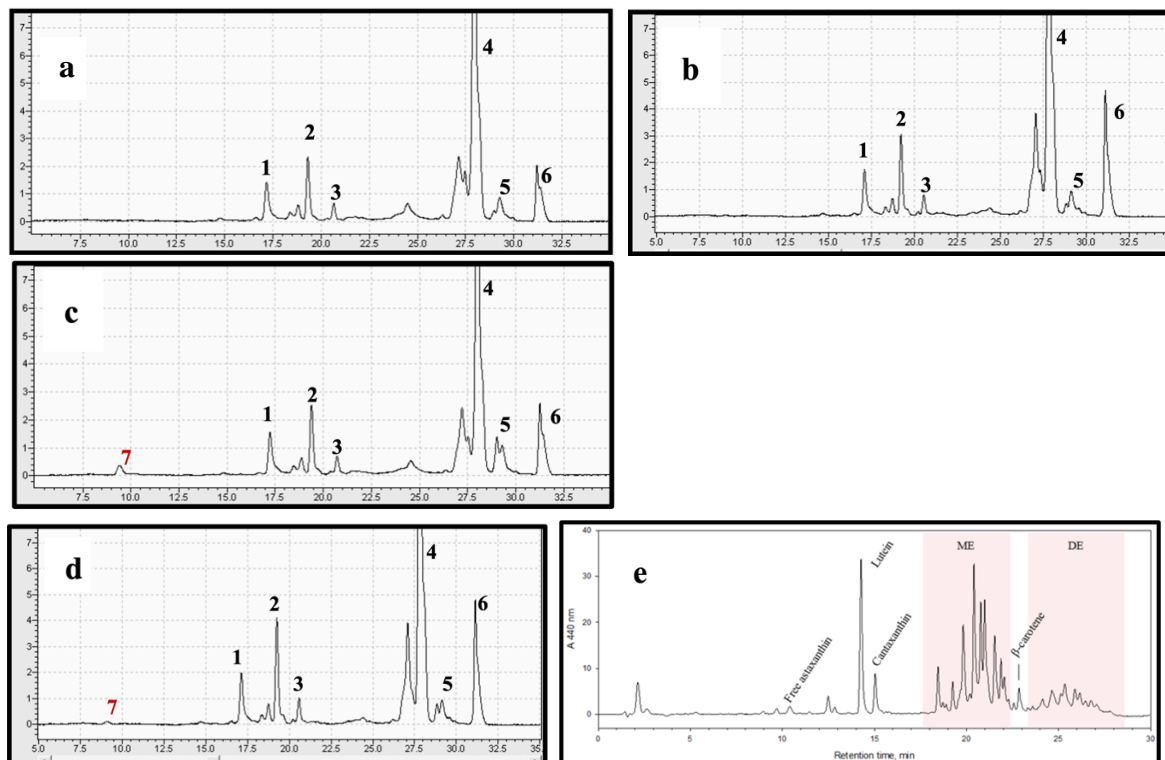


Figure 5.

HPLC chromatogram of carotenoid profiles. (a.) WTc at 1% NaCl, (b.) WTc at 2% NaCl, (c.) OX_BKT at 1% NaCl (d.) OX_BKT at 2% NaCl (e.) a HPLC chromatogram of *Haematococcus pluvialis* carotenoid extracts obtained from Jurčáková et al. (2023).

Abbreviation: ME, monoester astaxanthin; DE, dinoester astaxanthin.

HPLC chromatogram analysis revealed that both wild type (WT) and OX_BKT strains exhibited the same major carotenoid peaks at identical retention times, including peak 1 (myxoxanthophyll), peak 2 (zeaxanthin), peak 3 (3-hydroxyechinenone), peak 4 (chlorophyll *a*), peak 5 (echinenone), and peak 6 (β -carotene). However, under elevated salt stress conditions (1% and 2% w/v NaCl concentrations), an additional peak (peak 7) was detected in the OX_BKT strain, but it was not found in the WTc. In Figure 5e, the free astaxanthin peak was found around 11 minutes of retention time (Jurčáková et al., 2023). Similarly, carotenoid profiling in cyanobacteria has demonstrated that astaxanthin peaks generally appear before other carotenoids due to its higher polarity (Pniewski, 2020). It is worthy to note that the unidentified peak (peak 7) detected only in the OX_BKT strain also appeared at an early retention time. Although it remained unclear, the peak no.7 in the

OX_BKT strain was speculated to be free astaxanthin or a new carotenoid type, in particular induced by NaCl stress, in comparison with the WTc, due to the earlier retention time of the higher polarity of carotenoids. Previous studies suggested that successful astaxanthin biosynthesis requires the combined introduction of both heterologous β -carotene ketolase (*bkt*) and β -carotene hydroxylase genes from *H. pluvialis* (Liang et al., 2023). Despite this limitation, the appearance of an unidentified carotenoid peak in the OX_BKT strain suggested that heterologous *bkt* expression may potentially lead to the synthesis of new carotenoid species in *Synechocystis* sp. PCC 6803.

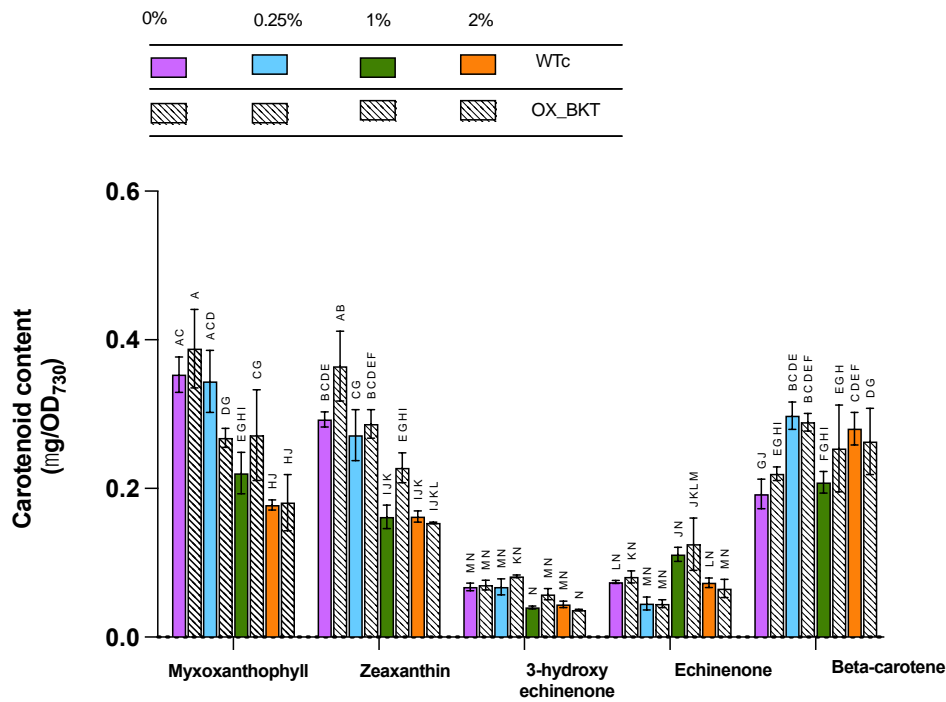


Figure 6.

Carotenoid contents in WTc and OX_BKT strains under different NaCl conditions. Data represent mean \pm SD ($n = 3$). Statistical analysis was performed using two-way ANOVA followed by Tukey's multiple comparisons test to determine significant differences between groups. Bars labeled with different letters indicate statistically significant differences ($p < 0.05$).

To investigate the carotenoid profiles of wild type (WTc) and OX_BKT strains, the contents of myxoxanthophyll and zeaxanthin were decreased with increasing NaCl concentration, while β -carotene and echinenone showed opposite trends (Figure 6). Specifically, β -carotene content was increased under salt stress and reached higher levels under 0.25% and 2% NaCl conditions in both WT and OX_BKT strains. These findings suggest that *Synechocystis* cells may attempt to maintain an overall carotenoid balance (Figure 4) by adjusting the proportions of carotenoid species (Figure 6), each of which could play a different role in salt stress. Our results indicate that salt stress can lead to a higher content of carotenoids in the carotene group, specifically β -carotene, compared to the xanthophyll group. This agrees with previous studies in microalgae, where moderate to high NaCl concentrations often promote β -carotene accumulation as a protective cell under oxidative stress (Wolf et al., 2021). Interestingly, echinenone showed the highest accumulation at 1% NaCl condition. Notably, at 1% NaCl condition, β -carotene content was lower compared to 0.25% and 2% NaCl conditions, while echinenone accumulation was at its



highest. This suggested that salt stress at 1% NaCl concentration may trigger the expression of both native and heterologous beta-carotene ketolase, which possibly catalyzes the conversion of beta-carotene into ketocarotenoids. Consequently, β -carotene was utilized as a substrate rather than stored, leading to enhanced echinenone production.

Conclusion:

This study demonstrated that heterologous expression of the β -carotene ketolase gene (*bkt*) from *Haematococcus pluvialis* in *Synechocystis* sp. PCC 6803 (OX_BKT) had influenced both growth rate and carotenoid accumulation under different NaCl conditions. OX_BKT showed the enhanced growth compared to WTc under normal and moderate salt stress. Chlorophyll *a* levels were increased under salt stress in both strains, whereas total carotenoid level in OX_BKT was decreased when increasing NaCl concentration. HPLC profiling confirmed the presence of native carotenoids in both strains, while an additional peak unique to OX_BKT under salt stress. This finding suggests that heterologous *bkt* expression may lead to the synthesis of novel carotenoid species. Furthermore, NaCl stress significantly altered carotenoid composition by reducing myxoxanthophyll and zeaxanthin while promoting β -carotene and echinenone accumulation, especially at 1% NaCl condition. Together, the heterologous *bkt* expression in *Synechocystis* sp. PCC 6803 not only affected the biosynthesis of carotenoid under salt stress, but it also served as a basis for further metabolic engineering projects that aim to produce high-value ketocarotenoids.

Acknowledgements:

This study was supported by the Development and Promotion of Science and Technology Talents Project, Thai government scholarship for financial support to Benjamat Sukkokee, and the Thailand Science Research and Innovation Fund Chulalongkorn University (BCG_FF_68_278_2300_070) to Saowarath Jantaro.

References:

1. Chamovitz D, Sandmann G, Hirschberg J. *J Biol Chem*. 1993;268(23):17348–17353.
2. Chen Y, Du H, Liang H, Hong T, Li T. *Int J Mol Sci*. 2023;24:11382.
3. Henríquez V, Escobar C, Galarza J, Gimpel J. Carotenoids in nature: biosynthesis, regulation and function. 2016;219–237.
4. Jurčáková Z, Ciglianová D, Mudroňová D, Tumová L, Bárcenas-Pérez D, Kopecký J, Hřčková G. *Antioxidants*. 2023;12(6):1144.
5. Kim SH, Ahn YO, Ahn MJ, Lee HS, Kwak SS. *Phytochemistry*. 2012;74:69–78.
6. Lagarde D, Vermaas W. *FEBS Lett*. 1999;454:247–251.
7. Liang H, Chen H, Liu X, Wang Z, Li P, Lu S. *Antioxidants*. 2023;12(10):1826.
8. Mantoura RFC, Llewellyn CA. *Anal Chim Acta*. 1983;151(2):297–314.
9. Makino T, Harada H, Ikenaga H, Matsuda S, Takaichi S, Shindo K, Sandmann G, Ogata T, Misawa N. *Plant Cell Physiol*. 2008;49:1867–1878.
10. Moran R. *Plant Physiol*. 1982;69(6):1376–1381
11. Pniewski F. *Biologia*. 2020;75(2):223–233.
12. Widomska J, Welc R, Gruszecki WI. *Biochim Biophys Acta Biomembr*. 2019;1861:845–851.
13. Wolf L, Cummings T, Müller K, Reppke M, Volkmar M, Weuster-Botz D. *Eng Life Sci*. 2021;21(3-4):115–125.4115–125.
14. Yazdani M, Tavakoli O. arXiv preprint arXiv:1911.11840. 2019.



COMPLETE GENOME INSIGHTS INTO A *bacillus cereus* GROUP ISOLATES FROM FOOD

Sawanya Potirungsee,¹ Phornphan Sornchuer,² Kritsakorn Saninjuk^{1,3,*}

¹ School of Science, Mae Fah Luang University, Chiang Rai, Thailand

² Microbiology and Immunology, Department of Preclinical Science, Faculty of Medicine, Thammasat University, Klongluang, Pathum Thani 12120, Thailand.

³ Microbial Products and Innovation Research Group, Mae Fah Luang University, Chiang Rai, Thailand

*e-mail: Kritsakorn.san@mfu.ac.th

Abstract:

Bacillus species are spore-forming, Gram-positive bacteria that are widely distributed in diverse ecological niches. The *B. cereus* group is particularly significant due to its implications for human health and food safety. Members of this group contaminate a variety of raw and processed foods and can survive heat treatments owing to the high resistance of their spores. *B. cereus* is an opportunistic pathogen capable of causing gastrointestinal illnesses, including diarrheal and emetic syndromes, as well as extra-intestinal infections. These conditions arise from the production of exotoxins such as hemolysin BL, non-hemolytic enterotoxin, and cytotoxin K, which are associated with diarrheal symptoms, and the emetic toxin cereulide, which induces nausea and vomiting. This clade exhibits notable medical and ecological diversity and is recognized for its resistance to multiple antibiotics, including β -lactam agents. Although tetracycline remains one of the most effective treatments, emerging resistance is increasingly reported. Furthermore, biofilm formation enhances persistence and virulence, posing challenges for both treatment and food safety. In this study, two *B. cereus* group isolates obtained from food in Thailand were subjected to whole-genome sequencing using Oxford Nanopore technology. Genomic analyses revealed features consistent with the *B. cereus sensu stricto* lineage. Comparative phylogenomic and average nucleotide identity (ANI) analyses positioned the isolates within the *B. cereus* clade, clustering closely with reference genomes such as *B. cereus* WPySW2 and AFA01. Both isolates harbored multiple virulence genes, including *nheA*, *nheB*, *nheC*, *entFM*, *cerA*, and *bceT*, indicating dual diarrheal and hemolytic pathogenic potential. These findings highlight the importance of understanding the pathogenicity, resistance mechanisms, and ecological adaptability of *B. cereus* for mitigating foodborne risks and informing public health interventions.

Introduction:

Bacillus species, which are spore-forming Gram-positive bacteria, are ubiquitous in nature as vegetative and spore cells. *B. cereus* group is a known human pathogen that can cause food poisoning that easily spreads to both raw and processed food such as rice, pasta, dairy products, vegetables, meat, and spices. This pathogen is capable of forming heat-resistant spores, allowing it to survive food processing and cooking conditions (1). Certain members of the *B. cereus* group are responsible for gastrointestinal illnesses including emetic and diarrheal types, as well as extra-intestinal infections, this can be severe in individuals with immunocompromised or ocular diseases. The *B. cereus* group, also referred to as *B. cereus sensu lato* (s.l), is composed of several closely related species as opportunistic pathogen towards extraintestinal infections, while *B. anthracis* is the causative agent of anthrax in humans and animals, and *B. thuringiensis* is widely applied as biopesticide, due to its insecticidal properties (2, 3). The group also compose with other species such as *B. mycoides* and *B. pseudomycoides*, which form rhizoidal colonies on agar media (3); *B. weihenstephanensis*, and *B. wiedmannii*, which are psychrotolerant (4-6); and *B. cytotoxicus*, noted for its thermotolerance. In addition, other members include *B. albus*, *B. bingmayongensis*, *B. fungorum*, *B. gaemokensis*, *B. luti*, *B. manliponensis*, *B. mobilis*, *B. nitratreducens*, *B. pacificus*, *B. paramycoides*, *B. paranthracis*, *B. proteolyticus*, *B. toyonensis*, and *B. tropicus*. Several more species have recently been classified within this group (7-9). Most foodborne illnesses are caused by cereulide, showing symptoms like nausea or vomiting within 15 minutes to 6 hours after ingesting contaminated food (10). Research suggests that cereulide activates 5-HT₃ serotonin receptors, which stimulate the vagus nerve and subsequently trigger the center of medulla oblongata causing vomit (11).

B. cereus shows resistance to many antibiotics like erythromycin, tetracycline, and streptomycin, which can arise from both genetic factors and environmental influences, but more often in β -lactam antimicrobial agents, including penicillin G, ampicillin, and cefotaxime, mainly because it produces β -lactamase enzymes. Tetracycline, a broad-spectrum antibiotic mostly effective against many *B. cereus*; however, cases of resistance have been documented in certain countries. In addition, biofilm formation further contributes to its pathogenic potential, as biofilms provide protection against antibiotic treatments and host immune defenses. This came from *B. cereus* secretion of damaging exotoxins such as hemolysins, phospholipases, pore-forming enterotoxins and emetic toxins. Among these, key pore-forming enterotoxins are hemolysin BL (HBL), non-hemolytic enterotoxin (NHE), and cytotoxinK (CytK) (12, 13). Hbl and Nhe are tripartite complexes (B, L1,L2) disrupt host cell membranes, which CytK is a single protein toxin capable of forming pores that lead to cell lysis, while enterotoxins are synthesized by vegetative cells that were introduced into the host cells or spores, within the small intestine causing abdominal cramps and watery diarrhea. Another tripartite complex (NheA, NheB, NheC), which forms pores in host cell membranes, induces cell death, and activates the NLRP3 inflammasome that leads to apoptosis (14). In contrast, the emetic toxin cereulide is a plasmid-encoded cyclic peptide that is pre-formed in contaminated food and induces vomiting after ingestion. *B. cereus* also produces degradative enzymes, most of which are regulated by the transcriptional activator PlcR (15). It functions as a quorum sensing system within *B. cereus*, this enables the bacterium to adjust to different environmental conditions. Two *B. cereus* group isolates from food were used in this experiment, and it is characterized by WGS using Oxford Nanopore sequencing, also the presence of genes related to virulence was observed in all isolates.



Methodology:

Bacterial strain and growth condition

Two *B. cereus* group isolates from foodstuff collected in 2018 in Pathum Thani province, Thailand, were performed in this study. The sampling procedure and microbiological analysis of the isolates were identified using both microbiological methods and API[®] 50 CHB/E Medium. The isolated bacteria were cultured on nutrient media and incubated at 35°C. The glycerol stocks of bacterial culture were stored at -80°C.

DNA extraction and Whole genome sequencing

The genomic DNA was isolated using Monarch HMW DNA Extraction Kits (NEB, Ipswich, MA, USA) according to the manufacturer's instructions and qualitatively characterized using a fluorometer. The DNA library preparation was performed using the Native Barcoding kit prior to sequencing on a flow cell (version R10.4.1/FLO-MIN114) using the MinION MK1c. Raw signals from the sequencer were base called using a superhigh accuracy model and demultiplexed using Guppy v.5.0.7 followed by adapter trimming using Porechop v.0.2.4. ONT raw reads were filtered with >1,000 bases in length using NanoFilt v.2.8.0. Quality control of filtered reads was checked by NanoPlot v.1.28.1. The sequence data was used for genome assembly using CANU v2.2. Taxonomic identification was performed using BTyper2 and GTDB-TK v1.5.1.

Genome annotation and circular map construction

The completeness and contamination levels were determined using CheckM v1.1.6. The assembled genomes were annotated using Rapid prokaryotic genome annotation (Prokka) with default parameters. The circular map for each genome was created using Genovi v0.4.3.

Whole-genome-based phylogenetic analysis and average nucleotide identity (ANI)

All complete genome sequences of the *B. cereus* group in complete genome level used in this study were obtained from the NCBI Genbank database. A maximum likelihood phylogenetic tree of xx strains was conducted using GToTree v1.8.3 with the hidden Markov model (HMM) source Firmicutes and default parameters. The resulting phylogeny was visualized using the web-based iTOL. Average nucleotide identities (ANI) based on BLAST alignment of whole-genome sequencing were calculated and visualized using pyANI v0.2.12.

Results and Discussion:

Whole genome sequencing and annotation were performed on two *Bacillus* isolates. Taxonomic classification using BTyper2 and GTDB-TK identified it as *B. cereus* based on average nucleotide differences and alignment fraction. The circular genome maps (Figure 1A and 1B) illustrate the distribution of coding sequences (CDSs), GC content, and GC skew across both genomes. The general feature of *B. cereus* B08 and B69 strains genome consists of one circular chromosome (B08; 5,368,653 bp and B69; 5,304,230 bp) with an overall GC content of 35.3%, consistent with previously reported *B. cereus* genomes. Genome annotation results revealed 5,721 coding sequences, 108 tRNA genes, and 42 rRNA genes for B08, and 5,407 coding sequences, 107 tRNA genes, and 39 rRNA genes for B69 (Table1). Functional classification of coding sequences using the Clusters of Orthologous Groups (COG) database revealed similar overall distribution patterns between the two isolates (Figure 1C and 1D). The most abundant functional categories included "Amino acid transport and metabolism (E)," "Carbohydrate transport and metabolism (G)," "Transcription (K)," and "General function prediction only (R)." Notably, both isolates contained a high proportion of genes associated with "Defense mechanisms (V)" and "Secondary metabolites biosynthesis, transport and catabolism (Q)," which are linked to antimicrobial resistance and toxin

protein processing and stability, such as posttranslational modification, protein turnover, and chaperones (O), are also well represented. Less frequent but biologically relevant categories include cell motility (N), intracellular trafficking and secretion (U), and mobilome-related genes such as prophages and transposons (X), which may contribute to horizontal gene transfer and genome plasticity.

Comparative genomic analysis of the *B. cereus* group isolates revealed clear clustering patterns consistent with species-level distinctions. The phylogenetic tree (Figure 2A), constructed from whole-genome sequence data using GToTree program, shows that the isolates segregate into distinct clades corresponding to recognized members of the *B. cereus* sensu lato complex, including *B. cereus* sensu stricto, *B. pacificus*, *B. paranthracis*, and *B. thuringiensis*. Isolates sequenced in this study (highlighted in blue) grouped closely with *B. cereus* strain MB1, AFA01, and WPySW2. Notably, two isolates clustered within the *B. cereus* s.s. clade, while others exhibited closer relationships to *B. thuringiensis* HM-311 and *B. thuringiensis* SA11 genomes. The ANI heatmap (Figure 2B) further supports these observations, with strong within-species similarity (>95% ANI) indicated by red diagonal blocks. Inter-species comparisons demonstrated ANI values of two *B. cereus* strains to *B. cereus* WPySW2 (B08; 98.92% and B69; 98.98%), *B. cereus* AFA01 (B08; 98.92% and B69; 98.99%), and *B. cereus* AFA01 (B08; 98.91% and B69; 98.99%).

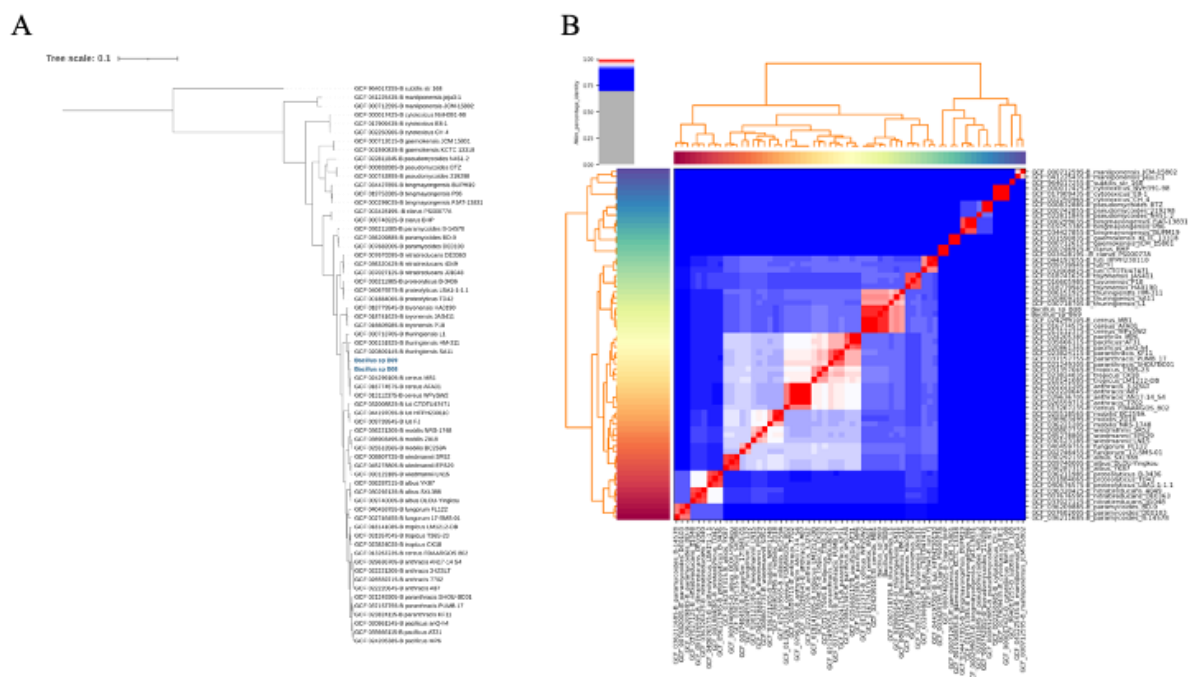


Figure 2.

Genome-based phylogenomics and Average Nucleotide Identity. (A) Maximum likelihood phylogenetic tree of two *B. cereus* strains (Blue font) and other strains of *B. cereus* group genome sequences, generated using the GToTree v1.8.3 workflow and visualized using the web-based tool iTOL v6. (B) Heatmap of whole genome-based average nucleotide identity (ANI) of the two *B. cereus* strains and other type strains of *B. cereus* group genome sequences, constructed using pyANI v0.2.12.

**Table 1.**

Genome characteristics of two *B. cereus* isolated from food sample from Pathum Thani province, Thailand

Sample	Genome length (bp)	GC content (%)	Number of CDS ^a	Number of rRNA	Number of tRNA
B08	5,368,653	35.3	5,721	42	108
B69	5,304,230	35.3	5,407	39	107

^aCDS; coding DNA sequences.

Virulence gene profiling of the two *B. cereus* group isolates was performed using BTyper2 against the Virulence Factor Database (VFDB). As shown in Table 2, both isolates (B08 and B69) carried multiple virulence genes commonly associated with diarrheal food poisoning, including the non-hemolytic enterotoxin complex (*nheA*, *nheB*, *nheC*), enterotoxin FM (*entFM*), and the diarrheal toxin gene (*bceT*). In addition, both isolates possessed cereolysin A (*cerA*), a pore-forming toxin contributing to hemolytic activity. All predicted genes showed high coverage (>97%) and nearly complete sequence identity (97–100%) to reference sequences in VFDB, suggesting strong conservation of these virulence determinants across the isolates. The identification of both diarrheal toxin genes (*nhe* complex, *entFM*, *bceT*) and hemolytic toxin genes (*cerA*) demonstrates the complexed pathogenic potential of these isolates. This dual toxin profile enables the production of enterotoxins that function within the gastrointestinal tract while simultaneously contributing to broader cytotoxic effects. These observations are consistent with previous studies indicating that foodborne *B. cereus* isolates frequently possess diverse enterotoxin repertoires, predisposing them to cause either diarrheal or emetic food poisoning syndromes depending on environmental conditions and differential gene expression patterns. The detection of highly conserved toxin genes across isolates emphasizes the significant threat these strains pose to food safety and public health. This genetic conservation suggests that pathogenic potential is maintained across diverse *B. cereus* populations, reinforcing the critical importance of implementing comprehensive genomic surveillance programs for foodborne pathogens to monitor virulence gene distribution and evolution in food production environments.

Table 2.Virulence genes predicted in two *B. cereus* isolates based on VFDB database using BTyper2.

Sample	Gene	Product	Source	Percent coverage	Percent identity
B08	<i>entFM</i>	enterotoxin	NP_831723.1	97.2	100
	<i>cerA</i>	cereolysin A	AGL98059.1	100	100
	<i>nheA</i>	non-hemolytic enterotoxin lytic component L2	NP_831582.1	99.7	100
	<i>nheB</i>	non-hemolytic enterotoxin lytic component L1	NP_831583.1	100	100
	<i>nheC</i>	enterotoxin C	NP_831584.1	98.9	100
	<i>bceT</i>	diarrheal toxin	BAA04134.1	99.4	97
	B69	<i>entFM</i>	enterotoxin	NP_831723.1	97.6
<i>cerA</i>		cereolysin A	AGL98059.1	97.7	100
<i>nheA</i>		non-hemolytic enterotoxin lytic component L2	NP_831582.1	99.7	100
<i>nheB</i>		non-hemolytic enterotoxin lytic component L1	NP_831583.1	100	100
<i>nheC</i>		enterotoxin C	NP_831584.1	99.4	100
<i>bceT</i>		diarrheal toxin	BAA04134.1	99.4	97

Conclusion:

This study provides genomic insights into two *B. cereus* groups isolated from food in Thailand, highlighting their potential threat to food safety and public health. Whole-genome sequencing using Oxford Nanopore technology revealed that both isolates possess genomic features consistent with the *B. cereus sensu stricto* lineage, including genome size (~5.3 Mb) and GC content (35.3%). Functional annotation and COG classification confirmed a broad metabolic versatility, with an overrepresentation of genes involved in amino acid and carbohydrate metabolism, defense mechanisms, and secondary metabolite biosynthesis, supporting their adaptability in diverse food environments. Comparative phylogenomic and ANI analyses positioned the isolates within the *B. cereus s.s.* clade, clustering closely with reference genomes such as *B. cereus* WPySW2 and AFA01. Importantly, virulence gene profiling demonstrated that both isolates carry highly conserved toxin genes including *nheA*, *nheB*, *nheC*, *entFM*, *cerA*, and *bceT*, with high coverage and identity to VFDB references. The presence of these diarrheal and hemolytic toxin genes underscores their dual pathogenic potential, consistent with strains associated with foodborne disease.

Acknowledgements:

This work was supported by New Researcher Grant from Mae Fah Luang University (Grant number 681A01001).

References:

1. Sornchuer P, Saninjuk K, Amonyngcharoen S, Ruangtong J, Thongsepee N, Martviset P, et al. Whole Genome Sequencing Reveals Antimicrobial Resistance and Virulence Genes of Both Pathogenic and Non-Pathogenic *B. cereus* Group Isolates from Foodstuffs in Thailand. *Antibiotics* (Basel). 2024;13(3).
2. Kolsto AB, Tourasse NJ, Okstad OA. What sets *Bacillus anthracis* apart from other *Bacillus* species? *Annu Rev Microbiol.* 2009;63:451-76.



3. Ehling-Schulz M, Lereclus D, Koehler TM. The *Bacillus cereus* Group: *Bacillus* Species with Pathogenic Potential. *Microbiol Spectr.* 2019;7(3).
4. Lechner S, Mayr R, Francis KP, Pruss BM, Kaplan T, Wiessner-Gunkel E, et al. *Bacillus weihenstephanensis* sp. nov. is a new psychrotolerant species of the *Bacillus cereus* group. *Int J Syst Bacteriol.* 1998;48 Pt 4:1373-82.
5. Hoton FM, Fornelos N, N'Guessan E, Hu X, Swiecicka I, Dierick K, et al. Family portrait of *Bacillus cereus* and *Bacillus weihenstephanensis* cereulide-producing strains. *Environ Microbiol Rep.* 2009;1(3):177-83.
6. Miller RA, Beno SM, Kent DJ, Carroll LM, Martin NH, Boor KJ, et al. *Bacillus wiedmannii* sp. nov., a psychrotolerant and cytotoxic *Bacillus cereus* group species isolated from dairy foods and dairy environments. *Int J Syst Evol Microbiol.* 2016;66(11):4744-53.
7. Liu X, Wang L, Han M, Xue QH, Zhang GS, Gao J, et al. *Bacillus fungorum* sp. nov., a bacterium isolated from spent mushroom substrate. *Int J Syst Evol Microbiol.* 2020;70(3):1457-62.
8. Liu Y, Du J, Lai Q, Zeng R, Ye D, Xu J, et al. Proposal of nine novel species of the *Bacillus cereus* group. *Int J Syst Evol Microbiol.* 2017;67(8):2499-508.
9. Bianco A, Capozzi L, Monno MR, Del Sambro L, Manzulli V, Pesole G, et al. Characterization of *Bacillus cereus* Group Isolates From Human Bacteremia by Whole-Genome Sequencing. *Front Microbiol.* 2020;11:599524.
10. Messelhauser U, Frenzel E, Blochinger C, Zucker R, Kampf P, Ehling-Schulz M. Emetic *Bacillus cereus* are more volatile than thought: recent foodborne outbreaks and prevalence studies in Bavaria (2007-2013). *Biomed Res Int.* 2014;2014:465603.
11. Breit S, Kupferberg A, Rogler G, Hasler G. Vagus Nerve as Modulator of the Brain-Gut Axis in Psychiatric and Inflammatory Disorders. *Front Psychiatry.* 2018;9:44.
12. Stenfors Arnesen LP, Fagerlund A, Granum PE. From soil to gut: *Bacillus cereus* and its food poisoning toxins. *FEMS Microbiol Rev.* 2008;32(4):579-606.
13. Beecher DJ, Macmillan JD. Characterization of the components of hemolysin BL from *Bacillus cereus*. *Infect Immun.* 1991;59(5):1778-84.
14. Que X, Zheng S, Song Q, Pei H, Zhang P. Fantastic voyage: The journey of NLRP3 inflammasome activation. *Genes Dis.* 2024;11(2):819-29.
15. Gohar M, Faegri K, Perchat S, Ravnum S, Okstad OA, Gominet M, et al. The PlcR virulence regulon of *Bacillus cereus*. *PLoS One.* 2008;3(7):e2793.
16. Sornchuer P, Saninjuk K, Prathaphan P, Tiengtip R, Wattanaphansak S. Antimicrobial Susceptibility Profile and Whole-Genome Analysis of a Strong Biofilm-Forming *Bacillus* Sp. B87 Strain Isolated from Food. *Microorganisms.* 2022;10(2).



MICROBIOME BIOMARKERS FOR COLORECTAL CANCER DIAGNOSIS VIA METAGENOMIC ANALYSIS

Kasidet Taweepon¹, Tavan Janvilisri², Joy Scaria³, Supeecha Kumkate¹, Phurt Harnvoravongchai^{1*}

¹Department of Biology, Faculty of Science, Mahidol University, Thailand

²Department of Microbiology, Faculty of Science, Chulalongkorn University, Thailand

³ Department of Veterinary Pathobiology, Oklahoma State University, USA

*e-mail: phurt.har@mahidol.edu

Abstract:

Colorectal cancer (CRC) is among the most common malignancies worldwide and contributes substantially to cancer-related mortality. CRC progression is frequently associated with delayed diagnosis and limited effectiveness of current therapeutic strategies, as tumors can acquire resistance to chemotherapy or radiotherapy. Treatment outcomes are generally more favorable in early-stage CRC than in metastatic disease, underscoring the importance of reliable diagnostic tools to improve patient survival. Various diagnostic approaches, including tumor characteristics and gut microbiome profiling, have been proposed as potential sources of biomarkers. However, universal biomarkers for CRC diagnosis have not yet been established. Moreover, most previous studies have focused on specific gut microbes using a single metric to distinguish healthy individuals from CRC patients.

In this study, we utilized a metagenomic gut microbiome database to identify potential microbial biomarkers for CRC. Multiple analytical metrics, including microbial diversity, differential abundance, and microbial interaction networks, were applied to evaluate the diagnostic potential of candidate gut microbes and their associations. Our findings revealed no significant differences in the top ten most abundant species among the three groups—control, adenoma, and cancer. Both alpha and beta diversity analyses indicated comparable microbial diversity across groups. Differential abundance analysis at the species level, based on three independent approaches, identified *Prevotella copri* as a potential biomarker for CRC, supported by its high LDA score and increased abundance in cancer samples compared to controls. Nevertheless, the interactions between *P. copri* and other microbial species remain unclear, and further investigation is required to elucidate its potential role in promoting or inhibiting colorectal carcinogenesis.

Introduction:

Colorectal cancer (CRC), an epithelial malignancy of the colon, is considered one of the five most common cancers worldwide, including in Thailand, due to its high incidence and mortality rates. According to the World Health Organization (WHO), the age-standardized incidence rate is approximately 20 per 100,000 individuals, ranking fourth globally, while the mortality rate is around 10 per 100,000. These statistics indicate that nearly half of CRC patients die from the disease¹.

The main contributors to CRC-related mortality are low survival rates and disease recurrence. The overall survival rate of patients with metastatic CRC treated at the University of Texas M.D. Anderson Cancer Center (UTMDACC) ranged from approximately 20–40%, reflecting limitations in treatment effectiveness and late diagnosis². Furthermore, recurrence rates are significantly higher in advanced stages of CRC compared to early stages. Both studies also suggested that longer delays until diagnosis reduce the effectiveness of treatment. Conversely, several studies reported survival rates up to 90–100% in cases of early detection³. Therefore, early diagnosis is crucial to reduce CRC mortality.



Conventional diagnostic methods, including patient history, biopsy, colonoscopy, and certain non-invasive tests, are not always efficient or reliable. The invasive standard approach of colonoscopy demonstrates high sensitivity (70–95%) and specificity (~90%)⁴, providing a reasonably accurate diagnosis; however, complications related to bowel preparation and procedure-related discomfort cannot be avoided. Carcinoembryonic antigen (CEA), a non-invasive biomarker, offers low sensitivity of approximately 50% for CRC diagnosis⁵. Additionally, factors such as comorbidities, infections, and bowel preparation can influence the accuracy of colonoscopy. Consequently, alternative diagnostic approaches are needed to improve reliability and patient comfort.

Biomarker characterization in CRC has focused on two main types: genetic biomarkers and gut microbiome profiles. Several studies have shown that CRC progression is associated with dysregulation of oncogenic genes. Comparisons between healthy individuals and CRC patients have also revealed significant differences in gut microbiota composition, where dysbiosis—characterized by an increase in opportunistic pathogens and a reduction in commensal flora—may promote carcinogenesis.

The human gut microbiome plays a critical role in disease development, including CRC. Alterations in microbial composition in dysbiosis patients highlight differential abundances of specific microorganisms. Most studies have focused on a single metric to identify potential microbial biomarkers for CRC diagnosis, which may limit the reliability and robustness of the findings.

To address this knowledge gap, we aim to investigate potential gut microbial candidates as CRC biomarkers using metagenomic analysis. A multi-metric microbial profiling, including diversity metrics, differential abundance analysis, and microbial interaction networks, will be employed to distinguish CRC patients from healthy individuals.

Methodology:

Sample dataset and preprocessing

A public fecal metagenomic shotgun sequencing of CRC dataset (PRJEB7774) was retrieved from NCBI. This dataset was retrieved from Austrian submitted by Beijing Genome Institute (BGI). Sequences were quality-filtered to remove low-quality reads and host contamination and assigned to their respective samples.

OTU and Operational taxonomic profiling

Filtered sequences were processed using the Quantitative Insights into Microbial Ecology 2 (QIIME2) pipeline with the Kraken2 classifier for species-level taxonomic profiling, referencing the Kraken2 database. Operational taxonomic units (OTUs) and taxonomic profiles were exported for downstream metric calculations.

Diversity, differential abundance, and network analysis

OTU tables and taxonomic profiles from QIIME2 were processed using the Phyloseq R package for preprocessing prior to differential abundance analysis. Alpha and beta diversity were analyzed across three groups (Control, Adenoma, and Cancer) using the vegan R package. Differential abundance was assessed using three approaches: LefSe (via the microbiomeMarker package), DESeq2, and ANCOMBC. Correlation networks of gut microbiomes in the three groups were constructed using the NetCoMi R package. Network metrics and properties were obtained and visualized in Cytoscape.

Statistical analysis

Alpha diversity indices and LefSe results were tested using the Kruskal–Wallis test for multiple-group comparisons. Differences in Bray–Curtis distances (PCoA) and network



properties from NetCoMi were assessed using permutation-based methods. Parametric tests for differential abundance were conducted using Wald tests (DESeq2, negative binomial distribution) and log-linear models (ANCOMBC). Statistical analyses were performed in R (version 4.5.0), with significance defined as $p < 0.05$. P-values from overall tests were adjusted for multiple comparisons using the Benjamini–Hochberg false discovery rate (FDR), with adjusted p-values < 0.05 considered significant.

Results and Discussion:

Diversity and taxonomic profiling

A total of 150 Austrian fecal samples were characterized based on the American Joint Committee on Cancer (AJCC) TNM staging system and classified into three groups: 63 samples from healthy individuals (Control), 47 samples from adenoma patients, and 46 samples from carcinoma (Cancer) patients. The Shannon index (Figure 1a) indicated no significant differences in alpha-diversity across the three groups in pairwise comparisons. Similarly, Bray–Curtis PCoA analysis of beta-diversity (Figure 1b) was plotted via PERMANOVA test across three group. It revealed significant difference with p-value = 0.012 between three groups. This microbial community alteration could be defined as a pair of control and cancer groups that had greater difference significantly from pairwise comparison analysis (p-value = 0.001). Adenoma did not exhibit significantly greater diversity compared to the control or cancer group. These results suggest that the overall gut microbiome diversity is substantially affected during cancer development, consistent with one of cohort which findings reported by Zhang et al⁶.

The mean relative abundances of species-level OTUs were calculated and visualized as stacked bar plots for the top 10 OTUs (Figure 1c). Overall, microbial profiles showed only slight variations among control, adenoma, and cancer groups. However, *Escherichia coli* was markedly increased in the adenoma and cancer groups, with approximately a tenfold higher mean relative abundance compared to the control group. Previous studies have reported that *E. coli* may contribute to colorectal carcinogenesis through the release of toxins that induce inflammation in the colorectal region.⁷

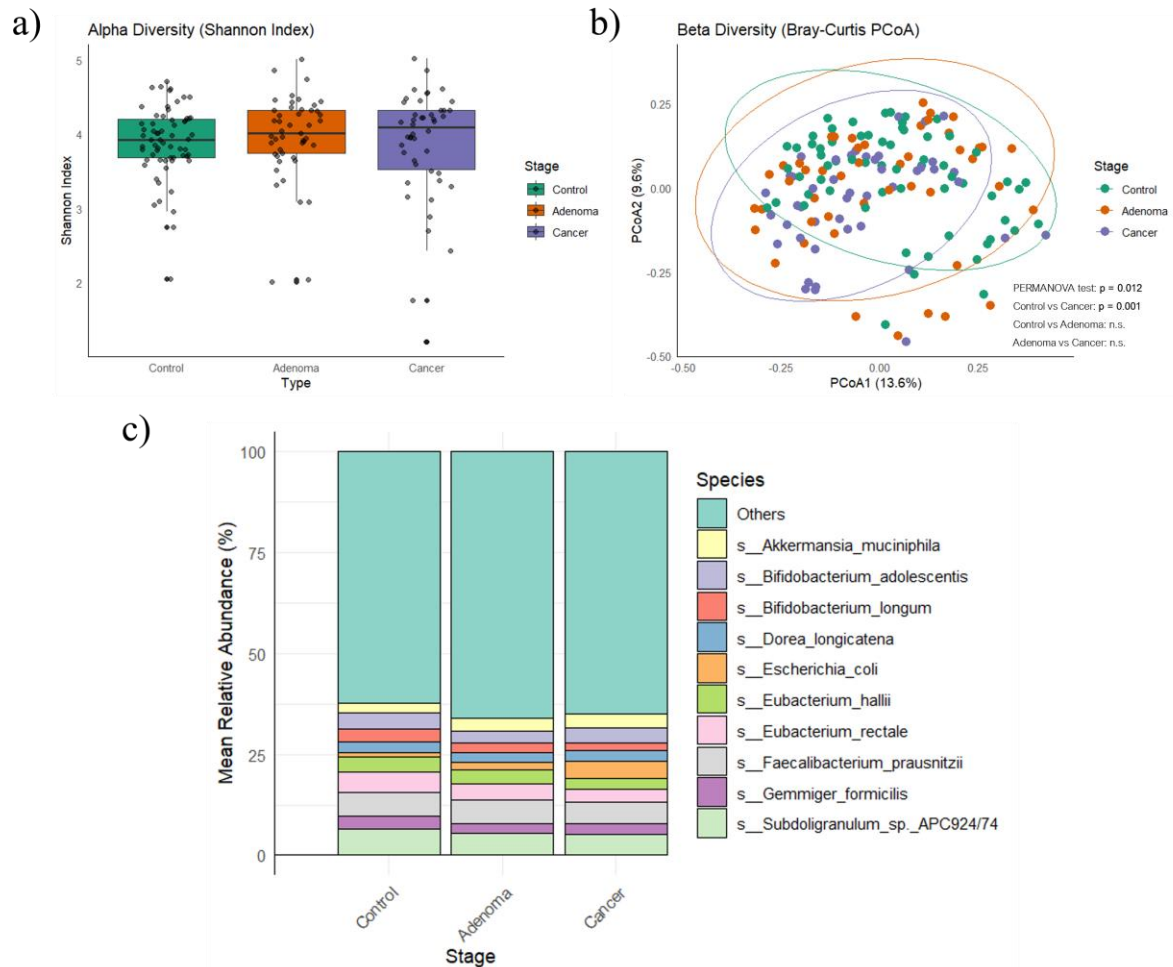


Figure 1 Gut Microbiome Diversity and Top 10 species relative abundance

The alpha diversity of gut microbiome in Control, Adenoma, and Cancer group was analyzed by Shannon diversity index (a). Beta diversity was assessed by Bray–Curtis principal coordinate analysis (PCoA) with PERMANOVA and pairwise tests (b). The mean relative abundance of species-level OTUs of the top 10 most abundant bacterial species were depicted in bar plots, with remaining species categorized as “Others” (c).

Differential abundance analysis

LEfSE with a threshold of False Discovery Rate (FDR) < 0.05 provided Linear Discriminant Analysis (LDA) scores to determine potential species that were differentially abundant among the three groups. Species with LDA scores > 3.5 were plotted (Figure 2a), including eight species, with *Prevotella copri*, *Escherichia coli*, and *Methanobrevibacter smithii* showing the highest LDA scores in the cancer group. Four species, two *Bacteroides* species, *Blautia*, and *Coprococcus*—were enriched in the adenoma group, with the highest LDA scores. In the control group, *Bacteroides vulgatus* and *Bifidobacterium breve* were identified as the top species with the highest scores. Previous studies have reported that the genus *Prevotella* serves as a common biomarker in colorectal cancer, supporting our findings. In addition, normal flora species observed in our analysis including *Bacteroides vulgatus* and *Bifidobacterium breve* have been characterized as cancer-preventive microbes due to their protective functions^{8,9}.

DESeq2 analysis was also performed to identify significant changes in microbial abundance by applying log fold change, Wald test, and FDR correction with a threshold of <



0.05. The results were visualized as a heatmap (Figure 2b), highlighting the top 10 differentially abundant species across all groups. Both adenoma and cancer groups exhibited higher abundances of several genera, including *Porphyromonas* and *Prevotella*, compared to the control group. Conversely, *Lactobacillus* was substantially reduced in adenoma and cancer groups.

Similarly, the ANCOM-BC method provided log fold change estimates combined with prevalence and robustness testing to identify potential differential abundances while accounting for zero inflation in microbiome data. This analysis revealed only minor differences between the control and adenoma groups, which did not reach significance after adjusted p-value, prevalence, and robustness testing (Figure 2c). In contrast, comparisons between cancer and control groups demonstrated a substantial increase in several species from the genera *Porphyromonas*, *Prevotella*, *Lachnospiraceae*, *Bifidobacterium*, and *Lactobacillus*, with absolute log fold change values > 1 . Among these, six species were identified as potential biomarkers through prevalence and robustness testing: *Porphyromonas asaccharolytica*, *Prevotella copri*, *Porphyromonas uenonis*, *Porphyromonas somerae*, *Porphyromonas sp. HMSC077F02*, and *Dialister pneumosintes*.

Zhang et al.⁶ reported universal diagnostic genera for colorectal cancer across multiple populations, including cohorts from Australia, China, France, Italy, Germany, and the United States. Their findings highlighted *Porphyromonas*, *Parvimonas*, and *Peptostreptococcus* as the main genera altered during CRC progression. Consistent with their study, our results also demonstrated a pronounced increase in several *Porphyromonas* species in the cancer group. Moreover, *Porphyromonas gingivalis* has been reported as a potential biomarker associated with colorectal cancer prognosis⁷. However, our analyses did not detect this species as significant in either LEfSE or ANCOM-BC.

Taken together, across the three differential abundance methods, *Prevotella copri* consistently emerged as a candidate biomarker. It demonstrated a high LDA score in LEfSE and significant enrichment in the cancer group with a log fold change of approximately 3 in both DESeq2 and ANCOM-BC analyses. Previous studies by Yao et al¹⁰. and Niccolai et al¹¹. have also emphasized the relevance of *P. copri* through mechanisms such as inflammatory responses mediated by IL-9 and its detection via quantitative PCR as a diagnostic tool. These findings support our results, underscoring *P. copri* as one of the most promising microbial biomarkers identified in this study.

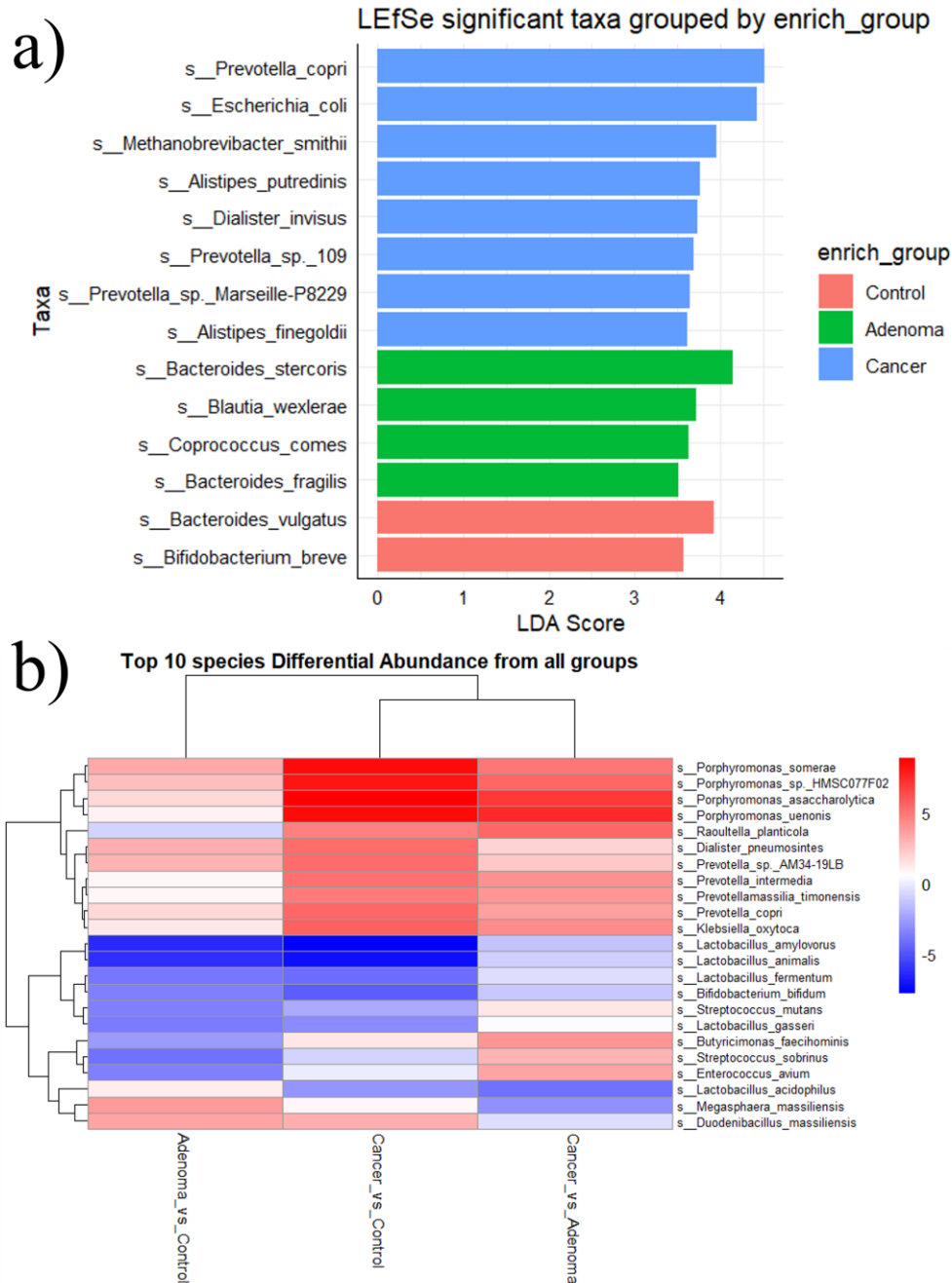


Figure 2 Biomarker discovery from Differential Abundance Analysis
Differential abundance analysis of species-level taxa based on three approaches: (a) LfSe, showing taxa with LDA scores > 3.5; (b) DESeq2, visualized as a heatmap of log fold changes across the three groups; (c–d) continued on next page

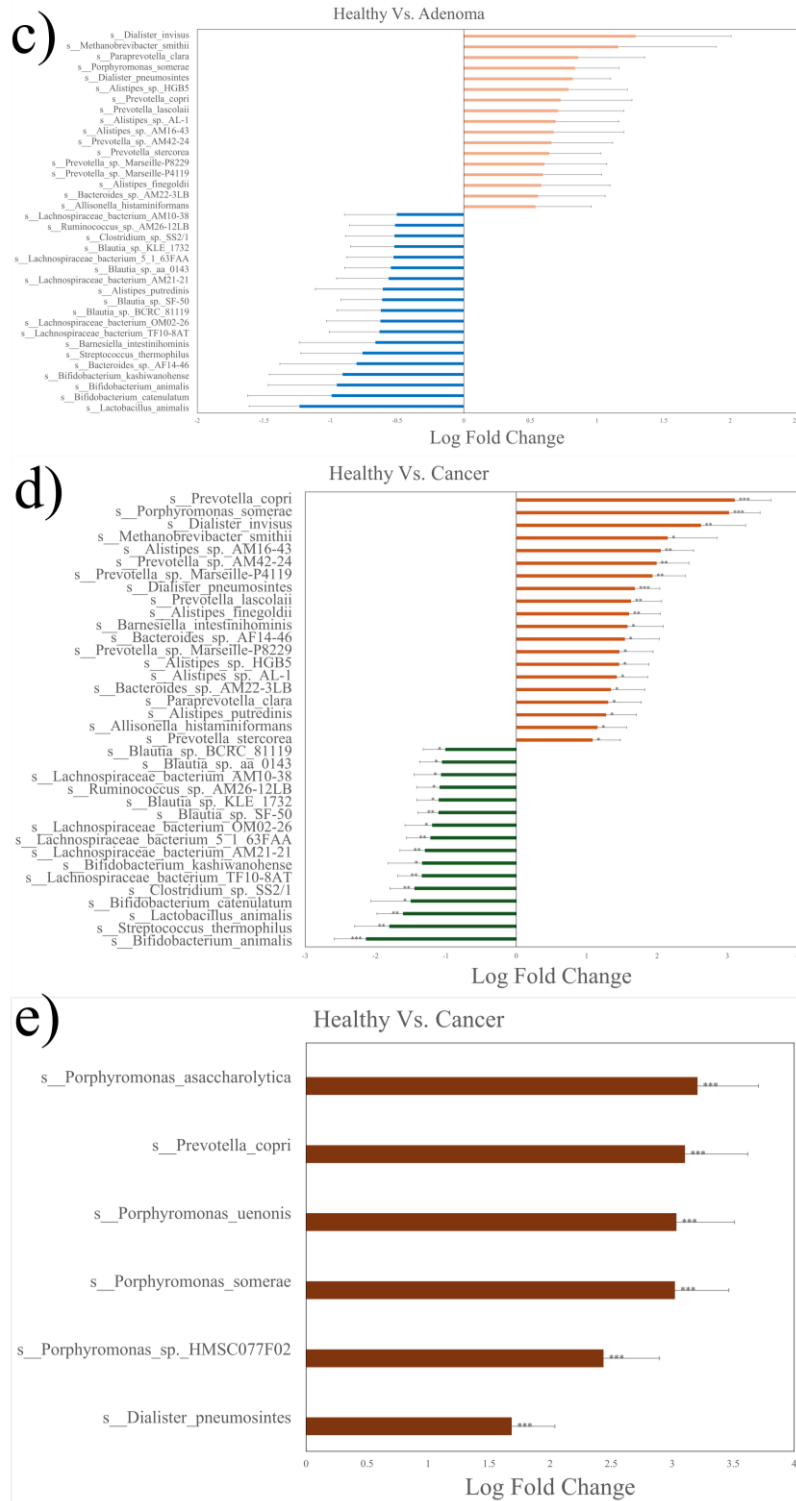


Figure 3 (continued) Biomarker discovery from Differential Abundance Analysis (c–d) ANCOM-BC, represented as bar plots of log fold changes for pairwise comparisons between Healthy vs. Adenoma and Healthy vs. Cancer. Thresholds were set at absolute log fold change > 0.5 for the Adenoma comparison and > 1 for the Cancer comparison. In ANCOM-BC, six species passed both prevalence and robustness tests and were identified as potential biomarkers (e). Adjusted p-values (FDR) were applied across all analyses, with significance thresholds indicated as $q < 0.05$ (*), $q < 0.1$ (**), and $q < 0.01$ (***)

Correlation Network Analysis

Our findings suggest that *Prevotella copri* may represent a crucial microbe in colorectal cancer development within this Austrian cohort. Correlation network analysis provided additional insights into its interactions with the surrounding microbial community. Using the NetCoMi R package and visualizing the results in Cytoscape (Figure 3), we observed that *P. copri* lost its negative associations with certain *Clostridia* and *Clostridium* species during the progression from adenoma to carcinoma. Furthermore, negative interactions with other *Prevotella* species, which similarly opposed *Clostridia* and *Clostridium*, were also lost. In contrast, positive associations between *P. copri* and other *Prevotella* species were retained across cancer stages compared to the control group.

To assess network-level differences, Jaccard indices were calculated for dissimilarity tests across the three groups, considering multiple centrality metrics (Degree, Betweenness, Closeness, Eigenvector, and Hub taxa) (Table 1). Statistical analysis of the top 10 nodes for each centrality measure did not reveal significant differences. However, comparison between the Control and Cancer groups indicated similarity in Eigenvector centrality, with $P(\geq \text{Jacc}) = 0.006$, suggesting that the key microbial contributors identified in this comparison were not significantly different between groups.

Prevotella copri as potential candidate of CRC biomarkers

Prevotella copri, a Gram-negative microbial species, is abundant in the human digestive system and has been identified in various microbiome profiles, both in beneficial and disease-associated contexts¹². A comparative study of gut microbiota between European and rural African children demonstrated that the *Prevotella* genus plays a key role in digesting polysaccharide-rich diets and provides protection against inflammation and colonic diseases caused by *Escherichia*, *Salmonella*, *Shigella*, and *Klebsiella* species¹³. In addition, studies on glucose metabolism in both human and mouse models have shown that the introduction of *Prevotella* improved glycogen storage¹⁴.

However, *P. copri* has also been associated with rheumatoid arthritis, as its high abundance was observed in fecal samples and in mouse models inoculated with *P. copri*. These mice exhibited increased colitis severity, which could contribute to a higher susceptibility to rheumatoid arthritis¹⁶.

Our findings indicate that *P. copri* was not among the top 10 most relatively abundant species in the gut microbiome of Austrian CRC cohorts, whether in healthy or cancer groups. Nevertheless, differential abundance analysis revealed significantly greater alterations in the cancer group compared to the healthy group, as determined by DESeq and ANCOM-BC approaches.

The study by Zhang et al⁶ identified differential abundance of *P. copri* and other microbial species using a two-sided Wilcoxon rank-sum test, comparing their relative abundance. In contrast, our study employed three differential analysis approaches to determine that *P. copri* may act as a key microbial regulator associated with colorectal cancer. In a DSS-induced mouse model, *P. copri* administration markedly increased susceptibility to rheumatoid arthritis¹⁵, and histological analysis of colon samples revealed enhanced colitis effects. Furthermore, previous studies investigating species abundance across different cohorts have identified *P. copri* as one of the top five most abundant species in colorectal cancer patients compared to healthy controls¹⁵.

These findings suggest that *P. copri* may contribute to colorectal cancer development by promoting inflammation, which can accelerate carcinogenesis. A study evaluating potential microbial biomarkers for CRC diagnosis by Yao et al¹⁰, also identified *P. copri* as one of the candidate biomarkers. However, *P. copri* alone may not serve as the most effective biomarker due to limitations in specificity and sensitivity. The most reliable diagnostic

markers for CRC are likely to involve a combination of multiple microbial species to achieve higher diagnostic accuracy.

Given that the gut microbiome composition varies substantially among different populations, further analyses in diverse cohorts are required to identify additional potential microbial candidates and to establish a consistent and reliable gut microbial biomarker profile for CRC diagnosis.

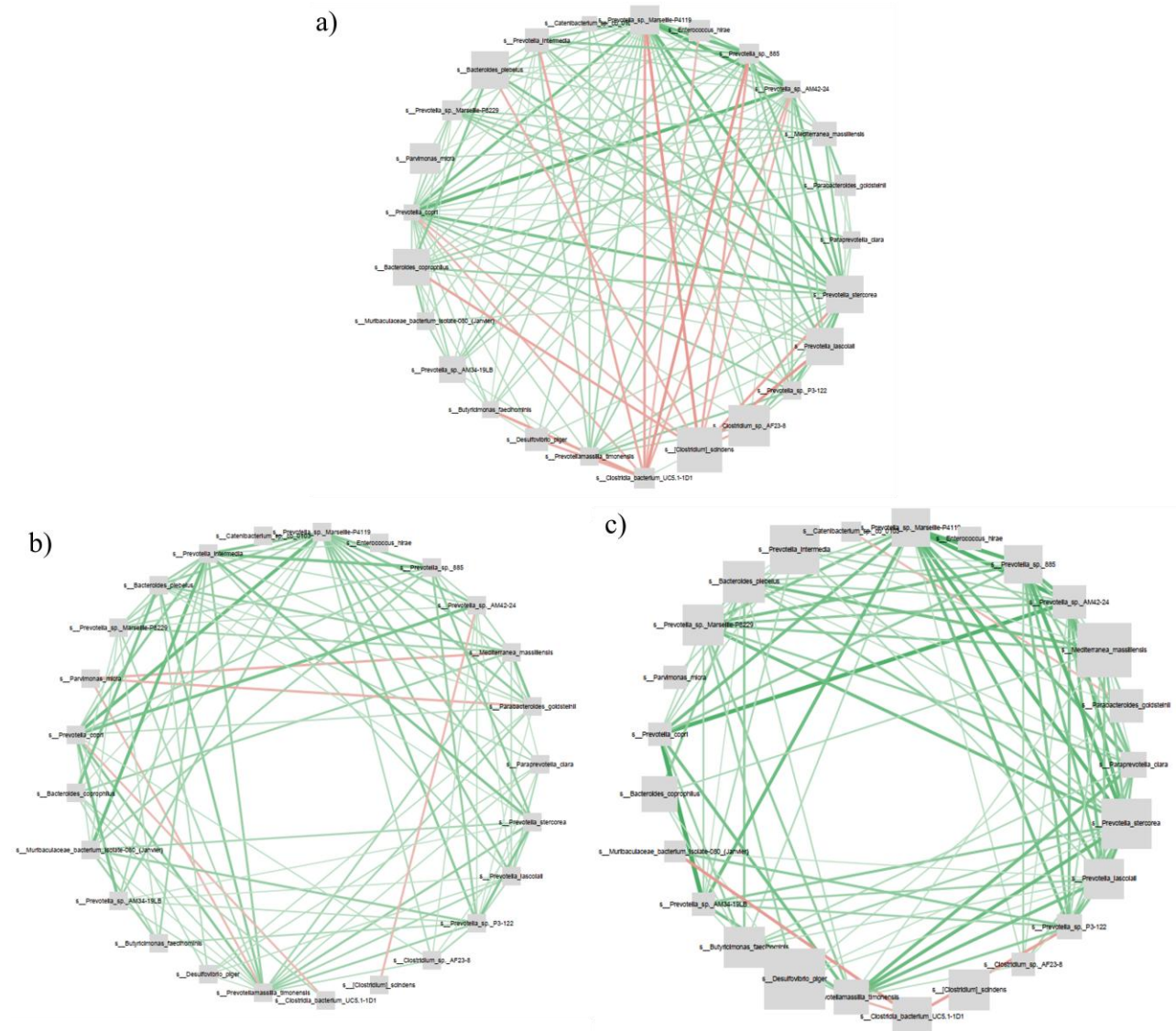


Figure 3 Correlation Network Interaction comparisons on *Prevotella copri*

Correlation networks centered on *Prevotella copri* were visualized across the three groups. Edges represent correlation metrics, with green lines indicating positive correlations and red lines indicating negative correlations. The strength of each correlation is depicted by line thickness, while node size reflects degree centrality. No significant differences were observed among the Control (a), Adenoma (b), and Cancer (c) groups (adjusted p -value < 0.5)



Table 1.
Global Jaccard Index comparison between Control Vs. Cancer

Centrality Value	Jaccard Index	(P(<=Jacc))	P(>=Jacc)
Degree	0.298	0.342	0.756
Betweenness	0.250	0.098	0.942
Closeness	0.311	0.416	0.686
Eigenvector	0.509	0.997	0.006**
Hub Taxa	0.231	0.322	0.863

*Footnote 1 p-value < 0.05

**Footnote 2 p-value < 0.01

Conclusion:

Based on the current findings, differential abundance analyses suggest that *Prevotella copri* may serve as a potential biomarker in colorectal cancer development. However, its interactions within the gut microbial community remain insufficiently characterized, limiting our understanding of its role in shaping microbiome dynamics.

Acknowledgements:

The author would like to thank the support of Department Biology, Faculty of Science, Mahidol university, Thailand and Animal Disease Research and Diagnostic Laboratory, Department of Veterinary and Biomedical Sciences, South Dakota State University, South Dakota, United of States for facilities usage and opportunity to assess research study expertise.

References:

1. Morgan E, Arnold M, Gini A, et al. Gut. 2023;72:338-344.
2. Zeineddine FA, Zeineddine MA, et al. NPJ Precis Oncol. 2023.
3. Swartjes H, van Rees JM, et al. Ann Surg Oncol. 2023;30:3915-3924.
4. Lin JS, Piper MA, et al. Cancers. 2023;15:5656.
5. Feng Q, Liang S, Jia H, et al. Nat Commun. 2015;6:6528.
6. Zhang H, Wu J, et al. Front Microbiol. 2022;13:1005201.
7. Kerdreux M, Edin S, et al. J Cancer. 2023;14:1479–1485.
8. Lu J, Zhang L, Zhang H, et al. NPJ Biofilms Microbiomes. 2023;9:98.
9. Wang M, Ahrné S, et al. FEMS Microbiol Ecol. 2005;54:219–231.
10. Yao Y, Ni H, et al. Front Cell Infect Microbiol. 2021;11:744049.
11. Niccolai E, Russo E et al. Front Immunol. 2020;11:573158.
12. Abdelsalam NA, Hegazy SM, et al. Gut Microbes. 2023;15:2249152.
13. De Filippo C, Cavalieri D, et al. Proc Natl Acad Sci U S A. 2010;107:14691-14696.
14. Kovatcheva-Datchary P, Nilsson A, et al. Cell Metab. 2015;22:971-982.
15. Scher JU, Sczesnak A, et al. eLife. 2013;2:e01202.
16. He T, Cheng X, et al. Bioengineered. 2021;12:7046-7060.



FUNCTIONAL ANALYSIS OF AROMATIC AMINO ACID TRANSPORTER GENE *aaaT* ON ANTIMICROBIAL RESISTANCE IN *Pseudomonas aeruginosa*

Pacharapon Phooanish,¹ Jintana Duang-nkern,² Saharit Wijitpittayanon,³ Adisak Romsang,^{1,3,*}

¹Department of Biotechnology, Faculty of Science, Mahidol University, Bangkok 10400, Thailand

²Laboratory of Biotechnology, Chulabhorn Research Institute, Bangkok 10210, Thailand

³Center for Emerging Bacterial Infections, Faculty of Science, Mahidol University, Bangkok 10400, Thailand

*e-mail: adisak.rom@mahidol.ac.th

Abstract:

Pseudomonas aeruginosa is a multidrug-resistant opportunistic pathogen capable of surviving diverse environmental stresses through efflux pumps, detoxification systems, and chemical transporters. Amino acid transporters have recently been recognized for roles beyond nutrient uptake, particularly in stress adaptation. In this study, the physiological function of the aromatic amino acid transporter gene (*aaaT*) was examined using knockout and complementation approaches, verified by sequencing. Plate sensitivity assays revealed that the *aaaT*-knockout strain exhibited pronounced sensitivity to paraquat (PQ), a superoxide generator, while complementation restored resistance, underscoring the role of *aaaT* in PQ tolerance. Strains with ectopic *aaaT* expression from a pBBR vector displayed growth defects compared with both wild-type and knockout strains, though no significant differences were observed under exposure to other oxidative agents, including hydrogen peroxide, cumene hydroperoxide, sodium hypochlorite, and N-ethylmaleimide. Antibiotic susceptibility testing by disk diffusion showed that the *aaaT*-knockout strain was more susceptible to ciprofloxacin and norfloxacin, but exhibited modestly increased resistance to cefepime, with no substantial changes to most other antibiotics. Collectively, these findings demonstrate that *aaaT* contributes to *P. aeruginosa* tolerance against oxidative stress and modulates its susceptibility to specific antibiotics, especially fluoroquinolones. Targeting *aaaT* may therefore represent a promising strategy to sensitize *P. aeruginosa* to existing antibiotics and enhance therapeutic efficacy.

Introduction:

Pseudomonas aeruginosa is a highly adaptable opportunistic pathogen that poses a significant challenge to public health due to its intrinsic and acquired resistance mechanisms against antibiotics and oxidative stress. The bacterium's resilience is attributed to its versatile metabolic pathways, efflux pumps, and stress response systems, which enable survival in diverse and hostile environments.¹ Proteins involved in amino acid transport and metabolism are increasingly recognized as pivotal in maintaining redox balance and cellular homeostasis.¹ However, the precise role in resistance and stress tolerance remains poorly understood.

Efflux pumps and amino acid transporters are key players in bacterial resistance to antibiotics and biocides. Efflux pumps, such as those from the resistance-nodulation-cell division (RND) family, actively expel toxic compounds, reducing their intracellular concentration and allowing bacteria to survive lethal exposures.² Amino acid transporters, primarily responsible for nutrient uptake, can also contribute to resistance by facilitating the uptake or expulsion of antibiotics and biocides. These systems often work synergistically, with efflux pumps providing a broad-spectrum defense and amino acid transporters offering a targeted mechanism to enhance survival.³



In *P. aeruginosa*, efflux pumps and amino acid transporters are critical contributors to its intrinsic and acquired resistance to antibiotics and biocides. The MexAB-OprM efflux pump, a member of the resistance-nodulation-division (RND) family, is well-known for conferring broad-spectrum resistance to antibiotics such as β -lactams, fluoroquinolones, and macrolides, as well as to biocides like chlorhexidine.⁴ Similarly, the MexCD-OprJ and MexEF-OprN systems provide resistance to fluoroquinolones and chloramphenicol, with their overexpression linked to reduced susceptibility to multiple antimicrobials.⁵ The interplay between efflux pumps and amino acid transporters highlights the complexity of resistance mechanisms in *P. aeruginosa*, emphasizing the need for targeted approaches to combat this pathogen's adaptability.

The primary aim of this study was to investigate the physiological role of *P. aeruginosa* aromatic amino acid transporter gene (*aaaT*) in the contribution to the bacteria's survival under host-mediated stress, and the assessment on the antibiotic susceptibility. Ultimately, the study sought to uncover the potential of targeting this gene as a strategy to overcome antibiotic resistance.

Methodology:

Bacterial growth conditions

Pseudomonas aeruginosa and *Escherichia coli* strains were grown in Luria-Bertani (LB) broth (Difco, USA) at 37 °C with continuous shaking at 180 rpm under aerobic conditions. As required for selective marker of plasmid, the medium was supplemented with 100 μ g/mL ampicillin (Amp) or 10 μ g/mL gentamicin (Gm) for *E. coli* cultivation while the medium was supplemented with 200 μ g/mL carbenicillin (Cb) or 30 μ g/mL gentamicin (Gm) for *P. aeruginosa* cultivation. All bacterial strains were cultured, maintained, and all experiments were performed in the BSL-2 laboratory according to the procedure MUSC2022-029, approved by the Biosafety Committee of the Faculty of Science at Mahidol University.

Construction of *P. aeruginosa aaaT*-mutant

A 339-bp fragment from the middle of the *aaaT* coding region in the PAO1 genome was amplified using primers EBI-1500 (5'-CTTCTTCGGTATCAGCCC-3') and EBI-1501 (5'-ACGAAGGTGGTCAGCATC-3'). The resulting PCR product was isolated, purified, and subsequently ligated into the cloning vector pKNOCK_{GM} at the *Sma*I restriction site. The ligated product, pKNOCK-*aaaT*, was transformed into *E. coli* BW20767 cells. Transformants were screened via PCR using primers BT543 (5'-TGACGCGTCCTCGGTAC-3') and EBI-1501 to confirm plasmid insertion and orientation. The plasmid was then sequenced to ensure accurate construction. Using a conjugation technique, plasmid pKNOCK-*aaaT* was transferred into the PAO1 wild-type strain. The *aaaT*-KO mutant was isolated based on its antibiotic resistance phenotype and confirmed through PCR amplification.⁶

Construction of *P. aeruginosa* full-length *aaaT*

The complete *aaaT* gene from the *Pseudomonas aeruginosa* genome was amplified using primers EBI-1499 (5'-GCCGCCTCCCGCACAATG-3') and EBI-1502 (5'-AAACAGCTA TGACCATG-3'), which are designed to cover the entire coding sequence. The resulting 1312-bp PCR product was cloned into the *Sma*I site of the expression vector pBBR1MCS-4. The recombinant plasmid carrying the *aaaT* gene was then transformed into competent *Escherichia coli* DH5 α cells. PCR screening with primers M13F (5'-GTAAAACGACGGCCAGT-3') and EBI-1500 were used to verify the insertion and orientation of the plasmid, followed by sequencing to confirm the accuracy of the construct.⁶



Physiological studies

Plate sensitivity assay

The plate sensitivity assay was conducted to evaluate bacterial growth on plates, reflecting the resistance levels of the PAO1 wild-type strain and various mutant strains against a range of oxidants. All *Pseudomonas aeruginosa* strains will initially be cultured in 3 mL of fresh L-broth containing suitable antibiotics. Overnight cultures were then subculture into 3 mL of fresh L-broth to adjust the OD₆₀₀ to 0.05 and incubated at 37 °C for 3 h. Exponentially growing cultures will be serially diluted 10-fold, and each dilution will be spotted onto L-agar plates with or without specific concentrations of oxidants. The plates were be incubated overnight at 37 °C, and the growth differences between strains will be observed. Resistance to oxidants will be quantified as the percent survival, calculated as the ratio of CFU on oxidant-containing plates to CFU on plates without oxidants, expressed as a percentage.⁷ Data will be presented as the mean and standard deviation from three independent biological replicates.⁶

Disk Diffusion Assay

The antibiotic susceptibility of *P. aeruginosa* PAO1 and its mutant derivatives was evaluated using the standard Kirby-Bauer disk diffusion method with a modification by Romsang et al.⁶ and Hudzicki.⁵ Briefly, bacterial cultures were grown aerobically in Mueller Hinton (MH) broth at 37 °C with 180 rpm shaking until the exponential phase, after which 50 µL of each culture was mixed with 15 mL of pre-warmed soft agar and poured onto MH agar base plates. Antibiotic-impregnated disks were placed on the solidified bacterial lawn and incubated at 37 °C for 18 h. The diameters of inhibition zones were measured in millimeters, and each assay was performed in triplicate.

Statistical statements

All groups of datasets were performed in mean ± standard deviation (SD). The student's *t*-test and ANOVA analyses were used to determine a difference between datasets with *p*-value < 0.05 which was considered significant.

Results and Discussion:

To investigate the physiological role of the *aaaT* gene in *P. aeruginosa*, four isogenic strains were constructed including *P. aeruginosa* wild-type control (PAO1/pBBR), *aaaT*-knockout strain (*aaaT*-KO/pBBR), *aaaT*-complemented strain (*aaaT*-KO/pBBR-*aaaT*), and *aaaT*-overexpression strain (PAO1/pBBR-*aaaT*). Sequencing confirmed correct insertion of the full-length *aaaT* gene into the pBBR vector without mismatches.⁸

When spotted on LB agar (LA) plates and incubated for 18 h, all strains displayed comparable colony numbers under non-stressed conditions. However, both the complemented and overexpression strains consistently exhibited smaller colony sizes compared with the wild-type and knockout strains, indicating a growth defect potentially associated with plasmid-based *aaaT* expression. Under oxidative stress conditions, no significant difference was observed on plates containing hydrogen peroxide (H₂O₂), cumene hydroperoxide (CHP), sodium hypochlorite (NaOCl), and N-ethylmaleimide (NEM) (Figure 1). In contrast, the *aaaT*-knockout strain showed marked sensitivity to paraquat (PQ), a phenotype that was restored upon complementation via a transformation of an ectopic *aaaT*-expression vector (Figure 1). Interestingly, the overexpression strain also displayed PQ sensitivity in addition to its colony size defect (Figure 1), further suggesting that the ectopic *aaaT* expression imposes a physiological burden. Collectively, these findings implicate *aaaT* in the superoxide stress response, with PQ sensitivity emerging as the most consistent phenotype. The data suggests that the *aaaT* gene encodes a transporter that is able to recognize and import paraquat due to

its structural similarity to aromatic amino acids. The selective susceptibility to paraquat, but not other oxidative agents, strongly supports the hypothesis that the primary role of the *aaaT* transporter in this context is the uptake of paraquat, rather than a general role in managing all forms of oxidative stress. Research in *E. coli* has shown that paraquat susceptibility is linked to polyamine uptake. Polyamines are small, positively charged molecules essential for cell growth. The polyamine transport system in *E. coli* is known to also transport paraquat, contributing to its toxicity. Mutants with defects in this transporter exhibit increased resistance to paraquat because the herbicide can no longer efficiently enter the cell.⁹

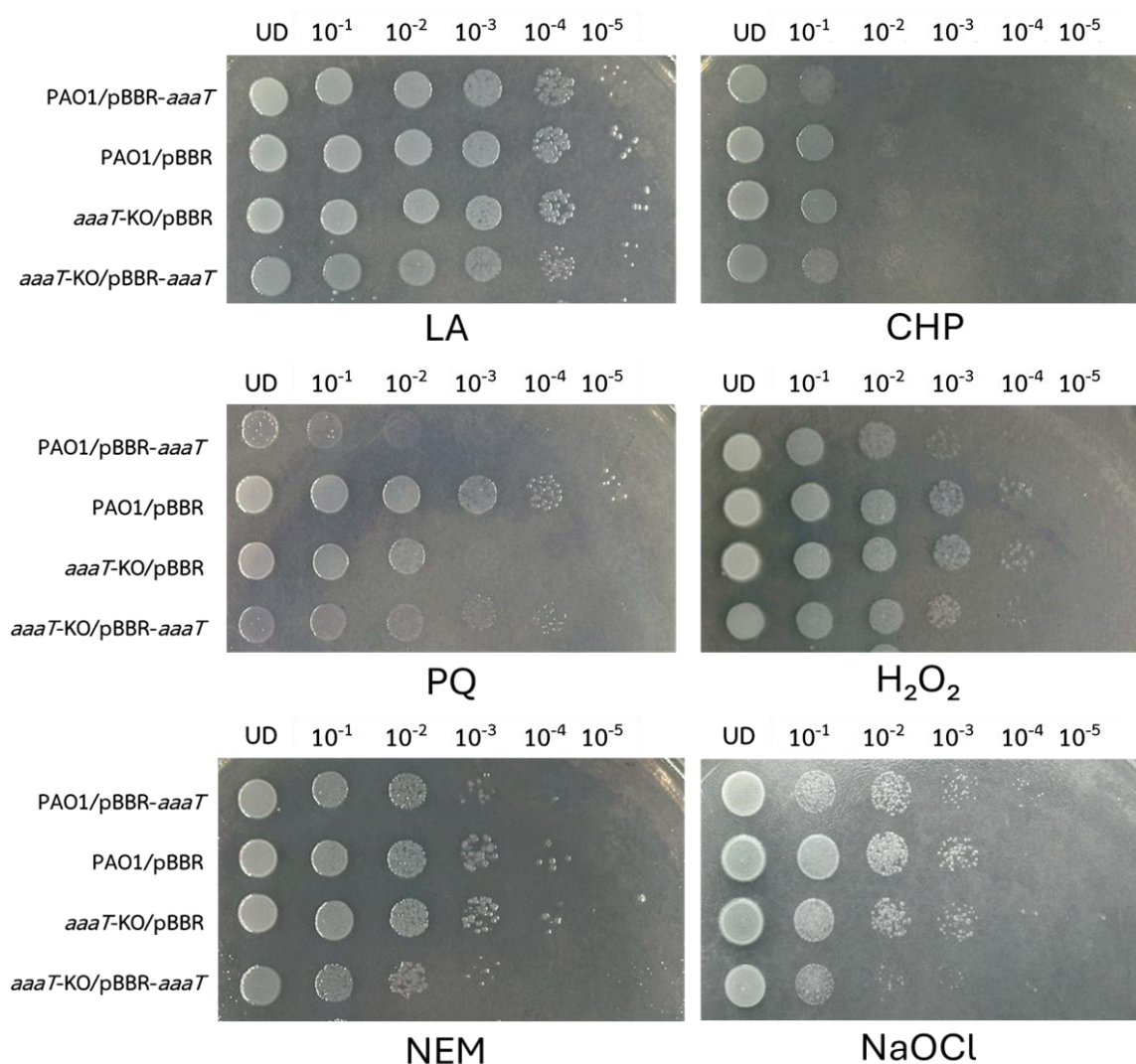


Figure 1.

Plate sensitivity assays under oxidative stress.

The exponential-phase cells of *P. aeruginosa* mutant strains were 10-fold serially diluted and spotted on LB agar (LA) plates with or without oxidants, including 2.1 mM CHP, 0.15 mM PQ, 0.35 mM H₂O₂, 0.75 mM NEM, and 8.88 mM NaOCl. After incubation at 37 °C for 18 h, growth between these strains was observed. The data presented were representative of three similar results.

Interestingly, we found that the *aaaT*-complemented and *aaaT*-overexpression strains displayed intrinsic growth defects on the LA and oxidant-containing plates (Figure 1). This intrinsic growth defect in the aromatic amino acid transporter gene *aaaT*-overexpression suggests that the delicate metabolic balance in the bacterial cells is disrupted by the

unregulated influx of aromatic amino acids or their toxic analogs,¹⁰ or by a significant energetic burden associated with maintaining the high number of transporters.¹¹⁻¹³ This finding highlights the critical importance of gene regulation for maintaining optimal cellular function, demonstrating that both the absence and the excessive presence of this AaaT transporter can be detrimental to the overall survival and growth in *P. aeruginosa*.

Next, the antibiotic susceptibility test was performed in the wild-type (PAO1/pBBR) and the *aaaT*-knockout mutant (*aaaT*-KO/pBBR). The Kirby-Bauer disk diffusion assay^{5, 6} revealed that most antibiotics produced comparable inhibition zone diameters between the two strains, supporting the notion that *aaaT* is not a broad determinant of intrinsic resistance. For example, no significant difference was observed in several antibiotics including imipenem (IPM10, $p = 0.37$), meropenem (MEM10, $p = 0.066$), ceftriaxone (CRO30, $p = 0.51$), ceftazidime (CAZ30, $p = 0.69$), fosfomycin (FOS50, $p = 0.68$), tetracycline (TE30, $p = 0.24$), polymyxin B (PB300, $p = 1.00$), and tobramycin (TOB10, $p = 0.12$), consistent with previous studies highlighting the dominant role of efflux pumps and other intrinsic mechanisms in *P. aeruginosa* resistance.^{1, 4}

Nevertheless, the *aaaT*-knockout strain exhibited a significant increase in the inhibition zones against ciprofloxacin (CIP5, $p = 0.0136$) and norfloxacin (NOR10, $p = 0.0244$), indicating dramatically increased sensitivity to fluoroquinolones (Figure 2). These results are consistent with the idea that amino acid transporters may indirectly influence quinolone susceptibility, possibly through effects on metabolic or redox balance.^{3, 10} Loss of *aaaT* could disrupt intracellular pools of metabolites required for redox homeostasis. This imbalance likely increases the susceptibility of the *aaaT*-knockout strain to PQ and fluoroquinolones, both of which generate ROS as part of their bactericidal action.¹⁴ Another explanation could be expressed that amino acid transporters and efflux systems are functionally linked in *P. aeruginosa*.^{1, 2} Knockout of *aaaT* may reduce efflux efficiency against fluoroquinolones, further sensitizing the mutant. Conversely, compensatory adjustments in efflux activity (e.g., MexAB-OprM upregulation) or changes in outer membrane permeability could selectively limit cefepime uptake, explaining the observed resistance phenotype. Together, these findings suggest that *aaaT* modulates susceptibility in a context-dependent manner: its loss predisposes cells to enhanced killing by ROS-inducing drugs (PQ, CIP, NOR) while paradoxically conferring a survival advantage under cefepime exposure. This dual effect underscores the complexity of metabolic–redox interactions in shaping antibiotic responses in *P. aeruginosa*.¹⁵

In contrast, the *aaaT*-knockout strain showed a smaller inhibition zone upon cefepime treatment (FEP30, $p = 0.0082$), a fourth-generation cephalosporin, compared to that in the PAO1/pBBR strain (Figure 2). This paradoxical outcome may reflect compensatory changes in efflux pump activity or outer membrane physiology that limit cefepime uptake. While cefepime requires specific porins for entry, the absence of the *aaaT* transporter may have triggered a global stress response within the cell. This response could lead to the upregulation of major multi-drug efflux pumps like the MexAB-OprM system, which are capable of expelling a broad range of antibiotics, including cephalosporins.¹⁶ This induced efflux system would effectively lower the intracellular concentration of cefepime, reducing its ability to reach its target and consequently resulting in increased resistance.

Altogether, these findings suggest that while *aaaT* is not a broad determinant of resistance, it contributes to enhanced sensitivity to fluoroquinolones and altered response to cephalosporins (Figure 2). This selective effect implies that *aaaT* may not directly interact with antibiotic targets but rather influence susceptibility through its role in maintaining cellular physiology. In particular, disruption of *aaaT* could perturb redox homeostasis or nutrient transport, indirectly altering the ability of *P. aeruginosa* to tolerate certain

antibiotics. Such context-dependent roles highlight the importance of considering metabolic background when studying resistance mechanisms.

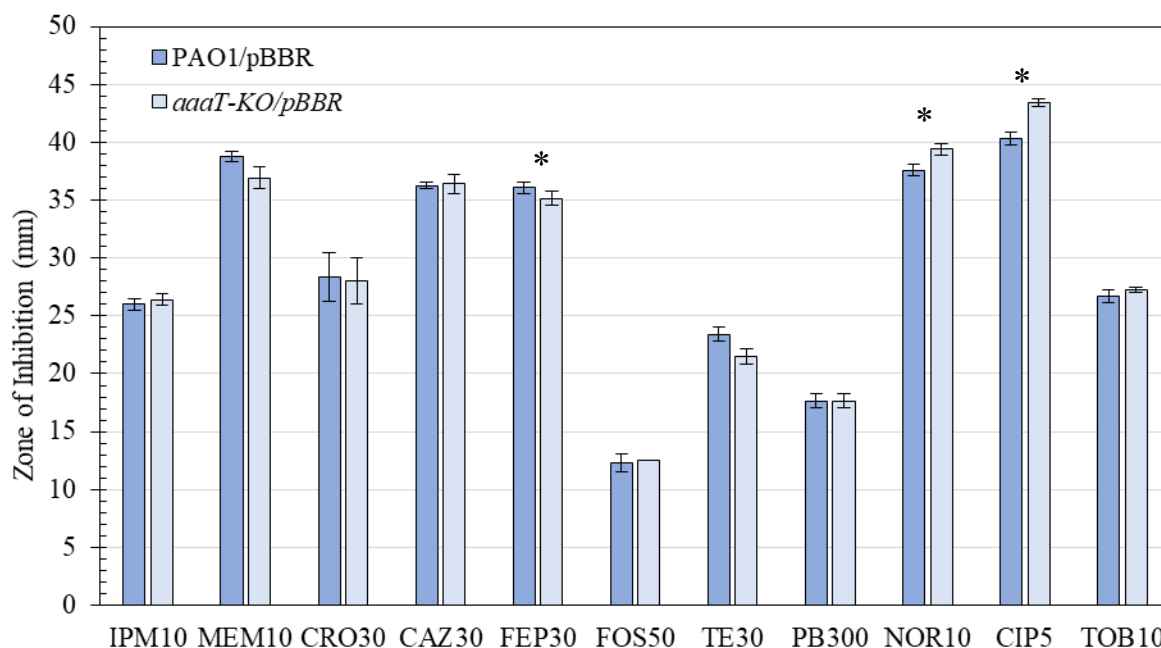


Figure 2.

Antibiotic susceptibility of *P. aeruginosa* PAO1 and its *aaaT* knockout derivative (*aaaT*-KO/pBBR) determined by the Kirby-Bauer disk diffusion assay. Bars represent the mean inhibition zone diameters (mm), and error bars indicate the standard deviation from three independent experiments. Asterisks (*) denote statistically significant differences between strains ($p < 0.05$, Student's *t*-test).

Taken together, these findings demonstrate that *aaaT* plays a specific role in the oxidative stress response and selectively modulates susceptibility to certain antibiotics. Rather than acting as a broad-spectrum resistance determinant, *aaaT* may indirectly influence drug tolerance through its role in maintaining cellular physiology and redox balance. Growth defects observed in complemented and overexpression strains highlight the limitations of plasmid-based systems and the importance of employing chromosomal integration approaches, such as mini-Tn7, to achieve balanced gene expression in future studies.^{1, 8, 10}

Conclusion:

This study concludes that the *aaaT* gene plays a crucial role in *P. aeruginosa* stress response and antibiotic susceptibility. The *aaaT*-knockout strain's sensitivity to paraquat confirms its involvement in superoxide stress tolerance. Furthermore, the gene's influence on antibiotic interactions is complex; its absence increases susceptibility to fluoroquinolones while paradoxically conferring a modest resistance to cefepime. The findings indicate that the *aaaT* gene plays a key role in protecting *P. aeruginosa* from oxidative stress and influences its susceptibility to specific antibiotics, particularly fluoroquinolones. These findings suggest that targeting the *aaaT* transporter could be a potential strategy for overcoming antibiotic resistance in *P. aeruginosa* by sensitizing the bacteria to existing antibiotics, thereby improving the efficacy of current treatment regimens.



Acknowledgements:

This research was supported by Mahidol University (Fundamental Fund: fiscal year 2023 by National Science Research and Innovation Fund (NSRF)) under A.R.'s project (Grant number FF-053/2566). P.P. was supported by a funding from Faculty of Graduate Studies, Mahidol University. Parts of this work are from P.P. thesis submitted for a Master degree in Biotechnology from Mahidol University.

References:

1. da Cruz Nizer WS, Inkovskiy V, Versey Z, Stempel N, Cassol E, Overhage J. *Pathogens*. 2021;10:1187.
2. Du D, Wang Z, James NR, Voss JE, Klimont E, Ohene-Agyei T, et al. *Nature*. 2014;509:512–5.
3. Masuda N, Sakagawa E, Ohya S, Gotoh N, Tsujimoto H, Nishino T. *Antimicrob Agents Chemother*. 2000;44:3322–7.
4. Gomez NO, Tetard A, Ouerdane L, Laffont C, Brutesco C, Ball G, et al. *Mol Microbiol*. 2021;115:84–98.
5. Hudzicki J. *Am Soc Microbiol*. 2009;15:1–23.
6. Romsang A, Atichartpongkul S, Trinachartvanit W, Vattanaviboon P, Mongkolsuk S. *J Bacteriol*. 2013;195:3299–308.
7. Hassett DJ, Ma JF, Elkins JG, McDermott TR, Ochsner UA, West SE, et al. *Mol Microbiol*. 1999;34:1082–93.
8. Choi KH, Schweizer HP. *Nat Protoc*. 2006;1:153–61.
9. Jung IL, Kim IG. *Cell Biol Toxicol*. 2003;19:29–41.
10. Nishino K, Yamasaki S, Nakashima R, Zwama M, Hayashi-Nishino M. *Front Microbiol*. 2021;12:737288.
11. Ceroni F, Algar R, Stan GB, Ellis T. *Nat Methods*. 2015;12:415–8.
12. Cook TB, Rand JM, Nurani W, Courtney DK, Liu SA, Pflieger BF. *J Ind Microbiol Biotechnol*. 2018;45:517–27.
13. Schuster LA, Reisch CR. *Nucleic Acids Res*. 2021;49:7189–202.
14. Ma JF, Ochsner UA, Klotz MG, Nanayakkara VK, Howell ML, Johnson Z, et al. *J Bacteriol*. 1999;181:3730–42.
15. Dulyayangkul P, Satapoomin N, Avison MB, Charoenlap N, Vattanaviboon P, Mongkolsuk S. *Front Microbiol*. 2021;11:592153.
16. Srikumar R, Paul CJ, Poole K. *J Bacteriol*. 2000;182:1410–4.



DISTRIBUTION OF *Vibrio* spp. IN RELATION TO WATER QUALITY IN THE SONGKHLA LAKE BASIN, THAILAND

Jutamas Manit,¹ Kurrotulayunee Kareeya,² Rattanaruji Pomwised^{1,*}

¹Division of Biological Science, Faculty of Science, Prince of Songkla University, Songkhla, Thailand

²Department of Biomedical Sciences and Biomedical Engineering, Faculty of Medicine, Prince of Songkla University, Songkhla, Thailand

*e-mail: rattanaruji.p@psu.ac.th

Abstract:

Songkhla lake basin is an important brackish water ecosystem in Thailand, supporting both biodiversity and aquaculture. Environmental changes and human activities affect water quality and the spread of *Vibrio* spp. which are associated with vibriosis in aquatic animals and severe infections in humans. This study investigated the occurrence of *Vibrio* spp. using the most probable number (MPN) method and examined correlations with water quality parameters. Isolates were identified using selective media, multiplex PCR for *Vibrio vulnificus*, and MALDI-TOF MS for other species. While *V. vulnificus* was not detected, *V. albensis* and other *Vibrio* species were present. Bacterial abundance correlated with elevated ammonia, nitrite, and organic matter, along with variations in pH, salinity, and temperature. These findings provide baseline data on *Vibrio* ecology in the Songkhla lake basin and underscore the importance of water quality monitoring to reduce risks for public health and aquaculture.

Introduction:

Climate change, particularly rising global temperatures, has significant impacts on public health and aquatic ecosystems. Increasing seawater temperatures and sea levels, together with pollution, have contributed to the rising incidence of *Vibrio*-associated illnesses and their emergence in previously unaffected regions^{1,2}. The genus *Vibrio* comprises Gram-negative, motile, curved rod-shaped bacteria that naturally inhabit estuarine and marine environments³. Under nutrient-rich conditions, such as those found in aquaculture systems, *Vibrio* spp. can proliferate rapidly, disrupting ecological balance and facilitating bacterial cycling⁴. In aquaculture, *Vibrio* infections (vibriosis) are a major cause of mortality in fish and crustaceans, leading to severe environmental consequences and economic losses⁵. Their persistence in sediments enables long-term survival and recurrent contamination within the same ecosystem. Several *Vibrio* species are also pathogenic to humans, including *V. cholerae*, *V. parahaemolyticus*, and *V. vulnificus*. Notably, *V. vulnificus* is an opportunistic pathogen responsible for gastroenteritis, wound infections, and septicemia in humans⁶.

In Thailand, *V. vulnificus* infections have been reported by the Thai Ministry of Health among government-based hospital between 2001-2006 with 6-12 per years or 0.016 cases per 100,000 populations per year. Septicemia by *V. vulnificus* infection causes rapid onset of limb swelling and hemorrhagic bullous skin lesion, septic shock with deadly disseminated intravascular coagulation⁷.

The Songkhla lake basin is the largest brackish water ecosystem in Thailand, encompassing three provinces: Songkhla, Phatthalung, and Nakhon Si Thammarat. This unique ecosystem supports high biodiversity and serves as a major aquaculture hub in southern Thailand. However, environmental changes and increasing human activities have significantly influenced water quality, creating favorable conditions for the proliferation of pathogenic bacteria⁸. Among the key bacterial groups inhabiting brackish water ecosystem, *Vibrio* spp. are of particular concern due to their dual role as natural inhabitants and opportunistic pathogens.



Changes in the physical and chemical properties of water systems, such as temperature, dissolved oxygen (DO)⁹, salinity¹⁰, and organic matter¹¹ resulting from human activity, can strongly impact the abundance and distribution of *Vibrio* spp. in the Songkhla lake basin. Understanding the distribution of these bacteria is important for monitoring and preventing the spread of pathogens that threaten both public health and the aquaculture sustainability. Therefore, this study aimed to investigate the distribution of *Vibrio* spp., with particular emphasis on *V. vulnificus* and related organisms, in the Songkhla lake basin. In addition, the relationship between water quality parameters and bacterial abundance was examined to better understand the environmental factors influencing *Vibrio* occurrence in this ecosystem. The findings of this study will contribute to identifying key diverse of *Vibrio* growth and provide a basis for water quality management strategies to reduce potential risks associated with seafood consumption and aquaculture production in the region.

Methodology:

Sample collection

Brackish water samples were collected from multiple sites around the Songkhla lake basin from November 2024 to February 2025, yielding a total of 16 samples, as shown in figure 1. At each site, water was aseptically collected in sterile bottles and stored at 4°C. All samples were transported to the laboratory and processed on the same day to minimize changes in microbial composition.

Enumeration of Vibrio spp. by MPN method

For bacterial enumeration, 25 ml of each brackish water sample was added to 225 ml of alkaline peptone water (APW, pH 8.5) to obtain a 1:10 dilution (total of 250 ml). The bacterial concentration was estimated using the three-tube most probable number (MPN) method. Briefly, ten-fold serial dilutions (10^{-2} , 10^{-3} , and 10^{-4}) were prepared in triplicate and incubated at 37 °C for 18–24 h. As a presumptive *Vibrio* test, all turbid tubes were streaked onto Thiosulfate Citrate Bile Salt Sucrose (TCBS) agar and incubated at 37 °C for 18–24 h. Tubes showing turbidity and yielding colonies on TCBS agar were considered positive. The number of positive tubes at each dilution was recorded and used to calculate the MPN values.

Identification of Vibrio spp. isolates

Colonies grown on TCBS agar were sub-cultured on CHROMagar™ *Vibrio* and incubated at 37°C for 18 – 24h. Turquoise colonies were presumptively identified as *V. vulnificus*.

Genomic DNA of bacterial isolates was extracted using the boiling method. In brief, a single colony from an overnight culture was suspended in 200 µl of sterile deionized water, boiled at 100°C for 10 min, cooled on ice for 10 min, and centrifuged at 14,000 rpm for 5 min. The supernatant was collected and used as DNA template for multiplex PCR.

Species identification was performed by multiplex PCR targeting the 16S rRNA gene, and the *vvhA* (cytolysin) gene, using MyTaq™ DNA polymerases (Bioline). Primer sequences are shown in Table 1. PCR conditions included an initial denaturation at 96 °C for 6 min, followed by 30 cycles of denaturation at 94 °C, annealing at 57.3 °C, and extension at 72 °C. A final extension was carried out at 72 °C for 7 min. PCR products were resolved on 1.5% agarose gels to confirm the presence of target amplicons for *V. vulnificus*.

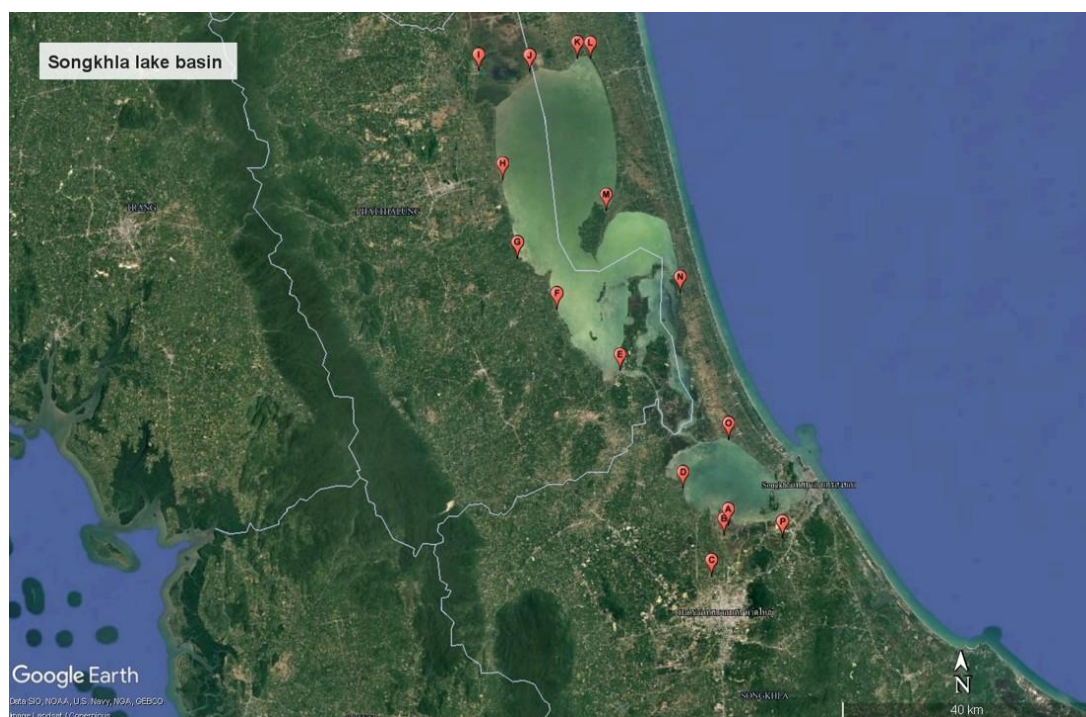


Figure 1.

Sampling sites of brackish water in Songkhla lake basin includes 16 sites.

In addition, unidentified isolates were analyzed using Matrix-Assisted Laser Desorption/Ionization Time-of-Flight Mass Spectrometry (MALDI-TOF MS) for species-level identification.

Table 1.

Primer sequence of targeted genes specific to *V. vulnificus*

Targeted gene	primer	Sequence (5'-3')	Tm (°C)	Size (bp)
16S rRNA ¹²	27-F	AGAGTTTGATCATGGCTCAG	53.7	1,465
	1492-R	TACGGCTACCTTGTTACGACTT		
<i>vvhA</i> ¹³	<i>vvh</i> -F	TTCCAACCTCAAACCGAACTATGA	59.4	205
	<i>vvh</i> -R	ATTCCAGTCGATGCGAATACGTTG		

Water quality analysis

Several water quality parameters were analyzed to evaluate their potential influence on the growth and distribution of *Vibrio* spp. Dissolved oxygen, ammonia, nitrite, sulfide, and total alkalinity were measured at the Central Equipment Division, Faculty of Science, Prince of Songkla University, using standard protocols. The temperature, salinity, and pH were determined *in situ* at the time of sample collection.



Results and Discussion:

1. Wate quality

The water quality was assessed using several parameters, including dissolved oxygen (DO), ammonia, nitrite, sulfide, total alkalinity, temperature, salinity, and pH (Table 2). DO levels ranged from 6.80 to 9.35 mg/L, which is considered acceptable, as concentrations above 5 mg/ml are generally sufficient to support aquatic life. Lower DO values typically indicate pollution or organic contamination.

Ammonia concentrations across the sampling sites ranged from 0.15 to 8.62 mg/L, exceeding the recommended safe level of < 0.1 mg/L for fish and aquatic animals¹⁴. Elevated ammonia levels may reflect sewage discharge or organic waste input into the water source¹⁵. Nitrite levels ranged from 0.13 to 1.41 mg/L, whereas the optimal nitrite concentration should remain below 1 mg/L. High nitrite value may indicate poor water associated with oxygen depletion and waste, which is in turn can stimulate microbial proliferation¹⁶. Notably, sulfide was not found in all samples sites. Sulfide is toxic to aquatic animals and typically indicates wastewater contamination. Its absence suggests limited direct sewage inflow.

Other parameters also provided insight into water quality. Total alkalinity ranged from 4.09 to 81.90 mg/L, with higher levels in some areas suggesting greater buffering capacity against pH fluctuations. The pH values ranged from 5.63 to 7.72, with the lowest value (5.63 at site B) potentially linked to sewage input. Temperature and salinity values ranged from 28.0 – 30.4 °C and 0.00 – 1.00 ppt, respectively, reflecting typical tropical brackish water conditions. Our results suggest that Songkhla lake basin provides an environment conducive to the persistence and growth of *Vibrio* spp.

Table 2.
Sampling sites, physical and chemical parameters of brackish water from Songkhla lake basin

Site	Isolates	Latitude	Longitude	Parameters							
				DO (mg/L)	Ammonia (mg/L)	Nitrite (mg/L)	Sulfide (mg/L)	Total alkaline (mg/L)	Temperature (°C)	Salinity (ppt)	pH
A	Vsb111	7°07'55.0 N	100°28'43.0 E	7.85	1.15	0.99	N	81.90	28.00	1.00	7.05
B	Vsb121	7°07'07.0 N	100°28'20.0 E	8.90	7.53	1.41	N	8.19	28.2	0.20	5.63
	Vsb122			8.80	8.62	1.12	N	4.09	28.00	0.00	6.02
C	Vsb 231	7°03'35.2 N	100°27'14.5 E	8.25	0.37	0.53	N	24.57	28.00	0.00	6.83
D	Vsb 241	7°11'06.7 N	100°24'48.9 E	9.00	0.24	0.47	N	20.48	28.20	0.00	7.13
	Vsb 242			9.35	0.18	0.35	N	20.48	28.00	0.00	7.09
E	Vsb 251	7°21'11.4 N	100°19'27.3 E	8.60	0.50	0.25	N	18.43	28.20	0.00	6.24
F	Vsb 261	7°26'26.1 N	100°14'01.7 E	6.80	0.19	0.38	N	18.43	28.40	0.00	7.72
G	Vsb 271	7°30'48.5 N	100°10'38.9 E	8.45	0.15	0.13	N	22.52	29.20	0.00	7.58
H	Vsb 281	7°37'33.4 N	100°09'24.6 E	9.05	0.18	0.24	N	40.95	29.00	0.00	7.04
I	Vsb 291	7°46'52.7 N	100°07'23.0 E	8.00	0.21	0.20	N	22.52	29.00	0.00	7.21
J	Vsb 2101	7°46'47.9 N	100°11'47.8 E	8.55	0.15	0.22	N	10.24	29.20	0.00	6.96
K	Vsb 2111	7°47'52.6 N	100°15'56.2 E	8.65	0.27	0.22	N	20.48	30.00	0.00	7.07
L	Vsb 2121	7°47'50.1 N	100°17'03.8 E	8.85	0.29	0.22	N	20.48	30.00	0.00	7.10
M	Vsb 2131	7°34'50.1 N	100°18'20.6 E	7.50	0.75	0.32	N	34.81	30.40	0.00	5.97
N	Vsb 2141	7°27'46.5 N	100°24'41.6 E	8.65	0.20	0.23	N	36.86	29.20	0.00	6.52
O	Vsb 2151	7°15'15.39 N	100°28'47.55 E	9.00	0.21	0.21	N	30.71	30.40	0.00	7.29
P	Vsb 2161	7°06'50.9 N	100°33'23.9 E	7.00	0.63	0.40	N	24.57	29.00	1.00	7.39

2. Most probable number (MPN)

The distribution of *Vibrio* spp. and related organisms in the Songkhla lake basin is summarized in Table 3. Site M and site N exhibited the highest bacterial concentration, each exceeding 1,100 MPN/g, followed by site B with the 1,100 MPN/g. The elevated abundance in these locations likely reflects localized accumulation of organic matter. This organic matter can enhance the growth of indigenous bacteria^{15,16}.

In contrast, site D, G, and H indicated relatively low bacterial concentration, ranging from 43 to 93 MPN/g. Bacterial counts at the remaining sites varied between 150 and 460 MPN/g. These findings indicate that bacterial abundance is not evenly distributed across the basin but instead follows site-specific patterns, likely influenced by differences in environmental and physicochemical conditions.

Table 3.
Abundance of *Vibrio* spp. in Songkhla lake basin by Three-tube MPN method

Site	Isolates	Positive tubes			MPN/g	Site	Isolates	Positive tubes			MPN/g
		0.1	0.01	0.001				0.1	0.01	0.001	
A	Vsb111	3	2	2	210	H	Vsb 281	3	1	0	43
	Vsb121	3	3	2	1100	I	Vsb 291	3	3	1	460
B	Vsb122	3	3	1	460	J	Vsb 2101	3	3	1	460
C	Vsb 231	3	3	1	460	K	Vsb 2111	3	3	1	460
	Vsb 241	3	1	0	43	L	Vsb 2121	3	2	1	150
D	Vsb 242	3	2	0	93	M	Vsb 2131	3	3	3	>1100
E	Vsb 251	3	3	1	460	N	Vsb 2141	3	3	3	>1100
F	Vsb 261	3	3	1	460	O	Vsb 2151	3	3	1	460
G	Vsb 271	3	1	0	43	P	Vsb 2161	3	3	1	460

3. Identification of *Vibrio* spp. isolates

Bacterial identification from the Songkhla lake basin was determined by using the selective media, CHROMagar™ *Vibrio*, followed by multiplex PCR and MALDI-TOF MS (Table 4). Several *Vibrio* species and related organisms were detected, reflecting their natural abundance in the lake environment. Turbid tubes from the MPN that yielded colonies on TCBS agar confirmed the widespread presence of *Vibrio* spp. and associated bacteria in the water samples.

To specifically investigate *V. vulnificus*, turquoise colonies from CHROMagar™ *Vibrio* were further analyzed by multiplex PCR. The suspected isolates including Vsb111, Vsb121, Vsb241, Vsb242, Vsb251, Vsb261, Vsb2141, Vsb2151, and Vsb2161 tested positive for the 16S rRNA gene but negative for the *vhA* gene, which is specific for *V. vulnificus*. This result indicated that none of them were *V. vulnificus*.

MALDI-TOF MS analysis identified some isolates as *V. albensis*, while others could not be reliably identified at the species level. All these results suggested that the Songkhla lake basin is a low-prevalence area for *V. vulnificus*, with other *Vibrio* species being more commonly represented.

4. Occurrence of *V. albensis*

Among the isolates analyzed, some were identified as *Vibrio albensis* using MALDI-TOF MS. *V. albensis* belongs to the non-O1/non-O139 *Vibrio cholerae* (NOVC) group¹⁷ and naturally inhabits aquatic environments where it can also associate with marine animals. Phylogenetically, this species shares more than 80% similarity with *V. cholerae*, reflecting its close genetic relationship.

Table 4.
Bacterial identification from sampling sites around Songkhla lake basin

Site	Isolates	CHROMagar™ Vibrio ^b	PCR (Multiplex)		MALDI-TOF MS ^c
			16S rRNA	<i>vvhA</i>	
A	Vsb111	+	+	-	No
B	Vsb121	+	+	-	No
	Vsb122	-	ND	ND	ND
C	Vsb 231	-	ND	ND	ND
D	Vsb 241	+	+	-	<i>V. albensis</i>
	Vsb 242	+	+	-	<i>V. albensis</i>
E	Vsb 251	+	+	-	<i>V. albensis</i>
F	Vsb 261	+	+	-	<i>V. albensis</i>
G	Vsb 271	-	ND	ND	ND
H	Vsb 281	-	ND	ND	ND
I	Vsb 291	-	ND	ND	ND
J	Vsb 2101	-	ND	ND	ND
K	Vsb 2111	-	ND	ND	ND
L	Vsb 2121	-	ND	ND	ND
M	Vsb 2131	-	ND	ND	ND
N	Vsb 2141	+	+	-	No
O	Vsb 2151	+	+	-	No
P	Vsb 2161	+	+	-	<i>V. albensis</i>

^aTCBS agar: + (Green colony), - (Yellow colony),

^bCHROMagar™ Vibrio : + (Green to turquoise colony), - (Purple and white colony)

^cMALDI-TOF MS: No (No Organism Identification Possible)

: ND (Not determine)

Although *V. albensis* is primarily considered an environmental bacterium, previous reports have documented its ability to infect humans¹⁸. Clinical cases have included gastroenteritis and septicemia, particularly in immunocompromised individuals. However, knowledge regarding its infection mechanisms and virulence factors remains limited compared with well-studied pathogenic *Vibrio* species¹⁹.

The detection of *V. albensis* in the Songkhla lake basin highlights the ecological diversity of *Vibrio* spp. in this environment. While its clinical relevance is less established than that of *V. vulnificus* or *V. parahaemolyticus*, its occurrence in a major aquaculture hub suggests the need for continued monitoring and further investigation into its potential pathogenicity.

5. Prevalence of *V. vulnificus* in relation to salinity

Although high concentrations of *Vibrio* spp. and related organisms were detected across the sampling sites, no *V. vulnificus* isolates were confirmed. Previous studies have demonstrated that both temperature and salinity strongly influence the ecology and life cycle of *V. vulnificus*²⁰. This species is known to proliferate over a wide salinity range, typically between 5 and 25 ppt²¹. In contrast, the salinity of the brackish water samples collected from the Songkhla lake basin during this study ranged from 0 to 1 ppt, which is below the optimal threshold for *V. vulnificus* growth.



Climatic conditions during the sampling period likely contributed to this observation. According to the Thai Meteorological Department, the northeast monsoon brings humid air from the Gulf of Thailand between October and February, often resulting in tropical depressions, storms, or typhoons that generate heavy rainfall in southern Thailand, including the Songkhla region²². The influx of freshwater during this period likely reduced salinity in the lake, creating an environment less favorable for *V. vulnificus* proliferation.

These findings suggested that in the Songkhla Lake Basin, *V. vulnificus* occurrence may be primarily regulated by salinity rather than temperature or organic matter availability. Consequently, seasonal fluctuations in salinity should be considered a critical factor when assessing the risk of *V. vulnificus* outbreaks in this ecosystem.

6. Environmental Factors Influencing Distribution

The distribution of *Vibrio* spp. in the Songkhla lake basin appeared to correlate with several physicochemical parameters of the water. For example, isolates Vsb2131 (Site M) and Vsb2141 (Site N) were recovered from areas with dissolved oxygen (DO) levels of 7.50 and 8.65 mg/L, respectively, where bacterial concentrations exceeded 1,100 MPN/g. As facultative anaerobes, *Vibrio* spp. and other indigenous aquatic bacteria do not require high DO for growth²³, which may explain their persistence in these environments.

Nutrient levels, particularly ammonia and nitrite, were also associated with bacterial distribution. Isolate Vsb122 was obtained from a site B with elevated ammonia (8.62 mg/L), while isolate Vsb121 was found at the same site where nitrite reached 1.41 mg/L. Both compounds are byproducts of protein decomposition in aquatic systems. Their accumulation can stimulate microbial growth by serving as nitrogen sources^{15,16}.

pH also appeared to influence bacterial abundance. Site B, with the lowest pH value (5.63), still supported concentrations up to 210 MPN/g. This suggests that *Vibrio* spp. and related bacteria are capable of adapting to suboptimal pH conditions, particularly in environments rich in organic matter.

Salinity was another key factor. Sites with low salinity (0.00 ppt) nevertheless contained bacterial concentrations exceeding 1,100 MPN/g, indicating that various *Vibrio* spp. and marine bacteria can thrive in both estuarine and nearly freshwater conditions. Temperature likely further supported this growth. Previous studies have shown that 25–35 °C provides favorable conditions for *Vibrio* proliferation¹⁰, consistent with the range observed in this study (28–30 °C).

Overall, these findings demonstrate that *Vibrio* spp. are highly adaptable and capable of persisting under diverse environmental conditions in the Songkhla Lake Basin. The interplay of nutrient availability, pH, salinity, and temperature collectively shapes their distribution and abundance, reinforcing the importance of environmental monitoring in managing microbial risks in aquaculture ecosystems.

Conclusion:

This study demonstrates the first evidence linking the distribution of *Vibrio* spp. in the Songkhla lake basin to water quality parameters. Key factors, including ammonia, nitrite, and temperature were strongly associated with bacterial diversity and abundance. DO and pH also influence growth directly. These findings highlight the importance of organic matter dynamics in shaping microbial communities within the basin.

Although *V. vulnificus* was not detected, the widespread presence of other *Vibrio* spp. and related microorganisms underscores the ecological significance of this environment and the potential risks to public health and aquaculture. Continuous monitoring of pathogenic *Vibrio* species is therefore essential to support sustainable aquaculture practices and safeguard seafood safety in this important ecosystem.



Acknowledgements:

This project is funded by the National Research Council of Thailand (NRCT). The funding is also supported by the Faculty of Science, Prince of Songkhla University. In addition, this study was supported by the Division of Biological Science, Faculty of Science, Prince of Songkla University, for research facilities.

References:

1. Choi G, Choi SH. Trends Microbiol. 2022;30:1205-1206.
2. Correa Velez KE, Norman RS. Front. Microbiol. 2021;12:754683.
3. Thompson Fabiano L, Iida T, Swings J. Microbiol. Mol. Biol. Rev. 2004;68:403-431.
4. Chandrakala N, Priya S. IJSRSET conference. 2017;3:1-9.
5. Hernández-Cabanyero C, Sanjuán E, Mercado L, Amaro C. Fish Shellfish Immunol. 2023;142:109131.
6. Hazards EPoB, Koutsoumanis K, Allende A, Alvarez-Ordóñez A, Bolton D, Bover-Cid S, *et al.* EFSA Journal. 2024;22:e8896.
7. Kiratisin P, Leelaporn A, Sangruchi T. Asian Biomed. 2012;6:495-502.
8. Naknaen A, Ratsameepakai W, Suttinun O, Sukpondma Y, Khan E, Pomwiset R. Toxins (Basel). 2021;13:631.
9. Jauregui I, Chiabai A, Neumann MB. Environ. Impact Ass. Rev. 2026;116:108126.
10. Sampaio A, Silva V, Poeta P, Aonofriesei F. DEI. 2022;14:97.
11. Geisser AH, Scro AK, Smolowitz R, Fulweiler RW. Front. Mar. Sci. 2025;12:2025.
12. Heuer H, Krsek M, Baker P, Smalla K, Wellington EM. Appl Environ Microbiol. 1997;63:3233-3241.
13. Panicker G, Myers ML, Bej AK. Appl Environ Microbiol. 2004;70:498-507.
14. El-Shafai SA, El-Gohary FA, Nasr FA, van der Steen NP, Gijzen HJ. Aquac. 2004;232:117-27.
15. Trach Y, Trach R, Kuznietsov P, Pryshchepa A, Biedunkova O, Kiersnowska A, *et al.* Sustainability. 2024;16:5835.
16. Zhang J-M, Fu B, Li Y-c, Sun J-H, Xie J, Wang G-J, *et al.* Aquac. 2023;562:738784.
17. Gherlan GS, Lazar DS, Florescu SA, Dirtu RM, Codreanu DR, Lupascu S, *et al.* Arch Clin Cases. 2025;12:5-16.
18. Ahmed AOE, Ali GA, Hassen SS, Goravey W. IDCases. 2022;29:e01551.
19. Araj GF, Taleb R, El Beayni NK, Goksu E. J Infect Public Health. 2019;12:712-3.
20. Martinez-Urtaza J, Bowers, JC, Trinanes J, DePaolo A. Food Res Int. 2010;43:1780-1790.
21. Fernández-Juárez V, Riedinger DJ, Gusmao JB, Delgado-Zambrano LF, Coll-García G, Papazachariou V, Herlemann DPR, Pansch C, Andersson AF, Labrenz M, Riemann L. MBio. 2024;15:e01569-24.
22. Noppradit P, Pradit S, Muenhor D, Doungsuwan N, Whangsani U, Sama N, Towatana P. IJAT. 2021;21:1507-1520.
23. Schultz P, Urban NR. Ecol. Model.. 2008;210:1-14.



PERFORMANCE TESTING OF A URINE MICROALBUMIN DIP TEST STRIPS DEVELOPED FOR PRELIMINARY KIDNEY DISEASE SCREENING

Umaporn Pimpitak^{1*}, Wanwisa Poonlapdecha² Anumart Buakeaw¹, Sirirat Rengpipat² and Kittinan Komolpis^{1,2,3}

¹The Institute of Biotechnology and Genetic Engineering, Chulalongkorn University, Bangkok, 10330 Thailand

²Qualified Diagnostic Development Center, Chulalongkorn University, Bangkok, 10330 Thailand

³Food Risk Hub, Research Unit of Chulalongkorn University, Bangkok 10330, Thailand

*Corresponding author. E-mail: Umaporn.p@chula.ac.th

Abstract:

This study describes the development of a novel lateral flow dipstick assay for the rapid screening of chronic kidney disease (CKD). The assay utilizes gold nanoparticles as a signal and is based on competitive antigen-antibody binding for the detection of microalbumin in urine, a key indicator of CKD. This point-of-care test is designed for convenient initial screening, particularly for microalbuminuria. The qualitative colorimetric dipstick, with a cutoff value of 20 µg/mL, provides results based on visual inspection of the color change, eliminating the need for specialized personnel. The method is cost-effective, provides rapid results, and can be implemented in various healthcare settings. In a study of 237 urine samples, the dipstick assay showed agreement with a standard reference method in 229 samples (51 positive, 178 negative), while 8 samples yielded discordant results. Statistical analysis revealed a sensitivity of 87.93%, a specificity of 99.44%, and an accuracy of 96.62% for the urine microalbumin dipstick. These results suggest that this dipstick assay is a promising tool for CKD screening by monitoring urine albumin levels for microalbuminuria, enabling physicians to make timely decisions regarding patient care. Positive results should be further confirmed by standard laboratory testing.

Introduction:

Chronic Kidney Disease (CKD) is a major public health challenge in Thailand. Patients with end-stage CKD often require hemodialysis or peritoneal dialysis. Early detection of declining kidney function is crucial, and monitoring protein leakage in urine is essential for assessing kidney health. Normally, the kidneys reabsorb proteins during filtration, preventing their excretion in urine. The presence of protein in the urine indicates a potential risk of CKD or other kidney diseases, which can severely impact health.

A standard and accurate method for assessing proteinuria involves analyzing protein leakage in urine over a 24-hour period. Albumin is the primary protein excreted; microalbuminuria is defined as albumin excretion in the range of 30-300 mg per 24 hours. Quantitative measurement of albumin in urine in clinical laboratories typically relies on immunoassays, such as immunoturbidimetry, immunofluorescence, ELISA, and radioimmunoassay. However, these methods require significant quantities of antibodies, expensive instrumentation, and trained personnel, leading to high costs and lengthy turnaround times.

The Microalbumin Dip Test Strip offers a rapid, point-of-care solution for detecting microalbumin in urine using a lateral flow immunochromatographic assay. This test is suitable for early-stage kidney disease screening by healthcare professionals and for convenient at-home testing. With a microalbumin detection cutoff value of 20 µg/mL, the test strip eliminates the need for complex analytical equipment. Results are available within 5-10 minutes by simply dipping the strip into urine for 10 seconds, enabling the preliminary



identification of kidney disease (microalbuminuria) in patients. Therefore, this study aims to assess the efficacy of a novel dip strip test for albumin detection in urine and to compare its performance against standard laboratory methods for the screening of individuals at risk of chronic kidney disease.

Methodology:

Preparation of Gold Nanoparticle and Monoclonal Antibody Conjugates

The monoclonal antibody (mAb) against human albumin was obtained from IBGE, Chulalongkorn University. The GNP-mAb conjugate was prepared following a previously described method (Pimpitak et al., 2020). Briefly, the optimal mAb to GNP ratio was first determined using the sodium chloride precipitation method. This ratio was then used for GNP-mAb conjugation.

To prepare the conjugate, 10 mL of mAb solution at the optimized concentration was added dropwise to 100 mL of the GNP solution. The mixture was gently stirred for 30 minutes at room temperature. Subsequently, 10 mL of 10% bovine serum albumin (BSA) in 20 mM sodium borate buffer, pH 8.2, was added. After gentle mixing for 10 minutes, the solution was centrifuged at $25,000 \times g$ at 4°C for 30 minutes. The resulting GNP-mAb conjugate pellet was washed three times with 20 mM sodium borate buffer containing 0.01% thimerosal. The conjugate solution was stored at 4°C until use.

Preparation of Dip Test Strip

The dip test strip comprised a 4×17 mm sample pad (Whatman® Standard 17; Whatman, Kent, UK), a 4×10 mm conjugate pad (Whatman® GF33; Whatman, Kent, UK), a 4×25 mm analytical pad AE 99 (GE Healthcare), and a 4×17 mm adsorption pad (Whatman® CF7; Whatman, Kent, UK). Human serum albumin (HSA) (4 mg/mL) and goat anti-mouse immunoglobulin (1 mg/mL) (Jackson ImmunoResearch, USA) were applied to the analytical pad at the test line (T-line) and control line (C-line) using a BioJet HR™ Non-Contact Solenoid Dispenser coupled with an XYZ3210 Dispense Platform (Biodot, CA, USA) at a flow rate of $1 \mu\text{L}/\text{cm}$. The GNP-mAb conjugate was applied to the conjugate pad at a flow rate of $15 \mu\text{L}/\text{cm}$. All pads were dried at 40°C for 30 minutes and then assembled onto a 4×60 mm plastic backing card (MIBA-080; DCN, CA, USA) in a conventional layout (Figure 1A) and covered with transparent plastic tape. The test strips were then placed in a sealed aluminum foil bag containing silica gel and stored in a humidity-controlled chamber ($\leq 20\%$ relative humidity) at room temperature until use.

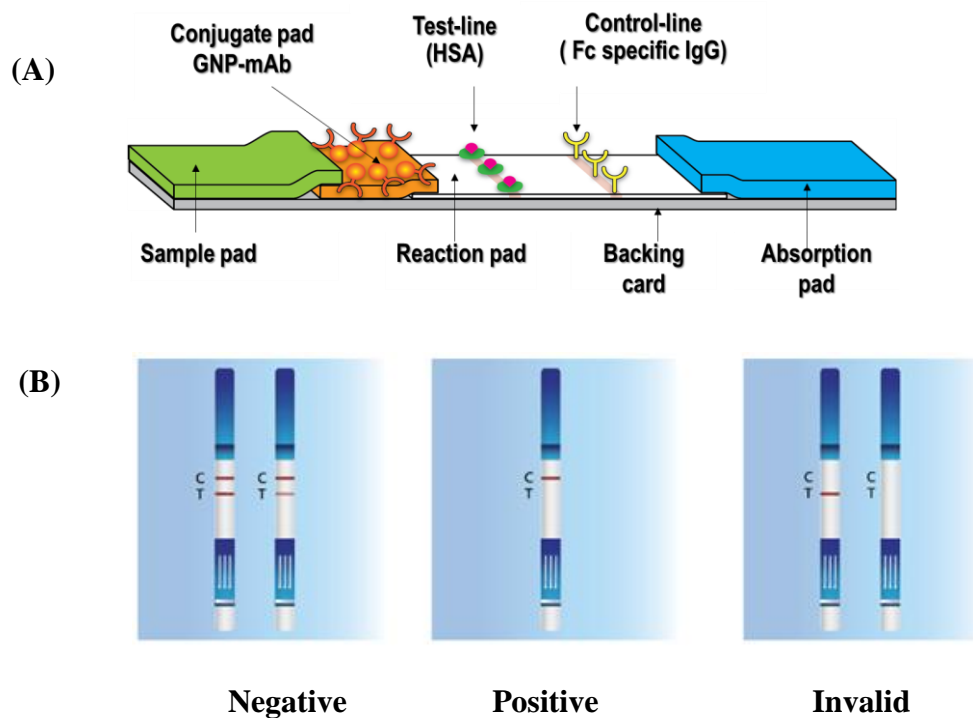


Figure 1.

(A) Schematic diagram of the microalbumin dip test strip. (B) Interpretation of test results.

Clinical performance study

The performance of the dip test strips was evaluated using urine samples with known albumin concentrations, as quantified by a standard microalbumin turbidimetric immunoassay.

Performance parameters were defined and calculated as shown in Tables 1 and 2.

Table 1.
Definition of Test Result

Dip Strip Test**	Immunoturbidimetry*		
	Positive	Negative	total
Positive	TP (True positive) = 51	FP (False positive) = 1	(TP+FP) = 52
Negative	FN (False negative) = 7	TN (True negative) = 178	(FN+TN) = 185
total	(TP+FN) = 58	(FP+TN) = 179	N = 237

* Positive when microalbuminuria > 20 µg/mL and negative when microalbuminuria ≤ 20 µg/mL

** Positive when the cherry red color was not observed at the T-line and negative when the cherry red color was observed at the T-line. In all cases, a cherry red color had to be observed at the C-line; otherwise, the test was classified as invalid.



Table 2.
Parameters Used for Dip Strip Test Performance.

Parameter	Calculation
Estimated Accuracy (%)	$[(TP+TN)/(N)] \times 100$
Estimated Specificity (%)	$[TN/(FP+TN)] \times 100$
Estimated Sensitivity (%)	$[TP/(TP+FN)] \times 100$
False Positive (%)	$[FP/(TP+FP)] \times 100$
False Negative (%)	$[FN/(FN+TN)] \times 100$
Based on evaluation specimens with disease prevalence (%)	$[(TP+FN)/(N)] \times 100$
Positive Predictive Value (PPV)	$[TP/(TP+FP)] \times 100$
Negative predictive value (NPV)	$[TN/(FN+TN)] \times 100$

Results and Discussion:

Clinical Performance of Microalbumin Dip test strips.

In-house produced Microalbumin Dip Test Strips were tested in a laboratory controlled according to ISO 13485:2016. Results were compared to a standard immunoturbidimetric method (gold standard) performed by an ISO 15189:2012-certified laboratory (Table 1). Relative accuracy (AC), specificity (SP), sensitivity (SE), positive predictive value (PPV), and negative predictive value (NPV) were calculated using the equations in Table 2.

The dip test strip's efficiency was assessed using urine samples from patients at the Center of Excellence in Critical Care Renal Disease, Chulalongkorn Hospital, Thai Red Cross Society. Figure 2 illustrates the dip test strips being tested in urine. Of the 237 samples, 51 tested positive and 178 tested negative by both the dip test strip and the standard method. Eight samples yielded discordant results (Table 1). Analysis of the test results (Table 3) revealed a sensitivity of 87.93%, a specificity of 99.44%, and an accuracy of 96.62%.

These results demonstrate that the developed prototype dip test strips are suitable for microalbuminuria detection in the early stages of CKD. The high sensitivity and low false negative rate (3.8%) indicate the potential of this test for early and accurate diagnosis.

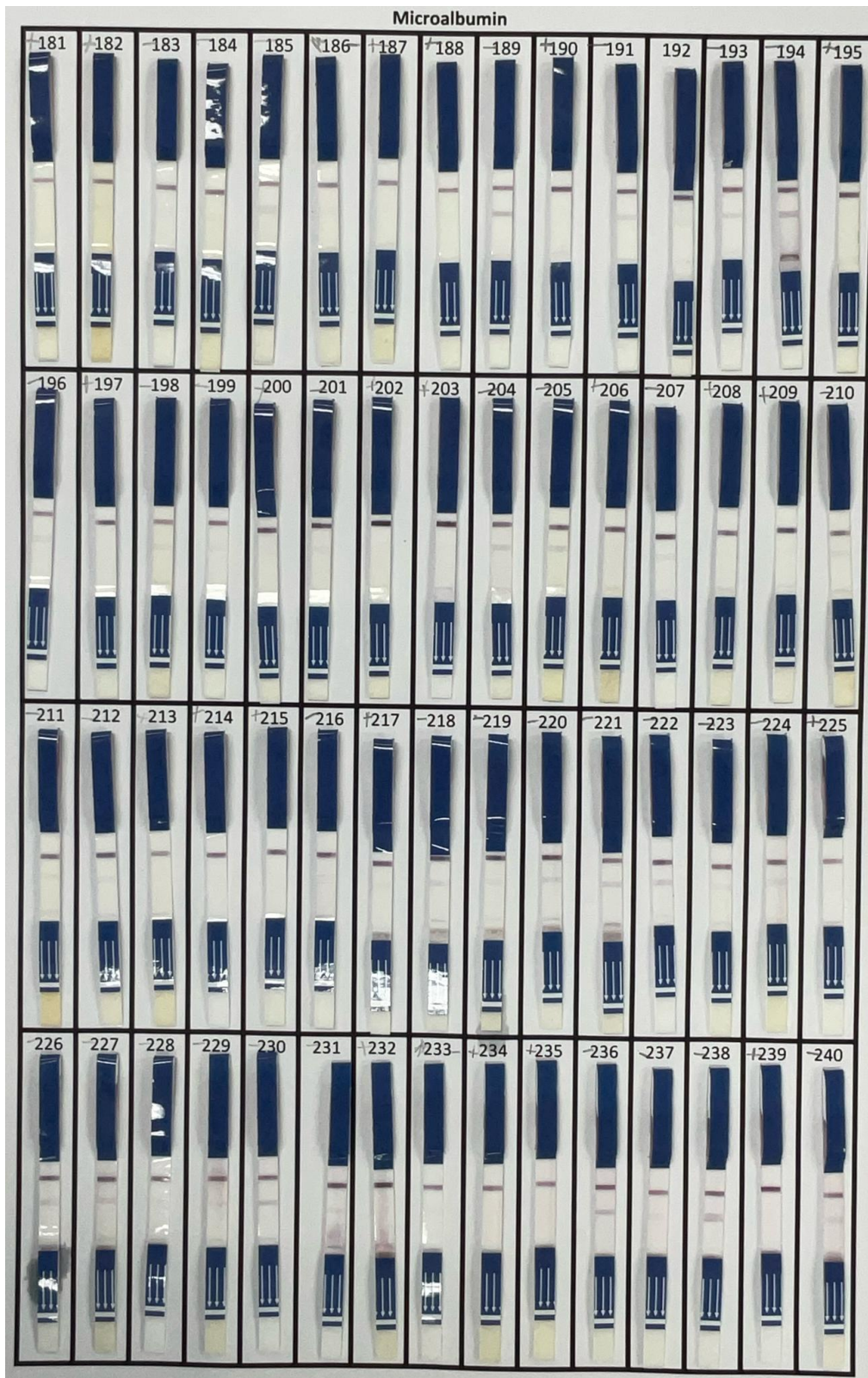


Figure 2
shows an example of microalbumin dip test strips when tested with a urine sample.



Table 3.
Clinical Performance of Microalbumin Dip Strip Test.

Parameter	
Number of samples	237
Estimated Accuracy (%)	96.62
Estimated Specificity (%)	99.44
Estimated Sensitivity (%)	87.93
False Positive (%)	1.9
False Negative (%)	3.8
Based on evaluation specimens with disease prevalence (%)	24.5
Positive Predictive Value (PPV) (%)	98.1
Negative predictive value (NPV) (%)	96.2

Conclusion:

The developed urine microalbumin dip test strips offer a promising point-of-care tool for early screening of chronic kidney disease, particularly in resource-limited settings. Early detection of kidney dysfunction is crucial for enabling timely interventions and lifestyle modifications to slow the progression of CKD. These dip test strips have the potential to improve patient outcomes and reduce the burden of CKD, especially in underserved communities.

Further research should focus on evaluating the long-term stability and shelf life of the dip test strips under various storage conditions. This is essential to ensure the reliability and effectiveness of the test in real-world settings, particularly in areas with varying climates and limited access to controlled storage facilities.

Acknowledgements:

The authors gratefully acknowledge the Excellence Center for Critical Care Nephrology, King Chulalongkorn Memorial Hospital, for providing urine samples. This research was supported in part by funding from the Qualified Diagnostic Development Center, Chulalongkorn University, and the Institute of Biotechnology and Genetic Engineering, Chulalongkorn University.

References:

1. Comper WD, Osicka TM. Detection of urinary albumin. *Adv Chronic Kidney Dis.* 2005;12(2):170 – 176.
2. Jafar TH, Chaturvedi N, Hatcher J, Levey AS. Use of albumin creatinine ratio and urine albumin concentration as a screening test for albuminuria in an Indo-Asian population. *Nephrol Dial Transplant* 2007 Aug;22(8):2194-200.
3. Ruggenti P, Gaspari F, Perna A, Remuzzi G. Cross sectional longitudinal study of spot morning urine protein:creatinine ratio, 24 hour urine protein excretion rate, glomerular filtration rate, and end stage renal failure in chronic renal disease in patients without diabetes. *BMJ* 1998 Feb 14;316(7130):504-9.
4. Hasslacher, C. 1993. Clinical significance of microalbumin and evaluation of the micral-test. *Clin Biochem.* Volume 26(4). pp. 283-287



5. Roberts, WL., Calcote, CB., Cook CB., Gordon DL., Moore ML., Moore S., et al. 1998. Comparison of four commercial urinary albumin (microalbumin) methods: implications for detecting diabetic nephropathy using random urine specimens. *Clinica Chimica Acta*. 273: 21-33.
6. Vutthikraivit, N., Kiatamornrak, P., Boonkrai, C., Pisitkun, T., Komolpis, K., Puthong, S., Lumlertgul, N., Peerapornratana, S., Thanawattano, C., Tungsanga, S., Praditpornsilpa, K., Tungsanga, K., Eiam-Ong, S., and Srisawat, N. 2021. Development and validation of point-of-care testing of albuminuria for early screening of chronic kidney disease. *J Clin Lab Anal*. 35: e23729. (<https://doi.org/10.1002/jcla.23729>)



ITS-BASED IDENTIFICATION OF COMMON POACEAE SPECIES FOUND AROUND BANGKOK

Lilian Haidvogl^{1,2}, Umaphorn Siriwattanaku^{2,3}, Wanichaya Chaiwimol³, Wisuwat Songnuan^{2,3,4,*}

¹Graduate Program in Toxicology, Faculty of Science, Mahidol University, Bangkok, Thailand

²Systems Biology of Diseases Research Unit, Faculty of Science, Bangkok, Thailand

³Department of Plant Science, Faculty of Science, Mahidol University, Bangkok, Thailand

⁴Center of Excellence on Environmental Health and Toxicology (EHT), Bangkok, Thailand

*E-Mail: wisuwat.son@mahidol.ac.th

Abstract:

Poaceae species—the main contributors to pollen allergy within Thailand—have almost identical pollen, often only differing significantly in size, so grains cannot be discriminated at species level visually. Exact taxonomical identification of grasses, necessary for research, is only achieved by experts when the entire plant, including inflorescence, is available. As this is often unobtainable, and sequencing can be time-consuming, other ways to verify a sample's classification must be found. Here, we demonstrate a way of aiding in the identification of 15 common grass species found around the Bangkok area, based on PCR amplification of its conserved internal transcribed spacer (ITS) region. Using eight different primers, a unique amplification pattern was created for each species, allowing to distinguish between the grasses of the Panicoideae and Chloridoideae families. While the close resemblance of all collected ITS sequences does not allow for precise characterization, directed PCR amplification may be used as an immediate species indicator, before the sequencing results return and verify the identification. However, the scarcity of ITS sequences for Thai grasses limits further improvement of this method. It is therefore important to also expand relevant databases to aid development of better processes, improving speed and quality of research.

Introduction:

The number of people experiencing allergic reactions to grass pollen in Asia is increasing¹⁻³, making it the third most common cause of airborne allergen-related allergies in Thailand. Palynological and allergological research has mostly focused on Western countries, with limited data, especially long-term, available on South-East Asia (SEA)⁴⁻⁶. This scarcity poses hurdles, given that the predominant allergenic plants differ depending on the geographical location. Consequently, there is a lack of regionally relevant data and specific allergenic components, and new emerging allergenic species remain inadequately studied^{7,8}. A key challenge lies in the first step, identification of relevant Poaceae species.

For this, it is essential for pollen research to determine the composition of a sample accurately. Traditionally, this is achieved through microscopic examination and comparison to known references. Poaceae species, however, lack distinctive differentiating features between pollen grains, often only varying significantly in size. Hence, this method is prone to overlooking contaminations and cannot discern different grasses accurately. Further, grass identification at species level is difficult, necessitating trained experts and mostly the entire plant including blade, sheath and most importantly inflorescence. An alternative to this expertise-dependent and labor-intensive process is DNA sequence analysis⁹⁻¹¹, which offers improved detection for different species from any part of a plant sample^{12,13}.

Identification through DNA barcoding¹⁴⁻¹⁶, using the internal transcribed spacer (ITS) region, is particularly suitable. The ITS region is present in all plants and comprises the standardized short sequences ITS1, 5.8S, and ITS2, located within the ribosomal RNA (rRNA) gene cluster. These regions, spanning approximately 590 to 630 base pairs, are easily



isolated and characterized by DNA sequencing, making them effective for species identification^{17–19}.

Sending each sample for sequencing is time-consuming and costly, so a fast, laboratory-based verification alternative should be available to identify species commonly dealt with within the lab. Due to the vast diversity of the Poaceae family, which encompasses over 11000 species (in 768 genera and 12 subfamilies)²⁰, out of which ca. 500 species are found within Thailand^{21,22}, a small assay that identifies all would not be feasible. Thus, this study focused on investigating species-specific digestion and amplification patterns to identify commonly found grasses around Bangkok.

Methodology:

Sample Collection

Plant samples—including leaves, inflorescence and roots—of Poaceae species found within the Bangkok area were collected. Species were identified by a taxonomic expert. DNA was extracted using a cold CTAB extraction protocol. Approximately 0.1 g of fresh tissue (blade, sheath, inflorescence, and/or pollen) sample was ground in liquid nitrogen and extracted with 2% CTAB buffer (1.5 M NaCl, 100 mM Tris-HCl pH 8, 20 mM EDTA pH 8.0, 0.2% β -mercaptoethanol) at a ratio of 1:20 (w/v).

Acquisition and Analysis of ITS Region Sequences

PCR amplification of extracted DNA with Vivantis[®] Taq DNA Polymerase (Vivantis, Malaysia) targeting the ITS region using the standard primers ITS4 (5'-TCCTCCGCTTATTGATATGC-3') and ITS5 (5'-GGAAGTAAAAGTCGTAACAAGG-3') (Macrogen Inc., Seoul, KOR) yielded amplicons of approx. 590–630 base pairs. Amplicon sequences were compared against the GenBank database using Blastn (BLAST[®], NLM, USA) and aligned using Multiple Sequence Alignment (Clustal Omega, EMBL-EBI, UK). Sequences were retrieved in RStudio 2024.04.2+764 using the packages ape for phylogenetics and comparative methods, and seqinr for nucleotide sequence management.

In Silico Cleaved Amplified Polymorphic Sequences (CAPS) assay

ITS sequences of collected specimens and publicly available GenBank sequences of interest were analyzed for interspecific differences. *In silico* restriction enzyme (RE) digestion was performed using the NEBcutter v3.0.19 tool (New England Biolab, UK) to identify the smallest number of restriction enzymes (RE) capable of producing distinguishable fragmentation patterns between the selected species.

Primer-Based Species Identification

Primers for differentiation were designed to amplify ITS regions of several specific species, thereby separating them into different groups via a decision tree based on the initially collected grass samples. The primer was deemed suitable if it successfully paired with standard ITS primer (ITS4 or ITS5) (Table 1). Further single species-specific primers were designed for final verification of each grass. PCR amplification was performed using genomic DNA as template, with each designed differentiation-primer and species-specific primer, in pair with the according standard ITS primer under conditions established for ITS amplification. PCR products were analyzed by gel electrophoresis on a 1.5% TAE-Gel, run at 100 V for 30 minutes.

Results and Discussion:

ITS Region

The internal transcribed spacer (ITS) region is widely used for DNA barcoding in plants, and hence may be used for taxonomical identification of Poaceae species when a matching

Table 1.

Differentiation primers. Primers designed for differentiation between the collected grass species, which were either designed as a pair with the standard primer ITS4 or ITS5

Primer	Sequence	Length (bp)	GC (%)	content	Tm (°C)
ITS5	5'-GGA AGT AAA AGT CGT AAC AAG G-3'	22	41.0		59.0
P1.	5'- GAA GGC GTC AAG GAI CAC -3'	18	55.6		60.3
P2.1.2	5'- CAA AAC AGA CIG TGA ACG TGT C -3'	22	45.5		61.9
P2.1.3	5'- GTG ACC CTT AAA CAA AAI AGA CC -3'	23	43.0		61.9
P3.2.	5'- GTG CAG CGA TIC TAT CTT AAT C -3'	22	41.0		59.0
P3.3	5'- GIA TGG CGT CAA GGA AAA C -3'	19	52.6		61.9

Reverse Primers with ITS 5 used as forward

Primer	Sequence	Length (bp)	GC (%)	content	Tm (°C)
ITS4	5'-TCC TCC GCT TAT TGA TAT GC-3'	20	45.0		60.0
P2.1.1	5'- GIC ICT GCA ICG AGA ACA AC-3'	20	50.0		61.0
P3.1	5'- GAA CAA CTT GIA GTC GCC CAC -3'	21	53.4		63.1
P2.2	5'- GTC ATC CAC CIT GTG CTG -3'	18	55.6		60.1

Forward Primers with ITS4 used as reverse reference sequence is available^{23–25}. However, for several of the 18 collected specimens in this study, reference sequences were either limited or entirely absent, therefore, confirmation of two species, *Cenchrus sp.* and *Echinochloa colona*, by sequencing was not possible.

The observed high conservation within the ITS region leads to close alignment between the different species and complicates determination of suitable unique segments for species differentiation. The collected ITS sequences span approximately 610–650 base pairs, but with the highly conserved 5.8S region^{26,27} excluded (159 bp in all collected sequences but for *Zea mays* with 160 bp), only 450–490 bp remain available for identifying RE cut sites. Further, this limited size and conserved nature of the ITS region restrict the number of unique primers that can be designed (Figure 1).

In most cases, sequence differences between individual species are limited to isolated single nucleotide polymorphisms (SNPs) rather than longer divergent regions, making it difficult to design primers with high specificity to one single species. This increases the likelihood of non-specific binding and cross-amplification. Additionally, the presence of point mutations due to geographical variation cannot be ruled out when working with field-



collected samples from different locations in the future^{28–30}. Nevertheless, in this study, the two specimens collected for *Urochloa reptans*, *Cynodon dactylon* and *Chloris barbata* at separate locations, all show identical sequences.

CAPS Assay

Digestion of collected samples using *Hinf*I, *Ngo*MIV, and *Bmg*BI restriction enzymes combined did not allow for unambiguous identification. Even within a single genus (*Urochloa*), analysis of ten sequences produced only six distinguishable CAPS profiles, demonstrating that genus-specific CAPS patterns are not feasible, as considerable overlap exists between species. However, intraspecific consistency was observed, with specimens collected at different locations showing identical restriction patterns. The repetition of digestion profiles in several related and unrelated species prevents direct identification of collected grass samples, nevertheless.

While simultaneous digestion with multiple REs may increase the variability between patterns, it would also produce many fragments under 100 bp, difficult to separate using gel electrophoresis, and limiting its practicality. Other alternative restriction enzymes could improve species differentiation; however, due to the diversity within Poaceae, it is unlikely that a single enzyme (or set of enzymes) will resolve all taxa. It may be more practical to develop CAPS profiles using readily available enzymes and validate them for target species groups relevant to local biodiversity or allergen studies.

Primer-based Differentiation

Eight primers were designed to enable species identification using a minimal number of PCR reactions, ideally following a decision tree. Alternatively, all primers may be run simultaneously to reduce experiment duration, especially when analysing an individual sample. As Primer 2.1.3 produces identical results to Primer 2.1.2 it was found redundant and may be excluded from the protocol. Due to the highly conserved 5.8S rRNA region between the ITS1 and ITS2 region, most differentiation primers were designed in close proximity and if bound amplified one band between 420–620 bp in length. However, the performed PCR amplifications did not match the predictions.

Across all primer sets, at least two more species were amplified than the design intended, which may be attributed to genomic repeats and non-target binding, and unspecific primer binding possibly due to short primer length and high GC content. Regardless, 12 distinctive amplification patterns for the 15 grasses were produced, based on presence/absence and fragment length (Table 2). Patterns were shared between multiple species in the case of *Eriochloa procera*, *Panicum repens* and *Megathyrsus maximus*. While all three are found in the same tribe, *Panicaceae*, other species belonging to this tribe had different amplification patterns. *Urochloa reptans*, *Eleusine indica* and *Dactyloctenium aegyptium*, which belong to different subfamilies, were amplified by every tested primer.

The limited sample size likely means that future additional species may share amplification patterns. Still, the current primers offer preliminary guidance for species identification within a known confined area. For instance, *Cynodon dactylon*, the most common cause of airborne grass allergen sensitization in Thailand³¹, could be identified here through a distinct amplification pattern out of a group of 16 species.

To enable fast in-lab identification, the total extracted plant DNA rather than purified ITS amplicons was used and primers were validated using standard PCR conditions. This allowed amplification of large (>1000 bp) fragments, due to non-target genomic binding sites outside the ITS region. Further, some unexpected amplifications may be a result of minor but frequent polymorphisms between sequences. Subsequently, when applied to purified ITS-

region amplicons, several primers (e.g., P1, P2.2, P3.2) amplified all species tested, and this approach was therefore abandoned.

The main challenge encountered was the lack of primer specificity. Even primers designed to only align to a single species amplified multiple. Out of 13 primer pairs tested, only the *U. reptans*-specific primer pair demonstrated species specificity. Again, the high sequence conservation across the Poaceae ITS region complicates the design of species-specific primers. Consequently, using these differentiation primers may narrow down species identity within established collection sites, but they cannot provide definitive identification.

Table 2.

Amplification Pattern. Resulting amplicons after PCR-amplification with differentiation primers for each Poaceae sample. Red indicates no amplification, while blue indicates a successful amplification.

Sample	Abbr.	Primer								
		1	2.1.1	2.1.2	2.1.3	3.1	3.2.	2.2	3.3	ITS
<i>Eriochloa procera</i>	EP	500	600	600	600	500	450	0	0	600
<i>Panicum repens</i>	PR	500	600	600	600	500	450	0	0	600
<i>Cenchrus echinatus</i>	CE	0	0	0	0	0	450	0	0	600
<i>Cenchrus sp.</i>	CS	500	600	600	600	500	450	500, 1000	0	600
<i>Echinochloa colona</i>	ES	500	600	600	600	500	450	0	600	600
<i>Megathyrsus maximus</i>	MM	500	600	650	600	500	450	0	0	600
<i>Digitaria bicornis</i>	DB	0	0	0	0	500	450	0	0	600
<i>Urochloa reptans</i>	UR	500	600	600	600	500	450	500	600	600
<i>Eragrostis tenella</i>	ET	500	0	600	600	500	450	500	600	600
<i>Zoysia matrella</i>	ZM	0	0	600	600	500	0	0	0	600
<i>Eleusine indica</i>	EI	500	600	600	600	500	450	500	600	600
<i>Cynodon dactylon</i>	CD	500	0	650	600	1000	450	500	600	600

<i>Chloris barbata</i>	CB	0	0	600	600	0	0	500	600	600
<i>Dinebra panicea</i>	DP	0	0	0	0	0	0	0	0	600
<i>Dactyloctenium aegyptium</i>	DA	500	600	600	600	500	450	500	600	600



Figure 1.

Schematic overview of the standard primer (ITS5 and ITS4) and designed differentiation primer locations in the ITS region.

Conclusion:

Rapid and reliable identification of the multitude of grasses is critical, particularly in allergen research, where timely sample confirmation affects both study accuracy and the ability to collect pollen of interest. While DNA sequencing is the most accurate approach, it is time-consuming and not always feasible in lab settings.

This study demonstrates that PCR-based primer amplification and CAPS (cleaved amplified polymorphic sequences) analysis offers preliminary guidance for verifying species identity. Although no single assay differentiated all species, a combination of the methods may distinguish between the 15 tested grasses.

However, the results also highlight important limitations. The high sequence conservation within the ITS region significantly reduces primer specificity, and unpredictable amplification patterns across species indicate that each primer must be empirically validated for every sample. Furthermore, the method's utility is currently restricted by the lack of ITS reference sequences for Thai Poaceae species in public databases. Expanding the available sequence data will improve the possibilities for grass species verification.

This is not only important for environmental and allergy-related studies, but also for broader applications supporting ecological and climate-related research^{32,33}. As such, the ITS region remains valuable for plant identification in various stages of growth through sequencing and DNA barcoding¹⁸, however, its limitations for fast, in-lab assays suggest the need for additional or alternative loci formats in future development.

Acknowledgements:

The authors are grateful to Dr. Watchara Arthan (Mahidol University, Thailand) for kindly identifying the grass samples.

References:

1. Pawankar R, Canonica GW, Holgate ST, Lockey RF. Allergic diseases and asthma: a major global health concern. *Curr Opin Allergy Clin Immunol*. 2012;12(1):39. doi:10.1097/ACI.0b013e32834ec13b
2. Pawankar R, Wang JY, Wang JJ, et al. Asia Pacific Association of Allergy Asthma and Clinical Immunology White Paper 2020 on climate change, air pollution, and biodiversity in Asia-Pacific and impact on allergic diseases. *Asia Pac Allergy*. 2020;10(1). doi:10.5415/apallergy.2020.10.e11
3. Singh AB, Mathur C. Climate Change and Pollen Allergy in India and South Asia. *Immunol Allergy Clin North Am*. 2021;41(1):33-52. doi:10.1016/j.iac.2020.09.007
4. Muzalyova A, Brunner JO, Traidl-Hoffmann C, Damialis A. Forecasting Betula and Poaceae airborne pollen concentrations on a 3-hourly resolution in Augsburg, Germany: toward automatically generated, real-time predictions. *Aerobiologia*. 2021;37(3):425-446. doi:10.1007/s10453-021-09699-3
5. Ravindra K, Goyal A, Mor S. Pollen allergy: Developing multi-sectorial strategies for its prevention and control in lower and middle-income countries. *Int J Hyg Environ Health*. 2022;242:113951. doi:10.1016/j.ijheh.2022.113951
6. Sofiev M, Siljamo P, Ranta H, Rantio-Lehtimäki A. Towards numerical forecasting of long-range air transport of birch pollen: theoretical considerations and a feasibility study. *Int J Biometeorol*. 2006;50(6):392-402. doi:10.1007/s00484-006-0027-x
7. Asam C, Hofer H, Wolf M, Aglas L, Wallner M. Tree pollen allergens—an update from a molecular perspective. *Allergy*. 2015;70(10):1201-1211. doi:10.1111/all.12696
8. Smith M, Jäger S, Berger U, et al. Geographic and temporal variations in pollen exposure across Europe. *Allergy*. 2014;69(7):913-923. doi:10.1111/all.12419
9. Codina R, Crenshaw RC, Lockey RF. Considerations About Pollen Used for the Production of Allergen Extracts. *J Allergy Clin Immunol Pract*. 2015;3(5):676-682. doi:10.1016/j.jaip.2015.04.003
10. Codina R, Crenshaw RC, Esch RE. Evaluation and Interpretation of the Purity of Pollen Used to Manufacture Allergen Extracts. *J Allergy Clin Immunol*. 2017;139(2):AB123. doi:10.1016/j.jaci.2016.12.396
11. Jarupund P, Sinthuvanich C, Jantrakulroj P, Suwanphakdee C. Evaluation of grass pollen quality control for allergy test kit production using pollen morphological characters. *Plant Sci Today*. Published online June 11, 2023. doi:10.14719/pst.2257
12. Agency EM. *Specific Requirement for the Production and Control of Allergen Products: European Medicines Agency*. European Medicines Agency; 1994.
13. Chen S, Yao H, Han J, et al. Validation of the ITS2 Region as a Novel DNA Barcode for Identifying Medicinal Plant Species. *PLOS ONE*. 2010;5(1):e8613. doi:10.1371/journal.pone.0008613
14. Kraaijeveld K, de Weger LA, Ventayol García M, et al. Efficient and sensitive identification and quantification of airborne pollen using next-generation DNA sequencing. *Mol Ecol Resour*. 2015;15(1):8-16. doi:10.1111/1755-0998.12288
15. Leontidou K, Vernesi C, De Groeve J, Cristofolini F, Vokou D, Cristofori A. DNA metabarcoding of airborne pollen: new protocols for improved taxonomic identification of environmental samples. *Aerobiologia*. 2018;34(1):63-74. doi:10.1007/s10453-017-9497-z
16. Longhi S, Cristofori A, Gatto P, Cristofolini F, Grando MS, Gottardini E. Biomolecular identification of allergenic pollen: a new perspective for aerobiological monitoring? *Ann Allergy Asthma Immunol*. 2009;103(6):508-514. doi:10.1016/S1081-1206(10)60268-2

17. Hebert PDN, Cywinska A, Ball SL, deWaard JR. Biological identifications through DNA barcodes. *Proc R Soc Lond B Biol Sci.* 2003;270(1512):313-321. doi:10.1098/rspb.2002.2218
18. Kress WJ. Plant DNA barcodes: Applications today and in the future. *J Syst Evol.* 2017;55(4):291-307. doi:10.1111/jse.12254
19. Wasti QZ, Sabar MF, Farooq A, Khan MU. Stepping towards pollen DNA metabarcoding: A breakthrough in forensic sciences. *Forensic Sci Med Pathol.* Published online December 26, 2023. doi:10.1007/s12024-023-00770-8
20. Soreng RJ, Peterson PM, Romaschenko K, et al. A worldwide phylogenetic classification of the Poaceae (Gramineae) II: An update and a comparison of two 2015 classifications. *J Syst Evol.* 2017;55(4):259-290. doi:10.1111/jse.12262
21. Chayamarit K, Pooma R, Pattharahirantricin N. *A Checklist of Plants in Thailand Vol. 1.* Office of Natural Resources and Environmental Policy and Planning; 2014:182-206.
22. Sungkaew S, Suddee S, Wong KM, Teerawatananon A. *Thyrsostachys* (Poaceae: Bambusoideae) in Thailand: taxonomy, lectotypification and natural distribution. *Thai For Bull Bot.* 2021;49(1):49-56. doi:10.20531/tfb.2021.49.1.05
23. Birch JL, Walsh NG, Cantrill DJ, Holmes GD, Murphy DJ. Testing efficacy of distance and tree-based methods for DNA barcoding of grasses (Poaceae tribe Poeae) in Australia. *PLOS ONE.* 2017;12(10):e0186259. doi:10.1371/journal.pone.0186259
24. Krinitsina AA, Omelchenko DO, Kasianov AS, et al. Aerobiological Monitoring and Metabarcoding of Grass Pollen. *Plants.* 2023;12(12):2351. doi:10.3390/plants12122351
25. Omelchenko DO, Krinitsina AA, Kasianov AS, et al. Assessment of ITS1, ITS2, 5'-ETS, and trnL-F DNA Barcodes for Metabarcoding of Poaceae Pollen. *Diversity.* 2022;14(3):191. doi:10.3390/d14030191
26. Harpke D, Peterson A. 5.8S motifs for the identification of pseudogenic ITS regions. *Botany.* 2008;86(3):300-305. doi:10.1139/B07-134
27. Jobes DV, Thien LB. A Conserved Motif in the 5.8S Ribosomal RNA (rRNA) Gene is a Useful Diagnostic Marker for Plant Internal Transcribed Spacer (ITS) Sequences. *Plant Mol Biol Report.* 1997;15(4):326-334. doi:10.1023/A:1007462330699
28. Graper AL, Noyszewski AK, Anderson NO, Smith AG. Variability in ITS1 and ITS2 sequences of historic herbaria and extant (fresh) *Phalaris* species (Poaceae). *BMC Plant Biol.* 2021;21(1):515. doi:10.1186/s12870-021-03284-z
29. Konieczny A, Ausubel FM. A procedure for mapping *Arabidopsis* mutations using co-dominant ecotype-specific PCR-based markers. *Plant J.* 1993;4(2):403-410. doi:10.1046/j.1365-313X.1993.04020403.x
30. Song J, Shi L, Li D, et al. Extensive Pyrosequencing Reveals Frequent Intra-Genomic Variations of Internal Transcribed Spacer Regions of Nuclear Ribosomal DNA. Vendramin GG, ed. *PLoS ONE.* 2012;7(8):e43971. doi:10.1371/journal.pone.0043971
31. Oncham S, Udomsubpayakul U, Laisuan W. Skin prick test reactivity to aeroallergens in adult allergy clinic in Thailand: a 12-year retrospective study. *Asia Pac Allergy.* 2018;8(2):e17. doi:10.5415/apallergy.2018.8.e17
32. Buters J, Clot B, Galán C, et al. Automatic detection of airborne pollen: an overview. *Aerobiologia.* Published online July 30, 2022. doi:10.1007/s10453-022-09750-x
33. Esterhuizen N, Berman DM, Neumann FH, et al. The South African Pollen Monitoring Network: Insights from 2 years of national aerospora sampling (2019–2021). *Clin Transl Allergy.* 2023;13(11):e12304. doi:10.1002/clt2.12304



ENHANCING SCOLIOSIS DETECTION USING AI: INTEGRATING DEEP LEARNING INTO THE MEDICAL FIELD

Pittayud Aursukitwattana,^{1*} Pakwalan Kiewwichai,² Sanghilan Limthong³,

¹Denla British School, Thailand

²King Mongkut's International Demonstration School, Thailand

³Concordian International School, Thailand

*e-mail: fringyronaldo@gmail.com

Abstract:

In the past, the study of biological conditions such as scoliosis relied heavily on physical detection through human eyes, with limited access to advanced technology. This often made it difficult for doctors to accurately identify and differentiate between each type of scoliosis, which are thoracic, thoracolumbar, and lumbar. Nowadays, with advancements in artificial intelligence, a deep learning image classification model can assist in recognizing these spinal curvatures more quickly and accurately. The model that is being used is the Xception model, trained using spinal X-ray images. The model achieved a validation accuracy of 68% and a test accuracy of 96%. This can potentially be introduced as a tool to aid in the detection of scoliosis. In the future, doctors can possibly compare their manual classification of scoliosis types with the model's predictions and discussed spinal.

Introduction:

Scoliosis is a spinal deformity that leads to an abnormal curvature and rotation of the spine.¹ Traditionally, it has been diagnosed through physical examinations and manual interpretation of X-ray images. These conventional methods, while foundational in medical practice, were limited by subjectivity and time consumption. In the past, healthcare settings did not have access to advanced diagnostic technologies. This makes early detection and precise classification of scoliosis type, including thoracic, thoracolumbar, and lumbar, more challenging.

With the advancement of artificial intelligence, particularly deep learning, the area of medical diagnostics has undergone a significant transformation. Deep learning, a branch of AI that simulates human neural processing, is now being utilized in hospitals to enhance the accuracy and speed of scoliosis detection.² By analyzing spinal X-rays, AI models can identify complex curvature patterns, predict disease progression, and support clinicians in classifying scoliosis types more efficiently than ever before.

The integration of AI into orthopedic diagnostics, especially for scoliosis, reflects a broader shift in modern medicine where data-driven tools are increasingly embedded into clinical workflows.³ As these technologies continue to evolve, their role in improving diagnostic precision, treatment outcomes, and healthcare efficiency becomes more critical.⁴ Scoliosis detection is just one example of how deep learning is reshaping the future of medical imaging and patient care.

Scoliosis classification plays an important role in spinal diagnostics and treatment planning. Clinically, scoliosis is often categorised based on the location of the spinal curvature, with thoracic, thoracolumbar, and lumbar types being the most common.⁵ Each type reflects a distinct pattern of spinal deviation observed in radiographic imaging. However, traditional diagnostic tools, such as manual interpretation of X-rays, can be limited by image quality and variability between practitioners. These limitations may hinder the early and accurate identification of scoliosis types, potentially delaying treatment, which might cause further damage. The integration of advanced technologies like deep learning has introduced a new level of precision in classification. This allows for more consistent analysis



of spinal curvature patterns and contributes to improved diagnostic accuracy and clinical outcomes.

A study by Zhu et al. demonstrates a method for the automated classification of scoliosis using spinal X-ray images.⁶ Deep learning techniques, particularly convolutional neural networks, are applied to analyze curvature patterns and vertebral alignment in the human body. The study shows that precise spatial features of spinal deviation, such as Cobb angle and curve location, are critical for the model to accurately classify scoliosis types.⁶ While there are numerous studies exploring the use of image processing and AI in medical imaging, many of these operate at a complex clinical or research level.⁶ Despite the progress, integration of AI-based scoliosis classification into a broader clinical setting remains limited, and accessibility outside of specialized institutions is still evolving.

Methodology:

In this study, the Xception model was trained with a total of 129 spinal X-ray images. The model was trained on the Google Colab platform. The methodology includes dataset preparation, model training, and performance evaluation. Three anatomical types of scoliosis are being classified: thoracic, thoracolumbar, and lumbar. A total of 129 spinal X-ray images were used, with 40-43 images per category. These images were sourced from public repositories. The dataset was divided into 60% for training, 20% for validation, and 20% for testing.

To enhance the model's generalizability, augmentation techniques such as image rotation, zooming, and horizontal flipping were applied. The data was split into 60-20-20 to minimize the risk of overfitting and enhance the model's reliability. The model was trained over 17 epochs. Its performance was measured through the accuracy curve of training and validation.

Results and Discussion:

This research developed a deep learning model for automated scoliosis classification, demonstrating strong performance using radiographic images. The Xception model is used to categorize thoracic, thoracolumbar, and lumbar scoliosis types. The model achieved an overall accuracy of 96%, suggesting that it can accurately distinguish features between the three scoliosis types. This high accuracy demonstrates the model's capability to generalize to unseen data. When the dataset is augmented before the classification process, the model performs better in terms of generalizability. This is crucial for application in clinical practice.

Figure 1 displays the training and validation curves over 17 epochs. By epoch 17, the training accuracy steadily increased from 24% in the very first epoch to 96%. At the last epoch, the validation accuracy was 96%, with a sign of overfitting of the data. While both the training and validation loss curves steadily decreased, the training loss dropped more significantly. This demonstrates how well the model works with the provided dataset. Furthermore, the model's remarkable capability of generalizing unknown data is demonstrated in Figure 2, which displays an example of predictions in which 15 out of 16 images are accurately identified. This high accuracy suggests the model's potential to generalize unseen data within the available dataset.

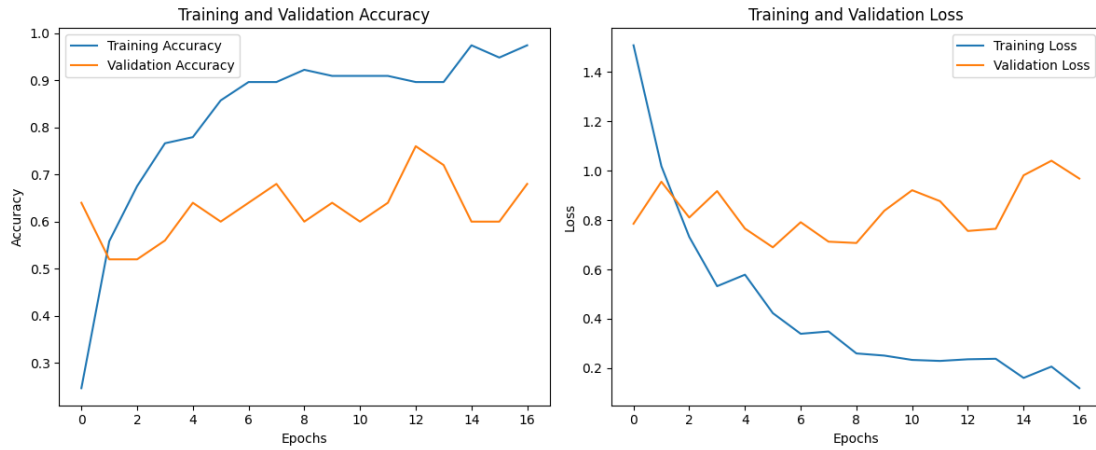


Figure 1.
Training and validation accuracy and loss curve

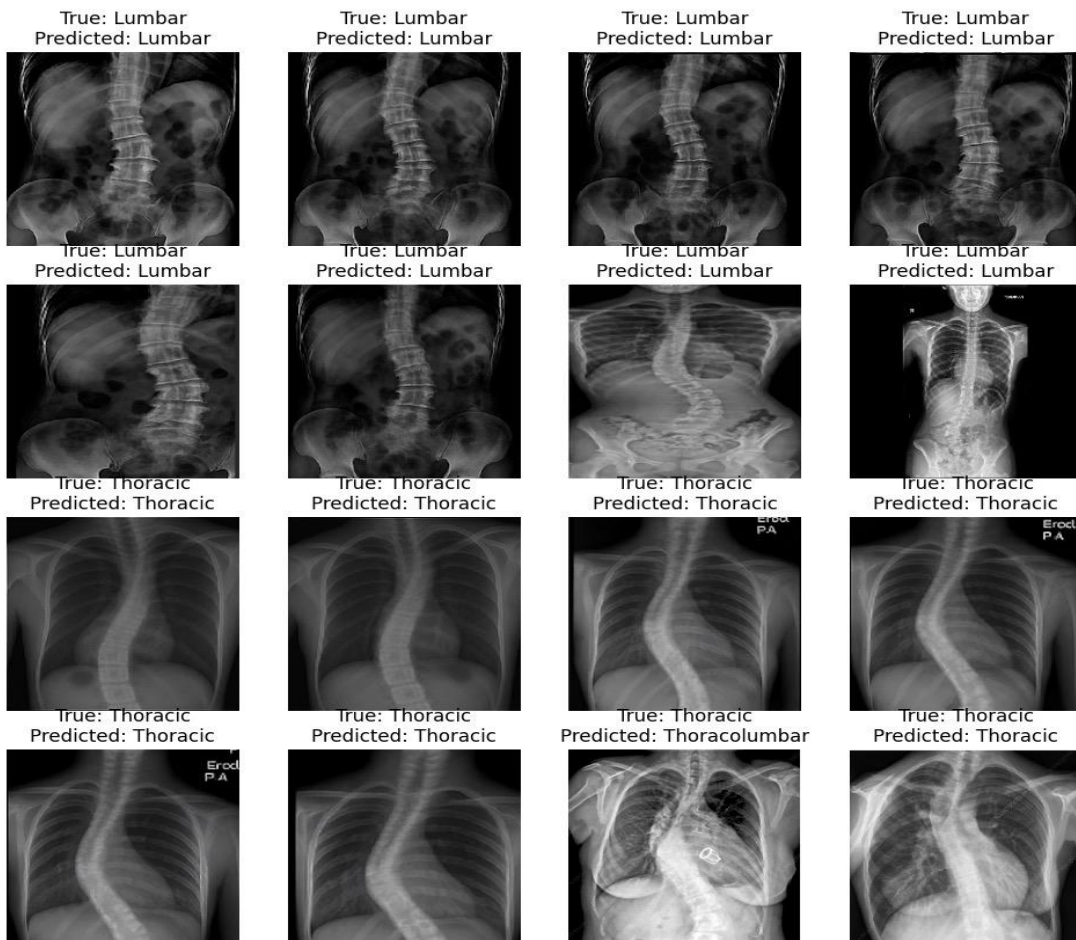


Figure 2.
Example of model predictions

A confusion matrix revealed strong classification performance across all three categories (thoracic, thoracolumbar, and lumbar scoliosis), though some overlap can be evident. The confusion matrix in Figure 3 shows that the model attains 100% accuracy in classifying thoracic scoliosis. This exceptional accuracy shows that the model can classify the features of the thoracic scoliosis well. However, there is a slight misclassification of

thoracolumbar and lumbar scoliosis. These results are consistent since the thoracolumbar curve exhibits features of both thoracic and lumbar abnormality, making it more challenging to classify. Also, some of the images that are being classified may lie on a spectrum rather than fitting into one specific category.

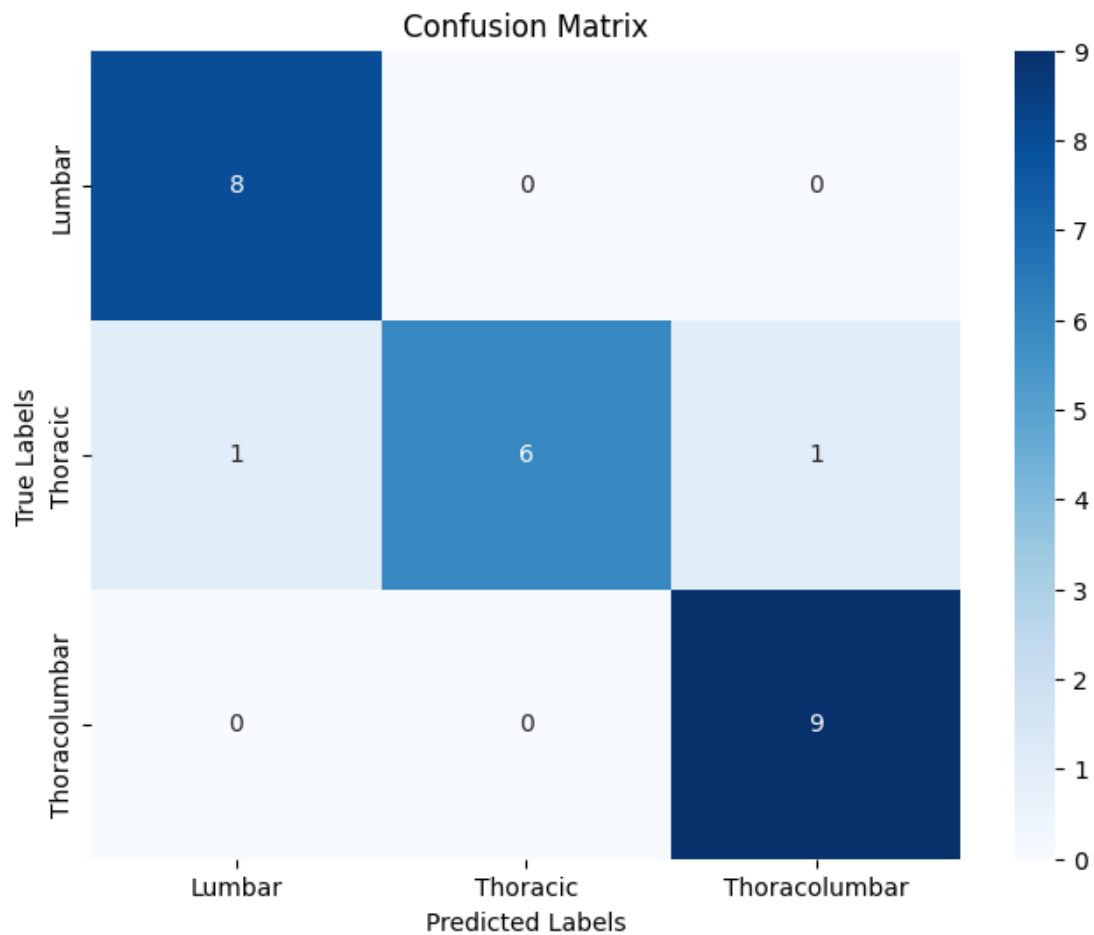


Figure 3.
Confusion matrix

Despite these minor misclassifications, the model can be highly applicable for real-world scenarios. Automated scoliosis classification using radiographic images presents a remarkable advancement in biomedical image analysis and diagnostic tools. Conventional classification of scoliosis mostly depends on manual interpretation by orthopedic surgeons or radiologists, which can be time-consuming.⁸ This diagnosis is difficult and subjective, especially for cases on a spectrum. In both clinical and remote locations, a 96% accurate AI-powered tool can be used as a decision support system, reducing diagnostic uncertainty and speeding up the screening process. This is highly beneficial in underdeveloped places with little access to a specialist.

The integration of these deep learning models with medical biotechnology tools suggests an advancement toward enhanced medical decision-making and precise diagnostics.⁹ The model can be improved by adding techniques like Grad-CAM. By making it easier to see what parts of the spinal imaging had the greatest influence on the model's prediction, this method can improve the interpretability of the model.¹⁰

Thus, the results indicate that our deep learning model is useful and accurate for medical diagnosis. This model has the potential to be a useful tool in orthopedic diagnostics



with additional validation on larger datasets and integration into easily accessible platforms. Its ability to automatically categorize different types of scoliosis makes an important contribution to the growing field of medical AI. It also demonstrates how deep learning can improve healthcare by providing a practical solution.

However, the data set is very small, which might cause overfitting and introduced bias to the model. Therefore, in future work, validation with the use of a larger and more diverse dataset collected from multiple hospitals to ensure that the model's generalizability across different groups of patients. In addition, X-ray images from different machines may vary in orientation, potentially influencing the model's performance. This model should be viewed as a diagnostic support tool, not replacing clinical expertise. Its integration into hospital workflows in the future could help doctors rapidly verify manual classifications, especially in hospitals with limited resources. Moreover, future improvements also should include additional evaluation metrics such as precision, recall, and F1-score to improve the reliability of accuracy and a more comprehensive evaluation. This would allow a more complete understanding of the model's performance and limitations. Cross-validation, such as k-fold, will also be included to increase generalization of the model.⁷

Conclusion:

This study explored the integration of a deep-learning image classification model in the medical field, focusing on the classification of types of scoliosis. The objective of the study was to use the advances in technology to aid in the detection of diseases in a medical way.

Three types of scoliosis have been classified using the Xception model: thoracic, thoracolumbar, and lumbar. The model was trained on a dataset of 129 images over 17 epochs. The Xception model achieved an accuracy of 96%. The model performed well in identifying thoracic; every image in this category was correctly identified.

This study demonstrates the potential of AI in enhancing clinical diagnostics. The model's predictions supported physicians in identifying and classifying scoliosis types more efficiently. This offers a supporting tool for the early detection of spinal deformities. In the future, by comparing the AI-generated classifications with their evaluations, doctors could cross-validate the result, investigate the misclassification, and refine diagnostic accuracy. This integration of deep learning into clinical workflows supports diagnostic consistency and informed decision-making.

Despite certain limitations, primarily related to the size of the dataset, the study demonstrates how AI can effectively enhance detection in medicine. By including a variety of datasets, future research may create platforms for broader clinical or medical use, evaluate long-term learning outcomes, and expand this model to include more classifications.

Overall, the results indicate that AI models developed in this work can significantly contribute to improving the identification of scoliosis. It can become a useful tool for doctors, especially for their accuracy, and reducing the time-consuming part of detection. While the findings indicate promising generalization capability, further testing on another separated datasets is required to confirm clinical applicability.

**References:**

1. Janicki J, Alman B. Paediatr Child Health. 2007;12:771–776.
2. Chakraborty C, Bhattacharya M, Pal S, Lee S. CRBIOT. 2023;7:100164.
3. Bajwa J, Munir U, Nori A, Williams B. Future Healthc J. 2021;8:188–194.
4. Sinha R. Discov Health Systems. 2024;3:1–14.
5. Harrop J, Naroji S, Maltenfort M, Ratliff J, Tjoumakaris S, Frank B, Anderson D, Albert T, Vaccaro A. Spine. 2011;36:21–25.
6. Zhu Y, Yin X, Chen Z, Zhang H, Xu K, Zhang J, Wu N. Spine Deformity. 2025;13:19–27.
7. Qiu J. AEMPS. 2024;99:69–72.
8. Liu D, Zhang L, Yang J, Lin A. Appl. Sci. 2023;13:3905.
9. Anyanwu E, Arowoogun J, Odilibe I, Akomolafe O, Onwumere C, Ogugua J. WJARR. 2024;21:2740–2752.
10. Zhang Y, Zhu Y, Liu J, Yu W, Jiang C. IEEE Internet Things J. 2025;12:3961–3970.



EVALUATION OF CHONDROCYTE CULTURE FORMATS FOR ENHANCING EARLY CARTILAGE MATRIX FORMATION

Matthuros Sonthisathaporn¹, Nattanan T-Thienprasert¹ and Chomdao Sinthuvanich^{1*}

Department of Biochemistry, Faculty of Science, Kasetsart University, Bangkok 10900, Thailand

*e-mail: chomdao.si@ku.th

Abstract:

Osteoarthritis (OA) is a chronic disease primarily affecting individuals over 60 years old, with a higher prevalence in females. The global incidence of OA is continuously rising due to aging populations and increasing rates of obesity and injury. Unlike other tissues, damaged cartilage has limited self-healing capabilities due to its avascular nature, low cell count, and abundant extracellular matrix (ECM). Current treatments for OA include surgical interventions such as drilling, subchondral abrasion, microfracture, and Autologous Chondrocyte Implantation (ACI). However, these approaches face challenges such as issues with cell handling and scaffold imperfections. This study aims to explore optimal *in vitro* culture conditions that support cartilage matrix production for potential application in cell-based therapies. Gene expression of Piezo2, ACAN, Col2A1 as well as glycosaminoglycan (GAG), DNA, and hydroxyproline content, were analyzed to identify which culture method best preserves the chondrocyte phenotype and promotes early-stage cartilage matrix synthesis. The results showed that the monolayer culture was superior in maintaining crucial gene expression. This culture also demonstrated enhanced extracellular matrix efficiency, as evidenced by significantly higher GAG/DNA and hydroxyproline/DNA ratios. These results suggest that monolayer culture provides a promising environment for *in vitro* cartilage matrix synthesis, paving the way for future injectable cell-based therapies for OA in both humans and animals.

Introduction:

Osteoarthritis (OA) is a chronic degenerative joint disease commonly found in the elderly, affecting small, medium, and large joints. It can occur in both males and females over the age of 60 years old, with the incidence rate in women being higher than that in men (Geng et al., 2023) and is a leading cause of disability among older adults. OA significantly impairs mobility and often requires costly treatments, especially joint replacement surgery in severe cases⁷. The knee joint, in particular, bears substantial mechanical load, and its articular surface is protected by cartilage tissue. This tissue has a thick layered structure of hyaline cartilage composed of chondrocytes embedded within an abundant extracellular matrix (ECM) containing water, collagen type II, and proteoglycans⁶. ECM plays a critical role in absorbing compressive forces and reducing friction during movement. These mechanical stimuli influence mechanosensitive ion channels, which in turn regulate mechanotransduction pathways crucial for cartilage maintenance and regeneration.

Chondrocytes express several types of mechanosensitive ion channels, including members of the Transient Receptor Potential (TRP) family and the recently identified Piezo channels, namely PIEZO1 and PIEZO2, which are involved in intracellular calcium regulation¹⁰. Additionally, Voltage-Gated Calcium Channels (VGCCs) mediate calcium influx in response to changes in membrane potential. Calcium ions (Ca²⁺) serve as vital second messengers in signaling pathways that control ECM synthesis. Specifically, Ca²⁺ can activate the MEK/ERK signaling pathway, which promotes GlcAT-I gene transcription by enhancing Sp1 binding to its promoter, thereby regulating glycosaminoglycan (GAG) synthesis². Furthermore, this signaling pathway also influences the expression of the SOX9 gene, which upregulates Col2A1, a key gene involved in collagen production (Sahu et al., 2020).

Currently, among the various treatment approaches for OA, only a limited number of surgical interventions are routinely recommended. Procedures including drilling, subchondral abrasion, and microfracture induce cartilage regeneration through the activation of bone marrow-derived mesenchymal stem cells; however, the regenerated tissue has consistently been reported as fibrocartilage, lacking the properties of native hyaline cartilage (Mitani et al., 2009). To address this critical need for functional cartilage regeneration, various tissue engineering methods have emerged. For instance, Autologous Chondrocyte Implantation (ACI), a tissue engineering method, allows for the regeneration of thick hyaline cartilage by implanting scaffold-embedded chondrocytes. However, concerns regarding scaffold adhesion and biocompatibility remain. The cell-sheet technique, a scaffold-free alternative, also regenerates thick hyaline cartilage by layering cultured chondrocyte sheets. However, its limitations include the fragility of single sheets, necessitating layering and prolonged culture periods¹⁴.

Recognizing these existing limitations in current cartilage regenerative strategies, especially regarding the quality of regenerated tissue, scaffold-related issues, and prolonged culture periods, this study aims to explore novel approaches by investigating the effects of various culture conditions on chondrocyte proliferation, extracellular matrix (ECM) production, and the expression of key cartilage-related genes in monolayer culture, ultimately working towards a simplified and efficient method for cartilage regenerative medicine.

Methodology:

Chondrocyte Isolation

Cartilage was collected from porcine knees and cut into 1 mm pieces under sterile conditions. The tissue was first incubated in chondrocyte culture medium containing 0.1% pronase at 37°C with 5% CO₂ for 1 hour to digest protein in the ECM of cartilage, followed by digestion in 0.1% collagenase type II under the same conditions for 14–16 hours to digest the collagen type II. The digested solution was filtered through 100 µm and 70 µm cell strainers, then centrifuged at 2,000 rpm for 15 minutes. The resulting cells were washed twice with phosphate-buffered saline (PBS) containing penicillin and streptomycin, followed by another centrifugation¹². The cell pellet was then resuspended in DMEM with HEPES buffer or HEPES buffer alone to achieve a final density of 1×10^8 cells/mL.

Cell culture

Cells were plated into T25 flasks containing 5 mL of chondrogenic medium at densities of 1×10^6 cells/mL and 5×10^5 cells/cm² for monolayer and cell sheet cultures, respectively. For pellet culture, 1 mL of cells was seeded at a density of 3×10^5 cells/mL in 15 mL conical tubes and centrifuged at 600 ×g for 5 minutes. The pellets were incubated overnight at 37°C with 5% CO₂. After incubation, the medium was replaced with high-glucose DMEM supplemented with HEPES buffer, 10% FBS, 0.4 mM L-proline, 0.25 mM ascorbic acid phosphate magnesium salt N-hydrate, 1 mM sodium pyruvate, and penicillin-streptomycin. The culture medium was changed every 3 days for a total of 7 days, after which the samples were subjected to biochemical analyses.

GAG Quantification

GAG content was measured using the dimethyl methylene blue (DMMB) assay. A 50-µL sample digested with papain in PBS (pH 7.5) was mixed with 200 µL of DMMB solution (46 µM DMMB, 40 mM NaCl, 40 mM glycine, pH 3). Absorbance was read at 525 nm. A standard curve was generated using chondroitin sulfate at 0–40 µg/mL in PBS⁵.



DNA Quantification

A 40- μ L papain-digested sample was mixed with 200 μ L of Hoechst 33258 dye (0.2 μ g/mL) in a 96-well black plate, in triplicate. Calf thymus DNA (0–1 μ g/mL in PBS) was used as the standard. Fluorescence intensity was measured with excitation at 365 nm and emission at 460 nm⁵.

Hydroxyproline Quantification

Samples were hydrolyzed in 2 M HCl at 121°C for 15 minutes, followed by neutralization with 2 M NaOH. To each 100- μ L sample, 625 μ L of 0.05 M chloramine-T was added and incubated at room temperature for 25 minutes, followed by the addition of 625 μ L of 1 M Ehrlich's reagent and incubation at 65°C for 20 minutes. The reaction was stopped with cold water, centrifuged at 600 \times g for 5 minutes, and 200 μ L of supernatant was transferred to a 96-well plate (in triplicate). Absorbance was measured at 550 nm^{3,8}.

Gene Expression Analysis (qRT-PCR)

RNA was extracted from the chondrocytes, followed by reverse transcription reaction to obtain complementary DNA (cDNA). Gene expression levels of GAPDH, TRPV, Piezo, Piezo2, Col2A1, ACAN, and SOX9 were measured using SYBR Green-based qRT-PCR. PCR conditions included an initial denaturation at 95°C for 10 minutes, followed by 40 cycles of 95°C for 15 seconds and 60°C for 60 seconds. Melting curve analysis was performed from 65°C to 95°C with a 0.2°C increment¹. Primer sequences for extracellular matrix gene analysis were as follows:

GAPDH, (forward 5'-ACCCCTTCATTGACCTCCAC-3', reverse 5'-ATACTCAGCACCAGCATCGC-3'), TRPV4, (forward 5'-CACCGTGGTGTGGTAAGGGT-3', reverse 5'-GGAGCTTTGGGGCTCTGT-3'), Piezo1, (forward 5'-GCCCCAACGGACCTGAAGC-3', reverse 5'-TGCGCAGCTGGATACGCACC-3'), Piezo2, (forward 5'-CCAGCTGGATCTGCGTGGAGG-3', reverse 5'-TGGTTGATCACC CCGGCGAC-3'), COL2A1, (forward 5'-GCTATGGAGATGACAACCTGGCTC-3', reverse 5'-TCACCGTGCAGCCATCCTTCAGAA-3') ACAN, (forward 5'-CGAGGAGCAGGAGTTTGTCAAC-3', reverse 5'-ATCATCACCACGCAGTCCTCTC-3')¹³, Sox9, (forward 5'-CAGGGCTCTGTGCTCTACTCC-3', reverse 5'-GGGTTACGGTCTTCTTCGGT-3')¹¹.

Results and Discussion:

Gene expression analysis of TRPV4, Piezo1, Piezo2, Col2A1, ACAN, and SOX9 revealed that on day 7 after culturing chondrocytes in different formats, which were pellet, monolayer, and cell sheet cultures, the expression levels of most genes tended to decrease compared to fresh cells, which were used as a control group (Figure 1). TRPV4 expression significantly decreased in all groups. This indicates that the culture environment could not maintain TRPV4 gene expression. Piezo1 and Piezo2 expression also decreased, with the monolayer culture showing the highest expression among the test groups, while the cell sheet culture had the lowest level. This suggests Piezo1 and Piezo2 responded differently depending on the culture format. Col2A1, a key gene for cartilage matrix, was drastically reduced in all culture formats, indicating that the culture conditions at this stage were not suitable for maintaining collagen type II gene expression. ACAN expressions also declined in all groups but remained detectable. The monolayer culture had the highest level (0.39-fold), while the pellet culture showed a marked decrease (0.01-fold). This suggests that monolayer culture may better preserve the chondrocyte phenotype at day 7. SOX9, a key transcription factor for cartilage development, also showed decreased expression in all groups. Overall, culturing for 7 days led to a marked decrease in the expression of mechanotransduction-related genes (TRPV4,

Piezo1, Piezo2) and cartilage-specific genes (Col2A1, ACAN, SOX9), especially in the pellet culture format. In contrast, the monolayer culture tended to maintain better gene expression, particularly for Piezo1, Piezo2, Col2A1, and ACAN, whereas the cell sheet culture did not show apparent efficacy in preserving gene expression.

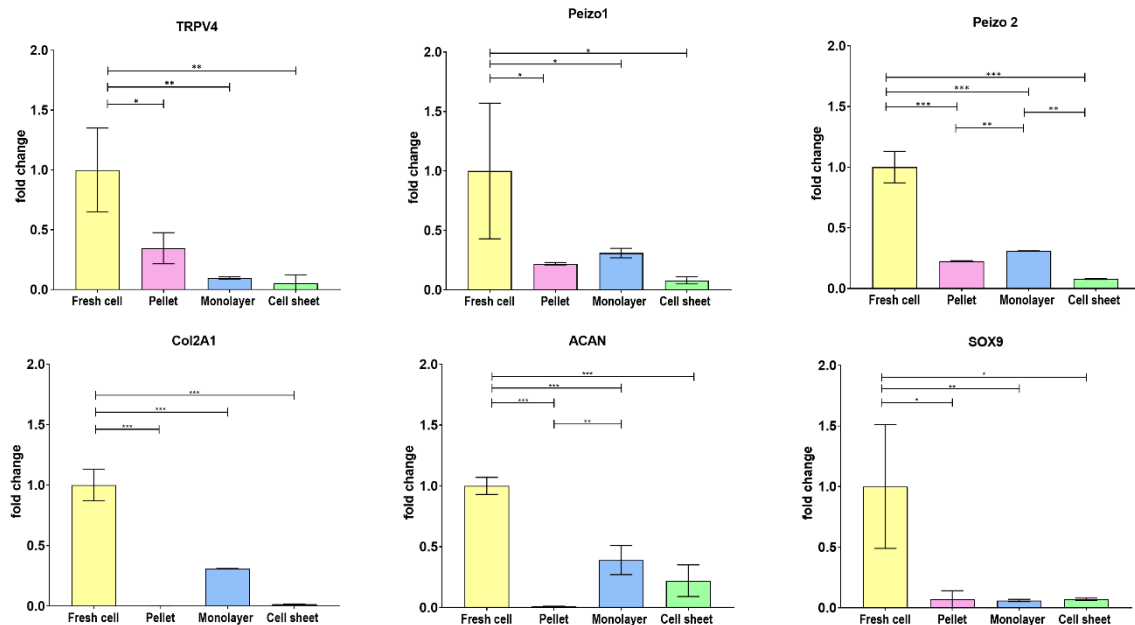


Figure 1.

Relative expression levels of mechanotransduction-related genes (TRPV4, Piezo1, Piezo2) and cartilage-specific genes (Col2A1, ACAN, SOX9). Values are expressed as fold changes relative to fresh cells. Statistical analysis was performed using one-way ANOVA.

DNA quantification showed that pellet culture had the highest DNA content ($0.34 \pm 0.04 \mu\text{g}/\text{sample}$), compared to monolayer culture ($0.04 \pm 0.004 \mu\text{g}/\text{mg}$) and cell sheet culture ($0.11 \pm 0.06 \mu\text{g}/\text{mg}$) ($p < 0.0001$). Thus, pellet culture maintained a higher cell number compared to monolayers and cell sheets within the same time frame, while monolayer culture resulted in the lowest DNA content (Figure 2).

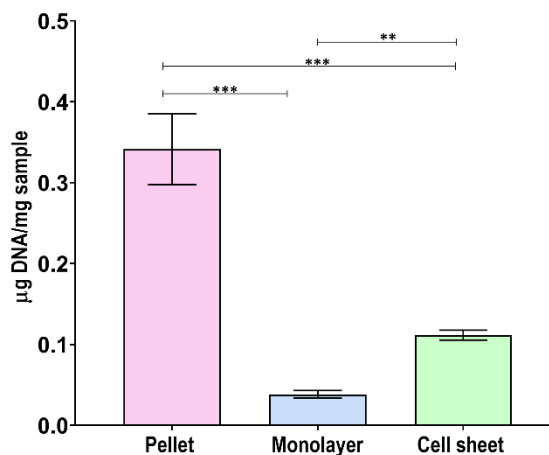


Figure 2.

DNA content in chondrocytes cultured under different conditions. Statistical analysis was performed using one-way ANOVA.

GAG quantification revealed that the pellet culture had a significantly higher GAG content ($1.18 \pm 0.1 \mu\text{g}/\text{sample}$) compared to the monolayer ($0.51 \pm 0.03 \mu\text{g}/\text{sample}$) and cell sheet ($0.57 \pm 0.22 \mu\text{g}/\text{sample}$) cultures. Pellet culture thus better promoted GAG synthesis, likely due to its three-dimensional nature, allowing greater cell-to-cell and cell-environment interaction. However, there was no significant difference between the cell sheet and the monolayer, indicating similar GAG production efficiency (Figure 3A).

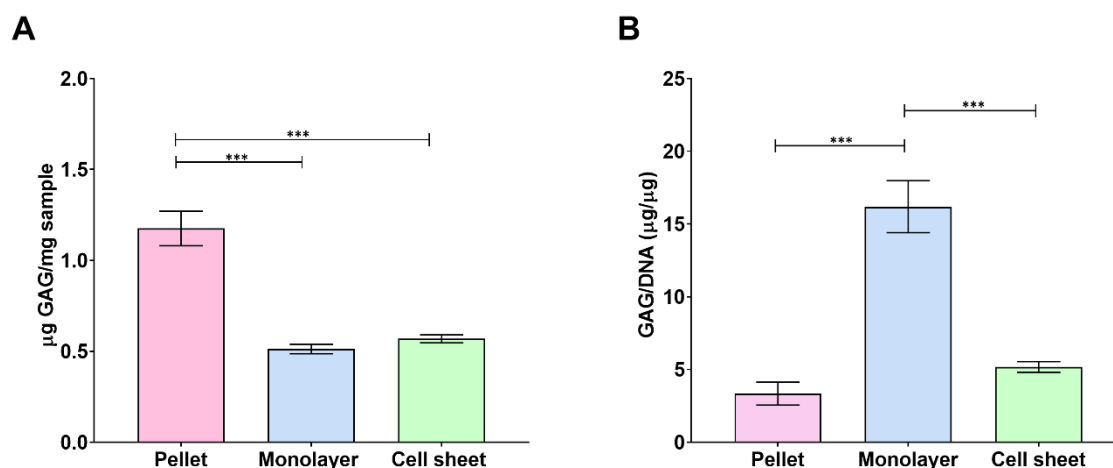


Figure 3.

GAG content in chondrocytes cultured under different conditions. (A) GAG content normalized by tissue weight ($\mu\text{g}/\text{sample}$), (B) GAG content normalized by DNA amount ($\mu\text{g}/\mu\text{g}$). Statistical analysis was performed using one-way ANOVA.

When the GAG/DNA ratio was analyzed, monolayer culture had the highest ratio ($16.19 \pm 1.79 \mu\text{g}/\mu\text{g}$), significantly higher than cell sheet ($5.18 \pm 0.37 \mu\text{g}/\mu\text{g}$) and pellet ($3.35 \pm 0.79 \mu\text{g}/\mu\text{g}$) ($p < 0.0001$) (Figure 3B). This shows that despite having the fewest cells, monolayer culture enabled the highest GAG production per cell. Pellet culture had the lowest GAG/DNA ratio, suggesting a lower ECM synthesis capability per cell. Although the cell sheet had a higher GAG/DNA ratio than the pellet, it remained significantly lower than the monolayer, possibly due to limitations in nutrient distribution or inefficiencies in early-stage matrix synthesis. Therefore, monolayer culture produces the most GAG per cell, despite having the lowest DNA content.

Hydroxyproline content, which is a direct correlation to total collagen content, showed that monolayer culture produced the most hydroxyproline ($0.77 \pm 0.24 \mu\text{g}/\text{sample}$), followed by pellet ($0.44 \pm 0.23 \mu\text{g}/\text{sample}$) and cell sheet ($0.34 \pm \mu\text{g}/\text{sample}$) cells. However, hydroxyproline content were not statistically significant between monolayer and cell sheet culture. This indicates that pellet culture promotes collagen synthesis more effectively than others within 7 days (Figure 4A).

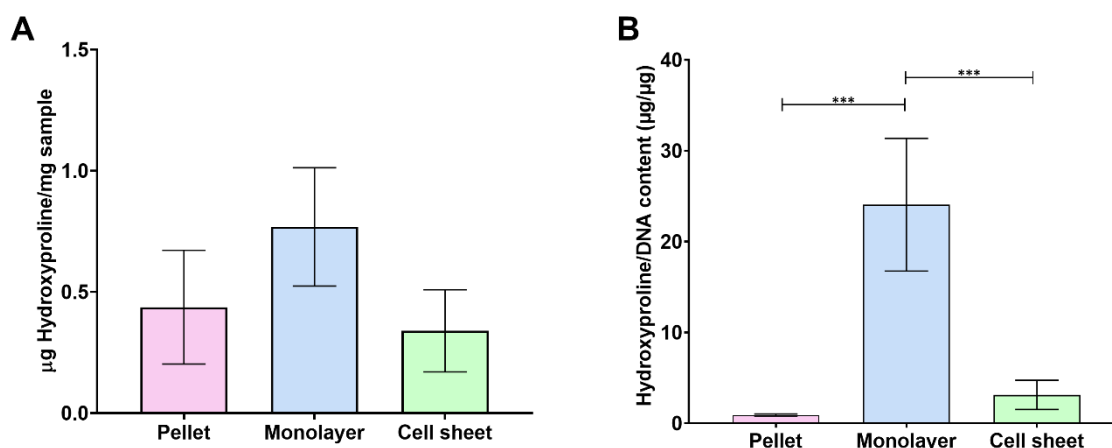


Figure 4.

Hydroxyproline content in chondrocytes cultured under different conditions. (A) Hydroxyproline content normalized by tissue weight. (B) Hydroxyproline content normalized by DNA amount. Statistical analysis was performed using one-way ANOVA.

Hydroxyproline/DNA ratio analysis revealed that monolayer culture had the highest total collagen production per cell at day 7 ($24.06 \pm 7.31 \mu\text{g}/\mu\text{g}$), significantly higher than pellet ($0.92 \pm 0.10 \mu\text{g}/\mu\text{g}$) and cell sheet culture ($3.14 \pm 1.62 \mu\text{g}/\mu\text{g}$) ($p < 0.001$) (Fig. 4B). This confirms that monolayer-cultured cells, despite being fewer, synthesized the most total collagen and GAG during the early culture period.

Overall, monolayer culture in the early stage (7 days) was the most efficient in promoting ECM production per cell, particularly GAG and collagen, which are key components of cartilage. Limitations of each culture format should be considered in designing future cartilage tissue engineering strategies. While monolayer culture demonstrated the highest ECM production efficiency per cell, its low DNA content indicates a smaller cell population, which may limit its capacity to generate sufficient tissue volume for therapeutic applications. Conversely, pellet culture supported a higher overall cell number, but the ECM synthesis efficiency per cell was considerably lower, suggesting that although pellet may provide greater tissue bulk, the quality of matrix production is reduced. Cell sheet culture showed intermediate performance, but its fragility and potential nutrient diffusion limitations restrict its practicality for large-scale applications.

Conclusion:

Each culture format presents trade-offs between cell number, ECM production efficiency, and structural feasibility, which should be carefully considered when designing cartilage tissue engineering strategies. Extending the time course will clarify whether the high ECM-per-cell observed in the monolayer at Day 7 is sustained or a transient response, and whether pellet or cell-sheet formats produce greater bulk matrix over a more extended period.

Acknowledgements:

The authors gratefully acknowledge financial support for this work from the Budget for the International Academic Conference (BIAC_Student) and the Graduate Studies Scholarship from the Faculty of Science, Kasetsart University.



References:

1. Asmar A, Barrett-Jolley R, Werner A, Kelly Jr R, & Stacey M. *Organogenesis*. 2016;12(2):94-107.
2. Barré L, Venkatesan N, Magdalou J, Netter P, Fournel-Gigleux S, & Ouzzine M. *Faseb j* 2006;20(10):1692-1694.
3. Cissell D D, Link J M, Hu J C, & Athanasiou K A. *Tissue Engineering Part C: Methods*. 2017;23(4):243-250.
4. Geng R, Li J, Yu C, Zhang, C, Chen F, Chen J, Ni H, Wang J, Kang, K, Wei Z, Xu Y, & Jin T. *Exp Ther Med*. 2023;26(4):481.
5. Hoemann C. D, Sun J, Chrzanowski V, & Buschmann M. D. *Analytical Biochemistry*. 2002;300(1):1-10.
6. Mitani G, Sato M, Lee J. I, Kaneshiro N, Ishihara M, Ota N, Kokubo M, Sakai H, Kikuchi T, & Mochida J. *BMC Biotechnology*. 2009;9(1):17.
7. O'Neill T. W, & Felson D. T. *Current Osteoporosis Reports*. 2018;16(5):611-616.
8. Reddy G, & Enwemeka C. *Clin. Biochem*. 1996;29:3-3.
9. Sahu N, Budhiraja G, & Subramanian A. *Stem Cell Research & Therapy*. 2020;11.
10. Savadipour A, Nims R J, Katz D. B, & Guilak F. *Connect Tissue Res*. 2022;63(1):69-81.
11. Savadipour A, Nims R J, Rashidi N, Garcia-Castorena J M, Tang R, Marushack G K, Oswald S J, Liedtke W B, & Guilak F. *Proceedings of the National Academy of Sciences*. 2023;120(30):e2221958120.
12. Sinthuvanich C, Haines-Butterick L A, Nagy K J, & Schneider J P. *Biomaterials*. 2012;33(30):7478-7488.
13. Sonthithai P, Hankamonsiri W, Lertwimol T, Uppanan P, & Janvikul W. *Biotechnology Progress*. 2022;38(3):e3240
14. Watanabe Y, & Shiraishi T. *Mechanical Engineering Journal*. 2024;11(5):24-00102.



OPTIMIZING A SPLIT LENTIVIRAL DELIVERY SYSTEM FOR CRISPR/CAS9-BASED GENE KNOCKOUT IN MESENCHYMAL STEM CELLS

Lanlalit Pongsasakulchot,¹ Kanok Keerati-Opasawat,¹ Natcha Gahawong,¹ Waracharee Srifa^{1,*}

¹Department of Biochemistry, Faculty of Medical Science, Naresuan University, 65000, Thailand

*e-mail: waracharees@nu.ac.th

Abstract:

Pooled CRISPR knockout (KO) screens enable large-scale functional analysis of genotypic-phenotypic relationships for cell line models, leading to insights into cellular functions and disease development. However, applying this approach to primary human cells remains challenging due to limited culture sizes and windows, as well as low delivery efficiency of CRISPR components. Here, we explored a CRISPR-based KO approach compatible with pooled screens using a split lentiviral system for the sequential delivery of sgRNA- and Cas9-expressing vectors in mesenchymal stem cells derived from human exfoliated deciduous teeth (SHED). Our results show that serial transduction using common CRISPR screening lentiviral vectors is compatible with SHED, with up to 76% guide RNA vector delivery efficiency and 56.8% Cas9 vector co-delivery efficiency in serial transduction. The delivery efficiency directly correlated with lentiviral doses with stable expression for both vectors. Gene knockout was validated at the *HBB* locus, resulting in an average indel mutations of 28%. Notably, knockout efficiency is considerably lower than Cas9 delivery efficiency, highlighting Cas9 vector delivery and CRISPR component expression as key limiting factors. These findings establish a proof-of-concept framework for split lentiviral CRISPR/Cas9 delivery in primary MSCs and provide a foundation for future pooled CRISPR screening in MSC models.

Introduction:

The CRISPR/Cas9 system is a powerful tool for inducing loss-of-function mutations at a specific gene through complementary sequences of guide RNA (gRNA) and the nuclease activity of Cas9. Following the precise introduction of double-strand breaks, error-prone repair via non-homologous end joining (NHEJ) generates insertion or deletion mutations (indels), leading to disruption of gene expression.¹ One of its most powerful applications is the pooled CRISPR knockout (KO) screen, which enables large-scale functional analysis of gene-phenotype relationships. Pooled CRISPR screens are a technique where genetic perturbations are introduced in a pooled library, and correlations between gene targets and phenotypes of interest are subsequently analyzed by sequencing-based quantification to reveal changes in guide RNA abundance after the pooled cells are challenged with a related selection pressure.²

Although pooled CRISPR screens are widely used with cell lines³, there are still challenges in primary human cells. Shalem and colleagues demonstrated that an all-in-one lentiviral vector is compatible with gene KO in genome-scale screening of pluripotent stem cells, but it resulted in low delivery and editing efficiencies due to lentiviral vector packaging limit.⁴ To overcome these limitations, a split lentiviral system, using separate vectors for gRNA (lentiGuide-Puro) and Cas9 (lentiCas9-Blast), has been developed, offering higher functional titers and improved delivery efficiency.⁵

Primary human mesenchymal stem cells (MSC) are multipotent stromal cells capable of triple-multilineage. Owing to their self-renewal ability, tissue regeneration potential, and immunomodulatory properties, MSCs have become a key candidate in tissue engineering and



cell-based therapies.⁶ However, further research is needed to better understand how MSC functions, improve their effectiveness and benefits, and develop guidelines for clinical use.⁷

In this study, we aimed to optimize a suitable protocol for pooled CRISPR screening using a split lentiviral delivery system for CRISPR/Cas9-based KO in dental tissue-derived MSC, namely, stem cells from human exfoliated deciduous teeth (SHED). Our approach involves sequentially delivering gRNA and Cas9 via a two-step lentiviral transduction protocol, using commonly used vectors for pooled CRISPR screens (lentiGuide-Puro and lentiCas9-EGFP vectors). We optimized the delivery protocols and evaluated delivery efficiencies and gene KO efficiencies using the aforementioned vectors to establish a protocol compatible with future pooled CRISPR screening in primary human MSCs.

Methodology:

2.1 Preparation of Lentivirus-Producing (HEK293T) and Target Cells (SHED)

Human embryonic kidney 293T (HEK293T; ATCC® CRL-3216™) cells were cultured in Dulbecco's Modified Eagle Medium high glucose media (DMEM high glucose; Gibco) supplemented with 10% fetal bovine serum (FBS; Gibco), 1% penicillin-streptomycin (Gibco). The cells were maintained at 37°C in a humidified incubator with 5% CO₂. The medium was replaced every 2 days. Upon reaching 80–90% confluency, the cells were subcultured at a 1:8 ratio in a T75 flask using TrypLE™ Express Enzyme (Gibco), according to ATCC recommendations. HEK293T cells were used exclusively for lentiviral vector production.

Stem cells from human exfoliated deciduous teeth (SHED) were kindly provided by Dr. Hathaitip Sritanaudomchai, Department of Oral Biology, Faculty of Dentistry, Mahidol University, Thailand. SHED were originally isolated from deciduous tooth pulp of healthy donors following informed consent, under protocols approved by the Mahidol University Ethics Committee (IRB 2014/041.2110).⁸ SHED were cultured in complete media consisting of Dulbecco's Modified Eagle Medium (DMEM, Gibco) supplemented with 10% fetal bovine serum (FBS, PAN-biotech GmbH), 1% penicillin-streptomycin (Gibco), and maintained at 37°C in a humidified incubator with 5% CO₂. The medium was replaced every 2–3 days, and cells were subcultured upon reaching 80–90% confluency using TrypLE™ Express Enzyme (Gibco). For all experiments, cells from two biological donors between passages 6–12 were used to minimize phenotypic drift. SHED identity was previously confirmed by their MSC marker expression and their fibroblast-like morphology.

2.2 Lentiviral production and transduction

The split lentiviral CRISPR/Cas9 system consisted of two plasmids: 1) lentiGuide-Puro was a gift from Feng Zhang (Addgene plasmid # 52963 ; <http://n2t.net/addgene:52963> ; RRID:Addgene_52963)⁵ and 2) lentiCas9-EGFP was a gift from Phil Sharp & Feng Zhang (Addgene plasmid # 63592 ; <http://n2t.net/addgene:63592> ; RRID:Addgene_63592).⁹ Lentiviral particles were produced in HEK 293T cells. In brief, 1x10⁶ HEK 293T cells were seeded in 6-well plates and overnight transfected with 2 μg of transfer vector plasmid (either lentiGuide-Puro or lentiCas9-EGFP), 1.5 μg of psPAX2 (a gift from Didier Trono (Addgene plasmid # 12260 ; <http://n2t.net/addgene:12260> ; RRID:Addgene_12260)), and 0.5 μg of pMD2.G (a gift from Didier Trono (Addgene plasmid # 12259 ; <http://n2t.net/addgene:12259> ; RRID:Addgene_12259)), using Lipofectamine™ 2000 Transfection Reagent (Thermo Fisher Scientific) according to manufacturer protocol. The lentiGuide-Puro viral supernatants were harvested after 24 hours, and lentiCas9-EGFP viral supernatants were harvested after 48 hours in complete SHED culture medium, then filtered through a 0.45 μm syringe filter (Sartorius™). Lentiviral volumes were added to SHED (seeded at 12,500 cells/cm²) at different percentages of the final transduction medium volume, including 3.125%, 6.25%,



12.5%, 25%, and 50% in complete medium, to evaluate dose-dependent delivery efficiency. After 24 hours, the transduction medium was replaced with fresh complete culture medium.

2.3 Measurement of lentiGuide-Puro vector delivery efficiency and long-term expression via puromycin resistance selection

Four days after lentiGuide-Puro transduction, cells were split into two groups, including non-treated ($Puro^-$) and puromycin-treated ($Puro^+$) groups. Puromycin (Gibco) ($2\mu\text{g/ml}$) was administered to $Puro^+$ group, whereas $Puro^-$ group served as a control. Delivery efficiency was measured at the endpoint of puromycin selection, defined as the time when all the $Puro^+$ non-transduced cells group (0% of lentiviral dose) were eliminated. And the delivery efficiency of lentiGuide-Puro was calculated as the percentage of viable cells in the $Puro^+$ group by that in the $Puro^-$ group at the same lentiviral dose. For long-term expression stability, the percentages of puromycin-resistant fraction were calculated for at least 3 passages after transduction. All experiments were performed in biological replicates.

2.4 Measurement of lentiCas9-EGFP vector delivery efficiency using flow cytometry

Following lentiCas9-EGFP transduction into SHED, green fluorescence protein (GFP) expression was assessed after two days by fluorescence microscopy (Zeiss; Axiocam 105 color) using a FITC channel set (excitation 488 nm, emission 509 nm) to qualitatively confirm successful transduction. Four days post-lentiCas9-EGFP transduction, the percentage of GFP-positive cells (GFP^+) was quantified by flow cytometry (Beckman Coulter, USA).

The samples were stained with propidium iodide (PI; Biolegend[®]) for 30 minutes at room temperature (RT) in the dark to monitor the viable cell population. An unstained PI control and a non-transduced negative control (GFP^- cells) were included to establish baseline control, serving as a reference to set the threshold for a positive GFP signal and minimizing false positives from autofluorescence. Flow cytometry data were acquired by recording at $30\mu\text{L}$ per sample. Sequential gating was applied to exclude debris (FSC/SSC), doublets (FSC-A vs. FSC-H), and dead cells (PI-positive), followed by quantification of GFP^+ cells within the viable population. Data were analyzed using the CytExpert software (Beckman Coulter). Results were expressed as the percentage of GFP^+ cells, with experiments performed in biological replicates.

2.5 Measurement of serial transduction efficiency

The two-step transduction strategy ensures that Cas9 activity is restricted to cells already carrying sgRNAs. By introducing the sgRNA-expressing cassette first and selecting gRNA-positive cells before delivery of Cas9, this approach avoids increasing cellular stress that would occur from puromycin selection concurrently with DNA double-strand breaks, which would occur if Cas9 were expressed before sgRNA delivery. In addition, for future pooled screening experiments, selecting gRNA-positive cells before Cas9 delivery allows additional proliferation steps to maintain the recommended coverage of 100–200 cells per target for positive selection screens and 500–1,000 cells per target for negative selection screens prior to the introduction of Cas9, thereby minimizing bottlenecks and preserving the quality of pooled CRISPR screens.²

First, SHEDs were seeded in a T75 flask at a density of 12,500 cells/cm². Two days later, the cells were transduced with the lentiGuide-Puro vector (*HBB* gene targeting) at a viral dose corresponding to 12.5% of the culture volume. Following 24 hours of incubation, the medium was replaced with fresh culture medium. Three days after transduction, puromycin ($2\mu\text{g/ml}$) was added for selection, allowing sufficient time for integration and expression of the puromycin-resistance gene. Puromycin selection eliminated non-transduced cells, thereby enriching the sgRNA-positive population. Once the puromycin-resistant cells



reached 80% confluency, they were subcultured and seeded into a 12-well plate at the same density (12,500 cells/cm²).

Two days after seeding, the cells were serially transduced with various lentiCas9-EGFP vector supernatant ratios (3.125%, 6.25%, 12.5%, 25%, and 50% in complete medium) to evaluate dose-dependent delivery efficiency. To confirm transduction, GFP expression was qualitatively assessed by fluorescence microscopy two days later. When the cells reached 80%-90% confluency after transduction, the percentage of GFP⁺ cells were quantified using flow cytometry. All experiments were performed in biological replicates.

2.6 Validation of gene knockout efficiency by measuring indel mutation percentage

Following the successful serial transduction and quantification, the efficacy of CRISPR-Cas9-mediated gene knockout was validated by measuring indel mutation frequencies at the *HBB* locus. Genomic DNA was extracted from cells that received a single lentiGuide-Puro and from cells that received serial lentiGuide-Puro and lentiCas9-EGFP transductions using the Genomic DNA Extraction Kit (BIOSEARCH technologies). The targeted genomic region (*HBB*) was amplified using polymerase chain reaction (PCR) with primers designed to produce 438 bp amplicon (Forward: 5'-TCTGTCTCCACATGCCAGT-3', Reverse: 5'-CAGGGCAGAGCCATCTATTG-3'). The resulting amplicons were analyzed using Sanger sequencing.

Sequencing chromatograms were analyzed using Inference of CRISPR Edits (ICE) software (ICE CRISPR Analysis, 2025, v3.0, EditCo Bio, URL: <https://ice.editco.bio/>) to calculate editing efficiency and identify profiles of insertion and deletion mutations, thereby providing a quantitative measure of gene knockout efficiency.

Results and Discussion:

This study focused on optimizing protocol of split lentiviral delivery system for CRISPR/Cas9-based gene knockout. The human beta globin (*HBB*) gene, which is not required for SHED function and therefore whose indel mutation should not affect cell viability or cellular behavior, was selected as a gene target to evaluate delivery of CRISPR components and gene knockout efficiencies.

First, we determined the optimal lentiviral dose for lentiGuide-Puro vector transduction (Figure 1A). Our study utilized the lentiGuide-Puro vector, which contains a U6 promoter (an RNA polymerase type III (Pol III) promoter) for sgRNA expression and an elongation factor-1 α (EF1 α) promoter (an RNA polymerase type II (Pol II) promoter) that drives stable expression of the puromycin resistance gene (PuroR), thereby enabling both gRNA expression and antibiotic selection of transduced cells (Figure 1B). We found that while puromycin (2 μ g/mL) was sufficient to induce cytotoxicity in non-transduced parental controls, it was much less cytotoxic to the transduced cells, thus demonstrating successful transduction of the lentiGuide-Puro transgene cassette (Figure 1C). Furthermore, we observed that delivery efficiencies were dependent on the lentiviral dose, with the highest estimated efficiency of 76.0% achieved at a 25% (v/v) lentiviral supernatant in culture medium (Figure 1D). The stable expression of the lentiGuide-Puro vector was confirmed at each dose for up to three passages post-transduction (Figure 1E). These results suggest that lentiGuide-Puro vector is compatible with SHED cells across different biological donors.

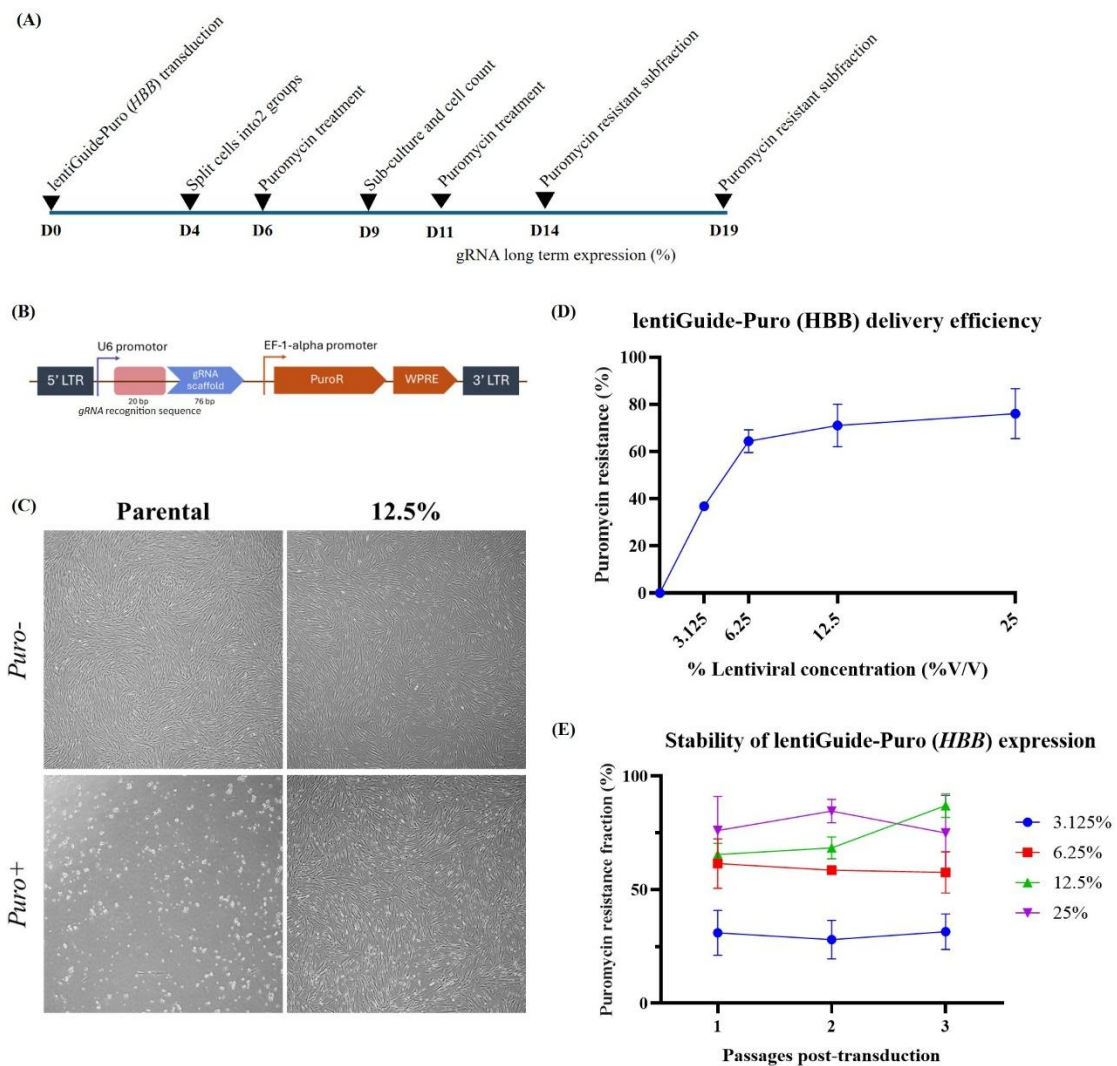


Figure 1.

Optimization for lentiGuide-puro vector transduction and long-term stability

- Schematic diagram of experiment for optimized lentiGuide-puro vector protocol
- Components of the lentiGuide-Puro vector
- Representative phase-contrast images of SHED cells after 3 days of puromycin selection at 50X magnification, demonstrating the resistance of transduced cells (12.5% lentiviral dose shown) to puromycin with selective pressure applied
- Dose-response curve showing the relationship between lentiviral concentration and delivery efficiency, indicated by percentage of puromycin-resistant cells
- Evaluation of the stability of lentiGuide-Puro expression over three passages, showing percentages of puromycin resistance fraction for SHED transduced at different viral dosages

Furthermore, we observed compatibility of lentiCas9-EGFP vector to SHED cells using various lentiviral doses with single- and serial-transductions (Figure 2A, 2B, respectively). We used the lentiCas9-EGFP vector, which contains an EF1 α promoter (a Pol II promoter) that drives stable expression of both Cas9 and GFP proteins (Figure 2C). The lentiCas9-EGFP vector was compatible with SHED, as confirmed by fluorescence microscopy at 100X magnification for GFP expression. Moreover, we observed that serial

transduction induced minimal cytotoxicity and preserved cell proliferation capacity (Figure 2D). As expected, the number of GFP⁺ cells correlated with the lentiviral dose, with up to 68.0% transduction efficiency of single-vector transduction using 50% lentiviral supernatant volume in culture medium. Importantly, the serial transduction groups showed a slightly lower percentage of GFP⁺ cells compared to the lentiCas9-EGFP only group, suggesting that a split CRISPR/Cas9 lentiviral delivery system is feasible but may be affected by slightly reduced transduction efficiency of the second vector (Figure 2E). Collectively, these findings demonstrate that the lentiCas9-EGFP vector is compatible with SHED in both single and serial transductions, with minimal cytotoxicity despite the reduced efficiency observed in the serial system.

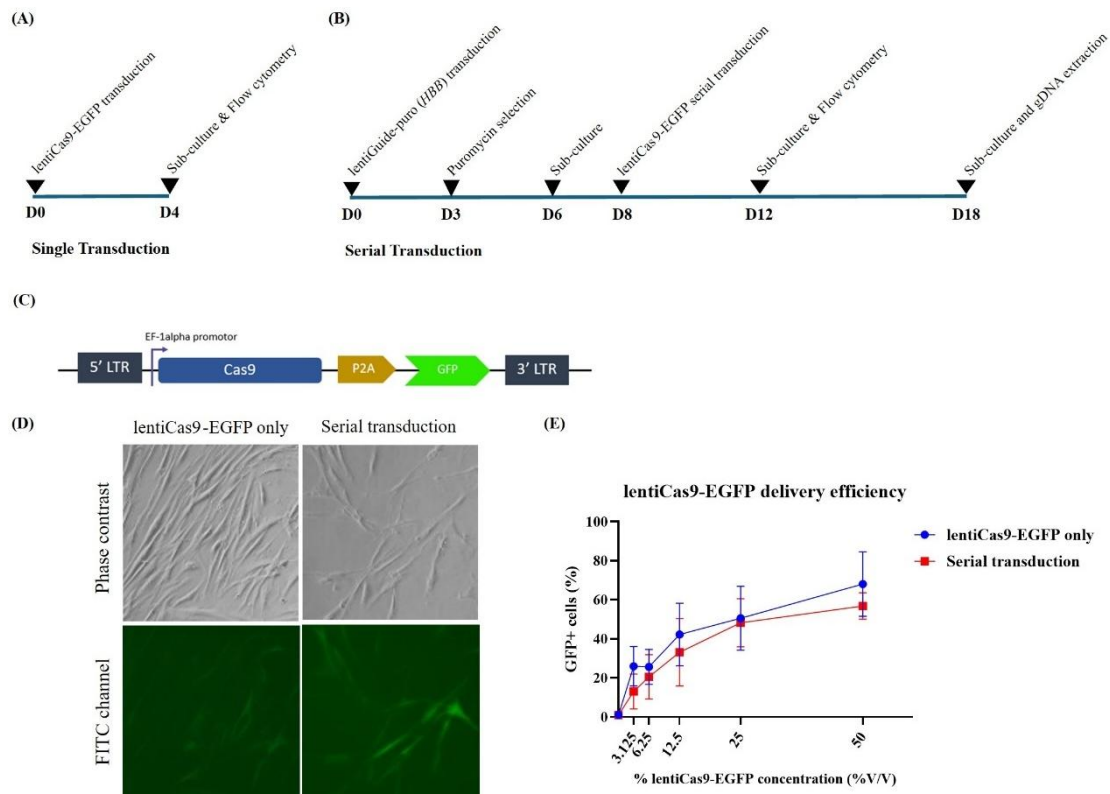


Figure 2.
Optimization for lentiCas9-EGFP vector transduction

- Schematic diagram of experiment for optimized single lentiCas9-EGFP vector protocol
- Schematic diagram of experiment for optimized serial lentiCas9-EGFP vector protocol
- Components of the lentiCas9-EGFP vector
- Representative phase-contrast and fluorescence images of SHED cells post lentiCas9-EGFP transduction versus serial transduction at 100X magnification (50% lentiviral dose shown)
- Dose-response curve showing the relationship between lentiviral concentration and percentage of GFP⁺ cells, comparing single transduction to serial transduction

Finally, we validated the gene knockout efficiency of the split lentiviral CRISPR/Cas9 system. PCR analysis confirmed the successful amplification of the target *HBB* gene, producing a 438 bp amplicon at the CRISPR/Cas9 cutting site (Figure 3A). Subsequently, the PCR products were sequenced using the Sanger sequencing technique. The resulting chromatogram of the serial transduced sample showed overlapping peaks downstream of the

target site, indicating a heterogeneous sequence and confirming gene editing that leads to indel mutation, represented by heterogeneity of the allelic sequences found in the serially transduced samples (Figure 3B upper row). This was in contrast with single lentiGuide-Puro (*HBB*) sample, well-defined peaks with no evidence of indel formation (Figure 3B lower row). ICE analysis of the sequencing data revealed an average indel mutation of 28% in the serially transduced sample. Furthermore, we found that the percentage of indel mutation was less than half of the lentiCas9-EGFP delivery efficiency (Figure 3C). Finally, we successfully generated gene knockout from split lentiviral CRISPR/Cas9 system.

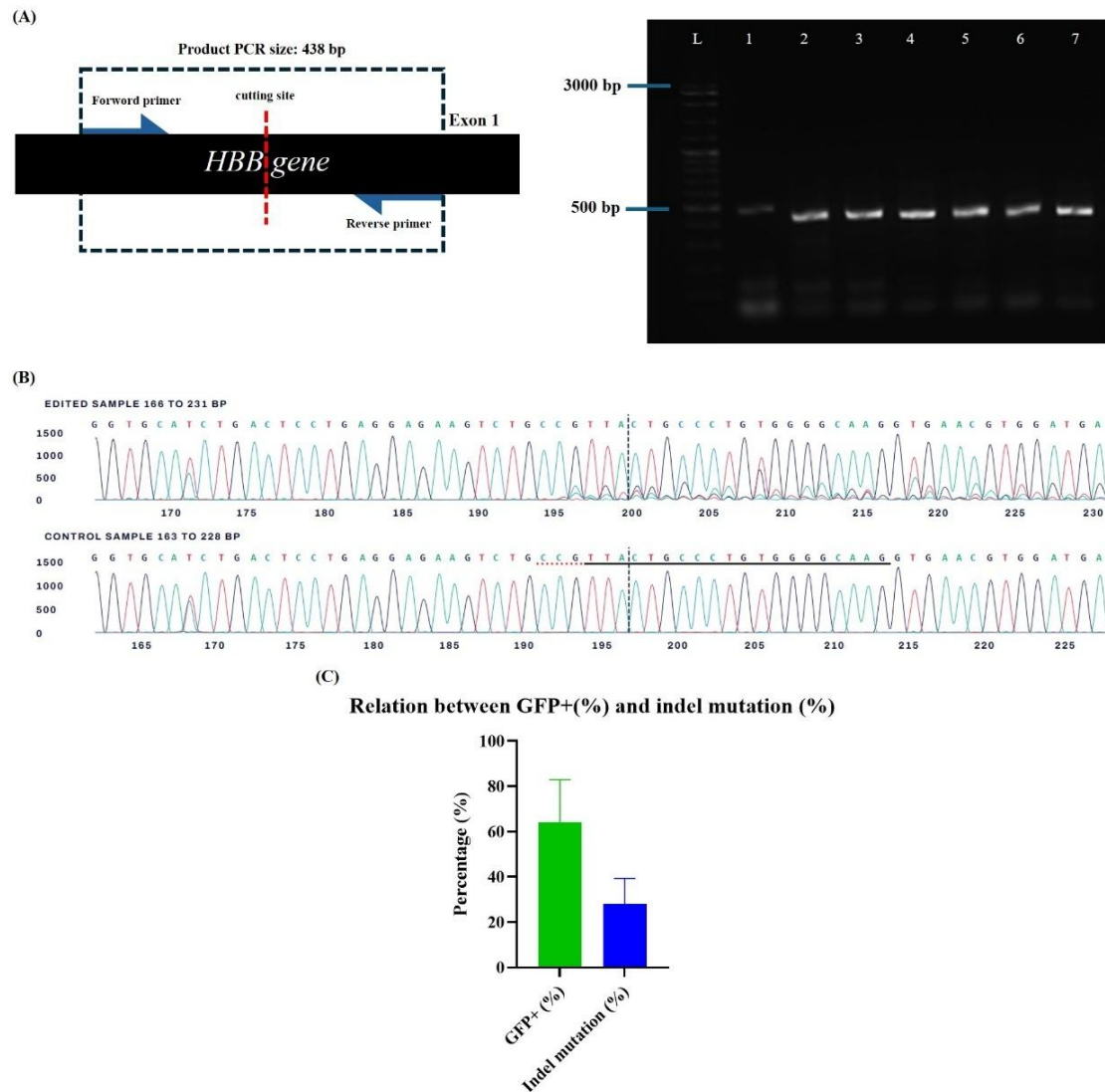


Figure 3.
Assessment of Gene Editing Efficiency

- Agarose gel electrophoresis of PCR products confirming the successful amplification of the target gene (L: VC 100 bp plus ladder; lane 1: no-template control lane; 2: lentiGuide-Puro only; 3-7 PCR products of serial transduction from 2 donors)
- Representative Sanger sequencing chromatograms validating indel mutations in the edited sample, indicated by overlapping peaks downstream of the target site, compared with the well-defined peaks of the control sample (lentiGuide-Puro only)
- Bar plots comparing lentiCas9-EGFP transduction efficiency (percentage of GFP-positive cells) and gene editing efficiency (percentage of indel mutation)



In this study, we investigated the application of a split lentiviral system for sequential delivery of sgRNA- and Cas9-expressing vectors in MSCs from human exfoliated deciduous teeth (SHED). Our findings demonstrate the technical feasibility of this approach, high efficiency delivery of sgRNA-expressing vector, and moderate frequency of the Cas9-expressing vector of choice. While the system was successfully adapted for SHED, its overall efficiency remained lower compared to immortalized cell lines, likely due to the heterogeneous biological characteristics of primary cells, their limited proliferation capacity, and high sensitivity to transgene-induced stress, as previously reported in other primary human cells.^{10,11} Previous studies have shown that the two-step Cas9 expressing cells serially transduced lentiGuide-Puro vector achieved higher knockout efficiency when compared to the one-step lentiCRISPRv2 system. However, this advantage was offset by reduced cell viability, particularly when targeting safe harbor genes in pooled CRISPR screens.¹²

Our findings underscore the critical importance of Cas9 expression levels in achieving efficient gene knockout. Elevated Cas9 expression has been shown to accelerate editing kinetics, thereby enhancing knockout efficiency.¹² Potential strategies include redesigning the vector backbone to optimize promoter strength and enhance Cas9 expression¹³, adopting non-viral delivery methods such as lipid nanoparticles¹⁴, electroporation¹⁵, or delivering Cas9 in alternative formats such as mRNA or protein.¹⁰

Conclusion:

In conclusion, our results demonstrate that the split lentiviral delivery system is compatible with primary human MSCs derived from dental tissue (subtype SHED), showing no cytotoxicity in single transductions and only minimal cytotoxicity in serial transductions. Future studies should further investigate the correlation between serial delivery efficiency and cell viability to quantitatively assess potential cytotoxic effects. Although the *HBB* gene was successfully edited, the efficiency was still lower than GFP⁺ cell frequencies in the puromycin-resistant fraction. Notably, the indel frequency correlated with Cas9 delivery efficiency, highlighting the importance of improving Cas9 delivery strategies to achieve higher knockout efficiency. However, excessive Cas9 activity may also increase cytotoxicity and off-target effects, underscoring the need for balanced optimization. The split delivery system, with Cas9 delivered after puromycin selection steps, would minimize the time window between Cas9 delivery and the beginning of screening assays. This helps reduce the chance of off-target mutations compared to an all-in-one vector, in which a puromycin selection step is added after the introduction of Cas9 and lengthening the gap between Cas9 expression and the start of screening assays. Regardless, potential off-target sites should be identified through computational predictions and help inform guide gRNA library design. Overall, these findings provide proof-of-concept that a split lentiviral delivery system can be applied in primary MSCs, and future optimization of Cas9 delivery will be critical to unlock its full potential for pooled CRISPR screens in future studies.

Acknowledgements:

We extend our sincere gratitude to Assoc. Prof. Dr. Hathaitip Sritanaudomchai for generously providing the SHED cells used in this study. This research was made possible through the comprehensive support of the Department of Biochemistry, Faculty of Medical Science, Naresuan University, including the provision of laboratory facilities and resources.

**References:**

1. Doudna JA, Charpentier E. *Science*. 2014;346(6213):1258096.
2. Bock C, Datlinger P, Chardon F, et al. *Nat Rev Methods Primers*. 2022;2:8.
3. Grimm S. *Nat Rev Genet*. 2004;5:179–189.
4. Shalem O, Sanjana NE, Hartenian E, et al. *Science*. 2014;343:84–87.
5. Sanjana NE, Shalem O, Zhang F. *Nat Methods*. 2014;11:783–784.
6. Dominici M, Le Blanc K, Mueller I, et al. *Cytotherapy*. 2006;8:315–317.
7. Fernández-Garza LE, Barrera-Barrera SA, Barrera-Saldaña HA. *Pharmaceuticals*. 2023;16:1334.
8. Gonmanee T, Thonabulsombat C, Vongsavan K, Sritanaudomchai H. *Arch Oral Biol*. 2018;88:34–41.
9. Chen S, Sanjana NE, Zheng K, et al. *Cell*. 2015;160:1246–1260.
10. Yudovich D, Bäckström A, Schmiderer L, Žemaitis K, Subramaniam A, Larsson J. *Sci Rep*. 2020;10:22393.
11. Hendel A, Bak RO, Clark JT, et al. *Nat Biotechnol*. 2015;33:985–989.
12. Fernandes Neto JM, Jastrzebski K, Lieftink C, et al. *bioRxiv*. 2021;2021.07.13.452178.
13. Li J, Liang Q, Zhou H, Zhou M, Huang H. *Cell Mol Biol Lett*. 2023;28:41.
14. Jamour P, Jamali A, Langeroudi AG, Sharafabad BE, Abdoli A. *BMC Mol Cell Biol*. 2024;25:15.
15. Shifrut E, Carnevale J, Tobin V, et al. *Cell*. 2018;175:1958–1971.e15.



OCT-4 ACTIVATING COMPOUND 1 ENHANCES DEVELOPMENTAL COMPETENCE AND PLURIPOTENCY OF PORCINE SCNT EMBRYOS

Thida Praeksamut¹, Phattarawadee Noita¹ and Rangsun Parnpai^{1,*}

¹ Embryo Technology and Stem Cell Research Center, School of Biotechnology, Institute of Agricultural Technology, Suranaree University of Technology, Nakhon Ratchasima, THAILAND

*e-mail: rangsun@g.sut.ac.th

Abstract:

Somatic cell nuclear transfer (SCNT) is an assisted reproductive technique involving a donor cell is transferred into an enucleated oocyte. Its efficiency remains low due to abnormal nuclear reprogramming. Previous studies have shown that SCNT blastocysts exhibit aberrant expression of *OCT-4* and related genes. *OCT-4* transcription factor is crucial for embryonic development, maintaining pluripotency, and regulating primordial germ cell formation. On the other hand, DNA methylation plays an important role in mammalian embryogenesis, such as gene imprinting, X chromosome inactivation, and genome stability. In the cloning technique, SCNT-derived embryos are highly methylated compared with *in vitro* fertilized embryos. Therefore, abnormal SCNT embryos may be caused by an incomplete reprogramming of DNA methylation. Enhancing *OCT-4* expression in SCNT embryos may improve their reprogramming efficiency. In this study, we investigated the optimal concentration and effects of OCT-4 Activating Compound 1 (OAC1) that was reported to induce the expression of *OCT-4* and *NANOG* in bovine SCNT embryos. Comparisons were made with porcine embryos derived from *in vitro* fertilization (IVF). The results of this study indicated that treatment with OAC1 at a concentration of 1.5 μM significantly increased the blastocyst formation rate and total cell numbers in SCNT embryos ($p < 0.05$). Furthermore, OAC1 enhanced the expression of *OCT-4*, *SOX2*, and *NANOG* specifically at the 8-cell stage, but did not significantly affect gene expression at other developmental stages. Regarding DNA methyltransferase (*DNMT*), IVF embryos exhibited lower expression levels than SCNT embryos during early development, with expression levels increasing from the 8-cell to the blastocyst stages involving re-methylation occurs and new genomic imprints are established by activating the methylation. In conclusion, OAC1 appears to exert beneficial effects on embryonic development in SCNT embryos by promoting *OCT-4* and related genes expression and reprogramming through modulation of DNA methylation.

Introduction:

Somatic cell nuclear transfer (SCNT) involves transferring a donor cell into an enucleated oocyte. Currently, SCNT has been successfully applied to a range of species. Animal production based on SCNT offers a range of opportunities in basic and applied research, in agriculture, genetic conservation, and human medicine [1]. However, SCNT efficiency is still low because of incomplete epigenetic reprogramming of donor cell nuclei [2]. Consequently, the improvement of epigenetic reprogramming is a crucial factor in enhancing the developmental efficiency of SCNT embryos [3].

OCT-4 (Octamer-binding transcription factor 4) is a major transcription factor in embryonic stem cells and primordial germ cells [4]. The *OCT-4* gene is essential for complete embryo development [5] and regulating pluripotency in embryonic stem cells [6].

Previous SCNT-related studies reveal that the expression level of the *OCT-4* gene in donor cells improves developmental efficiency, promotes nuclear reprogramming of SCNT embryos in bovine and porcine [7] and enhances the expression level of the *OCT-4* during cleavages resulting in a higher developmental rate of mouse SCNT embryos. Oct4-activating compound (OAC1) has been widely applied to increase the expression activity of the *OCT-4*



in mouse [9]. Moradi-Hajidavaloo et al. (2023) [10] reported that using 1.5 μM of OAC1 in IVC medium improves the quality of bovine SCNT embryos. However, the effects of OAC1 on porcine SCNT embryos have not yet been reported.

This study aimed to determine the optimal concentration and the effects of OAC1 as a small-molecule supplemented in IVC medium on cleavage rate, blastocyst formation rate, expression level of *OCT-4*, *SOX2*, *NANOG*, and *DNMT1* genes of porcine SCNT embryos.

Methodology:

Chemicals

Chemicals used in this research were purchased from Sigma-Aldrich Corporation (St. Louis, MO, USA), if not, specify additionally.

Preparation of oct-4 activating compound 1 (OAC1) solution

Commercially available OAC1 was dissolved in 1 ml dimethylsulphoxide (DMSO) to produce a 21.07 mM 1,000X stock solution. Porcine zygote medium-3 (PZM-3) was used to dilute the stock solution to obtain a working solution.

Donor cell preparation

Fibroblast cells were isolated from the ear skin tissues of a male piglet. The skin was washed with 70% alcohol, and root hair and cartilage were removed before being manually cut into small pieces. The tissue pieces were placed on culture dishes and covered with a sterilized glass slide. Four milliliters of culture medium were then added to each culture dish, and the tissues were cultured under a humidified atmosphere of 5% CO_2 at 37 °C. The culture medium consisted of Minimum Essential Medium Eagle, Alpha modification (αMEM) supplemented with 10% fetal bovine serum (FBS, Gibco, 10270-098), 1 mM L-glutamine, 100 IU/ml penicillin-G, and 100 $\mu\text{g}/\text{ml}$ streptomycin sulfate. The medium was changed every 3 days. After the fibroblasts reached at least 80% confluency, they were harvested using trypsin/EDTA and passaged until the third passage. At the third passage, the harvested cells were resuspended in freezing medium, loaded into 0.5 ml straws, stored at -80 °C overnight, and subsequently transferred to liquid nitrogen until use. For donor cell preparation, fibroblasts were thawed and cultured in a culture dish with 3 ml of culture medium under a humidified atmosphere of 5% CO_2 at 37 °C for 2–3 days. Porcine fibroblasts at the fourth passage were used as donor cells.

Oocyte collection and in vitro maturation (IVM)

Porcine ovaries were obtained from a local slaughterhouse and kept in 0.9% NaCl solution at room temperature within 2 h during transport to the laboratory. Then, cumulus-oocyte complexes (COCs) were collected from antral follicles using an 18-gauge needle equipped with a 10 ml syringe. COCs with homogeneous cytoplasm and at least three layers of intact cumulus cells were cultured in IVM-I medium (50 COCs/500 μl) in 4-well dishes covered with mineral oil under 5% CO_2 at 38.5 °C for 23 h, followed by culture in IVM-II medium under the same conditions for 22 h.

Somatic cell nuclear transfer (SCNT)

SCNT was performed following a previously published protocol [11]. Briefly, cumulus cells were removed from COCs after 42–44 h of IVM. Only A- and B-graded metaphase II (MII) oocytes were used, and the zona pellucida above the first polar body was cut before enucleation with a glass needle squeeze. Complete enucleation was confirmed by staining the extruded cytoplasm and the first polar body with 5 $\mu\text{g}/\text{ml}$ Hoechst 33342 and visualization under a fluorescence microscope (IX71, Olympus, Tokyo, Japan). Donor cells at passage 4



were inserted into the perivitelline space of enucleated oocytes. The oocyte–donor cell complexes were fused using an electro-cell fusion machine (SUT F-1, Suranaree University of Technology) with two DC pulses of 24 V for 16 μ sec. Reconstructed embryos were activated by incubation in 3 μ M Ionomycin diluted in TCM199H for 4 min at room temperature, followed by incubation in 2 mM 6-Dimethylaminopurine (6-DMAP) diluted in PZM-3 under 5% CO₂ in air at 38.5 °C for 3 h.

In vitro embryo culture with OAC1 treatment

After the SCNT processes, groups of 50 oocytes were cultured in 500 μ l of PZM-3 medium [12] supplemented with 0, 1.0, 1.5, or 3.0 μ M OAC1 in 4-well dishes covered with mineral oil at 38.5 °C under 5% CO₂, 5% O₂, and 90% N₂ for 6 days. Embryo development was examined on days 3 and 6 to record cleavage and blastocyst formation, respectively.

Total cell number of porcine SCNT embryos

Total cell numbers were determined using Hoechst 33342 staining [13]. After 144 h of IVC, 10 blastocysts per treatment were incubated with 25 μ g/ml Hoechst 33342 in PBS (without Ca²⁺ and Mg²⁺) for 5 min at room temperature. Stained embryos were mounted on glass slides and observed under a fluorescence microscope (IX71, Olympus, Tokyo, Japan).

In vitro fertilization (IVF)

Embryos from the IVF group were used as a positive control. After 44 h of IVM (2.4), oocytes were washed three times in modified pig-FM medium [14] containing 10 mM HEPES, 2 mM caffeine, and 5 mg/ml BSA. Fresh semen from the SUT farm was diluted in BTS extender [15] at 15–20 °C. Sperm were preincubated in washing medium (TCM199 with Earle's salts, 4.12 mM calcium lactate, 3.05 mM glucose, and 12% FBS, pH 7.8) under 5% CO₂ in air at 37 °C for 30 min, centrifuged, and resuspended in pig-FM to a final concentration of 1.0×10^6 /ml. For fertilization, 10–15 oocytes were co-incubated with a 50 μ l sperm droplet in 35-mm culture dishes covered with mineral oil under 5% CO₂ at 38.5 °C for 4–6 h. After fertilization, cumulus cells were removed by gentle pipetting, and embryos were cultured in PZM-3 medium under 5% CO₂, 5% O₂, and 90% N₂ at 38.5 °C. Developmental stages (PN, 2-, 4-, 8-cell, and blastocyst) were evaluated on days 1, 2, and 5–6, respectively.

Effect of OAC1 on the expression level of OCT-4, SOX2, NANOG and DNMT1 by qPCR

Embryos at PN, 2-, 4-, 8-cell, and blastocyst stages from IVF and SCNT groups were harvested in PBS (–) and stored at –80 °C until RNA extraction. Embryos at PN (n = 150), 2-cell (n = 120), 4-cell (n = 60), 8-cell (n = 40), and blastocyst (n = 20) stages were lysed in lysis buffer, and mRNA was extracted using the FavorPrep™ Tissue Total RNA Mini Kit (Favorgen Biotech, Pingtung, Taiwan) according to the manufacturer's protocol. mRNA was reverse-transcribed to cDNA using the biotechrabbit™ cDNA Synthesis Kit (Biotechrabbit, Berlin, Germany). The reaction was incubated at 25 °C for 30 s and 52 °C for 30 min, followed by 99 °C to inactivate reverse transcriptase. cDNA was stored at –20 °C until use. Quantitative real-time PCR (qPCR) was performed with the KAPA SYBR-Green PCR

Master Mix (Applied Biosystems, Carlsbad, CA, USA) on a CFX Opus 96 real-time PCR system (Bio-Rad, Hercules, CA, USA) using specific primers (Table 1). Relative gene expression was normalized to GAPDH (reference gene) and compared with IVF embryos (normal control) using the $2^{-\Delta\Delta C_t}$ method.

Table 1.
Primer sequences used in this study

genes	Primer Sequences5' to 3'	Product Length, bp	Accession No.
genes related to embryo development			
<i>OCT4</i>	F: TTTGGGAAGGTGTTTCAGCCAAACG R: TCGGTTCTCGATACTTGTCGGCTT	198	NM_001113060
<i>SOX2</i>	F: ATGCACAACCTCGGAGATCAG R: TATAATCCGGGTGCTCCTTC	130	NM_001123197
<i>NANOG</i>	F: GGTTTATGGGCCTGAAGAAA R: GATCCATGGAGGAAGGAAGA	98	NM_001129971
genes related to epigenetic reprogramming			
<i>DNMT1</i>	F: TCGAACCAAAACGGCAGTAC R: CGGTCAGTTTGTGTTGGACA	215	NM_001032355
<i>GAPDH</i>	F: GTCGGTTGTGGATCTGACCT R: TTGACGAAGTGGTCGTTGAG	207	NM_001206359

Statistical analysis

Statistical analysis was performed by GraphPad version 5 (GraphPadSoftware, San Diego, CA, USA), and data were represented as the mean \pm SEM. A value of $p < 0.05$ was considered significant with different superscript-case letters. The differences between data were indicated using a one-way analysis of variance (ANOVA), followed by the Tukey–Kramer Honest Significant Difference (HSD) Post hoc test to compare differences between the two groups.

Ethical Approval Statement

This study was approved by the Institutional Animal Care and Use Committee, Suranaree University of Technology. The protocol number is IACUC-67-43.

Results and Discussion:

Results

Cleavage and blastocyst rate of porcine SCNT cultured with OAC1

To evaluate the optimal concentration of OAC1 supplemented in IVC medium on porcine SCNT embryos development. After the SCNT process, the reconstructed embryos were cultured in IVC medium supplemented with 0, 1.0, 1.5, and 3.0 μ M OAC1. The results from Table 2 showed that supplemented with 1.5 μ M OAC1 significantly higher cleavage rate than the untreated group ($86.33 \pm 1.2\%$ vs $74.2 \pm 1.8\%$, $p < 0.05$). The blastocyst rate of the 1.0 and 1.5 μ M OAC1 was significantly higher than untreated group ($42.87 \pm 1.9\%$ and $48.07 \pm 0.8\%$ and $36.1 \pm 0.9\%$ $p < 0.05$, respectively) (Table 2)

Total cell number of porcine SCNT cultured with OAC1

In the next step, we examine the effect of OAC1 supplemented in IVC medium on the total cell number in the blastocysts. The results showed that total cell number of supplemented with 1.5 μ M OAC1 was significantly higher than the other group (Table 2).

Table 2

The effect of different concentrations of OAC1 on the development of porcine SCNT embryos

OAC1 concentration (μM)	No. of embryos cultured	No. of cleaved (mean \pm SEM, %)	No. of blastocysts (mean \pm SEM, %)	Total cell number in blastocyst (mean \pm SEM)
0	156	117 (74.2 \pm 1.8) ^c	57 (36.1 \pm 2.9) ^c	53.8 \pm 1.6 ^c
1.0	158	124 (79.0 \pm 1.7) _{bc}	68 (42.8 \pm 1.9) ^b	61.1 \pm 1.2 ^b
1.5	160	140 (86.3 \pm 1.2) ^a	76 (48.1 \pm 1.8) ^{ab}	66.0 \pm 1.8 ^a
3.0	158	130 (82.5 \pm 1.6) _{bc}	66 (41.53 \pm 2.0) ^{bc}	58.2 \pm 1.1 ^b

9 replicates were performed

^{a, b, c} Values with different superscripts in the same column are significantly different ($P < 0.05$)

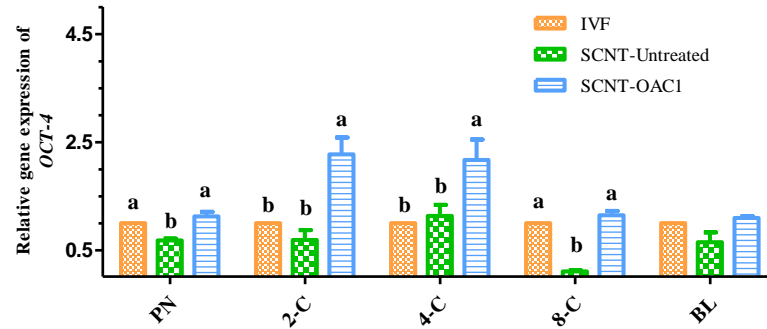
OAC1 affected the expression of genes related to the development and pluripotency of porcine SCNT embryos

We investigated the OAC1 that regulated the mRNA expression level of *OCT-4*, *SOX2*, and *NANOG* genes at PN, 2-, 4-, 8- cells and blastocyst stages between untreated SCNT embryos group as a negative control (SCNT-Untreated), IVF group as a positive control (normal control) and SCNT embryos treated with 1.5 μM of OAC1 as a treatment group (SCNT-OAC1) with the results shown in Figure 1

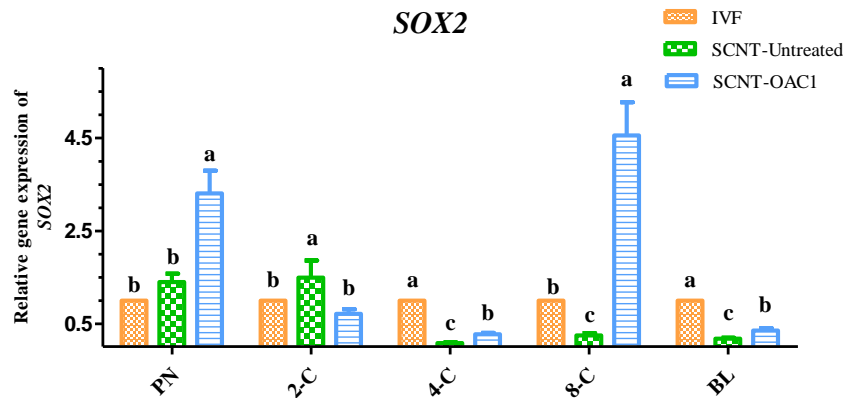
The expression level of the *OCT-4* gene in the treatment group showed variation across the developmental stages. At PN and 8-cell stages, the *OCT-4* expression level of the SCNT-OAC1 group was significantly higher than the SCNT-Untreated group ($p < 0.05$), but no significant difference when compared with the IVF group. At 2- and 4-cell stages, the *OCT-4* expression level of the SCNT-OAC1 group was significantly higher than the SCNT-Untreated and IVF groups ($p < 0.05$). Finally, at the blastocyst stage, the *OCT-4* expression level of the SCNT-OAC1 group had no significant difference when compared with the SCNT-Untreated and IVF groups. The expression level of the *SOX2* gene in the treatment group showed variation across different stages. At PN stage, the *SOX2* expression level of the SCNT-OAC1 group was significantly higher than SCNT-Untreated and IVF groups ($p < 0.05$). At the 2-cell stage, the *SOX2* expression level of the SCNT-OAC1 group was significantly lower than the SCNT-Untreated, but no significant difference when compared with the IVF groups. At 4-cell and blastocyst stages, the *SOX2* expression level of the SCNT-OAC1 group was significantly lower than the IVF group ($p < 0.05$), but was significantly higher than the SCNT-Untreated group ($p < 0.05$). Finally, at 8-cell stage, the *SOX2* expression level of the SCNT-OAC1 group was significantly higher than SCNT-Untreated and IVF groups ($p < 0.05$), but the IVF group was significantly higher than the SCNT-Untreated group ($p < 0.05$). The expression level of the *NANOG* gene in the treatment group showed variation across different stages. At PN and 4-cell stages, the *NANOG* expression level of the SCNT-OAC1 group was significantly lower than the IVF group ($p < 0.05$), but no significant difference when compared with the SCNT-Untreated group. At the 2-cell stage, the *NANOG* expression level of the SCNT-OAC1 group was significantly lower than the IVF group ($p < 0.05$), but was significantly higher than the SCNT-Untreated group. Finally, at 8-cell and blastocyst stages, the *NANOG* expression level of the SCNT-OAC1 group was significantly higher than the SCNT-Untreated group ($p < 0.05$), but no significant difference when compared with the IVF group.

OCT-4

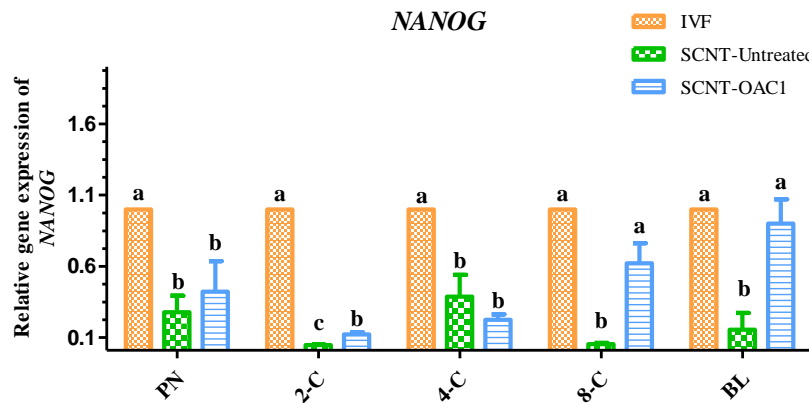
(A)



(B)

SOX2

(C)

NANOG**Figure 1**

Comparison of mRNA expression levels (mean \pm SEM) of genes related to development and pluripotency of porcine embryos between the SCNT-OAC1, IVF, and SCNT-Untreated groups at PN, 2-cell, 4-cell, 8-cell, and blastocyst stages: (A) Expression levels of *OCT-4* gene, (B) Expression levels of *SOX2* gene, and (C) Expression levels of *NANOG* gene. Embryos at PN stage (n=150), 2-cell stage (n=120), 4-cell stage (n=60), 8-cell stage (n=40), and blastocyst stage (n=20) were examined. ^a, ^b, and ^c Values with different superscripts indicate a significant difference ($p < 0.05$). Error bar = standard error of the mean.

OAC1 affected the expression of genes related to DNA methylation of porcine SCNT embryos
We investigated the *OAC1* that regulated the mRNA expression level of the DNA methylation of porcine SCNT embryos, including *DNMT1* genes at PN, 2-, 4-, 8- cells, and blastocyst stages between untreated SCNT embryos group as a negative control (SCNT-Untreated), IVF group as a positive control (normal control) and SCNT embryos treat with 1.5 μM *OAC1* as a treatment group (SCNT-*OAC1*) with the results shown in Figure 2.

The expression level of the *DNMT1* gene in the treatment group showed variation across different stages. At the PN stage, the *DNMT1* expression level of the SCNT-*OAC1* group was significantly higher than the IVF group ($p < 0.05$), but no significant difference when compared with the SCNT-Untreated group. At the 2-cell stage, the *DNMT1* expression level of the SCNT-*OAC1* group was significantly higher than SCNT-Untreated and IVF groups ($p < 0.05$), and the SCNT-Untreated group was significantly higher than the IVF group. At the 4-cell stage, the *DNMT1* expression level of the SCNT-*OAC1* group was significantly lower than the SCNT-Untreated group ($p < 0.05$), but no significant difference when compared with IVF group. Finally, at 8-cell and blastocyst stages, the *DNMT1* expression level of the SCNT-*OAC1* group was significantly lower than the IVF group ($p < 0.05$), but no significant difference when compared with the SCNT-Untreated group.

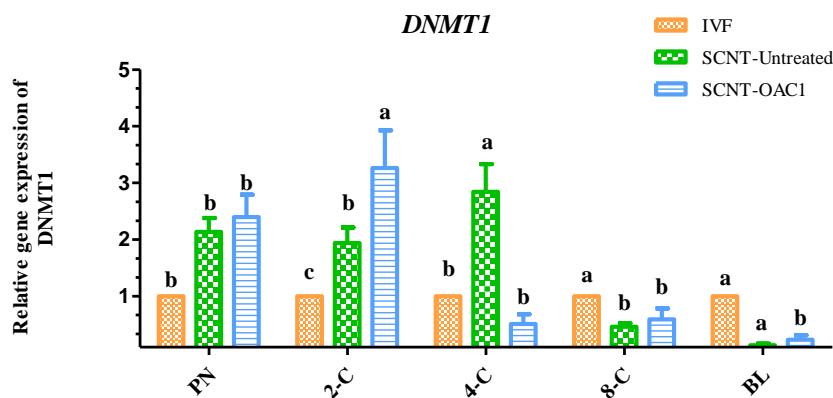


Figure 2

Comparison of mRNA expression levels (mean \pm SEM) of genes related to DNA methylation of porcine embryos between the SCNT-*OAC1*, IVF, and SCNT-Untreated groups at PN, 2-cell, 4-cell, 8-cell, and blastocyst stages. Embryos at PN stage (n=150), 2-cell stage (n=120), 4-cell stage (n=60), 8-cell stage (n=40), and blastocyst stage (n=20) were examined. ^a, ^b, and ^c Values with different superscripts indicate a significant difference ($p < 0.05$). Error bar = standard error of the mean.

Discussion:

In our study, first of all, we treated various concentrations of *OAC1* supplemented in IVC medium and cultured for 6 days to examined the optimal concentration by measuring the quality and development of porcine SCNT embryo (cleavage rate, blastocyst rate, and total cell numbers) between treated and untreated *OAC1*. The results showed that 1.5 μM of *OAC1* gives a significantly increased the embryo development particular at cleavage and blastocyst rates, and the total cell numbers of blastocyst-derived porcine SCNT. The results of this experiment are similar to a SCNT bovine embryo that was treated with 1.5 μM of *OAC1*, showing an increased developmental rate [10]. We used 1.5 μM of *OAC1* to investigate the mRNA expression of *OCT-4*, *SOX2*, and *NANOG* genes that pluripotency markers of embryonic cells play an important role in self-renewal and maintaining the

pluripotency of cloned embryos [16,17]. The effect of pluripotent markers induced by OAC1 has not yet been reported in a porcine SCNT embryo. However, the *OCT-4* expression in our study showed an increase in the SCNT-OAC1 group at the PN until 8-cell stages than the untreated and IVF group but no significant difference was observed at blastocyst stages between the untreated and IVF group. This result is consistent with the report in SCNT porcine embryo, the *OCT-4* expression level is detected until the 8-cell stage from transcription using maternal mRNA, and the zygote *OCT-4* expression being from 8 – 16-cell stage [18]. In addition, in mouse embryos, the loss of *OCT-4* expression showed at the blastocyst stage due to the occurrence of differentiation of totipotent cells to somatic lineages [19]. During early embryonic development, transcription factors (TFs) play a crucial role in determining the fate of blastomere by regulating the activation or suppression of *OCT-4*, the key development gene is a core component of the pluripotency regulation network, guiding blastomere to ICM, which later gives rise to embryonic stem cell or toward differentiation into trophoblast cell, with contribution to extra-embryonic structure [6]. Several studies have demonstrated a function of *OCT-4* in the embryo development [20]. Further studies on the transcription regulation of *OCT-4* in porcine improved the developmental efficiency of nuclei transfer embryos, suggesting that high *OCT-4* expression in donor cells are more efficient promote nuclei reprogramming [21,22]. However, the mRNA expression of *OCT-4* in porcine and bovine SCNT embryos was significantly lower than that derived by IVF [23]. Previous studies have made progress on identifying an *OCT-4* promoter-activating compound to promote the *OCT-4* expression to enhance the efficiency of reprogramming [24] and differentiated cells into pluripotent cells [10,24,25]. The *SOX2* expression level of SCNT-OAC1 group showed higher than untreated and IVF groups at PN and 8-cell stages, lower than IVF group at 4-cell and blastocyst stage but no difference at the 2-cell stage. *Sox2* acts cooperatively with *OCT-4* at promoters activating the transcription of several genes, which play important roles in embryo development [26]. The downregulate of *SOX2* expression is possible to decreasing *OCT-4* expression levels influence several transcription factors and induce developmental arrest [18].

The *NANOG* expression level in the OAC1 treatment group was lower than in the IVF group at the PN stage until the 4-cell stage, and there was no difference at the 8-cell to blastocyst stages. The results were consistent with the previous study, the *OCT-4* and *SOX2* network stimulates the expression of *NANOG* has shown that the expression of *OCT-4*, *SOX2*, and *NANOG* follows the same trend, with high expression level of *NANOG* at the 8-cell stage to the blastocyst stage [27,28] and the distinct expression pattern of *OCT-4* compared to *NANOG* at certain stages of embryo development supports previous studies indicating that OAC1 promotes the expression level of *OCT-4* and *NANOG* [24].

DNA methylation occurs at the fifth carbon of cytosine residues within CpG dinucleotides and is essential for long-term transcriptional silencing as well as normal mammalian embryonic development. Somatic cells with high levels of DNA methylation are often used as nuclear donors for cloning, resulting in cloned embryos that typically exhibit increased DNA methylation, which is abnormally hypermethylated [29]. *DNMT1*, a maintenance methyltransferase, is recruited to the replication fork during the S-phase of the cell cycle, where it methylates the newly synthesized DNA strand [30]. DNA demethylation occurs during early embryonic development, followed by re-methylation at later stages [31,32]. We investigate the mRNA expression of *DNMT1* involved in the dynamics of DNA methylation. The results showed that the expression of *DNMT1* in the OAC1 treatment group was higher than IVF group at PN, and 2-cell stages, but no significant difference at the 4-cell stage, and significantly lower than the IVF group at 8-cell to blastocyst stages. Normally, the *DNMTs* expression at the early stage of IVF is lower than SCNT embryos [33] but it could be higher than SCNT embryos that possible explanation may be the limitation of IVM oocytes to



process several spermatozoa entering the ooplasm [34]. Inconsistent reports of SCNT embryos can be high DNA methylation expression is partially retained its methylation pattern even after the nucleus has been structurally remodeled into a pronucleus-like state [35]. Another reason that porcine IVF embryos at early stages still increase more than SCNT embryos is that after fertilization, the parental epigenomes undergo significant changes to restore totipotency in the zygote. The tightly packed paternal genome quickly unravels, sperm protamines are replaced with histones, and DNA is actively demethylated without the need for replication [36,37]. In addition, from the 8-cell to the blastocyst stage, normalized DNA methylation levels continuously increased in IVF embryos, but contrasted to SCNT embryos that decreased DNA methylation is possibly the result of *de novo* methylation related to the activity of *de novo* DNA methyltransferases [38,39]. On the other hand, the report of global DNA methylation at an early stage and blastocyst stage does not differ between IVF and SCNT embryos but at the 8-cell stages, the IVF embryo increases more than the SCNT embryo possibly re-methylated occurs and new genomic imprints are established by activating the methylation [33,35,40]

Conclusion:

The optimal concentration of OAC1 at 1.5 μ M could enhance cleavage and blastocyst rates, as well as the total cell numbers. Additionally, it improved the expression of genes related to the pluripotency and DNA methylation of SCNT embryos, including *OCT-4*, *SOX2*, *NANOG* and *DNMT1* at the 8-cell to the blastocyst stages. However, more of the OAC1 dynamic on the development and epigenetic modification of porcine SCNT embryos need to be confirmed in the future. The suggestion of the study might be to investigate such as the optimal time to culture OAC1 after the SCNT process, the suitable period of treatment, the IVM or IVC period, the mechanism of OAC1, co-culture with another small molecule, another position of histone modification, and the number of healthy offspring after embryo transfer.

Acknowledgements:

This study was supported by Suranaree University of Technology. Thida Praeksamut received the One Research One Graduate (OROG) fellowships program. We would like to thank Betagro Public Co., Ltd. for providing the pig ovaries in our research.

References:

1. Campbell K, Fisher P, Chen W, Choi I, Kelly R, Lee J-H, Xhu J. *Theriogenology*. 2007; 68: S214–S231.
2. Long C, Westhusin R, Golding M C. *Molecular Reproduction and Development*. 2014; 81(2): 183–193.
3. Qiao F, Ge H, Ma X, Zhang Y, Zuo Z, Wang M, Zhang Y, Wang Y. *Theriogenology*. 2018; 114: 199–205.
4. Looijenga L H, Stoop H, De Leeuw H P, de Gouveia Brazao C A, Gillis A J, Van Roozendaal K E, Van Zoelen E J, Weber R F, Wolffenbuttel K P, Van Dekken H. *Cancer Research*. 2003; 63(9): 2244–2250.
5. Nichols J, Zevnik B, Anastassiadis K, Niwa H, Klewe-Nebenius D, Chambers I, Schöler H, Smith A. *Cell*. 1998; 95(3): 379–391.
6. Niwa H, Miyazaki J, Smith A G. *Nature Genetics*, 2000; 24(4): 372–376
7. Goissis M D, Suhr S T, Cibelli J B. *Cellular Reprogramming (Formerly" Cloning and Stem Cells")*. 2013; 15(1): 24–34.
8. Pfeiffer M J, Balbach S T, Esteves T C, Crosetto N, Boiani M. *International Journal of Developmental Biology*. 2010; 54(11–12): 1649–1657.

9. Li W, Tian E, Chen Z-X, Sun G, Ye P, Yang S, Lu D, Xie J, Ho T-V, Tsark W M. *Proceedings of the National Academy of Sciences*. 2012; 109(51): 20853–20858.
10. Moradi-Hajidavaloo R, Jafarpour F, Hajian M, Andani M R, Varnosfaderani S R, Nasr-Esfahani M H. *Theriogenology*. 2023; 198: 75–86.
11. Wei H, Qing Y, Pan W, Zhao H, Li H, Cheng W, Zeng Y. *PloS one*. 2013; 8(2): e57728.
12. Cao Z, Sui L, Li Y, Ji S, Zhang X, Zhang Y. *Zygote*. 2012; 20(3): 229–236.
13. Chazotte B. *Cold Spring Harbor Protocols*. 2011(1); pdb-prot5557.
14. Suzuki K, Asano A, Eriksson B, Niwa K, Nagai T, Rodriguez-Martinez H. *International Journal of Andrology*. 2002; 25(2): 84–93.
15. Bwanga C, De Braganca M, Einarsson S, Rodriguez-Martinez H. *Journal of Veterinary Medicine Series A*. 1990; 37(1-10): 651–658.
16. Keramari M, Razavi J, Ingman K A, Patsch C, Edenhofer F, Ward C M, Kimber S J. *PloS One*. 2010; 5(11): e13952.
17. Park S-J, Park H-J, Koo O-J, Choi W-J, Moon J, Kwon D-K, Kang J-T, Kim S, Choi J-Y, Jang G. *Cellular Reprogramming (Formerly" Cloning and Stem Cells")*. 2012; 14(5): 398–406.
18. Kirchhof N, Carnwath J, Lemme E, Anastassiadis K, Scholer H, Niemann H. *Biology of Reproduction*. 2000; 63(6): 1698–1705.
19. Pesce M, Schöler H R. *Stem Cells*. 2001; 19(4): 271–278.
20. Boiani M, Eckardt S, Schöler H R, McLaughlin K J. *Genes & Development*. 2002; 16(10): 1209–1219.
21. du Puy L, de Sousa Lopes S M C, Haagsman H P, Roelen B A. *Theriogenology*. 2011; 75(3): 513–526.
22. Lee J-H, Lee W-J, Jeon R-H, Lee Y-M, Jang S-J, Lee S-L, Jeon B-G, Ock S-A, King W A, Rho G-J. *Cellular Reprogramming (Formerly" Cloning and Stem Cells")*. 2014; 16(6): 428–438.
23. Garcia-Canovas M, Parrilla I, Cuello C, Gil M A, Martinez E A. *Animal Reproduction Science*. 2024; 107600.
24. Li W, Tian E, Chen Z-X, Sun G, Ye P, Yang S, Lu D, Xie J, Ho T-V, Tsark W M. *Proceedings of the National Academy of Sciences*. 2012; 109(51): 20853–20858.
25. Huang X, Lee M-R, Cooper S, Hangoc G, Hong K-S, Chung H-M, Broxmeyer H E. *Leukemia*. 2016; 30(1): 144–153.
26. Nishimoto M, Fukushima A, Okuda A, Muramatsu M. *Molecular and Cellular Biology*. 1999; 19(8): 5453–5465.
27. Kalmar T, Lim C, Hayward P, Munoz-Descalzo S, Nichols J, Garcia-Ojalvo J, Martinez Arias A. *PLoS Biology*. 2009; 7(7): e1000149.
28. Rodda D J, Chew J-L, Lim L-H, Loh Y-H, Wang B, Ng H-H, Robson P. *Journal of Biological Chemistry*. 2005; 280(26): 24731–24737.
29. Enright B, Kubota C, Yang X, Tian X. *Biology of Reproduction*. 2003; 69(3): 896–901.
30. Sharif J, Muto M, Takebayashi S, Suetake I, Iwamatsu A, Endo T A, Shinga J, Mizutani-Koseki Y, Toyoda T, Okamura K. *Nature*. 2007; 450(7171): 908–912.
31. Reik W, Santos F, Mitsuya K, Morgan H, Dean W. *Biological Sciences*. 2003; 358(1436): 1403–1409.
32. Ivanova E, Canovas S, Garcia-Martínez S, Romar R, Lopes J S, Rizos D, Sanchez-Calabuig M J, Krueger F, Andrews S, Perez-Sanz F. *Clinical Epigenetics*. 2020; 12: 1–18.
33. Kaneda M, Okano M, Hata K, Sado T, Tsujimoto N, Li E, Sasaki H. *Nature*. 2004; 429(6994): 900–903.



34. Gioia L, Barboni B, Turriani M, Capacchietti G, Pistilli M G, Berardinelli P, Mattioli M. *Reproduction*. 2005; 130(1): 29–39.
35. Deshmukh R S, Østrup O, Østrup E, Vejlsted M, Niemann H, Lucas-Hahn A, Petersen B, Li J, Callesen H, Hyttel P. *Epigenetics*. 2011; 6(2): 177–187.
36. Abdalla H, Yoshizawa Y, Hochi S. *Journal of Reproduction and Development*, 2009; 55(4): 356–360.
37. Fulka H, St. John J C, Fulka J, Hozák P. *Differentiation*. 2008; 76(1): 3–14.
38. Loi P, Beaujean N, Khochbin S, Fulka Jr J, Ptak G. *Bioessays*. 2008; 30(1): 66–74.
39. Bermejo-Alvarez P, Rizos D, Rath D, Lonergan P, Gutierrez-Adan A. *Physiological Genomics*. 2008; 32(2): 264–272.
40. Bonk A J, Li R, Lai L, Hao Y, Liu Z, Samuel M, Ferguson E A, Whitworth K M, Murphy C N, Antoniou E. *Molecular Reproduction and Development*. 2008; 75(2): 250–264.



ASSESSMENT OF THE ANTIOXIDANT AND ANTI-INFLAMMATORY PROPERTIES OF HUMAN PLACENTAL EXTRACT IN HUMAN MESENCHYMAL STEM CELLS

Kanda Rungboon, Nipha Chaicharoenaudomrung, Natchadaporn Sorraksa, Phongsakorn Kunhorm, and Parinya Noisa*

School of Biotechnology, Institute of Agricultural Technology, Suranaree University of Technology

*Corresponding e-mail: kandakdrb@gmail.com

Abstract:

Cellular senescence is a major concern for humans, caused by both natural aging and external environmental factors. From these factors, if the body accumulates oxidative stress in the body weakens physiological functions, leading to cellular deterioration, organ dysfunction, and aging. As a result, people are increasingly turning to dietary supplements or commercial cosmetic to maintain their health and beauty. However, one major problem with most products may have long-term side effects and could increase the risk of chronic diseases. Human placental extract (HPE) has gained increasing attention in scientific and clinical fields as a promising natural supplement whose advantages include being naturally sourced and having few side effects. It's rich in nutrients, cytokines, and growth factors. Which contribute to its antioxidant properties, restores cells, and delay cells senescent. Therefore, this study aims to evaluate the effects of human placental extract at optimal concentrations under both normal and oxidative stress conditions through MTT assay, DCFH-DA assay, and gene expression analysis using RT-PCR. The expected results suggest that HPE enhances antioxidant defense mechanisms by regulating the expression of antioxidant enzymes, thereby preventing ROS production and cause delay cells senescent.

Introduction:

Cellular senescence builds up in the organs of aging animals and is triggered by both internal and external factors [1]. External elements, such as ultraviolet radiation (UVR), can accelerate this process by increasing oxidative stress. UVR promotes the production of ROS in mitochondria, leading to DNA and protein damage, which weakens cell function and structure. This contributes to premature aging and the development of diseases like cancer, neurodegenerative disorders, and other age-related conditions [2, 3]. Antioxidant enzymes such as SOD, CAT, and GPX play a key role in neutralizing ROS and protecting cells from oxidative damage [4, 5].

Mesenchymal stem cells (MSCs) are versatile cells that can develop into different types of specialized cells, such as bone, cartilage, fat, and muscle cells [6]. They play an essential role in healing and tissue regeneration by replacing damaged cells and also have strong anti-inflammatory effects. Because of these abilities, MSCs have attracted growing attention in medical research for their potential use in treating various health problems, including joint disorders like osteoarthritis, heart diseases, and immune system conditions [7, 8].

Human placental extract (HPE) is a natural substance rich in bioactive compounds, including nutrients, peptides, enzymes, amino acids, fatty acids, vitamins, minerals, and growth factors like FGF-2, VEGF, and TGF- β [9, 10]. HPE has been shown to reduce oxidative stress, support anti-inflammatory activity [11] and promote autophagy, which helps rejuvenate skin by encouraging the formation of new cells and reducing signs of aging [12, 13]. It also helps regulate hormonal balance. because the placental is rich in beneficial molecules, HPE has become popular in the health and beauty industries [14]. Placental extracts from human is considered low-risk, cost-effective, and valuable for developing



therapeutic and commercial cosmetic products [15]. With its strong regenerative potential and safety profile, HPE continues to be explored for use in various medical therapeutic applications and commercial cosmetic [16, 17].

Materials and Methods:

Cell culture and MTT cells survival assay

The umbilical cord-derived human mesenchymal stem cells (UC-MSCs) were obtained from the American Type Culture Collection (ATCC) (Manassas, VA, USA). Cells were cultured in MEM alpha medium containing 10% (v/v) FBS, 1% (v/v) penicillin-streptomycin, 1% (v/v) nonessential amino acids, and 1% (v/v) L-glutamine in a humidified incubator with a 5% CO₂ atmosphere at 37 °C. Cells were cultured until they reached 80% confluence which was found to be optimal for both utilization and expansion. The determination of cell viability and cell proliferation was performed by using MTT (3-[4,5-dimethyl-2-thiazolyl]-2,5-diphenyl-2H-tetrazolium bromide) assays. MSCs were seeded in a 96-well plate at a density of 4×10^3 cells/well and incubated overnight until the cells were approximately 80% confluent. The cells were treated with various concentrations of 0.5, 1, 2, 5, 10, 50, 100, 1000, and 1800 µg/mL HPE for 24 hours. After treatment, cells were washed once with 1x PBS and incubated with MTT 0.5 mg/mL in serum-free medium with a 5% CO₂ atmosphere at 37 °C for 3 hours. The MTT solution was discarded and formazan crystals were solubilized by adding DMSO. The absorbance was measured at 570 nm by using a microplate reader. The cytotoxic effect of hydrogen peroxide (H₂O₂)-induce stress on MSCs was evaluated using cell viability assays. This experiment will continue like the previous one but will use H₂O₂ instead of human placental extract to find the appropriate concentration for MSCs to use as a model under induced conditions.

Measurement of ROS intracellular using DCF-DA assays

Intracellular ROS generation was determined using 2',7'-dichlorofluorescein diacetate (DCFH-DA). MSCs were seeded in a 96-well plate at a density of 5×10^3 cells/well and incubated for 24 hours. The cells were then pretreated with or without 1 mM H₂O₂ for 30 minutes before being treated with various concentrations of HPE standard (0.5, 1, 2, and 5 µg/mL) for 24 hours. Subsequently, the cells were exposed to 1 mM H₂O₂ alone or co-treated with 10 mM N-acetylcysteine (NAC) for 30 minutes. After treatment, all conditions were incubated with 10 µM DCF-DA at 37 °C under 5% CO₂ for 1 hour. The fluorescence intensity of DCF-DA was then measured using a fluorescence microplate reader.

Gene expression by RT-PCR

Cells were pretreated with or without 1 mM H₂O₂ for 30 minutes in 6-well plates. After pretreatment, cells were treated with various concentrations of HPE standard and incubated for 24 hours. Following incubation, cells were detached using 0.25% trypsin-EDTA and collected by centrifugation at 1500 rpm. Total RNA was extracted using the NucleoSpin RNA kit (Macherey-Nagel, Dueren, Germany) according to the manufacturer's instructions. Subsequently, 1 µg of total RNA was used to synthesize complementary DNA (cDNA) using TOYOBO kits. The RT-PCR reaction mixture was prepared with cDNA, 2X Taq Master Mix, nuclease-free water, and specific primers for the genes *SOD*, *GPX*, and *CAT*. Glyceraldehyde 3-phosphate dehydrogenase (*GAPDH*) was used as an internal control to normalize gene expression, as listed in **Table 1**. RT-PCR products were separated by agarose gel electrophoresis and visualized under UV light after staining with RedSafe™ Nucleic Acid Staining Solution. Electrophoresis was performed using the PowerPac™ Basic Power Supply (BIO-RAD).

Results:

Cytotoxicity of HPE and H₂O₂-induce in MSCs

To assess the effects of HPE on MSCs viability and cytotoxicity, MSCs were treated under normal conditions with various concentrations of HPE (0.5, 1, 2, 5, 10, 50, 100, 1,000, and 1,800 $\mu\text{g}/\text{mL}$) for 24 hours. To mimic oxidative stress conditions, MSCs were also exposed to different concentrations of H₂O₂ (0.1, 0.5, 1, 3, 5, 10, 20, 30, and 40 mM) for 30 minutes (Figure 1 B-C). Untreated MSCs served as the control group in both experiments to determine the optimal concentrations of HPE and H₂O₂ for cell viability. The results demonstrated that HPE at concentrations of 0.5 to 1000 $\mu\text{g}/\text{ml}$ did not significantly affect cell viability compared to the control. In contrast, treatment with HPE at concentrations of 1,800 $\mu\text{g}/\text{ml}$ significantly reduced cell viability. Based on these findings, HPE concentrations ranging from 0.5 to 5 $\mu\text{g}/\text{ml}$, which maintained high cell survival rates, were selected for use in subsequent experiments. In the oxidative stress model, MSCs exposed to H₂O₂ showed a significant obvious cytotoxicity in cells at concentrations range from 3 mM onwards. Meanwhile, H₂O₂ at a concentration of 1 mM of, cells began to show signs of stress but maintaining a certain level of viability. Therefore, 1 mM H₂O₂ was chosen as the optimal concentration for inducing oxidative stress in this model (Figure 1D). Moreover, the morphology of MSCs treatment with HPE remained cell viability similar to that of the control group in terms of size and flattened shape (Figure 1A).

HPE reduced oxidative stress in MSCs by activating antioxidant genes

The effect of HPE on the expression of antioxidant-related genes in MSCs was investigated. The mRNA expression levels of *CAT*, *GPX*, and *SOD* were analyzed by RT-PCR (Figure 2 A-B) in cells pretreated with or without 1 mM H₂O₂ for 30 minutes prior to HPE treatment. HPE was applied at concentrations from 0.5 to 5 $\mu\text{g}/\text{mL}$ under both normal and oxidative stress conditions and compared to the control group. The results revealed that HPE significantly upregulated the expression of antioxidant genes in a dose-dependent, indicating an enhancement of the cellular antioxidant defense system. Additionally, intracellular ROS levels were assessed using the fluorescent probe DCF-DA, confirm the antioxidant activity of HPE through a marked reduction in ROS production in MSCs (Figure 2 C).

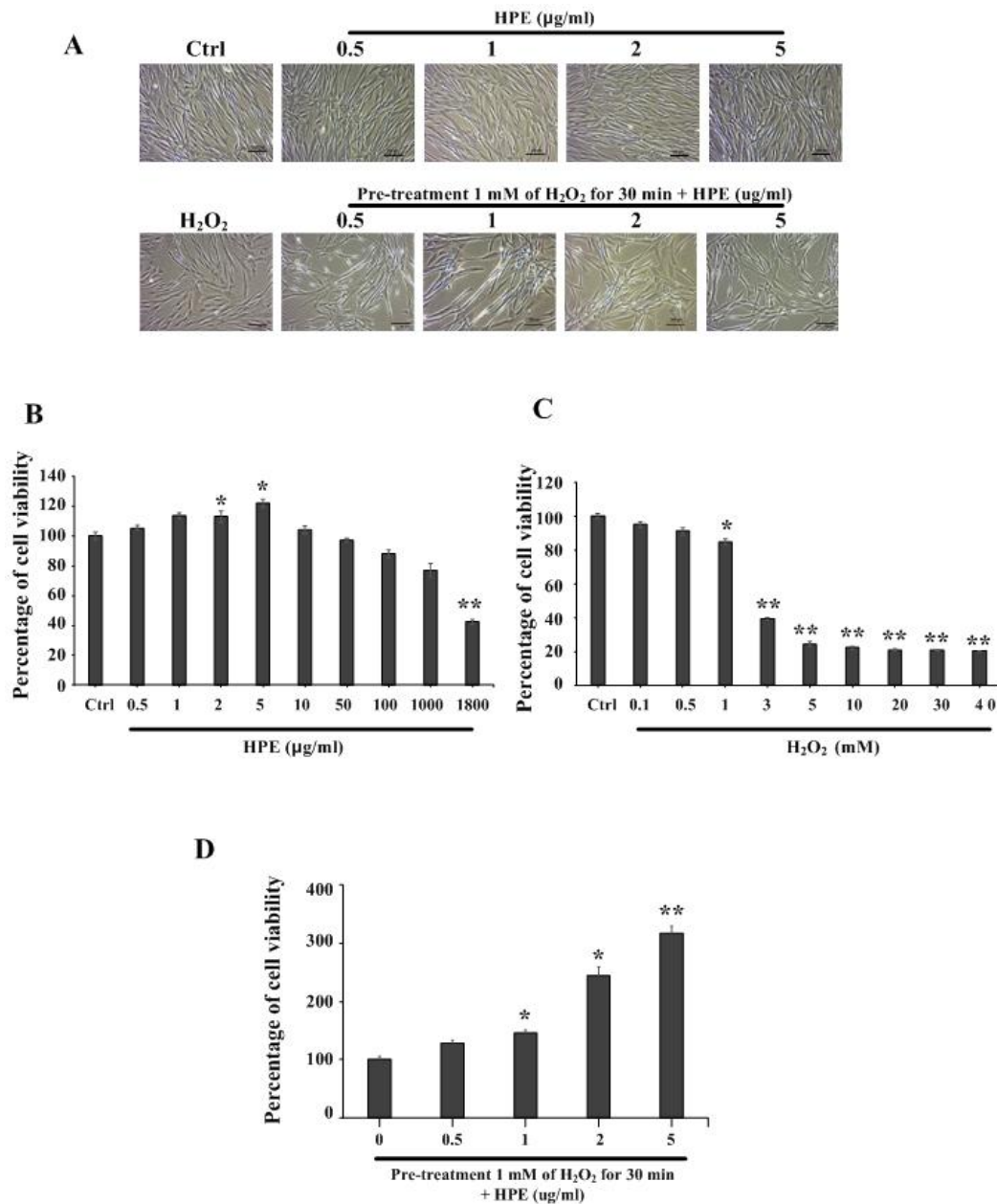


Figure. 1

The effect of HPE and H_2O_2 -induce on MSCs proliferation.

(A) The morphology of MSCs treated with HPE at 10X magnification was used to digitally capture the image; scale bar 100 μm . (B) The proliferation of cells treated with HPE was assessed using the MTT assay. (C) The effect of H_2O_2 -induced oxidative stress on MSC viability was also evaluated using the MTT assay. (D) The potential of HPE when pre-treated with H_2O_2 -induced oxidative stress on MSCs.

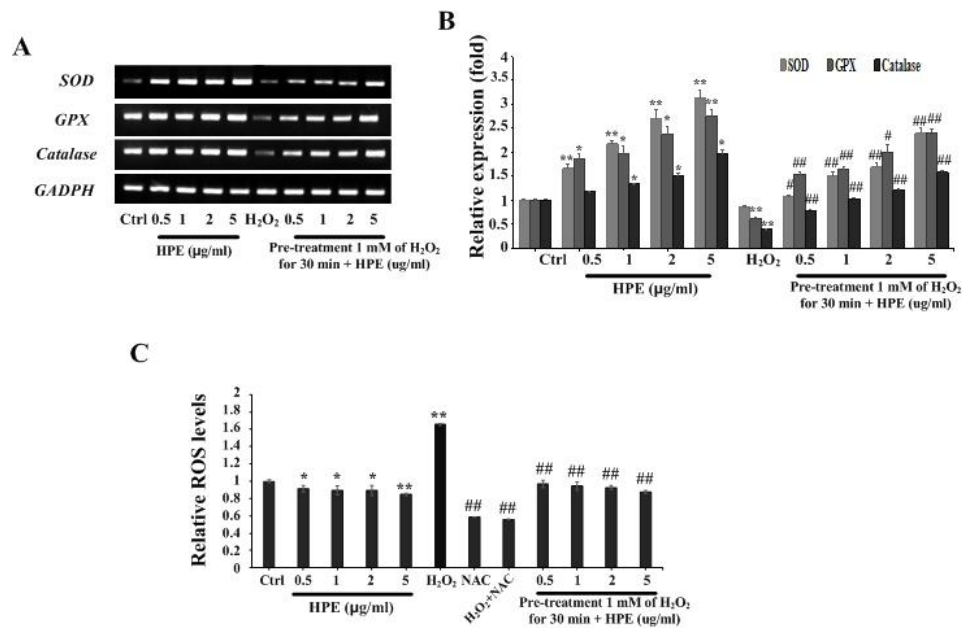


Figure. 2

The effect of HPE on mRNA expression in MSCs. (A-B)

The treatment of HPE-treated at concentrations 0.5 to 5 µg/mL either with or without 1 mM H₂O₂-induced for 30 minutes. upregulated the level of antioxidant genes in a dose-dependent by using GAPDH as the internal control. (C) To confirm antioxidant activity based on the reduction of intracellular ROS levels after treated with HPE was measured in MSCs using the fluorescent dye DCF-DA. Image j was used to analyze images of RT-PCR bands.

Discussion and Conclusion

Cellular senescence is a serious issue that affects human health and quality of life [18]. It can be caused by both internal aging, which is a natural biological process, and external factors such as pollution, chemicals, UVR, and certain lifestyle habits [19, 20]. A major factor in cellular aging is oxidative stress. This happens when the body produces too many ROS and its natural antioxidant system becomes weaker [21, 22]. High levels of ROS can harm important parts of the cell, like DNA, proteins, and mitochondrial membranes. This damage affects the balance inside the cell, lowers its ability to function properly, and reduces its ability to repair and divide. As a result, organs dysfunction, and signs of aging may appear throughout the body[23]. Antioxidants help fight oxidative stress by neutralizing ROS and protecting cells [5]. The body produces antioxidant enzymes such as SOD, GPX, and CAT to help control ROS levels. HPE has shown the ability to decrease oxidative stress, which helps delay cell senescence and prevent cell damage [11, 24]. Studies show that HPE can reduce ROS in stressed cells and increase the levels of antioxidant enzymes like SOD, GPX, and CAT in a dose-dependent. This benefit is likely due to the bioactive substances in HPE, including nutrients, enzymes, minerals, cytokines, vitamins, and growth factors. These components not only have antioxidant effects but also support cell repair and regeneration.

In conclusion, this study shows strong evidence from *in vitro* experiments that HPE can improve the body's antioxidant defenses in both normal and oxidative stress conditions. This action helps decrease the levels of ROS and delay cell senescence. The results suggest that HPE could be a natural option for reducing damage caused by oxidative stress, delaying the aging process in cells, and helping maintain healthy tissue function.

References

1. Franco, A.C., C. Aveleira, and C. Cavadas, *Skin senescence: mechanisms and impact on whole-body aging*. Trends in molecular medicine, 2022. **28**(2): p. 97-109.
2. Gough, D. and T. Cotter, *Hydrogen peroxide: a Jekyll and Hyde signalling molecule*. Cell death & disease, 2011. **2**(10): p. e213-e213.
3. Jomova, K., et al., *Reactive oxygen species, toxicity, oxidative stress, and antioxidants: Chronic diseases and aging*. Archives of toxicology, 2023. **97**(10): p. 2499-2574.
4. Dundar, Y. and R. Aslan, *Antioxidative stress*. Eastern Journal of Medicine, 2000. **5**(2): p. 45-47.
5. Huang, L., et al., *Human Placental Extract Delays In Vitro Cellular Senescence through the Activation of NRF2-Mediated Antioxidant Pathway*. Antioxidants, 2022. **11**(8): p. 1545.
6. Ding, D.-C., W.-C. Shyu, and S.-Z. Lin, *Mesenchymal stem cells*. Cell transplantation, 2011. **20**(1): p. 5-14.
7. Li, D., et al., *Biological characteristics of human placental mesenchymal stem cells and their proliferative response to various cytokines*. Cells Tissues Organs, 2007. **186**(3): p. 169-179.
8. Zupan, J., *Mesenchymal Stem/Stromal cells and fibroblasts: their roles in tissue Injury and Regeneration, and age-related degeneration*. Fibroblasts—Advances in Inflammation, Autoimmunity and Cancer, 2021: p. 1-25.
9. Chakraborty, P.D. and D. Bhattacharyya, *Aqueous extract of human placenta as a therapeutic agent*. Recent Advances in Research on the Human Placenta. Rijeka, Croatia: InTech, 2012: p. 77-92.
10. Chang, P.-Y., et al., *Human placental extract activates a wide array of gene expressions related to skin functions*. Scientific Reports, 2022. **12**(1): p. 11031.
11. Ghoneum, M. and M.S.A. El-Gerbed, *Human placental extract ameliorates methotrexate-induced hepatotoxicity in rats via regulating antioxidative and anti-inflammatory responses*. Cancer Chemother Pharmacol, 2021. **88**(6): p. 961-971.
12. Shin, J.Y., et al., *Mesenchymal stem cells enhance autophagy and increase β -amyloid clearance in Alzheimer disease models*. Autophagy, 2014. **10**(1): p. 32-44.
13. Jeong, K., et al., *The Inhibitory Effect of Human Placenta Extract (Laennec®) on Atopic Dermatitis-Like Skin Disease In Vivo and In Vitro*. 2023.
14. Kroløkke, C., E. Dickinson, and K.A. Foss, *The placenta economy: From trashed to treasured bio-products*. European Journal of Women's Studies, 2018. **25**(2): p. 138-153.
15. Szendzielorz, E. and R. Spiewak, *Placental extracts, proteins, and hydrolyzed proteins as active ingredients in cosmetic preparations for hair loss: A systematic review of available clinical evidence*. Applied Sciences, 2024. **14**(22): p. 10301.
16. Badrul Hisham, R., N.A. Tukiran, and M.A. Jamaludin, *Placenta in cosmetic products: an analysis from shariah and legal perspective in Malaysia*. ESTEEM Journal of Social Sciences and Humanities, 2024. **8**(1): p. 194-206.
17. Di Matteo, B., et al., *Placenta-Derived Products Demonstrate Good Safety Profile and Overall Satisfactory Outcomes for Treating Knee Osteoarthritis: A Systematic Review of Clinical Evidence*. Arthroscopy: The Journal of Arthroscopic & Related Surgery, 2023. **39**(8): p. 1892-1904.
18. Songjang, W., et al., *Porcine placenta extract induced Akt, ERK, and JNK signaling to heighten the osteogenic activity of human osteoblasts*. Journal of Applied Pharmaceutical Science, 2022. **12**(8): p. 018-025.
19. Sgarbieri, V.C. and M.T.B. Pacheco, *Healthy human aging: intrinsic and environmental factors*. Brazilian Journal of Food Technology, 2017. **20**: p. e2017007.



20. Song, S., et al., *Ultraviolet light causes skin cell senescence: from mechanism to prevention principle*. *Advanced Biology*, 2025. **9**(2): p. 2400090.
21. Hajam, Y.A., et al., *Oxidative stress in human pathology and aging: molecular mechanisms and perspectives*. *Cells*, 2022. **11**(3): p. 552.
22. Tan, B.L., et al., *Antioxidant and oxidative stress: a mutual interplay in age-related diseases*. *Frontiers in pharmacology*, 2018. **9**: p. 1162.
23. Farage, M.A., et al., *Characteristics of the aging skin*. *Advances in wound care*, 2013. **2**(1): p. 5-10.
24. Wang, Y., et al., *Superoxide dismutases: Dual roles in controlling ROS damage and regulating ROS signaling*. *Journal of Cell Biology*, 2018. **217**(6): p. 1915-1928.



NOVEL INSIGHTS INTO THE ROLE OF VESICLE- AND MONOLAYER-DERIVED EXTRACELLULAR VESICLES FROM BOVINE OVIDUCT EPITHELIAL CELLS IN ENHANCING EMBRYO QUALITY IN VITRO

Apisit Polrachom^{1,1}, Kamolchanok Tonekam², Worawalan Samruan³, Traimat Boonthai^{5,2} and Rangsun Parnpai^{6*}

1Embryo Technology and Stem Cell Research Center, School of Biotechnology, Institute of Agricultural Technology, Suranaree University of Technology, Nakhon Ratchasima 30000, Thailand

2Biological Science Program, Faculty of Science, Burapha University, Chon Buri 20131, Thailand

*e-mail: rangsun@g.sut.ac.th

Abstract:

This study investigated the effects of extracellular vesicles (EVs) derived from bovine oviduct epithelial cells (BOECs) on the development of bovine embryos during in vitro culture (IVC). EVs play an essential role in mimicking the oviductal microenvironment by transferring bioactive molecules such as proteins and RNAs, thereby facilitating intercellular communication and embryo development. In this experiment, EVs were isolated from two BOEC culture systems: a monolayer culture (BOEC-M-EVs) and a vesicle-forming culture (BOEC-V-EVs). These EVs were supplemented into the IVC medium at concentrations of 2×10^6 , 4×10^6 , and 8×10^6 particles/mL, while non-supplemented embryos served as controls. Supplementation with BOEC-M-EVs significantly increased total blastocyst cell numbers at all concentrations tested (132.8 ± 3.6 , 147.6 ± 5.6 , and 148.2 ± 1.7) compared with the control group (108 ± 5.2 , $P < 0.05$). Similarly, BOEC-V-EVs enhanced total cell numbers at 4×10^6 and 8×10^6 particles/mL (149.0 ± 1.7 and 158.6 ± 3.2 , $P < 0.05$). Both EV types improved blastocyst quality at higher concentrations, consistent with the upregulation of IFN τ , a gene essential for maternal recognition of pregnancy in ruminants. These findings demonstrate that BOEC-derived EVs support embryo development by recreating physiological cues of the oviduct and suggest their promising application for enhancing in vitro embryo production and reproductive efficiency in cattle.

Keywords: ruminant species, reproduction, oviduct epithelial cells, In vitro fertilization

Introduction:

In vitro embryo production (IVEP) is a widely used method for producing superior bovine embryos. However, embryos generated *in vitro* often exhibit slower developmental rates than their *in vivo* counterparts due to increased cell death caused by suboptimal culture conditions. As a result, improving the *in vitro* culture (IVC) environment is crucial to enhancing embryo quality and achieving results comparable to those seen *in vivo*. To address this, previous research has explored various culture media supplements, such as resveratrol and anethole from star anise, to improve the development of bovine embryos. Recently, extracellular vesicles (EVs) have emerged as promising candidates for enhancing embryonic growth in livestock. EVs promote intercellular communication by delivering biomolecules essential for early embryonic development, implantation, and pregnancy. While the benefits of EV supplementation have been extensively studied in species such as sheep and mice, little is known about their effects on bovine embryos. demonstrated that EVs derived from the bovine



uterus not only upregulated genes associated with embryo previous report¹, development, and implantation but also significantly increased inner cell mass and trophectoderm ratios. Similarly, in a previous study, researchers found that the addition of EVs to the *in vitro* maturation (IVM) medium enhanced both the trophectoderm and inner cell mass of bovine IVF embryos². Furthermore, EVs derived from bovine oviduct epithelial cells have been shown to improve mitochondrial activity, decrease lipid accumulation, and upregulate genes involved in blastocyst development. These findings suggest that EVs enhance embryo quality by regulating lipid metabolism and reducing the expression of apoptosis-related genes. Moreover,³ reported that EVs produced from monolayered bovine oviduct epithelial cells (BOEC-M-EVs) in IVC medium improved embryo quality by upregulating the expression of quality-related genes, outperforming fresh BOEC supplementation. However, no studies have yet investigated the effects of EVs derived from spheroid-derived or vesicle-shaped bovine oviduct epithelial cells (BOEC-V-EVs). Therefore, the objective of this study is to evaluate how BOEC-M-EVs and BOEC-V-EVs in IVC medium influence the development and quality of bovine embryos produced through IVF.

Methodology:

Chemicals and reagents

Unless stated otherwise, all chemicals and reagents were purchased from Sigma-Aldrich (St. Louis, USA). The cell culture media were purchased from Gibco (Paisley, UK), and plastic cell culture devices were obtained from SPL Life Sciences (Gyeonggi-do, Republic of Korea).

Preparation of EVs-depleted fetal bovine serum (dFBS)

Fetal bovine serum (FBS, Gibco, 10270-098) used in this study was removed EVs⁴. Briefly, the FBS was heated for 30 min at 56°C in a water bath, and then ultracentrifuged twice at 120,000xg for 90 min at 4°C. Subsequently, the supernatant was collected and kept at -20°C in conical tubes until used.

Preparation of bovine oviduct epithelial cells (BOEC)

Healthy oviducts from bovine ovaries were collected at the slaughterhouse during the post-ovulatory stage, which occurs between first five days of the estrus cycle⁵. Bovine oviducts were thoroughly rinsed with 0.9% NaCl solution, then placed in plastic bottles containing 0.9% NaCl solution, and kept at 4°C. Upon arrival at the laboratory, bovine oviducts were rinsed with 0.9% NaCl solution, soaked in PBS to remove any debris, and submerged in 70% ethanol. Connective tissues and blood vessels were discarded in a biosafety cabinet. Oviducts were subsequently rinsed twice in 70% ethanol after rinsing in PBS. Oviducts were rinsed in washing solution containing TCM199 HEPES supplement with bovine serum albumin (BSA). Next, oviductal segments were pressed into 1.5 ml microcentrifuge tubes using forceps. Three separate oviducts, at least, were combined. Retrieved cells separated by repeatedly taking in and out 10 times using a 21-gauge needle and a 25-gauge needle attached to a 1 ml syringe to isolate cells. Retrieved cells were transferred to a 15 ml conical tube containing 10 ml washing medium. The conical tube was incubated at 38.5°C for 5 min. Then, the supernatant was discarded and retrieved cells were washed with 10 ml washing medium twice. Subsequently, 100 µl retrieved cells were diluted with 10 ml culture medium (TCM199 supplemented with 10% FBS).



Preparation of conditioned medium from monolayered bovine oviduct epithelial cells (BOEC-M)

The BOEC were seeded in culture medium in a 100 mm petridish (Nunc, Denmark, 10mL/dish) and incubated at 38.5°C under a humidified atmosphere at 5% CO₂ in air for 48 h. The medium was changed and incubated at 38.5°C under humidified atmosphere at 5% CO₂ in air until confluence was reached. Then remove all medium and added 10 ml. TCM199 supplemented with 10%FBS and incubated at 38.5°C at days 2, 4, and 6 post-incubation, the conditioned medium was collected for EVs isolation and TCM199 supplement with 10% dFBS was added into the petridish. The collected conditioned medium was stored at -80°C until used.

Preparation of conditioned medium from vesicle-shaped bovine oviduct epithelial cells (BOEC-V)

The BOEC were cultured in culture medium in a 100 mm petridish and incubated at 38.5°C for 48 h as aforementioned. In order to gain only vesicle-shaped BOEC (BOEC-V), the conditioned medium and BOEC-V were transferred into a new 100 mm petridish and incubated at 38.5°C for 48 h. Afterward, the medium containing BOEC-V was selected and pipetted into 5 ml TCM199 supplemented with 10% FBS prior to incubation at 38.5°C for 48 h. The suspended BOEC-V was rinsed twice in TCM199 supplemented with 10% dFBS. After that, the suspended BOEC-V was cultivated in 60 mm dishes with 5 ml TCM199 supplemented with 10% dFBS. The conditioned medium was collected at days 2, 4 and 6 post-incubation and stored at -80°C as detailed previously.

EVs isolation

EVs were extracted from the collected BOEC-monolayer conditioned medium (BOEC-M-EVs) and BOEC-vesicle conditioned medium (BOEC-V-EVs) with minor modifications⁶. The collected BOEC-M-EVs and BOEC-V-EVs were separately centrifuged at 4°C, 300xg for 15 min. Then, the supernatant was collected and centrifuged again at 2,000xg, 4°C for 15 min. The supernatant was collected before centrifugation at 4°C, 12,000xg for 15 min. The supernatant was then ultracentrifuged at 4°C, 100,000xg for 90 min. The pellets were collected, resuspended in PBS(-), and filtered through a 0.22 µm filter. The BOEC-M-EVs and BOEC-V-EVs were kept at -80°C until use.

The particle size distribution by nanoparticle size analyzer

Particle size distribution was assessed using the Nanoparticle Tracking Analysis (NTA) (Malvern Panalytical, NanoSight Pro) following the manufacturer's instruction. In brief, isolated EVs were resuspended in PBS(-). Next, the EVs suspension was transferred into a glass cuvette before being placed in the Nano Particle Size and Zeta Potential Analyzer for analysis.

In vitro embryo production (IVEP)

Oocyte collection and in vitro maturation (IVM)

Bovine ovaries were collected from local abattoirs and stored in 0.9% NaCl solution at room temperature during transport to the laboratory. Upon arrival, ovaries were rinsed with 0.9% NaCl solution, and oocytes were aspirated from follicles diameter 3-8 mm. using 10ml. syring connected with 18G needle and examined under a stereo microscope. Cumulus-oocyte complexes (COCs) with at least 3 layers of cumulus cells and homogeneous cytoplasm were selected and placed in modified Dulbecco's phosphate-buffered saline (mDPBS)supplemented with 0.1% polyvinyl pyrrolidone (PVP). Then, the intact COCs were



cultured in a 60 mm culture Petri dish containing IVM medium covered with mineral oil (20 oocytes/drop). The composition of the IVM medium included TCM-199 supplemented with 10% FBS, human chorionic gonadotropin (HCG, Intervet, Netherlands) follicle-stimulating hormone (FSH, Antrin R10; Kyoritsu Seiyaku Co., Tokyo, Japan), and 17 β -estradiol. Oocytes were cultured in a humidified atmosphere of 5% CO₂ in air at 38.5°C for 23 h.

Sperm preparation and in vitro fertilization (IVF)

Frozen semen from a Wagyu Bull in 0.25 mL straws was thawed at 37°C in a water bath for 1 min and then centrifuged at 3000 rpm for 10 min through a gradient of 400 μ L of 45% and 400 μ L of 90% Percoll solution in a 1.5 mL Eppendorf tube. The sperm pellet was re-suspended in 1 ml of Tyrode's albumin lactate pyruvate (TALP)⁷ And centrifuged at 3000 rpm for 5 min. The pellet was re-suspended in TALP medium. and adjusted to a final concentration of 2 \times 10⁶ sperm/ml for IVF. Then 50 μ l droplets of sperm suspension were transferred to a 35 mm culture dish covered with mineral oil COCs were co-incubated with sperm (10 COCs/drop) under humidified atmosphere of 5% CO₂ in air at 38.5°C for 10 h.

In vitro culture (IVC) of presumptive zygotes

At 10 h of co-incubation of sperm and COCs, the presumptive zygotes were denuded by pipetting in TCM199 HEPES supplemented with 10% FBS. The presumptive zygotes were then cultured in CR1aa medium (Rosenkrans et al., 1993) [8] supplemented with 5% dFBS and either BOEC-M-EVs or BOEC-V-EVs at 3 concentrations (2 \times 10⁶, 4 \times 10⁶, and 8 \times 10⁶ particles/ml). The CR1aa medium supplement with 5% dFBS without EVs supplements was considered a negative control. The presumptive zygote was cultured in 80 μ l droplets of medium (12 zygote/drop) a 35 mm culture dish under a humidified atmosphere of 5% CO₂, 5% O₂, and 90% N₂ at 38.5°C for 7 days. The development of embryos was recorded at days 2 and 7 post-culture, respectively.

Embryo development

The cleavage rate was recorded on day 2 (48 h post-culture), and cumulative blastocyst yield was recorded on day 7. Throughout the study, IVM and IVF were performed 10 times at each treatment to produce more than 150 presumptive zygotes per treatment before culture in CR1aa medium supplemented with 5% dFBS and supplemented with either BOEC-M-EVs or BOEC-V-EVs.

Embryo quality

Differential staining

Blastocysts collected on day 7 post-cultured were stained with 0.1 mg/ml propidium iodide (PI) and 0.2% Triton X-100 in mDPBS supplemented with 0.1% PVP for 1 min. Afterward, embryos were placed into Hoechst 33342 solution dissolved in 99.5% ethanol for 5 min before being mounted with glycerol on a glass slide. Trophectoderm (TE) and inner cell masses (ICM) were counted under an inverted fluorescent microscope. ICM cells appeared blue due to Hoechst uptake, while TE cells were stained pink–red.

Quantitative real-time polymerase chain reaction (qPCR)

A group of 20 blastocysts from each experiment was pooled, washed with PBS(-), and stored at -80°C until mRNA extraction. The mRNA was extracted from the blastocysts using the Dynabeads® Oligo (dT)25 nucleotide method (Dynabeads mRNA DIRECT™ kit, Invitrogen, Waltham, Massachusetts, USA) according to the manufacturer's instructions. Complementary DNA (cDNA) was synthesized from the mRNA using reverse transcriptase and oligo-dT primers (biotech rabbit GmbH, Berlin, Germany). The cDNA was then used to

examine gene expression through qPCR analysis. Specific gene expressions were analyzed using KAPA SYBR FAST qPCR Master Mix (Applied Biosystems, Carlsbad, CA, USA) via the BIO-Rad system (CFX Opus 96 Real-Time PCR System). Melting curve analysis was performed to verify the specificity of the primers (Table 1). GAPDH was used as the housekeeping gene to normalize the target genes. Analysis of relative gene expression data was conducted in triplicate, and statistical analysis was performed using the $2^{-\Delta\Delta C_t}$ method.

Statistical analysis

Data are expressed as mean \pm SEM. The number of embryo development and total cell were tested for normality and homoscedasticity before statistical analysis. Differences in embryo development and total cell numbers were analyzed using a one-way ANOVA followed by Dunnett's Multiple Comparison for post-hoc comparison (GraphPad Prism 5.01 Inc., La Jolla, CA, USA). The level of significance for all analyses was $P < 0.05$.

Results and Discussion:

Extracellular vesicles (EVs) have been widely investigated in reproductive biology due to their crucial role in embryo–maternal communication. Initially, EVs were identified in human uterine luminal fluid (ULF) and later studied in various animal species, including ovine and bovine models^{6, 9, 10}. In cattle, several studies have successfully isolated EVs from epithelial cells of the oviduct and uterus, demonstrating their potential contribution to embryo development and implantation^{1, 3, 11}.

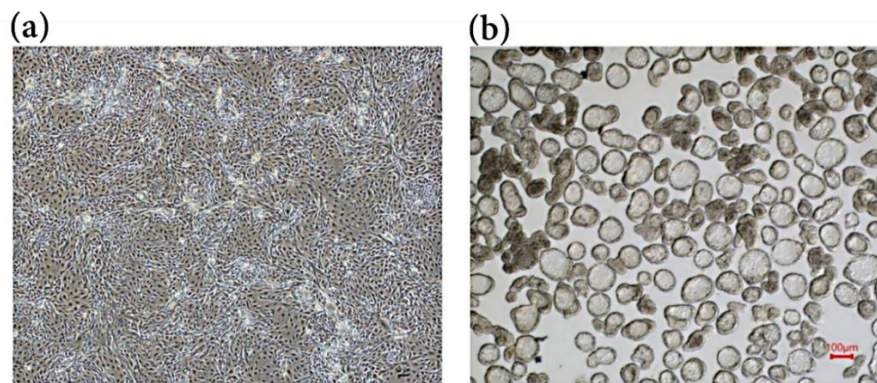


Figure 1.

Morphology of oviduct epithelial cells grown in TCM199+10%dFBS in this study:

A) monolayer culture (BOEC-M), and B) vesicle culture (BOEC-V)

A: Scale bar 10 μ m, B: Scale bar 100 μ m.

In the present study, EVs were successfully isolated from both monolayered BOECs (BOEC-M) and vesicle-shaped BOECs (BOEC-V) and supplemented into embryo culture medium. Importantly, this is the first study to report the successful isolation of EVs from BOEC-V-EVs. Nanoparticle Tracking Analysis (NTA) revealed that BOEC-M-EVs and BOEC-V-EVs exhibited round to cup-shaped morphologies, with average diameters of 131 nm and 189 nm, respectively, and concentrations of 1.89×10^{12} and 2.42×10^{11} particles/ml. These size ranges are consistent with previous reports, which have shown that EVs derived from bovine oviduct epithelial cells and uterus typically fall within the 150–200 nm range¹². In addition, Lopera-Vasquez et al. (2017) reported BOEC-M-EV diameters ranging from 80–150 nm¹³, while Almiñana et al. (2018) observed smaller EVs within 30–100 nm¹⁴. Similar particle sizes have also been observed in sheep EVs (148 nm)⁹ and human follicular fluid EVs (~220 nm)¹⁵. Taken together, these findings confirm the successful isolation of EVs

from both BOEC-M and BOEC-V cultures. However, further studies are needed to confirm EV identity, such as detecting CD9 or other EV-specific surface markers.

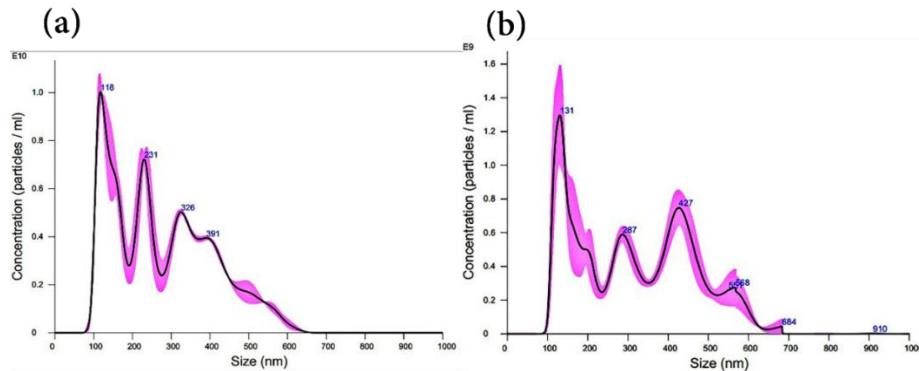


Figure 2.

The average particle size of BOEC-M-EVs (A) and BOEC-V-EVs (B) using the NTA.

Despite successful EV isolation, supplementation with BOEC-derived EVs at 4×10^6 and 8×10^6 particles/ml in IVC medium did not significantly improve cleavage, blastocyst, or hatching rates ($P > 0.05$). However, EV supplementation significantly enhanced blastocyst quality, as demonstrated by increased total cell numbers and upregulation of IFN τ expression ($P < 0.05$). These results agree with previous studies showing that EV supplementation primarily affects embryo quality rather than blastocyst yield. For example, Leal et al. (2022) reported that adding dFCS-EVs increased blastocyst cell numbers without affecting cleavage or blastocyst formation rates¹¹. Similarly, embryos co-cultured with BOECs or bovine amniotic membrane stem cells (bAMSCs) exhibited significantly higher survival rates after warming compared to controls.

Table 1.

Effect of BOEC-M-EVs and BOEC-V-EVs supplemented in IVC medium on bovine embryo development.

Types of EVs	EVs conc. in IVC medium (particles/ml)	No. IVC	Cleavage (%)	Blastocyst (%)
Control	-	200	132/200 (66.00 \pm 4.5)	45/200 (23.65 \pm 2.9)
BOEC-M-EVs	2×10^6	200	131/200 (65.50 \pm 1.3)	57/200 (28.50 \pm 2.3)
	4×10^6	200	152/200 (76.00 \pm 3.2)	67/200 (33.50 \pm 7.3)
	8×10^6	200	105/158 (65.00 \pm 4.0)	64/200 (32.00 \pm 4.4)
BOEC-V-EVs	2×10^6	200	135/200 (67.50 \pm 3.1)	52/200 (32.27 \pm 4.6)
	4×10^6	200	138/200 (69.00 \pm 3.5)	62/200 (31.00 \pm 5.0)
	8×10^6	200	76/200 (70.00 \pm 5.0)	60/200 (30.00 \pm 5.0)

ANOVA –test (10 Blastocysts) %: Mean \pm SEM.

The substantial increase in total cell numbers observed in this study may be related to the role of EVs in mediating intercellular communication and regulating gene expression during early embryonic development^{1,17}. Consistent with this, EVs extracted from the bovine uterus have previously been shown to enhance inner cell mass (ICM) and trophoctoderm (TE) ratios by upregulating genes involved in embryo development, quality, and implantation¹⁸. However, the beneficial effects were less pronounced at lower EV concentrations (2×10^5 particles/ml), suggesting that an insufficient EV dose may limit their influence on embryo competence.

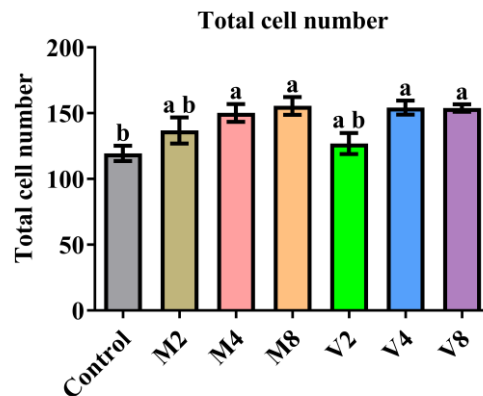


Figure 4.

Analysis of the TE, ICM, and total cell number of IVF embryos cultured in IVC medium supplemented with or without BOECs-M-EVs and BOECs-V-EVs. A total of 10 embryos per group were analyzed. Data are presented as mean \pm SEM, $P < 0.05$ (ANOVA test).

Moreover, several studies have confirmed that EV supplementation improves embryo quality by promoting cell proliferation and enhancing developmental competence. Sidrat et al. (2022) reported significant increases in IFN τ expression in embryos treated with BOEC-derived EVs¹³, while supplementation with BSA¹² and dFCS⁵ has yielded similar positive outcomes. Since IFN τ is a key signal for pregnancy recognition and successful maternal–embryo communication, its increased expression further supports the positive effects of BOEC-derived EVs¹.

Interestingly, our findings demonstrate that BOEC-V-EVs were comparable to BOEC-M-EVs in enhancing blastocyst quality, despite being derived from distinct culture systems. This similarity suggests that the bioactive cargo (e.g., proteins, mRNAs, microRNAs) contained in EVs may be conserved between BOEC-M and BOEC-V. However, we cannot rule out subtle compositional differences that may influence their functional effects. Previous studies have shown that cell culture conditions play a crucial role in shaping the molecular profile of secreted EVs, which can directly impact embryonic development. For example, Wei et al. (2022) demonstrated that heat stress at 42 °C altered EV content, leading to reduced embryo competence.

Overall, our results indicate that EVs derived from BOECs improve blastocyst quality rather than blastocyst formation rates, and that both BOEC-M-EVs and BOEC-V-EVs are equally effective under the tested conditions. Future research should investigate the molecular mechanisms underlying these effects and explore how EV cargo composition is influenced by culture conditions, with the aim of optimizing EV-based strategies in assisted reproductive technologies (ART).



Conclusion:

Using Nanoparticle Tracking Analysis (NTA), this study successfully isolated and characterized extracellular vesicles (EVs) from both monolayered BOECs (BOEC-M) and vesicle-shaped BOECs (BOEC-V), confirming their sizes to be predominantly below 200 nm. Supplementation of BOEC-derived EVs into *in vitro* culture (IVC) medium did not significantly improve cleavage or blastocyst formation rates. However, EV supplementation, particularly BOEC-V-EVs, significantly enhanced blastocyst quality by increasing total cell numbers and upregulating IFN τ expression, which plays a crucial role in pregnancy recognition and maternal–embryo communication.

These findings indicate that BOEC-derived EVs can contribute to improving embryo competence rather than increasing embryo production efficiency. To fully elucidate the molecular mechanisms underlying these effects and maximize the potential applications of EVs in assisted reproductive technologies (ART), further studies should investigate the bioactive cargo of EVs and their roles in regulating cell signaling pathways during early embryonic development.

Ethical approval:

The Animal Ethics Committee of Suranaree University of Technology (IACUC-67-42), Thailand, obtained ethical approval for using bovines in this study.

Acknowledgements:

This research was supported by the Suranaree University of Technology (SUT), the National Science, Research One Graduate (OROG) fellowship program, and the Research and Innovation Fund (NSRF) Grant Number: FF3-304-65-24-51(12). The authors thank all ESRC laboratory members for their support.

References:

1. Qiao F, Ge H, Ma X, et al. Bovine uterus-derived exosomes improve developmental competence of somatic cell nuclear transfer embryos. *Theriogenology* 2018; 114: 199–205.
2. Wei Y, Idrees M, Sidrat T, et al. BOEC–Exo Addition Promotes In Vitro Maturation of Bovine Oocyte and Enhances the Developmental Competence of Early Embryos. *Animals* 2022; 12: 424.
3. Lopera-Vasquez R, Hamdi M, Maillo V, et al. Effect of bovine oviductal extracellular vesicles on embryo development and quality in vitro. *Rev. Reprod.* 2017; 153: 461–470.
4. Aswad H, Jalabert A, Rome S. Depleting extracellular vesicles from fetal bovine serum alters proliferation and differentiation of skeletal muscle cells in vitro. *BMC Biotechnol.* 2016; 16: 1–12.
5. Almiñana C, Corbin E, Tsikis G, et al. Oviduct extracellular vesicles protein content and their role during oviduct–embryo cross-talk. *Rev. Reprod.* 2017; 154: 253–268.
6. Théry C, Amigorena S, Raposo G, et al. Isolation and characterization of exosomes from cell culture supernatants and biological fluids. *Curr. Protoc. Cell Biol.* 2006; 30: 3–22.
7. Lu K. Pregnancy established in cattle after transfer of embryos derived from in vitro fertilization of oocytes matured in vitro. *Vet. Rec., Lond.* 1988 ; 121: 259–260.
8. Rosenkrans Jr C, Zeng G, McNamara G, et al. Development of bovine embryos in vitro as affected by energy substrates. *Biol. Reprod.* 1993; 49: 459–462.
9. Burns G, Brooks K, Wildung M, et al. Extracellular vesicles in luminal fluid of the ovine uterus. *PloS one* 2014; 9: e90913.



10. Ng YH, Rome S, Jalabert A, et al. Endometrial exosomes/microvesicles in the uterine microenvironment: a new paradigm for embryo-endometrial cross talk at implantation. *PloS one* 2013; 8: e58502.
11. Leal CLV, Karina Cañón-Beltrán, Yulia N Cajas, et al. Extracellular vesicles from oviductal and uterine fluids supplementation in sequential in vitro culture improves bovine embryo quality. *J Anim Sci Biotechnol* 2022; 13: 116.
12. Lopera-Vasquez R, Hamdi M, Fernandez-Fuertes B, et al. Extracellular vesicles from BOEC in in vitro embryo development and quality. *PloS one* 2016; 11: e0148083.
13. Sidrat T, Khan AA, Joo M-D, et al. Extracellular vesicles improve embryo cryotolerance by maintaining the tight junction integrity during blastocoel re-expansion. *Reprod. (Cambridge, England)* 2022; 163: 219.
14. Alminana C, Tsikis G, Labas V, et al. Deciphering the oviductal extracellular vesicles content across the estrous cycle: Implications for the gametes-oviduct interactions and the environment of the potential embryo. *BMC genomics* 2018; 19: 1–27.
15. Tannetta D, Dragovic R, Alyahyaei Z, et al. Extracellular vesicles and reproduction—promotion of successful pregnancy. *Cell Mol Immunol* 2014; 11: 548–563.
16. Nejat-Dehkordi S, Ahmadi E, Shirazi A, et al. Embryo co-culture with bovine amniotic membrane stem cells can enhance the cryo-survival of IVF-derived bovine blastocysts comparable with co-culture with bovine oviduct epithelial cells. *Zygote* 2021; 29: 102–107.
17. Feliciano DM, Zhang S, Nasrallah CM, et al. Embryonic cerebrospinal fluid nanovesicles carry evolutionarily conserved molecules and promote neural stem cell amplification. *PloS one* 2014; 9: e88810.



ESTABLISHMENT OF THE GLYCOPROTEIN CD147 KNOCKOUT IN A HUMAN LEUKEMIA CELL LINE (K562) USING LENTIVIRUS-BASED CRISPR/CAS9 SYSTEM

Wannakan Jaikamlue¹, Kumpanat Pomlok², Suparat Lithanatudom³, Jiraprapa Wipasa⁴, Pathrapol Lithanatudom^{1,*}

¹ Department of Biology, Faculty of Science, Chiang Mai University, Chiang Mai, 50200, Thailand

² Department of Microbiology, Faculty of Science, Silpakorn University, Nakhon Pathom, 73000, Thailand

³ Program in Genetics, Faculty of Science, Maejo University, Chiang Mai 50290, Thailand

⁴ Research Institute for Health Sciences, Chiang Mai University, Chiang Mai, 50200, Thailand

*e-mail: pathrapol.l@cmu.ac.th

Abstract:

Cluster of differentiation 147 (CD147) is a plasma membrane-bound glycoprotein that functions as an adhesion molecule. While CD147 has been proposed as a promising biomarker in cancer and a potential antitumor targeting solid tumors/adherent cell model, its role in leukemia (suspension cells) has not been extensively studied. Therefore, this study aimed to establish the CD147-knockout leukemia models in a human leukemia cancer cell line (K562) using CRISPR-Cas9 technology. In this study, we successfully generated 6 stable cell lines bearing CD147-depletion namely KO1, KO6, KO8, KO9, KO10 and KO13. Flow cytometry analysis confirmed KO6 was the most significant reduction in CD147 expression. Besides, morphological analysis revealed that the CD147-depleted cells were relatively larger in size with an increased level of debris as compared to controls. We hypothesize that the type of cell death is most likely a necrotic-like cell death since the cell morphology after CD147-knockout are primarily associated with cellular enlargement and swelling. Taken together, we concluded that disruption in CD147 expression in K562 cells was detrimental to cell survival, thus, further studies should be conducted to explore the role of CD147-knockout in greater details, particularly focusing on the molecular mechanisms underlying the cellular aberration of CD147-depleted K562 cells.

Introduction:

Cancer remains a major global public health challenge due to its high incidence and mortality rates. Despite advancements in diagnosis and treatment, the ability to specifically target cancer cells while minimizing side effects continues to be a primary goal of current medical research. One of the most challenging cancers to treat is leukemia, which affects individuals across all age groups. Particularly, chronic myelogenous leukemia (CML) is more prevalent in children, where treatment options are more limited compared to adults. CML is closely associated with the *BCR-ABL* mutation and resistance to conventional therapies (1). Furthermore, patients with CML exhibit variable responses to targeted therapy. According to the European Leukemia Net guidance, some patients are unable to maintain long-term disease control with Tyrosine Kinase Inhibitor (TKI therapy). Therefore, appropriate management strategies are required, such as dose reduction to minimize treatment-related side effects. Recent advances in allogeneic stem cell transplantation have further expanded treatment options for these patients (2). The K562 cell line, derived from a patient in the blast crisis phase of CML, is widely used as a model for studying disease mechanisms and developing novel therapeutic approaches. In recent years, the emergence of CRISPR/Cas9 gene-editing technology has revolutionized biomedical research. This system enables precise manipulation of genes at the molecular level, allowing researchers to investigate gene



function and disrupt oncogenic pathways with high efficiency. In leukemia research, CRISPR/Cas9 has been applied to modify immune cells and target specific genes to enhance treatment efficacy and reduce side effects. Efficient delivery of the CRISPR/Cas9 system into target cells is a critical step in successful gene editing (3). Among various delivery methods, lentiviral vectors have gained popularity due to their ability to infect both dividing and non-dividing cells and stably integrate genetic material into the host genome. This makes them particularly suitable for editing hematopoietic and leukemia cells such as K562.

One such target protein of interest in cancer research is CD147, a glycoprotein that plays a key role in cancer cell processes including invasion, angiogenesis, immune evasion and prognostic biomarker (4). Overexpression of CD147 has been widely documented across a spectrum of human cancers, including but not limited to leukemia, breast cancer, lung cancer, and gastric cancer (5). This elevated expression often correlates with increased tumor aggressiveness, advanced disease stages, and poorer patient prognoses. Consequently, inhibiting CD147 function has emerged as a highly promising therapeutic strategy. By targeting CD147, researchers aim to disrupt multiple pathways critical for cancer growth and dissemination. This potentially leads to a reduction in tumor aggressiveness, enhanced sensitivity to existing treatments, and ultimately improved therapeutic outcomes for cancer patients.

Therefore, this study aimed to generate a model of CD147-knockout K562 leukemia cells using a lentivirus-based CRISPR/Cas9 system for further in-depth investigation of CD147 roles in leukemia progression. This approach may contribute to the development of more precise and effective treatments for leukemia in the future.

Methodology:

Preparation of CD147-knockout lentivirus.

HEK-293T cells (a gift from Asst.Prof.Dr. Alisa Tubsuwan, Mahidol University, Thailand) were transfected with the lentiCRISPR V2 plasmid (Addgene, 52961) containing sgRNA along with the packaging plasmids (psPAX2 and pMD2.G) (Addgene, 12260 and 12259) using a suitable transfection method for propagating the recombinant lentivirus (6) and then the lentivirus carrying CD147 knockout cassette was employed for transfection into a leukemia cell line (K562 cells) (a gift from Prof.Dr. Sumalee Tungpradabkul, Mahidol University, Thailand).

Generation of CD147-knockout models and clonal selection in K562 cell line.

CD147-knockout cassette was transfected into the leukemia cell line (K562 cells) with appropriate amount of lentiviral particles. Genome-edited cells were selected via the antibiotic selection using 1 µg/ml puromycin. After that, the selected single clones were expanded to obtain a homogeneous population of genetically edited cells (7).

Validation of CD147-knockout models.

Selected K562 clones with transfected CD147-knockout cassette were validated via flow cytometry to detect the expression level of CD147 and confirm the significant reduction of CD147 expression in the CD147-knockout cells compared with control cells (8, 9).

Observation of cell morphology and cell viability of transfected leukemic cell line.

Successfully validated K562 clones bearing CD147 depletion were subjected to cell viability and morphological screenings by visualized under an inverted light microscope.

Statistical analysis.

All experimental data were analyzed for statistically significant differences using SPSS software. One-way ANOVA was employed, with a P -value < 0.001 considered statistically significant.

Results and Discussion:

Generation of CD147-knock out cassette packaging in Lentivirus.

The lentivirus containing CD147-knockout construct was generated using the single guide RNA (gRNA) sequences as described elsewhere (10), including BSG-F (5'-CACCGTCTTCATCTACGAGAAGCGC) and BSG-RC (5'-AAACGCGCTTCTCGTAGA TGAAGAC). This construction was subsequently adopted in the recent study, which investigated the downregulation of CD147 in HeLa cells. The results revealed that this construct can disrupt CD147 expression in HeLa cells, leading to abnormal cellular changes (11). For the lentivirus production process, HEK-293T cells were transfected with the lentiviral cassettes including the Cas9-gRNA construct along with the packaging plasmids to generate the lentivirus containing CD147-knockout construct (Figure 1). Then, K562 cells were transduced to generate CD147-knockout K562 models.

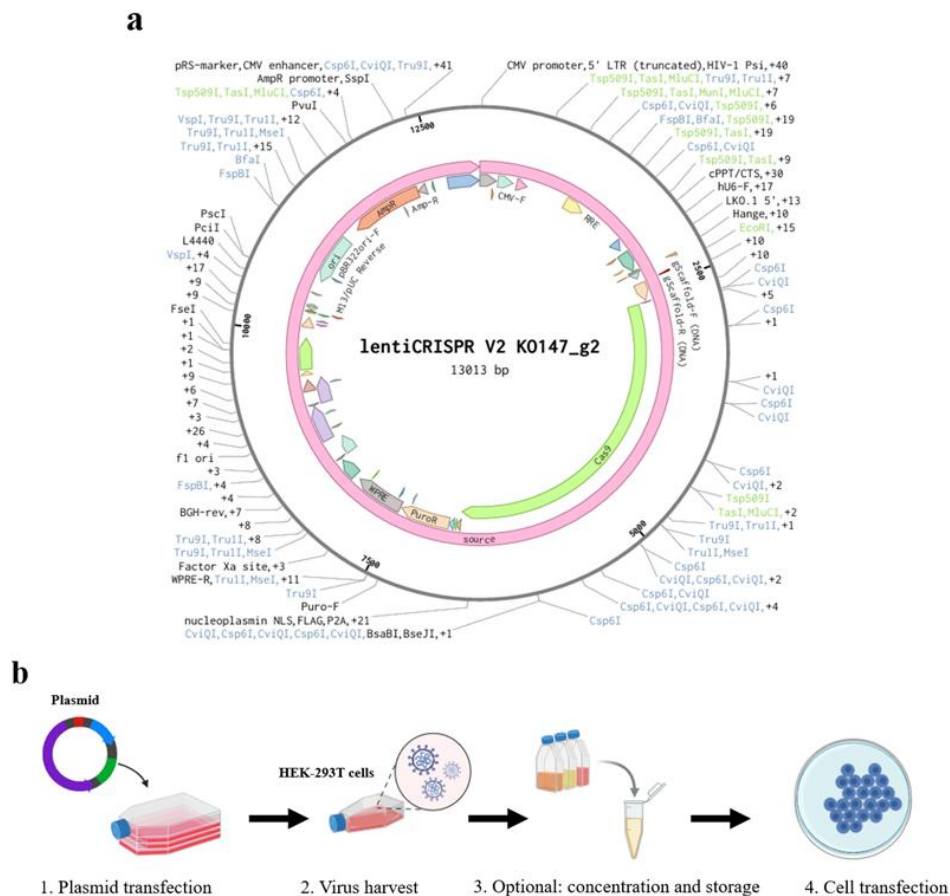


Figure 1

Schematic of viral propagation in HEK-293T cells. **(a)** Lentiviral construction for CD147 knockout. **(b)** The CD147-knockout cassette was transfected into HEK-293T cells to produce lentivirus. Subsequently, K562 cells were transduced with lentiviral particles and then were selected in medium containing puromycin.

Evaluation of CD147 Expression in K562 Cells Using Flow Cytometry.

Flow cytometry analysis was employed to assess the expression level of CD147 in CD147-knockout cells based on mean fluorescence intensity (MFI) data. Results revealed CD147 expression was noticeably decreased in the CD147-knockout K562 cell line as compared to the controls (Figure 2a) and the relative fold change of CD147 expression was shown in Figure 2b. Data indicated that the obtained two CD147-disrupted K562 clones (KO6 and K10) showed the significantly declined expression of CD147 (0.08 ± 0.01 , 0.55 ± 0.01 fold, respectively) as compared to wild-type (1.13 ± 0.08 fold) and empty vector (1 fold), as shown in Figure 2. According to the observation under a microscope, CD147-knockout cells displayed heterogeneous phenotypes (Figure 3). Interestingly, the severity of phenotypic changes is consistent with the different levels of CD147 downregulation. This was evidenced by the fact that the morphological observation in KO6, where CD147 was most efficiently knocked out, exhibited more severe than KO10 (a mild CD147-knockout model). Nevertheless, a subset of cell population could adapt to survive by compensating CD147 expression resulting in a better cell survival observed after several batches of cell cultivation after CD147 knockout. For instance, KO10 demonstrated the CD147 compensation by upregulating CD147 expression level and the overall phenotypes are more comparable to wild-type cells (Figure 3), resulting in two distinct peaks of cell populations observed (Figure 2a).

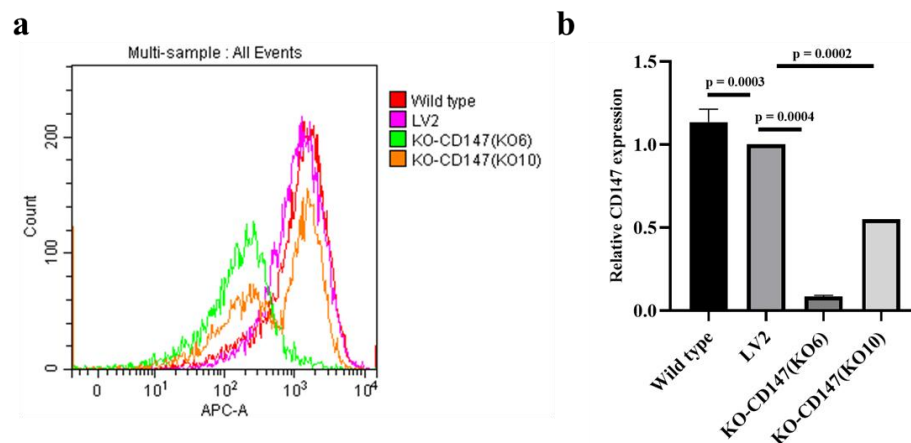


Figure 2

Assessment of CD147 expression level. **(a)** The histograms represent CD147 expression in CD147-knockout cells as compared to controls. **(b)** The relative fold change of CD147 expression is presented as the mean \pm standard deviation from each sample as duplicates.

The morphological differences in KO6 and KO10 expression levels

According to the CD147 expression results in K562 cells (Figure 2), CD147-depleted K562 clone KO6 exhibited more severe morphological characteristics, including the presence of enlarged cells, abnormal-shaped cells, and a higher number of dead cells in culture, as well as a slower proliferation rate as compared to KO10 where the moderate CD147 knockout was observed (Figure 3). According to the observation of abnormal cells, characterized by cellular enlargement and swelling, results revealed the percentage of aberrant cells significantly increased to $6.4 \pm 0.52\%$ and $4.2 \pm 0.94\%$ in KO6 and KO10, respectively, as compared to wild type ($1.8 \pm 0.2\%$). These findings suggest that KO6 cells, with the least CD147 expression, possess a higher proportion of abnormal cells.

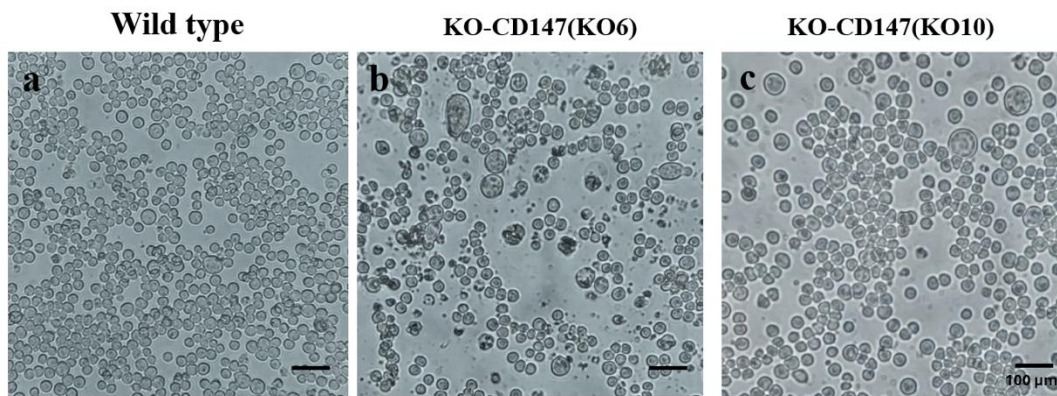


Figure 3

Comparison of cell morphology among (a) Wild type, (b) KO6 and (c) KO10 cells.

Morphological Observation of CD147-knockout K562 Cells.

After K562 cells were transduced with lentivirus targeting CD147-knockout cassette and subsequently cultured in selective medium for the clonal selection (12), it was observed that the expansion of selected cells (CD147-knockout cells) was slower than wild-type and empty vector controls. Furthermore, the observation under an inverted microscope revealed aberrant cell morphology in the CD147-knockout cell line (KO6) as evidenced by the presence of somewhat larger cells and the accumulation of cell debris (Figure 4). This finding supports a recent study, demonstrating that treatment of HepG2 cells with the IgM mAb targeting CD147 led to cell swelling and an increased level of cell death (13).

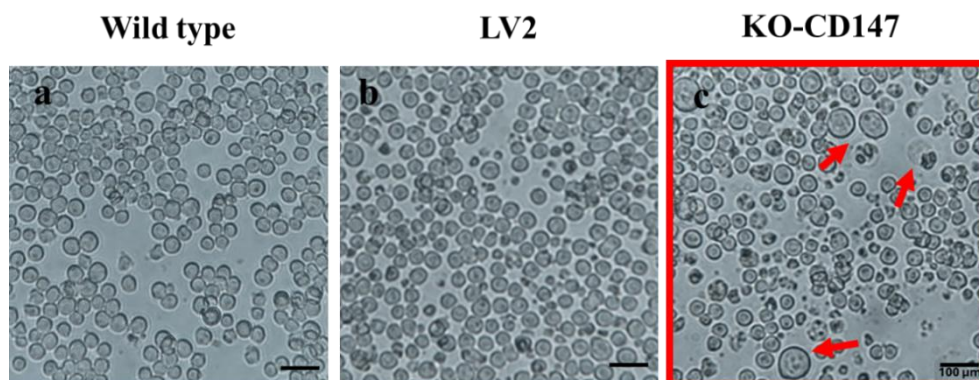


Figure 4

Morphological observation of K562 cell lines including (a) wild-type, (b) empty vector and (c) CD147-depleted K562 cells under an inverted microscope.

Conclusion:

In this study, we successfully established a CD147-knockout suspension model in the K562 leukemia cell line. The knockout efficiency was confirmed using flow cytometry, which demonstrated a significant reduction in CD147 expression in the knockout cells compared to controls. Notably, CD147-knockout K562 cells exhibited the increase in cell size. According to cell morphology observation, results revealed that CD147-knockout cells showed cell enlargement and a higher number of debris compared to controls. Besides, CD147-knockout cells also showed poorer cell survival compared to controls. Interestingly, we noticed that cells with CD147 depletion became swelling prior to death, together with the reduced cell survival. Hence, it is likely that the type of cell death associated with CD147 depletion is a



necrotic-like cell death. Taken together, our findings suggest the potential roles of CD147 in regulating cell size, cell morphology and cell viability in leukemia cells. Nevertheless, this study remains preliminary and further in-depth investigations in the molecular level such as those involving with signaling pathways, cell cycle arrest, and programmed cell death, are required to validate these findings in the future study.

Acknowledgements:

This research was supported by the Molecular Biology Laboratory, Department of Biology, Chiang Mai University.

References:

1. Chakraborty S, Rahman T. The difficulties in cancer treatment. *Ecancermedicalsecience*. 2012;6:ed16.
2. Apperley JF, Milojkovic D, Cross NCP, Hjorth-Hansen H, Hochhaus A, Kantarjian H, et al. 2025 European LeukemiaNet recommendations for the management of chronic myeloid leukemia. *Leukemia*. 2025;39(8):1797-813.
3. Vuelta E, García-Tuñón I, Hernández-Carabias P, Méndez L, Sánchez-Martín M. Future Approaches for Treating Chronic Myeloid Leukemia: CRISPR Therapy. *Biology (Basel)*. 2021;10(2).
4. Ulrich H, Weidle WS, Daniela Eggle, Stefan Klostermann and Hannes Stockinger. Cancer-related Issues of CD147. *Cancer Genomics & Proteomics*. 2010; 7 no. 3 157-169.
5. Nyalali AMK, Leonard AU, Xu Y, Li H, Zhou J, Zhang X, et al. CD147: an integral and potential molecule to abrogate hallmarks of cancer. *Front Oncol*. 2023;13:1238051.
6. Merten OW, Hebben M, Bovolenta C. Production of lentiviral vectors. *Mol Ther Methods Clin Dev*. 2016;3:16017.
7. Ye M, Wilhelm M, Gentshev I, Szalay A. A Modified Limiting Dilution Method for Monoclonal Stable Cell Line Selection Using a Real-Time Fluorescence Imaging System: A Practical Workflow and Advanced Applications. *Methods Protoc*. 2021;4(1).
8. Mishra M, Tiwari S, Gomes AV. Protein purification and analysis: next generation Western blotting techniques. *Expert Rev Proteomics*. 2017;14(11):1037-53.
9. Millán O, Brunet M. Flow Cytometry as Platform for Biomarker Discovery and Clinical Validation. In: Preedy VR, Patel VB, editors. *General Methods in Biomarker Research and their Applications*. Dordrecht: Springer Netherlands; 2015. p. 141-64.
10. Kanjee U, Grüring C, Chaand M, Lin K-M, Egan E, Manzo J, et al. CRISPR/Cas9 knockouts reveal genetic interaction between strain-transcendent erythrocyte determinants of *Plasmodium falciparum* invasion. *Proceedings of the National Academy of Sciences*. 2017;114(44):E9356-E65.
11. Kulaphisit M, Pomlok K, Jaitan N, Lithanatudom SK, Saenjum C, Wipasa J, et al. Multispectral imaging flow cytometry identifies the formation of polyploid giant cancer cells and cellular senescence induced by CD147 depletion. *Talanta*. 2025;297(Pt B):128653.
12. Xie Y-B, Li J-P, Shen K, Meng F, Wang L, Han G-X, et al. [Effect of HIF-1 α on Angiogenesis-Related Factors in K562 Cells]. *Zhongguo Shi Yan Xue Ye Xue Za Zhi*. 2019;27(5):1476-81.
13. Pomlok K, Pata S, Kulaphisit M, Pangnuchar R, Wipasa J, Smith DR, et al. An IgM monoclonal antibody against domain 1 of CD147 induces non-canonical RIPK-independent necroptosis in a cell type specific manner in hepatocellular carcinoma cells. *Biochimica et Biophysica Acta (BBA) - Molecular Cell Research*. 2022;1869(9):119295.

SORGHUM STEM JUICE VALORIZATION TO PRODUCE BIOETHANOL: PROCESS SIMULATION AND LIFE CYCLE ASSESSMENT

Jutima Tantrakool,¹ Aye Myat Theint Kyaw,² Penjit Srinophakun,² Anusith Thanapimmetha,² Maythee Saisriyoot,² Khemmathin Lueangwattanapong,² and Nutchapon Chiarasumran^{2,*}

¹Master of Engineering Program in Sustainable Energy and Resources Engineering, Faculty of Engineering, Kasetsart University, Bangkok, Thailand

²Department of Chemical Engineering, Faculty of Engineering, Kasetsart University, Bangkok, Thailand

*e-mail: fengnpc@ku.ac.th

Abstract:

The increasing global demand for renewable raw materials has intensified interest in bioethanol as a versatile chemical feedstock. This study adopts an industrial ecology perspective to valorize sorghum stem juice, a low-value agricultural byproduct associated with Thailand's furniture industry. Although limited utilized, it contains fermentable sugars that render it a promising substrate for bioethanol production. Two process scenarios were evaluated, the first utilized a mixture of sorghum stem juice and sugarcane molasses, while the second relied solely on molasses, a conventional feedstock. Process simulation was conducted using Aspen Plus V.14 to optimize the bioethanol production pathway, achieving an ethanol purity of 95%. In parallel, a life cycle assessment (LCA) was performed to evaluate the environmental impacts of both scenarios within the context of Thailand's expanding bio-based sector. The LCA was conducted using a cradle-to-gate approach and a functional unit of 1 kg of bioethanol. The results indicated that the co-utilization of sorghum stem juice and sugarcane molasses had more environmental benefits, with a global warming potential (GWP) of 5.62 kgCO₂eq, compared to 7.74 kgCO₂eq for the molasses-only pathway. The major environmental impacts were primarily attributed to the reliance on non-renewable energy sources in Thailand and the sugarcane cultivation stage.



Figure 1.

Bioethanol production pathways from sorghum and molasses for LCA

Introduction:

Fossil fuels, the predominant global energy source, emit harmful gases and particulate matter during combustion, contributing significantly to environmental degradation. This has stimulated the search for cleaner alternatives, among which bioethanol has emerged as a promising candidate due to its ability to reduce emissions and particulate matter. Bioethanol is primarily employed as a transportation fuel, commonly blended with gasoline, and has also been identified as a potential feedstock for sustainable aviation fuels. It may be utilized either as a complete substitute for gasoline or in blended forms. Beyond its energy applications, bioethanol functions as a solvent in pharmaceuticals, chemicals, and cosmetics, and as a versatile feedstock for the synthesis of resins, plastics, and other value-added products. Unlike petroleum-derived ethanol, bioethanol is produced from biomass, a renewable and biogenic resource, thereby offering a substantially lower carbon footprint.¹

Despite these advantages, commercial bioethanol production remains heavily dependent on food-based crops such as corn (USA), sugarcane (Brazil), wheat and cassava (China), and cassava and blackstrap molasses (Thailand)². As these substrates are simultaneously utilized in the food, feed, starch, organic acid, and alcoholic beverage industries, competition for raw materials often constrains the sustainable expansion of bioethanol production. Consequently, increasing research attention has been directed toward identifying alternative non-food energy crops.

Sorghum represents a particularly promising candidate owing to its high fermentable sugar content, short maturation period of 100–120 days compared with 270–360 days for sugarcane^{3,8}, and adaptability to diverse climatic and soil conditions. Furthermore, it requires less fertilizer and consumes only one-third of the water required for sugarcane cultivation⁴, rendering it a resource-efficient and sustainable bioethanol feedstock. In addition to its energy potential, sorghum offers considerable value for bio-based chemical manufacturing due to its carbohydrate-rich composition and bioactive compounds^{5,6}. With biomass yields reaching up to 60 tons of stems per hectare⁷, sorghum provides a reliable and scalable supply for downstream industries.

Beyond conventional and non-food biomass feedstocks, industrial waste streams have recently gained attention as alternative resources for bioethanol production. In particular, wastewater generated during sorghum juice extraction retains significant amounts of residual sugars that remain suitable for fermentation. While the solid biomass fraction is typically processed into wood pellets for fuel, the sugar-rich wastewater, frequently regarded as waste, presents additional value when valorized as a fermentation substrate which simultaneously supporting waste minimization and renewable energy generation.

To assess this potential, the present study compares two ethanol production pathways: the conventional route utilizing molasses and an alternative route employing sorghum stem juice. Process simulation is conducted using Aspen Plus to evaluate ethanol yields and process efficiencies, while life cycle assessment (LCA) is applied to examine the environmental implications of each pathway. By repurposing industrial waste and optimizing fermentation processes, this research seeks to advance sustainable practices and contribute to the development of a circular bio-based chemical industry.

Methodology:

The study was structured into two primary phases, process simulation modeling and environmental impact assessment of the final products. The simulation was performed using Aspen Plus V.14 software to evaluate the mass and elemental balances of all input and output streams across each stage of the bioethanol production process. Two feedstock scenarios were considered which are a mixture of sorghum stem juice and molasses (SSJ), and molasses alone, representing the conventional production pathway. The output data from the

simulation served as the basis for the life cycle inventory (LCI) phase. Subsequently, environmental impacts were assessed using a cradle-to-gate approach life cycle assessment (LCA) methodology through SimaPro software method ReCiPe 2016 midpoint (H) and endpoint (H), with clearly defined system boundaries as illustrated in figure. 2.

A life cycle assessment is covering the following stages: (i) cultivation, (ii) juice extraction, (iii) fermentation, and (iv) distillation. The functional unit was defined as 1 kg of bioethanol produced, reflecting the study's focus on ethanol as a chemical feedstock rather than as an energy carrier.

Beginning with the cultivation of sorghum and including all subsequent processing steps for the production of bioethanol from SSJ, sorghum cultivation and sugarcane molasses production were represented using LCA inventory data from Ecoinvent (2019) and AgriFootprint 5.0 for the Thailand region. The average yield of sorghum cultivation was assumed to be 15 tons per rai (2,400 m²). The primary feedstocks for fermentation, SSJ and sugarcane molasses, were obtained during the extraction stage. Several assumptions were applied in the analysis such as the production of fertilizers, pesticides, chemicals, and energy was included using market datasets, which aggregate all activities associated with a reference product within a given geographic region, including transportation. The transportation of sorghum to the extraction facility and from the extraction facility to the biorefinery was included. Capital goods, labor, and infrastructure were excluded from the system boundaries.

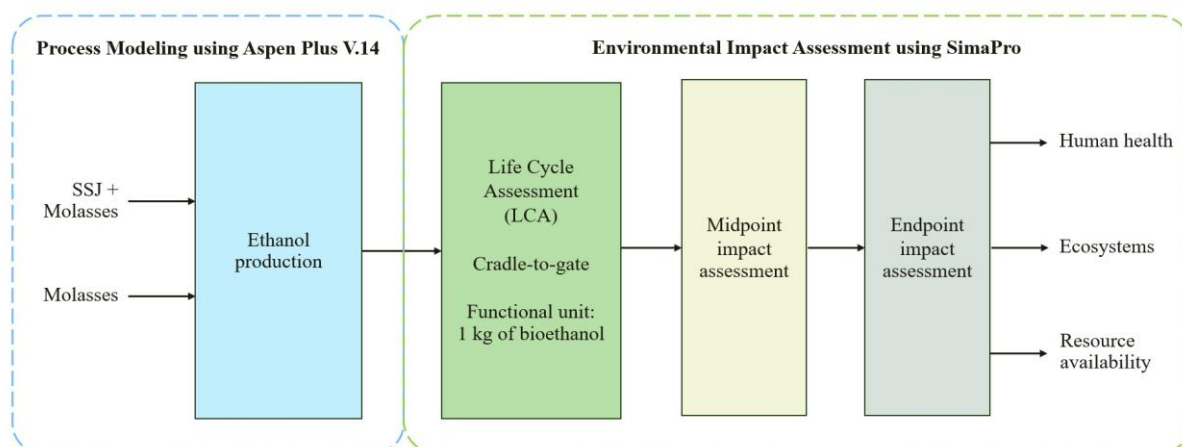


Figure 2.

System boundary of bioethanol production from SSJ and molasses

Juice extraction was a necessary step because the biomass portion of the sorghum stalks was intended for use as wood pellets, requiring the sugar-rich juice to be separated. This was carried out using a 6-roller mill, which is widely applied in sorghum and sugarcane industries due to its high extraction efficiency.⁹ The rollers crush the stalks progressively, releasing the juice while retaining the fibrous bagasse. After extraction, the juice was passed through a filtration cloth to remove suspended solids and fine bagasse particles, ensuring a cleaner substrate for subsequent fermentation. From the harvested sorghum, approximately 30 tons of juice were obtained, while the remainder was left as fibrous biomass. On a mass basis, the extracted juice accounted for about 30% of the stalk weight, with the remaining 70% retained as bagasse, consistent with reported values for sorghum processing.

Fermentation and distillation stages were simulated in Aspen Plus V.14 and using the non-random two-liquid (NRTL) method. Table 1 gives a brief explanation of each block used for simulation bioethanol production. The flowsheet diagram of process can be shown in figure 3. The process simulation begins with sorghum stem juice as the feedstock, which consists of 71.47 g/L total sugars by mass. Because the feed is highly diluted, achieving the



target ethanol purity of 95 vol.% presents a challenge. To address this, additional sugar is introduced by blending the feed with molasses from an external source containing 47% sugars by mass. Finally got 13.70 wt.% of sugar. While conventional case has 20 wt.% of sugar. The mixture is then sent to the fermenter, R-01 at 32°C, where *Saccharomyces cerevisiae* yeasts convert the sugars into bioethanol and CO₂ according to the following equation.



In the fermenter, sucrose was converted to ethanol obtaining 10.80 vol.% and 8.25 vol.% ethanol from molasses and SSJ, respectively. In this study, sugar was converted into ethanol at a sugar consumption rate of 81.7%. The mixture then enters flash separator S-01 to remove unwanted gases while the remaining stream was heated to 80 °C. After heating, distillation was performed with two rectification columns (T -01 and T-02). In the former, 20 stages were employed, while the latter used 15. Feeding for the first column occurred at the 17th stage, while for the second column, it was the 9th. From the first column, bioethanol was obtained with 88.56 vol.% and 51.14 vol.% for molasses and SSJ, respectively.

In the second column, the bioethanol collected from stream ETOH, is ethanol with 95 vol.% purity close to azeotropic bioethanol which is 95.60%. The by-product obtained in the first distillation unit (vinasse) was considered to be an avoided product. The inputs and outputs of both the SSJ and molasses employed in this study can be shown in Table 2.

Table 1.

Block description for bioethanol production simulation from SSJ and molasses

Block	Equipment	Description
M-01	Mixer	To mix sorghum stem juice with molasses
R-01	Rstoic	To convert raw material to ethanol through fermentation.
S-01	Sep	To remove carbon dioxide from the main stream
E-01	Heater	To heat the mainstream up to 80 Celsius
P-01	Pump	To increase the main stream pressure
T-01	RadFrac	To concentrate ethanol up to 51.14 vol.% and 88.56 vol.%
T-02	RadFrac	To concentrate ethanol up to 95 vol.%

Results and Discussion:

Table 2 presents the material balance of the ethanol production process from SSJ and molasses, as derived from the model simulation. These simulation results were employed as the primary basis for constructing the life cycle inventory, which constitutes a critical step in the life cycle assessment framework. The environmental performance of bioethanol production was evaluated under a cradle-to-gate system boundary, with the functional unit defined as 1 kg of bioethanol. The assessment was considered under conditions specific to Thailand in order to ensure regional relevance. Furthermore, electricity consumption was represented using the Thai national grid mix to account for country specific energy characteristics.

The impact assessment focused on seven environmental categories identified as having the highest normalization constants within the ReCiPe 2016 method. These categories include Global warming potential, Terrestrial ecotoxicity, Freshwater ecotoxicity, Human noncarcinogenic toxicity, Land use, Fossil resource scarcity, and Water consumption. The

detailed results of the impact assessment for ethanol production from SSJ and molasses are presented in Table 3.

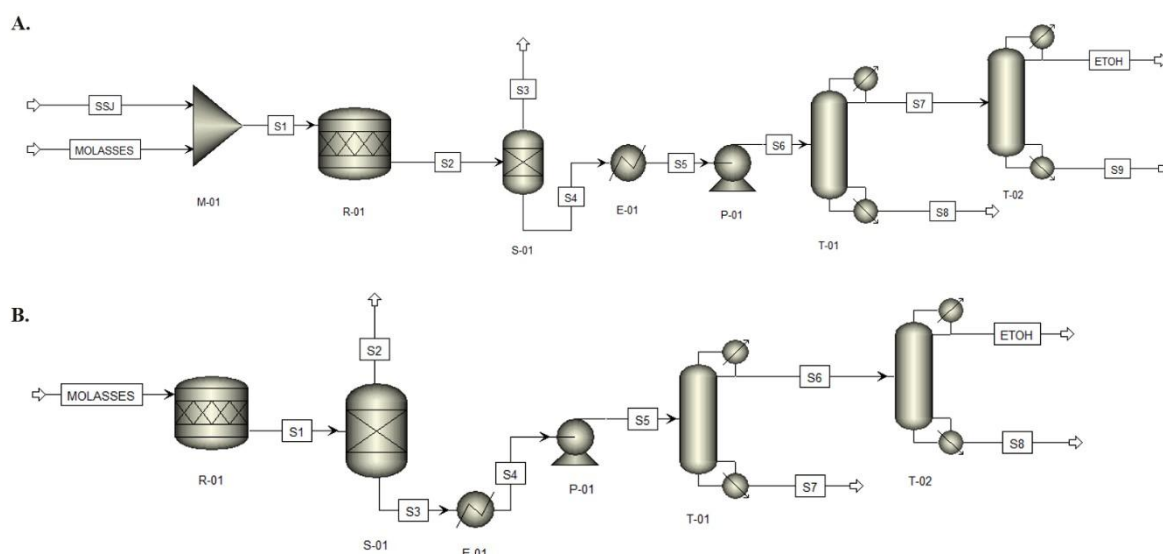


Figure 3.

Aspen Plus V.14 flow sheet simulation for the bioethanol production from A. SSJ and B. molasses

Table 2.

Inputs and outputs of the bioethanol production from molasses and sorghum stem juice (for functional unit 1 kg of bioethanol)

Process parameters	Unit	Molasses	SSJ
<i>Input</i>			
Sorghum stem juice	kg	-	11.86
Molasses	kg	9.70	2.33
Electricity used	kwh	2.33	5.26
<i>Output</i>			
Bioethanol	kg	1	1
<i>Emission to air</i>			
Carbon dioxide	kg	8.74E-01	8.68E-01
<i>Emission to water Bioethanol</i>			
	kg	9.98E-03	3.01E-03
Glucose	kg	4.95E-02	5.18E-02
Fructose	kg	4.95E-02	4.66E-02
Sucrose	kg	5.82E-02	3.36E-02
Carbon dioxide	kg	1.61E-07	1.46E-07

When comparing the two scenarios, bioethanol production from sorghum stem juice (SSJ) was found to have a relatively lower environmental burden across all considered impact categories. In terms of global warming potential (GWP), the conversion of SSJ to bioethanol resulted in greenhouse gas emissions of 5.62 kg CO₂-eq per kilogram of bioethanol, whereas molasses -based bioethanol accounted for 7.74 kg CO₂-eq. This indicates that the global



warming potential of bioethanol derived from molasses was 27.39% higher than that of SSJ. The dominant contributors to these emissions differed between the two feedstocks. For molasses, the major source of impact originated from transportation, as the market dataset incorporated truck transport over distances which is over 76% of GWP. In contrast, for SSJ, the principal contributor was electricity consumption. This higher energy demand is attributed to the relatively lower sugar concentration of SSJ, which requires additional processing energy to achieve the same ethanol quality and yield as molasses which is over 68%. The Thai electricity grid mix is primarily composed of natural gas, lignite, and hard coal, all of which are fossil-based sources and thus significantly contribute to the associated greenhouse gas emissions.

In term of terrestrial ecotoxicity, SSJ-based ethanol production resulted in 5.85 kg 1,4DCB-eq per kilogram of bioethanol, while molasses-based ethanol accounted for 10.89 kg 1,4DCB-eq. For molasses, the main source of impact was sugarcane cultivation, specifically fungicide and herbicide application, which contributed 77.47% of the total. For SSJ, the dominant sources were also agricultural inputs (34.59%) and electricity consumption (33.85%), highlighting the influence of both farming practices and energy requirements in this pathway. For freshwater ecotoxicity, SSJ-based ethanol production generated 0.20 kg 1,4DCB-eq per kilogram of bioethanol, compared with 0.30 kg 1,4-DCB-eq for molasses-based ethanol. In the molasses pathway, sugarcane cultivation was again the primary contributor (81.61%), largely due to the use of fertilizers, pesticides, and fungicides, which leach into water bodies through agricultural runoff. By contrast, in the SSJ pathway, the main source of impact was electricity consumption (50%), reflecting the higher energy intensity of processing SSJ. In terms of human non-carcinogenic toxicity, SSJ-based ethanol production resulted in 3.24 kg 1,4-DCB-eq per kilogram of bioethanol, whereas molasses-based ethanol accounted for 3.44 kg 1,4-DCB-eq. The principal contributor in the molasses case was sugarcane cultivation (52.87%), again driven by the application of fertilizers, pesticides, and fungicides, which release toxic residues into soils and water systems. In the SSJ case, electricity use was overwhelmingly dominant, contributing 89.23% of the total impact.

For land use, SSJ-based ethanol production required 2.41 m²a crop-eq per kilogram of bioethanol, of which 64.58% was attributed to sugarcane farming and 35.42% to sorghum cultivation. By contrast, molasses-based ethanol required 6.52 m²a crop-eq, entirely from sugarcane cultivation. The higher land use in the molasses case is explained by allocation rules in the Agri-footprint 5.0 database, which reports that one ton of sugarcane yields approximately 132 kg of sugar and only 31 kg of molasses. Consequently, a substantially larger amount of sugarcane must be cultivated to obtain sufficient molasses for ethanol production, leading to higher land use impacts. For fossil resource scarcity, SSJ-based ethanol production resulted in 1.65 kg oil-eq per kilogram of bioethanol, while molasses-based ethanol accounted for 2.38 kg oil-eq. The main contributor in the SSJ pathway was electricity consumption (68.09%), whereas in the molasses pathway, diesel use in sugarcane cultivation was the largest source of impact (76.43%). Finally, in terms of water consumption, SSJ-based ethanol production required 0.66 m³ per kilogram of bioethanol, with the majority of the burden attributed to sugarcane cultivation (72.60%) and the remainder to sorghum farming. In contrast, molassesbased ethanol required 2.01 m³ per kilogram of bioethanol, with sugarcane cultivation overwhelmingly dominating the impact (98.74%).

Table 3.
Life cycle Impact Assessment of bioethanol from SSJ and molasses

Impact categories	Unit	Molasses	SSJ
Global warming potential	kg CO ₂ eq	7.74	5.62
Terrestrial ecotoxicity	kg 1,4-DCB	10.89	5.85
Freshwater ecotoxicity	kg 1,4-DCB	0.35	0.20
Human non-carcinogenic toxicity	kg 1,4-DCB	3.44	3.24
Land use	m ² a crop eq	6.52	2.41
Fossil resource scarcity	kg oil eq	2.38	1.65
Water consumption	m ³	2.01	0.66

To complement the midpoint analysis, the assessment was extended to the endpoint (single-score) level, which provides a more comprehensive perspective on environmental damages. At this level, impacts are aggregated into three areas of protection which are human health, ecosystems, and resource availability, yielding indicators that are more directly interpretable in relation to societal and ecological concerns.

The single-score life cycle assessment (LCA) results are presented in Figure 4 and expressed in milliPoints (mPt). The findings indicate that the total environmental impact of ethanol produced from SSJ was 161.61 mPt, compared with 243.87 mPt for ethanol derived solely from molasses, demonstrating the lower overall burden of the SSJ pathway. When the impact categories are considered individually, the SSJ pathway consistently exhibited lower impacts across all categories. In the human health category, ethanol from SSJ accounted for 129.94 mPt, representing a reduction of approximately 28% compared to molasses-only ethanol (180.17 mPt). With respect to ecosystems, the SSJ route generated 26.17 mPt, which is nearly 51% lower than the 53.43 mPt associated with the molasses-only system. In terms of resource availability, the SSJ based scenario reported 5.50 mPt, compared to 10.27 mPt for molasses alone, reflecting a 46% decrease.

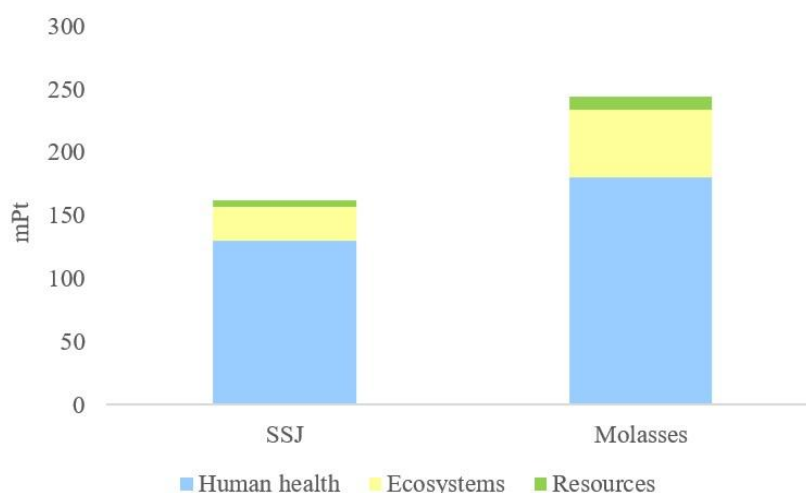


Figure 4.
Endpoint single-score results for bioethanol from SSJ and molasses

The endpoint results per impact category are summarized in Figure 5. For global warming, ethanol from SSJ accounted for 74.68 mPt, which is considerably lower than the 102.86 mPt observed for molasses-only ethanol. Similar improvements are seen in terrestrial ecotoxicity, where SSJ resulted in 0.037 mPt compared with 0.069 mPt for molasses, and in

freshwater ecotoxicity, where the values were 0.077 mPt for SSJ and 0.136 mPt for molasses, confirming the reduced toxic emissions from the SSJ pathway. In terms of human noncarcinogenic toxicity, both systems show comparable outcomes, with 9.34 mPt for SSJ and 9.91 mPt for molasses. A substantial difference is evident in land use, where the SSJ pathway reported 11.94 mPt, less than half of the 32.35 mPt associated with molasses. For fossil resource scarcity, ethanol from SSJ yielded 5.48 mPt, compared to 10.23 mPt for molasses, representing a reduction of nearly 47%. Water consumption also reflected this trend, with SSJ requiring 1.61 mPt compared to 2.26 mPt for molasses.

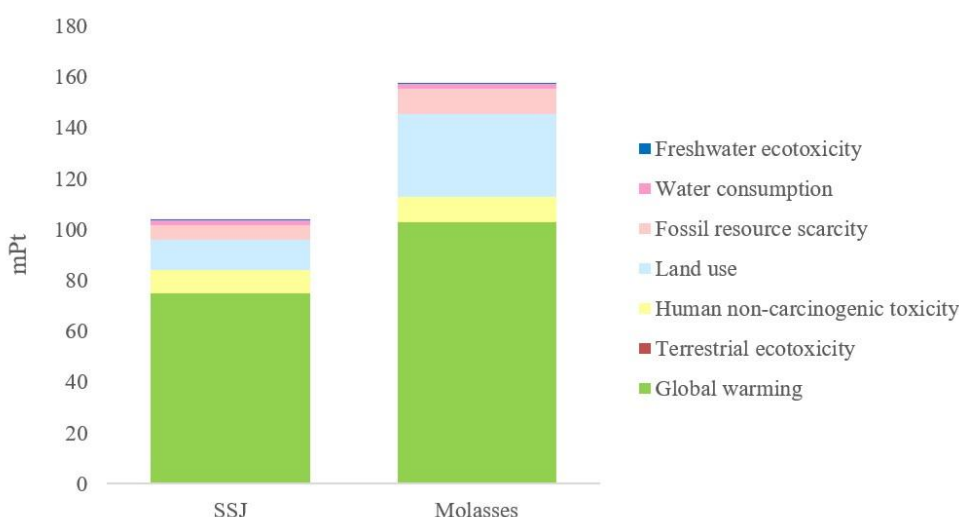


Figure 5.

Endpoint single-score results per impact categories for bioethanol from SSJ and molasses

Conclusion:

The comparative life cycle assessment demonstrated that using sorghum stem juice (SSJ) as a co-feedstock with molasses improves the overall sustainability of bioethanol production. At the inventory level, SSJ ethanol required more raw material input and higher electricity consumption compared with the molasses-only pathway. However, because sorghum is a more environmentally favorable feedstock than molasses, the higher input demand did not translate into greater impacts. At the impact assessment level, SSJ ethanol consistently outperformed molasses ethanol, with the global warming potential decreasing from 7.62 to 5.62 kg CO₂-eq/kg at the midpoint level. Endpoint results confirmed these advantages, showing reductions in global warming from 102.86 to 74.68 mPt. The total environmental impact of SSJ ethanol was 161.61 mPt, compared to 243.87 mPt for molasses ethanol. Overall, the results indicate that incorporating sorghum stem juice as a co-feedstock with molasses leads to substantial reductions in environmental burdens, with the most pronounced improvement observed in the ecosystem damage category. These findings highlight the environmental benefits of valorizing sorghum stem juice in ethanol production and underline its potential as a sustainable feedstock that can significantly enhance the performance and resilience of bioethanol supply chains.

Acknowledgements:

The authors would like to express their gratitude to the Master of Engineering Program in Sustainable Energy and Resources Engineering for providing financial support, and to the Department of Chemical Engineering, Faculty of Engineering, Kasetsart University, for granting access to research facilities.

**References:**

1. Sanyam J, Shushil K, Energy. 2024;296:131130.
2. Miftahul K, International Journal of Research and Review. 2024;11(8):568-574.
3. Ghorai AK, AJAEES. 2022; 40:497–502.
4. Prasad S, Singh A, Jain N, Joshi HC, Energy Fuels. 2007;21:2415–2420.
5. Ahmad Dar R, Ahmad Dar E, Kaur A, Gupta PU, Renew Sust Energy Rev. 2018;82:4070–90.
6. Vanamala JKP, Massey AR, Pinnamaneni SR, Reddivari L, Reardon KF. Crit Rev Food Sci. 2018;58(17):2867–81.
7. Hu W, Zhou L, Chen Jh, Biotechnol Biofuels.2022;15:72.
8. Tang S, Wang Z, Chen C, Xie P, Xie Q, J Agric Sci Bot. 2018;2(3):5–11.
9. Chibrikov V, Vakuliuk P, Sobczuk H, Crit Rev Food Sci Nutr. 2024;64(32):11850-11870.



ENHANCING BIOTRANSFORMATION OF CASSAVA PULP TO BIOMETHANE WITH LIQUID HOT WATER AND MICROBIAL PRETREATMENTS

Saengmany Phommakod,¹ Suppanut Varongchayakul,¹ Warinthorn Songkasiri,² Pawinee Chaiprasert^{1,*}

¹Biotechnology Program, School of Bioresources and Technology, King Mongkut's University of Technology Thonburi, Bangkok, Thailand

²National Center for Genetic Engineering and Biotechnology, National Science and Technology Development Agency, Pathum Thani, Thailand

*e-mail: pawinee.cha@kmutt.ac.th

Abstract:

Cassava pulp (CP), a major agro-industrial byproduct of cassava starch processing in Thailand, contains high residual organic matter, making it a potential feedstock for anaerobic digestion. However, much of its starch is trapped within the lignocellulosic cell wall, which limits biodegradability. This study investigated two pretreatment strategies to improve CP conversion: (a) liquid hot water (LHW) under optimized conditions, and (b) microbial hydrolysis and fermentation of starchy lignocellulose using *Clostridium manihotivorum* CT4^T (CT4^T), both aimed to disrupt the cell wall structure of CP and solubilized hemicellulose and starch into saccharides as well as enhancing volatile fatty acids (VFAs) production for biomethane generation. Under the selected optimum LHW condition (186.67 °C and 6.97 min), glucose was released at 444 mg/gTS-CP, along with detectable amount of galactose, xylose, L-arabinose and mannose. Inhibitory compounds, including furfural and hydroxymethylfurfural, were presented only at low concentrations (0.031 and 0.032 g/L, respectively). Biochemical methane potential tests of LHW-pretreated CP showed a biomethane yield of 328±2.59 mL/g VS and substrate degradation efficiency of 75.0±2.28%, representing a 35% improvement over untreated CP and reducing the anaerobic digestion time from 22 d to 10 d. These results demonstrated that LHW was an efficient, chemical-free pretreatment for enhancing CP biodegradability. In the biological pretreatment, CP hydrolysis and fermentation by CT4^T found only low sugar accumulation (0.21–0.24 mg/mL) but generated substantial yields of acetic acid (0.24–0.28 g/g VS) and butyric acid (0.29–0.32 g/g VS). Subsequent methanogenesis, initiated with a syntrophic-methanogenic consortium and fed with the VFAs-rich leachate, biomethane yielded of 325±3.94 mL/g VS, with a substrate degradation efficiency of 66.8±1.79%; a 30% improvement compared to untreated CP. Both LHW and CT4^T effectively disrupted the CP cell wall, releasing starch that was readily utilized and completely degraded. These pretreatment strategies significantly enhanced CP conversion to biomethane in a shorter time than non-pretreated CP. Overall, LHW and CT4^T provide environmentally friendly and promising approaches for accelerating and improving biomethane production in the cassava starch industry.

Keywords: Biological hydrolysis, Biomethane, Cassava pulp, *Clostridium manihotivorum* CT4^T, Liquid hot water, Pretreatment

Introduction:

The increase in global cassava demand cause Thailand, the world's biggest cassava supplier, try to fulfill the market demand by increasing cassava production. This means that increased cassava production will also increase waste generation from the manufacturing process. In 2019, the cassava-starch product manufacturing process in Thailand (5.12 million tons) was reported to annually generate two types of waste, including wastewater (21 million m³) and cassava pulp (CP) (9.5 million tons). The wastewater is being used directly by the cassavastarch factories with a biogas integrated system in Thailand for biogas generation,

while the high solids content in CP causing this waste requires special management to avoid pollution in the environment [1].

In order to implement the circular economy concept declared by the Thailand Government in the cassava starch industry aiming to combat the environmental issues associated with cassava waste, finding an effective strategy to manage CP waste would be promising. CP waste is mainly generated from cassava-starch industries with high residual organic content remnants. The residual organic content in CP is 60-75% starch, 4-15% cellulose, 4-5% hemicellulose, 1-3% lignin, 1-2% protein, 0.1-0.2% lipids, 2-12% ash, and 117% other materials [1]. Thus, it can be potentially used as biogas production feedstock that can further contribute to waste reduction, environmental improvement, and reduction in greenhouse gas emissions.

The main residual compound of CP is starch. However, this residual starch is in the form of starch granules entrapped inside the plant cell wall, namely lignocellulosic material that is recalcitrant to degradation [2]. Therefore, to achieve maximum digestion of CP, it is important to degrade the lignocellulosic plant cell wall to further release the starch for enzymatic digestion. In addition, being known as one of the easy compounds to be enzymatically degraded by microorganisms, high starch content might cause a limitation in anaerobic digestion (AD). In addition, due to the presence of lignocellulose and high starch content in CP, parallel limitations might be caused if it is used as the biogas production feedstock. The effective AD technology of CP can be obtained if the lignocellulose material that limits hydrolysis of microbial contact with the main organic residue is successfully degraded. Therefore, starch granules can be released freely and further utilized by microorganisms to produce organic acids. This means that AD technology that can enhance lignocellulose degradation is required. There are several techniques for enhancing the hydrolysis of lignocellulosic materials in AD, such as using pretreatment methods based on physical, chemical, and biological techniques [3]. Physical and chemical-based techniques are highly effective in hydrolyzing lignocellulose; these techniques require high operating costs and generate other types of waste that may harm the environment. Biological-based techniques have gained more attention in developing AD technology, which is cheaper and safer for the environment. The promising physico-chemical and biological-based strategies to enhance break down lignocellulosic plant cell wall, there were only a few pretreatment methods that had potential as cost effective and applied on an industrial scale. These methods were liquid hot water (LHW) and biological pretreatments [4]. The effective microbial consortia that specialize in AD of cellulosic waste, *Clostridium* species, are particularly notable because they can degrade into a broad range of substrates, from 1st-3rd generation (starch crops, lignocellulosic biomass, and C1 grasses) [5]. Mulyawati et al. [6] found *Clostridium butyricum*-rich microbial consortium able to degrade rice straw which is high in lignocellulosic content for up to >80% degradation. This versatility highlights their potential as robust microbial candidates for biorefinery applications. Additionally, *Clostridium manihotivorum* CT4^T is a mesophilic anaerobic bacterium isolated from the cassava landfill soil. It produces a complex enzyme mix amyolytic, hemicellulolytic, cellulolytic, and pectinolytic that enables CP degradation, generating acetic acid (AA) and butyric acid (BA), ethanol, propionate (PA), CO₂, and H₂ as major fermentation end-products [7].

Therefore, this study conducted two strategies of LHW and microbial pretreatments of CP for biomethane production. The selected optimization of LHW pretreatment in CP to disrupt the cell wall structure, solubilize starch, and recover produced sugars at 187 °C for 7 min was used and then biochemical methane potential assay of LHW pretreated CP and nonpretreated CP was also studied. Next biological strategy is carried out by separating the first step for hydrolysis and acidogenesis using a lignocellulolytic bacteria, *Clostridium manihotivorum* CT4^T, and the second step for acetogenesis and methanogenesis.



Furthermore, the result of this study will become a promising AD technology for massive CP waste minimization and biomethane as renewable energy production.

Methodology:

Cassava Pulp Characterization

The fresh CP used in this study was obtained from a cassava-starch factory in Chonburi Province, Thailand. The fresh CP was immediately homogenized before being stored at a cold temperature. Prior to use for the experiment, the fresh CP was dried in a laboratory-standardized oven at 50°C for 48 h and until the moisture content was below 10%. The dried CP was ground with mortar and pestle and then sieved through the mesh no.10 sieve (2.0 mm in size). The dry CP was then stored at room temperature (30–35°C). The CP was also characterized based on standard methods. These parameters were total solids (TS), moisture content, and volatile solids (VS) [8] including starch content [9] as well as cellulose, hemicellulose, and lignin contents [10].

Pretreatment

Liquid hot water and *C. manihotivorum* CT4^T were used to break down lignocellulosic cell wall to release free starch granules with solubilization and hydrolysis/fermentation, respectively.

Liquid hot water

The selected optimum condition for pretreatment was used at temperature of 186.67 °C and reaction time of 6.97 min from previous research study [2]. LHW pretreatment with loading 1.5% VS of CP was conducted in mini benchtop reactor (Parr Instruments, Moline, USA). The pressure was set as saturated vapor pressure at a specific temperature by N₂ gas with a vertical shaking system at 500 rpm. The heating jacket elevated the temperature inside the reactor with a heating rate of 10 °C/min. After reaching the targeted temperature and time of reactions, the cooling coil was applied to instantly terminate the heating process and rapidly decrease the temperature. Solid residue and clear hydrolysate fraction of the pretreated CP were separated by filter paper (Whatman No.1). The clear hydrolysate was collected for sugar composition analysis. The presences of inhibitors, such as furfural and hydroxymethylfurfural, which were probably generated during the pretreatment, were also observed. The solid residual fraction was analyzed for its starch content, lignocellulosic composition, and morphology of biomass structure. Scanning electron microscope (SEM) was used to reveal morphology and the disruption of the intact biomass structure. The results analyzed would be compared to non-pretreated CP.

Clostridium manihotivorum CT4^T

C. manihotivorum CT4^T (CT4^T) is a novel lignocellulolytic species isolated from the soil of cassava landfill. CT4^T was obtained from the Thailand Bioresource Research Center (TBRC). The microorganism was cultured anaerobically in an anaerobic chamber (Bactron Anaerobic Chamber: Model I, USA) at 37 °C in basal medium 7 using glucose as a carbon source for activating inoculum. When the optical density (OD₆₀₀) reached 0.9-1.1, 5% (v/v) CT4^T exponential phase culture and supplemented with 1.0 and 1.5% VS of dried CP in the basal medium. Hydrolysis and fermentation were conducted at 37 °C for 6 d, and biomass degradation and volatile fatty acids (VFAs) production were measured [7]. The BM7 medium containing 1.5 g/L KH₂PO₄, 2.9 g/L K₂HPO₄, 2.1 g/L Urea, 4.5 g/L yeast extract, 0.5 g/L cysteine-HCl, 0.001 g/L Resazurin, and 200 µL of a mineral solution containing 25 g/L MgCl₂·6H₂O, 37.5 g/L CaCl₂·2H₂O, and 0.3 g/L FeSO₄·6H₂O.

Biochemical methane potential (BMP) analysis

After CP pretreatment with LHW and CT4^T, the pretreated samples were carried out to determine BMP. In this experiment, two fractions such as clear hydrolysate and solid residual fraction from pretreated CP with LHW and CT4^T were also analyzed for their BMP. Nonpretreated CP was used as a control treatment. BMP assay was conducted with a working volume of 80 mL and the inoculum-to-substrate (ISR) used in this experiment was 1:1, which was identified as the suitable ratio based on a previous study [11]. The bottles were flushed with N₂ gas for 10 minutes for anaerobic conditions before being incubated at mesophilic temperatures (37 °C). The initial pH was adjusted to pH 7.0 using NaHCO₃, and this experiment was performed in triplicates. Biogas production and composition were determined by liquid displacement method and gas chromatography (GC) with a thermal conductivity detector (TCD) [11].

Statistical Analysis

All quantitative data obtained was statistically analyzed using analysis of variance of ANOVA followed by the Tukey Test to compare the significance of different. The data was presented as the mean and standard deviation. The threshold for statistical differences was set at $p \leq 0.05$.

Results and Discussion:

Characterization of cassava pulp

Fresh CP resembles starchy biomass with 21.4% TS and 78.6% moisture; it was characterized by high organic content (98.3% VS) and a starch-rich composition (47.9% starch) with 20.9% cellulose, 8.1% hemicellulose and 3.4% lignin. It was also observed that CP mainly contained 76.9% (dry basis) of carbohydrate polymer, especially starch and lignocellulosic components.

Cassava pulp pretreatment

Liquid hot water

The selected optimum condition for CP pretreatment was carried out at 187 °C for 6.97 min. The remaining solid residue after LHW pretreatment was approximately 22% TS. SEM revealed the structural morphologies of pretreated CP compared with non-pretreated CP as shown in **Figure 1**. For non-pretreated CP, starch granules were trapped inside the plant cell wall. Smooth surface without disruption of the cell wall was observed (**Figure 1a**). However, no entrapping starch granules were observed in the cell wall of pretreated CP due to the gelatinization of starch. SEM illustrated the appearance of disruption and breakdown of an intact cell wall structure of pretreated CP (**Figure 1b**).

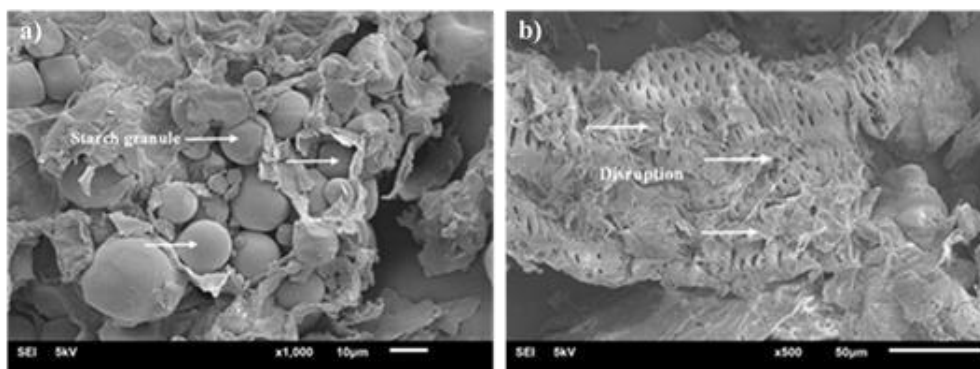


Figure 1.

The morphologies of the solid residues from a) non-pretreated CP at 1000x magnification and b) pretreated CP under optimum condition at 187 °C for 7 min at 500x magnification.

Starch, cellulose, hemicellulose, and lignin contents in solid residue before and after CP pretreatment were shown in **Figure 2**. Starch and hemicellulose were mostly removed from pretreated CP residue compared with non-pretreated CP, in which it was reduced from 47.9 to 0.1% and 8.1 to 1.7% (based on TS of non-pretreated CP), respectively. Starch and hemicellulose are highly hydrolyzed from pretreated CP into an aqueous phase. However, cellulose and lignin were partially hydrolyzed from pretreated CP. Cellulose and lignin were slightly reduced from 20.9 to 14.2% and 3.4 to 2.2%, respectively.

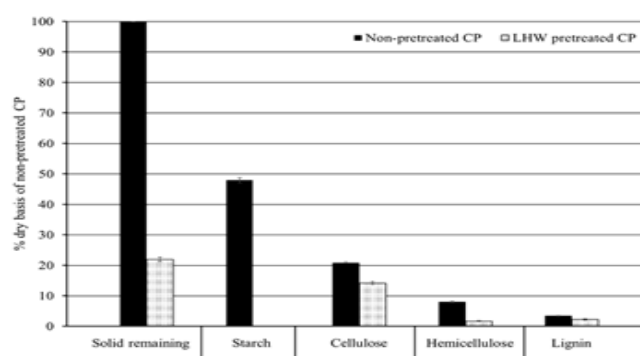


Figure 2.

Starch, cellulose, hemicellulose and lignin content in solid residue comparing to non-pretreated CP.

In clear hydrolysate fraction after pretreatment of CP, most sugar in form of disaccharides were observed maltose at 4 mg/g VS and monosaccharides form as glucose, xylose, galactose, L-arabinose, and mannose were found at 4, 2, 4, 9 and 2 mg/g VS, respectively. The total amount of glucose was 444 mg/g VS. The amount of solubilized glucose in the clear hydrolysate was calculated as 78% of total glucose in CP. Glucose in the clear hydrolysate was mostly hydrolyzed from starch (99.8% reduction). The amounts of furfural and hydroxymethylfurfural at optimum condition were 31 and 32 µg/mL, representing to 0.53 and 0.52 mg of FF and HMF per 1 g of pretreated CP, respectively. It was noticed that furfural and hydroxymethylfurfural in this pretreatment was lower than an inhibitory effect of FF and HMF on fermentative microorganisms presenting at a concentration of more than 1 mg/mL [12].

Clostridium manihotivorum CT4^T

The degradation efficiency of CP based on VS removal by microbial CT4^T pretreatment was measured. At 1.0 and 1.5 % VS CP concentration, CP removal was 66.8-69.5%. Starch was completely utilized within 96 h, while hemicellulose and cellulose were hardly degradable compared to starch (**Table 1**).

Table 1.
Substrate degradation rate on different starch concentration of CT4^T

Concentration (%VS)	Substrate degradation efficiency (%)			
	CP	Starch	Cellulose	Hemicellulose
1.0	69.5	99.6	47.4	54.0
1.5	66.8	99.2	39.6	55.5

Table 2 summarizes the degradation rate by CT4^T in CP as carbon source. The CP degradation rate was 0.0726-0.0834 g/L.h. In addition, degradation rate of existing substrate components in CP as the term of starch CP (0.0581-0.0759 g/L.h) was higher than cellulose (0.0041-0.0052 g/L.h) and hemicellulose (0.0025-0.0039 g/L.h) in CP approximately 14.214.6 times and 19.5-23.2 times, respectively. Degradation rate of starch in CP was higher than cellulose and hemicellulose in CP due to the CP mainly comprise of 37.43% starch content (dry basis) following of 24.6% cellulose and 12.63% hemicellulose. Hydrolysis of starch occurs more rapidly due to its simpler polymeric structure and the presence of amylolytic enzymes.

Table 2.
Degradation rate by CT4^T in CP as carbon source

CP concentration (%VS)	CP uptake (g/L.h)	Starch uptake (g/L.h)	cellulose uptake (g/L.h)	hemicellulose uptake (g/L.h)
1.0	0.0726±0.002	0.0581±0.003	0.0041±0.0002	0.0025±0.0001
1.5	0.0834±0.003	0.0759±0.003	0.0052±0.0002	0.0039±0.0002

To investigate physical structure changes of CP after pretreatment by CT4^T, nonpretreated and pretreated CP were analyzed by SEM. **Figure 3a** shows the rigid surface structure of non-pretreated CP, in which starch granules of CP are entrapped in the fibrous matrix containing the cellulose microfibrils embedded in the cross-linked hemicellulose lignin matrix [13], hindering their extraction and degradation. After hydrolysis of CP by the CT4^T for 72 h, the fibrous structure was disrupted and loosened by the action of the enzyme from CT4^T (**Figure 3b**). The degradation of the fibrous cell wall matrix resulted in the release of intact starch granules, allowing starch-degrading enzymes to access and degrade the starch granules.

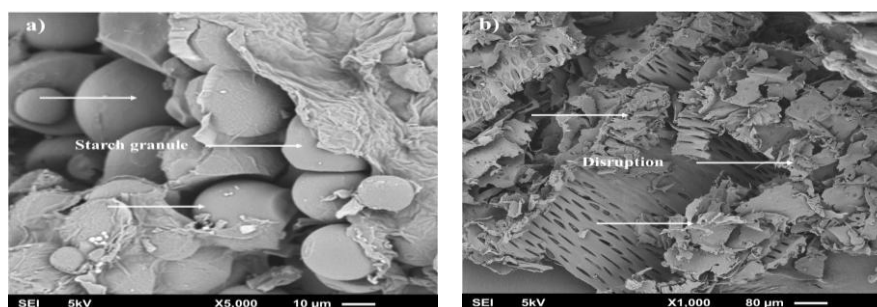


Figure 3.

Surface structures of non-pretreated CP (a) and pretreated CP with CT4^T for 72 h incubation (b) using scanning electron microscopy

CP hydrolysis and fermentation by CT4^T resulted in only low sugar concentrations (0.21–0.24 mg/mL), as the sugars were utilized by the bacteria for cellular growth and maintenance through oxidation–reduction reactions, leading to the production of VFAs during fermentation. From **Table 3** summarized the specific production rate and production yield of the major product including acetic and butyric acids. The estimated VFA production rate of CP for AA and BA were 0.0089–0.0093 and 0.0115–0.0120 g/h; and VFA yield for both acids were 0.2432–0.2805 and 0.2928–0.3225 g/g VS, respectively. The H₂ production rate and yield of CT4^T achieved was 12.26–19.85 mL/h and 174–193 mL H₂/g VS, respectively (**Table 4**). Comparison to *C. lentocellum* Cel10 [14] could utilize CP to generate H₂, and the H₂ yield reached 91 mL H₂/g VS.

Table 3.

Maximum concentration of end product by CT4^T in cassava pulp as carbon source

CP concentration (%VS)	CP removal (%)	VFA production rate (g/h)	VFA yield (g/g VS)	AA	BA
1.0	69.58	0.0089	0.2432	0.2928	0.0115
1.5	66.8	0.0093	0.2805	0.3225	0.0120

Table 4.

H₂ yield and kinetics coefficient of CT4^T on various cassava pulp concentration

CP concentration (%VS)	H ₂ yield (mL H ₂ /g VS)	H ₂ production rate (mL/h)
1.0	174.12	12.26
1.5	192.96	19.85

Biogas and methane production from pretreated CP

Liquid hot water

Pretreated CP contained two fractions of solid residue (SR) and clear hydrolysate (CH). In this study, pretreated CP named mixture (MX), SR, and CH at optimum condition were observed for their BMP. The cumulative biomethane production obtained from the AD of those pretreated CP and non-pretreated CP were monitored during the 60 d experimental period as illustrated in **Figure 4**. During 10 d of the initial stage, higher cumulative biomethane production from MX was observed (112 NmL) compared with non-pretreated CP (87 mL). The methane content of MX was sharply increased up to 61.2%, while nonpretreated CP was at 55.2%. After 10 d of incubation time, biomethane production from MX was slightly increased and reached a steady state, while that from non-pretreated CP still sharply increase until to d 22 and then slightly increased. The cumulative biogas and

biomethane production at d 60 of MX were 247 and 133 mL, while those of non-pretreated CP were 238 and 123 mL, respectively. Methane yields of CH, SR, and MX were 216, 70, and 328 mL/g VS within 10 d, respectively, while non-pretreated CP was 243 mL/g VS within 22 d.

The methane yield from LHW pretreated CP at 187 °C for 6.97 min was 35% higher than non-pretreated CP. Several literature searches were reported that the highest reducing sugar and maximum methane yield were obtained from LHW pretreatment of corn stove [15], *Sida hermaphrodita* [16], sugarcane press mud [17], and poultry slaughterhouse waste sludge [18]. LHW pretreatment, also known as hydrothermal or autohydrolysis processing, is a chemical-free method that minimizes equipment corrosion and operates over short reaction times. Hydronium ions generated through water autoionization act as a weak acid to disrupt lignocellulosic structures, promoting cell wall breakdown and starch solubilization. This approach enables high total sugar recovery with low inhibitor formation, thereby improving substrate degradability and enhancing biomethane production in AD [19-20].

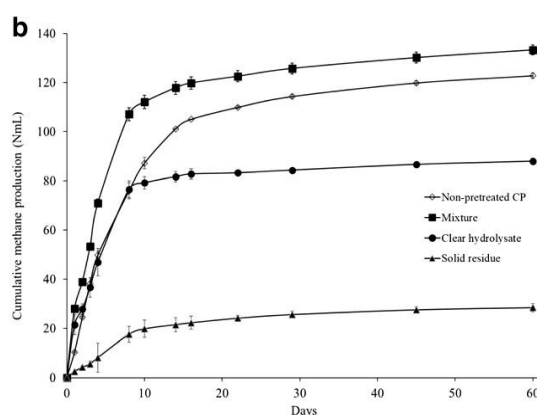


Figure 4.

Comparison of cumulative biomethane production from non-pretreated and pretreated CP as solid residue, clear hydrolysate, and mixture

Clostridium manihotivorum CT4^T

Leachate from CT4^T pretreated CP containing AA (0.56-1.22 g/L) and BA (1.10-1.40 g/L) was determined for potential of biogas and biomethane production by adding syntrophsmethanogens. The result was shown in **Figure 5**. The leachate from CT4^T exhibited high accumulated biomethane production (120 mL) and 80% biomethane composition (**Figure 5a**). Over 6 d, the accumulated biogas and biomethane yields were 409 and 325 mL/g VS, respectively, with COD removal efficiency of 90% (**Figure 5b**). Biomethane yield from CT4^T was compared with non-pretreated CP (NP-CP).

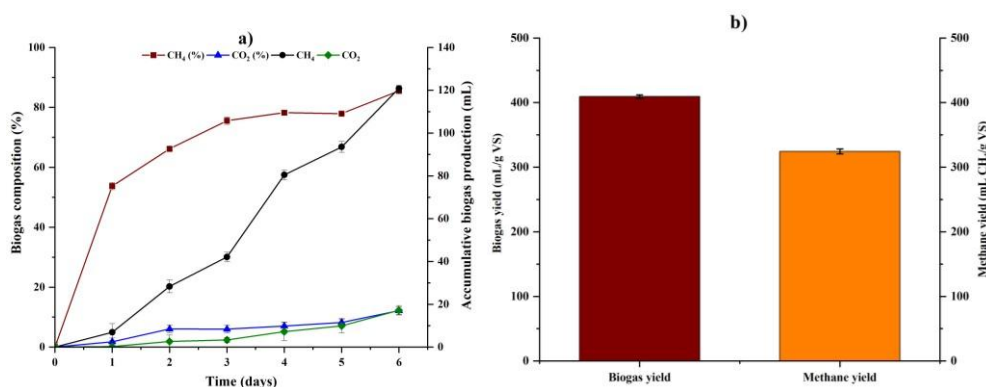


Figure 5.

Biogas production and composition (a) and gas yields (b) from CT4^T pretreated CP

Two consecutive batch incubations with NP-CP, NP-CP1 and NP-CP2, were determined biomethane production in 7 d. Over 7 d, the accumulated biomethane and carbon dioxide yields obtained from NP-CP1 and NP-CP2 were 221 and 250 mL/g VS, 131 and 150 mL/g VS, respectively. CP removal efficiency approached completely CP degradation (**Figure 6**). It was illustrated that CT4^T pretreatment of lignocellulosic CP feedstock promotes to increase biomethane yield by 30% compared with non-pretreated feedstock.

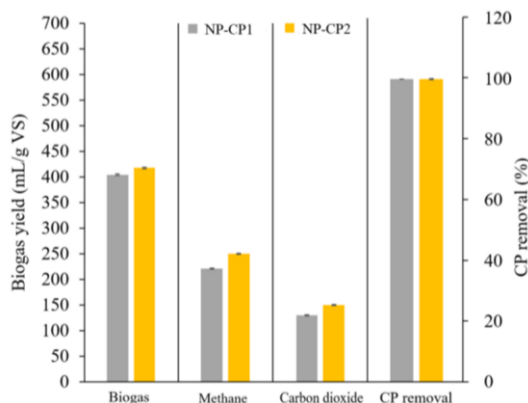


Figure 6.

CP removal and biogas yield of non-pretreated CP

Biological pretreatment with CT4^T provides a low-energy, cost-effective alternative for CP processing. CT4^T possesses a broad enzymatic profile, including amylolytic, cellulolytic, hemicellulolytic, and pectinolytic activities, enabling effective in situ degradation of starch, cellulose, and hemicellulose [7]. During pretreatment, CT4^T hydrolyzes complex polysaccharides into soluble sugars and VFAs, which can serve as direct substrates for methanogens in the subsequent AD stage.

The choice between LHW and CT4^T pretreatments involves a trade-off. LHW can rapidly enhance biomethane yields but demands high energy input and capital investment. CT4^T pretreatment is slower but more cost-effective, environmentally friendly, and produces intermediate products (VFAs, H₂) that allow for flexible biorefinery integration. A promising future direction could be hybrid pretreatment, where mild LHW condition will be applied to disrupt biomass structure, followed by CT4^T fermentation to further hydrolyze carbohydrates and initiate VFAs production before methanogenesis. This could be balanced with the advantages of rapid substrate accessibility from LHW with the cost-effectiveness and product diversification of biological pretreatment.

Comparison methane production from LHW and CT4^T pretreatment

At a CP concentration of 1.5% VS, LHW and CT4^T pretreatments achieved nearly complete starch degradation ($99.8\pm0.05\%$ and $99.2\pm0.03\%$, respectively). However, LHW pretreatment resulted in higher CP ($75.0\pm2.28\%$) and hemicellulose (78.8 ± 0.73) degradation compared to CT4^T pretreatment ($66.8\pm1.79\%$ and $55.5\pm0.83\%$, respectively), whereas cellulose degradation was slightly higher with CT4^T ($39.6\pm0.42\%$) than with LHW ($32.3\pm0.62\%$). Despite these variations, methane yields were comparable between the two methods (328 ± 2.59 vs. 325 ± 3.94 mL/g VS), indicating that both pretreatment strategies effectively enhanced biogas production from CP as illustrated in **Table 5**.

Table 5.
Substrate hydrolysis in CP by LHW and CT4^T

CP concentration (%VS)	Substrate CP	tion efficiency (%)			Methane yield (mL/g VS)
		degrada Starch	Cellulose	Hemicellulose	
LHW pretreatment method					
1.5	75.0 ± 2.28	99.8 ± 0.05	32.3 ± 0.62	78.8 ± 0.73	328 ± 2.59
CT4^T pretreatment method					
1.5	66.8 ± 1.79	99.2 ± 0.03	39.6 ± 0.42	55.5 ± 0.83	325 ± 3.94

Conclusion:

Both pretreatments of lignocellulosic CP by LHW and CT4^T with free chemical usage prior to bioconversion into biomethane illustrated that these effective pretreatment methods enhanced to break down cell wall plant and release free starch granules, which easily hydrolysis to glucose. After pretreatments, starch and hemicellulose were greatly removed from CP, while cellulose and lignin remained in the solid residue. The increasing of soluble sugar and by- products (AA and BA) especially from CT4^T pretreatment in hydrolysate and more disruption in the lignocellulosic matrix of a cell wall structure from these pretreatments resulted in higher biomethane production yield and maximum biomethane production rate comparing to non-pretreated CP. It was noticed that these pretreated CPs accelerated higher production of biomethane within a shorter time compared with non-pretreated CP. Moreover, biotransformation of CP into biomethane through pretreatment of LHW and CT4^T requires minimum operational cost and produces high-economy products while minimizing greenhouse gas emissions to the atmosphere. This next-generation CP waste pretreatment and utilization will be good application in the future by contributing to sustainable development goals.

Acknowledgements:

This research project was funded by King Mongkut's University of Technology Thonburi (KMUTT), Thailand Science Research and Innovation (TSRI), and National Science, Research and Innovation Fund (NSRF) in Fiscal year FRB670016/0164. Mr. Saengmany Phommakod and Mr. Suppanut Varongchayakul were supported by the "Scholarship for outstanding students" from School of Bioresources and Technology, KMUTT. The authors would like to thank Excellent Center of Waste Utilization and Management (ECoWaste) for research facility.

References:

1. Lerdlattaporn R, Phalakornkule C, Trakulvichean S, Songkasiri W. *Sustain Environ Res.* 2021;31(1):1-12.
2. Varongchayakul S, Songkasiri W, Chaiprasert P. *TSB2018.* 2018;BBE-O-06:313-322.
3. Zhou S, Zhang M, Zhu L, Zhao X, Chen J, Chen W, Chang C. *Biotechnol. biofuels bioprod.* 2023;16(1): 1-17.
4. Peral C. *Biotransformation of Agricultural Waste and By-Products.* 2016;Elsevier Inc:125-160.
5. Yang Z, Leero DD, Yin C, Yang L, Zhu L, Zhu Z, Jiang L. *Bioresour Technol.* 2022;361:127656.
6. Mulyawati AI, Suraraksa B, Chaiprasert P. *Bioenerg Res.* 2023;16:2314-2330.
7. Cheawchanlertfa P, Sutheworapong S, Jenjaroenpun P, Wongsurawat T, Nookaew I, Cheevadhanarak S, Kosugi A, Pason P, Waeonukul R, Ratanakhanokchai K, Tachaapaikoon C. *PeerJ.* 2020;8:1-28.
8. Mertens DR. *J AOAC Int.* 2002;85(6):1217-1240.
9. McCleary BV, Gibson TS, Mugford DC. *J AOAC Int.* 1997;80(3):571-579.
10. Van Soest Pv, Robertson J, Lewis B. *J Dairy Sci.* 1991;74(10):3583-3597.
11. Panichnumsin P, Nopharatana A, Ahring B, Chaiprasert P. *Biomass Bioenerg.* 2010;34(8):1117-1124.
12. van der Pol EC, Bakker RR, Baets P, Eggink G. *Appl Microbiol Biotechnol.* 2014;98(23):9579–9593.
13. Huang L, Zhang X, Xu M, An S, Li C, Huang C, Chai K, Wang S, Liu Y. *AIP Advances.* 2018; 8(10):1-12.
14. Zhang L, Li Y, Liu X, Ren N, Ding J. *RSC Advances.* 2019;9(20):11179-11185.
15. López González LM, Pereda Reyes I, Dewulf J, Budde J, Heiermann M, Vervaeren H. *Bioresour Technol.* 2014;169:284–290.
16. Song X, Wachemo AC, Zhang L, Bai T, Li X, Zuo X, Yuan H. *Bioresour Technol.* 2019; 289:121646.
17. Zieliński M, Kisielewska M, Dudek M, Rusanowska P, Nowicka A, Krzemieniewski M, Kazimierowicz J, Dębowski M. *Biomass Bioenerg.* 2019;128:105324.
18. Park S, Yoon Y-M, Han SK, Kim D, Kim H. *Waste Manag.* 2017;64:327-332
19. Mosier N, Wyman C, Dale B, Elander R, Lee YY, Holtzapple M, Ladisch M. *Bioresour Technol.* 2005;96(6): 673-686
20. Cara C, Ruiz E, Oliva JM, Sáez F, Castro E. *Bioresour Technol.* 2008;99(6): 1869-1876 21.

EFFECTS OF THAI HERBAL EXTRACTS ON MITIGATING ALACHLOR-INDUCED OXIDATIVE STRESS IN *Saccharomyces cerevisiae*

Pham Ngoc Nhi Huynh^{1,2} and Choowong Ausukaree^{1,2*}

¹Department of Biotechnology, Mahidol University, Bangkok, Thailand

²Mahidol University-Osaka University Collaboration Research Center for Bioscience and Biotechnology, Bangkok, Thailand

*e-mail: choowong.aue@mahidol.ac.th

Abstract:

Alachlor is a chloroacetanilide herbicide used to control broad leaf weeds and annual grasses in agricultural crops such as corn, soybean, and sorghum. Due to its intensive application, alachlor has been detected in soil and water resources worldwide at concentrations exceeding safety limits. In *Saccharomyces cerevisiae*, prolonged exposure to alachlor has been reported to result in increased reactive oxygen species (ROS) accumulation and the activation of antioxidant defenses. This study aimed to investigate the protective potential of three Thai medicinal extracts, namely *Cissus quadrangularis* L. (CQ), *Moringa oleifera* Lam (MO) and *Mucuna pruriens* (L.) DC. (MP), in alleviating alachlor-induced oxidative stress. Yeast cells exposed to alachlor and supplemented with ethanolic CQ, MO, or MP exhibited significantly enhanced growth compared with untreated controls. Moreover, all three extracts markedly decreased intracellular ROS levels compared with untreated controls, reflecting strong antioxidant capacity. These findings indicate that ethanolic extracts of CQ, MO, and MP play a protective role against alachlor-induced oxidative stress, likely through their antioxidant and cytoprotective properties. Overall, our results highlight the potential of these Thai herbal extracts, particularly in ethanolic form, as natural candidates for mitigating herbicide-induced oxidative damage.

Introduction:

In recent decades, the extensive use of pesticides in industrial agriculture has raised serious concerns regarding the environment, food safety, and human health. Approximately 2 million tons of pesticides are applied globally each year, and this number is expected to increase in the next few years¹. Moreover, according to the Food and Agriculture Organization (FAO), the proportion of herbicides in global pesticide consumption has increased rapidly, reflecting a 53% increase. Among them, alachlor [2-chloro-2',6'-diethyl-N-(methoxymethyl)-acetanilide], a chloroacetanilide herbicide widely applied for pre-emergent control of grasses and broadleaf weeds, is particularly concerning due to its persistence in soil and groundwater. Many studies suggest that alachlor disrupts key metabolic pathways in plants by inhibiting protein, lipid, gibberellin, and terpenoid biosynthesis, thereby reducing anthocyanin, lignin, very-long-chain fatty acids, and essential amino acids^{2,3,4}.

Alachlor has been classified by the United States Environmental Protection Agency as a probable human carcinogen, and epidemiologic studies have linked its exposure to increased risks of lymphohematopoietic cancers, laryngeal cancer, and myeloid leukemia^{5,6}. In the eukaryotic model *Saccharomyces cerevisiae*, prolonged exposure to alachlor induced intracellular ROS accumulation. To cope with the alachlor-induced oxidative stress, *S. cerevisiae* relied on cytosolic Cu/Zn-SOD as its primary defense, with glutathione as compensatory protection, especially when enzymatic antioxidant defenses are compromised⁷. Many plants are rich in natural antioxidants and have been used for medicinal purposes since ancient times. Their main antioxidants, including polyphenols, vitamins and carotenoids, have been shown to effectively mitigate oxidative stress induced by pesticides^{8,9}. Therefore, this study aims to investigate the protective role of three Thai herbal extracts, namely *C. quadrangularis* (CQ), *M. oleifera* (MO) and *M. pruriens* (MP), against alachlor-induced

oxidative stress in the eukaryotic model *S. cerevisiae*. Specifically, spot susceptibility assay was performed to examine the effects of these extracts on the growth of wild-type yeast cells underalachlor stress. In addition, the reactive oxygen species (ROS) levels were also measured to evaluate the ability of the extracts to alleviate oxidative stress induced byalachlor.

Methodology:

Yeast strains and growth conditions

The wild-type *S. cerevisiae* strain BY4742 (*MAT α* ; *his3 Δ 1*; *leu2 Δ 0*; *lys2 Δ 0*; *ura3 Δ 0*) was used in this study. Yeast cells were cultured in YPD medium containing 1% yeast extract, 2% peptone, and 2% glucose at 30 °C. Agar media were prepared by adding 2% agar.

Preparation of ethanolic extracts

A total of 83.33 g of each dried herb powder was mixed with 500 mL of absolute ethanol and incubated with shaking at 30 °C for 24 h. After the incubation period, the mixture was carefully pipetted to separate and retain the supernatant, which contains the ethanol-soluble fraction, and was kept at room temperature. The ethanolic extract was then evaporated and dried under reduced pressure to remove the ethanol, resulting in a concentrated extract. Before use, the dried ethanolic extract was reconstituted in absolute ethanol to achieve final concentrations.

Preparation of aqueous extracts

A total of 5 grams of each dried herb powder was suspended in 30 mL of distilled water. The suspension was vigorously vortexed for 1 min to ensure homogenization, followed by centrifugation at 13,000 rpm for 20 min at 4 °C. The supernatants were filtered through Whatman No. 42 filter paper to remove residual particulates. The resulting filtrates were concentrated under reduced pressure using a rotary evaporator and then lyophilized to dryness. Before use, the dried extracts were reconstituted in sterile distilled water to the desired concentrations and sterilized by membrane filtration through 0.22 μ m syringe filters (Acrodisc®, Pall, USA).

Table 1.
List of Thai herbs used in this study

Name in Thai	Scientific name	Part
มะรุม	<i>Moringa oleifera</i> Lam.	Leaves
เพชรสังฆาต	<i>Cissus quadrangularis</i> L.	Aerial parts
หมามุ่ย	<i>Mucuna pruriens</i> L.	Seeds

Determination of phenolic and flavonoid contents

The total phenolic content was determined using the Folin–Ciocalteu assay. Briefly, 100 μ L of extract was mixed with 100 μ L of Folin–Ciocalteu reagent and then diluted with 300 μ L of distilled water. After incubation for 5 min, 500 μ L of 8% (w/v) sodium carbonate solution was added, and the final volume was adjusted to 1.5 mL with distilled water. The mixture was left at room temperature in the dark for 30 min, after which absorbance was measured at 765 nm using a microplate reader. A standard curve was created using gallic acid (5–500 μ g/mL), and results were expressed as mg gallic acid equivalents (GAE) per g of dried extract.



The total flavonoid content was determined using the aluminum chloride colorimetric method. In this assay, 500 μL of extract was mixed with 500 μL of 2% (w/v) AlCl_3 solution and allowed to react at room temperature for 1 h. The mixture was measured at 420 nm using a microplate reader. A standard curve was generated using quercetin (5–200 $\mu\text{g}/\text{mL}$), and the TFC values were expressed as mg quercetin equivalents (QE) per g of dried extract.

DPPH and ABTS antioxidant assays

The antioxidant capacity of the extract was determined using 2,2-diphenyl-1-picrylhydrazyl (DPPH) and 2,2'-azino-bis-(3-ethylbenzothiazoline-6-sulfonic) acid (ATBS) assays.

For the DPPH assay, 100 μL of extract at various concentrations was mixed with 100 μL of 0.3 mM DPPH solution in ethanol. The mixture was incubated in the dark at room temperature for 30 min, and the absorbance was measured at 518 nm using a microplate reader. The antioxidant activity of the sample was expressed as the half-maximal inhibitory concentration (IC_{50}).

For the ABTS assay, the $\text{ABTS}^{\cdot+}$ radical cation was generated by mixing 7 mM ABTS solution with 2.45 mM potassium persulfate and incubating the mixture in the dark at room temperature for 16 h. The $\text{ABTS}^{\cdot+}$ solution was diluted with ethanol to an absorbance of 0.70 ± 0.02 at 734 nm. Next, 20 μL of extract was added to 180 μL of $\text{ABTS}^{\cdot+}$ solution and allowed to react for 6 min at room temperature. Absorbance was measured at 734 nm using a microplate reader. The antioxidant activity of the sample was expressed as the half-maximal inhibitory concentration (IC_{50}).

Spot susceptibility assay

Log-phase BY4742 cells ($\text{OD}_{600} \sim 1$) were treated with 1.5 mM alachlor in the presence and absence of 5 mg/mL of plant extracts, and then incubated at 30 °C for 16 h. Subsequently, 1 mL of each condition was collected and centrifuged at 7000 rpm for 5 min, washed twice, and resuspended in sterile reverse osmosis (RO) water. The cells were then subjected to 10-fold serial dilution (10^0 , 10^{-1} , 10^{-2} , 10^{-3} , and 10^{-4}) and 2.5 μL aliquots of each dilution sample were spotted onto YPD agar plates. The plates were incubated at 30 °C for 2 days.

Measurement of ROS level

Intracellular ROS levels were measured using the 2',7'-dichlorodihydrofluorescein diacetate probe (DCFH-DA; Sigma). Log-phase BY4742 cells ($\text{OD}_{600} \sim 1$) were treated with alachlor in the presence or absence of plant extracts and incubated at 30 °C for 16 h. Cells were then incubated with 0.1 mM DCFH-DA in the dark for 1 hour prior to harvesting, washed twice with PBS, and disrupted with glass beads by vortexing for 30 min. Supernatants were collected by centrifugation at 13,000 rpm for 10 min at 4 °C, and fluorescence was measured using a microplate reader (excitation 490 nm, emission 524 nm). ROS levels were normalized to protein content and expressed as relative DCF fluorescence.

Results and Discussion:

Antioxidant compositions and free radical scavenging activity

The total phenolic content (TPC), total flavonoid content (TFC) of ethanolic and aqueous extracts from the three Thai herbs are summarized in Table 2. Among the six extracts, aqueous *M. pruriens* (AMP) exhibited the highest TPC (132.08 ± 9.64 mg GAE/g DW), while ethanolic *M. oleifera* (EMO) showed the highest TFC (16.33 ± 0.41 mg QE/g DW). On the other hand, aqueous *C. quadrangularis* (ACQ) had the lowest TPC (4.51 ± 0.96 mg GAE/g DW), and aqueous *M. pruriens* (AMP) showed the lowest TFC (1.44 ± 0.19 mg QE/g DW). Overall, ethanolic extracts (EMP, ECQ, EMO) contained higher levels of both phenolics and flavonoids compared with their aqueous counterparts, except for AMP, which

exhibited remarkably high phenolic content. These results suggest that the type of solvent strongly influences the extraction efficiency of different antioxidant compounds. Ethanol is a more versatile solvent due to its intermediate polarity, which allows it to dissolve both polar and non-polar compounds, thereby enabling the extraction of a broader range of phytochemicals. In contrast, water is a highly polar solvent that is more efficient in extracting polar molecules¹⁰.

Antioxidant activity of the six extracts was evaluated by measuring the free radical scavenging capacity against DPPH and ABTS radicals, expressed as the concentration required to inhibit 50% of radical activity (IC_{50} values), as summarized in Table 2. For DPPH assay, AMP exhibited the lowest IC_{50} value (0.15 ± 0.00), consistent with its high TPC, indicating strong radical scavenging activity. ACQ showed the lowest activity ($IC_{50} = 14.52 \pm 1.24$ mg/mL). A similar trend was observed in the ABTS assay, where AMP displayed the highest IC_{50} (0.13 ± 0.01 mg/mL), while ACQ showed the lowest activity ($IC_{50} = 4.39 \pm 0.64$ mg/mL). EMO, despite its high flavonoid content, showed only moderate radical scavenging in both assays (DPPH $IC_{50} = 1.16 \pm 0.03$ mg/mL; ABTS $IC_{50} = 1.52 \pm 0.08$ mg/mL), suggesting that different antioxidant compounds contribute differentially to radical scavenging mechanisms. Overall, ethanolic extracts generally demonstrated stronger antioxidant activity than aqueous extracts. These findings provide a basis for the protective potential of Thai herbal extracts in alleviating herbicide-induced oxidative stress.

Table 2.
Total phenolic and flavonoid contents, and antioxidant capacities (DPPH and ABTS scavenging activities) of six extracts.

Extract	TPC (mg GAE/g DW)	TFC (mg QE/g DW)	DPPH IC_{50} (mg/mL)	ABTS IC_{50} (mg/mL)
EMP	24.18 ± 2.9	5.64 ± 0.49	0.87 ± 0.2	0.74 ± 0.07
AMP	132.08 ± 9.64	1.44 ± 0.19	0.15 ± 0.00	0.13 ± 0.01
ECQ	10.12 ± 1.16	6.41 ± 0.38	3.26 ± 0.18	2.34 ± 1.13
ACQ	4.51 ± 0.96	1.88 ± 0.05	14.52 ± 1.24	4.39 ± 0.64
EMO	25.7 ± 1.12	16.33 ± 0.41	1.16 ± 0.03	1.52 ± 0.08
AMO	25.98 ± 0.96	6.84 ± 0.35	1.46 ± 0.10	1.45 ± 0.13

Ethanolic extracts restore yeast growth underalachlor stress

The effects of six herbal extracts on the growth of *S. cerevisiae* underalachlor stress are shown in Figure 1. To evaluate whether the extracts reducealachlor toxicity, we examined the growth of wild-type cells incubated with 1 mM and 1.5 mMalachlor in the presence or absence of 5 mg/mL of each extract. We found that supplementation with ethanolic extracts markedly restored cell growth at both concentrations ofalachlor. On the other hand, the supplementation of aqueous extracts only slightly improved the growth of wild-type yeast cells at 1 mM, with minimal effects observed at 1.5 mM. Interestingly, although AMP contained high levels of phenolic compounds and displayed strong antioxidant activity, it was unable to recover growth at the higheralachlor concentration. It is likely that its antioxidant capacity alone could not counteract the cellular damage triggered by severe herbicide stress, suggesting that other protective mechanisms beyond ROS detoxification are required. These results suggest that the ethanolic extracts have the ability to protect yeast cells againstalachlor, possibly through their effects on alleviatingalachlor-induced oxidative stress. This

protective effect is consistent with their higher phenolic and flavonoid contents, which are associated with stronger antioxidant activity.

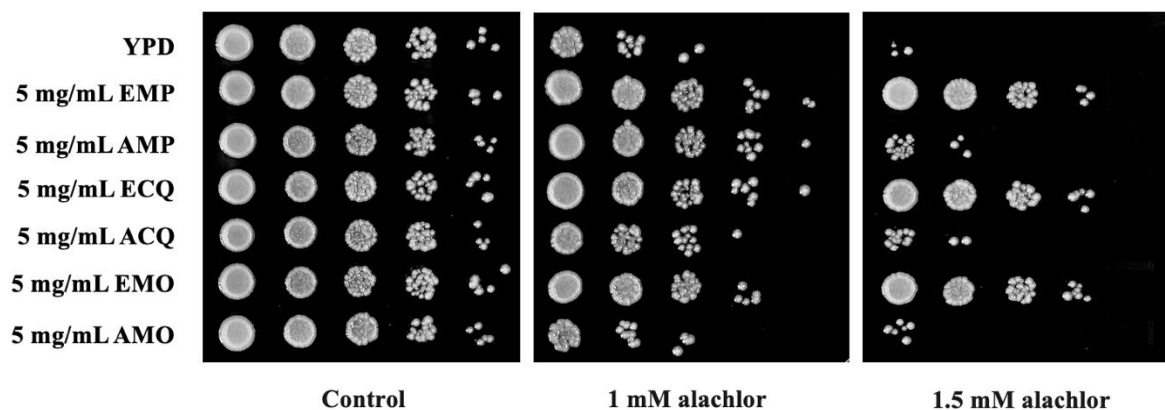


Figure 1.

Effects of Thai herbal extracts on yeast cell growth under alachlor stress conditions. The wild-type (BY4742) cells were incubated in YPD media containing 1 mM or 1.5 mM alachlor in the presence or absence of 5 mg/mL of each extract (Control) with shaking at 30 °C for 16 h.

Ethanollic extracts reduce intracellular ROS levels during exposure to alachlor

To further investigate the role of ethanollic extracts in inhibiting ROS generation, we measured the intracellular ROS levels of yeast cells exposed to 1.5 mM alachlor in the presence or absence of 5 mg/mL of each ethanollic extract. Our results showed that supplementation with 5 mg/mL of EMP, ECQ, and EMO dramatically reduced the intracellular ROS levels of alachlor-treated cells to normal levels. This reduction in ROS is consistent with the improved cell growth observed under 1.5 mM alachlor stress when supplemented with 5 mg/mL ethanollic extracts.

Previously, it has been reported that alachlor induces oxidative stress indirectly, primarily as a consequence of its direct effect on protein denaturation⁷. In this study, supplementation with 5 mg/mL of EMP, ECQ, and EMO significantly suppressed ROS accumulation in alachlor-treated yeast cells, indicating their strong antioxidant potential. The reduction in ROS levels suggests that these herbal extracts help restore redox balance and protect cells from oxidative damage. Together with the spot assay results, our findings demonstrate that ethanollic Thai herbal extracts can effectively alleviate alachlor-induced oxidative stress.

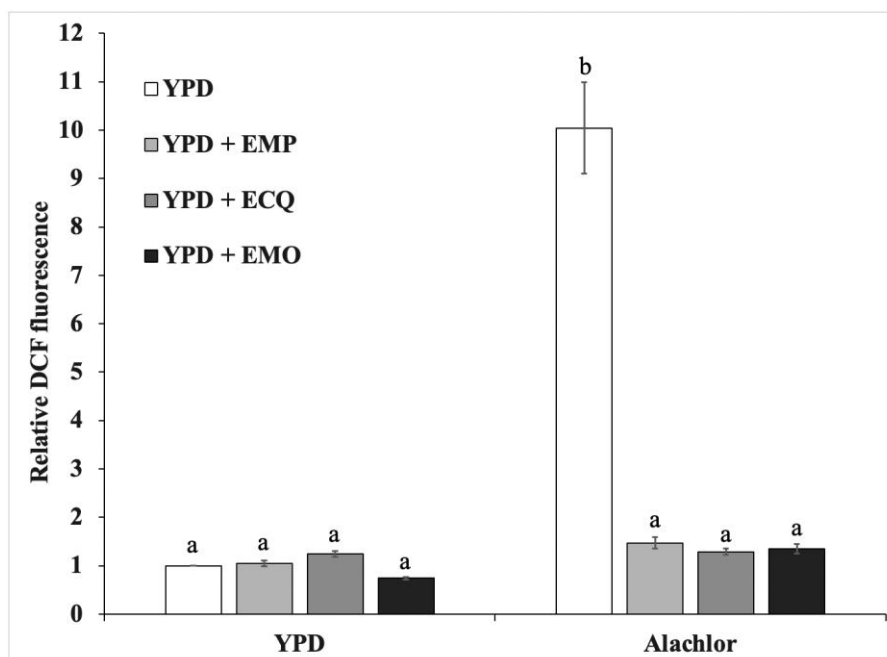


Figure 2.

Effects of ethanolic herbal extracts on intracellular ROS levels. ROS levels were measured using the DCFH-DA fluorescence assay. DCF fluorescence intensity of each sample was normalized to the untreated wild-type cells and expressed as relative DCF fluorescence. Data represent mean \pm SD from six independent experiments. Values with different superscript letters indicate statistically significant differences at $P < 0.05$.

Conclusions:

Conclusively, our data demonstrate that ethanolic extracts of *Mucuna pruriens* (EMP), *Cissus quadrangularis* (ECQ), and *Moringa oleifera* (EMO) have stronger free radical scavenging activity as measured by DPPH and ABTS assays, compared to their aqueous extracts. Consistent with the antioxidant potential, these extracts markedly restored the growth of wild-type (BY4742) yeast cells under alachlor stress and brought the intracellular ROS levels to baseline. Altogether, these observations suggest the protective role of ethanolic Thai herbal extracts in mitigating alachlor-induced oxidative stress in yeast, thereby providing a molecular basis for their cytoprotective effects. Nevertheless, further studies are necessary to elucidate the precise mechanisms underlying this protection.

References:

1. Sharma A, Kumar V, Shahzad B, Tanveer M, Sidhu GPS, Handa N, Kohli SK, Yadav P, Bali AS, Parihar RD. SN Appl. Sci. 2019;1:1-16
2. Molin WT, Anderson EJ, Porter CA. Pestic Biochem Physiol. 1986;25:105-111
3. Trenkamp S, Martin W, Tietjen K. Proc Natl Acad Sci USA. 2004;101:11903-11908
4. Wilkinson R. Pestic Biochem Physiol. 1982;17:177-184
5. Lee WJ, Hoppin JA, Blair A, Lubin JH, Dosemeci M, Sandler DP, Alavanja MC. Am J Epidemiol. 2004;159:373-380
6. Lerro CC, Andreotti G, Koutros S, Lee WJ, Hofmann JN, Sandler DP, Parks CG, Blair A, Lubin JH, Beane Freeman LE. J Natl Cancer Inst. 2018;110:950-958
7. Rattanawong K, Kerdsomboon K, Auesukaree C. Free Radic Biol Med. 2015;89:963-971
8. Elhalwagy ME, Darwish NS, Zaher EM. Pestic Biochem Physiol. 2008;91:81-89



9. Liu H, Wan Y, Wang Y, Zhao Y, Zhang Y, Zhang A, Weng Q, Xu M. *Nutrients*. 2018;10:1838
10. Liu X, Li Y, Zhang Q, et al. *Front Nutr*. 2023;10:1118761



SUGARCANE LEAF DERIVED-BIOCHAR ACID CATALYST FOR EFFICIENT ISOSORBIDE PRODUCTION FROM SORBITOL

Chonthicha Nilapornkul,¹ Pongtanawat Khemthong,² Bunyarit Panyapinyopol,¹ Wasawat Kraithong,² Pawan Boonyoung,² Saran Youngjan,² Jakkapop Phanthasri,² Tokla Eom,¹ Kamonwat Nakason,^{1,*}

¹Department of Sanitary Engineering, Faculty of Public Health, Mahidol University, Bangkok, Thailand

²National Nanotechnology Center (NANOTEC), National Science and Technology Development Agency (NSTDA), Pathumthani, Thailand

*e-mail: kamonwat.nak@mahidol.ac.th

Abstract:

Isosorbide is a high-value chemical used in food, pharmaceuticals, and plasticizers, commonly produced via acid-catalyzed sorbitol dehydration. While homogeneous acid catalysts are effective, they pose challenges such as corrosion, difficult separation, and environmental concerns. To address these issues, this study developed a heterogeneous acid catalyst from sugarcane leaves (SCL). The catalyst was synthesized through carbonization at 500 °C under CO₂ for 1 h, followed by sulfonation at 200 °C for 6 h using concentrated sulfuric acid. Its physicochemical properties were characterized using CHNS analysis, BET surface area, acidity, TGA/DTG, SEM, TEM, FTIR, and XPS. The resulting catalyst showed excellent properties, with a surface area of 154 m²/g, total acidity of 4.18 mmol/g, and sulfonic acid content of 2.31 mmol/g. Isosorbide synthesis was conducted at 200-240 °C for 6-27 h with catalyst loadings of 0-35 wt.%. Optimal yield (54.23 mol%) and selectivity (60.96%) were achieved at 220 °C for 21 h with 25 wt.% catalyst. Recyclability tests confirmed the catalyst's stability and reusability. These findings demonstrate that SCL-derived biochar is a promising, eco-friendly catalyst for dehydration reactions, advancing sustainable chemical production.

Keywords: Sorbitol conversion, Agricultural residues, Sugarcane leaf, Double dehydration, Isosorbide

Introduction:

Isosorbide, also known as Dianhydro-D-glucitol, is a biomass-derived diol produced via double dehydration of D-sorbitol (1, 2). Recognized as a high-value platform chemical, the global isosorbide market was valued at USD 413.3 million in 2020 and is projected to reach USD 700 million by 2027, with a CAGR of 7.9% (3). Owing to its safety, biocompatibility, and renewable origin, isosorbide serves as a sustainable alternative to petroleum-based diols in bio-based polymers and pharmaceuticals (2). Despite extensive research on isosorbide production, homogeneous acids, such as sulfuric acid and *p*-toluenesulfonic acid, remain the most commonly used catalysts. However, they present drawbacks including corrosion, difficult separation, environmental concerns, and lack of reusability(4). Recently, heterogeneous catalysts supported on biochars (e.g., rice husk, corncob, and cassava rhizome) have emerged as promising alternatives for dehydration reactions (5, 6). Sugarcane leaves (SCL), with over 16 million tons of annual surplus in Thailand (7), are a promising feedstock for biochar production. Their high contents of oxygen, volatile matter, cellulose, and hemicellulose (8) enable the formation of porous structures during devolatilization and facilitate the introduction of Brønsted acid sites via sulfonation (6). Utilizing SCL not only adds value to waste but also helps mitigate PM_{2.5}, CO, and GHG emissions from open burning (9). To the best of our knowledge, this is the first report on using SCL-derived solid



acid catalysts for sorbitol dehydration to isosorbide. Therefore, this study aims to synthesize a heterogeneous acid catalyst from SCL and evaluate its efficiency for isosorbide production.

Methodology:

1) Chemicals and Materials

SCL were collected from Phetchabun Province, Thailand. Prior to use, the SCL was oven-dried at 105 °C for 24 h and ground to a powder with particle sizes ranging from 150 – 600 μm. Sorbitol was purchased from Tokyo Chemical Industry Co., Ltd., while isosorbide (≥98%) was obtained from Sigma-Aldrich Co., Ltd. Concentrated sulfuric acid (H₂SO₄, 98%) and ethanol (CH₃CH₂OH) were supplied by Qrec Co., Ltd. (New Zealand). All chemicals and reagents were used without further purification or pretreatment.

2) Preparation of acid catalyst

Initially, 3 g of SCL was carbonized at 500 °C for 1 h under a CO₂ flow of 100 mL/min. Then, 1 g of the resulting biochar (CSCL) was sulfonated in 20 mL of concentrated sulfuric acid at 200 °C for 6 h. The solid product was separated by vacuum filtration and washed repeatedly with deionized water until the filtrate reached a neutral pH. The final solid was dried at 105 °C for 24 h to yield the acid catalyst (S-CSCL), which was stored in an amber glass bottle for further use.

3) Characterization

Untreated SCL was characterized by its lignocellulosic, proximate, and ultimate composition. The catalyst characterization was performed via several parameters, including acidic density was measured via an acid-base back-titration, ultimate composition, thermal decomposition properties, nitrogen sorption properties, and surface morphology. The lignocellulosic, ash, moisture, and volatile matter (VM) compositions of the SCL were measured via the method of NREL/ TP-510-42618 (10). The fixed carbon (FC) content was determined by subtracting the sum of ash and VM contents from 100 %. The ultimate compositions of carbon (C), hydrogen (H), nitrogen (N), and sulfur (S) contents were measured with an elemental analyzer. (LECO CHNS 628, LECO, USA). The oxygen (O) content was determined based on the existing mass fraction without ash content. Thermal decomposition properties were investigated using a thermogravimetric analyzer (TGA/DTG, NETZSCH STA 449 F5 Jupiter, Germany). Nitrogen sorption isotherms were determined by Belsorp Maxx (Quantachrome, USA). The specific surface area (SSA) and pore characteristics of the samples were determined via the Brunauer-Emmett-Teller (BET) equation and the Barrett-Joyner-Halenda (BJH) model, respectively. Surface chemical functional groups were identified by Fourier transform infrared spectroscopy (FTIR Thermo Scientific Nicolet 6700, Thermo Scientific, USA) through KBr method. Elemental chemical states were identified using X-ray photoelectron spectroscopy (XPS, Kratos Axis Ultra, Kratos, UK). Morphological features were observed via scanning electron microscopy equipped with energy dispersive X-ray spectroscopy (SEM-EDS, FEI-Versa 3D) and transmission electron microscopy (TEM, JEM-1400Flash Electron Microscope, JEOL, USA).

4) Isosorbide production

Isosorbide production was conducted in a 100 mL high-pressure stainless-steel batch reactor. In a typical batch, experiment, 1 g of sorbitol, 0.25 g of S-CSCL, and 20 mL of ultrapure water were loaded into the reactor. Reactions were performed at 200 - 240 °C for 6 - 27 h under 600 rpm continuous stirring, with catalyst loadings ranging from 0 - 35 wt.%. After reaction completion, the reactor was rapidly cooled to room temperature. The reaction mixture was filtered, and the solid was washed with ultrapure water and ethanol, then dried at



105 °C for 24 h for further analysis. Each experiment was conducted in duplicate, with a third replicate performed if the coefficient of variation (CV) exceeded 10%.

Liquid-phase products were analyzed using HPLC (Shimadzu, Japan). Sorbitol conversion, isosorbide yield, and isosorbide selectivity were calculated using Eqs. (1)-(3) (6), with isosorbide yield serving as the primary metric for optimizing reaction conditions.

One-way ANOVA (SPSS Statistics v30, IBM, USA) was used to assess the effects of temperature, reaction time, and catalyst loading on isosorbide yield. LSD post hoc tests were applied at a significance level of $p < 0.05$ to determine statistically significant differences and identify optimal conditions.

$$\text{Isosorbide yield (mol.\%)} = \left(\frac{\text{Isosorbide mass (mol)}}{\text{Initial substrate mass (mol)}} \right) \times 100\% \quad (1)$$

$$\text{Isosorbide selectivity (mol.\%)} = \left(\frac{\text{Isosorbide yield (mol.\%)}}{\text{Feedstock conversion (mol.\%)}} \right) \times 100\% \quad (2)$$

$$\text{Sorbitol conversion (mol.\%)} = \left(\frac{\text{Initial substrate mass (mol)} - \text{existed substrate mass (mol)}}{\text{Initial substrate mass (mol)}} \right) \times 100\% \quad (3)$$

Results and Discussion:

1) SCL properties

Table 1.
The SCL composition.

SCL composition		Amount
Proximate composition (wt.%)	Moisture	9.78
	Ash	9.71
	VM	65.20
	FC	17.50
Ultimate composition (wt.%)	C	43.13
	H	5.84
	N	1.32
	S	1.40
	O ^a	38.60
Lignocellulosic composition (wt.%)	Cellulose	32.02
	Hemicellulose	30.54
	Lignin	17.37

^a: Calculated by subtracting the combined contents of C, H, N, S, and ash from 100%.

The compositions of the raw material in Table 1 reveal that SCL is rich in carbon and oxygen, suggesting favorable thermal reactivity and a carbon-rich nature. These characteristics support the formation of a porous structure during carbonization (11), which is beneficial for catalytic applications. Additionally, the high cellulose and hemicellulose contents, known to thermally decompose within the 200 – 350 °C range, facilitate the development of micro- and mesoporous structures, thereby enhancing the material's suitability as a support for heterogeneous acid catalysts (2).

2) Catalyst characteristics

Table 2.
Elemental compositions, acid density, and textural properties of CSCL, S-CSCL, and 5th S-CSCL

Sample name	Elemental compositions (wt.%)						Total acidity (mmol/g)	Sulfonic acidity (mmol/g)	Surface properties	
	C	H	N	S	O	Ash			SSA (m ² /g)	Pore volume (cm ³ /g)
CSCL	58.36	2.94	1.68	0.05	8.02	28.61	0.60	0.00	6	0.015
S-CSCL	48.72	1.96	1.45	1.44	24.49	21.85	4.18	2.31	154	0.087
5 th spent S- CSCL	67.13	3.07	1.20	0.88	21.94	5.53	2.96	1.20	27	0.034

As presented in Table 2, the elemental compositions, total acidity, sulfonic acidity, and textural properties of CSCL, S-CSCL, and the 5th spent S-CSCL show that carbon was the dominant element in CSCL. The oxygen and hydrogen contents were significantly reduced compared to raw SCL due to their volatilization during carbonization, highlighting the effectiveness of the process in enhancing SCL's potential as a catalyst support. Furthermore, the nitrogen adsorption–desorption isotherms in Figure 1(a) reveal that S-CSCL exhibits a Type IV isotherm with a hysteresis loop, indicative of mesoporous materials (12). The pore size distribution in Figure 1(b) confirms that most pores fall within the mesoporous range (2–50 nm). Upon sulfonation, the specific surface area, sulfur content, and sulfonic acidity of CSCL significantly increased from 6–154 m²/g, 0.05–1.44 %, and 0.00–2.31 mmol/g, respectively (Table 2), confirming the successful introduction of sulfonic acid groups (13). However, after five catalytic cycles, the spent S-CSCL exhibited reduced surface area (27 m²/g), sulfur content (0.88 %), and sulfonic acidity (1.20 mmol/g), which may be attributed to pore blockage by residual organics and acid site leaching during the sorbitol dehydration process (14).

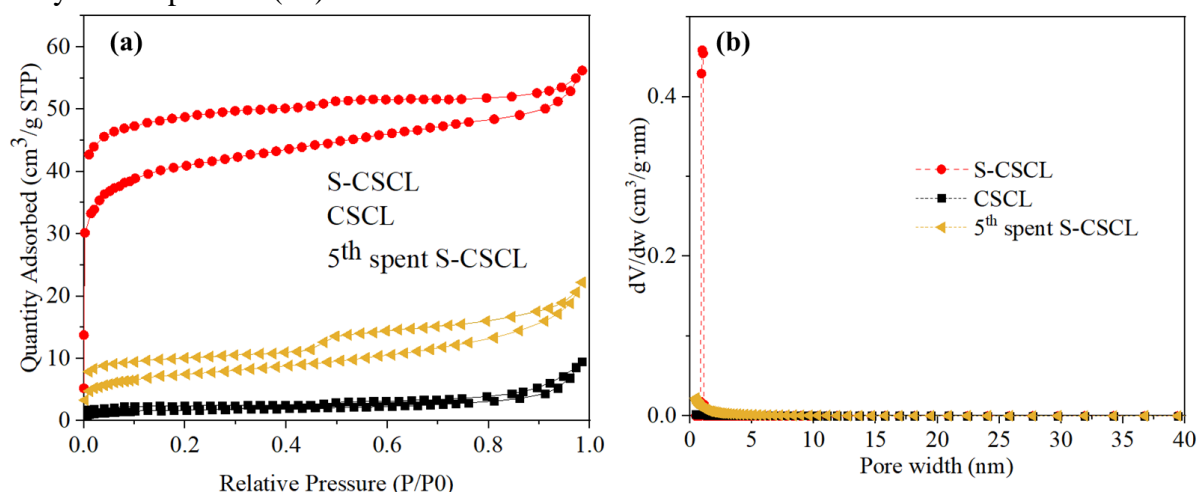


Figure 1.

(a) N₂ adsorption desorption isotherm, (b) pore size distribution of CSCL and S-CSCL.

The thermal stability profiles of SCL, CSCL, and S-CSCL are illustrated in Figure 2. The SCL shows three primary stages of weight loss. The initial stage, occurring between 50 – 120 °C, corresponds to the evaporation of moisture. The second stage, from 200 – 315 °C, is associated with the thermal decomposition of cellulose and hemicellulose. The final stage, observed above 400 °C, reflects the degradation of lignin (15). After carbonization, the CSCL sample exhibited enhanced thermal stability, as evidenced by reduced weight loss throughout the entire temperature range. In contrast, the S-CSCL sample demonstrated increased degradation within the 100 - 400 °C range, with a pronounced DTG peak between 150 - 250 °C. This behavior is attributed to the decomposition of sulfonic acid groups and oxygen-containing functional groups introduced during the sulfonation process (13).

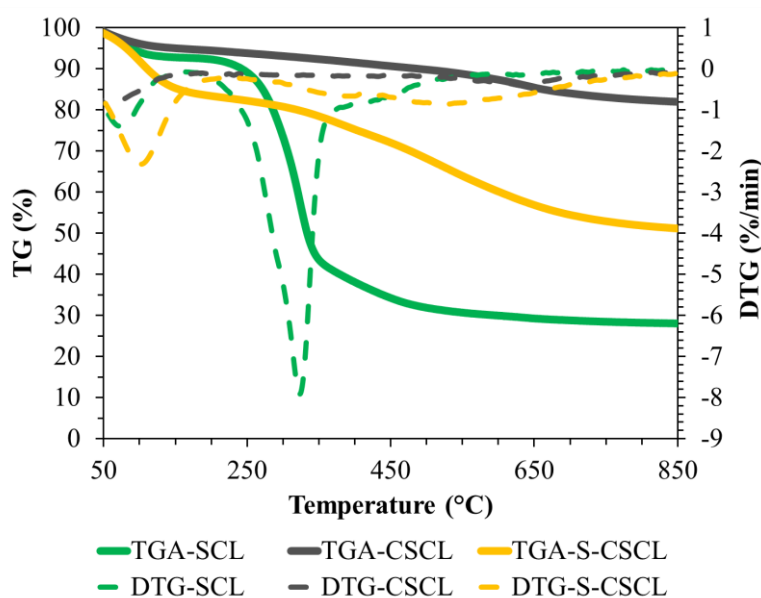


Figure 2.

TG and DTG curves of SCL, CSCL and S-CSCL.

The scanning electron microscopy (SEM) images reveal that the surface of S-CSCL (Figure 3b) became significantly rougher and more fragmented compared to CSCL (Figure 3a) after sulfonation, with clearly visible pore formation. This transformation is attributed to the corrosive action of concentrated sulfuric acid, which induces microcracks and promotes the development of fine porosity, consistent with the textural data in Table 2 (16, 17). Transmission electron microscopy (TEM) of CSCL (Figure 3d) shows a dense, compact morphology typical of untreated carbon. In contrast, S-CSCL (Figure 3e) exhibits a more transparent structure, likely due to the introduction of $-\text{SO}_3\text{H}$ groups that modify the carbon matrix. After five catalytic cycles (Figure 3f), the spent S-CSCL displays increased opacity, indicating the accumulation of humin, amorphous, carbonaceous byproducts known to clog catalyst pores. Furthermore, TEM-EDS elemental mapping (Figures 3h–i) confirms the homogeneous distribution of sulfur across the S-CSCL surface, verifying the successful incorporation of sulfonic acid groups. Post-reaction analysis of the 5th spent catalyst also reveals partial pore collapse and aggregation, likely resulting from humin deposition and acidic leaching during repeated use (18).

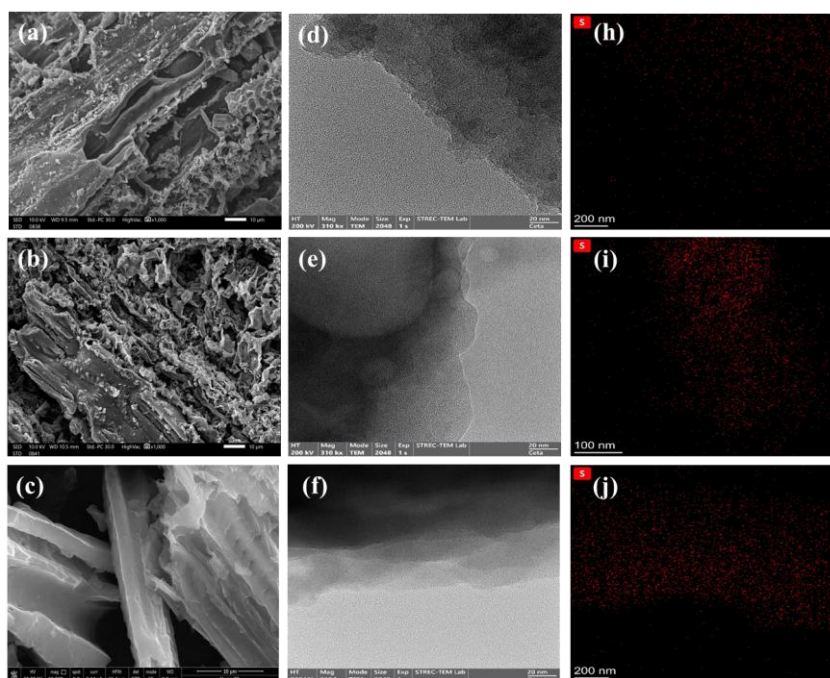


Figure 3.

SEM images of (a) CSCL, (b) S-CSCL, (c) 5th spent S-CSCL; TEM images and sulfur mapping of (d, h) CSCL, (e, i) S-CSCL, and (f, j) 5th spent S-CSCL.

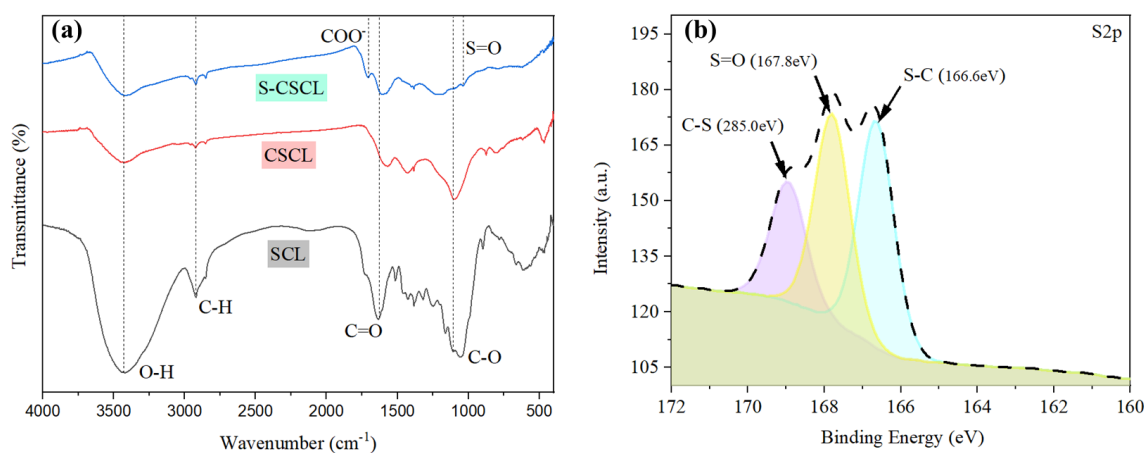


Figure 4.

(a) FTIR spectra of SCSL, CSCL, and S-CSCL and (b) XPS spectra of S-CSCL

Figure 4(a) demonstrates that carbonization effectively removes most oxygenated and aliphatic functional groups, such as O–H, C–H, and C=O, while enhancing the intensity of aromatic C=C bands. This shift indicates increased aromatic condensation and improved structural stability (19), making CSCL a chemically robust support for catalysis. Subsequent sulfonation introduces strong absorption bands near 1180 and 1040 cm^{-1} , corresponding to S=O and –SO₃H stretching vibrations, respectively, along with a partial recovery of O–H groups (20, 21). These modifications combine a stable aromatic carbon matrix with high surface acidity, rendering S-CSCL an efficient solid acid catalyst for biomass conversion. The XPS spectrum in Figure 4(b) confirms successful sulfonation, as evidenced by an S2p peak in the range of ~166–170 eV, characteristic of S⁶⁺ in –SO₃H groups (22, 23).

3) Catalytic performance of S-CSCL in isosorbide production

Isosorbide production from sorbitol was investigated at 200-240 °C for 6-27 h using catalyst loadings ranging from 0-35 wt.%. As shown in Figure 5(a), increasing the temperature from 200-220 °C significantly enhanced the isosorbide yield and selectivity from 20.80-54.23 mol.% and 44.64-60.96 %, respectively. However, further increasing the temperature to 240 °C slightly reduced the yield and selectivity to 53.08 mol.% and 55.74%. Similarly, the isosorbide yield and selectivity also varied with reaction time. Rising the time from 6-21 h elevated the yield and selectivity from 7.76-54.23 mol.% and 27.73-60.96 %, but a longer duration of 27 h led to decreases to 41.94 mol.% and 43.32 % (Figure 5(b)). Catalyst loading showed a comparable trend, with the yield and selectivity increasing from 0.02-54.23 mol.% and 0.13-60.96% as loading rose from 0-25 wt.%, before declining slightly to 53.12 mol.% and 59.52 % at 35 wt.% (Figure 5(c)). Statistical analysis confirmed that temperature ($F = 1721.20$), time ($F = 243.02$), and catalyst loading ($F = 3573.55$) significantly affected isosorbide yield ($p < 0.001$). Post hoc tests indicated no significant differences between 220 and 240 °C or among 15, 25, and 35 wt.% loadings, suggesting a plateau effect. Thus, 220 °C, 21 h, and 25 wt.% were identified as optimal.

The enhanced yield and selectivity are attributed to the double dehydration of sorbitol via a sorbitan intermediate, promoted by the $-\text{SO}_3\text{H}$ groups on the S-CSCL catalyst. Optimal conditions (220 °C, 21 h, 25 wt.%) ensured efficient conversion due to increased acid site density and surface area. Conversely, harsher conditions led to isosorbide degradation and humin formation, which reduced yield and selectivity (2). Additionally, side reactions under these conditions produced unwanted byproducts like levulinic acid and polyols, further decreasing efficiency (24).

Compared to previous studies, this work achieved a comparable yield (54.2 mol%) to a Ce(IV) sulfate catalyst (55.7 mol% at 180 °C, 6 h, 2 MPa N_2) (25), though lower than the 82.7% yield reported for a calcium citrate catalyst at 160 °C for 1.5 h (26), attributed to its superior porosity and acidity. However, from a sustainability standpoint, the S-CSCL catalyst, derived from agricultural waste, offers environmental benefits such as a potentially negative carbon footprint. In contrast, calcium citrate is synthetically produced and contributes more to carbon emissions. While S-CSCL's performance is slightly lower, its eco-friendly nature makes it a promising green alternative. Future improvements could target enhancing its surface area, porosity, and acidity to further boost efficiency.

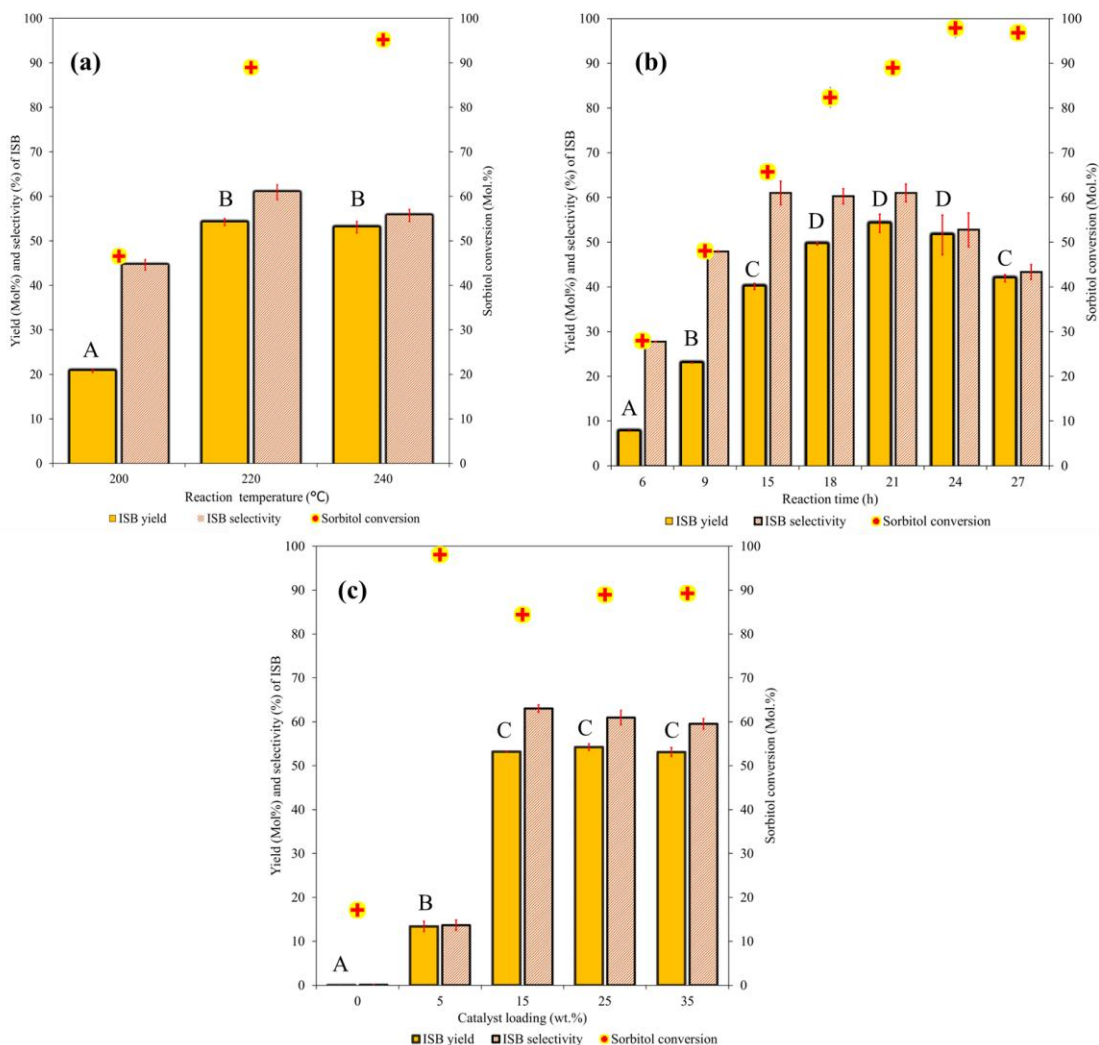


Figure 5.

Sorbitol conversion to isosorbide at different (a) reaction temperature (21 h reaction time, S-CSCL 25wt.%); (b) reaction time (220°C reaction temperature, S-CSCL 25wt.%); (c) Catalyst loading (21 h reaction time, 220°C reaction temperature). The different letters indicate a significant difference at $\alpha = 0.05$

4) Recycling test

In this study, the reusability of S-CSCL catalyst was evaluated under optimal reaction condition (220 °C, 21 h, 25 wt.% catalyst). After each cycle, the spent catalyst was washed with ethanol and dried prior to reusing. As shown in Figure 6, the catalytic reaction was repeated over five consecutive cycles. The isosorbide yield remained relatively stable during the first three runs, declining slightly from 50.56-48.05 mol%, indicating less than a 10% loss in catalytic performance. However, a significant drop was observed in the fourth cycle, with the yield decreasing to 28.60 mol%. This decline in activity may be attributed to the accumulation of humin and polymeric by-products on the catalyst surface, which block active sites, as well as the gradual loss of $-\text{SO}_3\text{H}$ functional groups essential for the dehydration reaction (27). Nonetheless, the ability of the S-CSCL catalyst to be reused for three consecutive cycles while maintaining high catalytic performance highlights its potential as a sustainable, biomass-derived solid acid catalyst for green chemical processes.

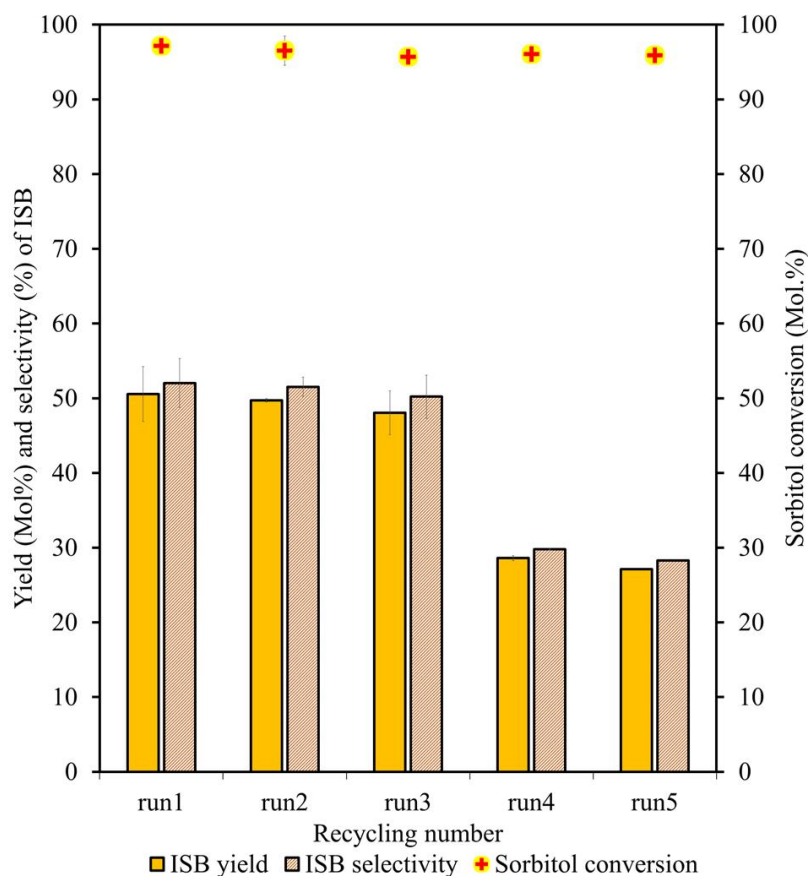


Figure 6.

Yield and selectivity of isosorbide, and sorbitol conversion after five running. Reaction condition: 220°C, 21h and 25wt.% catalyst loading.

Conclusion:

Agricultural waste in the form of SCL was utilized as a support material for a heterogeneous acid catalyst, which was applied to the hydrothermal conversion of sorbitol into isosorbide. The resulting S-CSCL catalyst achieved a maximum isosorbide yield of 54.23 mol% and a selectivity of 60.96 mol% at 220 °C for 21 h with a catalyst loading of 25 wt.%. Characterization results confirmed that the high density of sulfonic acid groups and the well-developed porous structure of the biochar support played critical roles in enhancing catalytic performance. Furthermore, the catalyst demonstrated good reusability, maintaining significant activity over three consecutive cycles. These findings underscore the potential of S-CSCL as a low-cost, renewable, and environmentally friendly catalyst for sustainable isosorbide production.

Acknowledgements:

This research project has been supported by Mahidol University (Fundamental Fund: fiscal year 2025 by National Science Research and Innovation Fund (NSRF)). The authors would like to express their gratitude to the National Science and Technology Development Agency (NSTDA) and the TGIST-Internship 2025 program for providing a short-term research grant to Ms. Chonthicha Nilapornkul, MSc student in Environmental Technology, Mahidol University.

References:

1. Stoss P, Hemmer R. *Adv Carbohydr Chem Biochem.* 1991;49:93-173.
2. Dussenne C, Wiatz V, Wyart H, Suisse I, Sauthier M. *Green Chem.* 2017;19:5332-4.
3. Zhao Z, Zhang S, Liang Y, Wu J, Song G. *Catal Today.* 2023;424:113747.
4. Shi Y, Yang J, Guo J, Wang S, Yuan D, Zhao N, et al. *Microporous Mesoporous Mater.* 2024;368:113009.
5. Galhardo TS, Simone N, Gonçalves M, Figueiredo FCA, Mandelli D, Carvalho WA. *ACS Sustainable Chem. Eng.* 2013;1:1381-9.
6. Nakason K, Sumrannit P, Youngjan S, Wanmolee W, Kraithong W, Khemthong P, et al. *Chem Eng Sci.* 2024;287:119729.
7. Board of Cane and Sugar. Bangkok; 2023.
8. Nakason K, Chukaew P, Utrarachkij F, Kuboon S, Kraithong W, Pichaiyut S, et al. *Sustain Mater Technol.* 2024;40:e00973.
9. Chokesawatnakit N, Jirathiwat P, Kamwilaisak K. *J Met Mater Miner.* 2021;31:46-53.
10. Sluiter A, Hames B, Ruiz R, Scarlata C, Sluiter J, Templeton D, et al. *NREL/TP-510-42618.* 2008.
11. Shu R, Jiang H, Xie L, Liu X, Yin T, Tian Z, et al. *Renew Energy.* 2023;202:1160-8.
12. Thommes M, Kaneko K, Neimark AV, Olivier JP, Rodriguez-Reinoso F, Rouquerol J, et al. *Pure Appl Chem.* 2015;87:1051-69.
13. Koziara BT, Kedzierzawski E, Ogiejko W, Nijmeijer K, Hempenius MA, Benes NE. *Macromol Mater Eng.* 2016;301:71-80.
14. Xie Q, Yang X, Xu K, Chen Z, Sarkar B, Dou X. *Environ Res.* 2020;188:109887.
15. Poletto M, Zattera AJ, Santana RMC. *Bioresour Technol.* 2012;126:7-12.
16. Adeyinka SY, Tang-Yue K, Porwal J. *RSC Adv.* 2022;12:10237-48.
17. Varkol M, Ghosh S, Omvesh, Palla VCS, Kumar P, Bhattacharjee S, et al. *Catalysts.* 2024;15:243.
18. Huang F, Li W, Liu Q, Zhang T, An S, Li D, et al. *Fuel Process Technol.* 2018;181:294-303.
19. Tu P, Zhang G, Wei G, Li J, Li Y, Deng L, et al. *Bioresour Bioprocess.* 2022;9:131.
20. Lam E, Luong JHT. *ACS Catal.* 2014;4:3393-410.
21. Fonseca JM, Spessato L, Cazetta AL, da Silva C, Almeida VC. *Chem Eng Process.* 2022;170:108668.
22. Liu XY, Huang M, Ma HL, Zhang ZQ, Gao JM, Zhu YL, et al. *Molecules.* 2010;15:7188-96.
23. Ferreira ARO, Silvestre-Albero J, Maier ME, Ricardo NMPS, Cavalcante CL, Luna FMT. *Mol Catal.* 2020;488:110888.
24. Srithep C, Jitsomboon S, Kanlayaporn Y, Boonyarattanakalin C, Kamwilaisak K. *Catalysts.* 2020;10:148.
25. Boupan M, Prompang K, Chompunuch A, Boonma P, Neramittagapong A, Theerakulpisut S, et al. *J Renew Mater.* 2023;11:2985-3000.
26. Zhang Y, Chen T, Zhang G, Wang G, Zhang H. *Appl Catal A Gen.* 2019;575:38-47.
27. Zhang S, Pan H, Huang J, Li Y, Zhang H. *Front Chem.* 2022;10:882235.



GENETIC IMPROVEMENT AND CHITINOLYTIC ENZYME PRODUCTION OF *Stenotrophomonas maltophilia* Mc_E05 ISOLATED FROM TERMITE EXOSKELETON

Chinnaphat Meeto,¹ Kittipong Chanworawit,¹ Pinsurang Deevong^{1,*}

¹Department of Microbiology, Faculty of Science, Kasetsart University, 10900, Bangkok, Thailand

*e-mail: fsciprd@ku.ac.th

Abstract:

Chitin is a crystalline polysaccharide polymer and difficult to decompose. The seafood industry produces large amounts of chitin waste, which rapidly accumulates in the environment. Accumulation of the chitin wastes leads to a range of pollutant effects on soil, water, and air. Chitinases play an important role in industry, agriculture, and the environment. These hydrolytic enzymes catalyze and degrade chitin materials to produce monomer and oligomer units. The chitinolytic bacterial isolate Mc_E05 used in this study was obtained from the exoskeleton of the termite *Microcerotermes* sp. and the 16S rRNA gene sequence analysis revealed that it was closely related to *Stenotrophomonas maltophilia*. The present study aimed to improve the chitinase production of the potential isolate using mutagenesis. The genetic improvement using ultraviolet (UV) irradiation and ethyl methane sulfonate (EMS) treatment enhanced the chitinolytic ability of bacteria. Based on the 10% survival rate of bacteria, almost thousand colonies were detected for their chitinase production using point inoculation on the nutrient agar (NA) supplemented with 1% colloidal chitin. Bacterial mutants with increased chitinase activity were collected and used for subsequent experiments. The selected mutants were determined the enzymatic activity using the 3,5-dinitrosalicylic acid (DNS) method. The mutant E05-UV2 exhibited the maximum chitinolytic activity of 142.30 ± 7.31 mU/mL (approximately 170% increased from wild-type) after 96 h of incubation, while the mutant E05-EMS2 exhibited the maximum chitinolytic activity of 85.45 ± 2.44 mU/mL (approximately 62% increased from wild-type) after 72 h of incubation. The result indicated that UV mutagenesis was effective for increasing the chitinase activity of *S. maltophilia*. Moreover, all treatments with UV irradiation showed significantly higher efficiency than those of EMS mutagenesis. The present study successfully improved the chitinolytic activity of the isolated termite gut bacterium, *S. maltophilia*, through mutagenesis. The resulting mutants and their chitinases provide valuable potential for applications in biotechnology and environmental bioremediation.

Introduction:

The increasing volume of industrial waste is generated annually in overall country in the world, comprising food scraps, chemicals, and various organic and inorganic substances. When there are large accumulations of waste, they lead to a range of pollutant effects on soil, water, and air. The presence of persistent organic pollutants can render the land infertile and unsafe for growing crops. Furthermore, it leads to water pollution, which is harmful to aquatic animals and plants, and it also produces foul odors. The decomposition of waste releases fine dust and particulate matter, which are harmful to breathe and spread of fungal spores. All these factors have a serious impact on both the environment and human health. Currently, the seafood industry produces shellfish waste, including crab and shrimp shells, which is approximately 75% of its total weight and chitin contains 20 – 58% of dry weight.¹ Chitin is a polymer of N-acetyl-glucosamine (NAG) with crystalline structure, strength, and not flexibility.³ Therefore, it is difficult to decompose and highly accumulated in the environment. Physical, chemical, and biological methods can be employed for the treatment

and disposal of waste. However, biological methods using microbial agents are more suitable because they are environmentally friendly, leave no chemical residues, and have the least impact on living organisms in the environment.

Chitinase is a catalytic enzyme that hydrolyzes chitin to simple sugar by cleavage of β -(1,4) glycosidic linkage and is found in many organisms (bacteria, fungi, plants, and animals), which play an important role in biological processes such as degradation of chitin-containing waste and control of pathogenic fungi.^{4, 5} Chitinase-producing bacteria were isolated from various habitats such as shellfish waste, compost, and hot springs. These chitinolytic bacteria, including the genera *Streptomyces*, *Aeromonas*, *Bacillus*, *Serratia*, *Pseudomonas*, and *Stenotrophomonas* have the ability to produce chitinase.⁶

A common biological method is the use of microorganisms and their enzymes to degrade chitin. The previous study reported that 10 isolates of chitin-degrading bacteria were isolated from dead termites, and the most efficient chitin-degrading bacteria in the study was classified as bacterial strain in the genus *Stenotrophomonas*.⁷ In the present study, we aimed to achieve genetic improvement of the chitinolytic *S. maltophilia* Mc_E05 obtained from the exoskeleton of termites to enhance the chitinase production. This mutagenic strain holds potential for future applications in the efficient biodegradation and disposal of chitin-containing wastes.

Methodology:

Bacterial strain and growth condition

The chitinolytic bacterium *Stenotrophomonas maltophilia* Mc_E05 (accession number: OQ293905.1) was isolated in a previous study by Chanworawit, Wangsoonthorn and Deevong^[8] from the exoskeleton of the wood-feeding termite *Microcerotermes* sp. This bacterial strain was cultured and maintained on nutrient agar (NA) at pH 7, and the temperature for culture incubation was 37°C.

Ultraviolet-radiation mutagenesis

UV-radiation mutagenesis was performed using the modified method described previously by Winston^[9]. For the UV mutagenesis, *S. maltophilia* Mc_E05 was cultured in 100 mL of nutrient broth (NB) and further incubated at 37°C for 24 h. The bacterial culture was adjusted to the cell turbidity of McFarland No. 0.5 (cell concentration of approximately 1.5×10^8 cells/mL). Then, the cell suspension was serially diluted to an appropriate cell number (30 – 300 colony-forming units (CFU) per plate) and spread on NA plates. The culture plates were exposed to UV light at 254 nm (30W, Germicidal lamp, SANKYO DENKI) for variable periods of 10, 30, 60, 90, 120, and 150 sec. After the UV exposure, the plates were incubated at 37°C for 48 h in darkness to prevent photoreactivation. Then, colony-forming units (CFU) were counted and quantified for the survival rate. The treated sample that demonstrated a 10% survival rate was selected for collecting bacterial colonies. In previous studies, this survival level showed a high probability of DNA repair with mutagenic effect.^{10, 11}

Chemical mutagenesis

Chemical mutagenesis using ethyl methane sulfonate (EMS) was performed using the modified method described previously by Biswas and Paul^[12]. For the EMS mutagenesis, *S. maltophilia* Mc_E05 was cultured as described above. After serial dilution, cell suspension was added with 100 μ g/mL of EMS and then shaken at 200 rpm at 37°C. The treated samples were collected at variable times of 10, 20, 30, 40, 50, and 60 min. After the mutagenesis, the reaction of EMS was stopped by adding with 20% (w/v) sodium thiosulfate. Then, the cell suspension was centrifuged at 10,000 rpm at 4°C and washed three times with sterile normal



saline (0.85% NaCl). Bacterial cell pellets were resuspended with 1 mL of normal saline and plated on NA plates. After incubation at 37°C for 48 h in darkness, colony-forming units (CFU) were counted and quantified for the survival rate. Then, the treated sample showing a 10% survival rate was selected for collecting bacterial colonies.

Screening of chitinase production from mutagenic strains

All bacterial colonies were pointed on the NA plate supplemented with 1% colloidal chitin and then incubated at 37°C for 120 h. The chitin hydrolysis zones of both the wild type and mutant strains were observed, and mutants that exhibited higher chitinase production than the wild type were selected and purified using the streak method on NA plate and used for subsequent experiments.

Chitinase activity assay

The strain *S. maltophilia* Mc_E05 was cultured in NB at 37°C for 24 h. After that, the bacterial culture was adjusted to the OD₆₀₀ value of 1.0, and 1% of the inoculum was inoculated into 100 mL NB supplemented with 1% colloidal chitin and then shaken at 200 rpm at 37°C for 7 days. Then, culture supernatant was collected by centrifugation at 10,000 rpm at 4°C for 10 min every day. The crude enzyme was determined for chitinase activity.

The chitinase activity was measured using the 3,5-dinitrosalicylic acid (DNS) method.¹³ To prepare the reaction mixture, 1 mL of colloidal chitin as a substrate was mixed with 1 mL of crude enzyme and then incubated at 37°C for 30 minutes. The reaction was stopped with 3 mL of DNS reagent and boiled in boiling water at 100°C for 5 min. The mixture was centrifuged at 10,000 rpm for 5 min, and the supernatant was measured at 540 nm using a spectrophotometer. Absorbance was compared with the NAG standard curve for calculated chitinase activity. One unit of chitinase activity was defined as the amount of enzyme that liberates 1 μmol of reducing sugar (NAG) per min under the conditions.

Statistical analysis

All experiments were performed in triplicate. The results are expressed as the mean ± standard deviation (S.D.). The data were analyzed using one-way ANOVA, followed by the Duncan Post Hoc test, in JASP version 0.19.3. Statistical significance level was set at $P < 0.05$ for all analyses.

Results and Discussion:

Mutagenesis and screening of mutagenic strains

After the mutagenesis of *S. maltophilia* Mc_E05 by UV irradiation and EMS treatment, bacterial survival was determined at different periods. The results showed that a 10% survival rate of bacteria was observed at 25 sec and 55 min, respectively. A total of 850 colonies were obtained from UV irradiation, and 1,150 colonies were derived from EMS treatment. After screening bacterial chitinase production on NA medium supplemented with 1% colloidal chitin, six mutagenic strains comprising E05-UV1, E05-UV2, E05-UV3, E05-EMS1, E05-EMS2, and E05-EMS3 exhibited the highest chitinase production and were selected for chitinase activity assay. The results showed that the survival rate of *S. maltophilia* Mc_E05 decreases exponentially with increasing exposure time to UV irradiation and EMS, with complete cell death occurring at 60 sec of UV irradiation and approximately 60 min of EMS treatment (**Figure 1**). The results were supported by previous reports involving bacterial chitinase production. For example, *Bacillus pumilus* SG2 was completely killed after 600 sec of UV irradiation¹⁴, while *Streptomyces halstedii* retained approximately 10% survival after 15 min of UV irradiation and 60 min of EMS treatment.¹⁵

The results of mutant screening shown in **Figure 2** indicated a variation in chitinase production among both UV- and EMS-induced mutants. Some mutants exhibited reduced chitinase production, while others showed an increased production compared with the wild-type strain. Several previous studies have reported the use of mutagenesis to improve enzyme production, including chitinase, protease, xylanase, and lipase.¹⁶⁻¹⁹ These findings suggested that the mutagenesis, whether induced by UV irradiation or the chemical mutagen EMS, can either enhance or reduce chitinase production in *S. maltophilia* Mc_E05.

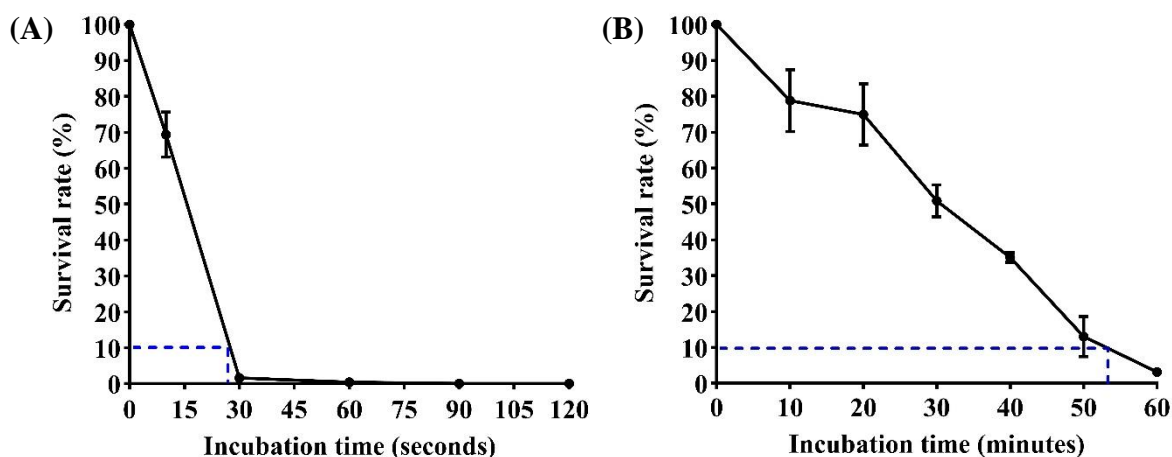


Figure 1.

Mutagenesis results of *Stenotrophomonas maltophilia* Mc_E05. Survival rates of bacteria after (A) UV treatment and (B) EMS treatment are presented.

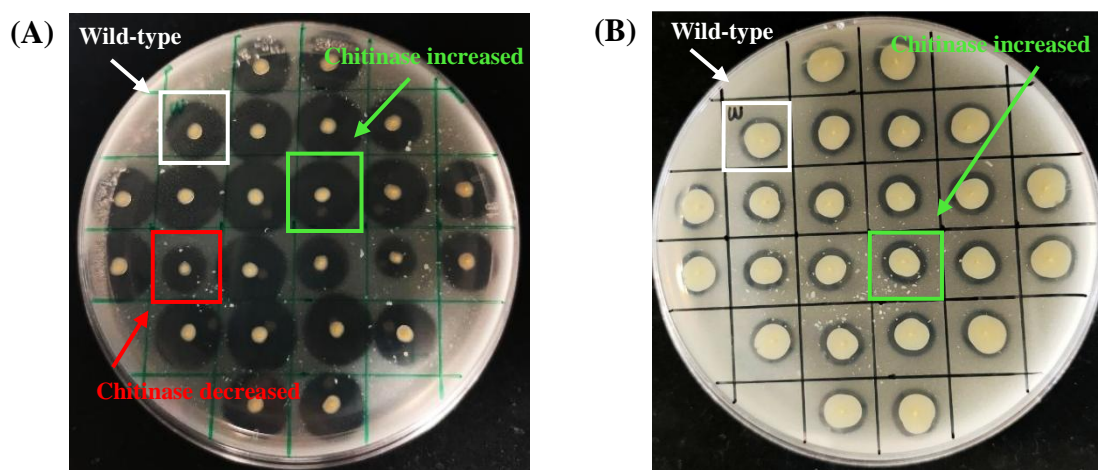


Figure 2.

The mutants produced chitinase with a larger clear zone compared with the wild-type strain. The results of (A) UV treatment and (B) EMS treatment are presented.

Chitinase activity of the promising mutants

The chitinase activity of mutant and wild-type strains is shown in **Figure 3**. The results indicated that the wild-type *S. maltophilia* Mc_E05 exhibited maximum chitinase activity of 52.72 ± 2.43 mU/mL at 96 h of incubation. All six selected mutants displayed significantly higher chitinase activity than that of the wild type. The highest chitinase activity was observed in mutant E05-UV2, with 142.30 ± 7.31 mU/mL (269.92%, or 1.7 folds higher than the wild type), followed by E05-UV3 and E05-UV1, which showed activities of $138.86 \pm$

4.88 mU/mL (263.39%, or 2.63 folds) and 113.01 ± 4.87 mU/mL (214.36%, or 2.14 folds), respectively. Meanwhile, the mutants E05-EMS2, E05-EMS1, and E05-EMS3 exhibited chitinase activities of 85.45 ± 2.44 mU/mL (162.08% or 1.62 folds), 82.00 ± 4.87 mU/mL (155.54% or 1.55 folds) and 75.84 ± 5.90 mU/mL (142.85% or 1.42 folds), respectively. Previous reports have also demonstrated improvements in chitinase production through mutagenesis. For example, *Bacillus pumilus* CHT11 had been enhanced its enzyme production by UV-mutagenesis, and its mutant strain BM33 exhibited up to a 5-fold increase in chitinase activity compared with the wild type.²⁰ Moreover, mutants of *Paenibacillus macerans* kh-B1 (strains kh-UVB-4 and kh-ESB-20) generated by UV and EMS mutagenesis could show higher chitinase activity than the wild type, with 41.6 U/mL (3.06 times) and 54.8 U/mL (4.02 times), respectively.²¹ Another study found that, *Streptomyces halstedii* MA-St-1 treated with UV and EMS could produce chitinase activity of 10.8 and 11.8 U/mL, respectively, while the wild-type produced 5.70 U/mL.¹⁵ **Table 1** summarizes the chitinase activities of chitinolytic bacteria and their mutants from this study and previous reports. The mutagenesis of chitinolytic bacteria demonstrated an increase in chitinase production in both UV- and EMS-induced mutants. In the present study, the UV-induced mutant strains exhibited a significantly greater increase in chitinase activity than the EMS-induced mutant strain, whereas the previous studies reported that the EMS-induced mutants showed higher enzyme activity than the UV-induced mutants. The results showed that the application of both UV- and EMS-mutagenesis resulted in different outcomes due to various influencing factors. These factors may include the type of microorganism, exposure duration, incubation period, and environmental conditions. Nevertheless, the findings of the present study demonstrated that both UV- and EMS-mutagenesis were effective in enhancing the chitinase activity of the chitinolytic *S. maltophilia* Mc_E05. Moreover, UV irradiation consistently showed higher efficiency than EMS treatment.

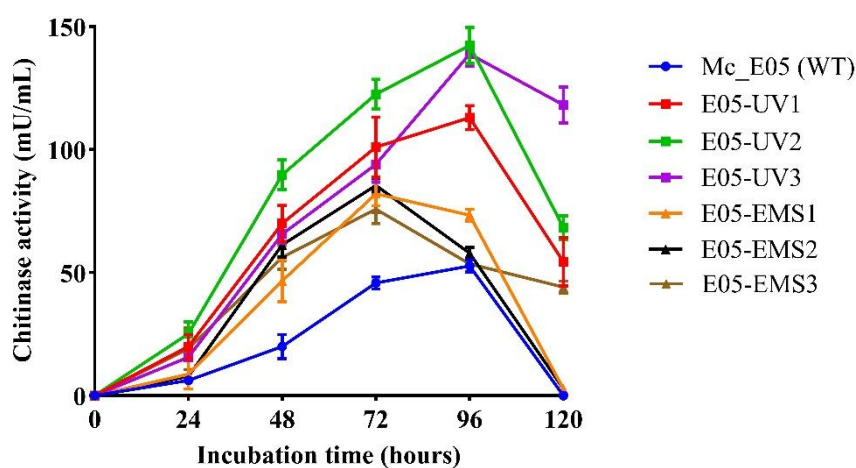


Figure 3.

Chitinase activity of *Stenotrophomonas maltophilia* Mc_E05 and their mutants at different incubation periods

Table 1.
Maximum chitinase activity of chitinolytic bacteria and their mutants

Isolates	Treatment	Maximum chitinase activity	Fold	%	Reference
<i>S. maltophilia</i> Mc_E05					
Wild-type	-	52.72 ± 2.43 ^a mU/mL	1.00	100.00	
E05-UV1	UV	113.01 ± 4.87 ^c mU/mL	2.14	214.36	
E05-UV2	UV	142.30 ± 7.31 ^d mU/mL	2.70	269.92	
E05-UV3	UV	138.86 ± 4.88 ^d mU/mL	2.63	263.39	This study
E05-EMS1	EMS	82.00 ± 4.87 ^b mU/mL	1.55	155.54	
E05-EMS2	EMS	85.45 ± 2.44 ^b mU/mL	1.62	162.08	
E05-EMS3	EMS	75.84 ± 5.90 ^b mU/mL	1.43	142.85	
<i>Paenibacillus macerans</i>					
kh-B1	-	13.6 U/mL	1.00	100.00	21
Wild-type					
Kh-UVB-4	UV	41.6 U/mL	3.06	305.88	
Kh-ESB-20	EMS	54.8 U/mL	4.02	402.94	
<i>Streptomyces halstedii</i>					
MA-St-1	-	5.70 U/mL	1.00	100.00	15
Wild-type					
UV/15-15	UV	10.8 U/mL	1.89	189.47	
E/60-12	EMS	11.8 U/mL	2.07	207.02	

Statistical significances were determined using one-way ANOVA in JASP version 0.19.3. The different superscripts indicate significant difference ($P < 0.05$).

Conclusion:

The UV-induced mutants (E05-UV1, E05-UV2, and E05-UV3) exhibited maximum chitinase activity at 96 h, whereas EMS-induced mutants reached their maximum activity at 72 h. The mutagenesis using UV irradiation and EMS has a good ability to enhance the chitinase production of *S. maltophilia* Mc_E05, with increasing chitinase activity by ~170% and ~62% compared to the wild-type, respectively. This study indicated that the chemical mutagen EMS could induce higher chitinase production within a shorter period. However, the UV-induced mutants displayed significantly higher maximum chitinase activity than the EMS-induced mutants. Among six selected mutants, the E05-UV2 mutant showed the highest chitinase activity of 142.30 ± 7.31 mU/mL at 96 h, which is ~1.7 fold higher than the wild-type strain. These results demonstrate that the UV mutagenesis was effective in increasing the chitinase production of Mc_E05, and all treatments with UV irradiation were more efficient than those of EMS. This study highlights the potential of enhancing chitinase production in *S. maltophilia* Mc_E05 using both UV irradiation and the chemical agent EMS, offering promising applications in biotechnology, agriculture, and industry, particularly for environmental bioremediation.



Acknowledgements:

This research was partially funded by the Undergraduate Research Matching Fund (URMF), Faculty of Science, Kasetsart University.

References:

1. Kuddus M, Ahmad I. *J Genet Eng & Biotechnol.* 2013;11(1):39-46.
2. Hamid R, Khan MA, Ahmad M, Ahmad MM, Abdin MZ, Musarrat J, Javed S. *J Pharm Bioallied Sci.* 2013;5(1):21-29.
3. Meunier L, Costa R, Keller-Costa T, Cannella D, Dechamps E, George IF. *Microbiol Spectr.* 2024;12(11):e00886-24.
4. Vaghela B, Vashi R, Rajput K, Joshi R. *Enzyme Microb Technol.* 2022;159:110055.
5. Ikeda M, Kakizaki H, Matsumiya M. *Int J Biol Macromol.* 2017;104:1672-1681.
6. Aly MM, Sediq AN, Baghdadi AM, Amasha RH. *IOSR J Pharm Biol Sci.* 2019;14:36043.
7. Jabeen F, Hussain A, Manzoor M, Younis T, Rasul A, Qazi JI. *Egypt J Biol Pest Control.* 2018;28(1):86.
8. Chanworawit K, Wangsoonthorn P, Deevong P. *Biosci Biotechnol Biochem.* 2023;87(9):1077-1091.
9. Winston F. *Curr Protoc Mol Biol.* 2008;82(1):13.3 B. 1-13.3 B. 5.
10. Sweet DM, Moseley B. *Mutat Res.* 1976;34(2):175-186.
11. Foster PL. *Methods Enzymol.* 1991;204:114-125.
12. Biswas J, Paul AK. *Curr Res Microbiol.* 2016;
13. Miller GL. *Anal Chem.* 1959;31(3):426-428.
14. Vahed M, Motalebi E, Rigi G, Noghabi KA, Soudi MR, Sadeghi M, Ahmadian G. *J Microbiol biotechnol.* 2013;23(11):1519-1528.
15. Shafi ME, Khattab AE-NA. *Adv Environ Biol.* 2020;14(1):7-19.
16. Soliman GM, El-Sawy SM, Salim RG, El-Sayed GM, Ramadan WA. *Jordan J Biol Sci.* 2023;16(2)
17. Irianto VS, Demirkan E, Cetinkaya AA. *Prep Biochem Biotechnol.* 2024;54(7):918-931.
18. Ghazi S, Sepahy AA, Azin M, Khaje K, Khavarinejad R. *Iran J Basic Med Sci.* 2014;17(11):844.
19. Bhuvanachandra B, Madhuprakash J, Podile AR. *BBA. Proteins and proteomics.* 2018;1866(3):407-414.
20. Aly MM, Tork S, Alakilli SY. *Universal scholar in Biotechnology.* 2011;1(2):14-21.
21. Sheikh HM, Hamshary O, Abd El-Hafez AE-N. *J Pure Appl Microbiol.* 2022;16(1):643-654.



REDUCING SUGAR EXTRACTION FROM OVER-ROASTED COFFEE BEANS AND COFFEE SILVERSKINS

Sukon Tantipaibulvut*, Patchanida Nuttipongpairroj, Areerat Khumpoln, Kanjanakorn Piyarat, Sukanya Yot-aon, Jirayut Euanorasetr, Sukanya Phuengjayaem

Laboratory of Biotechnological Research for Energy and Bioactive Compound, Department of Microbiology, Faculty of Science, King Mongkut's University of Technology Thonburi, Bangkok 10140, Thailand

*e-mail: sukon.tan@kmutt.ac.th

Abstract:

Significant amounts of waste are generated by the coffee industry, among them, coffee silverskin (CS) and over-roasted coffee beans (OCB) are the most abundantly generated during the beans roasting. In this study, this material was proximately analyzed and subsequently submitted to an acid hydrolysis aiming to extract reducing sugar. Reactions were performed to verify the effects of the variables H_2SO_4 concentration, temperature, and reaction time, on the efficiency of hydrolysis. After acid treatment, the hydrolysate was adjusted to the appropriate pH using sodium hydroxide solution. The conditions that gave a significant highest amount of reducing sugar were $90^\circ C$, 5% H_2SO_4 , and 3 hours, which yielded 14.57 ± 0.23 g sugar/L for OCB and 8.37 ± 0.20 g sugar/L for CS. Treatment the material at $70^\circ C$ for either 1 hour or 3 hours gave no significantly different amount of reducing sugar obtained for both CS and OCB, especially at 1% to 3% H_2SO_4 . The hydrolysate from acid treatment of OCB and CS can be used as substrate for lactic acid and bioethanol production.

Introduction:

Coffee is one of the most popular consumed food commodities and is the second-largest traded commodity after petroleum [1]. Coffee beans are the seeds of coffee berry and popularly used for the preparation of beverage. The global coffee consumption was approximately 10.38 million tons in year 2022-2023. From this consumption, the roasting processes produced 0.20 million tonnes of coffee silverskin [2]. The coffee silverskin (CS) is an integument of coffee bean obtained as a by-product of the roasting process. It contains 17.8% cellulose, 13.1% hemicellulose and 20% protein [2]. Pretreatment of CS biomass with Choline chloride/glycerol can be efficient in terms of both sugars yield and low formation of fermentation inhibitors. A glucose yield of 0.24 g glucose/g biomass was reached after Deep eutectic solvents pretreatment at $150^\circ C$ with a biomass to solvent ratio of 1/32 [3]. Kim et al. [4] had treated coffee residue after roasting with acid-chlorite three times after organic solvent extraction (OSE-3). The sugar yield obtained was 0.568 g sugar/g OSE-3.

Coffee roasting is the process of transforming a raw, green coffee bean into a dark brown bean, changing their form and developing the character. As heat is applied, a series of complex chemical reactions occur within the bean. Sugars caramelize, creating sweetness and depth of flavor. Acids break down, contributing to a smoother taste. Oils rise to the surface, adding richness. However, pushing the roast level too far can lead to over-extraction, burning the coffee and producing undesirable bitterness. These over-roasted coffee beans (OCB) can be another waste of the roasting process. By transforming this biomass into valuable products, the coffee sector can significantly reduce its environmental impact and create a more sustainable, resilient global coffee circle.

Even though the treatment temperatures of most research were higher than $100^\circ C$ using low acid concentration, this work aimed to use the lower temperature to reduce the energy used and using high concentration of sulfuric acid to investigated the amount of sugar

obtained. Reducing sugar, as a biomass precursor, can be further transformed to fuel alcohol or lactic acid in a fermentation process by means of yeast or lactic acid bacteria, respectively.

Methodology:

Coffee samples.

The coffee silverskins (CS) and over-roasted coffee beans (OCB) were obtained from the mixtures of Arabica and Robusta coffee (unknown ratio) from a coffee shop in Bangkok, Thailand. The OCB was dried since it was taken from the coffee shop. The CS was dried at 42°C for 1 day. All were ground by means of a domestic mill (Braun), passed through a 16-mesh sieve (Tyler series) and kept at 4°C for further use.

Proximate composition.

The proximate composition of CS and OCB was analyzed by the method of AOAC [5]. The moisture content was determined by oven-drying at 105°C for 3 h. The crude protein content was measured by Kjeldahl method. The crude fat content was analyzed using the Soxhlet apparatus and petroleum ether as the extraction solvent. The ash content was analyzed by ignition at 550°C for 1 h in an electric furnace. Proximate compositions are expressed as a percentage of the sample weight. The content of carbohydrates was calculated by subtracting the moisture content, crude protein content, crude fat content, and ash content from 100.

Hydrolysate preparation.

The reaction conditions used for CS and OCB hydrolysis composed of 10 g of CS or OCB in a 100 ml of sulfuric acid solution with variables concentration (1%, 2%, 3%, 5% and 10% (v/v)). The reactions were performed in 500-ml Duran bottle, immersed in a water-bath of 70°C or 90°C for 1 h or 3 h. At the end of the reaction, the bottles were immediately cooled by running tap water. The hydrolysates were then separated from the solid residue by filtration through cheese cloth. To be used as fermentation medium, the pH of hydrolysates was adjusted to 5.5 by the addition of 2 M NaOH solution. The content of reducing sugar (RS) in the hydrolysate was determined by using dinitrosalicylic acid reagent [6]. All experiments and assays were performed at least twice. All results are expressed as the mean \pm standard deviation. The effect of the pretreatment factor on the amount of released reducing sugar was statistically analyzed by ANOVA using the Prism 10.5 program.

Results and Discussion:

Proximate composition of CS and OCB

Table 1 reports the proximate composition of CS and OCB compared to another report. The moisture content of CS and OCB in this work was about 9%. As mentioned by Laukalčja et al. [7] and Kim et al. [8], the moisture content of dark roasted and very dark roasted coffee beans (VDCB) was $2.0 \pm 0.0\%$ and $0.89 \pm 0.04\%$, respectively. The moisture content of CS that has been reported was $2.78 \pm 0.30\%$ [9] and $4.76 \pm 0.10\%$ [10]. The higher moisture content of CS and OCB in our report may be due to the long storage at room temperature. However, the protein content of CS in our results are close to data from Costa et al. [10] and Martuscelli et al. [9] which was 19% and $18.15 \pm 2.17\%$, respectively. The proximate composition (g/100 g) of very dark roasted coffee beans (VDCB) reported by Kim et al. [8] was shown in Table 1. The protein content of OCB in our report was higher than that reported by Kim et al. [8], while the carbohydrate content was lower. The content of ash and crude fat was nearly the same. This may be due to the use of different types of coffee beans in each study. The concentration of total saturated fatty acid, total monounsaturated fatty acid, and total polyunsaturated fatty acid in dark-roasted coffee was 5.9%, 1.3% and 6.1% (w/w), respectively [7].

Table 1.
Proximate composition of coffee silver-skins and over-roasted coffee beans

Properties (g/100 g)	CS	CS [9]	OCB	VDCB [8]
Moisture	9.91 ± 0.02	2.78 ± 0.30	8.58 ± 0.30	0.89 ± 0.04
Ash	5.58 ± 0.04	6.79 ± 0.78	4.25 ± 0.02	4.61 ± 0.02
Crude fat	1.68 ± 0.34	2.31 ± 0.50	11.71 ± 0.10	12.99 ± 1.07
Crude protein	18.83 ± 0.03	18.15 ± 2.17	17.88 ± 0.26	12.91 ± 1.23
Carbohydrate	64.00 ± 0.10	69.97*	57.58 ± 0.18	68.59 ± 0.83

*This value is obtained by subtracting the moisture content, crude protein content, crude fat content, and ash content from 100.

Reducing sugar in the hydrolysates

The contents of RS in the hydrolysates of CS and OCB treated with varied concentration of sulfuric acid, temperature and reaction time are presented in Figure 1. The conditions that gave a significant highest amount of reducing sugar were 90°C, 5% H₂SO₄, and 3 hours, which yielded 14.57±0.23 g sugar/L for OCB and 8.37±0.20 g sugar/L for CS. Treatment the material at 70°C for either 1 hour or 3 hours gave no significantly different amount of reducing sugar obtained for both CS and OCB, especially at 1% to 3% H₂SO₄. The hydrolysate of CS and OCB that treated with 10% sulfuric acid had lower concentrations of RS than that treated with 5% sulfuric acid; even though the higher the acid concentration, the more the yield of RS should be obtained. To improve the RS yield of CS, the autoclave conditions have been carried out. It appeared that the maximum RS yield of 12.60 ± 0.11 g/L was obtained at 5% (v/v) H₂SO₄ concentration hydrolyzed in an autoclave at 121°C for 15 min.

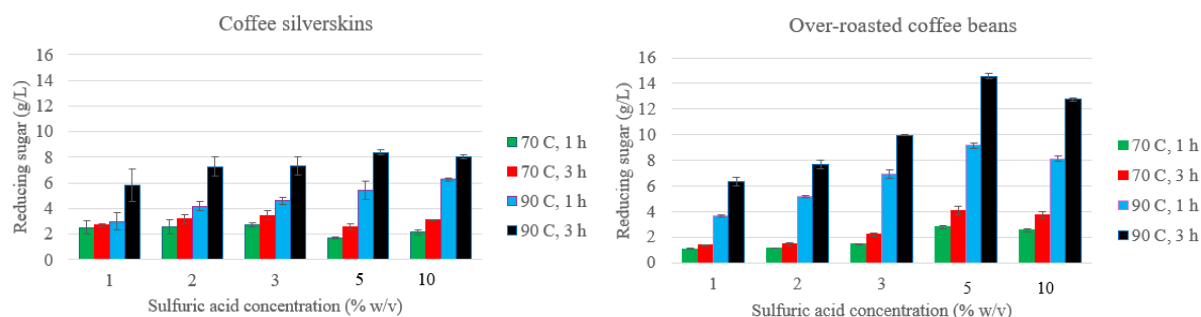


Figure 1.

Reducing sugar in the hydrolysate of coffee silver skins (left) and over-roasted coffee beans (right) after acid treatment at various conditions

Ghazali et al. [11] found that the highest sugar yield was obtained from durian seeds pre-treated using 0.6% H₂SO₄ and 5% substrate concentration, heated in an autoclave at 130°C for a retention time of 30 minutes. The obtained yield was 23.5 g/L. Further increase in acid concentration gave no meaningful increase in sugar yield. Pachuau et al. [12] had treated *Mirabilis jalapa* seed kernels with dilute H₂SO₄ concentrations (1 – 5%, v/v) at 121°C and reaction time of 15 to 45 mins. They found that with biomass loading of 10%, the maximum reducing sugar yield (1.90 ± 0.04 mg/g) was obtained at 2% (v/v) H₂SO₄ concentration hydrolyzed for 15 mins. Further increase in acid concentration (> 2.0%, v/v) and pretreatment time resulted in decrease in sugar yield. This decrease in sugar yield could be due to the increase in production of interferences with increasing acid concentration and reaction time. Prolongation of reaction duration and high acid concentration frequently



resulted in the conversion of monomeric sugars to inhibitory compounds such as furfural and 5-hydroxyl methyl furfural (5-HMF) from pentose and hexose sugars respectively [12]. The treatment of defatted soybean meal at 135 °C, 2.0% H₂SO₄, and 45 min produced the highest content of fermentable sugars, 32.2 g per 100 g of initial SBM, such treatment generated relatively low 5-HMF and furfural levels (0.0018 g/L and 0.32 g/L, respectively), and 0.87 g/L of acetic acid [13]. NAVIA P. et al. [14] had subjected the juice from mucilage and coffee pulp to an acid hydrolysis treatment, which consisted in heating it with 37% purity hydrochloric acid at 95°C for 900 seconds, at a rate of 6.0 x 10⁻⁶ m³ of acid per 1.0 x 10⁻⁴ m³ of juice. The obtained reducing sugar was 64.4 kg/m³. Constantino et al. [15] had carried out experiments to extract soluble sugar from green coffee beans using orbital shaker and microwave. The varying factors studied were the sample amount (300, 400, and 500 mg), time (30, 60, and 90 min), and temperature (30, 45, and 60 °C). They found that the optimum conditions were using 500 mg ground green coffee, 90 min, and 60 °C. The concentration of sugar obtained (per liter) was 2.16 g sucrose, 0.1 g glucose and 0.2 g fructose.

Conclusion:

Based on the obtained results, it was observed that the optimum conditions for acid pretreatment of the materials were: 5% (v/v) H₂SO₄ and hydrolysis time of 3 h at 90°C. Autoclave condition can give better yield of RS than 90°C and 3 h reaction time. Although, the pretreatment improved the production of reducing sugar, it may produce inhibitors, including acetic acid, furfural and 5-HMF that could obstruct the fermentation process. Further studies should be done on pretreatment processes to monitor and reduce the inhibitor effect on fermentation. The results of this study have shown that with the application of proper pretreatment, the potential for production of reducing sugar from coffee silver-skins and over-roasted coffee beans is possible. This gives the idea to utilize the waste biomass to produce the value-added product.

Acknowledgements:

The authors would like to thank the Department of Microbiology, KMUTT for providing chemicals and laboratory equipment necessary to carry out this work.

References:

1. Arya SS, Venkatram R, More PR, Vijayan P. *J Food Sci Technol.* 2022;59(2):429-444.
2. Coffee Development Report 2022-2023, International Coffee Organization.
3. Procentese A, Rehmann L. *Bioresour. Technol. Rep.* 2018; 4:174-180.
4. Kim HM, Choi YS, Lee DS, Kim YH, Bae HJ. *Bioresour. Technol.* 2017; 236: 194-201.
5. Association of Official Analytical Chemists (AOAC). *Official Methods of Analysis of AOAC International.* 16th ed. Association of Official Analytical Chemists, Arlington, VA, USA (1995)
6. Miller GL. *J. Anal. Chem.* 1959; 31:426-428.
7. Laukalča I, Krūma Z, Cinkmanis I. *Proc. Latv. Acad. Sci.* 2022; 76(1):145-151.
8. Kim I, Jung S, Kim E, Lee J-W, Kim C-Y, Ha J-H, Jeong Y. *Food Sci Biotechnol.* 2021; 30: 235–244.
9. Martuscelli M, Esposito L, Di Mattia CD, Ricci A, Mastrocola D. *Foods.* 2021; 10:1367.
10. Costa ASG, Alves RC, Vinha AF, Costa CSG, Costa MA, Nunes AA, Almeida A, Santos-Silva Oliveira MBPP. *Food Chem.* 2018, 30:28–35.



11. Ghazali KA, Salleh SF, Riayatsyah TMI, Aditiya HB, Mahlia TMI. IOP Conf. Series: Earth and Environmental Science 32 (2016) 012058, doi:10.1088/1755-1315/32/1/012058
12. Pachuau L, Paul D and Bez G. J. Himalayan Ecol. Sustain. Dev. 2023;18:116-125.
13. Luján-Rhenals DE and Morawicki RO. BioRes. 2016; 11(4): 8155-8165.
14. NAVIA P Diana P, VELASCO M, Reinaldo de J, HOYOS C, José L. Vitae, 2011, 18(3): 287-294.
15. Constantino LV, Zeffa DM, Koltun A, Urbano MR, Sanzovo AWS and Nixdorf SL. Acta Chromatographica. 32(4): 242-246.



CHARACTERIZATION OF UV-MUTATED *Kluyveromyces marxianus*: ISOBUTANOL TOLERANCE AND XYLOSE UTILIZATION

Krittaporn Thungmuthaswade¹, Navaphorn Pinrenu², Thanyalak Vorawongsakul², Jirasin Koonthongkaew^{1,*}

¹Department of Microbiology, Faculty of Science, Chulalongkorn University, Phayathai Rd., Pathumwan, Bangkok 10330, Thailand

²Department of Biotechnology, Faculty of Science, Chulalongkorn University, Phayathai Rd., Pathumwan, Bangkok 10330, Thailand

*e-mail: Jirasin.K@chula.ac.th

Abstract

Isobutanol has been of interest as a second-generation biofuel because it possesses higher energy density, lower vapor pressure, and potential as a platform chemical to produce materials with additional value, including isobutylene and biojet fuels, which are better than traditional ethanol. However, one of the main obstacles to reaching high fermentation titer is its acute toxicity to microorganisms, with concentrations above 8–10 g/L often reported as inhibitory to yeasts. To date, reports on the isobutanol tolerance of *Kluyveromyces marxianus* remain scarce. In this study, the wild-type strain *K. marxianus* G3-10(2) was mutated with ultraviolet (UV) irradiation and screened in culture media containing a high concentration of isobutanol. The obtained mutant 2(3) was evaluated for isobutanol tolerance in YPD medium with the addition of 10–14 g/L isobutanol. The mutant exhibited consistently stronger growth than the wild type, showing 1.2-fold, 1.1-fold, and 1.3-fold higher OD₆₀₀ values at 72 h under 10, 12, and 14 g/L isobutanol stresses, respectively. Microscopic and colony morphology observations showed that both the mutant and wild-type strains exhibited oval budding cells and creamy, circular colonies. A spot assay at pH 4 and 7, with cultures grown at 30°C and 37°C, also confirmed the greater tolerance of the mutant, particularly at neutral pH at 30°C. In addition, a xylose utilization test revealed that both strains were able to metabolize xylose as the sole carbon source, with the mutant strain showing better cell growth compared to the wild-type strain. These observations show that UV mutagenesis can effectively improve *K. marxianus* mutants having high isobutanol tolerance and enhanced pentose utilization. Although the strains have not been tested for isobutanol production, the mutant represents a promising host platform for future metabolic engineering toward efficient isobutanol biosynthesis.

Keywords: *Kluyveromyces marxianus*, isobutanol tolerance, ethanol tolerance, pentose utilization, UV mutagenesis

Introduction

As global energy demands continue to rise and fossil fuel reserves decline, the urgency to develop renewable energy solutions is an important situation to focus on. Biofuels have long been recognized as sustainable alternatives that can reduce dependence on fossil carbon and mitigate the environmental consequences of climate change. Isobutanol has become a very promising option among the many different types of biofuels being studied. Compared with ethanol, isobutanol offers several superior properties, including a higher energy density, lower vapor pressure, and a higher-octane number, all of which make it more compatible with existing gasoline infrastructure.¹ Significantly, isobutanol functions as a multifaceted platform chemical its dehydration to isobutylene yields a crucial intermediary for biojet fuels and several industrial products.² These characteristics have placed isobutanol at the forefront of next-generation biofuels. Despite this potential, large-scale biological production of isobutanol remains a challenge. The most widely studied yeast, *Saccharomyces cerevisiae*,

produces isobutanol only in trace amounts through valine catabolism and the Ehrlich pathway. Even with intensive metabolic engineering, product yields remain far below theoretical maximums due to redox imbalance, flux competition with ethanol, and sensitivity to alcohol toxicity.³⁻⁴ This situation underscores the need for alternative microbial platforms that combine robust growth with tolerance to industrial stresses.

Kluyveromyces marxianus has drawn increasing attention. As a non-conventional yeast, *K. marxianus* grows rapidly, tolerates high temperatures, and can utilize a wide variety of carbon sources, including pentoses and disaccharides that are abundant in lignocellulosic hydrolysates.⁵ These traits make it particularly attractive for second-generation biofuel processes, where cost-effective use of complex feedstocks and resistance to harsh process conditions are critical. Moreover, its weak glucose repression provides greater metabolic flexibility than *S. cerevisiae*.⁶⁻⁷ Taken together, *K. marxianus* represents a strong candidate for expanding the biofuel portfolio beyond ethanol to include higher alcohols such as isobutanol. However, *K. marxianus* has been extensively studied for its ethanol tolerance and thermotolerance, reports specifically addressing its tolerance to isobutanol are scarce. There, no previous studies have systematically characterized isobutanol tolerance in *K. marxianus*. In this study, which focuses on the development and characterization of UV-mutated *K. marxianus* strains with enhanced tolerance to isobutanol, one of the main bottlenecks remains its sensitivity to isobutanol toxicity. High concentrations of isobutanol can compromise membrane integrity, destabilize proteins, and impose oxidative stress, ultimately lowering cell viability and product yield.⁸⁻⁹ In comparison, concentration is often reported as toxic above 8–10 g/L in yeasts.⁹ Overcoming this limitation is therefore a crucial step in making *K. marxianus* an industrially viable producer of advanced biofuels. Several strategies have been proposed to improve microbial tolerance to alcohol, ranging from metabolic engineering and adaptive evolution to classical mutagenesis. While metabolic rewiring has been extensively explored in *S. cerevisiae*, the development of diverse mutant libraries through UV mutagenesis remains an accessible, cost-effective, and powerful approach for *K. marxianus*.¹⁰⁻¹¹ UV mutagenesis induces random DNA damage, generating a broad spectrum of genetic variation that can be rapidly screened for traits such as solvent tolerance or enhanced alcohol production.¹⁰ When combined with selective screening, this strategy offers a pragmatic route to identify promising strains without the requirement for complex genetic tools.

Methodology

Culture media and starter culture preparation

Prepare YPD agar (yeast extract 10 g/L, peptone 20 g/L, glucose 20 g/L, agar 20 g/L) or YNB (yeast nitrogen base 6.7 g/L, peptone 20 g/L, glucose 20 g/L, agar 20 g/L) and YPD broth (yeast extract 10 g/L, peptone 20 g/L, glucose 20 g/L) were prepared to grow *K. marxianus*. The wild-type yeast strain in this research, *K. marxianus* (isolated G3-10(2)), was originally isolated from sugarcane juice at Thai Sugar Industry Co., Ltd., Kanchanaburi, Thailand¹² and mutant strain 2(3) was preserved in 80% glycerol tubes and stored at -80°C.

Screening mutants by using conventional methods

Single colonies of yeast strains grown on YPD agar at 30°C for 48 h were pre-cultured in 15 ml tubes containing 10 ml YPD medium under shaking condition at 200 rpm and incubated at 30°C for 24 h. The cells were collected by centrifugation at 5,000 rpm at room temperature for 3 min. Subsequently, the cell suspension was washed and diluted with sterile distilled water 10⁴-10⁵ times. 1 ml of the suspension was spread on a plastic cover plate. The cells were exposed to ultraviolet (UV) radiation at a wavelength of 254 nm, approximately 25 cm from the cover plate, for 4 min. The UV-irradiated yeast was then spread on a YPD agar plate



and incubated at 30°C until colonies appeared. To screen for isobutanol tolerant mutants, colonies obtained after UV treatment were inoculated into YPD broth supplemented with 10 g/L isobutanol and incubated at 30°C with shaking at 200 rpm. Cultures that showed visible growth were subsequently spread onto YPD agar plates. From these plates, a single colony that exhibited robust growth was isolated and designated as mutant strain 2(3).

Cell and colony morphology determination

The colony morphology of *K. marxianus* was examined on YPD agar plates incubated at 30°C for 48 h. Single colonies were directly picked from the agar surface and suspended in sterile distilled water. Cell morphology was observed under a light microscope at 100× magnification.

Isobutanol tolerance

To evaluate isobutanol tolerance, a single colony was inoculated into a 15 mL test tube containing 3 mL of YPD medium and incubated at 30°C with shaking at 200 rpm for 24 hours. Subsequently, 500 µL of pre-culture was inoculated into a 50 mL test tube containing 10 mL of YPD medium supplemented with 10, 12, and 14 g/L of isobutanol. The optical density of the samples was measured at 600 nm every 24 h for 3 days to monitor cell growth.

Spot assay under different pH and temperature conditions

To evaluate the growth performance of yeast strains under acidic and neutral environments, a single colony of the yeast strain was inoculated into a 15 mL test tube containing 3 mL of YPD medium and incubated at 30°C with shaking at 200 rpm for 24 h and then adjusted to an OD₆₀₀ of 1.0. The cell suspension was collected by centrifugation at 12,000 rpm at 4°C for 1 min, then diluted 10¹-10⁵ times, and 2 µl of the suspension was spotted on YPD plates at pH 4 and 7. The plates were incubated at 30°C and 37°C for 24-48 h, and growth was assessed by comparing colony formation across conditions.

Xylose utilization test

To evaluate the ability of *K. marxianus* strains to utilize xylose as an alternative carbon source to glucose, a single colony of the yeast strain was inoculated into a 15 mL test tube containing 3 mL of YNB medium and incubated for 24 h. The pre-culture was inoculated with an initial inoculum adjusted to an optical density at 600 nm (OD₆₀₀) of 0.1 per mL into a 50 mL test tube containing 10 mL of YNB medium supplemented with 20 g/L xylose as the sole carbon source (YNX) and incubated at 30°C with shaking at 200 rpm. Cell growth was monitored by measuring OD₆₀₀ at 24 and 48 h to investigate the growth of the yeast.

Results and Discussion

1. Isobutanol tolerance

After UV mutagenesis was performed, a mutant colony designated as 2(3) was obtained. Therefore, both the wild-type strain G3-10(2) and the mutant 2(3) were evaluated for their growth in YPD medium supplemented with 10–14 g/L isobutanol to determine their tolerance to isobutanol toxicity.

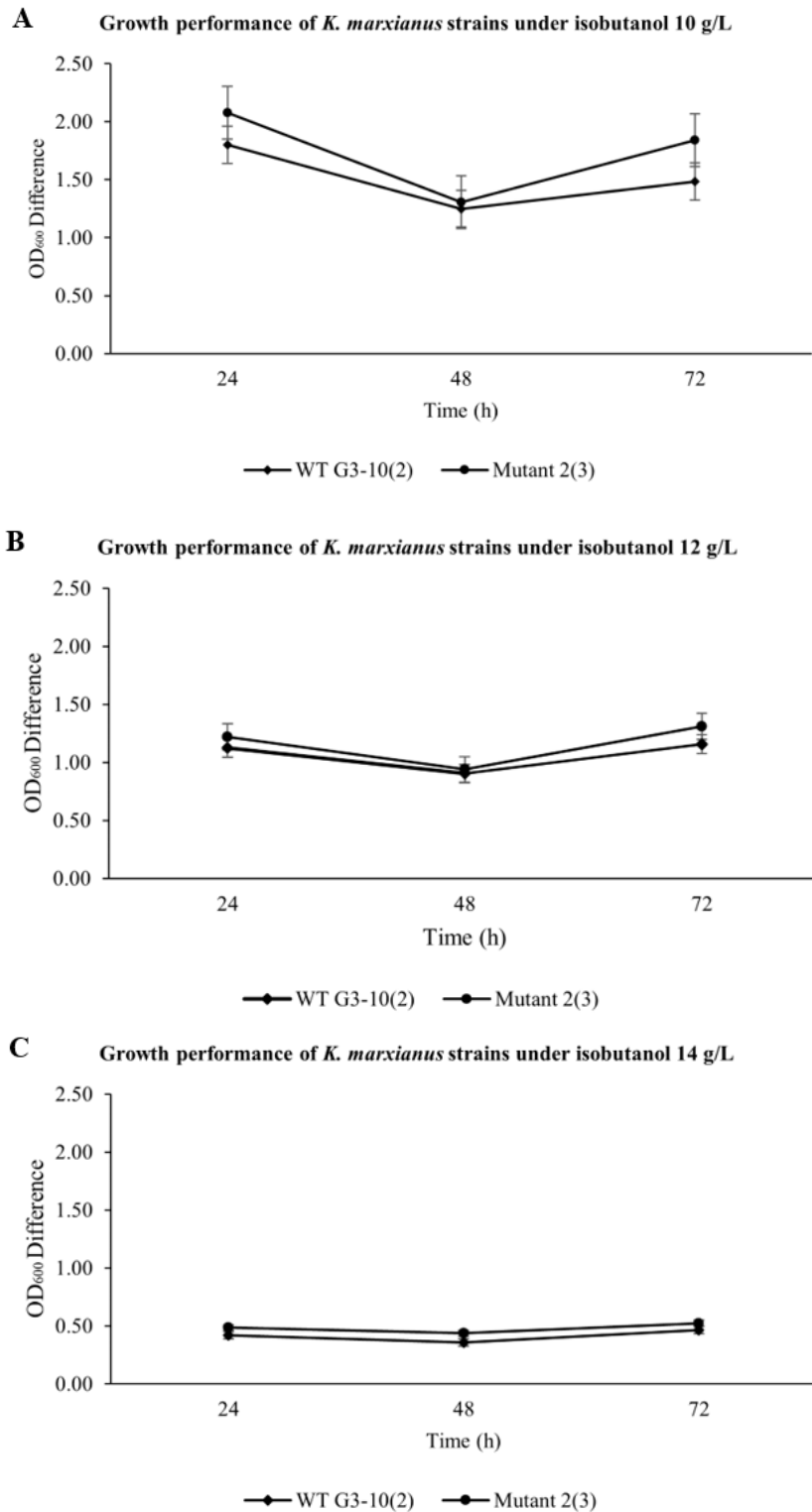


Figure 1.

Growth performance of *K. marxianus* strains under different isobutanol concentrations as indicated by OD₆₀₀ differences compared with initial values. (A) isobutanol 10 g/L, (B) isobutanol 12 g/L, and (C) isobutanol 14 g/L.

Figure 1 shows the growth performance of wild-type strain G3-10(2) and UV-derived mutant 2(3) of *K. marxianus*, which were tested for their resistance against isobutanol stress in YPD medium containing 10–14 g/L of isobutanol. At 10 g/L (Figure 3A), both strains were able to grow, and the mutant consistently exhibited 1.2-fold higher OD₆₀₀ values at 72 h than the wild-type G3-10(2), showing higher tolerance and better adaptation to isobutanol stress. At 12 g/L of isobutanol (Figure 3B), the cell growth was generally reduced for two strains, but the mutant still maintained 1.1-fold higher OD₆₀₀ than the wild-type. At the highest concentration of 14 g/L isobutanol (Figure 3C), the cell growth for both strains was repressed, but the mutant still retained a measurable increase in OD₆₀₀ that was 1.3-fold higher than the wild-type at 72 h, which suggested a stronger inhibitory effect of isobutanol on the wild-type strain. These results indicate that UV mutagenesis was able to develop a mutant strain of *K. marxianus* with improved performance in isobutanol tolerance up to 14 g/L.

2. Cell morphology and microscopy

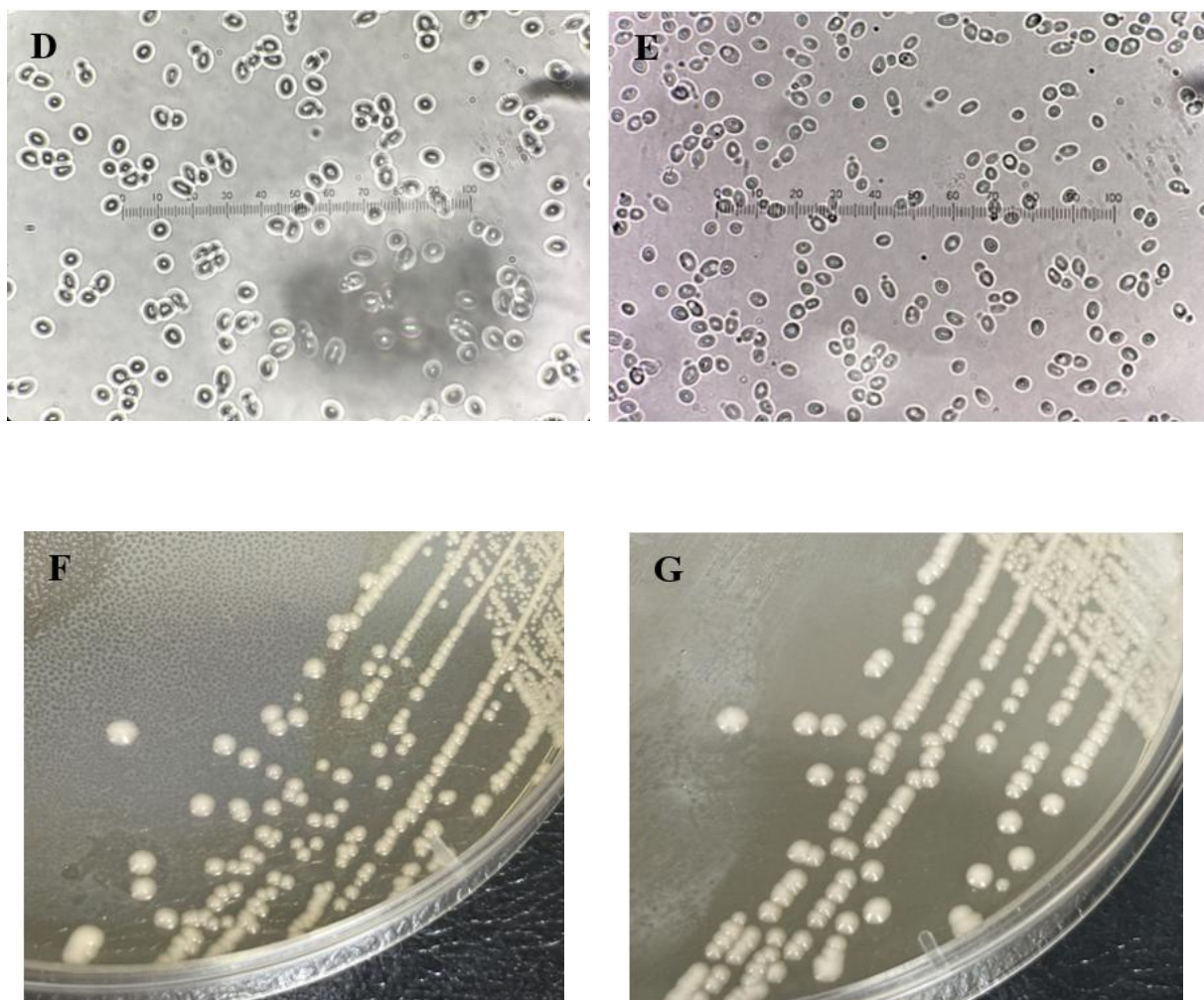


Figure 2.

Colony and cell morphology of *K. marxianus*. (D) Microscopic image of mutant strain 2(3) at 100× magnification; (E) Microscopic image of wild-type strain G3-10(2) at 100× magnification; (F) Mutant strain 2(3) colonies; (G) Wild-type strain G3-10(2) colonies.

Microscopic and cell morphology observations were carried out to compare the mutant with the wild-type strain G3-10(2). Both the mutant strain (Figure 2A) and the wild-type strain (Figure 2B) consisted of unicellular, oval to round cells with distinct budding sites. On YPD agar plates, the mutant (Figure 2C) and wild-type colonies (Figure 2D) showed a creamy white, circular appearance. Both colonies appeared large, dense, and regularly shaped. These phenotypic traits are consistent with the reported morphology of *K. marxianus*³⁻⁵. The observed similarities in cell size, shape, budding pattern, and colony characteristics indicate that the UV-derived mutant and the wild type share common morphological features typical of *K. marxianus*.

3. Effect of pH and temperature on growth

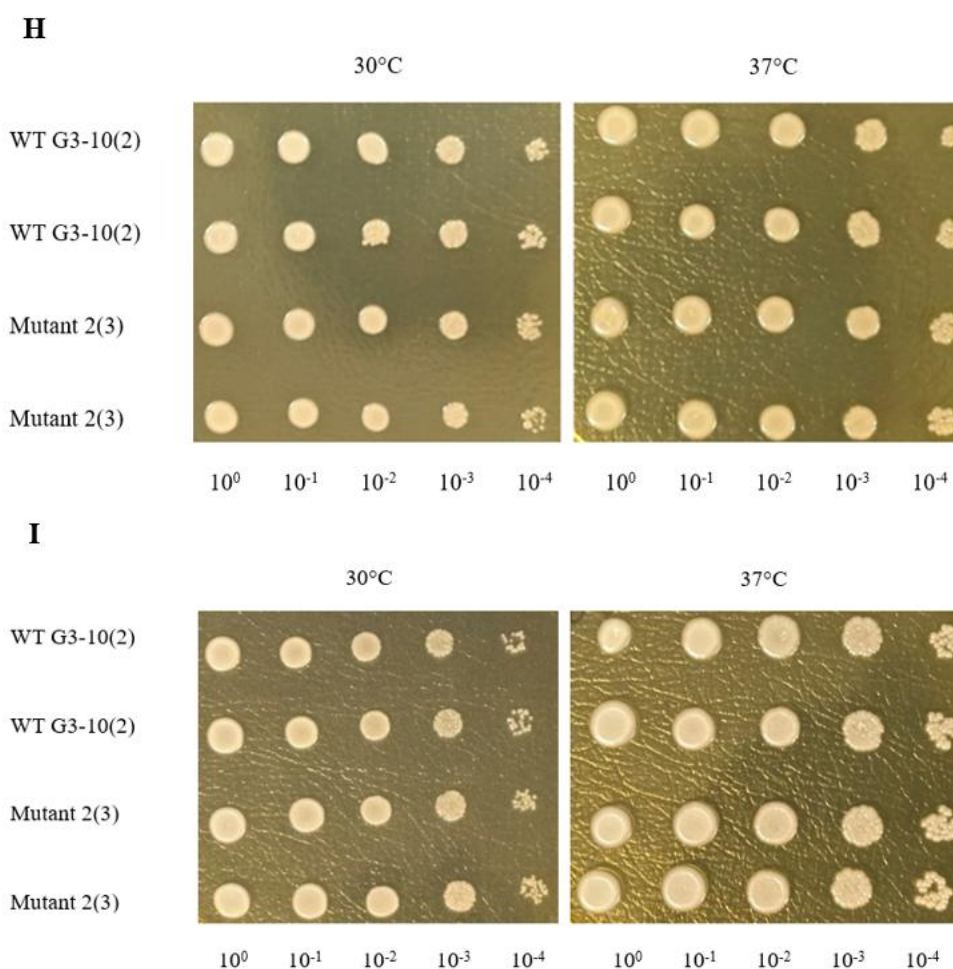


Figure 3.

Spot assay of *K. marxianus* strains under different pH and temperature conditions: (H) pH 4 and (I) pH 7, each tested at 30 °C and 37 °C. Serial dilutions (10⁰–10⁻⁴) of wild-type strain G3-10(2) and mutant strain 2(3) were spotted onto YPD agar plates and incubated for 48 h.

K. marxianus was known to have a thermotolerant phenotype, and in biofuel production the initial pH is normally around 4.5–5.0 to optimize yeast performance and fermentation efficiency.^{11,19} To investigate the effects of pH and temperature on yeast growth, spot assays were performed for both wild-type G3-10(2) and mutant 2(3) strains under different environmental conditions (Figure 3). At acidic pH 4.0 (Figure 3H) and neutral pH 7.0 (Figure

3D), both strains showed visible growth across serial dilutions up to 10^{-4} . Colony size appeared comparable between the wild-type and mutant, indicating similar tolerance under these pH conditions. Temperature also influenced growth potential. At 37°C , both strains can maintain growth comparable to that at 30°C , demonstrating the intrinsic thermotolerant phenotype of *K. marxianus*. This observation is consistent with previous reports that *K. marxianus* can grow well within the temperature range of $30\text{--}40^{\circ}\text{C}$.^{18,19} Both strains can sustain growth at higher dilutions under acidic and elevated temperature conditions, suggesting a robust tolerance to environmental stresses relevant for industrial bioethanol fermentation.

4. Xylose utilization test

A xylose utilization test was conducted to assess the capability of *K. marxianus* strains, wild-type strain G3-10(2) and mutant 2(3), to use xylose as an alternative carbon source to glucose. Notably, xylose is abundant in hemicellulose structure of lignocellulosic biomass.

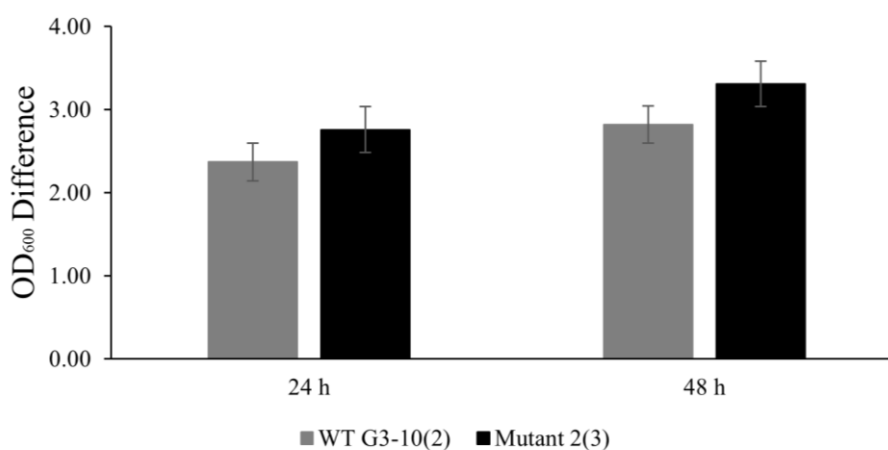


Figure 4.

Growth performance of *K. marxianus* strains under xylose as the sole carbon source as indicated by OD₆₀₀ differences compared with initial values.

Figure 4 shows the xylose utilization ability of the wild-type strain G3-10(2) and the mutant strain 2(3). Both strains were able to grow on xylose as the sole carbon source. But wild-type G3-10(2) was showed a moderate increase in OD₆₀₀, reaching about 2.4 at 24 h and 2.8 at 48 h, while mutant 2(3), exhibited higher growth, with OD₆₀₀ values of 2.7 at 24 h and 3.3 at 48 h. When compared to the wild-type, the mutant displayed approximately a 1.1-fold higher OD₆₀₀ at 24 h and a 1.2-fold higher OD₆₀₀ at 48 h. These results showed that mutant strain utilized xylose more efficiently than wild-type strain, which suggested that random mutagenesis by UV-irradiation able to be conferred improved metabolic adaptation toward pentose sugars which needs further investigation. This enhanced capacity to metabolize xylose, a major component of lignocellulosic hydrolysates, indicates that the mutant strain could serve as a valuable platform for future research aimed at producing second-generation biofuel.

Conclusion

In this study UV mutagenesis was used to an effective approach to improve isobutanol tolerance in *K. marxianus*. The mutant strain 2(3) exhibited higher growth capacity than the wild-type G3-10(2) under isobutanol stress, particularly at $10\text{--}12\text{ g/L}$ and showed robustness across different pH and temperature conditions. The potential of strain improvement



strategies to tolerate the toxicity of isobutanol can expand the applicability of *K. marxianus* in advanced biofuel production. Microscopy and colony morphology observations confirmed that the mutant retained the typical characteristics of *K. marxianus*. Importantly, both strains were able to utilize xylose as a sole source of carbon, but mutant strain 2(3) exhibited much higher utilization, showing higher ability to metabolize xylose sugars that are relevant to lignocellulosic hydrolysates. In future work, we aim to integrate targeted metabolic engineering with mutagenesis to establish *K. marxianus* as a robust host platform that not only tolerates higher levels of isobutanol but can also be engineered for efficient production of isobutanol. Meanwhile, the mechanism of isobutanol toxicity tolerance and xylose utilization of this *K. marxianus* mutant will be investigated.

References

1. Janković T, Straathof AJJ, Kiss AA. *Energy Convers Manag* X. 2024;21:100520.
2. Songdech P, Runguphan W, Yamada R. *Renew Energy*. 2024;223:119598.
3. Avalos JL, Fink GR, Stephanopoulos G. *Nat Biotechnol*. 2013;31:335–341.
4. Wess J, Brinek M, Boles E. *Biotechnol Biofuels*. 2019;12:173.
5. Sene S, Nonato RV, Rodrigues RCLB, Gomes FCO, Oliveira J. *Bioresour Technol Rep*. 2023;21:101310.
6. Lane MM, Burke N, Morrissey JP. *Antonie Van Leeuwenhoek*. 2011;100:507–517.
7. Lane MM, Morrissey JP. *Fungal Biol Rev*. 2010;24:17–26.
8. Ding J, Huang X, Zhang L, Zhao N, Yang D, Zhang K. *Appl Microbiol Biotechnol*. 2009;85:253–263.
9. Sánchez Nogué V, Karhumaa K. *Biotechnol Lett*. 2015;37:761–772.
10. Leonel LV, Silva GP, Reis VCB, Lopes ML, Basso TO. *FEMS Yeast Res*. 2021;21:foab054.
11. Lawrence CW, Christensen R. *Genetics*. 1976;82:207–232.
12. Tolieng V, Kunthiphun S, Savarajara A, Tanasupawat S. *J Appl Pharm Sci*. 2018;8(02):136–142.
13. Park JB, Kim JS, Jang SW, Hong E, Ha SJ. *J Korean Soc Biotechnol Bioeng*. 2015;30:125–133.
14. Papapetridis I, van Dijk M, van Maris AJA, Pronk JT. *Biotechnol Biofuels*. 2017;10:107.
15. Pal U, Vij S. *Biocatal Agric Biotechnol*. 2022;45:102533.
16. Mavrommati M, Papanikolaou S, Aggelis G. *Process Biochem*. 2023;124:280–289.
17. Pan Y, Xia S, Dong C, Pan H, Cai J, Huang L, Xu Z, Lian J. *ACS Synth Biol*. 2021;10:2440–2446.
18. Fonseca GG, Heinzle E, Wittmann C, Gombert AK. *Appl Microbiol Biotechnol*. 2008;79:339–354.
19. Kurtzman CP, Fell JW, Boekhout T. *The Yeasts: A Taxonomic Study*. 2011;5th ed:Elsevier.
20. Pal U, Vij S. *Biocatal Agric Biotechnol*. 2022;45:102533.
21. Park S, Nicaud JM, Ledesma-Amaro R. *Appl Microbiol Biotechnol*. 2018;102:9567–9578.



FACTORS INFLUENCING ON DEVELOPMENT OF TREHALOSE PRODUCTION BY *Saccharomyces cerevisiae*

Warissara Chotiwanee,¹ Sitanan Thitiprasert,^{2,3} Nuttha Thongchul^{2,3*}

¹Program in Biotechnology at Faculty of Science, Chulalongkorn University, Thailand

²Center of Excellence in Bioconversion and Bioseparation for Platform Chemical Production, Institute of Biotechnology and Genetic Engineering, Chulalongkorn University, Bangkok, Thailand

³Institute of Biotechnology and Genetic Engineering, Chulalongkorn University, Bangkok, Thailand

*e-mail: Nuttha.T@chula.ac.th

Abstract:

Trehalose is a non-reducing disaccharide comprising two glucose units that are linked by an α,α -1,1-glycosidic linkage, exhibits remarkable versatility across various industries applications. The most unique characteristic of trehalose is that its function as an osmolyte compound that protects against numerous environmental stresses in a wide range of microorganism and plants. Conventional industrial trehalose production employs a sequential enzymatic process utilizing maltooligosyltrehalose synthase (EC 5.4.99.15) followed by maltooligosyltrehalose trehalohydrolase (EC 3.2.1.141), with starch serving as the primary substrate. Nevertheless, recent advances in sustainable biotechnology have stimulated the development of microbial trehalose biosynthesis pathways, thereby diversifying production methodologies. This study aims to design the fermentation process of trehalose production using *Saccharomyces cerevisiae*, leveraging its inherent capacity for trehalose synthesis under stress conditions. Based on the concept that trehalose could protect the yeast cells against environmental stresses, osmotic stress and high temperature control were examined. Additionally, the influence of yeast cell age on trehalose synthesis was determined to identify the optimal growth phase of yeast cells. A two-phase fermentation approach was applied for trehalose production by *S. cerevisiae* in shaken flask scale. *S. cerevisiae* was initially grown in cell production medium, containing 100 g/L glucose to produce high cell density and ethanol. The late-log phase cells were transferred into trehalose induction medium containing 100 g/L glucose and various ethanol concentrations, which were cultivated under at 45 °C. The experimental results demonstrated that supplementation with 25 g/L ethanol during the production phase significantly enhanced both extracellular and intracellular trehalose accumulation compared to alternative conditions. The extracellular trehalose production was 0.330 ± 0.010 g/L with a yield of 0.003 ± 0.000 g/g and a productivity of 0.055 ± 0.002 g/L·h, while the intracellular trehalose production was 0.180 ± 0.002 g/L, which corresponding to 0.429 ± 0.003 g trehalose/g cell. These findings indicate that stress conditions, particularly osmotic and thermal stress, can effectively improve trehalose production in *S. cerevisiae*.

Introduction:

Trehalose (C₁₂H₂₂O₁₁) is a non-reducing disaccharide formed by a glycosidic bond. Naturally, trehalose is synthesized by microorganisms, plants, and animals [1,2]. It functions as a protectant molecule, stabilizing proteins and cell membranes under various environmental stresses such as nutrient deprivation, oxidative stress, freezing, high temperature, and osmotic pressure [3]. Trehalose is known for its stability, safety, and lack of color, odor, and reducing properties. It is approved as a safe food additive by both the European Union and the U.S. Food and Drug Administration (FDA). Due to its properties, trehalose is widely used in food, pharmaceutical, and cosmetic industries [4,5]. Trehalose can be synthesized through chemical or biological means. Chemical synthesis involves reactions between specific glucose

derivatives but is limited by low yield and high cost [6]. In contrast, industrial-scale biological production utilizes enzymatic conversion of starch using maltooligosyltrehalose synthase (EC 5.4.99.15) and maltooligosyltrehalose trehalohydrolase (EC 3.2.1.141) [7]. Microorganisms, especially *Saccharomyces* spp., are capable of naturally synthesizing and accumulating trehalose under stress conditions. These yeasts are recognized as GRAS (Generally Recognized as Safe) by the U.S. FDA and are widely used in fermentation industries, including beer, wine, ethanol, and baked goods [8]. Notably, *Saccharomyces* spp. can tolerate ethanol concentrations up to 18% (w/v) [9] and adapt well to environmental stress. Trehalose biosynthesis in *Saccharomyces* sp. involves the conversion of glucose-1-phosphate to UDP-glucose by UDP-glucose-dependent trehalose synthase (TPS), followed by trehalose-6-phosphate (T6P) production via TPS1 and finally conversion into trehalose by TPS2 [10]. Increased attention has been given to trehalose synthesis in yeast due to its link with improved stress resistance and ethanol production. This study aims to develop a trehalose production process in *S. cerevisiae* by examining key factors that enhance cell growth and trehalose biosynthesis under flask-scale fermentation.

Methodology:

1. Yeast cultivation and inoculum preparation

S. cerevisiae preserved in 25% (v/v) glycerol at -80°C was activated in seed culture 1 at 30°C and 200 rpm for 18 hours. The seed culture 1 was Yeast-Peptone-Dextrose (YPD) media, containing 20 g/L glucose, 10 g/L yeast extract, and 20 g/L peptone. Subsequently, seed culture 1 was transferred into fresh YPD medium to prepare seed culture 2, which served as the inoculum for cell production with the inoculum size of 3% (v/v). Seed culture 2 was then incubated at 30°C and 200 rpm for 6 hours. After incubation, the seed culture 2 was collected for further use in the fermentation step and for monitoring yeast growth.

2. Two-phase fermentation of trehalose production in shake flask scale

Seed culture 2 was transferred into cell production media containing 100 g/L glucose, 10 g/L yeast extract, 0.3 g/L KH_2PO_4 , and 0.25 g/L $\text{MgSO}_4 \cdot 7\text{H}_2\text{O}$ with the inoculum size at 10% (v/v) to promote cell growth and ethanol production. The culture was incubated at 30°C and 200 rpm for a duration sufficient to allow the yeast cells to reach the exponential (late-log) phase. Fermentation broth was collected every 4 h to determine yeast growth, glucose consumption, ethanol, and byproducts using spectrophotometry and high-performance liquid chromatography (HPLC) techniques.

After that yeast cells were harvested using centrifugation technique under 4°C at 12,000 rpm for 5 minutes. The cell pellets were washed twice with sterile deionized (DI) water, followed by centrifugation under the same conditions to remove the wash solution. Subsequently, the cell pellets were resuspended in trehalose induction media, containing 100 g/L glucose, 10 g/L yeast extract, 0.3 g/L KH_2PO_4 , 0.25 g/L $\text{MgSO}_4 \cdot 7\text{H}_2\text{O}$ and supplementing ethanol with various concentrations (0, 25, and 50 g/L). The culture was incubated at 45°C and 200 rpm for 6 hours. The fermentation broth was collected every 30 minutes to determine yeast growth, glucose consumption, and trehalose concentration.

3. Sample analysis

3.1 Cell growth of *S. cerevisiae* and fermentation kinetics

Fermentation samples were collected for the determination of yeast growth, glucose consumption, and trehalose production. The fermentation broth was centrifuged at 10,000 rpm for 5 min to separate yeast cells from the fermentation broth. The cell pellet was resuspended in deionized water to measure the optical density at a wavelength of 600 nm, while the supernatant was collected to determine the glucose consumption, trehalose

concentration and byproducts. The concentration of glucose concentration, trehalose concentration, and byproducts was analyzed using HPLC. For analyses of the remaining glucose, trehalose, and byproducts, supernatant was automatically injected (SIL 20A HPLC autosampler (Shimadzu Corp., Kyoto, Japan) into an organic acid analysis column (Aminex HPX-87H ion exclusion organic acid column; Biorad) and maintained at 65 °C in a column oven. Sulfuric acid at 0.005 M was used as eluent at a flow rate of 0.6 mL/min. A reflective index detector was used to detect target compounds. To determine sample concentration, external standards containing 0 – 2 g/L of glucose, glycerol, acetic acid, ethanol and trehalose were injected as the references.

3.2 Trehalose production

3.2.1 Yeast cell extraction preparation

The fermentation broth samples were centrifuged at 4 °C, 12,000 rpm for 5 minutes. The supernatant and pellet were separated. The cell pellets were washed twice with 0.85% NaCl, and the salt solution was removed by centrifugation under the same conditions. Subsequently, 1 mL of 0.05 M potassium phosphate buffer (pH 7.2) and 0.5 g of unwashed glass beads (425–600 µm) were added to 0.5 g of wet cell pellet. Cell disruption was then performed using an ultrasonic disruptor for 5 minutes (45 s sonication interval with 60 s break) under cooling conditions. After cell disruption, the mixture was centrifuged again at 4 °C, 12,000 rpm for 5 minutes, and the supernatant was collected and stored at refrigerator temperature for subsequent trehalose quantification by HPLC.

3.2.2 Trehalose quantification

Trehalose concentration was analyzed from both the fermentation broth and the supernatant obtained from cell extraction. Both sample types were filtered through a 0.22 µm Polytetrafluoroethylene (PTFE) filter before injection. The filtered samples were analyzed using HPLC equipped with an Aminex® HPX-87H column (300 mm × 7.8 mm, Biorad). The mobile phase consisted of 0.005 M H₂SO₄, with a flow rate of 0.6 mL/min, and the column temperature was maintained at 65 °C. Detection was performed using a refractive index (RI) detector. To determine sample concentration, external standards containing 0 – 2 g/L of glucose, glycerol, acetic acid, ethanol and trehalose were injected as the references.

Results and Discussion:

A two-phase fermentation approach was applied for trehalose production by *S. cerevisiae*. Yeast cells were initially cultivated to promote growth and ethanol accumulation, thereby priming the metabolic pathways of *S. cerevisiae* to activate trehalose synthesis as a cellular stress response mechanism. During the cell production phase, glucose was completely consumed within 12 h, resulting in high cell density with an OD₆₀₀ of 55.13 ± 0.551. The growth profile of yeast cells demonstrated that the log phase occurred during 0-8 h, followed by entry into stationary phase from 12 h onward until the end of the 24-hour fermentation time. Additionally, ethanol, glycerol, and trehalose were identified as major metabolites produced during the cell induction phase, with concentrations of 46.200 ± 1.848 g/L, 2.200 ± 0.066 g/L, and 0.690 ± 0.014 g/L, respectively (Fig. 1a). Furthermore, intracellular metabolite analysis during the cell production phase revealed the accumulation of glucose, ethanol, glycerol, acetic acid, and trehalose within yeast cells, demonstrating dynamic temporal changes throughout the fermentation process (Fig. 1b). These metabolite concentration fluctuations reflect the cellular physiological state and indicate metabolic flux redistribution within central carbon metabolism pathways [11,12]. The observed intracellular metabolite dynamics may be associated with the establishment of metabolic balance within yeast cells

under osmotic stress conditions [12,13], where trehalose accumulation serves as a key osmolyte for maintaining cellular homeostasis during environmental perturbations [14,15].

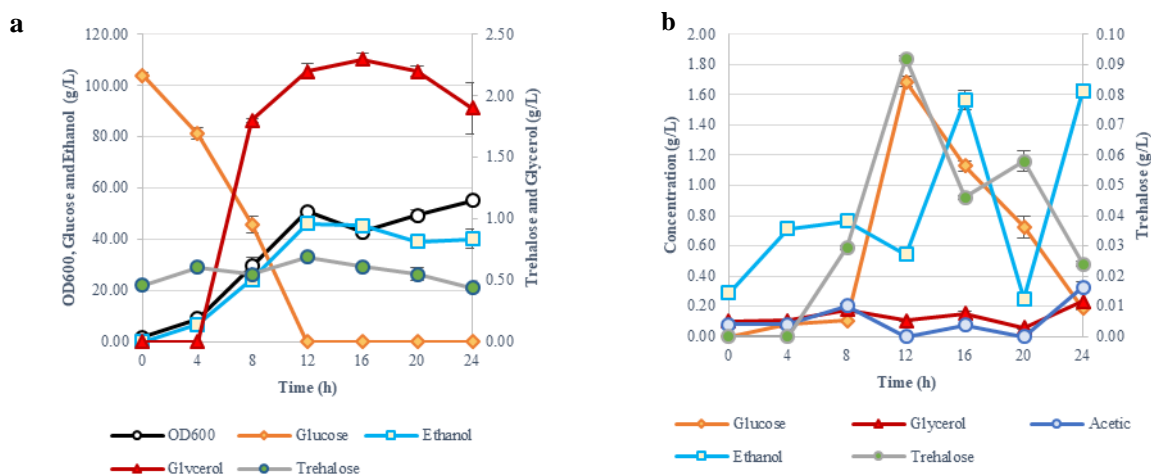


Figure 1.

Fermentation profiles of *S. cerevisiae* cultivated in cell production medium. (a) Time course of cell growth, glucose consumption, and extracellular metabolites formation. (b) Intracellular metabolites accumulation during the cultivation period.

After finishing the cell production step, yeast cells at the age of 8 h were transferred to trehalose production medium and incubated at higher temperature (45°C) to induce trehalose formation. During this stage, ethanol supplementation was investigated at concentrations of 25 g/L and 50 g/L to evaluate its effect on trehalose synthesis in *S. cerevisiae*, compared to the control trehalose production medium without ethanol addition.

The results revealed that thermal conditions and ethanol supplementation significantly influenced the fermentation performance of yeast cells (Fig. 2). In the case of trehalose production medium without ethanol addition, yeast cells exhibited limited growth with OD₆₀₀ values ranging from 2.967 ± 0.089 to 5.807 ± 0.232 . Although glucose was poorly utilized, the yeast cells demonstrated adaptive responses through the formation of ethanol, trehalose, and glycerol as protective metabolites, as shown in Fig. 2a. Furthermore, examination of intracellular metabolites revealed that yeast cells cultivated at higher temperature above their optimal growth range resulted in a reduced cellular uptake of glucose, consequently leading to substantial glucose accumulation remaining in the culture system. Additionally, the production of various metabolites was observed, particularly ethanol and glycerol, which indicated the activation of cellular protective mechanisms in yeast cells under thermal stress conditions (Fig 2b). At 25 g/L ethanol, yeast cells maintained viable growth with OD₆₀₀ values of 2.213 ± 0.155 to 3.507 ± 0.245 while showing enhanced production of protective metabolites, including trehalose (0.260 ± 0.013 to 0.420 ± 0.013 g/L) and glycerol (0.150 ± 0.005 to 0.430 ± 0.017 g/L) (Fig. 2b-2c; Table 1). These results indicate successful activation of stress response pathways and establishment of cellular protective mechanisms. However, at 50 g/L ethanol, yeast cells showed severely reduced growth (OD₆₀₀ values of 2.527 ± 0.025 to 3.227 ± 0.097) and were unable to utilize glucose or produce any metabolites (Fig. 2e-2f; Table 1). This concentration appears to exceed the threshold for cellular adaptation, resulting in metabolic dysfunction and compromised cell viability rather than protective responses.

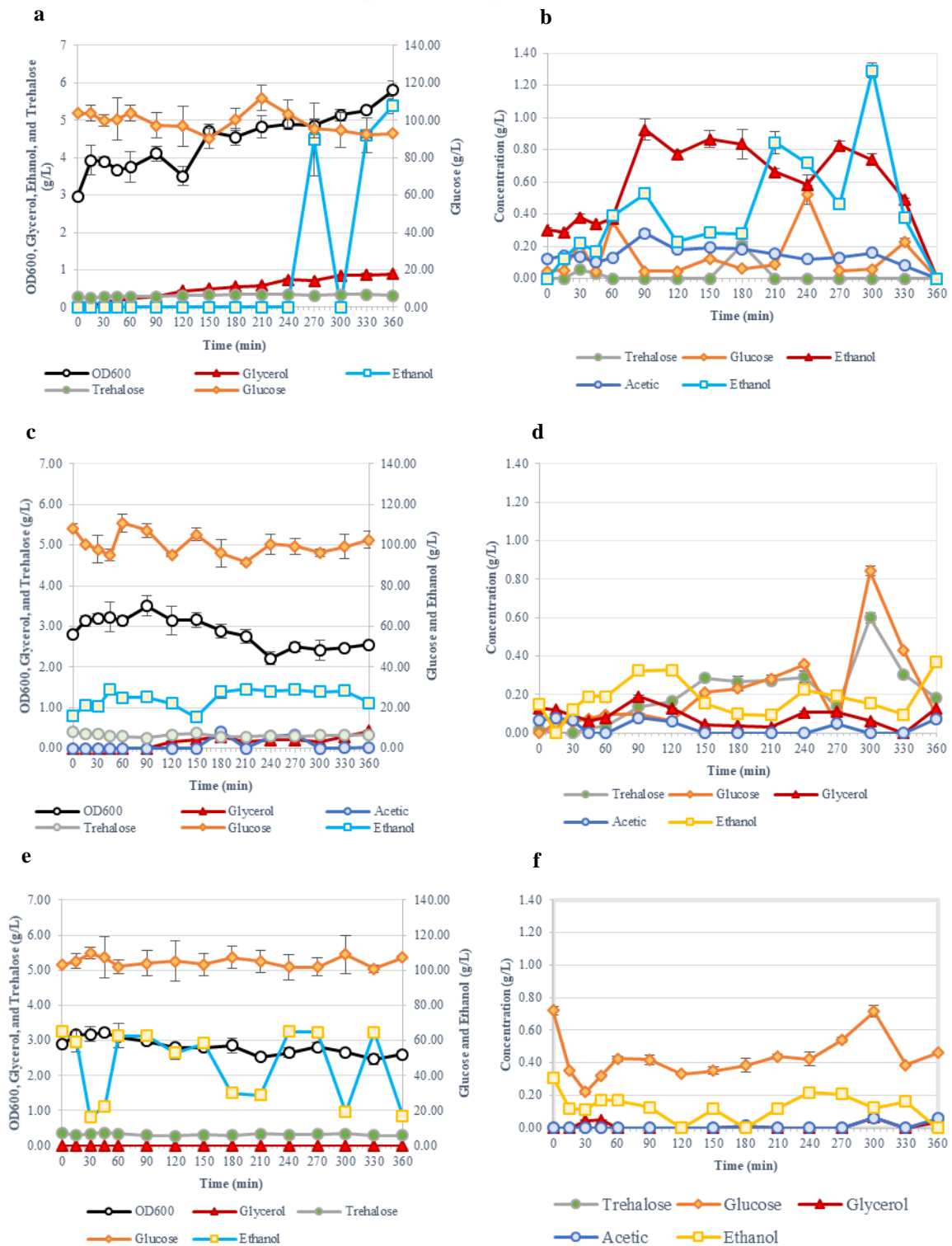


Figure 2.

Fermentation profile of *S. cerevisiae* in trehalose production medium cultivated at 45 °C for 6 h. (a) Extracellular metabolites profile presented in medium without ethanol. (b) Intracellular metabolites profile during cell cultivated in medium without ethanol. (c) Extracellular metabolites profile presented in medium supplemented with 25 g/L ethanol. (d) Intracellular metabolites profile during cell cultivated in medium supplemented with 25 g/L ethanol. (e) Extracellular metabolites profile presented in medium supplemented with 50 g/L ethanol. (f) Intracellular metabolites profile during cell cultivated in medium supplemented with 50 g/L ethanol.

Table 1.
Fermentation kinetics of *S. cerevisiae* at the end of 6 h fermentation time under different trehalose fermentation media

Fermentation kinetics	Fermentation media		
	Initial glucose 100 g/L without ethanol concentration	Initial glucose 100 g/L with initial ethanol concentration 25 g/L	Initial glucose 100 g/L with initial ethanol concentration 50 g/L
Growth (OD ₆₀₀)	5.807 ± 0.233 ^a	2.547 ± 0.026 ^b	2.600 ± 0.104 ^b
Trehalose (g/L)	0.310 ± 0.012 ^b	0.330 ± 0.010 ^a	0.300 ± 0.012 ^b
Productivity (g/L·h)	0.052 ± 0.002 ^{ab}	0.055 ± 0.002 ^a	0.050 ± 0.002 ^b
Yield (g trehalose/g glucose)	0.003 ± 0.000 ^a	0.003 ± 0.000 ^a	0.003 ± 0.000 ^a
Yield (g trehalose/g cell biomass)	0.160 ± 0.000 ^c	0.389 ± 0.008 ^a	0.347 ± 0.028 ^b

Values are presented as Mean ± S.D. (n=3). In the same row, means with different letters (^a, ^b, ^c) are significantly different (p < 0.05)

Conclusion:

This study demonstrated the effectiveness of two-phase fermentation for trehalose production by *S. cerevisiae* under controlled stress conditions. The combination of thermal stress (45°C) and moderate ethanol supplementation (25 g/L) significantly enhanced trehalose synthesis, with yeast cells producing trehalose (0.260 ± 0.013 to 0.420 ± 0.013 g/L) and glycerol (0.150 ± 0.005 to 0.430 ± 0.017 g/L) while maintaining viable growth. However, excessive ethanol concentration (50 g/L) resulted in severe growth inhibition and metabolic dysfunction. The results indicate that moderate dual-stress conditions effectively activate cellular protective mechanisms and redirect metabolic flux toward trehalose biosynthesis, while excessive stress overwhelms cellular adaptive capacity. This approach provides valuable insights for optimizing trehalose production in yeast fermentation systems.

Acknowledgements:

This work was financially supported by Center of Excellence in Bioconversion and Bioseparation for Platform Chemical Production, Institute of Biotechnology and Genetic Engineering, Chulalongkorn University. We thank the Program in Biotechnology, Faculty of Science, Chulalongkorn University for partial supporting and facilitating this research and TSB conference participation.

References:

1. Qiao Y, Wang W, Lu X. Engineering cyanobacteria as cell factories for direct trehalose production from CO₂. *Metabolic Engineering*. 2020;62:161-71.
2. Elbein AD, Pan YT, Pastuszak I, Carroll D. New insights on trehalose: a multifunctional molecule. *Glycobiology*. 2003;13(4):17r-27r.
3. Chen A, Tapia H, Goddard JM, Gibney PA. Trehalose and its applications in the food industry. *Compr Rev Food Sci Food Saf*. 2022;21(6):5004-37.
4. Chang SW, Liu PT, Hsu LC, Chen CS, Shaw JF. Integrated biocatalytic process for trehalose production and separation from rice hydrolysate using a bioreactor system. *Food Chemistry*. 2012;134(4):1745-53.



5. Agarwal N, Singh Sudhir P. A Novel Trehalose Synthase for the Production of Trehalose and Trehalulose. *Microbiology Spectrum*. 2021;9(3):e01333-21.
6. Lama L, Nicolaus B, Trincone A, Morzillo P, De Rosa M, Gambacorta A. Starch conversion with immobilized thermophilic archaeobacterium *Sulfolobus solfataricus*. *Biotechnology Letters*. 1990;12(6):431-2.
7. Cai X, Seitzl I, Mu W, Zhang T, Stressler T, Fischer L, et al. Biotechnical production of trehalose through the trehalose synthase pathway: current status and future prospects. *Applied Microbiology and Biotechnology*. 2018;102(7):2965-76.
8. Johnson EA, Echavarri-Erasun C. Chapter 3 - Yeast Biotechnology. In: Kurtzman CP, Fell JW, Boekhout T, editors. *The Yeasts (Fifth Edition)*. London: Elsevier; 2011. p. 21-44.
9. Bandara A, Fraser S, Chambers PJ, Stanley GA. Trehalose promotes the survival of *Saccharomyces cerevisiae* during lethal ethanol stress, but does not influence growth under sublethal ethanol stress. *FEMS Yeast Research*. 2009;9(8):1208-16.
10. Chen A, Gibney P. Intracellular trehalose accumulation via the Agt1 transporter promotes freeze-thaw tolerance in *Saccharomyces cerevisiae*. *Journal of Applied Microbiology*. 2022;133.
11. Noordlander B, Krantz M, Hohmann S. Hog1-mediated metabolic adjustments following hyperosmotic shock in the yeast *Saccharomyces cerevisiae*. In: *Stress-activated protein kinases*. Berlin: Springer; 2008. p. 141-58.
12. Duveau F, Cordier C, Chiron L, Le Bec M, Pouzet S, Seguin J, et al. Yeast cell responses and survival during periodic osmotic stress are controlled by glucose availability. *eLife*. 2024;13:e88750.
13. Kus-Liskiewicz M, Fickers P, Lognay G. Sodium transport and redox regulation in *Saccharomyces cerevisiae* under osmotic stress depending on oxygen availability. *Scientific Reports*. 2024;14(1):23878.
14. Li Y, Jiang G, Long H, Liao Y, Wu L, Huang W, et al. Metabolic characteristics of intracellular trehalose enrichment in salt-tolerant *Zygosaccharomyces rouxii*. *Frontiers in Microbiology*. 2022;13:935756.
15. Wangpaiboon K, Padungros P, Rattanaphan N. High glucose is a stimulation signal of the salt-tolerant yeast *Zygosaccharomyces rouxii* on thermoadaptive growth. *Foods*. 2024;13(6):898.



NITRATE REDUCING BACTERIA FROM OIL SLUDGE AND THEIR POTENTIAL ROLES ON METAL CORROSION INHIBITION

Luxnapol Marturunkakul, Chutima Rotchum, Ekawan Luepromchai*

Microbiology and Microbial Technology Program, Department of Microbiology, Faculty of Science, Chulalongkorn University, Bangkok, Thailand, 10330

*e-mail: ekawan.l@chula.ac.th

Abstract:

Microbiologically influenced corrosion (MIC) is a chronic problem that leads to economical loss in oil and gas industries. Although sulfate-reducing bacteria (SRB) are a major MIC promoter, roles of other bacterial groups on corroded surface such as nitrate-reducing bacteria (NRB) are equally important. Using six assorted media, eight potential NRB isolates (*Citrobacter cronae* SJ1, *Pseudomonas aeruginosa* SJ5, *Stutzerimonas balearica* SJ26, *Halomonas johnsoniae* SJ33, *Pseudomonas kurunegalensis* SJ21P, *Brucella cytisi* SJ21T, *Stutzerimonas stuzeri* SJ29 and *Pseudomonas khazarica* SJ37) were enriched from oil sludge. An aerobic metal corrosion experiment was then conducted in simulated produced water containing selected bacterial strains and L80-1 carbon steel coupons. After 30-day, the abiotic control decreased the metal weight by 17.9 mg/coupon, whereas strain SJ26, SJ33 and SJ37 decreased the metal weight by 4.8, 5.2 and 4.2 mg/coupon, respectively. The low metal weight loss was corresponded with the formation of biofilm, which suggested that these bacteria protected the metal surface from abiotic oxidation. *H. johnsoniae* SJ33 also produced significant ammonia indicating the reduction of nitrate, which was probably due to the anoxic condition in the bacterium biofilm. In conclusion, the NRB under aerobic condition were non-corrosive and inhibited metal corrosion. Further study will investigate the interactions between NRB and SRB on MIC.

Introduction:

Microbiologically influenced corrosion or MIC is a term referring to a phenomenon in which the activities of microorganisms in the system directly or indirectly deteriorate materials, particularly metals. To prevent and repair the damage caused by MIC, many industries, especially oil and gas, have to face an enormous economic burden; an estimated 2.7 trillion dollars is spent annually as a result of biocorrosion^{1,2}. Despite a century of research and studies, scientists still struggle to fully comprehend the scope and mechanistic details of the system which is due largely to its complexity, dynamic behaviors and interdisciplinarity^{3,4}. From a microbiological point of view, several types of microorganisms take part in the MIC, with bacteria figuring in as a chief contributor³. Corrosion-influencing bacteria can, in turn, be classified into various categories including sulfate-reducing bacteria (SRB), acid-producing bacteria (APB), nitrate-reducing bacteria (NRB), sulfur-oxidizing bacteria (SOB), iron-oxidizing bacteria (IOB), iron-reducing bacteria (IRB) and slime-forming bacteria^{3,5,6}. Theoretically, some bacteria are capable of corroding metallic structures solitarily, yet they are naturally found to work in cooperation, mostly in a form of biofilm⁷. Indeed, it is the process by which these bacteria affect each other that controls and determines the cohesion as well as the practical applications of the bacterial consortia³. Furthermore, the intricacies of the system can be intensified by the surrounding environmental factors making every cluster of bacteria unique in its composition and properties^{7,8}.

Of all the key bacterial groups, SRB which is recognized as the pre-eminent corrosive bacteria have attracted the most attention from scientists in the related fields and a great deal of research has been undertaken to investigate mechanisms and activities of this organisms^{3,5}. However, the corrosive impact of SRB alone is no match for the full extent of corrosion that a natural biofilm in the real-world environment can achieve^{1,7}. Accordingly, activities of the

remaining bacteria in the system are not to be overlooked and studies of other corrosive species are necessary. This research study, therefore, focuses on enrichment and isolation of bacteria other than SRB from oil sludge collected from a metal corrosion site. The bacteria were identified from 16S rDNA sequences and later determined their activities in a metal corrosion experiment under aerobic condition, an initial state in MIC. These bacteria were considered as representatives of minor bacterial populations relevant to MIC. The expected outcome is to provide new insights into the roles of relatively obscured microorganisms in an oilfield, a major corrosion-affected area.

Methodology:

Bacterial enrichment

An oil sludge sample was collected by a pigging technique where a sponge-like device was sent running through corroded petroleum pipelines to sweep any deposits on their surface. The produced water inside the pipeline has neutral pH with an average salinity of 2.6-2.8 %. Six different minimal culture media were selected from literatures with the aim of enriching aerobic bacteria relevant to metal metabolism, which feature in the early stages of metal corrosion (Table 1). These media share some nutrients and energy sources, but, together, cover a wide range of pH from extremely acidic to mildly alkaline, thereby rendering a decent prospect for the cultivation of broad yet specific groups of bacteria. After adding 20% (w/v) of oil sludge, the media were incubated at room temperature with a shaking speed of 150 rpm. This condition was used in accordance with the previous studies. Every 7-12 days, 10% (v/v) of culture broth was transferred to a new medium with the total of 6 times to ensure the growth of dominant targeted bacteria.

Table 1.
The list of enrichment media

Medium	Main component(s)	pH range
Medium 1 ⁹	FeSO ₄ ·7H ₂ O, (NH ₄) ₂ SO ₄	~ 2
Medium 2 ¹⁰	FeSO ₄ ·7H ₂ O	~ 2
Medium 3 ¹¹	Bacto-peptone, Ferric ammonium citrate, Na ₂ S ₂ O ₃	~ 7
Medium 4 ¹²	Na ₂ S ₂ O ₃ , NH ₄ Cl, KNO ₃ , CH ₃ COONa	7-9
Medium 5 ¹³	Na ₂ S ₂ O ₃ , (NH ₄) ₂ SO ₄	4.4-4.7
Medium 6 ¹⁴	Na ₂ S ₂ O ₃	4-5

Bacterial isolation and sequencing

After the final transferring, the enriched bacteria were isolated by spread plate and streak plate techniques. Diluted culture broth was spreaded on agar plates of their respective media and any distinct colonies were streaked on new plates. A Gram-staining method was then employed to each isolate. The bacterial isolates were grouped based on Gram stain result and colony's form and color. Subsequently, one bacterium from each group was designated to be identified by a 16S rDNA sequencing technique.

Metal corrosion experiment

Following the bacterial sequencing, information of each species was gathered and evaluated, and three most engaging microbes were selected for a metal corrosion test. A month-long experiment was set up, with modified simulated produced water¹⁵ replacing the enriched media as a liquid agent. Metal coupons were prepared from a carbon steel, L80 type 1 pipe (L80-1). L80-1 was cut into a-cubic-centimeter-sized coupons with each coupon having an average weight around 4.2 – 4.6 g. There were four experimental sets including (i) a control

group in which one cleaned and sterile metal coupon alone was immersed into the medium; (ii) a replica of group i, plus 10% (v/v) inoculum of the first bacterium; (iii) a replica of group i, plus 10% (v/v) inoculum of the second bacterium; and (iv) a replica of group i, plus 10% (v/v) inoculum of the third bacterium. The experiment was conducted under a static aerobic setting, at room temperature. Each set was performed in triplicate. At the end of the test, the coupon was retrieved for a measurement of the weight loss as well as the biofilm attached on the metal surface for which a drop plate technique was used. The solution was collected for a quantification of pH and concentrations of sulfate and ammonia using a pH meter and a multiparameter photometer, respectively. Finally, ANOVA and Tukey Post-Hoc Test were conducted using jamovi (Version 2.3).

Results and Discussion:

Bacterial enrichment, isolation and sequencing

MIC in the oil field is a direct consequence of elaborate bacterial activities, yet the deterioration of structures is generally attributed to SRB while contributions of other microbes is often underrated¹⁶. In seeking to shed light on the roles and manner of these peripheral bacteria in biocorrosion, six minimal media of varying pH ranges (Table 1) were first used for the promotion of them. Prior to the second subculturing, two media with highly acidic pH (i.e. Media 1 & 2) were terminated as they had not been able to accommodate any culturable bacteria. This, nevertheless, corroborates the fact that the oil field from which the oil sludge was sampled has neutral pH. Though these two media contain no carbon source, the apparent absent of organisms in the media coupled with the nature of the oil field suggests that some corrosive acidophilic chemolithoautotrophs are unlikely to exert solid influence on MIC of the relatively neutral oil fields. Eventually, the other four media did succeed in culturing bacteria (Figure 1). Next, a comparative analysis of colony and cell morphology was carried out to arrange the obtained pure cultures into groups where their identities were later confirmed by a 16S rDNA sequencing method. Intriguingly, all the isolates are found to be rod-shaped Gram-negative bacteria under the microscopic observation (Table 2). Taking into account that the pipelines are constantly flooded with biocides, Gram-negative bacteria with their double-layer efflux system, are probably more tolerant to toxic substances than Gram-positive bacteria¹⁷.

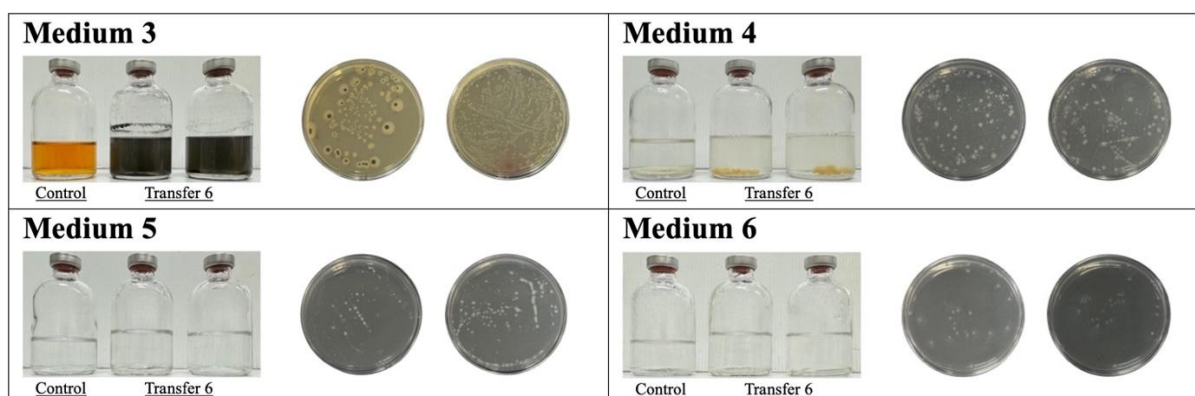
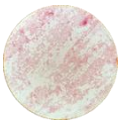


Figure 1.
Bacterial enrichment of Medium 3-6

Subsequent to the identification, eight distinct bacteria were obtained, each of which displayed a similarity to its related species beyond 98.8% (Table 2). Still, the phylogenetic analysis of some bacteria proved insufficient to specify the bacterial species, hence the morphological features were drawn on to reinforce the classification. Ultimately, strain codes

were given to the isolated bacteria as follows: *Citrobacter cronae* SJ1, *Pseudomonas aeruginosa* SJ5, *Stutzerimonas balearica* SJ26, *Halomonas johnsoniae* SJ33, *Pseudomonas kurunegalensis* SJ21P, *Brucella cytisi* SJ21T, *Stutzerimonas stuzeri* SJ29 and *Pseudomonas khazarica* SJ37. Among them, only *P. aeruginosa* and *S. balearica* were present in more than one type of enrichment media demonstrating their ability to thrive in a wide range of pH and atmosphere. The isolation of *Halomonas johnsoniae* was corresponded with the salinity of the produced water.

Table 2.
16S rDNA sequencing and gram-stain

Code	Closely related species	% Similarity	Gram-stain	Enrichment medium
SJ1	<i>Citrobacter cronae</i> / <i>Citrobacter braakii</i>	99.52 (MN548424/ NAEW01000064)		Medium 3 ¹¹
SJ5	<i>Pseudomonas aeruginosa</i> / <i>Pseudomonas paraeruginosa</i>	100.00 (BAMA01000316/ ON359917)		Medium 3 ¹¹ , Medium 5 ¹³ , Medium 6 ¹⁴
SJ26	<i>Stutzerimonas balearica</i>	99.79 (CP007511)		Medium 4 ¹² , Medium 6 ¹⁴
SJ33	<i>Halomonas johnsoniae</i>	100.00 (AM941399)		Medium 4 ¹²
SJ21P	<i>Pseudomonas kurunegalensis</i>	99.93 (AM911650)		Medium 5 ¹³
SJ21T	<i>Brucella cytisi</i> / <i>Brucella anthropi</i>	100.00 (AY776289/ CP000758)		Medium 5 ¹³
SJ29	<i>Stutzerimonas stuzeri</i>	99.52 (CP002881)		Medium 4 ¹²
SJ37	<i>Pseudomonas hydrolytica</i> / <i>Pseudomonas guguanensis</i> / <i>Pseudomonas khazarica</i>	98.87 (MK248116/ FNJJ01000024/ KX712072)		Medium 4 ¹²

Potential functions of the isolated bacteria

With eight identified bacteria, relevant literature was reviewed to identify their potential functions relevant to MIC in the oil field. Moreover, potential bacterial categories were assigned to each strain based on the reviewed information (Table 3). Some of the assigned categories, however, contradicted the enrichment results. For instance, *H. johnsoniae*, a potential IRB, was not found in Medium 3 which has ferric ammonium citrate as a main component. This is probably due to bacterial competitions during enrichment, the deprivation of vital nutrients in some media, or the specific culture condition used in this study. Further studies are required in order to explain the absence of certain bacteria in some media and to

confirm the metabolic ability of each bacterium. As thiosulfate ($S_2O_3^{2-}$) constitutes the only main energy source contained in all four media, it is quite perplexing that SOB was not the most abundant bacterial group enriched; APB were also low in number but were more likely given the non-acidic characteristic of the corrosion site. Instead, it turned out that all the cultivated bacteria appeared to possess an ability to reduce nitrate, a typical of NRB, what's more, seven of these bacteria even tend towards capacity for ferric reduction making them IRB as well. Both NRB and IRB are versatile bacteria which favor neutral pH^{18,19} and can utilize some hydrocarbons like toluene as carbon source¹⁶, thus they are predominant in petroleum pipeline. It is probable that MIC in the oil field is greatly affected by the metabolic functions of NRB and IRB. Currently, the roles of NRB in the biocorrosion are rather ambiguous. On the one hand, NRB are regarded as a biological tool for the mitigation of MIC since the proliferation of nitrate reducers can effectively combat the growth of SRB, thus limiting the production H_2S ¹⁶. On the other hand, numerous studies preferred to label NRB as a vigorous corrosive species. The fact that the combined iron oxidation and nitrate reduction yields higher redox potential than the reaction between iron oxidation and sulfate reduction meant that NRB are, in some context, perceived to be no less detrimental than SRB⁵. In addition, starved NRB can activate a special energy pathway known as extracellular electron transfer (EET) which allows them to extract electrons from the elemental iron (Fe^0) itself²⁰. Likewise, the involvement of IRB is also a paradoxical one. Whilst IRB can shield metal surface through oxygen absorption and protective film formation, they can also indirectly corrode metals through the dissolution of 'iron oxide deposits' leaving the surface unprotected, not to mention the recycling of IOB-generated ferric ions by IRB which resupplies IOB with ferrous ions^{1,6,21}. This vagueness concerning the role of NRB and IRB is due partly to the subtle differences between species which further stresses the need to investigate every bacteria individually²¹.

In this research, *Stutzerimonas balearica*, *Halomonas johnsoniae* and *Pseudomonas khazarica* were chosen from seven bacteria presumed to be both NRB and IRB for further study. *P. aeruginosa* and *S. stuzeri* are multi-functional bacteria with proven corrosive traits, but since their notoriety are, to a certain extent, securely established, they were not consonant with the objective of this project.

Stutzerimonas balearica, formerly known as *Pseudomonas balearica*, is a facultative denitrifying bacteria chiefly spotted in oil-contaminated areas^{22,23}. Several *S. balearica* strains were isolated from petroleum-based sources including one from an oil-storage floating vessel suffered from a corrosion^{22,24}. Crucially, the usage of produced water and injected water in oil recovery processes has permanently introduced *S. balearica* into the oil and gas infrastructures²³. Through its tenacity towards biocides, *S. balearica* was evidently found to dominate the microbial population in produced water and injected water of some oil industries, an alarming sign suggesting that the bacteria might become problematic in the future^{23,25}.

Halomonas johnsoniae is also a nitrate reducing bacteria where its existence is first realized in 2010²⁶. Though little is known about *H. johnsoniae*, the bacterium is believed to have shared a common evolutionary ancestor and many 'clade-specific signature genes' with a certain prominent corrosive bacterium, *Halomonas titanicae*²⁷; *H. titanicae* is a facultative nitrate- Fe^{3+} reducing bacteria which restrains oxygen corrosion in an aerobic state but turns corrosive itself in an anaerobic environment²¹. Regarding the close link between *H. johnsoniae* and *H. titanicae*, there is a good chance that some qualities of *H. johnsoniae* might parallel that of *H. titanicae*.

Pseudomonas khazarica is probably the most recent species discovered of all three. Isolated in 2020, *P. khazarica* is found to be gifted with a catabolic pathway of degrading polycyclic aromatic hydrocarbons and an ability to use nitrate as an electron acceptor²⁸.

Despite the scarce information, its very genus (i.e. *Pseudomonas*) coupled with its oil-related functions are enough for *P. khazarica* to be suspected of playing a part in the oil field MIC.

Table 3.
Classification of the isolated bacteria

Type of bacteria	Major functions	Reference genus/species	Isolated bacteria
Sulfate-reducing bacteria (SRB)	- Reduce SO_4^{2-} to S^{2-} - Generate hydrogen sulfide ³ - Perform EET ²⁰	<i>Citrobacter</i> sp. ²⁹	<i>C. cronae</i> SJ1
Nitrate-reducing bacteria (NRB)	- Reduce NO_3^- into NO_2^- , NH_4^+ or N_2 - Induce iron oxidation thermodynamically ⁵ - Perform EET ^{20,30}	<i>P. aeruginosa</i> ^{5,31} , <i>S. stuzeri</i> ³² , <i>B. anthropi</i> ³³ , <i>B. cytisi</i> ³⁴ , <i>P. khazarica</i> ²⁸ , <i>Pseudomonas</i> sp. ³⁵ , <i>H. johnsoniae</i> ²⁶ , <i>H. titanicae</i> ³⁶ , <i>S. balearica</i> ²⁴ , <i>C. freundii</i> ³⁷	<i>P. aeruginosa</i> SJ5, <i>S. balearica</i> SJ26, <i>H. johnsoniae</i> SJ33, <i>P. kurunegalensis</i> SJ21P, <i>B. cytisi</i> SJ21T, <i>S. stuzeri</i> SJ29, <i>P. khazarica</i> SJ37, <i>C. cronae</i> SJ1
Sulfur-oxidizing bacteria (SOB)	- Oxidize $\text{S}^{2-}/\text{S}_2\text{O}_3^{2-}$ into SO_4^{2-} - Produce H^+ ions ⁶	<i>S. balearica</i> ²² , <i>S. stuzeri</i> ³⁸ , <i>Pseudomonas</i> sp. ³⁸	<i>S. balearica</i> SJ26, <i>P. kurunegalensis</i> SJ21P, <i>S. stuzeri</i> SJ29, <i>P. khazarica</i> SJ37
Iron-oxidizing bacteria (IOB)	- Oxidize Fe^{+2} to Fe^{+3} - Create an oxygen-free environment providing a habitat for SRB ⁵	<i>Pseudomonas</i> sp. ³⁹ , <i>Brucella</i> sp. ⁴⁰ , <i>S. balearica</i> ⁴¹ , <i>C. freundii</i> ³⁷	<i>S. balearica</i> SJ26, <i>P. kurunegalensis</i> SJ21P, <i>B. cytisi</i> SJ21T, <i>P. khazarica</i> SJ37, <i>C. cronae</i> SJ1
Iron-reducing bacteria (IRB)	- Reduce Fe^{+3} into Fe^{+2} - Destroy protective films precipitated by other microbes ¹	<i>P. aeruginosa</i> ⁴² , <i>S. stuzeri</i> ⁴³ , <i>Citrobacter</i> sp. ⁴⁴ , <i>Pseudomonas</i> sp. ⁶ , <i>H. titanicae</i> ²¹	<i>P. aeruginosa</i> SJ5, <i>S. balearica</i> SJ26, <i>H. johnsoniae</i> SJ33, <i>P. kurunegalensis</i> SJ21P, <i>S. stuzeri</i> SJ29, <i>P. khazarica</i> SJ37, <i>C. cronae</i> SJ1
Acid-producing bacteria (APB)	- Generate organic acid ⁵ - Indirectly hinder the development of a protective film ⁵	<i>P. aeruginosa</i> ³¹ , <i>S. stuzeri</i> ⁴³ , <i>B. anthropi</i> ³³	<i>P. aeruginosa</i> SJ5, <i>B. cytisi</i> SJ21T, <i>S. stuzeri</i> SJ29
Slime-forming bacteria	- Secrete extracellular polymeric substances - Create an anaerobic niche ⁶	<i>P. aeruginosa</i> ⁴⁵ , <i>S. stuzeri</i> ⁴³ , <i>Citrobacter</i> sp. ⁴⁴ , <i>Pseudomonas</i> sp. ⁶ , <i>S. balearica</i> ²² , <i>H. titanicae</i> ⁴⁶	<i>C. cronae</i> SJ1, <i>P. aeruginosa</i> SJ5, <i>S. balearica</i> SJ26, <i>H. johnsoniae</i> SJ33, <i>P. kurunegalensis</i> SJ21P, <i>S. stuzeri</i> SJ29, <i>P. khazarica</i> SJ37



Effect of the selected bacterial strains on metal coupons

Oil field MIC is symbolized by anaerobic corrossions, yet it has never been a solely anaerobic affair and oxygen occasionally took part in the biocorrosion^{2,7}. In this experiment, MIC was studied by immersing metal coupon in the produced water containing 1.6% salinity under aerobic condition (Figure 2). On day 3, a noticeable growth of all bacteria was observed, and the biotic samples remained turbid till the end of the study. The results indicated that *S. balearica*, *H. johnsoniae* and *P. khazarica* grew well in saline solution. Additionally, biofilm of each strain gradually formed on the coupon surfaces as well as at the bottom of the vials. Throughout the study, brownish deposits were apparently developed in the abiotic control set suggesting abiotic oxidation of metal. The metal coupons and solutions were separately collected and analyzed at day 30 (Table 4). Without supplementary nutrients, all three bacteria did manage to survive in large numbers, roughly 10^7 CFU/cm², in a form of biofilm attached to the metal coupon. After corrosion products on the metal samples were discarded, weight loss of each coupon was calculated. The control set lost an average of 17.9 mg/coupon of its weight whereas the strain SJ26, SJ33 and SJ37 sets lost only 4.8, 5.2 and 4.2 mg/coupon, respectively. In the environment where oxygen is accessible, it appeared that the bacteria not only posed no harm to the carbon steel but also minimized corrosion caused by abiotic factors. It is very likely that these bacteria covered the outer layer of metals with biofilm which, in turn, prevented oxygen from reaching it. Similarly, *H. titanicae* – a fellow NRB and IRB – depreciated the DO concentration through oxygen metabolism undermining a spontaneous cathodic reaction to keep a curb on metal corrosion²¹. Considering the potential advantages of the biofilm, a further quantitative analysis on the biofilm thickness will be conducted. As for the recovered liquid phase, pH in the experimental group was found to be just slightly lower than the control group which can be inferred that there were no highly acidic compounds produced. Yet, the difference between abiotic and biotic sets was obvious in the detected sulphate concentrations. Even though none of the genera is famed for having sulfate reduction features, it seemed that sulfate was metabolized by these bacteria which led to a marked drop in its contents. Lastly, a sign of nitrate reduction could be witnessed in solution harboring *H. johnsoniae* SJ33 biofilm where the ammonium ions made a steep rise to 1.1 mg/L, more than twice as high as the other groups. The reduction of nitrate was probably due to the anoxic condition in the bacterium biofilm. *S. balearica* SJ26 and *P. khazarica* SJ37 were able to produce ammonia but at lower amounts of 0.3-0.4 mg/L. The results indicate that these selected bacteria should be classified as NRB.

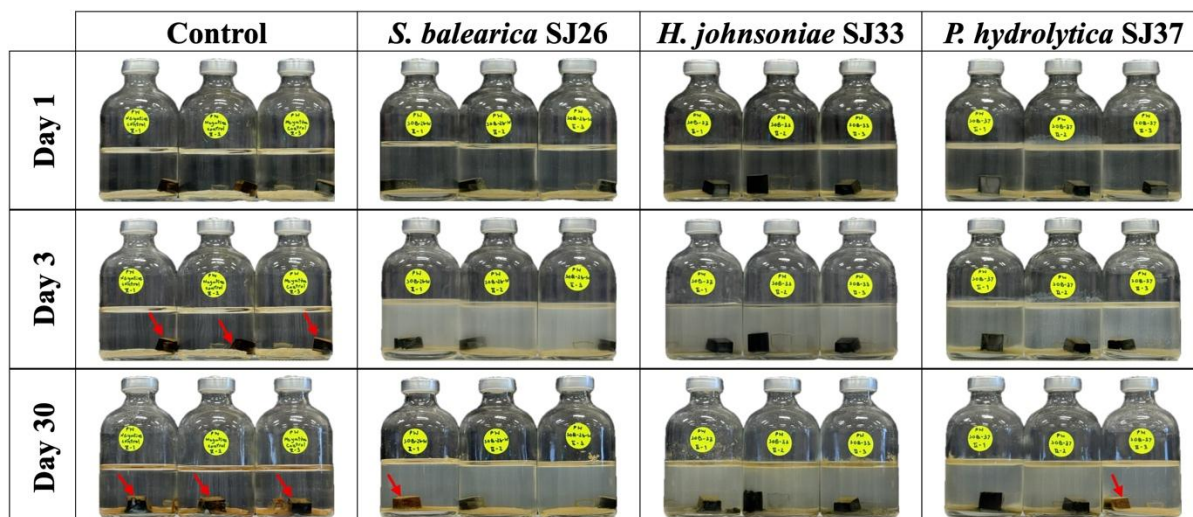


Figure 2.

Metal corrosion experiments showing the changes of metal coupons overtime with and without selected bacterial strains. Arrows indicate the rust formation on coupons.

Table 4

pH, Ions, biofilm and metal weight loss measured at day 30 of the experiment

Parameters	Control	<i>S. balearica</i> SJ26	<i>H. johnsoniae</i> SJ33	<i>P. hydrolytica</i> SJ37
pH	9.4±0.0*	8.8±0.2	8.9±0.1	8.9±0.1
Sulfate (SO ₄ ²⁻) (mg/L)	720.0±10.0 *	670.0±10.0	676.7±5.8	683.3±11.5
Ammonia (NH ₄ ⁺) (mg/L)	0.0	0.4±0.0	1.1±0.3*	0.3±0.1
Biofilm (CFU/cm ²)	-	6.4x10 ⁷ ±4.7x10 ⁷	3.8x10 ⁷ ±2.6x10 ⁷	8.3x10 ⁷ ±2.9x10 ⁷
Metal weight loss (mg/coupon)	17.9±0.1*	4.8±2.2	5.2±0.6	4.2±0.9

* Indicates that the value is significantly different from other conditions ($p < 0.05$).

Conclusion:

Oil fields are full of bacterial species that relevant to MIC, many of which are yet to be revealed and scrutinized. In this research, eight Gram-negative bacteria which appeared to be NRB were successfully isolated from an oil sludge sample. Most of them have never been described as corrosion-related microorganisms. The effects of three selected strains namely *S. balearica* SJ26, *H. johnsoniae* SJ33 and *P. khazarica* SJ37 on carbon steel coupon were then studied under aerobic condition. As it turned out, all bacteria largely safeguarded the metal surface with their colonized biofilm. Further study will investigate the interactions between NRB and SRB on MIC. In addition, the behaviors of isolated NRB when deprived of oxygen require further investigation. The acquired information will contribute towards the elucidation of MIC that will lead to an invention of effective inhibiting means to nullify the bacterial corrosive activities.



References:

1. Vigneron A, Head IM, Tsesmetzis N. *Appl Microbiol Biotechnol.* 2018;102:2525-33.
2. Xu D, Gu T, Lovley DR. *Nat Rev Microbiol.* 2023;21:705–718.
3. Qi P, Zeng Y, Zhang D, et al. *Cell Rep Phys Sci.* 2025;6:102500.
4. de Andrade MF, De Conti D. *Physica A.* 2025;675:130800.
5. Jia R, Unsal T, Xu D, et al. *Int Biodeterior Biodegrad.* 2019;137:42-58.
6. Aslan C, Baihaqi B, Devianto H, et al. *Biomass Bioenerg.* 2025;201:108075.
7. Knisz J, Eckert R, Gieg LM, et al. *Fems Microbiol Rev.* 2023;47:1-33.
8. Li Z, Sun W, Zhou H, et al. *Corrosion Sci.* 2025;256:113211.
9. Chen H, Yang B, Chen X. *Microbiol Res.* 2009;164:613-23.
10. Chen H, Kimyon O, Lamei Ramandi H, et al. *Int J Min Sci Technol.* 2021;31:357-63.
11. Ali A, Amrullah A, Andi J, et al. *Aacl Bioflux.* 2020;13:2886-96.
12. Luo J, Tian G, Lin W. *J Environ Sci.* 2013;25:1393-9.
13. Beard S, Paradela A, Albar JP, et al. *Front Microbiol.* 2011;2:00079.
14. Starosvetsky J, Zukerman U, Armon RH. *J Microbiol Methods.* 2013;92:178-82.
15. Wang J, Shi P, Du M, et al. *Corrosion Sci.* 2024;227:111771.
16. Little BJ, Blackwood DJ, Hinks J, et al. *Corrosion Sci.* 2020;170:108641.
17. Wickham G. *Biosci Horiz.* 2017;10:008.
18. Herrera LK, Videla HA. *Int Biodeterior Biodegrad.* 2009;63:891-5.
19. Xu M, Zhang Q, Xia C, et al. *ISME J.* 2014;8:1932-44.
20. Li Y, Xu D, Chen C, et al. *J Mater Sci Technol.* 2018;34:1713-8.
21. Wang Y, Wu J, Sun L, et al. *Corrosion Sci.* 2021;182:109263.
22. Salvà-Serra F, Pérez-Pantoja D, Donoso RA, et al. *Front Microbiol.* 2023;14:1159176.
23. Bedoya K, Niño J, Acero J, et al. *Int Biodeterior Biodegrad.* 2021;157:105137.
24. Medina LR, Silva LCF, Lima HS, et al. *Heliyon.* 2024;10:39436.
25. Zhou H, Huang X, Jiang L, et al. *Environ Technol Innov.* 2023;32:103280.
26. Kim KK, Lee KC, Oh HM, et al. *Int J Syst Evol Microbiol.* 2010;60:369-77.
27. de la Haba RR, Arahall DR, Sánchez-Porro C, et al. *Front Microbiol.* 2023;14:1293707.
28. Tarhriz V, Nouioui I, Spröer C, et al. *Antonie van Leeuwenhoek.* 2020;113:521-32.
29. Shahryari Z, Gheisari K, Motamedi H. *Mater Chem Phys.* 2019;236:121799.
30. Qian HC, Chang WW, Liu WL, et al. *Bioelectrochemistry.* 2022;143:107953.
31. Tang J, Guo R, Zhang X, et al. *Heliyon.* 2022;8:12588.
32. Fu Q, Wei B, Xu J, et al. *Corrosion Sci.* 2023;216:111084.
33. Holmes B, Popoff M, Kiredjian M, et al. *Int J Syst Evol Microbiol.* 1988;38:406-16.
34. Zurdo-Piñeiro JL, Rivas R, Trujillo ME, et al. *Int J Syst Evol Microbiol.* 2007;57:784-8.
35. Song X, Zhang G, Zhou Y, et al. *Sci Total Environ.* 2023;895:165034.
36. Lu S, Dou W, Gu T, et al. *Corrosion Sci.* 2023;217:111125.
37. Li B, Pan X, Zhang D, et al. *Ecol Eng.* 2015;77:196-201.
38. Li P, Yuan W, Huang Y, et al. *BMC Microbiol.* 2022;22:137.
39. Zhou X, Su H, Wang Q, et al. *Bioelectrochemistry.* 2023;150:108359.
40. Li S, Fan S, Peng X, et al. *iScience.* 2024;27:108595.
41. Salgar-Chaparro Silvia J, Castillo-Villamizar G, Poehlein A, et al. *Microbiol Resour Ann.* 2020;9:00275-20.
42. Huang L, Chang W, Zhang D, et al. *Corrosion Sci.* 2022;199:110159.
43. Zhang S, Dong B, Zhao D, et al. *Bioelectrochemistry.* 2025;162:108846.
44. Venkidusamy K, Hari AR, Megharaj M. *Front Microbiol.* 2018;9:349.
45. Li C, Wu J, Zhang D, et al. *Water Res.* 2023;232:119708.
46. Fu M, Xia M, Lai L, et al. *Corrosion Sci.* 2025;246:112758.



EFFECT OF POTENTIALLY PATHOGENIC AND PLASTIC-DEGRADING BACTERIAL CO-CULTURE ON POLYLACTIC ACID MICROPLASTICS

Nutthamon Boonlum¹, Chonchanok Muangnapoh¹, and Ekawan Luepromchai^{1,2*}

¹Department of Microbiology, Faculty of Science, Chulalongkorn University, Thailand

²Center of Excellence in Microbial Technology for Marine Pollution Treatment (MiTMaPT), Chulalongkorn University, Thailand

*e-mail: ekawan.l@chula.ac.th

Abstract:

Compostable plastics such as polylactic acid (PLA) can generate microplastics (MPs) due to their incomplete degradation and deterioration. PLA MPs can persist in the environment and create new ecological niches for microorganisms. Previous studies have shown that pathogenic bacteria are often among the pioneer colonizers on microplastic surfaces due to their biofilm-forming ability. Biofilm formation also alters the physicochemical properties of microplastics, thereby promoting the subsequent colonization and activity of other microbial groups. This study therefore investigated the synergistic effects of potentially pathogenic and plastic-degrading bacteria on PLA MPs when cultured as monocultures and co-cultures. The PLA MPs used in this study were prepared from PLA cup waste and cut into fragments of approximately 3×3 mm (< 5 mm in diameter). Initially, growth, colonization, and biofilm formation of four bacterial strains (*Stenotrophomonas pavanii* EA33, *Bacillus pumilus* STUV10, *Vibrio parahaemolyticus* PA7_5, and *Staphylococcus saprophyticus* PF11_E1) on PLA MPs were compared. PLA MPs in liquid medium enhanced growth and biofilm formation of all bacteria compared with the control without PLA MPs. The co-culture of *S. pavanii* EA33 (PLA-degrading bacterium) and *V. parahaemolyticus* PA7_5 (potentially pathogenic bacterium) showed synergistic enhancement of PLA MP degradation. The weight loss of PLA MP in co-culture was 39% at day 20, while only 14% was degraded in the monoculture. Morphological observations confirmed progressive erosion, cracking, and fragmentation of PLA MPs. In addition, *V. parahaemolyticus* PA7_5 showed better growth in co-culture (~ 8 log CFU/mL) than that of monoculture (~ 7 log CFU/mL). Overall, this study indicated the dual roles of PLA MPs as degradable substrates and carrier for pathogens. The findings will be used to determine the fate of PLA microplastics and pathogens in natural ecosystems.

Introduction:

Poly(lactic acid) (PLA) is a compostable plastic made from renewable natural resources such as corn, starch, and sugarcane. It has good biodegradability and mechanical properties, which are widely used as packaging and account for approximately 45% of the global biodegradable plastic market.^{1, 2} PLA can be rapidly degraded under very specific conditions (high temperature, moisture, presence of microorganisms and enzymes), however its degradation rate in the natural ecosystems is often not feasible, and complete mineralization is difficult to achieve.³ Similar to petroleum-based plastics, bio-based plastics also produce microplastics (< 5 mm in diameter) throughout their life cycle and can even produce more particles than petroleum-based plastics.⁴ Recent studies showed that bio-based microplastics pose certain ecological and environmental risks.²

Due to their small size, high specific surface area, and hydrophobicity, microplastics readily attract microorganisms to form biofilms on their surfaces, making them good carriers for microbial colonization and translocation.⁵ Biofilm primarily consists of microbial cells and extracellular polymeric substances (EPS). Compared to the surrounding environment, the surface biofilm of microplastics has been shown to have a distinct microbial community



structure.⁶ Additionally, microplastics can easily migrate through hydrodynamic processes, making them carriers of spreading harmful microorganisms.⁷

Potential opportunistic pathogens have been identified as pioneer colonizer on the surface of microplastics.⁸ For example, *Vibrio*, *Enterobacteriaceae*, and *Tenacibaculum* have been recognized on various types of microplastics, including polyethylene (PE), polylactic acid (PLA), and polystyrene (PS), in the marine environment due to biofilm formation ability.⁸⁻¹⁰ Several studies have demonstrated that microbial colonization on microplastic surfaces is divided into different successional stages: firstly, pioneer microorganisms that can effectively adhere to microplastics randomly through biofilm, secondly, microorganisms with the ability to degrade polymers are enriched, and finally, plastic-degrading microorganisms are replaced by other organisms and exit the core role.^{11, 12} Various bacteria capable of degrading microplastics from microplastic-associated biofilm including *Bacillus*, *Pseudomonas*, *Alcanivorax*, *Stenotrophomonas*, *Alteromonas*, etc. have shown a promising ability to degrade various microplastic.¹³⁻¹⁶

Currently, most studies focus on isolating microbial strains capable of degrading plastics from contaminated environments, as well as describing the stages of biofilm formation and providing taxonomic insights into bacteria colonizing microplastics.¹⁷ However, there remains a significant knowledge gap regarding how potentially pathogenic and plastic-degrading bacteria interact on compostable plastics such as PLA, and how these interactions affect both biofilm development and microplastic degradation.

Thus, this study aims to investigate the interactions between potentially pathogenic and plastic-degrading bacteria on PLA MPs. We hypothesized that co-culture of both bacterial groups will result in altered biofilm formation and PLA MPs degradation compared with monocultures. The obtained knowledge enables understanding of bacterial communities affecting MPs degradation and potential public health risk mediated by microplastic contamination.

Methodology:

Materials and strain maintenance

PLA microplastics (PLA MPs) were prepared from plastic cup waste collected from a local coffee shop, following a modified methodology of Mistry et al. (2022). The PLA cups were cut into 3x3 millimeters (mm) pieces using sterilized scissors. The microplastics were pretreated with UV-C irradiation by placing them in an ultraviolet chamber (15 W and 50 Hz) for 24 hours (h) to simulate long-term exposure of sunlight. Subsequently, the PLA was sterilized by soaking in absolute ethanol and rinsing with sterile distilled water, drying in a laminar airflow cabinet, and 10 minutes (min) of UV irradiation.

Two plastic-degrading bacteria *Stenotrophomonas pavanii* EA33 and *Bacillus pumilus* STUV10, along with two potentially pathogenic bacteria *Vibrio parahaemolyticus* PA7_5 and *Staphylococcus saprophyticus* PF11_E1, were obtained from the MSCU culture collection of the Department of Microbiology, Faculty of Science, Chulalongkorn University, Thailand. These bacterial strains were previously isolated and identified from plastic-contaminated environments. The bacteria were separately cultivated in 0.25x Tryptone Soya Broth (0.25xTSB), except for *V. parahaemolyticus* PA7_5 that was cultivated in 0.25xTSB supplemented with 3% NaCl. The flasks were incubated at room temperature (30°C) with 150 rpm for 16 h (the late logarithmic phase). The inoculum (OD₆₀₀ = 0.5, 10⁸ CFU/mL) was suspended in a 0.85% (w/v) NaCl solution before use.

Monoculture and co-culture experiment

A total of 5 mL of the bacterial inoculum was inoculated into 45 mL of Zobell Marine Broth (ZMB) supplemented with 5 mg/mL of PLA MPs. The flasks were incubated at room



temperature (30°C) with shaking at 150 rpm for 30 days. The abiotic control contained PLA MPs without bacterial inoculum, while the biotic control contained bacterial inoculum without PLA MPs. Three replicate flasks were collected at days 0, 10, 20, and 30 for analysis of bacterial growth in ZMB, bacterial attachment on microplastic surface, and biofilm formation.

A potentially pathogenic and a PLA-degrading bacteria were selected for the co-culture system. Prior to co-culture preparation, the selected bacteria were tested for antagonistic effects using the cross-streak method, and only compatible isolates were used. The co-culture was prepared at a 1:1 (v/v) ratio and the co-culture experiment was conducted under the same conditions as the monoculture experiment. Bacterial growth in ZMB, bacterial attachment on microplastic surface, biofilm formation, and PLA microplastic degradation (weight loss measurement) were determined.

Analysis of bacterial growth and biofilm formation

Bacterial growth in ZMB

The bacteria growth in ZMB was analyzed by plate count technique. Firstly, the culture broth was diluted with a ten-fold dilution technique. Diluted cultures were spread on Tryptone Soya Agar (TSA), while TSA with 3% NaCl was used for *V. parahaemolyticus* PA7_5. The plates were incubated at room temperature (30°C) for 2 days. In the co-culture experiment, the number of bacterial colonies was enumerated separately based on the distinct colony color and morphology observed on TSA.

Bacterial attachment on microplastic surface

PLA MPs were removed from culture broth using strainer. The attachment of bacterial cells in biofilm over PLA MP surface were monitored, following a modified methodology of Maheswaran et al. (2023). Microplastics were washed with distilled water to remove loosely attached bacteria and liquid medium, then vortexed and sonicated in 1 mL of 0.85% (w/v) saline solution to remove the bacterial biofilm. An aliquot was serially diluted and plated on TSA, while TSA with 3% NaCl was used for *V. parahaemolyticus* PA7_5. The plates were incubated at room temperature (30°C) for 2 days. In the co-culture experiment, the number of bacterial colonies was enumerated separately based on the distinct colony color and morphology observed on TSA.

Biofilm formation

PLA MPs were gently washed with sterile distilled water (DW) to remove loosely attached bacterial cells. The washed PLA microplastics were then immersed in 5 mL of 3% (w/v) crystal violet solution for 15 min. Following staining, the PLA microplastics were rinsed with DW to remove excess dye. The biofilm-stained PLA microplastics were extracted by immersing them in 3 mL of 95% (v/v) ethanol. The optical density (OD) of the extracted stain in ethanol was measured at 590 nm using a spectrophotometer to quantify biofilm formation.²⁰

PLA MPs degradation

Weight loss measurement

Weight loss analysis was conducted by washing PLA MPs multiple times with 2% (w/v) sodium dodecyl sulfate (SDS), followed by washing with water and a final wash with 70% (v/v) ethanol. Finally, the samples were dried overnight at 60°C before weighing. The degradation efficiency was calculated using the equation (1):

$$\text{Degradation efficiency of PLA MPs (\%)} = (W_0 - W_1) / W_0 \times 100\% \quad (1)$$

Where W_0 was the weight of the PLA MPs before degradation and W_1 was the weight after degradation.

Results and Discussion:

Growth of bacterial monoculture in ZMB medium with and without PLA microplastics

Figure 1 shows the growth of four bacterial monocultures, including the plastic-degrading bacteria *S. pavanii* EA33 and *B. pumilus* STUV10, along with the potentially pathogenic bacteria *V. parahaemolyticus* PA7_5 and *S. saprophyticus* PF11_E1, in ZMB medium with and without PLA MPs. In ZMB with PLA MPs (Fig. 1a), all strains exhibited a rapid increase in cell numbers during the first 10 days. *S. pavanii* EA33 and *B. pumilus* STUV10 reached the highest densities (~ 9 log CFU/mL) and remained stable until day 30, whereas *V. parahaemolyticus* PA7_5 and *S. saprophyticus* PF11_E1 also increased during the early phase but showed slightly lower maximum values (~ 8 log CFU/mL). In contrast, in ZMB without PLA MPs (Fig. 1b), all strains showed limited growth and their cell numbers gradually declined after day 6. The calculated specific growth rates (μ) supported these observations. In the presence of PLA MPs, all strains displayed positive μ values (0.016–0.019 d^{-1}), while those without MPs showed negative or near-zero μ values (-0.015 to 0.005 d^{-1}).

The results indicate that PLA MPs enhance bacterial growth and survival compared to controls without MPs. The stable cell densities observed in PLA-containing cultures suggest that microplastics acted as potential carbon source through slow degradation. Moreover, the presence of microplastics in the environment may also increase the risk of proliferation of pathogenic bacteria. These findings are consistent with previous studies reporting that compostable plastics such as PLA can sustain microbial colonization and contribute to long-term bacterial persistence.²¹

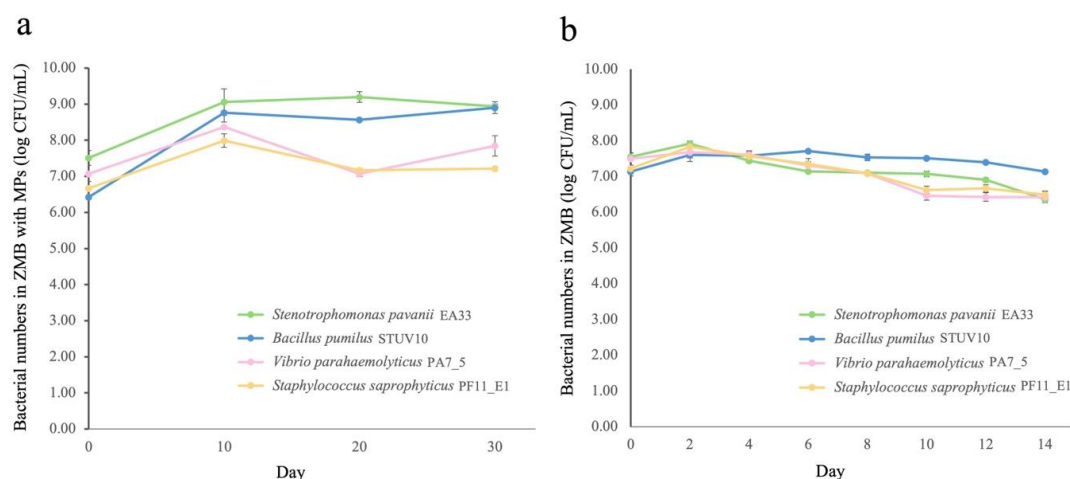


Figure 1

Bacterial growth of monoculture in ZMB medium with (a) and without PLA MPs (b).

Growth and biofilm formation of bacterial monoculture on PLA microplastic surfaces

Figure 2 shows the growth and biofilm formation of four bacterial strains on the surface of PLA MPs during 30 days of incubation. On the MP surface (Fig. 2a), all strains maintained high viable counts ($6\text{--}8$ log CFU/cm²) throughout 30 days. *S. pavanii* EA33 consistently showed the highest densities, followed by *B. pumilus* STUV10, *V. parahaemolyticus* PA7_5, and *S. saprophyticus* PF11_E1. This trend was consistent with their growth in ZMB medium with MPs. Although slight fluctuations were observed, no significant decline occurred, indicating stable colonization on MPs.

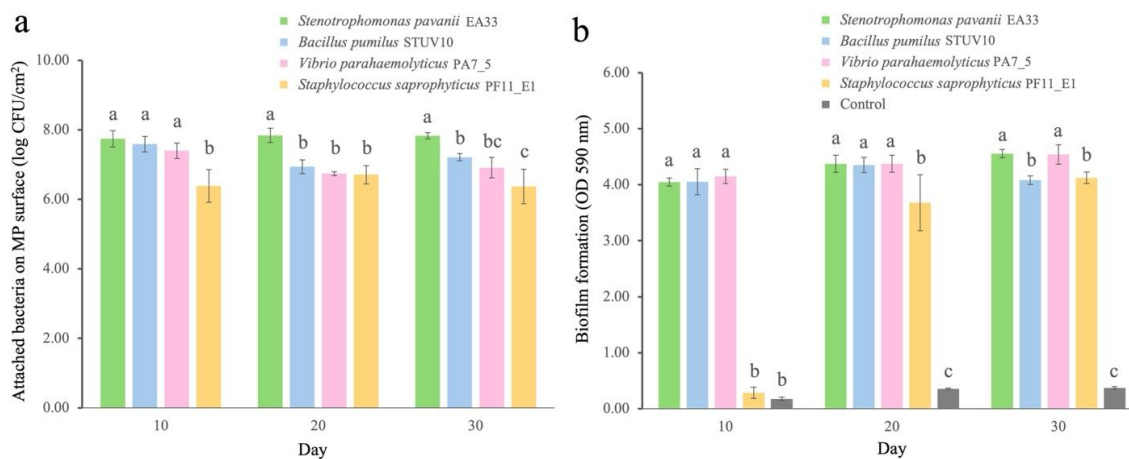


Figure 2

Numbers of attached bacteria (a) and biofilm formation (b) of monoculture on PLA MP surface. Different letters indicate significant difference between bacterial strains at the same sampling time ($p < 0.05$).

Biofilm quantification by four bacterial monocultures over PLA MP surface was evaluated by crystal violet assay (Fig. 2b). Among them, the highest biofilm formation was observed by *V. parahaemolyticus* PA7_5 and *S. pavanii* EA33 after 30 days of incubation, while *B. pumilus* STUV10 and *S. saprophyticus* PF11_E1 produced slightly lower biofilm. These results demonstrated that MP surfaces can be colonized by various microorganisms over time. Previous studies have reported that bacterial biofilm on microplastics can alter their physicochemical properties, such as crystallinity, functional groups, hydrophilicity, and surface morphology, providing suitable niches for microbial colonization.²² Moreover, these aggregates formed by microplastics and microbial biofilms play a crucial role in vertical transport and sedimentation, potentially affecting long-term microplastic fate and diagenetic processes.²³

Based on these results, *S. pavanii* EA33 was selected as the representative plastic-degrading bacteria due to its higher attachment ability and biofilm formation on PLA MP surface than *B. pumilus* STUV10. For the potentially pathogenic bacteria, *V. parahaemolyticus* PA7_5 was selected because it exhibited higher biofilm formation than *S. saprophyticus* PF11_E1. These selected bacteria were used to prepare the co-culture in the following experiment.

Growth and biofilm formation of plastic-degrading and pathogenic bacterial co-culture on PLA microplastics

Figure 3 shows the interaction between *S. pavanii* EA33, a plastic-degrading bacteria, and *V. parahaemolyticus* PA7_5, a potentially pathogenic bacteria, through antagonistic assay, bacterial growth in ZMB medium with PLA MPs, bacterial attachment on PLA MP surfaces, and biofilm formation.

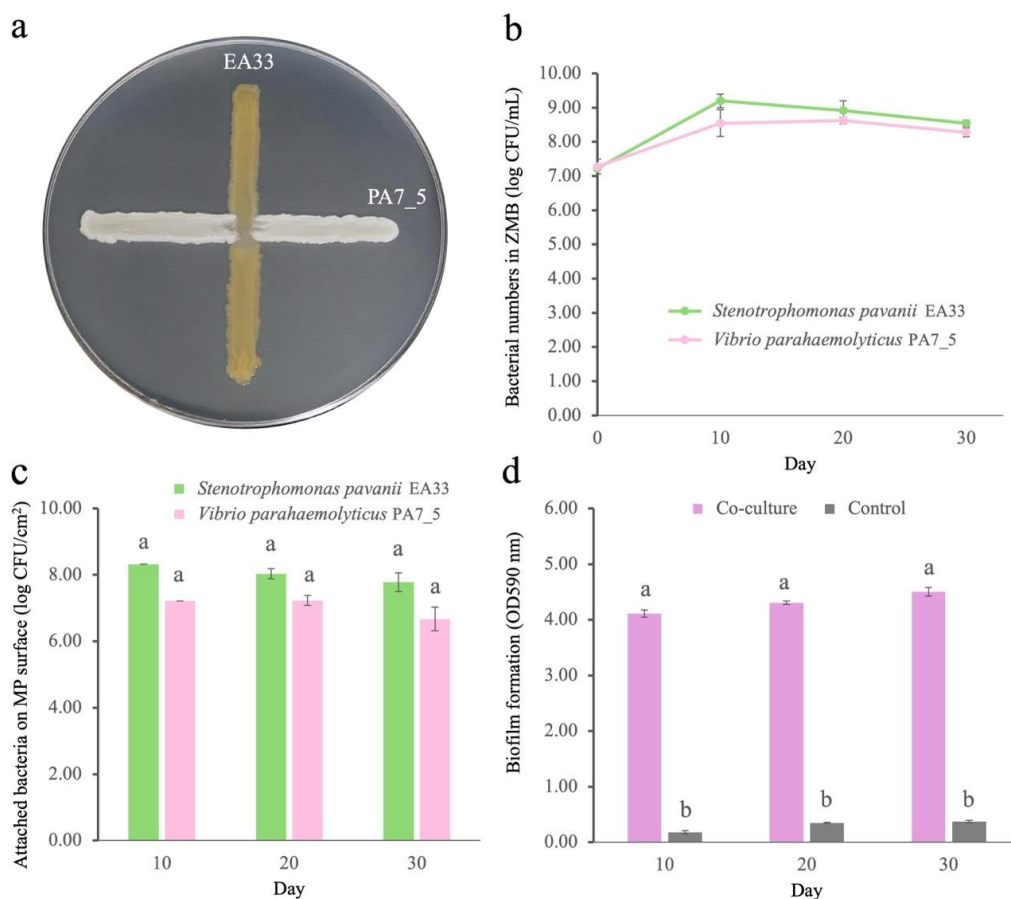


Figure 3

The interaction between co-culture of a plastic-degrading bacteria and a potentially pathogenic bacteria, i.e., antagonistic assay (a), bacterial growth in ZMB with PLA MPs (b), bacterial attachment on PLA MP surfaces (c), and biofilm formation (d). Different letters indicate significant difference between bacterial strains at the same sampling time ($p < 0.05$).

Both strains (*V. parahaemolyticus* PA7_5 and *S. pavanii* EA33) showed no antagonism (Fig. 3a) and grew rapidly in ZMB medium, reaching approximately 9 log CFU/mL by day 10 and remaining stable until day 30 (Fig. 3b). On PLA MP surfaces, both strains successfully colonized and maintained viable populations between 7 and 8 log CFU/cm² throughout 30 days (Fig. 3c). *S. pavanii* EA33 displayed slightly higher viability compared to *V. parahaemolyticus* PA7_5, but both showed strong persistence, demonstrating that PLA MPs provided suitable niches for sustained attachment and growth.

Moreover, when comparing bacterial numbers between co-culture (Fig. 3b) and monoculture in ZMB (Fig. 1a), *V. parahaemolyticus* PA7_5 showed better growth in co-culture (~8 log CFU/mL) than in monoculture (~7 log CFU/mL). This may be because of the incomplete degradation of PLA by *S. pavanii* EA33 that generated PLA oligomers or other breakdown products for *V. parahaemolyticus* PA7_5 to use as an additional carbon source. Such cross-feeding interactions are common in microbial consortia and may explain the enhanced persistence of pathogens in the presence of plastic degraders.

The co-culture had the highest amount of biofilm on day 10, 20, and 30 at an absorbance value of around 4 as showed in Figure 3c. The biofilm formation by co-culture suggested synergistic interactions between the two species in colonizing the microplastic surface. Biofilm formation over plastic is an essential criteria for plastic biodegradation, where plastic-degrading bacteria localizes extracellular degradative enzymes on the PLA MP

surface, leading to enhanced degradation efficiency and protected the bacterial cells from severe hostile environmental condition.¹⁸ Meanwhile, biofilm formation by pathogenic bacteria enhanced the accumulation and provide higher possibilities for transportation of pathogenic bacteria to new habitats.⁷

PLA MP degradation by plastic-degrading and pathogenic bacterial co-culture

Figure 4 shows the degradation of PLA MPs in the co-culture system using weight loss analysis over 30 days of incubation. The co-culture of *S. pavanii* EA33 and *V. parahaemolyticus* PA7_5, degraded 39% PLA MPs in the first 20 days, which was higher than that of *S. pavanii* EA33 alone (Fig. 4a). In addition, PLA MPs showed signs of physical disintegration during incubation (Fig. 4b). The biodegraded PLA MPs showed clear signs of surface erosion, cracking, and fragmentation over time. On day 30, PLA MPs degraded to 65% by the co-culture and showed fragmentation into smaller pieces. In contrast, PLA MPs in the abiotic control retained their original morphology throughout the experiment, with no visible changes.

The weight loss and morphological analyses provide clear evidence that PLA MPs are susceptible to microbial degradation and that the co-culture enhanced this process, particularly during the early stages of incubation. The co-culture of *S. pavanii* EA33 and *V. parahaemolyticus* PA7_5 achieved significantly higher degradation efficiency than the monoculture of *S. pavanii* EA33, suggesting that their interactions facilitated effective colonization and breakdown of the polymer.

These results emphasize the importance of bacterial interactions on the fate of compostable plastics in the environment. Importantly, the findings may help predict the environmental fate of microplastics such as PLA MPs when they are colonized by both potentially pathogenic and plastic-degrading bacteria.

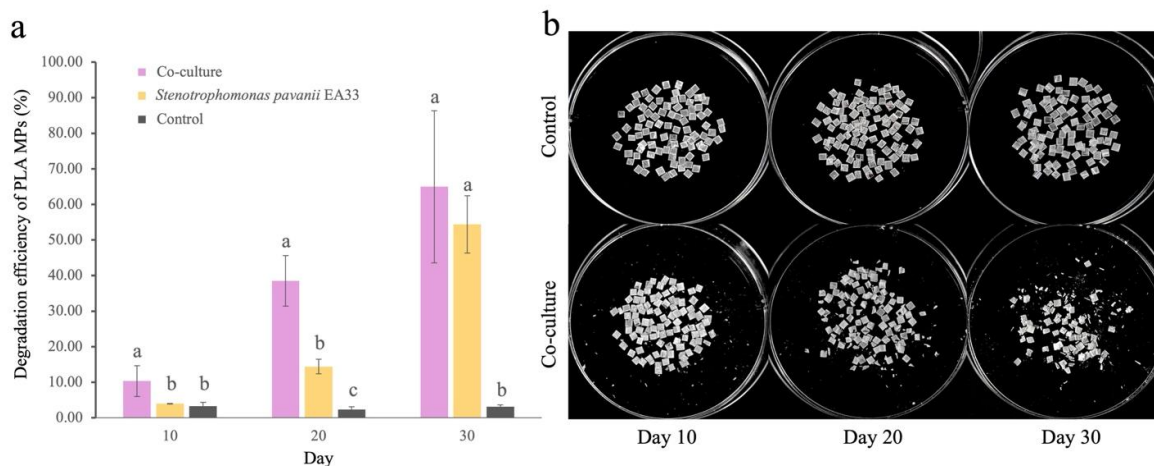


Figure 4

Degradation of PLA MPs by co-culture of *S. pavanii* EA33 and *V. parahaemolyticus* PA7_5 (a). Morphological changes of PLA MPs after 10, 20, and 30-d incubation with co-culture compared with abiotic control (b). Different letters indicate significant difference between bacterial strains at the same sampling time ($p < 0.05$)

Conclusion:

This study demonstrates that PLA MPs enhance growth, colonization, and biofilm formation of both plastic-degrading and potentially pathogenic bacteria. The co-culture of *S. pavanii* EA33 and *V. parahaemolyticus* PA7_5 showed synergistic enhancement, which significantly increased bacterial growth and early-stage degradation at a higher extent than that of



monoculture. The PLA MPs degradation of 39% was achieved from the co-culture within the first 20 days. This study verified the effects of PLA MPs on plastic-degrading and pathogenic bacteria, as well as their interactions on PLA surfaces. These findings can be used for understanding the fate of PLA microplastics and bacterial pathogens in natural ecosystems.

Acknowledgements:

This work was financially supported by Center of Excellence in Microbial Technology for Marine Pollution Treatment (MiTMaPT), Chulalongkorn University.

References:

1. Swetha TA, Bora A, Mohanrasu K, Balaji P, Raja R, Ponnuchamy K, Muthusamy G, Arun A. *Int J Biol Macromol*. 2023;234:123715.
2. Tang B, Zhang L, Salam M, Yang B, He Q, Yang Y, Li H. *Environ Pollut*. 2024;344:123347.
3. Pinaeva LG, Noskov AS. *Sci Total Environ*. 2024;947:174445.
4. Liu X, Ahmad S, Ma J, Wang D, Tang J. *J Hazard Mater*. 2023;460:132343.
5. Wang J, Guo X, Xue J. *Environ Sci Technol*. 2021;55(19):12780–12790.
6. Huang H, Wang F, Ma S, Yuan X, Li J, Chen H, Yuan R, Luo S, Gai N. *Rev Environ Contam Toxicol*. 2024;262(1):15.
7. Kaur K, Reddy S, Barathe P, Oak U, Shriram V, Kharat SS, Govarthanan M, Kumar V. *Chemosphere*. 2022;291:133005.
8. Keszy K, Labrenz M, Scales BS, Kreikemeyer B, Oberbeckmann S. *Microorganisms*. 2021;9(1):76.
9. Deng H, Fu Q, Li D, Zhang Y, He J, Feng D, Zhao Y, Du G, Yu H, Ge C. *J Clean Prod*. 2021;319:128774.
10. Lim JH, Kang JW. *Water Res*. 2024;254:121379.
11. Wang P, Liu J, Han S, Wang Y, Duan Y, Liu T, Hou L, Zhang Z, Li L, Lin Y. *J Hazard Mater*. 2023;442:130045.
12. Wright RJ, Gibson MI, Christie-Oleza JA. *Microbiome*. 2019;7(1):85.
13. Jeyavani J, Al-Ghanim KA, Govindarajan M, Nicoletti M, Malafaia G, Vaseeharan B. *Sci Total Environ*. 2024;918:170499.
14. Joshi G, Goswami P, Verma P, Prakash G, Simon P, Vinithkumar NV, Dharani G. *J Hazard Mater*. 2022;425:128005.
15. Khandare SD, Chaudhary DR, Jha B. *Mar Pollut Bull*. 2021;169:112566.
16. Zadjelovic V, Chhun A, Quareshy M, Silvano E, Hernandez-Fernaund JR, Aguilo-Ferretjans MM, Bosch R, Dorador C, Gibson MI, Christie-Oleza JA. *Environ Microbiol*. 2020;22(4):1356–1369.
17. Monràs-Riera P, Avila C, Ballesté E. *Mar Pollut Bull*. 2024;208:116961.
18. Mistry AN, Kachenchart B, Wongthanoj A, Somwangthanoj A, Luepromchai E. *Polym Degrad Stab*. 2022;202:110051.
19. Maheswaran B, Al-Ansari M, Al-Humaid L, Sebastin Raj J, Kim W, Karmegam N, Mohamed Rafi K. *Chemosphere*. 2023;310:136757.
20. Taghavi N, Singhal N, Zhuang WQ, Baroutian S. *Chemosphere*. 2021;263:127975.
21. Nie Z, Wang L, Lin Y, Xiao N, Zhao J, Wan X, Hu J. *Environ Pollut*. 2022;315:120343.
22. Jia H, Zhang M, Weng Y, Li C. *J Hazard Mater*. 2021;403:123679.
23. Rogers KL, Carreres-Calabuig JA, Gorokhova E, Posth NR. *Limnol Oceanogr Lett*. 2020;5(1):18–36.



INVESTIGATION OF THE ANTIOXIDANT ACTIVITY OF A SELECTED COMPOUND DERIVED FROM *Curcuma comosa* ROXB. IN *Saccharomyces cerevisiae*

Trin Tangnaratchakit¹, Anyaporn Sangkaew¹, Apichart Suksamrarn², Chulee Yompakdee^{1,*}

¹Department of Microbiology, Faculty of Science, Chulalongkorn University, Bangkok 10330, Thailand

²Department of Chemistry and Center of Excellence for Innovation in Chemistry, Faculty of Science, Ramkhamhaeng University, Bangkok 10240, Thailand

*e-mail: chulee.y@chula.ac.th

Abstract:

Excess reactive oxygen species (ROS) can cause oxidative stress, damaging macromolecules and organelles like mitochondria, and contributing to chronic diseases such as cancer, cardiovascular, and neurodegenerative disorders. Exogenous antioxidant supplementation helps neutralize ROS, preventing cellular damage. *Saccharomyces cerevisiae* is an excellent eukaryotic model for studying oxidative stress due to its highly conserved redox-regulatory pathways with higher eukaryotes. *Curcuma comosa* Roxb. is an abundant source of many bioactive compounds. This study aimed to screen and evaluate the antioxidant activity of pure compounds derived from *C. comosa*. Using DPPH and ABTS assays to screen compounds with *in vitro* antioxidant activity, ASCY181 showed the highest antioxidant activity among thirteen compounds tested with 70.13% and 81.9% in the DPPH and ABTS assays, respectively. To further investigate the *in vivo* antioxidant capability, intracellular ROS levels and cell viability in wild-type and $\Delta sod2$ mutant yeast were measured. ASCY181 significantly protected the wild-type strain from H₂O₂-induced oxidative stress by markedly reducing intracellular ROS levels. However, its efficacy was diminished in the $\Delta sod2$ mutant strain, where only a slight reduction in ROS levels was observed. Taken together, our findings indicate that *SOD2* is crucial for the protective role of ASCY181 against oxidative stress. Nonetheless, whether ASCY181 engages additional mechanisms contributing to its antioxidant activity remains to be investigated.

Introduction:

Reactive oxygen species (ROS) are small molecules produced by the incomplete one-electron reduction of oxygen, are typically extremely reactive, and unstable. ROS encompass superoxide, peroxide, hydroxyl radicals, and singlet oxygen, which are generated during the metabolic process in cells.¹ Furthermore, several environmental factors, such as pollution, tobacco smoke, industrial chemicals, and ultraviolet (UV) radiation, possess the potential to induce the production of ROS.² Excess abundances of ROS can provoke oxidative stress, leading to damage to macromolecules such as nucleic acids, proteins, lipids, membranes, and organelles such as mitochondria.³⁻⁴ Oxidative stress results from an imbalance between free radicals and the ability of antioxidant defense systems and cellular repair mechanisms. It is linked to various chronic diseases, including cardiovascular diseases, cancer, neurodegenerative disorders, and other age-related conditions.⁵ Numerous antioxidant defense mechanisms have been reported to mitigate the impact of free radicals, hence alleviating oxidative-mediated cellular damage.⁶ Exogenous antioxidant supplementation is crucial for neutralizing free radical reactions, thereby averting cellular damage.⁷ Bioactive compounds obtained from plant extracts function as common antioxidant agents. Quercetin is an antioxidant flavonoid that is naturally present in various fruits and vegetables. In numerous model species, it can safeguard cells from oxidative stress by decreasing apoptotic and oxidative stress.⁶

The budding yeast *Saccharomyces cerevisiae* serves as an impressive eukaryotic model organism for investigating oxidative stress.⁸ It is a simple, accessible, and genetically

manipulable organism, with roughly 30% of human disease-related genes having yeast orthologues.⁹ *S. cerevisiae* possesses comparable antioxidant defense mechanisms that closely mirror those of mammals. Numerous fundamental cellular pathways, especially those related to oxidative stress response, are remarkably well conserved between yeast and humans, making *S. cerevisiae* an invaluable model for elucidating the molecular basis of oxidative stress and related physiological processes.¹⁰ Yeast enzymatic antioxidant systems, including superoxide dismutase (SOD), catalase (CAT), and glutathione peroxidase (GPX), serve as essential defenses for the scavenging of ROS.¹¹ SODs convert superoxide into hydrogen peroxide (H₂O₂), which is then transformed into water and oxygen by CAT or GPX. Eukaryotic cells typically possess two evolutionarily distinct types of superoxide dismutases (SODs) that function to neutralize superoxide. A copper/zinc-dependent superoxide dismutase (SOD1) largely localized in the cytoplasm and a manganese-dependent superoxide dismutase (SOD2) found in the mitochondrial matrix. SOD2 is located inside the superoxide-generating mitochondrial respiratory chain, and its deficiency leads to substantial consequences, including increased oxidative damage, shortened lifespan, and decreased resistance to various environmental stressors.¹² Any genetic alteration, such as deletion or mutation in the yeast model, contributes to locating specific gene targets for potential therapeutic molecules within oxidative stress response pathways.⁶

Curcuma comosa Roxb, also known as Waan-Chak-Motluk, a member of the *Zingiberaceae* family, is a native Asian plant that is often seen in Malaysia, Indonesia, and Thailand.¹³ It has been extensively employed in Thai traditional medicine to alleviate postpartum uterine hemorrhage. Its estrogenic activity has been well-characterized in both *in vitro* and *in vivo* models.¹⁴ The most specific biological activities have been investigated for their influence, such as anti-inflammatory and antioxidant.¹⁵⁻¹⁷

Therefore, this study focuses on screening and evaluating the antioxidant activity of the compounds derived from *C. comosa* using the DPPH and ABTS assays. A compound with the highest antioxidant activity was assessed cellular toxicity and protective effect against oxidative stress generated by H₂O₂ in *S. cerevisiae*.

Methodology:

1. Screening of the compounds from *C. comosa* for *in vitro* antioxidant activity using DPPH assay

Thirteen compounds kindly gifted by Professor Dr. Apichart Suksamrarn, Department of Chemistry, Faculty of Science, Ramkhamhaeng University, Bangkok, Thailand, were screened. All test compounds were dissolved in dimethyl sulfoxide (DMSO) to obtain a concentration of 10 mg/ml as a stock solution.

The antioxidant properties of test compounds were assessed by the DPPH radical scavenging assay as described by Blois (1958).¹⁸ The compound at a concentration of 0.1 mg/ml was incubated with the DPPH (Sigma-Aldrich, USA) solution (0.06 mM in methanol) for 30 minutes. The reaction was measured at 515 nm using a microplate reader (Perkin Elmer, USA). The antioxidant activity was determined using the following equation 1.

$$\text{DPPH scavenging activity (\%)} = [(A-B) \div A] \times 100 \quad (1)$$

where 'A' and 'B' are absorbances of the DPPH without and with the compound, respectively. In this study, the antioxidant activity of ascorbic acid was used as the positive control. All samples undergo tested in triplicate.



2. Screening of the compounds from *C. comosa* exhibiting *in vitro* antioxidant activity using ABTS assay

The ABTS assay was conducted following the method described by Re et al. (1999) with some modifications by mixing 7 mM ABTS (AK Scientific, Inc., USA) with 2.45 mM potassium persulfate in equal volumes.¹⁹ The mixture solution was incubated in the dark at room temperature for 16 hours and subsequently diluted to an absorbance of 0.7 ± 0.02 at 734 nm with distilled water. The test compounds (0.1 mg/ml) were incubated with the diluted ABTS^{•+} solution for 10 minutes. The absorbance was measured using a microplate reader (Perkin Elmer, USA). The antioxidant activity was calculated as described in the DPPH assay. Ascorbic acid was used as a positive control. All samples undergo tested in triplicate.

3. Cytotoxicity test of the selected compound in yeast

S. cerevisiae wild-type strain BY4741 (*MATa his3Δ1 leu2Δ0 met15Δ0 ura3Δ0*) was used in this experiment. Yeast cells were cultured in yeast peptone dextrose (YPD) liquid medium (2% peptone, 2% glucose, and 1% yeast extract). Overnight cultures were adjusted to an OD 660 nm = 0.2, transferred to a 96-well plate in synthetic defined (SD) liquid medium with and without the candidate compound at various concentrations in ranging from 0.25 to 100 μg/ml, and incubated at 30°C for 48 hours to reach the stationary phase. The effect of the selected compound on cytotoxicity was monitored by determining the viable cells with the methylene blue staining method. The numbers of viable (seen as bright cells) and dead cells (stained blue) were counted with a microscope. A total of 200-300 cells were counted in order to increase the accuracy of the cell count. The percentage of viable cells (% viability) was calculated using the following equation 2.²⁰ Then, cell viability of the treated cells was normalized and represented as a percentage with respect to the untreated control. The appropriate concentration of the selected compound was used in further experiments.

$$\text{The percentage of viable cells (\% viability)} = [A \div (A+B)] \times 100 \quad (2)$$

where 'A' and 'B' are the number of viable cells and the number of dead cells, respectively.

4. Measurement of the intracellular ROS

2',7'-dichlorodihydrofluorescein-diacetate (DCFH₂-DA) (Sigma-Aldrich, USA), was the most widely used fluorogenic probe for the detection of oxidative stress, used as described in van der Laan et al. (2020).²¹ Firstly, the *S. cerevisiae* BY4741 wild-type and the isogenic *Δsod2* mutant strain were inoculated in YPD medium with and without the candidate compound at an appropriate concentration. For the untreated control, cells were inoculated in YPD medium with 1% DMSO at final concentration. Following incubation at 30°C overnight, the cells were undergoing treatment with an appropriate concentration of H₂O₂ for 1 hour. Thereafter, the yeast cell suspension was incubated with DCFH₂-DA at 30°C for 30 minutes in the dark. The cell pellet was collected and then resuspended in 100 μl of 0.1 M phosphate buffer (pH 7.4). The ROS level was measured using a microplate reader (Perkin Elmer, USA) using fluorescence excitation and emission at 504 nm and 525 nm. The positive control for this experimental analysis was 8 μg/ml of quercetin.

5. Determining the yeast cell survival against H₂O₂-induced oxidative stress

S. cerevisiae BY4741 wild-type or isogenic *Δsod2* strain was inoculated in YPD medium, with and without treatment of the candidate compound with an appropriate concentration at 30°C, 200 rpm. For the untreated control, cells were inoculated in YPD medium with 1% DMSO at final concentration. After overnight incubation, cell suspension was aliquoted and treated with an appropriate concentration of H₂O₂ for 1 hour. Thereafter, the cell pellet was

collected and then resuspended in 0.1 M phosphate buffer (pH 7.4). Then, cell suspension was diluted by 10-fold serial dilution with 0.1 M phosphate buffer (pH 7.4). The qualitative analysis of cell viability was conducted via spot assay. The yeast cell suspension (5 μ l) of each dilution was spotted on YPD agar plate, and after incubation for 2 days at 30°C, the yeast colonies on the plate were visualized.²² Quercetin at a concentration of 8 μ g/ml was used as a positive control. All the experiments were independently performed in triplicate.

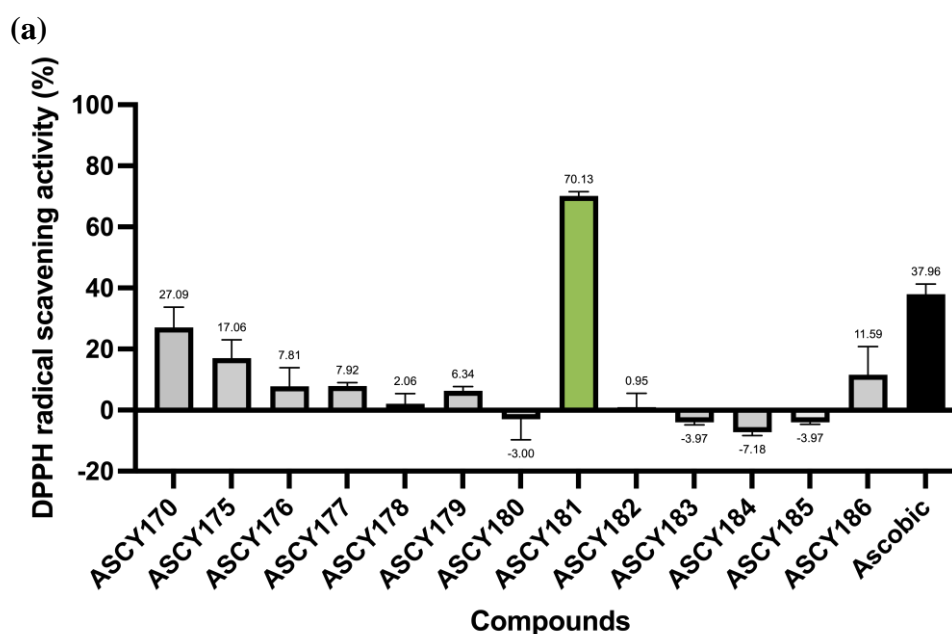
6. Statistical analysis

All experiments were conducted in triplicate. The results were reported as means \pm standard errors. Statistical analyses were performed with GraphPad Prism version 10.6.0 (GraphPad Inc., USA). One-way analysis of variance (ANOVA) was applied to test for significant differences.

Results and Discussion:

1. The ASCY181 compound exhibiting potent antioxidant activity *in vitro*

This study utilized two widely used antioxidant assays, 2,2-diphenyl-1-picrylhydrazyl (DPPH) and 2,2'-azino-bis-3-ethylbenzthiazoline-6-sulphonic acid (ABTS), to assess the radical scavenging properties of the test compounds. Ascorbic acid, known as an antioxidant compound, was utilized as a positive control.²³ Thirteen bioactive compounds-derived from *C. comosa*, were screened using the DPPH and ABTS assays. The results showed that a tested compound ASCY181 had the strongest antioxidant property, with 70.13% and 81.9% in the DPPH and ABTS assays, respectively (Figure 2). It effectively neutralizes free radicals within hydrophilic and lipophilic systems, as demonstrated in the hydrophilic system of ABTS assay, as well as in hydrophobic system in the DPPH experiment.²⁴ Hence, ASCY181 was selected for further investigation of its potential in this work.



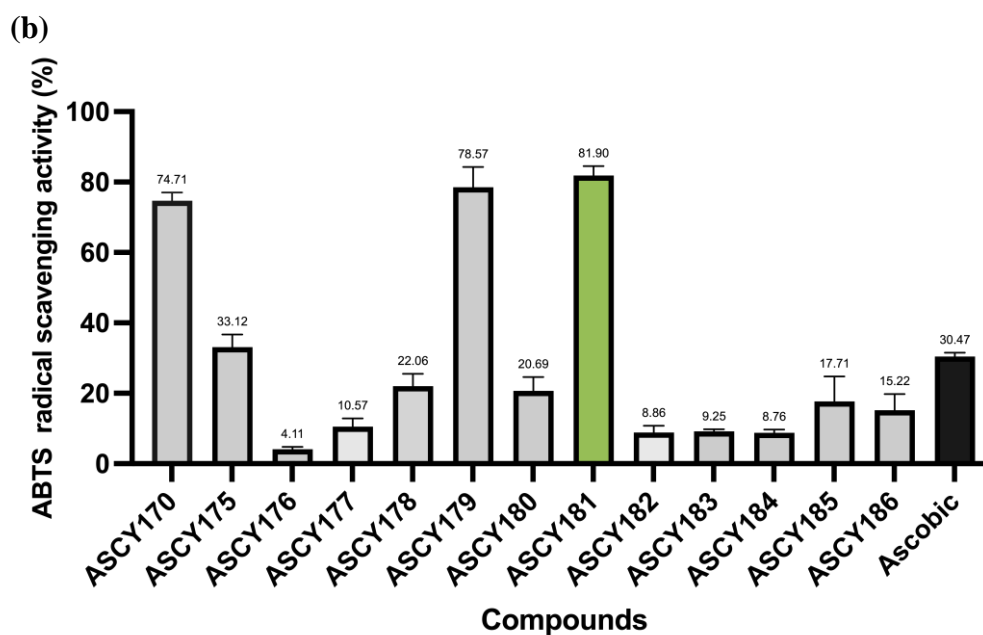


Figure 1.

In vitro free radical scavenging activity of compounds derived from *C. comosa*. Test compounds were determined in both DPPH (a) and ABTS (b) assays. Each compound was tested at 0.1 mg/ml. Ascorbic acid (0.03 mg/ml) was used as a positive control. All the experiments were conducted in triplicates.

2. Effect of ASCY181 on the cell viability of *S. cerevisiae*

To determine the optimal concentration of ASCY181 with no detectable cytotoxicity, *S. cerevisiae* BY4741 wild-type strain was cultivated in the absence and presence of the ASCY181 compound at various concentrations ranging from 0.25 to 100 $\mu\text{g/ml}$ for overnight. The cell viability was determined using the methylene blue staining method. As shown in Figure 2, there was no significant difference in cell viability was observed at concentrations of 0.25, 0.5, and 1 $\mu\text{g/ml}$ of ASCY181 compared with the untreated control. Although treatment with ASCY181 at 4 and 20 $\mu\text{g/ml}$ resulted in a slight decrease in cell viability, the reduction was not statistically significant. However, at a concentration of 100 $\mu\text{g/ml}$, treatment with ASCY181 resulted in a significant decrease in cell viability compared with the untreated control. Therefore, a concentration of 1 $\mu\text{g/ml}$ of ASCY181 was chosen for subsequent experiments.

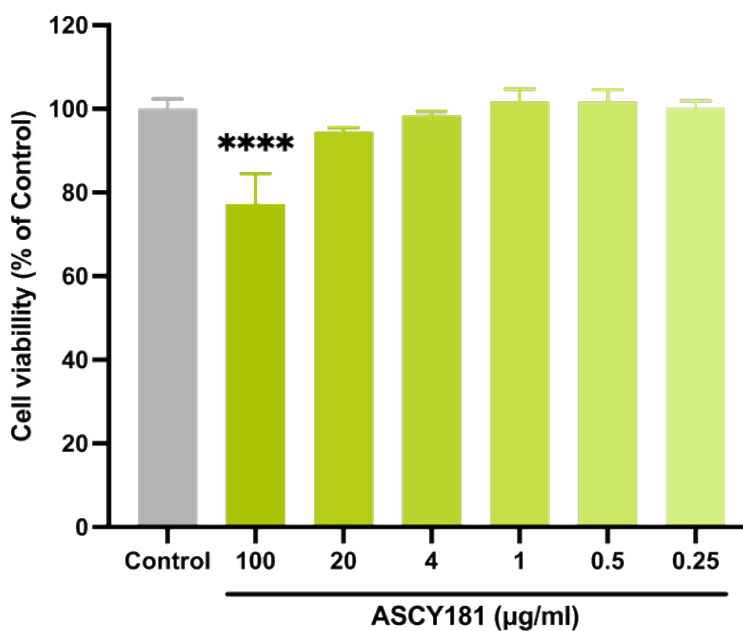


Figure 2.

The effect of the ASCY181 on cell viability of *S. cerevisiae* BY4741 wild-type strain. Viability of yeast cells was determined using the methylene blue staining method. The experiment was performed in triplicates. The analysis was performed by using GraphPad Prism, one-way analysis of variance (ANOVA), and Dunnett's multiple comparison test. All treatments were compared with untreated control. **** $p < 0.0001$.

3. The protective effect of the ASCY181 compound against H₂O₂-induced oxidative stress in *S. cerevisiae*

From the screening of the antioxidant activity of compounds derived from *C. comosa* using the *in vitro* DPPH and ABTS assays, the results showed that ASCY181 had the strongest antioxidant property in both the DPPH and ABTS assays. Therefore, the protective effect of the ASCY181 against H₂O₂-induced oxidative stress in yeast cells was assessed. *S. cerevisiae* wild-type BY4741 and its isogenic mutant lacking the gene coding for manganese superoxide dismutase (MnSOD) ($\Delta sod2$ strain) were investigated. *SOD2* was chosen for investigation due to its crucial role as an antioxidant enzyme that is essential for neutralizing ROS. A working concentration of H₂O₂ was determined by performing a dose-response experiment. Figure 3a and 3b showed that the concentration of H₂O₂ at 6-8 mM significantly elevated intracellular ROS levels in both strains as compared to their respective control (0 mM H₂O₂). Therefore, the concentration of H₂O₂ at 6 mM was chosen for use in further experiments.

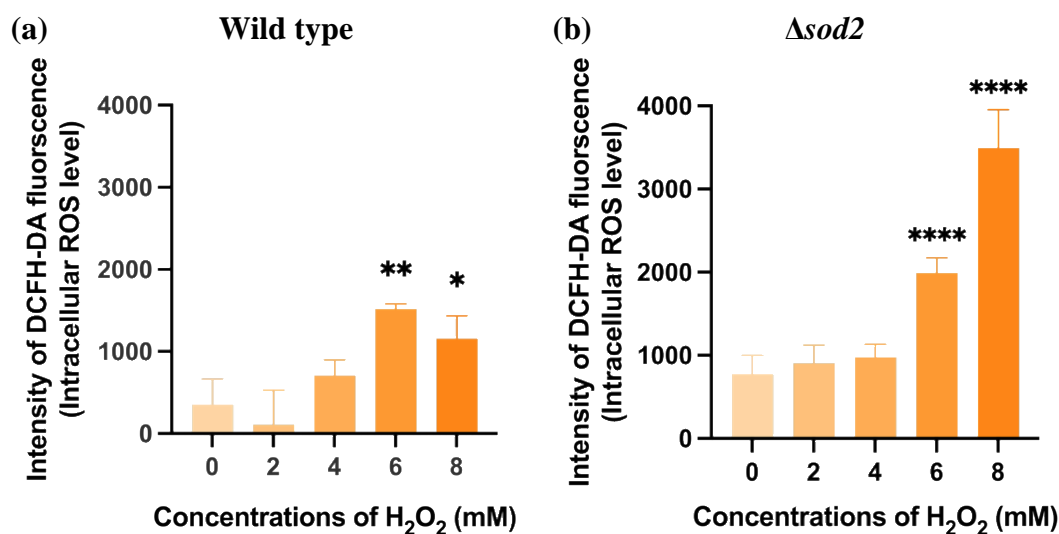


Figure 3.

The effect of H₂O₂ on intracellular ROS level in *S. cerevisiae*.

S. cerevisiae BY4741 wild-type (a) and $\Delta sod2$ strains (b) were treated with H₂O₂ at various concentrations. The intracellular ROS level was measured by DCFH₂-DA. The experiment was performed in triplicates. The analysis was performed by using GraphPad Prism, one-way analysis of variance (ANOVA), and Dunnett's multiple comparison test was applied to test for significant differences. All treatments have been compared with 0 mM of H₂O₂ treatment.

* $p < 0.05$, ** $p < 0.01$, and **** $p < 0.0001$.

To determine the protective effect of ASCY181 against H₂O₂-induced oxidative stress, DCFH₂DA assay and a spot assay using an agar plate were performed. H₂O₂-induced oxidative stress resulted in a significant elevation of intracellular ROS levels in both wild-type and the $\Delta sod2$ mutant strains relative to their respective non-stressed controls (Figure 4a and 4c). However, treatment with ASCY181 at 1 μ g/ml markedly reduced ROS accumulation in the wild-type strain ($p < 0.0001$) compared with the untreated stressed control (Figure 4a), whereas only a slight but significant reduction ($p < 0.01$) was observed in the mutant strain (Figure 4b).

These results indicate that the ASCY181 compound can efficiently counter H₂O₂-induced oxidative stress and *SOD2* is important for the ability of the ASCY181 compound to resist H₂O₂-induced oxidative stress. Consistently, spot assay revealed that ASCY181 improved cell viability under H₂O₂-induced oxidative stress in the wild-type strain (Figure 4c), while only a subtle improvement was observed in the $\Delta sod2$ strain (Figure 4d). The results demonstrated that *SOD2* may represent a direct or indirect molecular target of ASCY181. Notably, treatment of the $\Delta sod2$ mutant strain with ASCY181 under oxidative stress led to a slight but significant decrease in intracellular ROS levels relative to the untreated stressed control. This suggests that ASCY181 may exert its protective effects not only through *SOD2* but also via additional mechanisms including modulation of cellular signaling pathways, regulation of transcription factors, regulation of mitochondrial ROS production, energy metabolism, and proteostasis.²⁵

Together, these results support the role of ASCY181 in alleviating oxidative stress. Thus, further investigation is required to elucidate the protective effect of ASCY181 against H₂O₂-induced oxidative stress in other mutant strains. For instance, the investigation on yeast mutants that lack enzymes involved in the antioxidant pathway, such as catalase (CAT) and glutathione peroxidase (GPX), which are located downstream of *SOD2*.

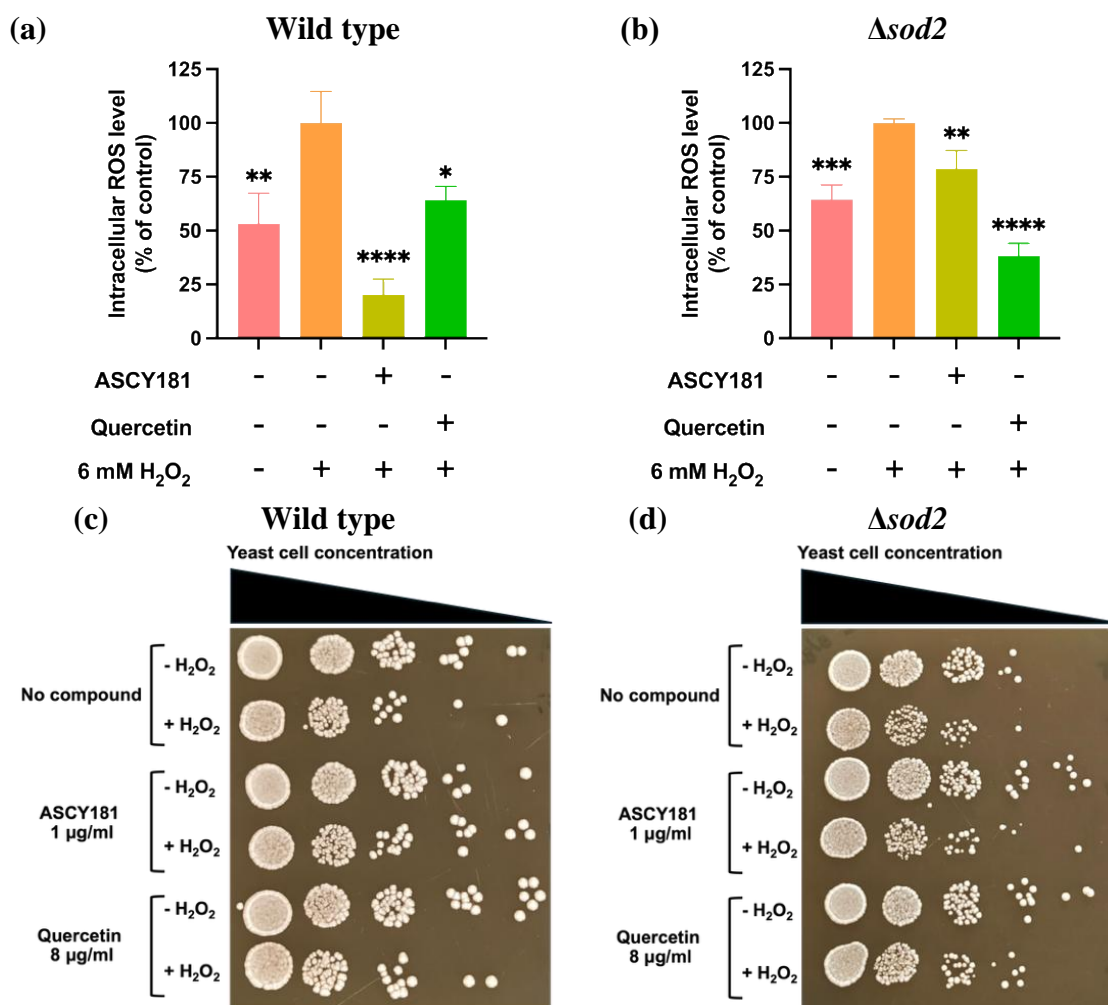


Figure 4.

In vivo investigation of the protective effects of the ASCY181 on H₂O₂-induced oxidative stress. Relative intracellular ROS level in *S. cerevisiae* BY4741 wild-type (a) and $\Delta sod2$ strain (b). The cell survival of yeast wild-type (c) and $\Delta sod2$ strain (d) against H₂O₂-induced oxidative stress. The yeast wild type and $\Delta sod2$ strain were pre-treated with ASCY181 at the concentrations of 1 μg/ml and then incubated with 6 mM of H₂O₂. Quercetin at 8 μg/ml was used as the positive control. Independent replicates were performed to validate the results.

The analysis was performed by using GraphPad Prism, one-way analysis of variance (ANOVA), and Dunnett's multiple comparison test. All treatments have been compared with untreated control, treated with H₂O₂. * $p < 0.05$, ** $p < 0.01$, *** $p < 0.001$, and **** $p < 0.0001$.

Conclusion:

This study identified the compound displaying *in vitro* antioxidant activity. From screening, the ASCY181 showed the greatest antioxidant activity with 70.13% and 81.9% measured by DPPH and ABTS assays, respectively. ASCY181 exhibited a potent protective effect against oxidative stress induced by H₂O₂ in the wild-type strain, as observed by elevating intracellular ROS levels and alleviating growth defect. As the yeast $\Delta sod2$ mutant, the efficacy of the ASCY181 compound to combat H₂O₂-induced oxidative stress was diminished compared to those in wild-type strain. These findings indicate that *SOD2* plays an important role for the ability of ASCY181 compound to resist H₂O₂-induced oxidative stress and could potentially act as a direct or indirect molecular target of the ASCY181 compound.



However, the additional mechanisms of the ASCY181 compound on antioxidant activity required further investigated.

Acknowledgements:

This research was supported by the 90th Anniversary of Chulalongkorn University Scholarship under the Ratchadapisek Somphot Endowment Fund.

References:

1. Uttara B, Singh AV, Zamboni P, Mahajan RT. *Curr Neuropharmacol*. 2009;7(1):65-74.
2. Phaniendra A, Jestadi DB, Periyasamy L. *Indian J Clin Biochem*. 2015;30(1):11-26.
3. Belinha I, Amorim MA, Rodrigues P, de Freitas V, Moradas-Ferreira P, Mateus N, Costa V. *J Agric Food Chem*. 2007;55(6):2446-2451.
4. Bhattacharyya A, Chattopadhyay R, Mitra S, Crowe SE. *Physiol Rev*. 2014;94(2):329-354.
5. Cheeseman KH, Slater TF. *Br Med Bull*. 1993;49(3):481-493.
6. Alugoju P, Periyasamy L, Dyavaiah M. *Lett Appl Microbiol*. 2020;71(3):272-279.
7. Lobo V, Patil A, Phatak A, Chandra N. *Pharmacogn Rev*. 2010;4(8):118-126.
8. Gershon H, Gershon D. *Mech Ageing Dev*. 2000;120(1-3):1-22.
9. Mager WH, Winderickx J. *Trends Pharmacol Sci*. 2005;26(5):265-273.
10. Khurana V, Lindquist S. *Nat Rev Neurosci*. 2010;11(6):436-449.
11. Jamieson DJ. *Yeast*. 1998;14(16):1511-1527.
12. Luk E, Carroll M, Baker M, Culotta VC. *Proc Natl Acad Sci U S A*. 2003;100(18):10353-10357.
13. Hemtong W, Chuncharunee A, Sreekanth GP. *Future Pharmacol*. 2022;3(1):1-13.
14. Chuncharunee A, Khosuk P, Naovarat R, Kaliyadan F, Sreekanth GP. *Saudi J Biol Sci*. 2021;28(10):5937-5946.
15. Jariyawat S, Kigpituck P, Suksen K, Chuncharunee A, Chaovanalikit A, Piyachaturawat P. *J Nat Med*. 2009;63(4):430-436
16. Sodsai A, Piyachaturawat P, Sophasan S, Suksamrarn A, Vongsakul M. *Int Immunopharmacol*. 2007;7(4):524-531.
17. Suksen K, Charaslertrangsi T, Noonin C, Jariyawat S, Devakul Na Ayutthaya W, Suksamrarn A, Tuchinda P, Piyachaturawat P. *Pharm Biol*. 2016;54(5):853-862.
18. Blois MS. *Nature*, 1958;181:1199-1200.
19. Re R, Pellegrini N, Proteggente A, Pannala A, Yang M, Rice-Evans C. *Free Radic Biol Med*. 1999;26(9-10):1231-1237.
20. Painting K, Kirsop B. *World J Microbiol Biotechnol*. 1990;6(3):346-347.
21. van der Laan KJ, Morita A, Perona-Martinez FP, Schirhagl R. *Nanomaterials (Basel)*. 2020;10(2):372.
22. Spencer J, Phister TG, Smart KA, Greetham D. *BMC Res Notes*. 2014;7:151.
23. Njus D, Kelley PM, Tu YJ, Schlegel HB. *Free Radic Biol Med*. 2020;159:37-43.
24. Granados-Guzmán G, Salazar-Aranda R, Garza-Tapia M, Castro-Ríos R, Waksman de Torres N. *Curr Anal Chem*. 2017;13(6):499-507.
25. Lennicke C, Cochemé HM. *Mol Cell*. 2021;81(18):3691-3707.



***Cratoxylum formosum* EXTRACT ATTENUATES INFLAMMATION IN LPS-ACTIVATED MACROPHAGES BY REDUCING IL-6 EXPRESSION**

Tuangtong Vongpipatana,^{1,*} Talayboon Pooyoi,¹ Kotchakorn Srikhong¹

¹Department of Biochemistry, Faculty of Science, Kasetsart University, 50 Ngamwongwan Rd, Lat Yao, Chatuchak, Bangkok 10900, Thailand

*e-mail: fscittv@ku.ac.th

Abstract:

Inflammation is the defensive process against harmful stimuli. Although inflammation is beneficial for body protection, long-lasting inflammation is the cause of various diseases. Therefore, inflammation must be controlled for an appropriate period of time. It is well known that plants are an important source of bioactive compounds, which have many activities, including antioxidant activity, antimicrobial activity, and anti-inflammatory activity. *Cratoxylum formosum* is a native plant in Southeast Asia, and it has been reported that the ethanolic extract has bioactive compounds for reducing free radicals. In this study, we aim to reveal the effects of aqueous extract from fresh *C. formosum* leaves on anti-inflammation using lipopolysaccharide (LPS)-activated Macrophages as a model for inflammation. We found that crude *C. formosum* extract at 15.63, 62.50, and 250.0 µg/ml significantly decreased nitric oxide production in LPS-activated macrophages in a dose-dependent manner. Quantitative RT-PCR analysis was performed to determine the expression level of pro-inflammatory cytokines. The expression of IL-6 mRNA was inhibited in LPS-activated macrophages treated with 250.0 µg/ml of *C. formosum* crude extract. These results indicate that the aqueous extract from fresh *C. formosum* leaves is able to reduce inflammation and provide information for an alternative way to treat inflammation-associated diseases in the future.

Introduction:

Inflammation is an immunological process for defending the body against pathogens, injury, and other harmful stimuli. Acute inflammation is the inflammation that immediately responds to the injurious causes and ends with resolution. Suppose the acute inflammation prolongs and fails to resolve. In that case, it is a transition from acute to chronic inflammation, leading to tissue damage, fibrosis, and loss of organ function as seen in many diseases such as atherosclerosis, heart failure, and asthma [1-3].

During acute inflammation, inflammatory cells, especially macrophages, are activated, producing nitric oxide from inducible nitric oxide synthase (iNOS). Moreover, it has been reported that iNOS expression is found in chronic inflammatory diseases [10], suggesting that nitric oxide is involved in the pathogenesis of chronic inflammation.

In addition to nitric oxide production, activated macrophages produce inflammatory mediators including interleukin 6 (IL-6), interleukin 1 β (IL-1 β), and tumor necrosis factor α (TNF α). IL-6, an inflammatory cytokine, plays an important role in the inflammatory response in many aspects. For example, IL-6 induces fever, activates acute-phase protein production, and induces the maturation of B cells into plasma cells [4]. Because of the several functions of IL-6, IL-6 production is tightly controlled, and aberrant expression of IL-6 is a cause of various diseases such as chronic inflammatory diseases, autoimmune diseases, and cancer [4-6]. For instance, it has been reported that the increase in IL-6 levels was found in serum and synovial fluid of rheumatoid arthritis (RA) patients [5, 7], and the IL-6 levels correlate with the increased activity of RA disease [8-9]. Therefore, regulation of IL-6 expression is a key target for the treatment of inflammation and inflammation-associated diseases.



Since ancient times, plants have been the primary source of bioactive compounds that have been used in traditional medicine. Many plant compounds have anti-inflammatory activity. For instance, quercetin is a flavonoid found in fruits and vegetables such as apples, berries, grapes, onions, and Ginkgo biloba [11-13], which contains anti-inflammatory ability by decreasing the expression of IL-6, IL-1 β , and TNF α [14].

Cratoxylum formosum is a plant grown in Southeast Asia and used by locals as a side dish. It has been revealed that the ethanolic extract of *C. formosum*, containing chlorogenic acid, has gastroprotective activity due to its antioxidant activity [15]. Furthermore, it has been reported that the methanolic extract partitioning with dichloromethane of stem bark from *C. formosum* reduced the expression of IL-1 β and TNF α in macrophages derived from U397 cells [16]. However, the anti-inflammatory effects of aqueous extract from fresh leaves on IL-6 expression are still unknown. In this study, we aim to investigate the inhibitory effects of *C. formosum* aqueous extract on IL-6 mRNA expression in lipopolysaccharide (LPS)-activated macrophages, RAW 264.7 cells, to gain insights into its anti-inflammatory mechanisms.

Methodology:

Plant extraction preparation

The aqueous extract was prepared from fresh *C. formosum* leaves, harvested from a local field in Rayong Province, Thailand. The 500 g of leaves were cleaned with water, chopped, and boiled with 2 L of water for 30 min. After filtration, the crude extract was lyophilized and stored at -20°C until used.

Cell culture

Mouse macrophage, Raw 264.7 cells, were cultured in complete media containing DMEM (Gibco) with 10% fetal bovine serum (Gibco) and 1% antibiotic penicillin–streptomycin (Gibco) at 37°C with 5% CO₂ and were maintained until 70–80% confluence before being used.

Nitric oxide measurement

RAW 264.7 cells were seeded in a 96-well plate for 24 hours. After incubation with crude *C. formosum* extract at a final concentration of 15.63, 62.50, and 250.0 μ g/ml for 2 hours, cells were treated with 2 μ g/ml of lipopolysaccharide (LPS) overnight. Griess Reagent was used to examine nitric oxide produced by LPS-activated cells.

Quantitative RT-PCR (qRT-PCR) analysis

Total RNA was isolated from RAW 264.7 cells by TRIzol reagent (Thermo Fisher Scientific) and subsequently converted to cDNA using an iScript™ Reverse Transcription Supermix for RT-qPCR kit (BIO-RAD) according to the manufacturer's protocol. The mRNA expression of IL-6 was quantified with SYBR green-based qRT-PCR using iTaq™ Universal SYBR® Green Supermix (Bio-Rad) on a CFX Connect Real-Time PCR Detection System (Bio-Rad) and was calculated by the $\Delta\Delta$ Ct method. The mRNA level was normalized to that of β -actin. The sequences of the specific primers were as follows: *IL-6* Forward 5'-ACCGCTATGAAGTTCCTCTCTGCA-3', *IL-6* Reverse 5'-AAGCCTCCGACTTGTGAAG TGGT-3'; *β -actin* Forward 5'-GTGCTATGTTGCTCTAGACTTCG-3' and *β -actin* Reverse 5'-ATGCCACAGGATTCCATACC-3'.

Statistical analyses

Statistical analyses were performed using GraphPad Prism 10 software. Results were displayed as the mean \pm standard error of three independent experiments' mean (SEM).

Results and Discussion:

In this study, LPS, found on the outer membrane of Gram-negative bacteria, was used to activate an inflammatory response in macrophages [17]. Given that nitric oxide, a crucial inflammatory mediator, is highly expressed in activated macrophages [18], we examined the inhibition of nitric oxide production in LPS-activated RAW 264.7 cells treated with crude *C. formosum* extract at 15.63, 62.50, and 250.0 $\mu\text{g/ml}$. The results revealed that treatment of crude *C. formosum* extract significantly inhibited nitric oxide production in a dose-dependent manner (**Figure 1**). These findings indicated that crude *C. formosum* extract contained anti-inflammatory ability. Consistent with previous reports, the extracts from dried *C. formosum* leaves, collected from Vietnam, contained flavonoids including quercetin, isoquercitrin, hyperin, and quercitrin that were able to decrease nitric oxide production in LPS-activated RAW 264.7 cells by suppressing the expression of iNOS [19]. The inhibition of iNOS expression has also been reported in the *C. formosum* spp. pruniforum root extract [20].

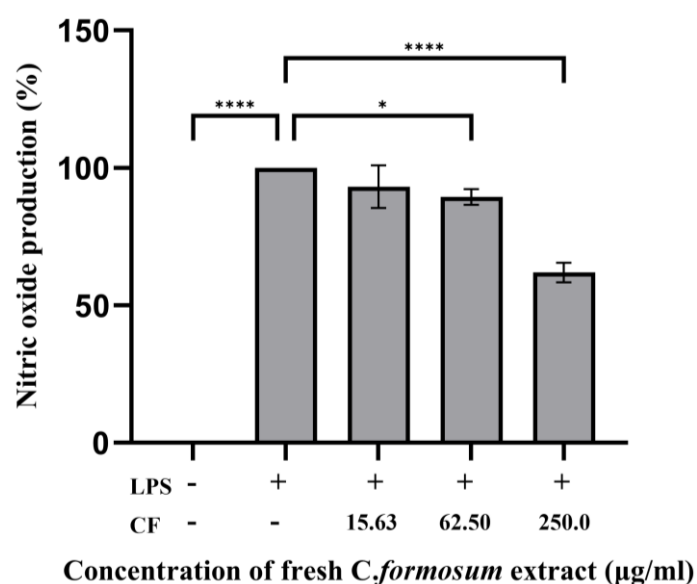


Figure 1

Inhibition of nitric oxide production in macrophages treated with various fresh *C. formosum* crude extract concentrations. Bars represent the percentage \pm SEM of three independent experiments (one-way ANOVA with Dunnett's multiple comparisons test, ** $p < 0.0021$, *** $p < 0.0002$, and **** $p < 0.0001$ versus the control group).

To test whether fresh *C. formosum* crude extract inhibited pro-inflammatory cytokine expression in activated macrophages, we measured the expression of *IL-6* mRNA. As shown in **Figure 2**, LPS activation significantly increased *IL-6* mRNA level, and *C. formosum* crude extract treatment at concentration 250.0 $\mu\text{g/ml}$ decreased *IL-6* mRNA expression compared to LPS-activated cells.

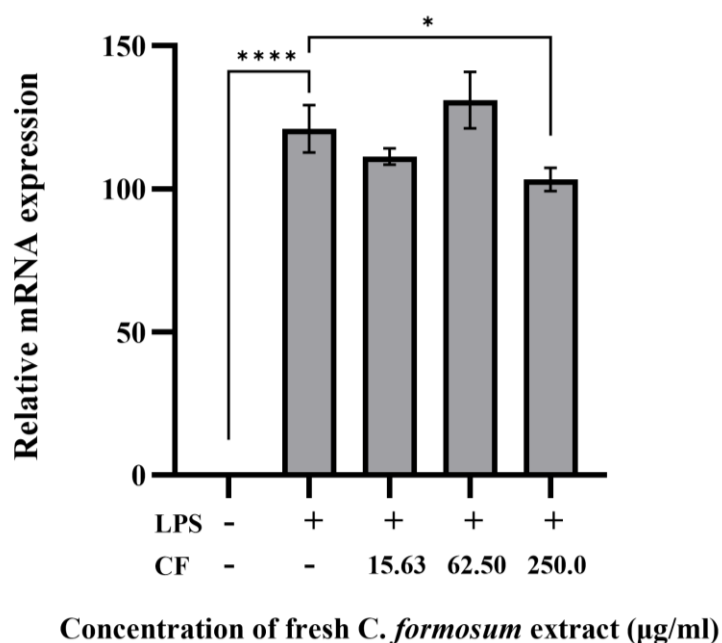


Figure 2

The relative expression of IL-6 mRNA in macrophages treated with various fresh *C. formosum* crude extract concentrations. Bars represent the percentage \pm SEM of three independent experiments (one-way ANOVA with Dunnett's multiple comparisons test, ** $p < 0.05$ and **** $p < 0.0001$).

In response to LPS or other pathogen-associated molecular patterns (PAMPs), macrophages increase the expression of pro-inflammatory cytokine genes such as IL-1 β , IL-6, and TNF- α through the activation of the NF- κ B signaling pathway [21]. Our results show that IL-6 mRNA was reduced in LPS-activated macrophages treated with fresh *C. formosum* crude extract. It has been reported that aqueous extract from fresh *C. formosum* leaves decreased the phosphorylation of NF- κ B in human cholangiocarcinoma (CCA) KKU-M156 cells [22]. Furthermore, the stem extract from the plant in the same genus, *Cratoxylum cochinchinense*, has been revealed to block the NF- κ B signaling pathway in HT-29 human colon cancer cells [23]. The results obtained from this study suggest the possible role of fresh *C. formosum* crude extract in the regulation of IL-6 mRNA expression via the NF- κ B signaling pathway.

In the present study, we revealed only the effect of fresh *C. formosum* crude extract on the nitric oxide production and IL-6 mRNA expression. These results suggest the anti-inflammatory effects of fresh *C. formosum* crude extract. However, the protein level of IL-6 needs to be examined by ELISA or Western blotting in further studies to check the IL-6 protein levels, as the protein levels sometimes do not correlate with their transcriptional products due to the complex layers of biological control, such as post-transcriptional regulation, translational regulatory mechanisms, and many post-translational modifications, that affect the mRNA and protein levels. The effects of fresh *C. formosum* crude extract on the mRNA and protein levels of other pro-inflammatory cytokines, including IL-1 β and TNF- α , must also be determined to broaden understanding of the anti-inflammatory activities of fresh *C. formosum* crude extract. Moreover, further investigation is required to confirm the inhibitory mechanism of fresh *C. formosum* crude extract on the NF- κ B signaling pathway to ameliorate inflammation in LPS-activated RAW 264.7 cells.



Conclusion:

The anti-inflammatory action of fresh *C. formosum* crude extract is associated with the reduction of nitric oxide production and IL-6 mRNA expression, which may come from the activity of fresh *C. formosum* crude extract to control the NF- κ B signaling pathway. However, the relationship between its activity and its inhibition of the NF- κ B signaling pathway needs to be further investigated.

Acknowledgements:

We would like to thank Assoc. Prof. Dr. Kiattawee Choowongkomon (Kasetsart University) for providing Raw 264.7 cells. This work was supported by the Kasetsart University's Academic Development Promotion Project (KU-ADPP-66).

References:

1. Sansbury BE, Spite M. *Circ Res.* 2016;119(1):113-130.
2. Frangogiannis NG. *Curr Opin Cardiol.* 2015;30(3):240-245.
3. Gillissen A, Paparoupa M. *Clin Respir J.* 2015;9(3):257-69.
4. Aliyu M, Zohora FT, Anka AU, Ali K, Maleknia S, Saffarioun M, Azizi G. *Int Immunopharmacol.* 2022;111:109130.
5. Tanaka T, Narazaki M, Kishimoto T. *Cold Spring Harb Perspect Biol.* 2014;6(10):a016295.
6. Beyranvand Nejad E, Labrie C, van Elsas MJ, Kleinovink JW, Mittrücker HW, Franken KLMC, Heink S, Korn T, Arens R, van Hall T, van der Burg SH. *J Immunother Cancer.* 2021;9(4):e002460.
7. Hirano T, Matsuda T, Turner M, Miyasaka N, Buchan G, Tang B, Sato K, Shimizu M, Maini R, Feldmann M, et al. *Eur J Immunol.* 1988;18(11):1797-801.
8. Burska A, Boissinot M, Ponchel F. *Mediators Inflamm.* 2014;2014:545493.
9. Madhok R, Crilly A, Watson J, Capell HA. *Ann Rheum Dis.* 1993;52(3):232-4.
10. Kröncke KD, Fehsel K, Kolb-Bachofen V. *Clin Exp Immunol.* 1998;113(2):147-156.
11. Wiczowski W, Romaszko J, Bucinski A, Szawara-Nowak D, Honke J, Zielinski H, Piskula MK. *J Nutr.* 2008;138(5):885-888.
12. Williamson G, Manach C. *Am J Clin Nutr.* 2005;81(1 Suppl):243S-255S.
13. Li Y, Yao J, Han C, Yang J, Chaudhry MT, Wang S, Liu H, Yin Y. *Nutrients.* 2016 15;8(3):167.
14. Tang J, Diao P, Shu X, Li L, Xiong L. *Biomed Res Int.* 2019;2019:7039802.
15. Sripanidkulchai K, Teepsawang S, Sripanidkulchai B. *J Med Food.* 2010;13(5):1097-1103.
16. Rodanant P, Rodanant R, Srichan R, and Korsuwanwong S. *J. Med. Plants Res.* 2012;6(23):4063-4068.
17. Erridge C, Bennett-Guerrero E, Poxton IR. *Microbes Infect.* 2002;4(8):837-851.
18. Sharma JN, Al-Omran A, Parvathy SS. *Inflammopharmacology.* 2007;15(6):252-9.
19. Choi SJ, Tai BH, Cuong NM *et al.* *Food Sci Biotechnol.* 2012;21: 587–595.
20. Boonak N, Chantrapromma S, Tewtrakul S. *et al.* *Arch. Pharm. Res.* 2014;37:1329-1335.
21. Liu T, Zhang L, Joo D, Sun SC. *Signal Transduct Target Ther.* 2017;2:17023.
22. Senggunprai L, Thammaniwit W, Kukongviriyapan V, Prawan A, Kaewseejan N, Siriamornpun S. *Nutr Cancer.* 2016;68(2):328-41.
23. Ren Y, Matthew S, Lantvit DD, Ninh TN, Chai H, Fuchs JR, Soejarto DD, de Blanco EJ, Swanson SM, Kinghorn AD. *J Nat Prod.* 2011;74(5):1117-25.



CHITINASE PRODUCTION BY *Aeromonas caviae* EW02 NEWLY ISOLATED FROM GIANT MUD CRAB POND AND POTENTIAL TO DEGRADE CHIRONOMID EGG MASSES (*Chironomus plumosus*)

Chirath Pitakkhuamdee,¹ Kittipong Chanworawit,¹ Piyangkun Lueangjaroenkit,¹ Pinsurang Deevong^{1,*}

¹Department of Microbiology, Faculty of Science, Kasetsart University, 10900, Bangkok, Thailand

*e-mail: fsciprd@ku.ac.th

Abstract:

Chitin is a naturally occurring polymer that is a fundamental structural component of crustacean shells and insect exoskeletons. This slow-decomposing polymer accumulates in the environment, contributing to pollution. In addition to bioremediation, the structural polymer of chitin has been broken down by chitinolytic bacteria and chitinase enzymes as a green alternative agent for biocontrol. Chironomids or non-biting midges (Chironomidae) are associated with several problems, including allergic reactions in humans, contamination of food and water supplies, impacts on health, nuisance, and economic damage. Chironomid eggs are embedded in a gelatinous matrix composed of glycoproteins and chitin. In the present study, chitinolytic bacterial isolates were obtained from a water sample in a giant mud crab pond using a microbial enrichment method. A semi-quantitative assay of chitinase production performed using the drop assay revealed that bacterial isolate EW02 exhibited the highest chitinase production value of 1.61 ± 0.09 in Luria–Bertani (LB) agar supplemented with 0.5% colloidal chitin. Based on 16S rRNA gene sequence analysis, the isolate EW02 was closely related to *Aeromonas caviae* (99.93% identity). In the chitinase activity assay, the chitinolytic EW02 exhibited the highest chitinase activity of 1.49 ± 0.04 U/ml at 48 h of incubation. After partial purification by ammonium sulfate precipitation and dialysis, the specific activity of chitinase was increased to 3.64 U/mg protein with a 4.17-fold purification. Moreover, both the bacterial cell suspension and the dialyzed chitinase from EW02 significantly inhibited chironomid egg hatching, with inhibition rates of $86.67 \pm 5.78\%$ and $26.67 \pm 5.78\%$, respectively. The findings suggest that chitinolytic *A. caviae* EW02 newly isolated from crab pond has potential as a green biocontrol agent for the control of chironomids collected from natural water environments.

Keywords: chironomids, *Chironomus plumosus*, *Aeromonas caviae*, chitinase, chitinolytic bacteria, giant mud crab

Introduction:

Chitin is a long-chain polymer of N-acetyl-D-glucosamine (GlcNAG) linked by β -1,4 glycosidic bonds, and it is an insoluble structural component of arthropod exoskeletons and fungal cell walls. Chitinase is an enzyme that hydrolyzes chitin through the cleavage of β -1,4 glycosidic linkages, producing diacetyl chitobiose, chitotriose, and chitotetraose as the main products.¹ This enzyme is found in a variety of microorganisms, including actinobacteria, fungi, and bacteria.²⁻⁴ Chitinases are classified into two main groups: (1) Endochitinases (EC 3.2.1.14), which randomly cleave internal β -1,4-glycosidic linkages of chitin chains, generating soluble chito-oligosaccharides of varying lengths, and (2) Exochitinases (EC 3.2.1.200), which hydrolyze β -1,4-glycosidic linkages from the non-reducing ends of the polymer, releasing mainly GlcNAG. In some cases, exochitinases are further classified into chitobioses, which release chitobiose units, and N-acetyl-D-glucosaminidases, which release monomeric GlcNAG.⁵



Chironomids, also known as non-biting midges, are mosquito-like insects that, unlike mosquitoes, do not feed on blood and thus do not directly bite humans. These insects are often used as indicators of ecological conditions in inland waters. They are highly tolerant of a wide range of environmental conditions and commonly found in polluted or organically enriched water bodies. Although they are not hematophagous, chironomids can still cause significant nuisance and health concerns. Their hemoglobin-containing larvae, as well as adults, are known to trigger allergic reactions in sensitive individuals, leading to respiratory and dermatological symptoms.⁶ The control of chironomid populations remains a challenge in areas where they proliferate rapidly. The most effective strategy involves integrated approaches, such as raising community awareness regarding the importance of maintaining clean and unpolluted water sources to prevent excessive breeding. In addition, chemical methods such as the application of insecticides or mosquito control agents have been employed, although their long-term environmental impact remains a concern.^{7, 8} Recently, biological control approaches, including the use of chitinolytic bacteria or chitinase enzymes that interfere with chironomid egg development, have gained attention as sustainable and environmentally friendly alternatives. In previous studies, *Aeromonas dhkanesis* 3K1C15 exhibited the ability to inhibit chironomid egg hatching.⁹ In the present study, chitinolytic bacteria were isolated from a giant mud crab pond using an enrichment method. After screening for chitin hydrolysis ability, the promising isolate was selected for chitinase activity assay, partial purification, and evaluation of its ability to inhibit chironomid egg hatching. The study provided knowledge of chitinolytic bacteria from crab ponds and promising bacteria for sustainable biocontrol of chironomids.

Methodology:

Sample collection and bacterial isolation

The water sample in the giant mud crab (*Scylla serrata*) farming pond was collected from a soft-shell crab farm in Chanthaburi province, Thailand (12°35'11.0"N 101°54'44.4"E). The water sample was microbially enriched in colloidal chitin broth (CCB) supplemented with 1% colloidal chitin and then incubated with shaking at 150 rpm for 7 days at 30°C.¹⁰ After enrichment, the sample was diluted in 0.85% NaCl and spread on colloidal chitin agar (CCA). After incubation for 7 days at 37°C, the morphologically different colonies with clear zones of chitin hydrolysis were collected and purified using streak-plate method on CCA. The chitinolytic isolates were characterized based on macroscopic and microscopic approaches.

Semi-quantitative assay of chitinase production

A semi-quantitative assay of chitinase production was according to the method of Salas-Ovilla, Gálvez-López [11] with minor modification. Chitinolytic bacterial isolates were cultured in Luria–Bertani (LB) broth supplemented with 0.1% colloidal chitin and then incubated with shaking at 200 rpm for 18 h at 37 °C. The bacterial culture was adjusted to the OD₆₀₀ value of 0.2 and the suspension (2 µL) was dropped on LB agar supplemented with 0.5% colloidal chitin. After incubation at 37°C for 7 days, the chitin hydrolysis zone was observed and calculated for the rate of chitinase production using the formula: Rate of chitinase production = bacterial colony diameter (mm) / chitin hydrolysis zone diameter (mm).

Bacterial identification

Bacterial genomic DNA was extracted using TIANamp Bacteria DNA Kit (TIANGEN BIOTECH, BEIJING, China) according to the manufacturer's instruction. Amplification of 16S rRNA gene was performed using the universal primer pair: forward 616V (5' AGA GTT



TGA TYM TGG CTC 3') and reverse 1492R (5' GGY TAC CTT GTT ACG ACT T 3'). The PCR condition was according to the method of Loy, Schulz [12]. DNA sequencing was conducted by Macrogen, Inc. (Seoul, Republic of Korea). The raw sequence data was error-corrected and sequence assembly was done using BioEdit version. The nucleotide sequence of the 16S rRNA gene was compared with nucleotide sequences in the EzBioCloud 16S database (<https://www.ezbiocloud.net/>) and constructed for the phylogenetic tree by MEGA version X software after multiple sequence alignment using Clustal W.

Crude enzyme preparation

To prepare bacterial crude enzyme, bacterial isolate was cultured in LB broth containing 1% colloidal chitin with shaking at 200 rpm for 7 days at 37°C. The bacterial culture was collected every day, and the cell-free supernatant (CFS) was collected by centrifugation at 12,000 rpm at 4°C for 10 min and used as a crude enzyme.

Chitinase activity assay and determination of protein concentration

Chitinase activity of the bacterial isolate was determined by the releasing of N-acetyl-D-glucosamine (GlcNAG) from chitin degradation using Schales' method.¹³ In preparation of the reaction mixture, 0.1 mL of crude enzyme was mixed with 0.1 mL of 1% colloidal chitin in 50 mM phosphate buffer (pH 7.0). After incubation at 37°C for 30 min, 1 mL of Schales' reagent was added into the mixture and boiled in boiling water at 100°C for 10 min. An absorbance was measured at 420 nm using a spectrophotometer. One unit (U) of chitinase activity is defined as the amount of enzyme that is required to release 1 µmol of GlcNAG per minute. The protein concentration was determined using Lowry-Folin procedure.¹⁴

Partial purification of chitinase

The crude enzyme was precipitated with solid ammonium sulfate at 75% saturation and subsequently dialyzed using a dialysis bag with a molecular weight cutoff of 12 – 14 kDa. The dialyzed enzyme was then stored at –20 °C and used in the next step.

Test of chironomid egg hatching inhibition

Chironomid eggs of *Chironomus plumosus* were collected from Bangkok, Thailand. Healthy eggs were selected under a stereomicroscope and washed three times with sterilized distilled water. The eggs (n = 10) were placed in sterile petri dishes and treated with 1 mL of either a chitinolytic bacterial cell suspension (1.5×10^8 cells/mL) or dialyzed chitinase. After incubation at 30°C for 24 h in darkness, egg hatching was quantified and calculated using the following formula: Inhibition of egg hatching (%) = (hatching eggs / total eggs) × 100. Damage of chironomid eggs caused by chitinolytic bacteria and their dialyzed chitinase was observed by 500× and 4,000× magnification in a FEI Quanta 450 scanning electron microscope (SEM) of the Scientific Equipment Center, Faculty of Science, Kasetsart University.

Animal use protocol

The animal use protocol in the current research was approved by the Kasetsart University Institutional Animal Care and Use Committee, Bangkok, Thailand (Approval ID. ACKU68-SCI-011) and was in accordance with the Guidelines of Animal Care and Use under the Ethical Review Board of the Office of National Research Council of Thailand for conducting scientific research.



Statistical analysis

All tests were performed at least in triplicate. The results are expressed as the mean \pm standard deviation (S.D.). The data were analyzed using one-way ANOVA, followed by the Duncan post hoc test, in SPSS v. 25.0. Significance was set at $p < 0.05$.

Results and discussion:

Isolation of chitinolytic bacteria and screening of chitinase production

A water sample from a giant mud crab pond was collected and microbially enriched in CCB medium for isolation of chitinolytic bacteria. In the isolation step, several morphologically different isolates were selected and used for a semi-quantitative assay on LB agar supplemented with 0.5% colloidal chitin. The results showed that the isolate EW02 exhibited the highest chitinase production rate with 1.61 ± 0.09 and this bacterial isolate had potential for use in subsequent experiments. Chitinolytic bacteria have previously been isolated from various sources, including riverbank soils at Ambo, Western Ethiopia; European sea bass gut; the gut of Indian tropical insectivorous black-bearded tomb bat; and the water of a sand dune lake, Sakata, in Niigata, Japan.¹⁴⁻¹⁷

Bacterial identification

The bacterial isolate was identified based on molecular identification. The 16S rRNA gene sequence (approximately 1.5 kb) of the isolate EW02 shared 99.93% identity with *Aeromonas caviae* CTCE 838 and the phylogenetic tree based on the 16S rRNA sequence is shown in **Figure 1**. In previous study, potential chitinolytic bacteria isolated from zooplankton was identified as *A. caviae*. Aquaculture environments are found as microbial habitat of chitinolytic bacteria, such as *Pseudoalteromonas piscicida* from marine environments and *Pseudoalteromonas lipolytica* from deep-sea sediments. Moreover, chitin-degrading bacteria have been isolated from terrestrial animals and ecosystems, for example *Bacillus thuringiensis* from termite *Microcerotermes*; *Stenotrophomonas maltophilia* and *Bacillus paramycoides* from *Duttaphrynus melanostictus*; *Pseudomonas* spp. from dune soil; *Streptomyces rimosus* from agricultural soil in the center of Poland; *Lysinibacillus fusiformis* from the roots of an apple plant; and *Paenibacillus tyrfis* from the soil.¹⁸⁻²⁵

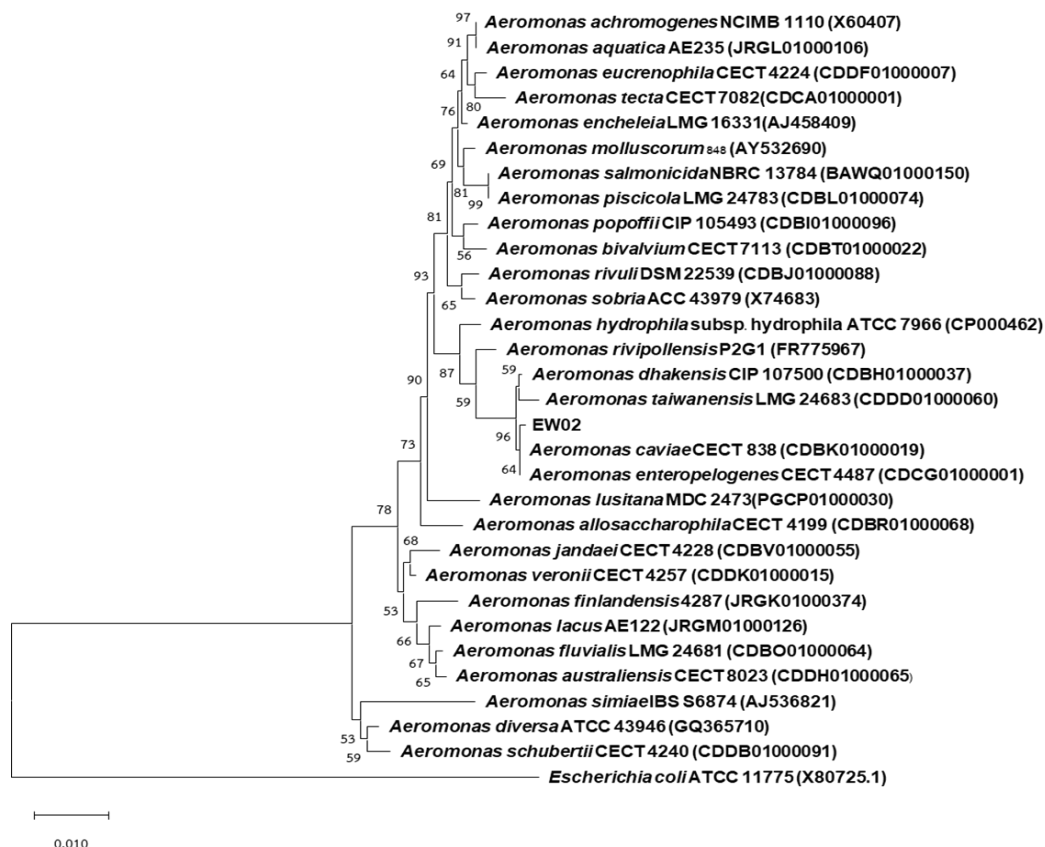


Figure 1.

Phylogenetic relationship based on 16S rRNA gene sequences of the isolate EW02 and their relative species belonging to the genus *Aeromonas*. The phylogenetic tree was constructed using MEGA X. Numbers at the nodes indicate the value of bootstrap (%) based on Neighbor-Joining (NJ) method with 1,000 resampled datasets. The bacterial strain *Escherichia coli* ATCC 11775 was used as an outgroup.

Chitinase activity assay and partial purification of chitinase

Bacterial growth and chitinase activity at different incubation times of *A. caviae* EW02 are shown in **Figure 2**. The highest chitinase activity of EW02 was expressed at the incubation period of 48 h with 1.49 ± 0.04 U/mL, and slightly decreased after 48 h of incubation. Comparable to previous reports, *A. caviae* CHZ306 exhibited chitinase activity of approximately 30.1 U/L, while *Stenotrophomonas maltophilia* showed 0.0513 U/mL.^{19, 26}

In the present study, the crude enzyme from *A. caviae* EW02 was partially purified by 80% saturated ammonium sulfate precipitation followed by dialysis. The specific chitinase activity of the dialyzed enzyme increased from 0.87 U/mg to 3.64 U/mg with a 4.17-fold purification compared with the crude enzyme. The results indicated that ammonium sulfate precipitation could enhance the enzyme purity by removing non-chitinolytic proteins. **Table 1** represented the partial purification profile of chitinase from *A. caviae* EW02.

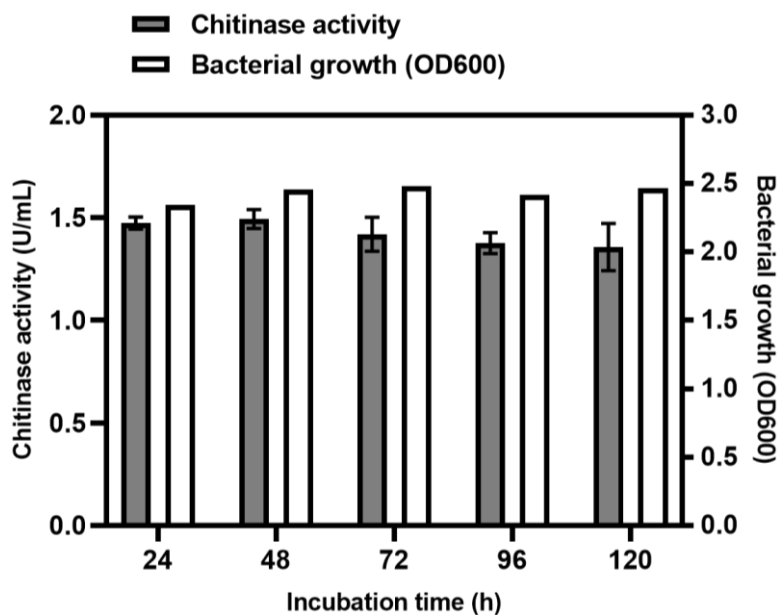


Figure 2.

Time course of chitinase activity (U/mL) and bacterial growth (OD₆₀₀) of the chitinolytic *Aeromonas caviae* EW02

Table 1.

Partial purification steps of chitinase from *Aeromonas caviae* EW02

Step	Protein (mg/mL)	Total protein (mg)	Enzyme activity (U/mL)	Total activity (U)	Specific activity (U/mg)	Yield (%)	Purification (fold)
Crude enzyme	1.006	84.504	0.876	73.584	0.871	100	1
Dialyzed enzyme	0.214	1.391	0.779	5.064	3.640	6.881	4.17

Test of chironomid egg hatching inhibition

Inhibition of chironomid egg hatching after treatment with cell suspension and dialyzed enzyme from *A. caviae* EW02 is shown in **Figure 3**. The treatments with bacterial cell suspension and dialyzed enzyme demonstrated a significant inhibition of egg hatching with $86.67 \pm 5.77\%$ and $26.67 \pm 5.77\%$ compared with the control, respectively. Interestingly, these results indicated that bacterial cell suspension was more effective for inhibiting egg hatching than the dialyzed enzyme likely due to additional metabolites acting on eggs composed of multiple components, including glycoproteins.⁹ In contrast, chitinase contributed to egg hatching inhibition, but its activity was limited to hydrolyzing chitin in the eggs. Therefore, the use of *A. caviae* cell suspension to inhibit egg hatching is of considerable interest for sustainable and eco-friendly applications as a biocontrol agent. The morphological change of chironomid eggs was observed using SEM after treatment with cell suspension and dialyzed chitinase, and the results suggested that the untreated eggs (control) displayed a smooth surface. In contrast, eggs treated with the dialyzed chitinase or bacterial cells showed obvious surface changes, including extensive delamination, and numerous cracks were observed across the surface. These results supported the hypothesis of Laviad, Golan [27] that chitin is a key structural component of chironomid eggs.

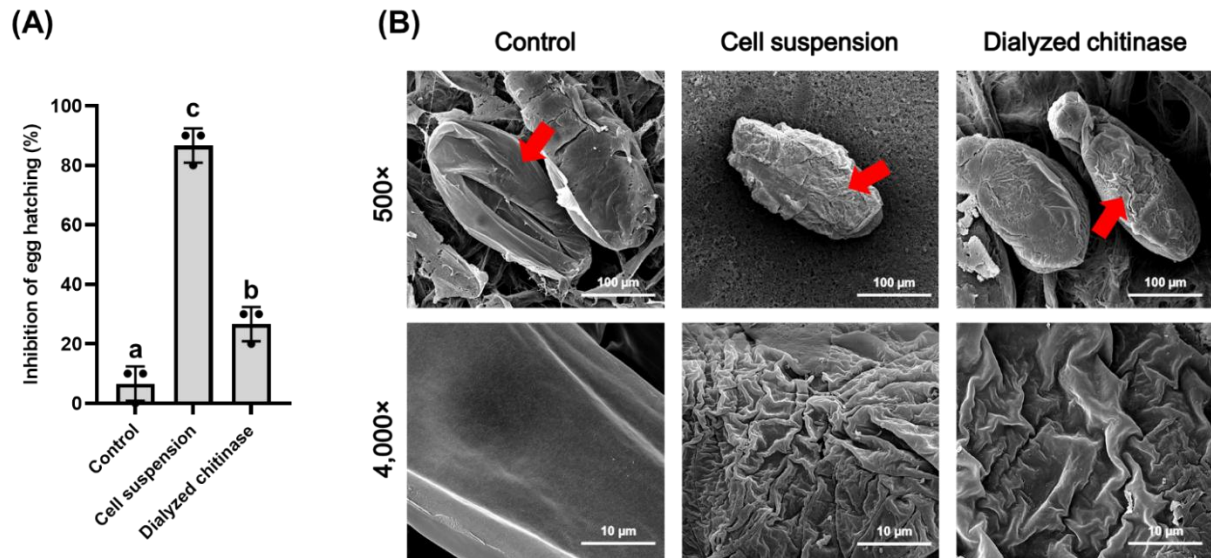


Figure 3.

Inhibition percentage of chironomid egg hatching after treatment with cell suspension and dialyzed chitinase from *Aeromonas caviae* EW02 (A); and damage of chironomid eggs under 500 \times and 4,000 \times magnification in a FEI Quanta 450 scanning electron microscope (SEM) (B). Each value represents the mean \pm S.D. (n = 3). Different superscripts indicate significant difference ($p < 0.05$).

Conclusion:

The present study obtained chitinolytic bacterial isolates from a giant mud crab pond. The isolate EW02 exhibited the highest value in the semi-quantitative assay of chitinase production, and this isolate was closely related to *A. caviae* based on the analysis of the 16S rRNA gene sequence. At 48 h of incubation, *A. caviae* EW02 exhibited the highest chitinase activity. After partial purification by ammonium sulfate precipitation and dialysis, both specific activity and purification fold were higher compared to the crude extract. Moreover, both the cell suspension and dialyzed chitinase from EW02 significantly inhibited chironomid egg hatching. This study provided knowledge of potential chitinolytic bacteria from crab pond environments. Our results suggested that the chitinolytic *A. caviae* EW02 obtained from the study was a promising candidate as a microbial agent for the biological control of chironomids.

Acknowledgments:

Thanks to Ms. Putsawee Tomtong, Mr. Pachara Wangsoonthorn, Mr. Chinnphat Meeto, Mr. Metas Chaleesaen, Mr. Jirun Thanompreechachai and Mr. Rapeepat Thippunyawong for helping and supporting.

References:

1. Sahai A S, Manocha M S. FEMS Microbiol. Rev. 1993;**11**(4):317-338.
2. Abo-Zaid G, Abdelkhalek A, Matar S, Darwish M, Abdel-Gayed M. J. Fungi. 2021;**7**(3):167.
3. Hartl L, Zach S, Seidl-Seiboth V. Appl Microbiol Biotechnol. 2012;**93**(2):533-43.
4. Veliz E A, Martínez-Hidalgo P, Hirsch A M. AIMS Microbiol. 2017;**3**(3):689-705.
5. Tanaka T, Fukui T, Imanaka T. J. Biol. Chem. 2001;**276**(38):35629-35635.
6. Seldén A I, Calo A, Mölleby G, Hultgren O. Med Vet Entomol. 2013;**27**(3):346-8.
7. Ali A, Morris C. IFAS, Univ. of Florida Medical Entomology Laboratory Technical Bulletin. 1992(4).



8. Gray E, Fusco R, Royals C, Noblet R, Wyatt R. *Journal of the J. Am. Mosq. Control Assoc.* 2011;**27**:173-6.
9. Halpern M, Gancz H, Broza M, Kashi Y. *Appl Environ Microbiol.* 2003;**69**(7):4200-4204.
10. Chanworawit K, Wangsoontorn P, Deevong P. *Biosci Biotechnol Biochem.* 2023;**87**.
11. Salas-Ovilla R, Gálvez-López D, Vázquez-Ovando A, Salvador-Figueroa M, Rosas-Quijano R. *PeerJ.* 2019;**7**:e6102.
12. Loy A, Schulz C, Lücker S, Schöpfer-Wendels A, Stoecker K, Baranyi C, Lehner A, Wagner M. *Appl Environ Microbiol.* 2005;**71**(3):1373-1386.
13. Imoto T, Yagishita K. *Agric Biol Chem.* 1971;**35**(7):1154-1156.
14. Tran D M, Sugimoto H, Nguyen D A, Watanabe T, Suzuki K. *Biosci Biotechnol Biochem.* 2018;**82**(2):343-355.
15. Gonfa T G, Negessa A K, Bulto A O. *Heliyon.* 2023;**9**(11):e21643.
16. Gracy Jenifer S, Marimuthu G, Raghuram H. *J Basic Microbiol.* 2021;**61**(10):940-946.
17. Rangel F, Santos R A, Monteiro M, Lavrador A S, Gasco L, Gai F, Oliva-Teles A, Enes P, Serra C R. *Biology.* 2022;**11**(7):964.
18. Brzezinska M S, Jankiewicz U, Walczak M. *Int Biodeterior Biodegradation.* 2013;**84**:104-110.
19. Cardozo F, Feitosa V, Pillaca-Pullo O, Pessoa A. *Bioengineering (Basel).* 2023;**10**(4).
20. De Boer W, Klein Gunnewiek P J A, Lafeber P, Janse J D, Spit B E, Woldendorp J W. *Soil Biol. Biochem.* 1998;**30**(2):193-203.
21. Dhole N P, Phuge S, Dar M A, Pandit R S. *Environ. Technol. Innov.* 2022;**28**:102929.
22. Jin B, Liang X, Wang X, Peng L-H, Yang J-L. *Mar Genom.* 2025;**82**:101203.
23. Passera A, Rossato M, Oliver J S, Battelli G, Shahzad G-I R, Cosentino E, Sage J M, Toffolatti S L, Lopatriello G, Davis J R, Kaiser M D, Delledonne M, Casati P. *Microbiol Res.* 2021;**244**:126665.
24. Paulsen S S, Andersen B, Gram L, Machado H. *Mar Drugs.* 2016;**14**(12):230.
25. Tran D M, Do T O, Nguyen Q V. *Data in Brief.* 2024;**53**:110087.
26. Aktas C, Ruzgar D, Gurkok S, Gormez A. *Prep Biochem.* 2023;**53**(7):797-806.
27. Laviad S, Golan A, Shaked T, Vaizel-Ohayon D, Halpern M, Pick E. *Environ Microbiol Rep.* 2016;**8**(1):30-7.



***Phyllosticta capitalensis*, AN ENDOPHYTIC FUNGUS ISOLATED FROM *Ocimum sanctum* WITH ANTIBACTERIAL ACTIVITY**

Pattaranan Ounjai, Khwanruedee Sangjan, Onchapron Jitkumkoon, Urarux Romruen, Eakaphun Bangyeekhun*

Department of Microbiology, Faculty of Science, Silpakorn University, Nakhon Pathom, Thailand

*e-mail: Bangyeekhun_e@su.ac.th

Abstract:

Endophytic fungi are recognized as prolific sources of novel bioactive metabolites. This study aimed to isolate endophytic fungi from *Ocimum sanctum*, *Ocimum basilicum*, and *Mentha cordifolia* (Lamiaceae) and to evaluate their antimicrobial potential. A total of 25 fungal isolates, designated MSSU01–MSSU025, were obtained. Antibacterial screening against *Bacillus subtilis*, *Staphylococcus aureus*, *Escherichia coli*, and *Pseudomonas aeruginosa* revealed that 44% of the isolates exhibited inhibitory activity, with isolate MSSU017 showing the strongest and broad-spectrum effects. Ethyl acetate extraction of MSSU017 culture filtrate yielded 0.93 ± 5.1 mg/mL of a dark green to blackish-viscid crude extract, with a maximum solubility of 3.5 mg/mL in 10% DMSO. Broth microdilution assays demonstrated minimum inhibitory concentrations (MICs) of 437.5–875.0 $\mu\text{g/mL}$, with bactericidal activity against Gram-positive strains but no detectable MBC values for Gram-negative bacteria. Phytochemical screening indicated the presence of terpenoids, consistent with previous reports of terpenoid-type metabolites in endophytic fungi. Morphological and molecular identification confirmed MSSU017 as *Phyllosticta capitalensis*, representing the first report of this species isolated as an endophyte from *O. sanctum*. These findings highlight the potential of *P. capitalensis* MSSU017 as a source of bioactive compounds for future pharmaceutical and biotechnological applications.

Introduction:

Fungi are eukaryotic organisms that obtain nutrients from organic matter. They occur as either unicellular or multicellular forms, and their cells typically grow as filamentous hyphae with chitin as the major component of the cell wall. Reproduction occurs via both sexual and asexual spores. Endophytic fungi are a unique group of fungi that inhabit the internal tissues of plants—such as leaves, stems, roots, flowers, fruits, and seeds—without causing disease symptoms. These fungi may reside within plant cells or in intercellular spaces, usually establishing mutualistic or commensal relationships with their host plants.¹

Endophytic fungi play important roles in ecosystems. Previous studies have demonstrated that they can enhance host plant tolerance to unfavorable environmental conditions. For instance, *Neotyphodium* spp. promote host survival under drought stress and improve growth compared to non-colonized plants. Plants harboring these endophytes often develop denser root systems with elongated root hairs, which may enhance water and nutrient uptake. In addition, endophytes produce secondary metabolites such as phenolic compounds with strong antioxidant properties, protecting plant cells from oxidative stress during drought.² Moreover, endophytic fungi are recognized as prolific producers of diverse bioactive compounds. For example, *Taxomyces andreanae*, isolated from *Taxus brevifolia*, synthesizes paclitaxel (Taxol), a potent anticancer agent.³ *Talaromyces radicus* from *Catharanthus roseus* produces vincristine-like alkaloids with cytotoxic activity.⁴ *Penicillium* sp. and *Talaromyces* sp. isolated from *Artemisia annua* generates emodin and physcion with antimalarial activity.⁵ *Chaetomium globosum* from *Ginkgo biloba* produces chaetoglobosin A, a metabolite showing phytotoxic and cytotoxic activity.⁶ Similarly, *Paecilomyces* sp. from



Schnella splendens yields phomoxanthone A, which exhibits antimicrobial and antiparasitic properties.⁷

Although research on endophytic fungi in Thailand has expanded in recent years, it remains limited compared to studies in other countries. Thailand, located in the tropical region and recognized as a biodiversity hotspot, possesses a wide variety of medicinal and economically important plants that may serve as reservoirs for novel endophytic fungi and their bioactive metabolites. The present study aimed to isolate endophytic fungi from members of the family Lamiaceae and to evaluate the antibacterial activity of their extracts. These findings are expected to contribute to applications in medicine, agriculture, and biotechnological industries in Thailand.

Methodology:

Isolation of endophytic fungi

Healthy plant samples were surface-sterilized following a standard protocol with minor modifications.⁸ Briefly, samples thoroughly washed with tap water and cut into pieces of approximately $1 \times 1 \times 1$ cm using a sterile scalpel. Surface sterilization was performed by sequential immersion of the samples in 70% ethanol for 1 min, followed by 10% commercial bleach solution (Haitec) containing 0.05% Tween 20 (equivalent to 0.6% sodium hypochlorite) for 5 min, then 70% ethanol for 30 s, and finally rinsing in sterile distilled water for 1 min. The sterilized plant fragments were placed onto half-strength Sabouraud Dextrose Agar (HS-SDA) medium (20 g/L dextrose, 5 g/L peptone, and 15 g/L agar, pH 5.6) and incubated at 30 °C for 3–7 days. Emerging fungal hyphae were transferred onto fresh HS-SDA plates and incubated at 30 °C for 3 days. Pure cultures were maintained at 4 °C as stock cultures.

Cross-streak assay for antibacterial activity

Antibacterial activity was assessed by the cross-streak method.⁹ Endophytic fungi were cultured on HS-SDA at 30 °C for 3 days. Using a sterile inoculating loop, fungal mycelium was streaked as a straight line approximately one-quarter of the plate's diameter from the edge and incubated at 30 °C for 3 days.

Test bacteria included *Bacillus subtilis* TISTR 008, *Escherichia coli* TISTR 887, *Pseudomonas aeruginosa* TISTR 1287, and *Staphylococcus aureus* TISTR 885, all obtained from the Thailand Institute of Scientific and Technological Research. Each bacterial strain (1–3 colonies) was suspended in 1 mL of 0.85% NaCl and adjusted to 0.5 McFarland standard ($\sim 1.5 \times 10^8$ CFU/mL). Sterile cotton swabs were dipped into each suspension and streaked perpendicularly across the fungal growth line, with one bacterial species per line. The plates were incubated at 37 °C for 24 h, and the distance of the clear zone (in mm) between fungal and bacterial growth was measured.

Extraction of bioactive metabolites

Endophytic fungi were cultured on HS-SDA at 30 °C for 3 days. Five mycelial plugs (0.5 cm in diameter) were inoculated into 1 L of HS-SDB in a 3 L Erlenmeyer flask and incubated at 30 °C for 15 days under shaking at 80 rpm. The culture broth was filtered through sterile gauze and Whatman No. 4 filter paper to separate the mycelia. The filtrate was extracted with ethyl acetate in a 1:2 (v/v) ratio using a separatory funnel. The organic phase was collected and evaporated under reduced pressure using a rotary evaporator. The crude extract was weighed, and the extraction yield was calculated as: Extraction yield = amount of crude extract (mg) / volume of culture filtrate (mL). The extract was dissolved in 10% dimethyl sulfoxide (DMSO) to obtain a stock concentration of 3.5 mg/mL (the maximum solubility concentration).



Determination of minimum inhibitory concentration (MIC) and minimum bactericidal concentration (MBC)

The MIC and MBC values of fungal extracts were determined by broth microdilution in 96-well microplates.¹⁰ Bacterial cultures were prepared by incubating the test strains on Nutrient Agar (NA) medium (peptone 5 g/L, beef extract 3 g/L, sodium chloride 5 g/L and agar 15 g/L, pH 7.4) at 37 °C for 24 h. One to three colonies were suspended in 0.85% NaCl and adjusted to 0.5 McFarland standard (1.5×10^8 CFU/mL), followed by a 1:100 dilution in 0.85% NaCl and further dilution (1:20) in NB to obtain $\sim 7.5 \times 10^4$ CFU/mL.

Each well received 50 μ L of NB medium. Serial two-fold dilutions of extracts were prepared by adding 50 μ L of extract (3.5 mg/mL) into the first well, then transferring 50 μ L sequentially through wells 2–8. Controls included medium alone, 10% DMSO, and Tetracycline (0.2–25.0 μ g/mL). Finally, 50 μ L of the bacterial suspension was added to each well. The final test concentrations ranged from 6.8 to 875.0 μ g/mL. Plates were sealed and incubated at 37 °C for 24 h.

To determine MBC, bacterial growth from each well was streaked onto NA plates and incubated at 37 °C for 24 h. MIC values were determined using resazurin dye (0.02%, 30 μ L per well) after incubation for 1 h. Wells with no bacterial growth remained blue (–), while metabolically active cells reduced resazurin to pink resorufin (+). MIC was defined as the lowest concentration with no visible growth, and MBC as the lowest concentration that killed bacteria, confirmed by three independent replicates. All assays were performed in triplicate.

Phytochemical screening

Qualitative phytochemical analysis of crude extracts was performed in triplicate as follows:¹¹ Alkaloids: 1 mL of extract was treated with three drops of Mayer's reagent (1.36 g mercuric chloride and 5 g potassium iodide in 100 mL distilled water). A cream-colored precipitate indicated alkaloids. Caffeine and 10% DMSO were used as positive and negative controls, respectively.

Phenolics: 5 mL of extract was mixed with five drops of 10% neutral ferric chloride solution. A green, blue, purple, or black coloration indicated phenolic compounds. Tea infusion and 10% DMSO were used as positive and negative controls, respectively.

Saponins: 5 mg of extract was boiled in 3 mL distilled water for 5 min, then shaken for 1 min. Persistent froth for 30 min indicated saponins. Soybean extract and 10% DMSO were used as positive and negative controls, respectively.

Terpenoids: 5 mL of extract was mixed with 2 mL chloroform and 3 mL concentrated sulfuric acid. A red interface indicated terpenoids. Eucalyptus oil and 10% DMSO were used as positive and negative controls, respectively.

Morphological characterization and identification of endophytic fungi

Fungal isolates were cultured on HS-SDA at 30 °C for 7 days. Colony characteristics, including surface and reverse pigmentation, were recorded. Microscopic morphology of vegetative and reproductive structures was examined. Molecular identification was carried out using ITS1 and ITS4 primers in a standard PCR protocol.¹² The amplified PCR amplicon was sequenced, and the resulting sequence was compared to those available in the GenBank database through BLASTn analysis at the National Center for Biotechnology Information (NCBI).

Results and Discussion:

A total of 25 endophytic fungal isolates (designated MSSU01–MSSU025) were successfully obtained from three Lamiaceae species, namely *Mentha cordifolia* Opiz ex Fresen, *Ocimum*

basilicum L.f. var. *citratum* Back., and *Ocimum sanctum* L. Antibacterial screening of all isolates against *B. subtilis*, *S. aureus*, *E. coli*, and *P. aeruginosa* revealed that 7 isolates (28%) inhibited *B. subtilis*, 9 isolates (36%) inhibited *S. aureus*, 2 isolates (8%) inhibited *E. coli*, and 5 isolates (20%) inhibited *P. aeruginosa*, whereas 14 isolates (56%) exhibited no antibacterial activity (**Table 1**).

Table 1.
Endophytic fungi isolated from Lamiaceae and their antibacterial activity.

Host	Fungal isolates	Clear zone (mm.)			
		Gram-positive bacteria		Gram-negative bacteria	
		<i>B. subtilis</i>	<i>S. aureus</i>	<i>E. coli</i>	<i>P. aeruginosa</i>
<i>M. cordifolia</i> (Leaf)	MSSU01	3	3	-	1
<i>M. cordifolia</i> (Leaf)	MSSU02	11	8	-	-
<i>M. cordifolia</i> (Stem)	MSSU03	2	2	-	1
<i>O. basilicum</i> (Flower)	MSSU04	-	-	-	-
<i>O. basilicum</i> (Leaf)	MSSU05	-	3	-	-
<i>O. basilicum</i> (Leaf)	MSSU06	-	-	-	-
<i>O. basilicum</i> (Leaf)	MSSU07	10	10	5	-
<i>O. basilicum</i> (Leaf)	MSSU08	-	-	-	-
<i>O. basilicum</i> (Root)	MSSU09	-	-	-	1
<i>O. basilicum</i> (Root)	MSSU10	-	-	-	-
<i>O. basilicum</i> (Root)	MSSU11	-	-	-	-
<i>O. basilicum</i> (Stem)	MSSU12	-	-	-	-
<i>O. basilicum</i> (Stem)	MSSU13	-	-	-	-
<i>O. sanctum</i> (Leaf)	MSSU14	-	-	-	-
<i>O. sanctum</i> (Leaf)	MSSU15	-	-	-	-
<i>O. sanctum</i> (Leaf)	MSSU16	-	-	-	-
<i>O. sanctum</i> (Leaf)	MSSU17	20.5	25	9	5
<i>O. sanctum</i> (Leaf)	MSSU18	-	-	-	-
<i>O. sanctum</i> (Leaf)	MSSU19	-	-	-	-
<i>O. sanctum</i> (Leaf)	MSSU20	9	8	-	-
<i>O. sanctum</i> (Leaf)	MSSU21	-	-	-	-
<i>O. sanctum</i> (Leaf)	MSSU22	-	-	-	-
<i>O. sanctum</i> (Leaf)	MSSU23	-	-	-	-
<i>O. sanctum</i> (Stem)	MSSU24	-	2	-	-
<i>O. sanctum</i> (Stem)	MSSU25	3	2	-	5

“ - ” indicates there was no clear zone detected.

When considered by host plant, all endophytes (100%) isolated from *M. cordifolia* (66.6% from leaves and 33.3% from stems) displayed antibacterial activity. In contrast, only 30% of isolates from *O. basilicum* (20% from leaves and 10% from roots) and 33.3% of isolates from *O. sanctum* (16.6% from leaves and 16.6% from stems) exhibited inhibitory effects. These results are consistent with previous reports by Mamangkey et al.,¹³ who demonstrated that Lamiaceae species harbor diverse endophytic fungi with antimicrobial potential.

Overall, 36% of the isolates inhibited Gram-positive bacteria with inhibition zones ranging from 2–25 mm, while 24% inhibited Gram-negative bacteria with smaller inhibition zones of 1–5 mm. These findings suggest that endophytic fungi in this study were more

effective against Gram-positive bacteria, likely due to differences in cell wall architecture. Among the isolates, MSSU017 demonstrated the strongest and broad-spectrum antibacterial activity, producing inhibition zones greater than 20 mm against both *B. subtilis* and *S. aureus* (**Table 1, Figure 1**). This broad-spectrum activity led to the selection of MSSU017 for further investigation.

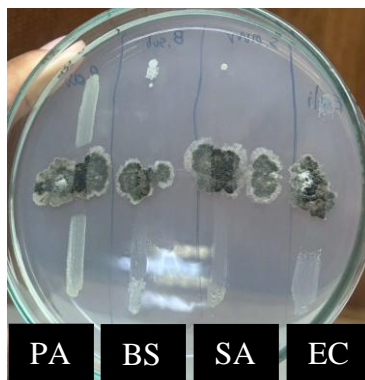


Figure 1.

Antibacterial activity of endophytic fungi isolate MSSU17 on tested bacteria.
(PA = *P. aeruginosa*, BS = *B. subtilis*, SA = *S. aureus*, and EC = *E. coli*)

Cultivation of isolate MSSU017 in HS-SDB medium for 15 days, followed by ethyl acetate extraction of the culture filtrate, yielded a dark green to blackish-viscid extract (yield: 0.93 ± 5.1 mg/mL from three independent experiments). The physical appearance suggested the possible presence of melanin, polyketides, or phenolic-type metabolites, which are commonly produced by endophytic fungi with antimicrobial potential.¹⁴ The maximum solubility of the extract in 10% DMSO was determined to be 3.5 mg/mL.

MIC and MBC values of the ethyl acetate extract were determined by the broth microdilution method (**Table 2**). The extract exhibited MIC values ranging from 437.5 to 875.0 μ g/mL against the tested bacteria. MBC values were not detected for Gram-negative bacteria, indicating resistance. These results corroborated the cross-streak assay, further indicating that bioactive metabolites from MSSU017 likely interfere with peptidoglycan biosynthesis or integrity, consistent with stronger inhibition of Gram-positive bacteria.

Phytochemical screening revealed that the ethyl acetate extract of MSSU017 belongs to the terpenoid class of metabolites, rather than alkaloids, phenolics, or saponins. This finding aligns with previous work by Trepa et al.,¹⁵ who reported that fungal terpenes and terpenoids possess antibacterial, antioxidant, anti-inflammatory, anti-cancer, and anti-tyrosinase properties, supporting their potential applications in pharmaceutical and dermatological products. Further structural elucidation of MSSU017 metabolites using GC-MS, LC-MS, and NMR is warranted.

Table 2.

Determination of minimum inhibition concentration (MIC) and minimum bactericidal concentration (MBC) of ethyl acetate extract of endophytic fungus isolate MSSU17 against tested bacteria.

Test	Bacteria	Extract (µg/ml)	Tetracycline (µg/ml)
MIC	<i>B. subtilis</i>	875 ± 0.0	6.3 ± 0.0
	<i>S. aureus</i>	437.5 ± 0.0	0.4 ± 0.0
	<i>E. coli</i>	437.5 ± 0.0	0.8 ± 0.0
	<i>P. aeruginosa</i>	729.2 ± 252.6	25 ± 0.0
MBC	<i>B. subtilis</i>	875 ± 0.0	3.1 ± 0.0
	<i>S. aureus</i>	nd	0.4 ± 0.0
	<i>E. coli</i>	nd	nd
	<i>P. aeruginosa</i>	nd	25 ± 0.0

“nd” (not detected) indicates undeterminable of MIC or MBC value at the maximum tested concentration.

Morphological characterization of MSSU017 revealed colonies with irregular shape, dark green to black pigmentation, and flat texture. Microscopic examination showed septate hyphae approximately 7.5 µm in width with pigmented cell walls; however, no sporulation was observed. Molecular identification based on ITS sequencing demonstrated 100% identity (631nt/631nt) with *Phyllosticta capitalensis* (accession numbers MT649668.1, MF495391.1, and MF993436.1) in the NCBI database.

The genus *Phyllosticta* is known to include both plant pathogens and endophytes. In our study, no sporulation was observed in the isolate. This is likely because *P. capitalensis* produces conidia within pycnidia only when growing on its host plant. Consequently, the absence of sporulation under standard culture conditions was expected. Wikee et al.¹⁶ recommended the use of pine needle agar (PNA) or synthetic nutrient-poor agar (SNA), combined with incubation under near-UV light, to induce sporulation in this genus.

Several studies have highlighted ability of *Phyllosticta* spp. to produce antibacterial compounds. Chukeatirote et al.¹⁷ reported *Phyllosticta* extracts active against *B. cereus*, *S. aureus*, *M. luteus*, *B. subtilis*, *E. coli*, *P. aeruginosa*, and *S. typhimurium*, which agrees with our observations. Wikee et al.¹⁶ further demonstrated that different *Phyllosticta* species exhibit varying antibacterial profiles, with *P. capitalensis* displaying the broadest spectrum of activity. Our findings therefore confirm the identity of isolate MSSU017 as *P. capitalensis* and support its strong antibacterial potential.

Additional reports have shown that *P. capitalensis* produces a diversity of metabolites. Talukdar et al.¹⁷ identified 1-octacosanol and other functional groups in GC-MS analyses of *P. capitalensis* extracts, while Chingath et al.¹⁸ described meroterpenoids such as Guignardone A and cyclic dipeptides from this species, highlighting the importance of terpenoid-type metabolites. Together, these findings support our phytochemical data and reinforce the potential of *P. capitalensis* as a prolific source of bioactive compounds.

P. capitalensis is a cosmopolitan endophyte and saprobe that has been isolated from diverse plant hosts. Given that *O. sanctum* is widely cultivated, the co-occurrence of *P. capitalensis* in this plant is plausible. To our knowledge, this is the first report of an endophytic *P. capitalensis* isolated from *O. sanctum*. Considering the broad spectrum of antibacterial activities and the range of bioactive metabolites documented for this species, *P. capitalensis* MSSU017 represents a promising candidate for further biotechnological



exploration. Toxicity assessments will, however, be essential prior to considering applications in food or pharmaceutical contexts

Conclusion:

This study successfully isolated 25 endophytic fungi from members of the family Lamiaceae in Thailand, of which 44% exhibited antibacterial activity. Among them, isolate MSSU017, identified as *Phyllosticta capitalensis*, demonstrated broad-spectrum antibacterial potential, particularly against Gram-positive bacteria. Phytochemical screening suggested the presence of terpenoids, supporting its bioactive nature. To our knowledge, this is the first report of *P. capitalensis* isolated from *Ocimum sanctum*. The findings underline the significance of endophytic fungi from medicinal plants as promising reservoirs of antibacterial metabolites. Future work should focus on purification, structural elucidation, mechanism of action, and toxicity assessment to evaluate their potential applications in pharmaceutical and biotechnological fields.

Acknowledgements:

This work was financially supported by the Department of Microbiology, Faculty of Science, Silpakorn University.

References:

1. Hashem AH, Attia MS, Kandil EK, Fawzi MM, Abdelrahman AS, Khader MS, Khodaira MA, Emam AE, Goma MA, Abdelaziz AM. MCFs. 2023;22:e107.
2. Malinowski DP, Belesky DP. Grassl. Sci. 2006;52:1-14.
3. Stierle A, Strobel G, Stierle D. Science. 1993;260:214-216.
4. Palem PP, Kuriakose GC, Jayabaskaran C. PloS one. 2015;10:e0144476.
5. Alhadrami HA, Sayed AM, El-Gendy AO, Shamikh YI, Gaber Y, Bakeer W, Sheirf NH, Attia EZ, Shaban GM, Khalifa BA. Sci. Rep. 2021;11:e2770.
6. Li H, Xiao J, Gao Y-Q, Tang JJ, Zhang A-L, Gao J-M. J. Agric. Food Chem. 2014;62:3734-3741.
7. Ramos GdC, Silva-Silva JV, Watanabe LA, Siqueira JEdS, Almeida-Souza F, Calabrese KS, Marinho AMdR, Marinho PSB, Oliveira ASd. Antibiotics. 2022;11:e1332.
8. Handayani D, Muslim RI, Syafni N, Artasasta MA, Riga, R. J. Appl. Pharm. Sci. 2024;14:182-188.
9. Maliehe TS, Mbambo M, Ngidi LS, Shandu JSE, Poe OJ, Masoko P, Selepe TN. BMC Complement. Med. Ther. 2022;22:e258.
10. da Silva MM, Nicolete G, Lopes BD, Morita CH, de Souza JM, Winkelstroter LK, Rodrigues MVP. Adv. Microbiol. 2018;8:270-285.
11. Chakraborty A, Majumdar S, Bhowal J. Arch. Microbiol. 2021;203:6091-6108.
12. Bellemain E, Carlsen T, Brochmann C, Coissac E, Taberlet P, Kausrud H. BMC Microbiol. 2010;10:e189.
13. Mamangkey J, Hartanto A, Rumahorbo CGP. Acta Microbiol. Bulg. 2023;39:140-6.
14. Lin L, Xu J. J. Fungi. 2020;6:e280.
15. Trepa M, Sułkowska-Ziaja K, Kała K, Muszyńska B. Molecules. 2024;29:e1183.
16. Wikee S, Lombard L, Crous PW, Nakashima C, Motohashi K, Chukeatirote E, Alias SA, McKenzie EHC, Hyde KD. Fungal Divers. 2013;60:91-105.
17. Chukeatirote E, Wikee S, Hyde K. Micol. Apl. Int. 2015;27:1-9.
18. Talukdar R, Wary S, Mili C, Roy S, Tayung K. J. Appl. Pharm. Sci. 2020;10:99-106.
19. Chingath DS, Bhagirathan U, Varghese L. Nat. Prod. Res. 2025:1-6.
<https://doi.org/10.1080/14786419.2025.2509879>



SCREENING OF POTENT FLAVOR COMPOUNDS PRODUCED BY NON-*Saccharomyces* YEAST

Naphattarachon Thammapanyaphong, Thamonwan Tassanaset, Jirasin Koonthongkaew*
Department of Microbiology, Faculty of Sciences, Chulalongkorn University, Phayathai Rd.,
Pathumwan, Bangkok 10330, Thailand

* e-mail: Jirasin.K@chula.ac.th

Abstract:

Saccharomyces cerevisiae is widely applied in beverage fermentation for its strong fermentation ability and stress tolerance, but its limited aroma profile can generate undesirable flavors. Non-*Saccharomyces* yeasts provide flavor diversity but often show lower ethanol productivity. This study aimed to identify a non-*Saccharomyces* strain with improved aroma potential. A total of 19 yeast isolates were obtained from 5 isolated from potato peels, 5 isolated from pineapple, and 9 from sugar factory samples, of which four non-*Saccharomyces* strains were identified by colony morphology and biochemical profiling using the API 32C system. Among them, strain JK319, isolated from a sugar factory, was identified as *Kluyveromyces marxianus* and selected for further evaluation. Growth curves in Synthetic Dextrose medium demonstrated its rapid exponential growth compared to the control *S. cerevisiae* strain Lalvin EC-1118. A sensory panel consisting of one certified evaluator and three trained panelists compared the aroma profiles of both yeasts. Fermentation assays in Yeast Nitrogen base medium showed similar CO₂ production, and both yeasts tolerated pH 2–10. Notably, *K. marxianus* tolerated up to 16% ethanol, a concentration inhibitory to *S. cerevisiae* strain Lalvin EC-1118. Sensory evaluation described *S. cerevisiae* strain Lalvin EC-1118 as producing astringent alcohol and musty notes, whereas *K. marxianus* generated citrus and lime peel aromas. These findings highlight *K. marxianus* JK319 as a promising alternative yeast for industrial fermentation under stressful conditions. Future studies will quantify ethanol and volatile compounds by HPLC and GC–MS and apply transcriptomic analysis to elucidate genes involved in aroma biosynthesis and stress tolerance.

Introduction:

Alcoholic beverages are globally popular products. According to Market Data Forecast (2024), the global alcoholic beverage market was valued at USD 585.16 billion in 2024 and expected to increase to USD 1,091.14 billion by 2032. In the commercial alcoholic beverage industry, yeast plays a crucial role in determining alcohol quality as well as the sensory and flavor characteristics of the final product. Key odor groups in alcoholic beverages include esters, aldehydes, ketones, and higher alcohols, such as ethyl octanoate, decanal, limonene, and 2-phenylethanol, which impart fruity, floral, roasted, and green aromas, respectively (1). *Saccharomyces cerevisiae* is the most widely used species due to its high ethanol productivity and strong tolerance to industrial stress conditions (2). However, *S. cerevisiae* has a relatively limited ability to produce complex aroma and flavor compounds, which can sometimes result in less distinctive sensory profiles in alcoholic beverages (3).

Non-*Saccharomyces* yeasts are therefore being explored as alternative options for alcoholic beverage production. Previous studies have shown that Non-*Saccharomyces* species such as *Torulospora delbrueckii*, *Wickerhamomyces anomalus*, *Metschnikowia pulcherrima*, and *Lachancea thermotolerans* produce metabolites associated with floral, fruity, citrus, and honey-like sensory attributes (4). Comparative studies between *S. cerevisiae* and Non-*Saccharomyces* species, including *Hanseniaspora uvarum*, *Hanseniaspora guilliermondii*, and *Pichia kluyveri*, found that *S. cerevisiae* produces lower amounts of key aroma compounds such as fatty acids, higher alcohols, and esters than the Non-*Saccharomyces*



strains. (5). However, many Non-*Saccharomyces* species exhibit lower ethanol yields, slower fermentation rates, and reduced tolerance to stress conditions such as high sugar concentrations and ethanol levels, which limits their independent use in large-scale fermentation (5, 6).

Herein, this study aims to screen and isolate Non-*Saccharomyces* yeasts capable of producing high concentrations of VOCs (Volatile compounds) for potential application in the alcoholic fermentation industry. Strains were isolated from multiple sources and identified using the biochemical test kit API 32C and morphological characterization. Preliminary screening included fermentation trials and sensory evaluation by special panelist, evaluated against a commercial wine yeast strain *S. cerevisiae* strain Lalvin EC-1118. Promising isolates were subsequently evaluated for growth phenotypes and for alcohol and acid-base tolerance, in comparison with the commercial wine yeast. The identified strains may serve as potential starters for enhancing the aromatic profile of alcoholic beverages in industrial-scale production.

Methodology:

1. Screening of isolated yeast

1.1 Preparation of medium for the screening of yeast strains

Prepare YPD solid medium (yeast extract 10 g/L, peptone 20 g/L, glucose 20 g/L, agar 20 g/L) or solid YNB (yeast nitrogen base 6.7 g/L, peptone 20 g/L, glucose 20 g/L, agar 20 g/L) and liquid YPD medium (yeast extract 10 g/L, peptone 20 g/L, glucose 20 g/L) or YNB liquid medium (yeast nitrogen base 6.7 g/L, peptone 20 g/L, glucose 20 g/L) for separating yeast from potato peels, pineapple and sugar factory.

Prepare SD liquid medium (yeast nitrogen base without amino acids and ammonium sulphate 1.7 g/L, glucose 20 g/L, ammonium sulphate 2.5 g/L) for study growth characteristics and tolerance to various stresses on yeast.

1.2 Screening and identification yeast by biochemical test

Yeasts were isolated from three sources: potato peels, pineapple, and sugar factory samples. All isolates were streaked onto YPD agar and incubated at 30 °C for 24–48 h. The obtained colonies were examined for colony and cellular morphology under a light microscope. Preliminary identification was performed using the biochemical API 32C kit (bioMérieux). Yeast strains were further characterized based on their ability to assimilate different sugars, and the resulting profiles were analyzed and interpreted using the APIWEB™ database. Non-*Saccharomyces* isolates were distinguished from *Saccharomyces cerevisiae* primarily by their cell morphology (shape and budding pattern) and by differences in biochemical assimilation profiles obtained from the API 32C test. These criteria enabled reliable differentiation of non-*Saccharomyces* strains for subsequent experiments.

1.3 Fermentation test and measurement CO₂ loss accumulation

Single yeast culture was suspended in 5 mL of Yeast Nitrogen Base (YNB) liquid medium in a shaking incubator at 200 rpm 30 °C for 24 h. Cells were harvested by centrifugation at 7000 rpm at room temperature for 3 minutes. Cells were resuspended in sterile distilled water and transferred to the YNB broth containing 250 g/L glucose (YNB+25% glucose) with a volume of 1220 mL, an initial inoculum of 0.1 absorbance at 600 nm (OD₆₀₀ = 0.1), in the dark at room temperature, without aeration. Fermentation capacity was measured for 14 days by comparing the initial weight and calculating the fermentation capacity based on the amount of gas lost from the sugar of net carbon dioxide loss (accumulative CO₂ loss)



2. Assessment volatile compounds generated during fermentation using primary sensory evaluation

Volatile compounds generated during fermentation were assessed by a sensory panel consisting of one certified evaluator with formal training in sensory evaluation and three additional panelists who had received basic training in aroma sniffing. The panel evaluated the aroma characteristics of the isolates in comparison with a commercial wine yeast strain.

3. Growth phenotype determination of isolated yeasts

A single yeast colony was cultured in 50 mL of SD broth in a flask at 30 °C for 36–48 h. The inoculum was transferred to fresh medium at $OD_{600} = 0.1$ and incubated with shaking at 200 rpm at 30 °C. Growth was monitored by measuring OD_{600} every 4 h for 36 h to study the growth characteristics of the yeast strains at different time points.

4. Examination of alcohol and acid-base tolerance in isolated yeasts

A single yeast colony was suspended in Synthetic Dextrose (SD) broth at 30 °C for 36–48 h. Subsequently, 5% (v/v) inoculum was transferred to SD broth containing ethanol concentrations of 0, 8, 10, 12, 14, and 16% (v/v) and different pH levels (2, 4, 6, 8, and 10). Growth was measured by OD_{600} at 0–48 h.

Result and Discussion:

A total of 19 yeast isolates were obtained: 5 isolated from potato peels, 5 isolated from pineapple, and 9 isolated from sugar factory samples, which were designated JK301–JK319. Based on colony morphology and the API 32C test, 4 isolates (JK301, JK302, JK304, and JK319) were selected as Non-*Saccharomyces* strains and confirmed to be non-pathogenic. Colony morphology, isolation source, and biochemical identification by the API 32C test are summarized in Table 1.

Table 1.

Characterization, isolation source, and biochemical identification of the isolated yeast strains

Yeast	Colony morphology	Isolation sources	API 32C
JK301	Circular, rough, undulate, pearly	Pineapple	<i>Cryptococcus humicola</i>
JK302	Circular, smooth, entire, pearly	Pineapple	<i>Candida colliculosa</i>
JK304	Circular, rough, undulate, pearly	Potato peels	<i>Cryptococcus humicola</i>
JK319	Circular, smooth, entire, pearly	Sugar factory	<i>Kluyveromyces marxianus</i>

Fermentation performance, based on CO₂ loss accumulation, was compared between non-*Saccharomyces* yeasts and the commercial *S. cerevisiae* strain Lalvin EC-1118, as shown in **Figure 1**

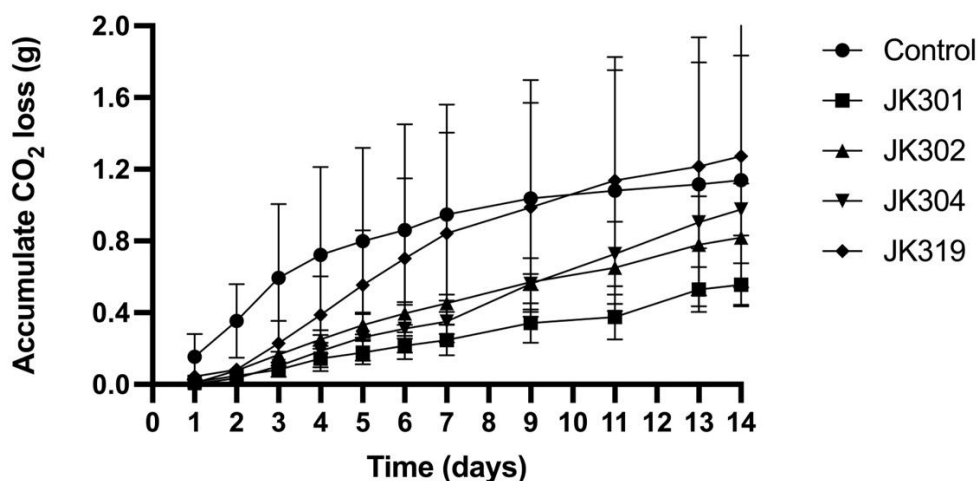


Figure 1.

The sugar assimilation capacity tests for yeast isolates JK301, JK302, JK304, and JK319 derived from potato peels, pineapple, and sugar factory, in comparison to the commercial control yeast, *Saccharomyces cerevisiae* Lalvin yeast EC-1118

From Day 1 to Day 7, *S. cerevisiae* EC1118 exhibited a markedly higher CO₂ loss accumulation, reaching 0.947 ± 0.614 g on Day 7. Within the non-*Saccharomyces* group,

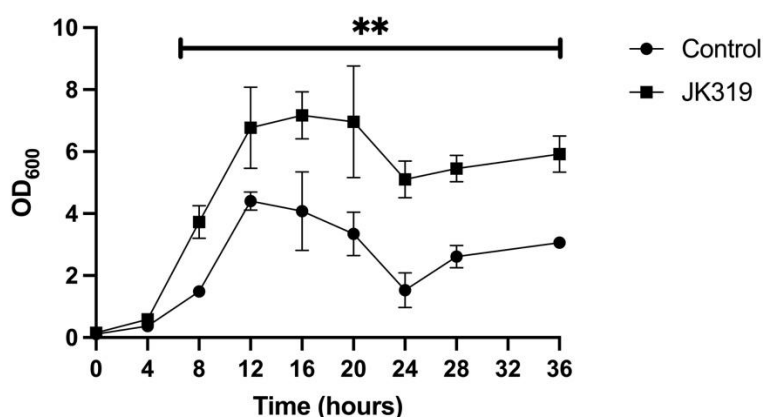
K. marxianus JK319 recorded the highest CO₂ loss 0.843 ± 0.562 g on Day 7 compared with the other non-*Saccharomyces* strains. By Day 9, CO₂ loss in *S. cerevisiae* strain Lalvin EC-1118 1.037 ± 0.662 g and *K. marxianus* JK319 0.987 ± 0.584 g became comparable. Notably, on Day 14, *K. marxianus* JK319 reached the highest CO₂ loss among all strains tested (1.273 ± 0.732 g), which was comparable to the commercial wine yeast *S. cerevisiae* strain Lalvin EC-1118 (1.140 ± 0.697 g). In contrast, other non-*Saccharomyces* strains showed lower CO₂ loss values, including *C. humicola* JK304 0.977 ± 0.146 g, *C. colliculosa* JK302 0.820 ± 0.026 g, and *C. humicola* JK301 0.557 ± 0.120 g. The comparable CO₂ loss observed in *K. marxianus* JK319 and *S. cerevisiae* strain Lalvin EC-1118 suggests that this non-*Saccharomyces* strain could be a promising candidate for industrial alcoholic fermentation, providing acceptable fermentation efficiency. As expected, *S. cerevisiae* strain Lalvin EC-1118 exhibited strong fermentative performance throughout the process. Interestingly, *K. marxianus* JK319 reached CO₂ loss values not only comparable to *S. cerevisiae* strain Lalvin EC-1118 by Day 9 but even surpassed it by Day 14. This indicates that *K. marxianus* JK319 possesses considerable fermentative capacity.

Table 2.

Characterisation of the flavor profiles derived from the assessment of each yeast strain's fermentation

Yeast isolated	Sensory descriptions
Control	Astringent alcohol, smooth, mushrooms, vegetables, slightly musty
JK301	Sour odour, absence of alcoholic scent, mushroom, soy sauce, shiitake mushroom, oyster sauce, putrid odour, traditional Chinese medicine
JK302	Clean, earthy tones, slightly fragrant, similar to red wine, with floral notes at the end
JK304	Whale oil, carbon dioxide, citrus fruits
JK319	Citrus fruits, mushrooms and lemon peel

The flavor profiles resulting from yeast fermentation are presented in Table 2. Based on sensory evaluation, the panelists recommended yeast isolate *K. marxianus* JK319 for its desirable scents, including citrus fruits, mushrooms, and lemon peel. These scents were consistent with ester, terpene and aldehyde groups (1). Nevertheless, the aroma profile should be further confirmed using analytical techniques such as gas chromatography–mass spectrometry (GC–MS). Based on the combined results of fermentation efficiency and sensory evaluation *K. marxianus* JK319 can be suitable candidate for further investigation.

**Figure 2.**

Growth curves of the control strain *S. cerevisiae* strain Lalvin EC-1118 and *K. marxianus* JK319 at different time points (0–36 hours), measured by optical density at 600 nm (OD₆₀₀). Statistically verified by student's t-test, $p < 0.05$

The growth phenotypes of the control strain *S. cerevisiae* strain Lalvin EC-1118 and *K. marxianus* JK319 were monitored over a 36-h period by measuring optical density at 600 nm (OD₆₀₀). Growth curves **Figure 2** showed that both strains exhibited a typical sigmoidal pattern. *K. marxianus* JK319 demonstrated a rapid exponential phase within the first 16 h, reaching a maximum OD₆₀₀ of 7.167 ± 0.759 . In comparison, *S. cerevisiae* strain Lalvin EC-

1118 grew more slowly, reaching a maximum OD₆₀₀ of 4.407 ± 0.297 at 12 h. At 20–24 h, the OD₆₀₀ values of both strains decreased (5.100 ± 0.595 for *K. marxianus* JK319 and 1.525 ± 0.565 for *S. cerevisiae* strain Lalvin EC-1118), which may be attributed to glucose depletion in the medium, resulting in a temporary decline in growth. At the later stage (28–36 h), OD₆₀₀ values increased again, likely due to the utilization of ethanol and other secondary metabolites as alternative carbon sources. At the final time point (36 h), the OD₆₀₀ values were 5.917 ± 0.588 for *K. marxianus* JK319 and 3.060 ± 0.183 for *S. cerevisiae* strain Lalvin EC-1118. These growth characteristics are consistent with previous reports. In *S. cerevisiae*, rapid sugar consumption under high-glucose conditions often leads to ethanol accumulation (Crabtree effect) and reduced biomass yield, with cells later shifting to ethanol utilization once glucose is exhausted (7). In *K. marxianus*, adaptive responses during the transition from glucose to ethanol metabolism have been reported under oxygen-limited and nutrient-depleted conditions, reflecting the strain's metabolic flexibility and stress tolerance (8). Therefore, *K. marxianus* JK319 was selected as the representative non-*Saccharomyces* strain for further characterization, due to its superior growth performance and metabolic adaptability compared to *S. cerevisiae* strain Lalvin EC-1118.

Table 3.

Evaluation of alcohol tolerance in the different yeast strains tested in this study

Yeasts	Alcohol concentrations					
	Alc 0%	Alc 8%	Alc 10%	Alc 12%	Alc 14%	Alc 16%
Control	++	++	+	+	-	-
JK319	++	+	++	++	++	++

Note:

'-' means cannot grow/grows slightly

'+' means grows well

'++' means grows very well

'-' indicates an OD₆₀₀ value less than 0.00 per mL

'+' indicates an OD₆₀₀ value between 0.00 and 1.00 per mL

'++' indicates an OD₆₀₀ value greater than 1.00 per mL

The alcohol tolerance of the yeast strains is summarized in Table 3. Under the control condition 0% ethanol, both *S. cerevisiae* strain Lalvin EC-1118 and *K. marxianus* JK319 exhibited normal growth. At 8% ethanol, both strains were able to grow, with *S. cerevisiae* showing moderate growth. *K. marxianus* JK319 demonstrated superior tolerance, maintaining robust growth at 10–12% ethanol. Remarkably, at 14% and 16% ethanol, *K. marxianus* JK319 continued to grow vigorously, whereas *S. cerevisiae* Lalvin EC-1118 was unable to grow under these conditions. These findings indicate that *K. marxianus* JK319 possesses higher alcohol tolerance than the commercial wine yeast, highlighting its potential for industrial fermentation applications.



Table 4.
Evaluation of pH levels in the different yeast strains tested in this study

Yeasts	pH levels				
	pH2	pH4	pH6	pH8	pH10
Control	+	++	++	++	++
JK319	+	++	++	++	++

Note:

'-' means cannot grow/grows slightly

'+' means grows well

'++' means grows very well

'-' indicates an OD₆₀₀ value less than 0.00 per mL

'+' indicates an OD₆₀₀ value between 0.00 and 1.00 per mL

'++' indicates an OD₆₀₀ value greater than 1.00 per mL

The acid-base tolerance of the yeast strains was summarized in Table 4. Both strains exhibited similar growth across a pH range of 2 to 10. The ability of both strains to grow across a broad pH range 2 to 10 indicates their robustness under varying acidic and alkaline conditions commonly encountered during industrial fermentation. Notably, *K. marxianus* JK319 maintained growth comparable to the commercial wine yeast *S. cerevisiae* strain Lalvin EC-1118, suggesting its suitability as a potential starter culture for alcoholic fermentation processes that may involve fluctuating pH conditions.

Conclusion:

In this study, Non-*Saccharomyces* yeast strains were isolated from pineapple, potato peels, and sugar factory samples and characterized for their colony morphology, biochemical profile, fermentation performance, aroma production, and stress tolerance. Among the strains tested, *K. marxianus* JK319, isolated from the sugar factory, exhibited superior fermentative capacity, as evidenced by CO₂ loss comparable to the commercial wine yeast *S. cerevisiae* strain Lalvin EC-1118, robust growth under various conditions, high alcohol tolerance, and the production of desirable aroma compounds, including citrus and lemon peel notes. These combined traits highlight *K. marxianus* JK319 as a promising candidate for industrial alcoholic fermentation. Future studies should focus on analytical confirmation of volatile compounds via GC-MS and on investigating the mechanisms underlying volatile compound synthesis and stress tolerance.

References:

1. Zhang S, Petersen M, Liu J, Toldam-Andersen T. Influence of Pre-Fermentation Treatments on Wine Volatile and Sensory Profile of the New Disease Tolerant Cultivar Solaris. *Molecules*. 2015;20:21609-25.
2. Ji X-X, Zhang Q, Yang B-X, Song Q-R, Sun Z-Y, Xie C-Y, et al. Response mechanism of ethanol-tolerant *Saccharomyces cerevisiae* strain ES-42 to increased ethanol during continuous ethanol fermentation. *Microbial Cell Factories*. 2025;24(1):33.
3. Romano P, Braschi G, Siesto G, Patrignani F, Lanciotti R. Role of Yeasts on the Sensory Component of Wines. *Foods*. 2022;11(13).
4. Gunhan M. With Advantages and Disadvantages The Role of Non-*Saccharomyces* Yeast In The Wine Industry. *Turkish Journal of Food and Agriculture Sciences*. 2022;4:13-7.



5. Lai Y-T, Hsieh C-W, Lo Y-C, Liou B-K, Lin H-W, Hou C-Y, et al. Isolation and identification of aroma-producing non-Saccharomyces yeast strains and the enological characteristic comparison in wine making. *LWT*. 2022;154:112653.
6. Mandakovic D, Pulgar R, Maldonado J, Mardones W, González M, Cubillos F, et al. Fungal Diversity Analysis of Grape Musts from Central Valley-Chile and Characterization of Potential New Starter Cultures. *Microorganisms*. 2020;8:956.
7. Bertozzi Silva J, Sauvageau D. Bacteriophages as antimicrobial agents against bacterial contaminants in yeast fermentation processes. *Biotechnology for biofuels*. 2014;7:123.
8. Signori L, Passolunghi S, Ruohonen L, Porro D, Branduardi P. Effect of oxygenation and temperature on glucose-xylose fermentation in *Kluyveromyces marxianus* CBS712 strain. *Microbial Cell Factories*. 2014;13(1):51.



ANTIMICROBIAL ACTIVITY AGAINST *Cutibacterium acnes* OF CORN AGRO-RESIDUES EXTRACT AS WASTE UTILIZATION FOR COSMETIC APPLICATION

Natthawut Thitipramote^{1,2*}, Ranchana Samaniam², Prinyaporn Pradmeeteekul¹, Junniphaphorn Nimkamnerd¹, Thiyapan Noppakoon¹, and Witayapan Nantitanon²

¹ Center of Excellence in Natural Products Innovation (CENPi), Mae Fah Luang University, Chiang Rai, 57100, Thailand

² School of Cosmetic Science, Mae Fah Luang University, Chiang Rai 57100, Thailand

*e-mail: natthawut.thi@mfu.ac.th

Abstract:

Corn agro-residues (CARs) productions or cultivations (e.g. tassels, leaves, and stalks) have higher amounts and low value. The most of these CARs are either as natural fertilizer or burnt. Agricultural burning is one of the causes of the particulate matter (PM_{2.5}) that reached a hazardous point of human health and environment. Thus, this study aimed to utilize corn agro-residues (CARs) as bioactive in cosmetic application. CARs (tassels-CRT, leaves-CRL, and stalks-CRS) were extracted with two solvents (ethyl acetate-EA and ethanol-ET) using shaking extraction 24 hours. Bioactive compounds (total phenolic; TPC, and total flavonoid; TFC contents) and antibacterial activity against *Cutibacterium acnes* [using agar well diffusion method (AWD), minimum inhibitory concentration (MIC) and minimum bactericidal concentration (MBC)] as well as the cytotoxicity of these CARs extracts were investigated. The results showed that ethanolic CARs extract tended to exert greater TPC than ethyl acetate extract at the same CARs part. The highest TPC was found in the CRT-ET extract (773.7 ± 17.2 mg GAE/g extract, $p < 0.05$). However, the highest TFC was found in the CRT-EA extract (876.3 ± 2.5 mg QE/g extract, $p < 0.05$). The results of antimicrobial activity against *C. acnes* showed that the inhibition zone was mostly found at high concentration of CARs extracts (≥ 5 mg/mL). In terms of MIC, corn leaves extracted with ethyl acetate (CRS-EA) showed the lowest MIC value (3.12 mg/mL). The MBC of CARs extracts, all three parts extracted with ethyl acetate (CRS-EA, CRL-EA and CRT-EA) showed highest effectiveness of MBC (12.50 mg/mL). The ethanolic extracts of CARs showed no toxicity at concentrations of 0.5 and 1 mg/mL (\square 85% cell viability). Thus, CARs extracts can be value-added by being used as a natural active ingredient in cosmetic applications and other related products.

Keywords: Agro-residues; Antibacterial; Bioactive compounds; Corn; *Cutibacterium acnes*; Cytotoxicity; Utilization

Introduction:

In Northern Thailand, the most significant economic activity is agriculture. Corn (*Zea mays*) is one of the major farming areas, especially in Chiang Rai province, accounting for 67.24%. Chiang Rai has approximately 0.3 million rai of corn farming area, which is the second largest in the northern region of Thailand¹. After harvesting, all of the agro-residues (tassels, leaves, and stalks) became fertilizer or were taken to a landfill. Moreover, agricultural burning was performed to dispose of residues and clear the land in preparation for the next crop cycle. This is the major cause of the smoke haze situation and particulate matter (PM_{2.5})², resulting in a negative impact on human health in the nearby area and environment, such as skin diseases, eye diseases, lung cancer, depression, cardiovascular diseases, and respiratory diseases.

Cutibacterium acnes is the most abundant source of microbiota on normal human skin. *C. acnes* is a gram-positive anaerobic facultative bacterium that helps to preserve and

support the natural microbial balance of the skin. However, under certain conditions, it can also substantially alter its local environment and cause disease³. *C. acnes* was first isolated from a patient with chronic acne vulgaris (AV), chronic inflammatory disease of the pilosebaceous unit, in the 1900s⁴. Inflammatory lesions can lead to scar formation, which is the result of inflammation of the acne dermis, and these processes tend to occur on the face, neck, chest, and back of AV patients⁵. However, there can be an overgrowth that can occur when factors like excess sebum production, hormonal changes, or inflammation create conditions favorable for bacterial proliferation⁶.

Previous studies showed that the ethanolic extract from corn silk had higher phenolic and flavonoid contents that had the potential as a bioactive source to inhibit the growth of acne-related bacteria, *Propionibacterium acne* or *Cutibacterium acne*, *Staphylococcus epidermidis*, and *Staphylococcus aureus*^{7,8}. Furthermore, a part of corn agro-residues; tassels, leaves, and stalks are presented with phenolic and flavonoid contents. Moreover, DPPH radical scavenging activity showed statistically significant antioxidant and anti-tyrosinase activity of corn residues⁹. Antibacterial activity of crudes from corn agro-residues extracts described by Odelola *et al.*, (2023)¹⁰ showed the highest inhibitory effects on *Pseudomonas aeruginosa*, *Klebsiella pneumoniae*, *Staphylococcus aureus*, *Escherichia coli*, and Coagulase-Negative *Staphylococci*. However, the study of their activity on *Cutibacterium acnes* inhibition of corn residues (tassels, leaves, and stalks) as agro-residuals has been little investigated. Previous studies showed that ethanol and ethyl acetate solvent extraction could exert both phenolic compounds and flavonoids in corn silk, stems, and tassels; therefore, these solvents were chosen in this study¹¹. Furthermore, their agro-residues might have antibacterial activity against *C. acnes* due to these plants composed of phenolic and flavonoid contents and can be developed as a natural active ingredient for cosmetic formulations or natural products to increase value, utilization, and reduce negative impact on human nearby communities and the environment. Therefore, this study aimed to investigate antibacterial activity of extracts from agro-residues of corn (tassels, leaves, and stalks) production against *Cutibacterium acnes* (*C. acnes*) and to evaluate cytotoxicity of corn agro-residues extracts that might be used as a natural active ingredient in cosmetic applications for maximum utilization.

Methodology:

Chemicals and reagents

All chemicals and solvents were of analytical grade. aluminum chloride (AlCl₃), dimethyl sulfoxide (DMSO), ethanol, ethyl acetate, gallic acid, quercetin, were purchased from Sigma Chemical (St.Louis, MO, USA). Folin-Ciocalteu reagent, ferric chloride, potassium acetate (CH₃COOK), and sodium carbonate (Na₂CO₃) were purchased from Merck (Darmstadt, Germany).

Plant preparation and extraction

Corn (*Zea mays*) agro-residues (CARs) were procured from a local farmer in Chiang Rai province, Thailand. The samples were separated into tassels, leaves, and stalks, and then were cleaned and dried in a hot air oven at 45°C until a constant sample weight. The dried sample was milled into powder and stored in a desiccator until use.

CARs were extracted by two different solvents: ethyl acetate (EA) and ethanol (ET), using shaking extraction at a ratio of sample: solvent (1:10 w/v) with an incubator shaker at 200 rpm at room temperature for 24 hours. All extracts were filtered by Whatman filter paper No.1. Organic solvents were removed by rotary evaporator at 50°C. CARs extracts were freeze-dried and kept at -20°C until used.

Determination of bioactive compounds

Total phenolic content (TPC) was measured with slight modification⁹. Briefly, 20 μL of CARs extracts were reacted with 100 μL of 0.2 M Folin-Ciocalteu reagent and 80 μL of 7.5% Na_2CO_3 . The mixture was left to stand in the dark for 30 minutes at room temperature. The absorbance was measured at 765 nm using a microplate reader. Gallic acid was used as a reference standard. The results were expressed as mg gallic acid equivalents (GAE)/g extract.

Total flavonoid content (TFC) was measured with slight modification⁹. Briefly, 25 μL of CARs extracts were mixed with 75 μL of ethanol, 140 μL of DI water, 5 μL of 10% (w/v) AlCl_3 , and 5 μL of 1M CH_3COOK , respectively. The mixture was incubated in the dark for 30 minutes at room temperature. The absorbance was measured at 415 nm. Quercetin was used as a reference standard, and the results were expressed as mg quercetin equivalents (QE)/g extract.

Anti-microbial activity against *Cutibacterium acnes*

Agar well diffusion (AWD)

Agar well diffusion (AWD) was used only for screening of antimicrobial activity from CARs (tassels, leaves, and stalks) extracts. Gram-positive *C. acnes* DMST 14916 strain was used in this study. Bacteria were first grown in brain heart infusion (BHI) and incubated at anaerobic condition with 37°C for 4 days. After incubation, the bacteria were adjusted to 0.5 on the McFarland scale, corresponding to 1.5×10^8 colony-forming units (CFU) mL^{-1} by suspending the bacteria in 0.85% normal saline. To modify the work of Domingos *et al.*, (2021)¹², the suspension was spread on BHI by cotton stick, 4 mm deep wells have been cut into the agar surface and then filled with 30 μL for each extract at concentrations 1, 5, 25 and 50 mg/mL in Dimethyl sulfoxide (DMSO) and incubated at 37°C for 4 days. Ampicillin (as an antibiotic) and phenoxyethanol (as a cosmetic preservative) were used as a positive control.

Minimum Inhibitory Concentration (MIC)

The minimal inhibitory concentration (MIC) is the lowest concentration of an antibacterial agent, completely preventing visible growth of the test strain of an organism¹³. MICs were assessed in 96-well plates using three replications of each microdilution assay being conducted. To modify the work of Domingos *et al.*, (2021)¹², the CARs extracts were diluted by a serial dilution of 50 mg/mL – 0.097 mg/mL in brain heart infusion broth (BHI broth). Ampicillin and Phenoxyethanol are also diluted concentrations of 25 $\mu\text{g}/\text{mL}$ – 0.048 $\mu\text{g}/\text{mL}$. After dilution, each bacterial strain suspension was adjusted to 0.5 on the McFarland scale, added in 96-well plates for 100 μL . Finally, the plates were incubated at 37°C for 4 days. After incubation, 30 μL of resazurin 0.015% (w/v) was added to all wells and further incubated for 2 hours to observe the color change¹⁴. MIC value was defined as the extreme lowest concentration of plant extract which inhibited the growth of bacteria¹⁵

Minimum Bactericidal Concentration (MBC)

The minimum bactericidal concentration (MBC) is determined by directly plating the contents of wells with concentrations greater than the MIC value¹³. According to Elshikh's work¹³, subcultures were made of four wells that did not show bacterial growth (two wells with higher MICs value and one wells which a lower MIC value). The bacteria were grown in BHI and incubated at 37°C for 4 days. The MBC was determined as the minimum concentration of the tested samples that had no bacterial population in the BHI plates¹⁶.



Cytotoxicity of CARs extracts

Ethanol CARs extracts were tested for cell toxicity on a Human immortalised non-tumorigenic keratinocyte cell line (HaCaT) (CLS Cell Lines Service, Eppenheim, Germany) using the MTT assay. HaCaT were cultured in Dulbecco's modified Eagle's culture medium (DMEM) supplemented with 10% heat-inactivated fetal bovine serum, 50 IU/mL of penicillin, and 50 µg/mL of streptomycin. Cells (1×10^4 cells/mL) were cultured in 24 well plate at 37°C in 5% CO₂ at 95% humidity. Samples were cytotoxicity tested at concentrations of 0.5 and 1 mg/mL. A 1% Triton X was used as a standard reference. Results were expressed as relative cell viability (%).

Statistical analysis

The obtained data were expressed in Mean \pm SD. An analysis of variance (ANOVA) test using Duncan's multiple range test for parametric analysis and Kruskal-Wallis for non-parametric analysis was used to statistically analyze the differences in each parameter between the groups (IBM SPSS version 21.0). The significance level was at $p < 0.05$.

Results and Discussion:

The extract yield was calculated on a dry basis (% yield). Table 1 showed the extraction yields of each part of corn with different solvents. Among solvent extractions, the ethanol extraction tended to have a higher yield than ethyl acetate. The highest yield was found in CRL-ET (13.25 % yield). The lowest yield was found in the CRS-EA (0.40 % yield).

Bioactive compound contents

The results showed a significant difference bioactive compounds (TPC and TFC) among CARs extracts ($p < 0.05$) as shown in Table 1. The ethanol solvent extraction tended to exert greater TPC than ethyl acetate extraction. The CRT-ET had the highest TPC (773.7 ± 17.2 mg GAE/g extract) and the lowest TPC was found in CRL-EA extract (267.5 ± 33.3 mg GAE/ g extract; $p < 0.05$).

In contrast to TPC, the ethyl acetate extracts tended to have higher TFC than the ethanol extracts. The highest TFC was found in the CRT-EA (876.3 ± 2.5 mg QE/g extract, $p < 0.05$) as shown in Table 1. However, the lowest TFC occurred in the CRL-ET, CRL-EA, and CRST-ET (455.3 ± 11.5 , 520.4 ± 11.5 , and 479.0 ± 4.3 mg QE/g extract, respectively $p < 0.05$).

Similar to previous study, this study showed that the CRT-ET had higher total phenolic content than other solvents¹⁷. This study also showed that each part of CARs tended to have higher TFC than TPC. Flavonoids, commonly found in plants, are an indispensable part of the human diet, were found in corn silk and corn husks^{18,19}.

Table 1.

Extractable yield and bioactive compounds [total phenolic (TPC) and flavonoid (TFC) contents] of CARs extracts, including tassels, leaves, and stalks, with two different solvent extractions (ethanol: ET and ethyl acetate: EA)

CARs Extracts	Solvents	Yield of extracts (% dry basis)	Bioactive compound	
			TPC (mg GAE/g extract)	TFC (mg QE/g extract)
Tassels (CRT)	Ethanol (CRT-ET)	7.63	773.7 ± 17.2 ^a	570.8 ± 3.8 ^c
	Ethyl Acetate (CRT-EA)	4.60	401.4 ± 8.6 ^c	876.3 ± 2.5 ^a
Leaves (CRL)	Ethanol (CRL-ET)	13.25	551.6 ± 5.5 ^b	455.3 ± 11.5 ^d
	Ethyl Acetate (CRL-EA)	3.84	267.5 ± 33.3 ^d	520.4 ± 11.5 ^d
Stalks (CRS)	Ethanol (CRS-ET)	6.98	602.4 ± 9.5 ^b	479.0 ± 4.3 ^d
	Ethyl Acetate (CRS-EA)	0.40	454.8 ± 10.4 ^c	655.0 ± 1.4 ^b

Note: Values are given as mean ± S.D. (n=3). Different superscribe letters (a-d) in the same column indicated significant differences in values ($p < 0.05$, ANOVA, Duncan's test).

Agar well diffusion (AWD)

The antibacterial activity of each part of CARs extracts (tassels leaves and stalks) at various concentrations 1, 5, 25 and 50 mg/mL was determined by the agar well-diffusion assay. The results showed that the inhibition zone mostly occurred in all CARs extracts at concentration ≥ 5 mg/mL, except CRS-ET extract (Table 2; Figure 1). Moreover, the CRT-ET and CRT-EA extracts showed the inhibition zone for *C.acnes* at concentrations 5, 25 and 50 mg/mL that ranged 18.95 – 22.29 and 13.97 – 19.03 mm, respectively. The inhibition zone of CRL-ET and CRL-EA extracts at concentrations ≥ 5 mg/mL ranged from 9.25 – 18.25 mm and 13.02 – 19.84 mm, respectively. The CRS-ET showed the inhibition zone at only one concentration (50 mg/ml) (10.80 ± 0.64 mm). While, the CRS-EA extracts exhibited the inhibition zone at all concentration (1-50 mg/mL) that ranged from 8.63 – 14.14 mm (Table 2; Figure 1).

Table 2.

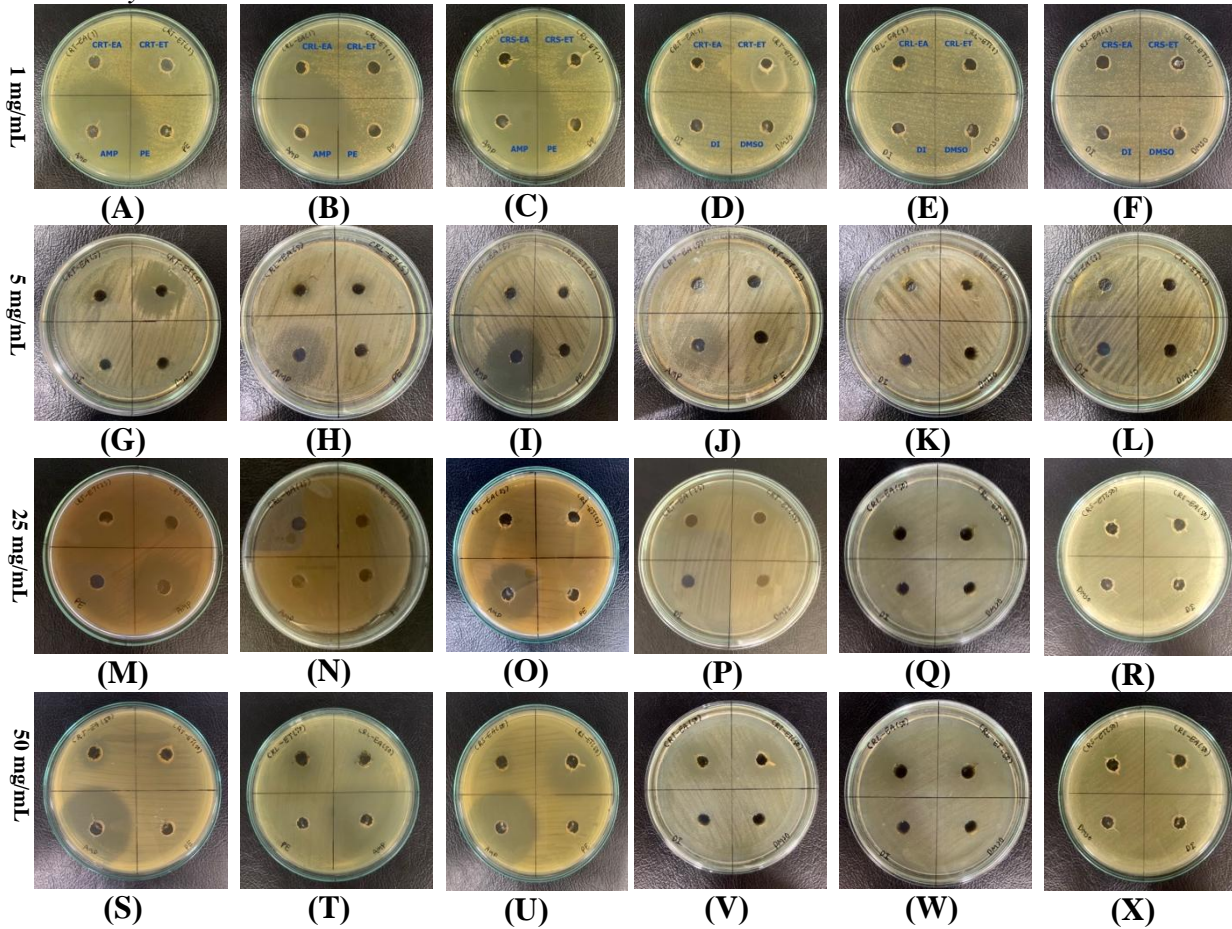
Inhibition zone of corn agro-residues (tassels, leaves, and stalks) extracts by agar well diffusion (AWD)

Groups	Samples	Solvents	Concentration	Units	Inhibition zone of <i>C. acnes</i> (mm)
Positive control	Ampicillin (AMP)		10	$\mu\text{g/mL}$	$9.08 \pm 0.76^{\text{h}}$
			25	$\mu\text{g/mL}$	$36.40 \pm 3.05^{\text{a}}$
Negative control	DMSO		-	-	ND
	DI water		-	-	ND
CARs extract	Tassels (CRT)	Ethanol (CRT-ET)	1	mg/m	ND
			5	L	$20.54 \pm 0.94^{\text{b,c,d}}$
			25	mg/m	$22.29 \pm 1.33^{\text{b}}$
		50	L	$18.95 \pm 1.77^{\text{c,d,e}}$	
			mg/m		
			L		
	Ethyl acetate		1	mg/m	ND
			5	L	$13.97 \pm 1.24^{\text{f,g}}$

Groups	Samples	Solvents	Concentration n	Units	Inhibition zone of <i>C. acnes</i> (mm)
		(CRT-EA)	25	mg/m	18.65 ± 4.08 ^{d,e}
			50	L	19.03 ± 1.57 ^{c,d,e}
				mg/m	
				L	
				mg/m	
				L	
	Leaves (CRL)	Ethanol (CRL-ET)	1	mg/m	ND
			5	L	9.25 ± 1.12 ^h
			25	mg/m	16.15 ± 3.27 ^{e,f}
			50	L	18.25 ± 1.07 ^{d,e}
				mg/m	
				L	
				mg/m	
				L	
		Ethyl acetate (CRL-EA)	1	mg/m	ND
			5	L	13.02 ± 0.38 ^{f,g}
			25	mg/m	19.84 ± 3.69 ^{b,c,d}
			50	L	17.74 ± 2.47 ^{d,e}
				mg/m	
				L	
				mg/m	
				L	
	Stalks (CRS)	Ethanol (CRS-ET)	1	mg/m	ND
			5	L	ND
			25	mg/m	ND
			50	L	10.80 ± 0.64 ^{g,h}
				mg/m	
				L	
				mg/m	
				L	
		Ethyl acetate (CRS-EA)	1	mg/m	11.25 ± 1.03 ^{g,h}
			5	L	8.63 ± 0.82 ^h
			25	mg/m	14.14 ± 2.40 ^{f,g}
			50	L	13.50 ± 1.91 ^{f,g}
				mg/m	
				L	
				mg/m	
				L	

Note: Values are given as mean ± S.D. (n = 5). Different superscript letters (a-h) in the same column indicated significant differences values (ANOVA, Duncan's, $p < 0.05$). ND indicated No Detected.

Zea mays L.



Note: A-F indicated inhibition zone of 1 mg/mL; G-L indicated inhibition zone of 5 mg/mL; M-R indicated inhibition zone of 25 mg/mL, and S-X indicated inhibition zone of 50 mg/mL of CRT, CRL, and CRS extracts, respectively. Positive control: Ampicillin (AMP) and phenoxyethanol (PE). Negative control: DI water (DI) and Dimethyl sulfoxide (DMSO).

Figure 1.

Inhibition zone size of corn tassels (CRT), leaves (CRL), and stalks (CRS), extracted with different solvents (ethyl acetate: EA and ethanol: ET) by agar well diffusion (AWD) at concentrations of 1, 5, 25, and 50 mg/mL against *C. acnes*.

Minimum inhibitory concentration (MIC)

Minimum Inhibitory Concentration (MIC) of CARs extracts was shown in table 3. The CRL-EA showed the lowest MIC value at a concentration of 3.12 mg/mL. Moreover, positive control was strongly effective for antimicrobial properties, that MIC values were 0.39 μ g/mL of ampicillin and 4.00 mg/mL of phenoxyethanol (Table 3).

Minimum bactericidal concentration (MBC)

Results of MBC values from CARs extracts showed that all samples extracted with ethyl acetate (CRS-EA, CRL-EA, and CRT-EA) demonstrated the highest effectiveness at a concentration of 12.50 mg/mL. In the control group, ampicillin showed MBC values of 0.39 μ g/mL and phenoxyethanol showed MBC values of 4.00 mg/mL (Table 3; Figure 2).

Table 3

Minimum Inhibitory Concentration (MIC) and Minimum Bactericidal Concentration (MBC) of tested samples.

Groups	Samples	Solvents	Units	<i>C. acnes</i>	
				MIC	MBC
Positive control	Ampicillin (AMP)	-	μ g/mL	0.39 \pm	0.39 \pm
		-	mg/mL	0.00	0.00
	Phenoxyethanol (PE)			4.00 \pm	4.00 \pm
CARs extract	Tassels (CRT)	ethanol (CRT-ET)	mg/mL	12.50 \pm	25.00 \pm
				0.00	0.00
		Ethyl acetate (CRT-EA)	mg/mL	6.25 \pm	12.50 \pm
				0.00	0.00
	Leaves (CRL)	ethanol (CRL-ET)	mg/mL	12.50 \pm	25.00 \pm
				0.00	0.00
	Ethyl acetate (CRL-EA)	mg/mL	3.12 \pm	12.50 \pm	
			0.00	0.00	
Stalks (CRS)	ethanol (CRS-ET)		mg/mL	12.50 \pm	25.00 \pm
				0.00	0.00
	Ethyl acetate (CRS-EA)	mg/mL	6.25 \pm	12.50 \pm	
				0.00	0.00

Note: Values are given as mean \pm S.D. (n = 2).

Antibacterial activity of CARs extracts is corroborated by Odelola *et al.* (2023)¹⁰, The phytochemical analysis of the methanol and aqueous extracts of corn husks and silks revealed the presence of saponins, tannins, flavonoids, steroids, terpenoids, and cardiac glycosides. The aqueous extract of corn husk showed the highest inhibitory effects on *P. aeruginosa*, *K. pneumoniae*, *S. aureus*, *E. coli*, and Coagulase-Negative *Staphylococci* with zones of inhibition ranging from 14.80 \pm 1.89 mm to 24.40 \pm 2.51 mm at 200 mg/mL. Findings from this study revealed the antibacterial potential of corn silks and husk extracts at varying concentrations.

The results of this study showed antibacterial activity of *Zea mays* against *C. acnes*. According to previous studies, CARs extract contains saponin, tannins, flavonoids, and terpenoids that have antibacterial activity by destruction of cell membranes²⁰. Therefore, stalks, leaves, and tassels of corn extract might be associated with their potent antibacterial activity.

Cytotoxicity of CARs extracts

This study showed that the ethanolic extracts of CARs contained a high amount of TPC and exhibited antimicrobial activity. Although the antibacterial activity of these ethanolic extracts were lower than that of the ethyl acetate extract, the ethanol extraction uses as a green solvent that is environmentally and consumer-friendly. Therefore, this study conducted a preliminary toxicity test on the ethanolic extract to provide information for future application. Thus, these ethanolic extracts of CARs were tested with the human keratinocyte (HaCAT) cell line at concentrations of 0.5 and 1 mg/mL for 48 hours. The percentage of cell viability more than 85% was classified to be no toxic for the cell. The results showed that cell viability of all ethanolic extracts in each part of CARs (at 0.5 and 1 mg/mL) was higher than 85% (table 4). The highest cell viability was found in the ethanol of stalks extract at 0.5 mg/mL ($140.8 \pm 18.4\%$; $p < 0.05$; table 4). Triton X-100 as negative control showed low cell viability ($10.8 \pm 0.6\%$; table 4). Thus, the ethanolic extracts of CARs might be safe for use as an active ingredient in cosmetic products or other related products.

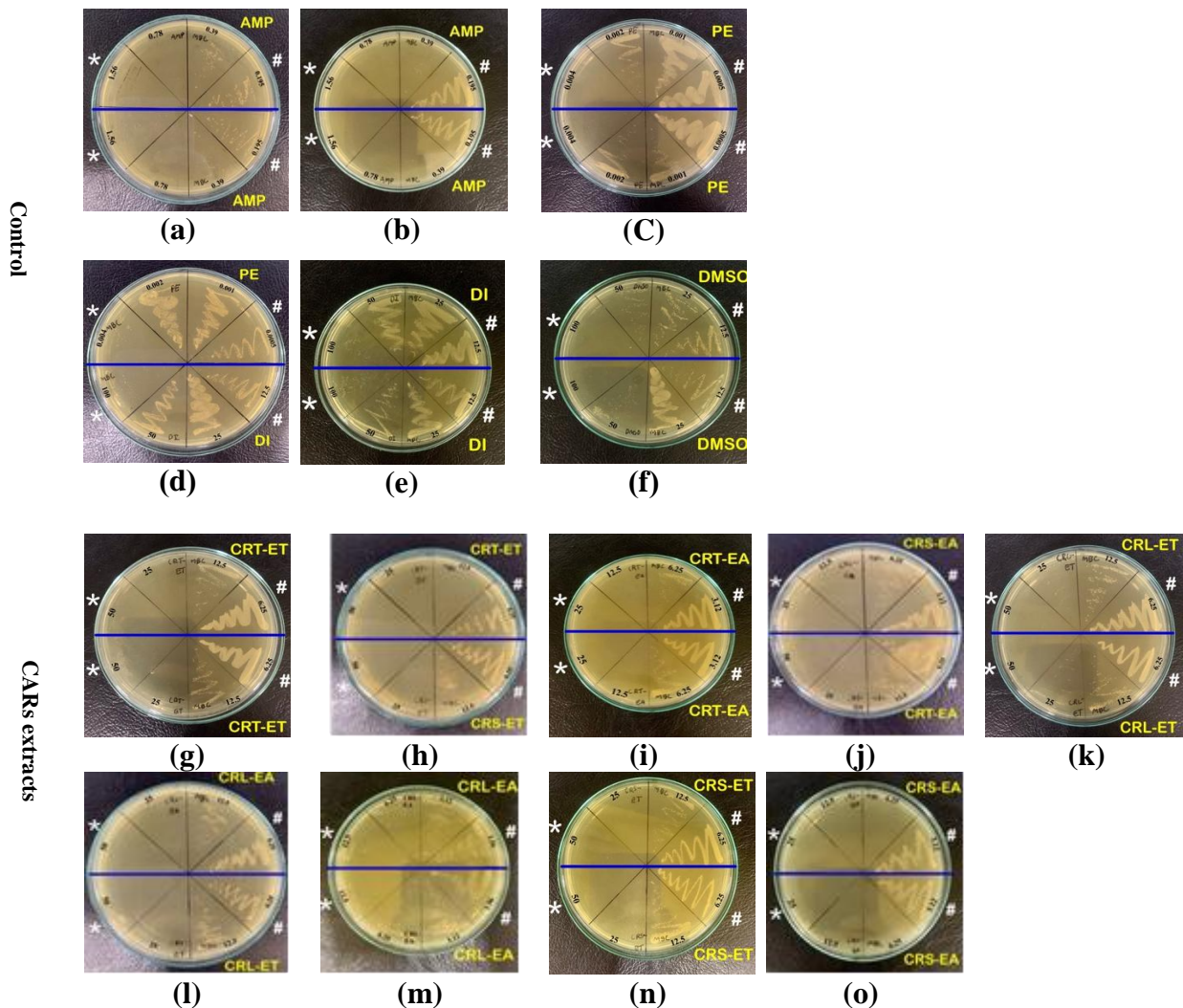


Figure 2.

Minimum Bactericidal Concentration (MBC) of the CARs (tassels, leaves, and stalks) extracts against *C. acnes* (g-o) with two different solvents (ethanol: ET and ethyl acetate: EA) and Asterisks (*) indicate the highest concentration to the lower concentration (#).

**Table 4**

Cytotoxicity of the ethanolic extracts of CARs, including tassels, leaves, and stalks at a concentration 0.5 and 1 mg/ml.

Group	Sample	concentration	% Cell viability
Control	No treated	-	100.0 ± 0.0 ^b
	Triton X-100	0.01 mg/mL	10.8 ± 0.6 ^c
CARs extract	Tassels-Ethanol (CRT-ET)	0.5 mg/mL	128.1 ± 19.9 ^a
		1 mg/mL	90.1 ± 5.3 ^b
	Leaves-Ethanol (CRL-ET)	0.5 mg/mL	139.4 ± 5.0 ^a
		1 mg/mL	93.1 ± 3.3 ^b
	Stalks-Ethanol (CRS-ET)	0.5 mg/mL	140.8 ± 18.4 ^a
		1 mg/mL	91.0 ± 6.1 ^b

Note: Values are given as mean ± S.D. (n=3), Different superscript letters (a-b) in the same column indicate significant differences in values ($p < 0.05$, ANOVA, Duncan's test).

Conclusion:

Corn agro-residues from corn cultivation (tassels, leaves, and stalks) have these bioactive compounds; TPC and TFC. The highest TPC was found in the ethanolic of corn tassels extract. While, the highest TFC was found in the ethyl acetate of corn tassels extract. For antibacterial activity was determined by the agar well-diffusion assay, the highest inhibition zone of was found on the ethanolic of corn tassels extract (CRT-ET). While the ethyl acetate of corn leaves extract (CRL-EA) showed the lowest minimum inhibitory concentration. Furthermore, the minimum bactericidal concentration was found on the ethyl acetate in all parts of corn. Moreover, the ethanolic of CARs showed no toxicity in HaCAT cells. Otherwise, corn agro-residues can be valuable-added and utilized for use as alternative source for natural active ingredients to formulation developed against acne vulgaris purposes in cosmetics or others related field.

Acknowledgements:

The authors are grateful to the Center of Excellence in Natural Products Innovation (CENPi), School of Cosmetic Science, and others in Mae Fah Luang University for financial and facilities supports.

References:

1. Ho P, Thepchalerm T. IJMMT. 2021;5(2):47–55.
2. Sirimongkonlertkun N. Environ. Nat. Resour. J. 2014;12(2):29–34.
3. Cros MP, Mir-Pedrol J, Toloza L, *et al.* Sci Rep. 2023;13:16058.
4. Mayslich C, Grange PA. Microorganisms. 2021;9:303.
5. Sun C, Na Y, Wang Z, Zhu T, Liu X. Front Pharmacol. 2024;15:1476670.
6. Sá S, Fernandes R, Gestoso Á, Macedo JM, Martins-Mendes D, Pereira AC, Baylina P. Appl. Sci. 2023;13:12086.
7. Nurani F, Rejeki N, Setyoputri T, Wardani P, Ridwan F, Suparmi S, Harlisa P. Bangladesh J. Med. Sci. 2022; 21:84-89.
8. Yucharoen R, Srisuksomwong P, Julsrigival J, Mungmai L, Kaewkod T, Tragoolpua Y. Antibiotics (Basel). 2023;12(9):1443.
9. Thitipramote N, Imsonpang S, Sukphopetch P, Pradmeeteekul P, Nimkamnerd J, Nantitanon W, Chaiyana W. Cosmetics. 2022;9(6):111.
10. Odelola OS, Oyetayo VO, Ogundare AO, Omoya FO, Ajayi OE. Int. J. pathog. Res. 2023;12(2):37–51.



11. Sheng S, Li T, Liu R. Corn phytochemicals and their health benefits. *Food Sci Hum Well*. 2018;7(3):185-195.
12. Domingos SCB, Clebis VH, Nakazato G, de Oliveira AG Jr, Takayama Kobayashi RK, Peruquetti RC, Pereira CD, Santa Rosa MT, Dos Santos Medeiros L. *J Sci Food Agric*. 2021;101(5):2072-2077.
13. Kowalska-Krochmal B, Dudek-Wicher R. *Pathogens*. 2021;10(2): 165.
14. Elshikh M, Ahmed S, Funston S, Dunlop P, McGaw M, Marchant R, Banat IM. *Biotechnol. Lett*. 2016; 38(6):1015-1019.
15. Rajagopal R, Kuppusamy P, Sathya R, Nandhakumari P, Bensy AD, Biji GD. *Physiol Mol Plant Pathol*. 2022;119:101813.
16. Parvekar P, Palaskar J, Metgud S, Maria R, Dutta S. *Biomaterial investigations in dentistry*, 2020; 7(1):105-109.
17. Mohsen SM, and Ammar ASM. *Food Chem*. 2009;112:595–598.
18. Tian S, Sun Y, Chen Z. *J Food Qua*. 2021; 1-9.
19. Zuorro A, Lavecchia R, González-Delgado AD, García-Martínez JB, L'Abbate P. *Processes*. 2019;7(11):804.
20. Jannah JK, Franyoto YD, Wulandari W, Widyasti JH. *JOHMPE*, 2023;1(1).



OPTIMIZATION OF PECTIN YIELD FROM *Cyclea barbata* MIERS LEAVES USING RESPONSE SURFACE METHODOLOGY

Witayapan Nantitanon^{1*}, Pimpailin Rodpradit¹, and Natthawut Thitipramote^{1,2}

¹School of Cosmetic Science, Mae Fah Luang University, Chiang Rai 57100, Thailand

²Center of Excellence in Natural Products Innovation (CENPi), Mae Fah Luang University, Chiang Rai, 57100, Thailand

*e-mail: witayapan.nan@mfu.ac.th

Abstract:

Pectin is a polysaccharide widely used in the food, pharmaceutical, and cosmetic industries as a gelling, stabilizing, emulsifying agent, prebiotic, and an attractive moisturizing agent ingredient in skin care, resulting in a continuously growing global demand. *Cyclea barbata* Miers is a traditional local plant widely distributed in Southeast Asia, including Thailand. It grows rapidly and is abundant in rural areas. Its leaves are rich in pectin, making them a sustainable raw material compared with conventional fruit peels. However, no study has yet optimized the extraction process from this plant. This work employed central composite design (CCD) to determine the optimal conditions for pectin extraction, especially examining the effects of temperature (70–90 °C), extraction time (30–60 min), and solution pH (1.5–3.5). The finding indicated that the quadratic model provided a superior fit ($p < 0.001$) with a non-significant lack of fit ($p > 0.6418$). Both individual factors and the interaction of temperature with pH and extraction time significantly influenced the obtained pectin yield. The optimal condition to give the experimental pectin ($14.23 \pm 0.17\%$) was established at 81.80 °C, pH 2.08, and 59.50 min under a sample-to-solution ratio of 1:20 (w/v) in an ultrasonic bath. The obtained pectin yield at this condition deviated by less than 5% from the predicted value, confirming the reliability of the quadratic model.

Keywords: *Cyclea barbata* Miers; Cosmetics; Optimization; Pectin; RSM

Introduction:

Pectin is a structurally complex polysaccharide, composed mainly of esterified D-galacturonic acid residues linked in linear chains.¹ It has gained considerable attention as a natural gelling agent, stabilizer, and emulsifier in both the food, pharmacy, and cosmetic industries.² In addition, pectin also exerts beneficial effects on human health, including lowering cholesterol levels and regulating serum glucose.³ Traditionally, commercial pectin has been extracted primarily from citrus peels and apple pomace.⁴ However, the growing demand for sustainable and diversified raw materials has driven the search for alternative botanical sources.

Among the potential candidates, *Cyclea barbata* Miers, commonly known as green jelly and belonging to the family Menispermaceae, has recently attracted attention as a novel and underutilized source of pectin.⁵ The leaves of this plant are rich in polysaccharides that may serve as valuable substrates for pectin extraction with promising functional applications. In addition to its nutritional value, green jelly leaves have been traditionally used in herbal medicine to alleviate digestive disorders and reduce fever, suggesting a broader spectrum of bioactivity.⁶

The efficiency of pectin extraction is strongly influenced by critical parameters such as pH, temperature, and extraction time.⁷ Conventional optimization approaches, which typically focus on one factor at a time, are labor-intensive and often overlook the interactions among multiple variables.⁸ Response Surface Methodology (RSM), a well-established statistical and mathematical approach, has emerged as a powerful tool to optimize multivariable processes while minimizing the number of experimental trials.⁹ By applying

RSM, researchers can not only enhance pectin yield but also gain insights into the synergistic effects of extraction conditions.

Despite the promising potential of green jelly leaves as a source of pectin, systematic studies addressing extraction efficiency and process optimization remain scarce. Therefore, the aim of this study was to determine the optimal extraction parameters for pectin yield of *Cyclea barbata* Miers leaves using RSM. Effect of temperature, pH, and extraction time on pectin yield were evaluated employing a central composite design (CCD) to develop predictive models and validate process performance.

Methodology:

Chemicals

Ethanol, hydrochloric acid, sodium hydroxide, and other analytical grade chemicals were purchased from Sigma Chemical (St. Louis, MO, USA).

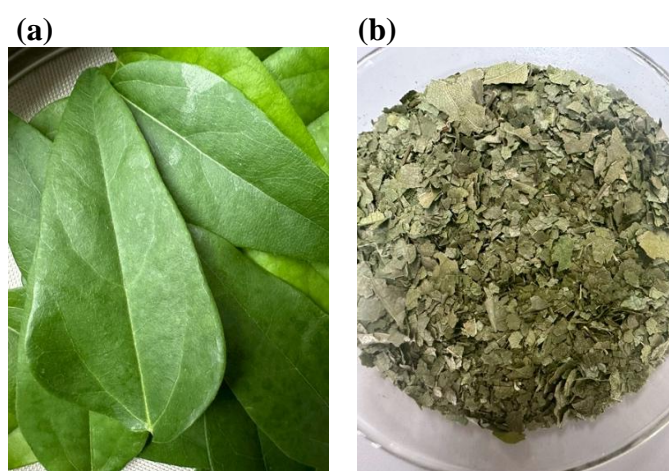


Figure 1.

Appearance of *Cyclea barbata* Miers fresh leaves (a) and dried leaf powder (b).

Plant material

Cyclea barbata Miers leaves were collected from Witayapan garden located in Chiang Rai, Thailand during April 2024. The fresh leaves were rinsed and subsequently dried at 50°C until a consistent weight was achieved. The dried leaves were ground to obtain a fine powder, which was then put in a sealed bag and kept at 4°C for the extraction process.

Extraction of pectin

Pectin is tightly crosslinked with the plant cell wall.² Many studies reported that pH, temperature, extraction time, and the solid-to-liquid ratio could facilitate pectin solubilization during extraction.¹⁰ Previous studies indicated that pH value of 1-3 is the most effective to break pectin out from the plant cell wall, allowing pectin to dissolve more easily into the solvent.¹¹ Other factors such as temperature, extraction temperature, and sample-to-solvent ratio have been frequently used in conventional acid extraction in the range of 50-95 °C, 30-120 minutes, and 1:10 and 1:50 (w/v), respectively, to obtain the highest pectin yield and quality of the extracted pectin.^{11,12} However, the optimized condition depends on the physical characteristics of the raw material and the desired concentration of pectin in the extract. Therefore in this study, condition of pectin extraction firstly designed using a Central Composite Design (CCD) with three-level of extraction parameters: pH (1.5-3.5), temperature (70-90 °C), and extraction time (30-60 min) while maintaining a sample-to-

solution ratio of 1:20 (w/v) established to balance efficient solubilization with manageable solvent consumption, as insufficient solvent volumes limit diffusion while excessive volumes increase operational cost and wastewater generation in ultrasonic bath. A total of 20 extraction conditions designed are presented in Table 1. Pectin from dried powder of *Cyclea barbata* Miers leaves was extracted with each designed condition. Briefly, five grams of the dried powder were slurried in each pH solutions in an Erlenmeyer flasks and extracted under the specified conditions. After extraction, the slurries were cooled to room temperature and centrifuged at 8000 rpm for 15 min. The obtained supernatant was then mixed with four volumes of absolute ethanol at 4 °C for 24 h, and then centrifuged at 8000 rpm for 20 min. The obtained precipitated pectin was washed twice with ethanol, re-dissolved in distilled water, and freeze-dried. The pectin yield (YP) was calculated using the following equation.

$$\% \text{ Yield pectin} = (\text{Dried weight of pectin} / \text{Dried weight of the dried powder}) \times 100$$

Table 1.

Experimental condition for pectin extraction of *Cyclea barbata* Miers leaves designed with Central composite design (CCD).

Run	Independent parameter			Pectin Yield (%w/w)	
	Temperature (°C)	pH	Time (min)	Experimental	Predicted
1	70	1.5	30	9.22	9.12
2	90	3.5	60	9.61	9.68
3	80	2.5	60	14.89	14.67
4	80	2.5	45	13.87	13.88
5	80	2.5	45	13.72	13.88
6	80	2.5	45	13.56	13.88
7	80	2.5	45	13.91	13.88
8	90	1.5	60	12.96	13.07
9	80	1.5	45	13.34	13.46
10	80	2.5	30	12.35	12.68
11	90	3.5	30	7.82	7.82
12	80	3.5	45	10.61	10.60
13	90	2.5	45	12.77	12.68
14	70	1.5	60	11.25	11.22
15	90	1.5	30	12.06	11.96
16	70	2.5	45	11.03	11.23
17	70	3.5	60	9.57	9.64
18	80	2.5	45	14.40	13.88
19	80	2.5	45	14.04	13.88
20	70	3.5	30	6.91	6.77

Results and Discussion:

Model fitting and Statistical analysis

Experimental parameters, namely pH, temperature, and extraction time, were used to run the RSM program in order to implement the optimal model. The summary fit of each model for pectin yield was summarized in Table 2. The finding indicated that a quadratic model was the most appropriate for describing the experimental data, confirmed from $p < 0.0001$, non-significant Lack-of-Fit ($p = 0.6418$), Adjusted R^2 (0.9865), and Predicted R^2 (0.9715), respectively. In contrast, the linear and 2FI models showed poor fit ($p > 0.05$), low Adjusted R^2 values, and negative Predicted R^2 values, indicating poor prediction ability. The cubic model, although it presented a relatively high Adjusted R^2 (0.9859) but was aliased, making it unsuitable for interpretation.

Table 2.

Fit summary of different model of pectin extracted from each designed condition.

Source	Sequential p-value	Lack of Fit p-value	Adjusted R^2	Predicted R^2	Remarks
Linear	0.0652	<0.0001	0.2340	-0.1527	
2FI	0.9162	<0.0001	0.0924	-3.4649	
Quadratic	<0.0001	0.6418	0.9865	0.9715	Suggested
Cubic	0.5226	0.5732	0.9859	0.6235	Aliased

Table 3 provides the variance analysis of a quadratic model. The Model having an F-value of 155.01, and the P value (<0.0001) indicated that noise was only responsible for 0.01% of the model. The study also found that individual factors (temperature, pH, and extraction time), including some interactions (temperature with pH and extraction time, respectively) exerting promoted the pectin produced. The non-significant Lack of Fit (p value >0.6418) indicated that the quadratic model effectively predicted pectin yield. The coefficient of determination (R^2) was 0.9929, which is nearly 1. This means that the independent variables indicate 99.29% of the variance in pectin production. This also implies that about 0.71% of the differences are ignored by the model. The adjusted R^2 (0.9865) and predicted R^2 (0.9715) values are close enough to the model's R^2 value to be useful. An adequate precision greater than 4 showed that the signal was sufficiently powerful. A higher CV value typically means that an experiment is less accurate. It's notable to notice that the CV value of this study (2.24) emphasized that the experimental runs were more reliable. The equation of developed quadratic model for predicting the pectin yield extracted from *Cyclea barbata* Miers leaves is provided below:

$$\text{Pectin yield (\% w/w)} = 13.88 + 0.72A - 1.43B + 0.99C - 0.45AB - 0.25AC + 0.19BC - 1.92A^2 - 1.85B^2 - 0.20C^2$$

Effects of extraction parameters on pectin yield

Figure 2 explores that pectin yield was affected by parameters used: temperature, pH, and extraction time. The yield of pectin increased as the pH increased, but the yield declined when the pH rose over 2.0. This phenomenon can be defined as acidic conditions facilitating the hydrolysis of pectin that interacts with the plant cell wall, transforming the insoluble parts of pectin into soluble forms, thereby improving the efficiency of pectin extraction.⁷ However, when the pH is low, the molecular weight of pectin declines due to its partial dissolution from plant tissues without breaking down the structure. These conditions cause pectin to precipitate, which lowers the yield of the extraction. Temperature also affected to pectin yield due to increasing diffusivity and solubility of pectin and other pectineous compounds in the

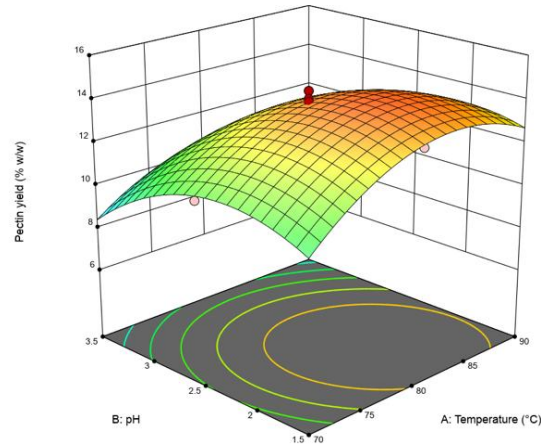
extraction solution.¹³ Additionally, extraction time is critical to the breakdown of pectin since thermal accumulation from heat energy absorption accelerates its solubilization into the extraction solution. The amount of pectin that is produced can be increased by prolonging the extraction time, but performing this over a longer duration of time diminishes the pectin's quality and limits its application in food and cosmetic formulations.¹⁰ Extended extraction times may cause the pectin molecular chains to degrade, which could immediately.⁷

Table 3.
Analysis variance (ANOVA) for pectin yield of *Cyclea barbata* Miers leaves

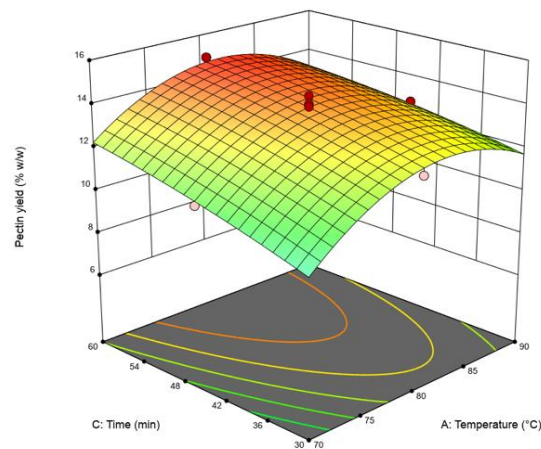
Source	Sum of Squares	df	Coefficient estimate	F-value	p-value	Remarks
Model	99.47	9	13.88	155.01	< 0.0001	Significant a
A-Temperature	5.24	1	0.7240	73.51	< 0.0001	
B-pH	20.48	1	-1.43	287.19	< 0.0001	
C-Time	9.84	1	0.9920	138.01	< 0.0001	
AB	1.62	1	-0.4500	22.72	0.0008	
AC	0.5000	1	-0.2500	7.01	0.0244	
BC	0.2888	1	0.1900	4.05	0.0719	
A ²	10.15	1	-1.92	142.31	< 0.0001	
B ²	9.37	1	-1,85	131.41	< 0.0001	
C ²	0.1110	1	-0.2009	1.56	0.2406	
Residual	0.7130	10	0.0713			
Lack of Fit	0.2961	5	0.0592	0.7102	0.6418	not significant
Pure Error	0.4169	5	0.0834			
Cor Total	100.19	19				
R²	0.9929					
Adjusted R²	0.9865					
Predicted R²	0.9715					
Adequate Precisions	41.8174					
C.V. %	2.24					

Remarks: Significant at 95% confidence level.

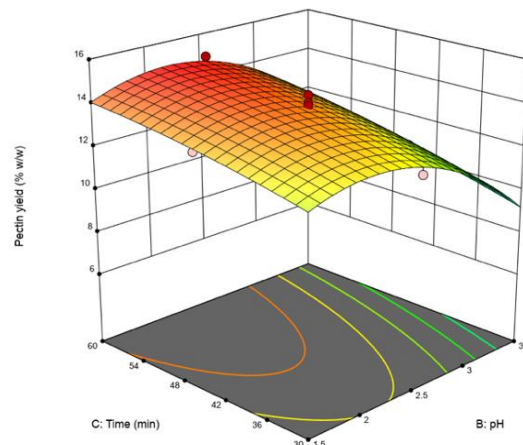
(a)



(b)



(c)

**Figure 2.**

Response surface plot of process paramitors (pH, temperature, and extraction time) affecting to pectin yield extracted from *Cyclea barbata* Miens leaves.

Validation of quadratic model for pectin yield

The optimal condition at 81.80 °C, pH 2.08, and 59.50 min (Figure 3), which provides a desirability value of 1.000, was further validated. Under this condition, the actual pectin yielded $14.23 \pm 0.17\%$, showing less than 5% deviation from the predicted value calculated

from the fit quadratic model (14.91%). This close agreement indicated that the developed model was accurate and reliable for predicting pectin yield. When compared with other plant sources, pectin yield can vary substantially depending on the raw material and extraction method.^{3,14} Commercial pectin typically yielded 13.4-37.5% from citrus peel and 4.2–19.8% from apple pomace, while non-traditional sources such as passion fruit peel (10-12.7%) and banana peel (5.2-12.2%) exhibited moderate yields influenced by pH, temperature, and extraction time.^{14,15} Therefore, pectin yield obtained from the *Cyclea barbata* leaves in this study fell within the typical range for non-peel plant materials. The appearance of the extracted pectin under the optimized condition is shown in Figure 4. The precipitated pectin (Figure 4a) exhibited a translucent yellow–brown, gel-like texture, indicating successful coagulation of the polysaccharide network after ethanol precipitation. After freeze-drying, The pectin became darker and brittle with a film-like structure (Figure 4b). The final ground pectin (Figure 4c) appeared as a coarse brown powder.

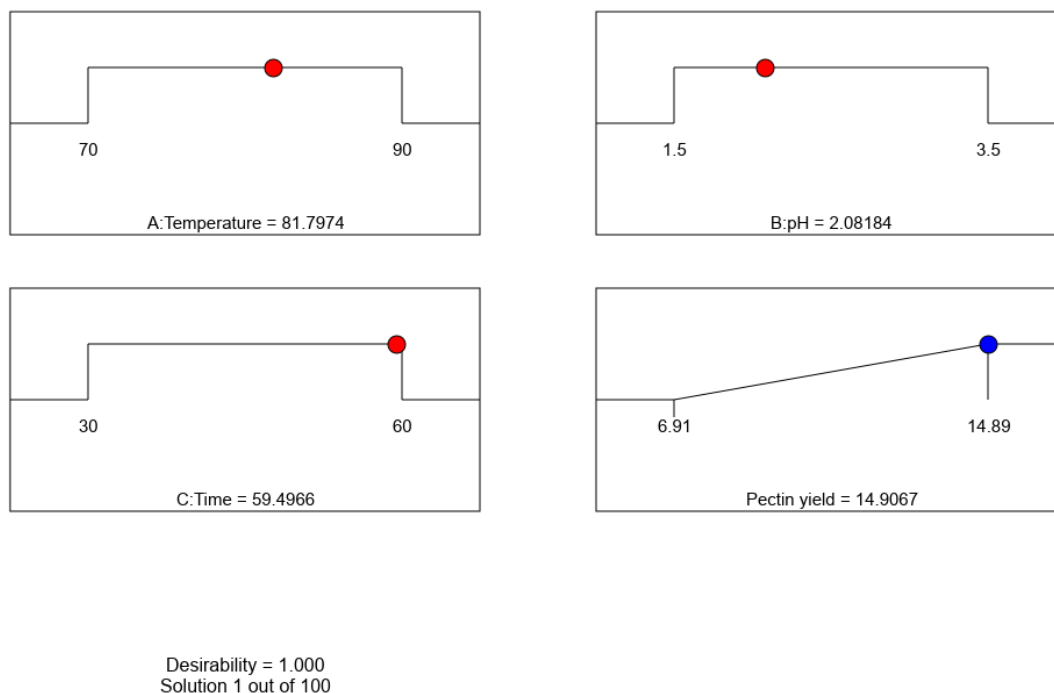


Figure 3.

Optimal condition for extraction of pectin yield from *Cyclea barbata* Miers leaves.

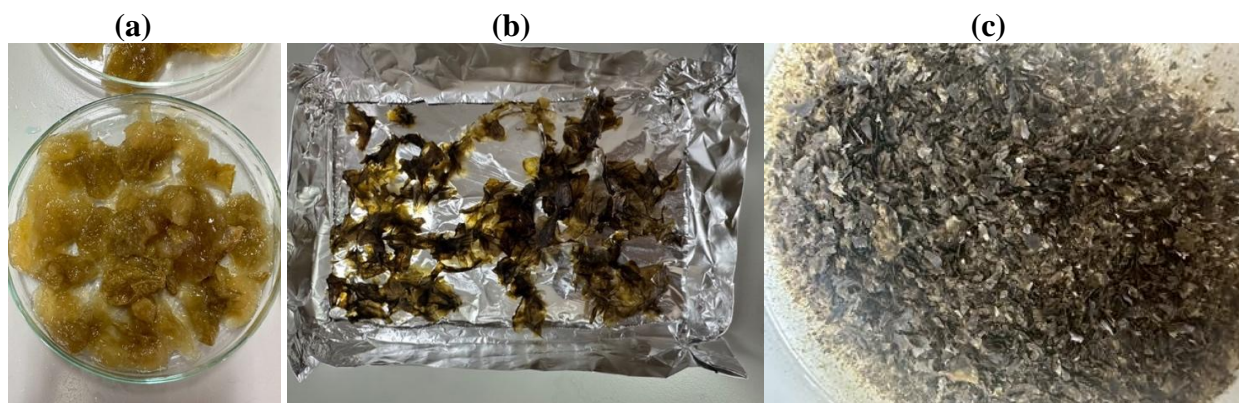


Figure 4.

Appearance of precipitated (a), dried (b), and ground (c) pectin obtained from *Cyclea barbata* Miers leaves under the optimal extraction condition.

Conclusion:

The quadratic model had a good fit for the prediction of pectin yield of *Cyclea barbata* Miers leaves. Parameters used: temperature, pH, and extraction time had a significant influence on pectin yield. The condition at 81.80 °C, pH 2.08, and 59.50 min gave the highest pectin yield ($14.23 \pm 0.17\%$), which value is close to the predicted value, having an error deviation of less than 5%. In further, structural characteristics and rheological behavior of the extracted pectin should be evaluated for application in the cosmetic field.

References:

1. Christiaens S, Van Buggenhout S, Houben K, Jamsazzadeh Kermani Z, Moelants KR, Nguoumazong ED, et al. *Crit Rev Food Sci Nutr*. 2016;56:1021–42.
2. Freitas CMP, Coimbra JSR, Souza VGL, Sousa RCS. *Coatings*. 2021;11:922.
3. Roman-Benn A, Contador CA, Li M-W, Lam H-M, Ah-Hen K, Ulloa PE, et al. *Food Chem Adv*. 2023;2:100192.
4. Gallery C, Agoda-Tandjawa G, Bekaert D, Gitto L. *Food Hydrocoll*. 2024;152:109950.
5. Yuliarti O, Chong S, Goh K. *Int J Biol Macromol*. 2017;103:1146–54.
6. Yuliarti O, Othman RMB. *Food Hydrocoll*. 2018;81:300–11.
7. Methacanon P, Kongsin J, Gamonpilas C. *Food Hydrocoll*. 2014;35:383–91.
8. Bagherian H, Ashtiani FZ, Fouladitajar A, Mohtashamy M. *Chem Eng Process Process Intensif*. 2011;50:1237–43.
9. Muthusamy S, Manickam LP, Murugesan V, Muthukumaran C, Pugazhendhi A. *Int J Biol Macromol*. 2019;124:750–8.
10. Marić M, Grassino AN, Zhu Z, Barba FJ, Brnčić M, Brnčić SR. *Trends Food Sci Technol*. 2018;76:28–37.
11. Raji Z, Khodaiyan F, Rezaei K, Kiani H, Hosseini SS. *Int J Biol Macromol*. 2017;98:709–16.
12. Ripoll CSS, Hincapié-Llanos GA. *Food Biosci*. 2023;51:102278.
13. Chan S-Y, Choo W-S. *Food Chem*. 2013;141:3752–8.
14. Dranca F, Oroian M. *Food Res Int*. 2018;113:327–50.
15. Oliveira TÍS, Rosa MF, Cavalcante FL, Pereira PHF, Moates GK, Wellner N, et al. *Food Chem*. 2016;198:113–8.



BIOMASS PRODUCTION OF *IN VITRO* *Microchirita involucrata* ROOTS AND EVALUATION OF BIOLOGICAL ACTIVITY OF ROOT CULTURE EXTRACTS ELICITED WITH ELICITORS

Adsadayu Thonnondang¹, Onrut Inmano², Anupan Kongbangkerd², Apinun Limmongkon^{1*}

¹Department of Biochemistry, Faculty of Medical Science, Naresuan University, Phitsanulok, 65000, Thailand

²Department of Biology, Faculty of Science, Naresuan University, Phitsanulok 65000, Thailand

*e-mail: apinunl@nu.ac.th

Abstract:

Microchirita involucrata is a plant from the Gesneriaceae family that produces secondary metabolites with antioxidant and antimicrobial properties. This study aimed to optimize auxin hormone treatments for enhancing root biomass and to evaluate the biological activity of culture medium extract under elicitor conditions. Roots were cultured with Indole-3-acetic acid (IAA), 1-Naphthaleneacetic acid (NAA) and Indole-3-butyric acid (IBA) at varying concentrations of 0.5, 1.0, 2.0 and 4.0 mg/L, while methyl jasmonate (MeJA) and cyclodextrin (CD) served as the elicitor. TLC and HPLC were used for metabolite profiling, and antioxidant activity was measured via the ABTS assay. Roots were treated with 4 mg/L IBA produced the highest biomass (6.11 ± 0.75 g). Elicitation led to medium color changes and intensified TLC bands. HPLC revealed major peaks at 15–25 mins retention time, indicating enhanced metabolite accumulation. The ABTS assay showed significant increase of antioxidant activity in IBA-treated roots under elicitor treatment (TEAC 2.44 ± 0.36 μ mol Trolox equivalents/g extract) compared to the unelicited control (TEAC 0.74 ± 0.08 μ mol Trolox equivalents/g extract). This study demonstrates that optimized hormone application can effectively promote root biomass and bioactive compounds production in *M. involucrata*, supporting potential industrial applications.

Introduction:

Microchirita involucrata var. *capitis* (Craib) C. Puglisi belongs to the Gesneriaceae family. Originally, this plant was classified under the genus *Chirita* and it was reclassified under *Didymocarpus* sect. *Microchirita*.¹ Over 166 compounds, including terpenoids, flavonoids, and phenolics, have been identified in *Didymocarpus*, exhibiting antimicrobial,² anticancer,³ antidiabetic,⁴ and antioxidant^{5,6} activities. *M. involucrata* grows more rapidly than most Gesneriaceae species, enabling efficient and consistent biomass production for metabolite extraction. In addition, *M. involucrata* possesses a distinct metabolite profile and a well-documented ethnomedicinal background, further supporting its consideration as a species of significant pharmaceutical interest. Plants synthesize secondary metabolites in various tissues, including leaves, flowers, and roots, as a defense against environmental stressors such as pathogens, chemicals, and drought.^{7,8,9,10}

Root-promoting hormones, including Indole-3-acetic acid (IAA), 1-Naphthaleneacetic acid (NAA), and Indole-3-butyric acid (IBA), have been widely studied for root proliferation in various plants. NAA has been reported to enhance root development in *Camellia sinensis* by upregulating genes involved in root initiation,¹¹ while IBA effectively induces root formation in *Dracocephalum kotschyi*.¹² Increasing root biomass through hormone application is essential for mass production, providing a larger biomass source for metabolite extraction and enhancing bioactive compound scalability for pharmaceutical and industrial use. However, the optimal conditions for hormone application in *M. involucrata* remain unexplored. Elicitors like methyl jasmonate (MeJA) and cyclodextrin (CD) enhance secondary metabolite production by activating plant defense mechanisms. Preliminary TLC



and HPLC analyses indicate that both MeJA and CD influence the metabolite profiles in the root of *M. involucrata* that were not treated with hormone (unpublished data). Thus, combining root-promoting hormones with elicitors may be a promising approach to boosting root biomass and secondary metabolite production for pharmaceutical and medical applications, as well as serving as a valuable database for future studies.

Methodology:

1. Optimization of hormone concentration and exposure duration

Root tissue segments of approximately 1.0 cm in length were cultured on semi-solid MS¹³ medium supplemented with different types and concentrations of auxins, including IAA, NAA, and IBA at 0, 0.5, 1.0, 2.0, and 4.0 mg/L. The root tissues were incubated in a controlled environment at $25 \pm 2^\circ\text{C}$. The experiment was conducted in triplicate, each replicate consisted of 10 root segments. Root fresh weight was recorded over a period of four weeks.

2. Elicitation of *M. involucrata* using elicitors

Root tissue cultures were maintained in liquid medium. The root cultures were then induced using 50 μM MeJA and 4 mM CD. The culture flasks were incubated in the dark on a shaker for 72 hours.

3. Extraction of culture medium of *M. involucrata*

After elicitor treatment, the culture medium was separated from the root tissues. The culture medium was mixed with ethyl acetate in a 1:1 ratio in a separating funnel. The upper organic phase was collected, and the extraction process was repeated three times. The combined ethyl acetate extracts were evaporated using a rotary evaporator, and the obtained crude extract was used for subsequent bioactivity testing.

4. Component analysis using Thin Layer Chromatography (TLC)

TLC plates coated with silica gel were prepared as the stationary phase and the mobile phase consist of hexane and ethyl acetate at a ratio of 2.1:0.9 mL. The result was observed under UV of 254 nm and 365 nm. To further classify the compounds, the plates were treated with anisaldehyde reagent, and the resulting color bands were observed after heating with a hot air blower. Additionally, the antioxidant activity of the separated compounds was tested using the DPPH assay.

5. Examination of the components using High Performance Liquid Chromatography (HPLC)

The components present in the extract were separated and analyzed using HPLC system (Shimadzu LC-10 ADVP), equipped with a Luna 5 μm C18 column (250x4.6 mm, Phenomenex Inc.). The extract was prepared at a concentration of 5 mg/mL and filtered prior to analysis. The mobile phase used for the separation consisted of acetonitrile and 2% formic acid in distilled water (18.2 m Ω), mixed in a 30:70 ratio with gradient elution. The signals were detected using a UV-Vis detector (Shimadzu SPD-10 AVP) at wavelengths of 280 nm.

6. ABTS antioxidant assay

Antioxidant activity was determined using the ABTS assay. For the assay, 20 μL of extract was mixed with 180 μL ABTS^{•+} solution, and absorbance was measured at 734 nm after 6 min. Each sample was evaluated using three independent biological replicates ($n = 3$), with each replicate further analyzed in triplicate as technical replicates ($n = 3$). Results were



expressed as Trolox Equivalent Antioxidant Capacity (TEAC, μmol Trolox equivalents/g extract).

7. Statistical analysis

The data were statistically analyzed using SPSS (version 23) software, and mean differences among treatment groups were assessed using Duncan's New Multiple Range Test (DMRT) to determine statistical significance

Results:

1. Optimization of auxin hormone concentration and exposure duration

Root tissue segments were cultured on semi-solid MS medium supplemented with various types and concentrations of auxins, including IAA, NAA, and IBA at 0, 0.5, 1.0, 2.0, and 4.0 mg/L. After three days of culture, root tissues in all treatments remained white, with browning was observed on the cut surfaces, and no significant morphological development was noted. By the first week, root branching became evident in all treatments, particularly at higher auxin concentrations, as detailed in **Table 1**. After two weeks, root development became more apparent. Media supplemented with IAA promoted increased branching with elongated roots and the emergence of fine lateral roots. In contrast, NAA-treated roots appeared dense and compact without elongation and exhibited light brown coloration. Roots cultured in IBA-supplemented medium were long, highly branched with large fluffy structures, and light brown in color, as shown in **Table 2**. After four weeks of culture, all treatments exhibited extensive root branching and full development, occupying the entire culture vessel. In the IAA-supplemented medium, the roots were slender, elongated, and light brown. NAA-treated roots remained dense and short, with dark brown coloration. The IBA treatment resulted in the longest and most highly branched roots, with dark brown coloration, as shown in **Table 3**.

Fresh weight analysis indicated an increase in root biomass across all treatments, with the highest fresh weight observed in the 4 mg/L of IBA treatment (6.11 ± 0.75 g), which was significantly greater than all other treatments. The second highest fresh weight was recorded in the 4 mg/L NAA treatment with 4.83 ± 0.63 g, while the lowest root weight was observed in the 0.5 mg/L IAA treatment, with a weight of 0.92 ± 0.32 g, as shown in **Table 4**.

Table 1.
Growth of the *M. involucrata* root towards auxin after 1 week.

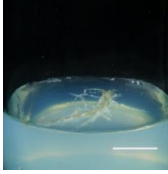
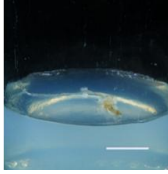
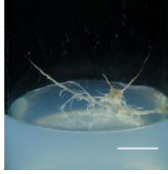
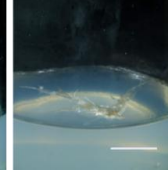
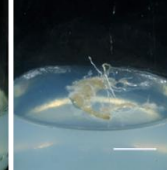
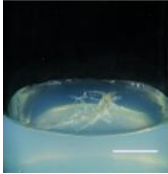
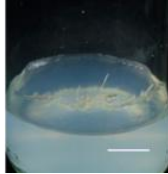
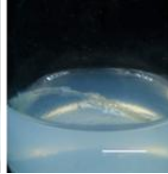
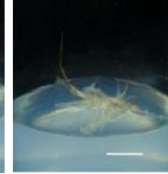
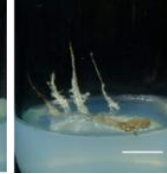
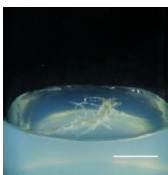
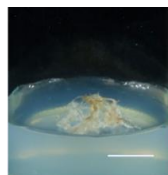
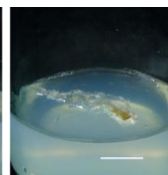
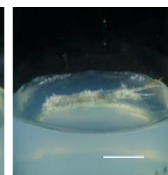
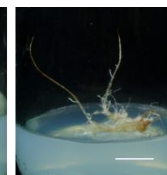
Effects of auxin hormones on root tissue segments of <i>M. involucrata</i> after 1 week (Scale = 1 cm)					
	Control	0.5 mg/L	1.0 mg/L	2.0 mg/L	4.0 mg/L
IAA					
NAA					
IBA					

Table 2.
Root tissue development and growth of *M. involucrata* roots after 2 weeks in response to various auxin concentrations

Effects of auxin hormones on root tissue segments of <i>M. involucrata</i> after 2 weeks (Scale = 1 cm)					
	Control	0.5 mg/L	1.0 mg/L	2.0 mg/L	4.0 mg/L
IAA					
NAA					
IBA					

Table 3.

Root tissue development and growth of *M. involucrata* roots after 4 weeks in response to various auxin concentrations

Effects of auxin hormones on root tissue segments of *M. involucrata* after 4 weeks (Scale = 1 cm)

	Control	0.5 mg/L	1.0 mg/L	2.0 mg/L	4.0 mg/L
IAA					
NAA					
IBA					

Table 4.

Fresh weight of root tissue segments of *M. involucrata* after 4 weeks in response to various auxin concentrations

Treatments (mg/L)		Root weight (g)
	Control	0.63 ± 0.29 e*
IAA	0.5	0.92 ± 0.32 e
	1.0	1.61 ± 0.19 e
	2.0	1.21 ± 0.08 e
	4.0	1.39 ± 0.20 e
NAA	0.5	3.89 ± 0.12 bcd
	1.0	4.30 ± 0.20 bc
	2.0	4.67 ± 0.13 bc
	4.0	4.83 ± 0.63 b
IBA	0.5	3.08 ± 0.08 d
	1.0	3.67 ± 0.27 cd
	2.0	4.23 ± 0.15 bc
	4.0	6.11 ± 0.75 a

* Values are means ± SE of 3 replications (10 roots per replication). Different letters within the same column show significant differences analyzed by Duncan's New Multiple Range tests at $p < 0.05$



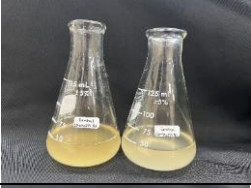
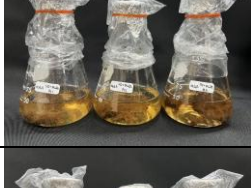
To identify the most effective auxin for inducing root growth and maximizing the potential of roots to produce valuable compounds, further studies were conducted using root tissues induced by each auxin treatment. The roots were elicited with MeJA and CD for three days, followed by extraction of compounds. The profiles of valuable compounds produced after elicitation were analyzed. Based on these results, the most suitable auxin for subsequent experiments was determined.

2 Effect of combined MeJA and CD elicitation on auxin-induced root cultures of *M. involucrata*

Root tissues 5 grams previously cultured with each auxin treatment were transferred into 50 mL of liquid ½ MS medium supplemented with 50 µM MeJA and 4 mM CD. A non-elicited group was used as a control (CT). The cultures were incubated in the dark and shaken on a rotary shaker for three days. Observations were recorded on changes in the color of both the root tissues and culture medium before and after elicitation. Prior to elicitation, roots pre-treated with 4 mg/L IAA appeared yellow-brown, and the culture medium remained clear. Following elicitation with MeJA and CD, the roots turned dark brown to black, and the culture medium became turbid yellow. In comparison to the non-elicited control, no obvious differences were observed. Similarly, roots pre-treated with 4 mg/L NAA exhibited a yellow-brown coloration and a clear medium before elicitation. After elicitation, the roots turned dark brown, and the medium shifted to a light-yellow color. For roots pre-treated with 4 mg/L IBA, the roots were yellow brown with a clear medium before elicitation. After treatment, the roots turned dark brown, and the medium became a deeper yellow compared to the control. The results are shown in **Table 5**.

Table 5.

 Root tissues and culture medium of *M. involucrata* cultured with different types of auxins and elicited with 50 μ M MeJA and 4 mM CD, observed at 0 and 3 days of treatment.

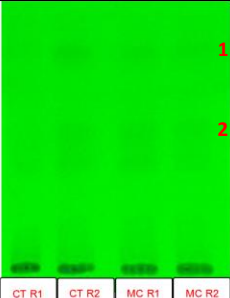
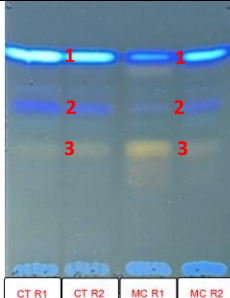
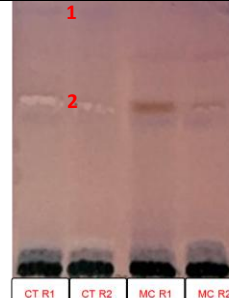
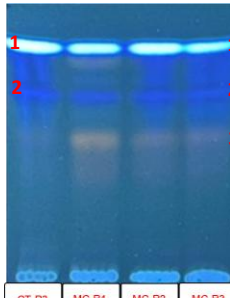
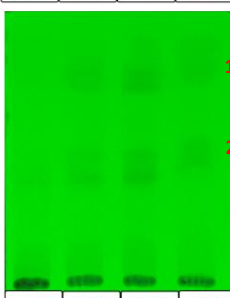
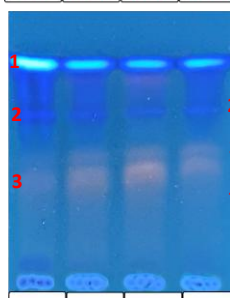
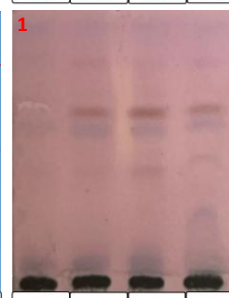
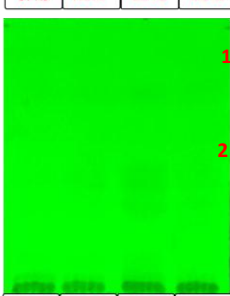
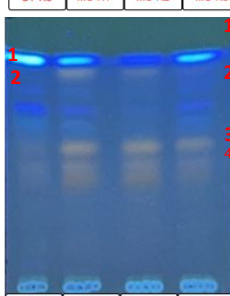
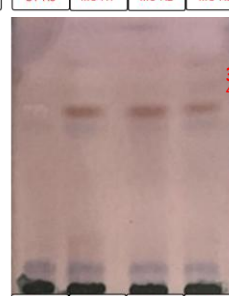
Types of hormones		Root and medium appearance (Day 0)	Root and medium appearance (Day 3)	Medium color
Non hormone	Control			
	50 μ M MeJA + 4 mM CD			
IAA	Control			
	50 μ M MeJA + 4 mM CD			
NAA	Control			
	50 μ M MeJA + 4 mM CD			
IBA	Control			
	50 μ M MeJA + 4 mM CD			

3 TLC analysis of culture medium extracts elicited with MeJA and CD

Preliminary phytochemical analysis of the extracts was performed using TLC. The TLC plates were visualized under UV light at 254 nm and 365 nm, followed by staining with anisaldehyde reagent to detect characteristic color bands of various compounds. Antioxidant activity of the separated bands was assessed by staining the TLC plate with DPPH solution, and monitoring the color change from purple to yellow, indicating free radical scavenging activity as demonstrated in **Table 6**.

Table 6.

TLC profiles of root culture medium extracts of *M. involucrata* elicited with MeJA and CD. CT: control group; MC: elicited group treated with MeJA and CD.

Auxin type	254 nm	365 nm	Anisaldehyde	DPPH
Non hormone				
IAA				
NAA				
IBA				

Under UV light at 254 nm, several dark bands were observed, indicating the presence of compounds containing conjugated double bonds or aromatic structures, such as phenolic compounds or other aromatic metabolites. Clear dark bands (bands 1 and 2) were detected on

the TLC plates of the non-hormone group with elicitors, the NAA-treated group with elicitors, and the IBA-treated group with elicitors. In contrast, the IAA-treated group exhibited only very faint bands that could not be clearly identified.

Under UV light at 365 nm, fluorescent bands were observed, indicating the presence of compounds with extended conjugated systems or polycyclic aromatic structures capable of fluorescing under higher UV wavelengths. Blue fluorescent bands (band 1) were observed in all groups, along with additional blue bands (band 2). An orange fluorescent band (band 3) observed in the non-hormone group under both elicited and non-elicited conditions. In the IAA-treated group, a faint orange fluorescent band (band 3) was detected in the non-elicited condition, with the band becoming more intense following elicitor treatment. The NAA-treated group exhibited two orange fluorescent bands (bands 3 and 4) after elicitation, with greater intensity compared to the non-elicited condition. Similarly, the IBA-treated group showed two intense orange fluorescent bands (band 3 and 4) upon elicitation, whereas only weaker bands were present under non-elicited condition.

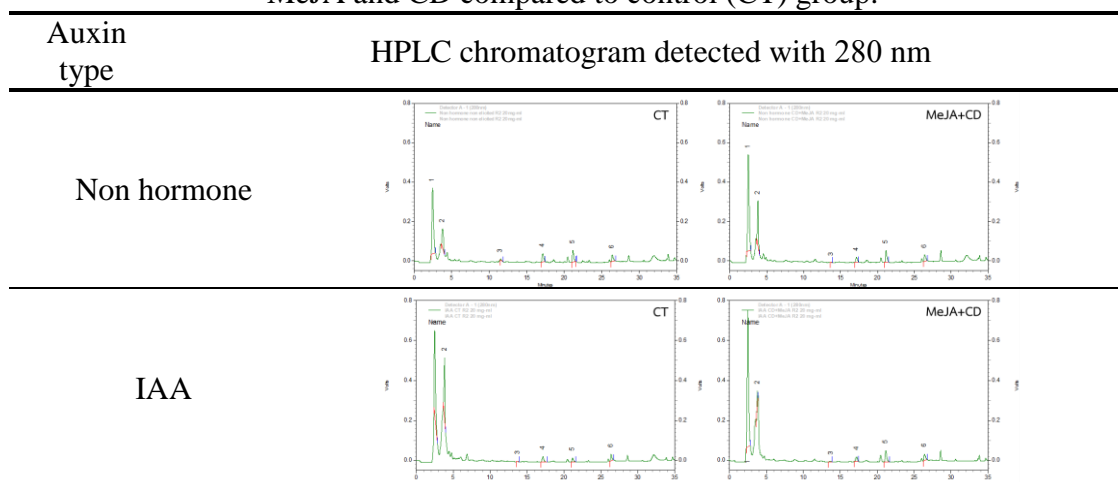
Following staining with anisaldehyde, band color changes were observed. A reddish-brown band (band 3) appeared in the elicited samples of non-hormone, NAA-treated and IBA-treated groups. In contrast, no colored bands were detected in the IAA-treated group, regardless of elicitor treatment. Staining with DPPH, used to identify antioxidant compounds based on the color shift from purple to yellow (reduced form), revealed yellow bands (band 1) in all groups, indicating antioxidant activity. The intensity of the yellow bands was greater in elicitor-treated samples compared to the non-treated control, as shown in **Table 6**.

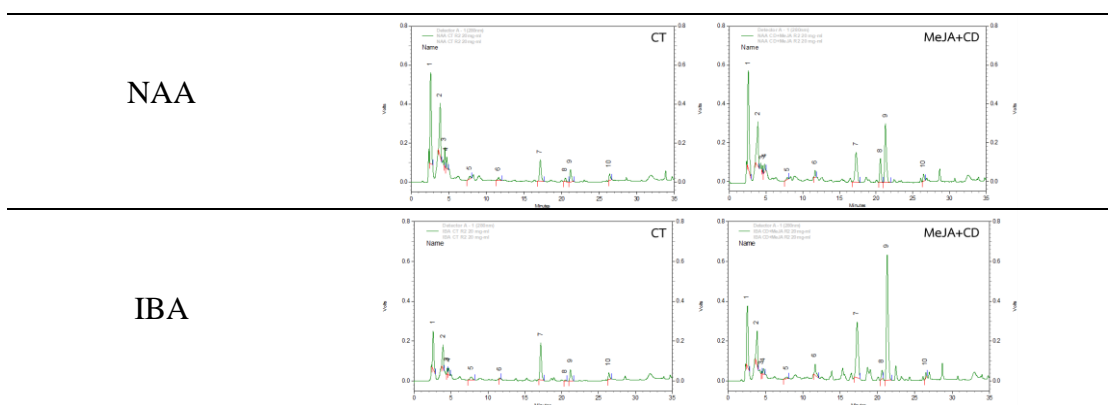
4 HPLC analysis of culture medium extracts elicited with MeJA and CD

The results of the HPLC analysis of crude extracts from the culture medium of *M. involucrata* treated with combined MeJA and CD are presented in **Table 7**. Analysis at a wavelength of 280 nm revealed distinct chromatographic patterns between the non-hormone group and the hormone-treated groups. The extract from the IBA-treated group exhibited several distinct, unidentified peaks at various retention times, suggesting the presence of multiple constituents compared to other auxin-treated groups. In contrast, extracts from groups treated with other auxins, particularly NAA and IAA, displayed prominent peaks in more polar retention time regions.

Table 7.

HPLC chromatogram of extract components from the culture medium treated with combined MeJA and CD compared to control (CT) group.





5 Antioxidant activity by ABTS assay

Based on the distinct metabolite profile observed in the IBA-treated root extract compared to other auxin-treated groups, IBA-treated roots subjected to MeJA+CD elicitation were selected for subsequent antioxidant evaluation against the unelicited control. The results demonstrated that IBA-treated roots elicited with MeJA+CD exhibited a significantly higher antioxidant capacity (TEAC 2.44 ± 0.36 μmol Trolox equivalents/g extract) compared with the unelicited control (TEAC 0.74 ± 0.08 μmol Trolox equivalents/g extract). Collectively, these findings indicate that IBA treatment in combination with MeJA+CD elicitation markedly enhances the antioxidant potential of root cultures.

Discussion:

The present study demonstrated that treatment with IBA at a concentration of 4 mg/mL significantly enhanced root growth, giving an average root biomass of 6.11 ± 0.75 grams. This was higher than those observed in cultures treated with IAA and NAA, indicating a superior efficacy of IBA in promoting root development. The greater effectiveness of IBA may be explained by its higher stability, together with its ability to interact with endogenous auxin pools. Evidence from *Arabidopsis* indicated that exogenous IBA, in combination with residual endogenous IAA, efficiently induced adventitious root formation, whereas IAA alone was less effective.¹⁴ These results are consistent with the findings of Anukul et al.,¹⁵ who reported that IBA at 2,000 ppm significantly increased root number (17.51 roots per cutting), fresh weight (0.78 g), and dry weight (0.06 g) in *Jatropha curcas* L. stem cuttings compared to NAA at 1,000 ppm.

In addition, the application of MeJA and CD induced a noticeable yellow coloration in the culture medium of *M. involucrata* within 3 days, which may indicate early-stage accumulation and secretion of secondary metabolites. This observation is consistent with previous report in peanut hairy roots, where MeJA and CD significantly enhanced the production of phenolic and stilbene compounds¹⁶. Therefore, the visible color change may serve as a preliminary indicator of elicitor-induced metabolic responses.

TLC analysis further supported these findings, which revealed intensified bands in the IBA-treated roots following under elicitor treatment, indicating an elevated accumulation of specific secondary metabolites compared to the untreated control. HPLC profiles revealed a prominent peak within the retention time range of 15–20 min. As the phytochemical profile of *M. involucrata* remains uncharacterized, terpenoids and flavonoids are considered potential major metabolites, consistent with reports from *Didymocarpus* and other Gesneriaceae species.¹⁷ This assumption is further supported by the prominent peaks observed in the HPLC chromatograms of the NAA- and IBA-treated groups under MeJA and CD elicitation compared to unelicited control. This profile is consistent with the report by Pilaisangsuree et al.,¹⁶ which showed distinct chromatographic patterns in hairy root cultures



treated with CD alone and co-treated with MeJA and CD, corresponding to enhanced phenolic compound secretion into the culture medium.

Conclusion:

The present study demonstrates that the combination of IBA with MeJA and CD effectively promotes both root biomass and secondary metabolite accumulation in *M. involucrata* root cultures. The observed yellowing of the culture medium, along with supporting evidence from TLC and HPLC profiles, confirms the elicitor-induced production and secretion of specific bioactive compounds. These findings highlight the potential of using optimized hormone and elicitor combinations as a practical strategy for large-scale production of root-derived phytochemicals with promising pharmaceutical and industrial applications.

Acknowledgement:

This work was supported by Naresuan University (NU) and the National Science, Research and Innovation Fund (NSRF) [grant number R2569B087].

References:

1. Chun WY. Sunyatsenia. 1946;6:290.
2. Biswas P, Bhattacharyya A, Bose PC, Mukherjee N, Adityachaudhury N. *Experientia*. 1981;37:397–398.
3. Gowda PJ, Ramakrishnaiah H, Krishna V, Narra S, Jagannath N. *Nat Prod Commun*. 2012;7(11):1535–1538.
4. Mittal AK, Bhardwaj R, Arora R, Singh A, Mukherjee M, Rajput SK. *ACS Omega*. 2020;5(39):24239–24246.
5. Kaur G, Lone IA, Athar M, Alam MS. *Chem Biol Interact*. 2007;165:33–44.
6. Lone IA, Ali M, Alam MS, Lone SA. *J Pharmacogn Phytochem*. 2016;5(1):36.
7. Creelman RA, Mullet JE. *Annu Rev Plant Physiol Plant Mol Biol*. 1997;48:355–381.
8. Franceschi VR, Krokene P, Christiansen E, Krekling T. *New Phytol*. 2005;167:353–376.
9. Rasmann S, Agrawal AA. *Plant Physiol*. 2008;146(3):875–880.
10. Li Z, Rubert-Nason KF, Jamieson MA, Raffa KF, Lindroth RL. *J Chem Ecol*. 2021;47(3):313–321.
11. Wang Y, Pang D, Ruan L, Zhang Y, Liu J, Li X. *BMC Plant Biol*. 2022;22:319.
12. Sharafi A, Sohi HH, Azadi P, Sharafi AA. *Physiol Mol Biol Plants*. 2014;20(2):257–262.
13. Murashige T, Skoog F. *Physiol Plant*. 1962;15:473–497.
14. Ludwig-Müller J, Vertocnik A, Town CD. Analysis of indole-3-butyric acid-induced adventitious root formation on *Arabidopsis* stem segments. *J Exp Bot*. 2005;56(418):2095–2105.
15. Anukul K, Abdulakassim S, Pagamas P. *Khon Kaen Agric J*. 2017;45(SUP):1–5.
16. Pilaisangsuee V, Neerachaikul S, Srisawat T, Chaiyasuta S, Luecha P. *Plant Biotechnol Rep*. 2018;12(3):189–197.
17. Verdan MH, Stefanello EA. *Chem. Biodivers*. 2012; (9): 2701–2731.)



ANTIFUNGAL ACTIVITY OF *Priestia aryabhatai* PTKU-123 CRUDE EXTRACT AGAINST *Fusarium* spp. ASSOCIATED WITH DURIAN DIE-BACK DISEASE

James Konkoy, Nisit Watthanasakphuban, Paiboon Tunsagool*

Special Research Incubator Unit of Fermentomics, Department of Biotechnology, Faculty of Agro-Industry, Kasetsart University, Bangkok, Thailand

*email: paiboon.tu@ku.ac.th

Abstract:

Durian (*Durio zibethinus*) production is increasingly threatened by fungal pathogens, including *Fusarium* spp., that was recently discovered to be implicated in die-back disease. Sustainable alternatives to synthetic fungicides are urgently required. This study investigated the antifungal potential of crude metabolites produced by *Priestia aryabhatai* strain PTKU-123. The bacterial isolate, maintained on nutrient agar, was fermented in Luria-Bertani broth, and metabolites were recovered through acid precipitation and ethanol extraction. Crude extracts were profiled using thin-layer chromatography (TLC), which revealed bands with Rf values consistent with lipopeptide fractions, as confirmed by ninhydrin and iodine staining. Antimicrobial efficacy was assessed using the poison food technique against *Fusarium* spp., a pathogen isolated from diseased durian tissue and validated by morphological and ITS-based identification. The crude extract significantly inhibited fungal growth in a concentration-dependent manner, with complete inhibition achieved at 5 mg/mL. These findings highlight *P. aryabhatai* PTKU-123 as a promising biocontrol candidate for durian disease management and provide a foundation for further purification and characterization of its antifungal metabolites.

Introduction:

Durian (*Durio zibethinus*) is one of Southeast Asia's most economically important fruit crops, with Thailand standing as the world's leading producer and exporter.¹ However, durian production is increasingly threatened by destructive fungal diseases that reduce both yield and fruit quality, leading to significant economic losses for growers.² Among these, black die-back disease has emerged as a particularly concerning problem. The disease is characterized by leaf yellowing, branch wilting, die-back of shoots, and in severe cases, death of the entire tree, posing a major challenge to orchard long-term sustainability.³

Recent investigations have identified *Fusarium* species as key pathogens associated with durian die-back. Morphological and molecular studies have confirmed the presence of *Fusarium incarnatum* and related species in diseased tissues, highlighting their role as emerging threats to durian health.⁴ This finding emphasizes the need for more precise management strategies, as conventional control methods in addressing *Fusarium*-induced infections.

Biological control using beneficial microorganisms offers a promising alternative to chemically synthesized fungicides, especially in perennial crops like durian where long-term soil health is vital. *Priestia aryabhatai*, a soil-dwelling bacterium, has gained attention for its ability to produce bioactive secondary metabolites, including lipopeptides, which are known for strong antifungal and biosurfactant activities.⁵ These natural compounds have been reported to disrupt fungal cell membranes and suppress the growth of phytopathogens such as *Fusarium*.⁶⁻⁸

In this study, we evaluated the antifungal efficacy of crude extracts from *P. aryabhatai* PTKU-123 against *Fusarium* spp. isolated from diseased durian tissues. The objective was to screen for possible bioactive metabolites with potential use in managing durian die-back disease, thereby contributing to alternative disease control strategies.

Methodology:

Microorganisms:

Priestia aryabhatai strain PTKU-123, isolated from agricultural soil and previously identified at the Omics Sciences & Bioinformatics Center (Chulalongkorn University, Thailand). The isolate was maintained on nutrient agar (NA) plates and stored at -20°C for short-term preservation. To ensure culture viability and purity, working stocks were routinely sub-cultured on fresh NA plates and incubated at 37°C prior to experimental use. This approach provided a consistent and reliable bacterial inoculum for downstream metabolite extraction and analytical studies.

The target fungal pathogen, *Fusarium* spp., was obtained from naturally infected durian tissues exhibiting die-back symptoms. The isolate was maintained on potato dextrose agar (PDA) under standard laboratory conditions and served as the test organism in antifungal bioassays. Identification of the fungal strain was carried out using a combination of morphological and molecular approaches. Microscopic examination revealed characteristic *Fusarium* conidia with distinctively curved or bent spores, a diagnostic feature of the genus. Molecular confirmation was performed through amplification and sequencing of the internal transcribed spacer (ITS) region, conducted by the Thailand Bioresource Research Center (TBRC, Thailand).

Fermentation and crude extract formation:

For the cultivation of bacteria, a loopful of *P. aryabhatai* PTKU-123 colonies grown on NA plates was inoculated into seed cultures containing Luria-Bertani (LB) broth and incubated at 37°C with agitation at 250 rpm for 24 h. These seed cultures were subsequently transferred into larger Erlenmeyer flasks containing fresh LB broth for fermentation. Cultures were maintained under identical shaking conditions (250 rpm, 37°C) for approximately 72 h, reaching the late exponential to early stationary phase, a period associated with optimal secondary metabolite synthesis.

Following incubation, the fermentation broth was harvested by centrifugation at 11,000 rpm and 4°C to obtain a cell-free supernatant. Crude metabolite extracts were obtained as following the previous research work protocol.⁹ The extracts were prepared using an acid precipitation method: the supernatant was adjusted to pH 2.0 with HCl and stored at 4°C for at least 24 h to facilitate precipitation. The precipitate was then collected by centrifugation, re-suspended in 80% ethanol, and centrifuged again to remove residual debris. The ethanol extract was concentrated under vacuum evaporation at 60°C, separating the dissolved metabolites from the solvent.¹⁰ The dried residue was subsequently re-dissolved in ethanol, yielding the crude extract preparation used for further analysis.

Screening for metabolites using thin layer chromatography:

Crude extract obtained from the fermentation broth was subjected to thin-layer chromatography (TLC) to provide preliminary evidence for the presence and diversity of secondary metabolites. TLC was selected as a rapid and cost-effective technique to separate complex mixtures, allowing detection of both hydrophilic and hydrophobic compounds within the crude extract.

Silica gel F254 TLC plates (60 µm, Merck, Darmstadt, Germany) were employed as the stationary phase, while a chloroform-methanol-water solvent system (65:25:4, v/v) served as the mobile phase, following previous research works.^{11,12} After sample application, plates were developed in a saturated and equilibrated TLC chamber and subsequently air-dried. For metabolite screening, multiple detection methods were used. TLC plates were first observed under UV light at 254 nm to detect fluorescent compounds, which may indicate aromatic or conjugated structures. Iodine vapor staining was then employed to reveal



hydrophobic compounds, which form reversible brown complexes with iodine. Finally, ninhydrin (0.2%) dissolved in water-saturated butanol was applied to identify amino acid/peptide-containing metabolites, producing purple coloration upon reaction. The combination of these visualization techniques enabled detection of both peptide- and lipid-associated compounds. After processing the TLC plates, the retention factor (Rf) values of visible bands will be calculated using the formula:

$$Rf = \frac{\text{Distance traveled by compound}}{\text{Distance traveled by solvent front}}$$

Antimicrobial bioassay of Priestia's crude extract:

The antifungal potential of *P. aryabhatai* PTKU-123 crude extract was assessed against *Fusarium* spp. using the poison food technique.¹³ Potato dextrose agar (PDA) plates were amended with defined concentrations of the crude extract, while solvent-treated and untreated PDA plates served as negative controls. Mycelial plugs (0.5 cm diameter) of actively growing *Fusarium* cultures were placed at the center of each plate and incubated at 25 °C for 5 days. Radial mycelial growth was recorded, and the percentage inhibition of fungal growth relative to controls was calculated according to the previous research work.¹⁴ All treatments were performed in triplicate to ensure reproducibility and statistical accuracy.

Results and Discussion:

Identification of fungal isolate by ITS sequencing and microscopy:

Microscopic characterization of the isolate from symptomatic durian tissues revealed slender, elongated macroconidia that were slightly sickle-shaped with a distinct apical bend. These conidia possessed 3-5 septa and measured approximately 10-15 µm in length by 3-5 µm in width (Figure 1). Such traits are consistent with classical taxonomic descriptions of the genus *Fusarium*, which produce bent, multi-septate macroconidia of similar dimensions. Comparable findings have been documented in durian-related studies, where bent conidial morphology has been highlighted as a reliable diagnostic feature.^{3,4}

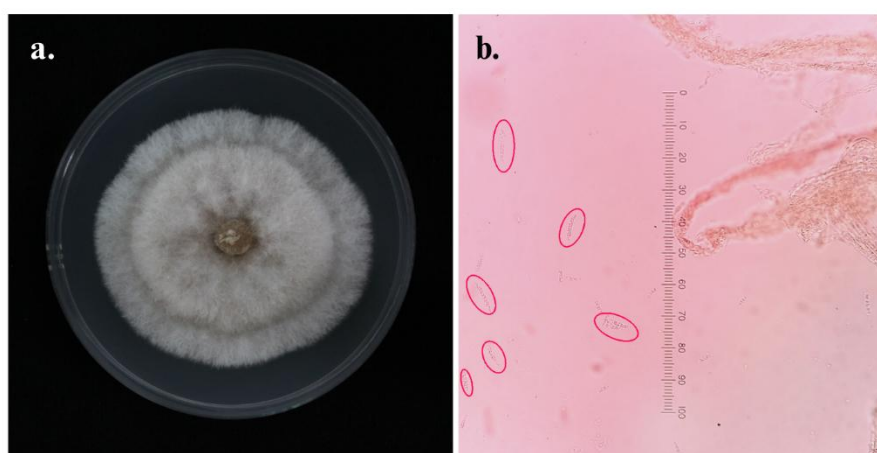
Molecular identification further supported this classification. ITS sequencing revealed 100% identity with several *Fusarium* reference strains, including *F. perambucanum* (ON054310.1), *F. equiseti* (OM326826.1), and *F. incarnatum* (MH290471.1) (Table 1). While this confirms placement at the genus level, the close similarity among ITS sequences prevented precise species-level resolution, a common limitation in *Fusarium* taxonomy that often necessitates additional loci (e.g., TEF1- α , RPB2) for higher resolution.

Together, the morphological and molecular data firmly establish the isolate as *Fusarium* sp. associated with durian die-back disease. This is consistent with recent reports highlighting *Fusarium* as a major pathogen affecting durian trees in Thailand. The presence of bent, septate macroconidia along with molecular identity strengthens the conclusion that *Fusarium* plays a significant role in durian decline.^{3,4}

Table 1.

Comparison of the fungal isolate's quantified ITS rDNA region with the reference strains using BLAST engine.

Rank	Scientific name	Max score	Total score	Query (%)	Identity (%)	Accension
1	<i>Fusarium pernambutanum</i> strain KUMCC-21-0688	1009	1009	100	100	ON054310.1
2	<i>Fusarium equiseti</i> strain MCC7	1007	1007	100	100	OM326826.1
3	<i>Fusarium incarnatum</i> strain GSS210	1005	1005	100	100	MH290471.1
4	<i>Fusarium sulawesiense</i> strain NRRL 66472	1005	1005	100	100	PP336544.1
5	<i>Fusarium equiseti</i> strain FUS-34-2	1005	1005	100	100	MH879250.1

**Figure 4.**

Morphological characteristics of *Fusarium* spp. (a) *Fusarium* isolate grown on PDA; (b) *Fusarium* spores (circled in red) visualized under the microscope with 400x magnification; the measurement range presents 0-100 μm .

TLC profiling of the crude extract:

The TLC analysis of the crude extract from *P. aryabhatai* PTKU-123 revealed both prominent and minor metabolite fractions that are consistent with lipopeptide production. Under UV and iodine visualization, a single dominant band was consistently observed at Rf 0.63, indicative of a major hydrophobic compound (Figure 2a-b). This Rf closely aligns with the range reported for surfactin derivatives (Rf 0.65-0.75) in earlier studies^{15,16}, suggesting that the primary metabolite in the extract may be surfactin-like in nature.

In contrast, derivatization with ninhydrin exposed a more complex metabolic profile, with five distinct peptide-containing bands at Rf values of 0.76, 0.69, 0.54, 0.29, and 0.16 (Figure 2c). These findings are parallel to previous reports where ninhydrin staining enhanced detection of lipopeptide fractions^{15,16,17}. Specifically, the bands at Rf 0.76, 0.69 and 0.54 correspond well to the surfactin range (0.55-0.75), confirming the presence of surfactin isoforms. The band at Rf 0.54 lies intermediate between surfactin and iturin ranges, suggesting possible co-production of these structurally related lipopeptides. Meanwhile, the band at Rf 0.29 overlaps with reported bacillomycin fractions (Rf ~0.3)¹⁵, and the band at Rf

0.16 is consistent with fengycin (Rf ~0.1-0.11)^{15,16}. The appearance of multiple peptide-reactive fractions suggests that *P. aryabhatai* PTKU-123 synthesizes not just surfactin-like compounds, but also several lipopeptides as presented in (Table 2).

When viewed alongside prior studies, these results reinforce the importance of TLC as a screening tool for differentiating between lipopeptide families. For example, the previous report studies demonstrated that crude extracts often contain overlapping surfactin, iturin, and fengycin families, each with distinct antifungal targets.^{15,16} The TLC profile of *P. aryabhatai* PTKU-123 mirrors this pattern, with detectable fractions corresponding to all three major lipopeptide classes. This metabolite diversity is of particular significance for biocontrol, as the combined presence of surfactin-, iturin-, bacillomycin-, and fengycin-like compounds can act synergistically, thereby broadening the antifungal spectrum and enhancing efficacy against *Fusarium* spp.

Table 2.

Potential secondary metabolites separated through thin-layer chromatography (TLC) system, by applying chloroform-methanol-water (65:25:4 v/v) as the mobile phase.

Rf value	Secondary metabolites	References
0.75, 0.65, 0.55	Surfactin	[15], [16], [17]
0.4, 0.32	Iturin	[15], [16]
0.3	Bacillomycin	[15]
0.1, 0.11	Fengycin	[15], [16]

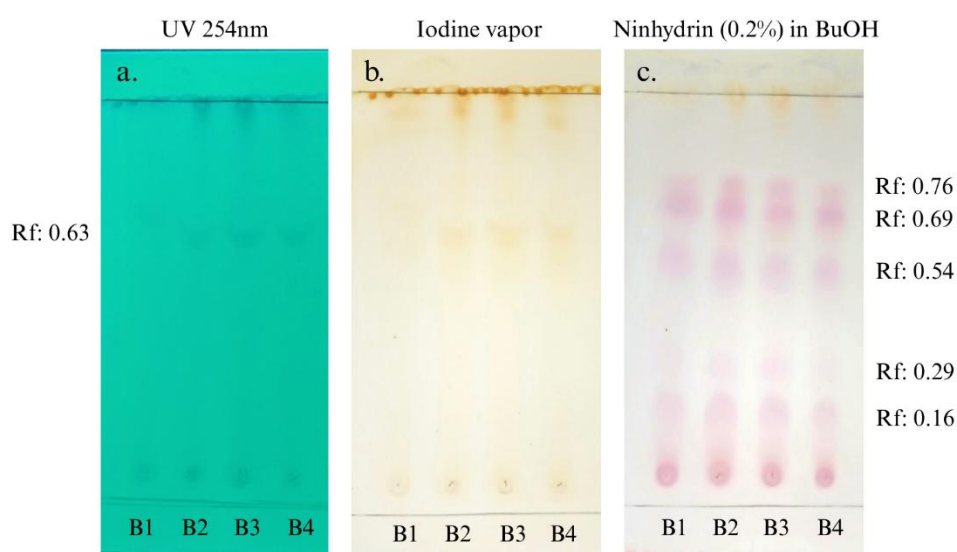


Figure 5.

Thin-layer chromatography profile of crude extract.

Visualization was performed under (a) UV (254 nm); (b) iodine vapor, and (c) ninhydrin staining (0.2% in water-saturated butanol).

Antifungal activity of Priestia's crude extract against Fusarium spp.:

The antifungal activity of the *Priestia aryabhatai* PTKU-123 crude extract was evaluated against *Fusarium* spp. using the poison food technique, with growth inhibition compared to the chemical fungicide metalaxyl and the biocontrol agent *Trichoderma* (Figure 3). A starting

concentration of 2 mg/mL was selected, as previous report indicates that metalaxyl achieves complete inhibition (100%) at 2-4 mg/mL against *Phytophthora*.¹⁸ Likewise, *Trichoderma*-based preparations are often evaluated in the same range, providing a comparative baseline.

At 2 mg/mL, the crude extract reduced mycelial growth to 11.3 ± 0.653 cm, corresponding to 44.55% inhibition (Table 3). Increasing the concentration to 3 mg/mL drastically enhanced activity, with inhibition rising to 97.78%. At 4 mg/mL, inhibition was nearly complete (99.91%), and at 5 mg/mL, full suppression of mycelial growth was achieved (100% inhibition). In contrast, the biological control agent *Trichoderma* (2 mg/mL) suppressed mycelial growth by 63.18%, while metalaxyl at the same concentration was notably less effective (14.72% inhibition). This highlights two key findings: (i) *Fusarium* isolates from durian exhibit reduced susceptibility to metalaxyl, a chemical fungicide commonly used in durian orchards, and (ii) the PTKU-123 crude extract demonstrates superior antifungal efficacy over the chemically synthesized fungicide, achieving complete inhibition at higher concentrations.

Table 3.

Mycelial growth and inhibition percentage of different test materials against *Fusarium* spp. using poison food bioassay.

Test material	Concentration (mg/ml)	Mycelial growth (cm)	Inhibition percentage (%)
Ethanol (control)	0	17.7 ± 1.491^b	-
Crude extract	2	11.3 ± 0.653^c	44.55
Crude extract	3	2.8 ± 0.602^a	97.78
Crude extract	4	1.0 ± 0.000^a	99.91
Crude extract	5	0.0 ± 0.000^a	100.00
<i>Trichoderma</i> (control)	2	11.6 ± 2.462^c	63.18
Metalaxyl (control)	2	18.8 ± 1.710^b	14.72

The data of mycelial growth are presented as Mean \pm SD.

The values sharing a common superscripted letter are not significantly different from each other at $p < 0.05$ value according to Turkey's HSD test.

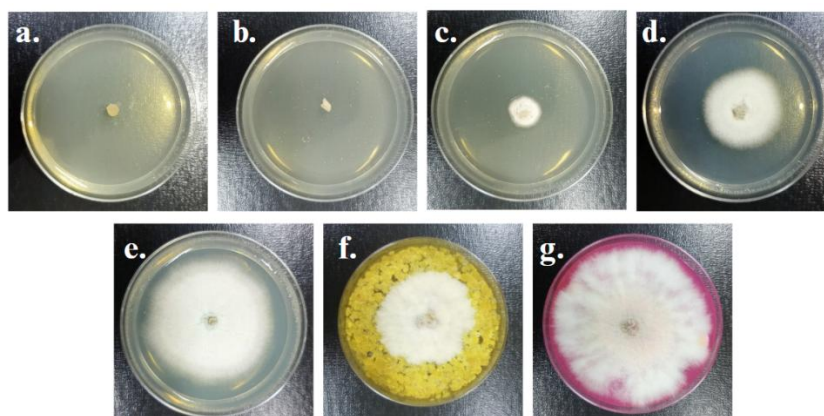


Figure 6.

Growth of *Fusarium* spp. on poison food bioassay with different concentrations of test material (a) 5 mg/ml of crude extract; (b) 4 mg/ml of crude extract; (c) 3 mg/ml of crude extract; (d) 2 mg/ml of crude extract; (e) control sample; (f) 2 mg/ml of *Trichoderma* as commercial control; (g) 2 mg/ml of metalaxyl as commercial control.

Implications for die-back disease management in durians:

The antifungal bioassay demonstrated that the crude extract of *P. aryabhatai* PTKU-123 effectively suppressed the radial growth of *Fusarium* sp., a pathogen implicated in durian die-back disease. At lower concentrations, partial inhibition was observed, while complete inhibition of fungal growth was achieved at 5 mg/mL. This level of efficacy is comparable to synthetic fungicides such as metalaxyl, which are typically effective at concentrations of 2-4 mg/mL, and to established biocontrol agents like *Trichoderma* spp. The ability of the bacterial crude extract to achieve full inhibition suggests strong antifungal potential, with the possibility that further purification could lower the effective dose required.

TLC profiling of the crude extract revealed the presence of multiple bioactive metabolites. A dominant band was consistently detected at an R_f value of 0.63 under iodine vapor visualization, suggesting a major compound with potential antifungal activity. Additional bands at R_f values of 0.76, 0.69, 0.54, 0.29, and 0.16 were observed after ninhydrin staining, indicating the presence of peptide-like metabolites. The diversity of these bands suggests that the crude extract consists of multiple secondary metabolites, which may act synergistically to enhance antifungal activity. This metabolite complexity is advantageous for field application, as mixtures of bioactive compounds are less likely to lead to rapid resistance development compared to single-compound fungicides.

The findings hold important implications for durian disease management. The suppression of *Fusarium* sp. by PTKU-123 extract demonstrates its potential as a natural and environmentally friendly alternative to chemically synthesized fungicides. Incorporating microbial-based antifungal agents into durian production systems could reduce chemical inputs, mitigate fungicide resistance, and improve orchard sustainability. Furthermore, the ability of *P. aryabhatai* PTKU-123 to produce diverse lipopeptide-like metabolites positions it as a promising candidate for the development of a biological control product tailored for durian die-back management.

Conclusion:

This study demonstrated that the crude extract of *P. aryabhatai* strain PTKU-123 possesses strong antifungal activity against *Fusarium* sp., a pathogen discovered to be associated with durian die-back disease. Complete inhibition of mycelial growth was achieved at a concentration of 5 mg/mL, indicating that the extract is highly effective, with comparable efficacy to certain chemical fungicides and biological control agents. Such potent inhibition suggests that further purification of the extract could reduce the effective inhibitory concentration, enhancing its practical application as a biocontrol agent. TLC profiling of the crude extract revealed the presence of multiple metabolite fractions, with a dominant band at R_f 0.63 observed under UV and iodine staining, and additional peptide-containing bands detected with ninhydrin. These findings indicate that *P. aryabhatai* produces a mix of lipopeptide-like compounds, among which the major fraction is likely responsible for the observed antifungal effect. Together, the results highlight the potential of *P. aryabhatai* PTKU-123 as a promising microbial source of antifungal metabolites for sustainable management of durian pathogens. Future work focusing on purification, structural characterization, and in-plant efficacy testing will be essential to validate its role as a biocontrol alternative to conventional fungicides.

Acknowledgements:

The authors gratefully acknowledge the financial support from the *Kasetsart Agro-Industry Scholarship 2024*, which enabled the successful completion of this research. Sincere appreciation is extended to our advisor and co-advisor for their continuous guidance, constructive feedback, and invaluable encouragement throughout the study. We also thank the Department of Agro-Industry, Kasetsart University, for providing laboratory facilities and technical support.

References:

1. Ali, N. A. W. A., Wong, G. R., Tan, B. C., Lum, W. S., & Mazumdar, P. (2025). Unleashing the potential of durian: Challenges, opportunities, and the way forward. *Applied Fruit Science*, 67(3). <https://doi.org/10.1007/s10341-024-01237-y>
2. Siriphanich, J. (2011). Durian (*Durio zibethinus* Merr.). In Elhadi M. Yahia (Ed.), *Postharvest biology and technology of tropical and subtropical fruits, vol. 3, cocona to mango* (pp. 80–116e). Woodhead Publishing Series in Food Science, Technology and Nutrition.
3. Pongpisutta, R.; Rattanakreetakul, C.; Bincader, S.; Chatchaisiri, K.; Boonruanfrod, P. Detection of fungal pathogen causing durian dieback disease. *Khon Kaen Agr. J.* 2020, 48, 703-714. [10.14456/kaj.2020.65](https://doi.org/10.14456/kaj.2020.65)
4. Pongpisutta, R., Keawmanee, P., Sanguansub, S., Dokchan, P., Bincader, S., Phuntumart, V., & Rattanakreetakul, C. (2023). Comprehensive investigation of die-back disease caused by *Fusarium* in durian. *Plants*, 12(17), 3045. <https://doi.org/10.3390/plants12173045>
5. Sreelakshmi, K. P., Madhuri, M., Swetha, R., Rangarajan, V., & Roy, U. (2024). Microbial lipopeptides: Their pharmaceutical and biotechnological potential, applications, and way forward. *World Journal of Microbiology and Biotechnology*, 40(3), 98. <https://doi.org/10.1007/s11274-024-03908-0>
6. Jiang, J., Gao, L., Bie, X., Lu, Z., Liu, H., Zhang, C., Lu, F., & Zhao, H. (2016). Identification of novel surfactin derivatives from NRPS modification of *Bacillus subtilis* and its antifungal activity against *Fusarium moniliforme*. *BMC Microbiology*, 16, 31. <https://doi.org/10.1186/s12866-016-0645-3>
7. Liang, C., Xi-xi, X., Yun-xiang, S., Qiu-hua, X., Yang-yong, L., Yuan-sen, H., & Ke, B. (2023). Surfactin inhibits *Fusarium graminearum* by accumulating intracellular ROS and inducing apoptosis mechanisms. *World Journal of Microbiology and Biotechnology*, 39, 340. <https://doi.org/10.1007/s11274-023-03790-2>
8. Liu, L., Jin, X., Lu, X., Guo, L., Lu, P., Yu, H., & Lv, B. (2023). Mechanisms of surfactin from *Bacillus subtilis* SF1 against *Fusarium foetens*: A novel pathogen inducing potato wilt. *Journal of Fungi*, 9(3), 367. <https://doi.org/10.3390/jof9030367>
9. Tunsagool, P., Kruaweangmol, P., Sunpapao, A., Kuyyogsuy, A., Jaresitthikunchai, J., Roytrakul, S., & Vongsangnak, W. (2023). Global metabolic changes by *Bacillus* cyclic lipopeptide extracts on stress responses of para rubber leaf. *Emerging Science Journal*, 7(3), 974–990. <https://doi.org/10.28991/esj-2023-07-03-022>
10. Abdel-Mawgoud, A. M., Aboulwafa, M. M., & Hassouna, N. A. (2008). Characterization of surfactin produced by *Bacillus subtilis* isolate BS5. *Applied Biochemistry and Biotechnology*, 150(3), 289–303. <https://doi.org/10.1007/s12010-008-8153-z>
11. Smyth, T. J., Rudden, M., Tsaousi, K., Marchant, R., & Banat, I. M. (2014). Protocols for the isolation and analysis of lipopeptides and bioemulsifiers. In *Hydrocarbon and Lipid Microbiology Protocols* (pp. 3-28). Springer. https://doi.org/10.1007/8623_2014_29



12. Smyth, T.J.P., Perfumo, A., McClean, S., Marchant, R., Banat*, I.M. (2010). Isolation and Analysis of Lipopeptides and High Molecular Weight Biosurfactants. In: Timmis, K.N. (eds) Handbook of Hydrocarbon and Lipid Microbiology. Springer, Berlin, Heidelberg. https://doi.org/10.1007/978-3-540-77587-4_290
13. Al-Nadabi, H. H., Al-Buraiki, N. S., Al-Nabhani, A. A., Maharachchikumbura, S. N., Velazhahan, R., & Al-Sadi, A. M. (2021). In vitro antifungal activity of endophytic bacteria isolated from date palm (*Phoenix dactylifera* L.) against fungal pathogens causing leaf spot of date palm. *Egyptian Journal of Biological Pest Control*, 31, 65. <https://doi.org/10.1186/s41938-021-00413-6>
14. Gamliel, A., Katan, J., & Cohen, E. (1989). Toxicity of chloronitrobenzenes to *Fusarium oxysporum* and *Rhizoctonia solani* as related to their structure. *Phytoparasitica*, 17, 101–106. <https://doi.org/10.1007/BF02979517>
15. Arrebola, E., Sivakumar, D., Bacigalupo, R., & Korsten, L. (2010). Combined application of antagonist *Bacillus amyloliquefaciens* and essential oils for the control of peach postharvest diseases. *Crop Protection*, 29(4), 369–377. <https://doi.org/10.1016/j.cropro.2009.08.001>
16. Razafindralambo, H., Paquot, M., Hbid, C., *et al.* (1993). Purification of antifungal lipopeptides by reversed-phase high-performance liquid chromatography. *Journal of Chromatography*, 639(1), 81–85. [https://doi.org/10.1016/0021-9673\(93\)83091-6](https://doi.org/10.1016/0021-9673(93)83091-6)
17. Hong, S.-Y., Lee, D.-H., Lee, J.-H., Haque, M. A., & Cho, K.-M. (2021). Five Surfactin Isomers Produced during *Cheonggukjang* Fermentation by *Bacillus pumilus* HY1 and Their Properties. *Molecules*, 26(15), 4478. <https://doi.org/10.3390/molecules26154478>
18. Phetkhajone, S., Siriwattanakul, U., Putaporntip, N., Pichakum, A., & Songnuan, W. (2024). Bioassay for validation of metalaxyl persistence to control *Phytophthora palmivora* infection in durian. *Tropical Plant Pathology*, 49, 209–217. <https://doi.org/10.1007/s40858-023-00621-5>



BIOLOGICAL PROPERTIES OF ALKALINE LIGNIN FROM LONGAN PEEL FOR COSMETIC APPLICATION

Kittiya Phiguntong¹, Jidapha Tinoi^{2,3,*}

¹Interdisciplinary Program of Biotechnology, Multidisciplinary and Interdisciplinary School, Chiang Mai University, Chiang Mai, Thailand

²Department of Chemistry, Faculty of Science, Chiang Mai University, Chiang Mai, Thailand

³Center of Excellence in Materials Science and Technology, Chiang Mai University, Chiang Mai 50200, Thailand

*e-mail: jidapha.tinoi@cmu.ac.th

Abstract:

Longan peel is a significant by-product generated in large quantities during the processing of longans. It has been found to contain lignin, an essential component with biological properties. The purpose of this study was to extract and apply lignin as a cosmetic ingredient. Lignin was extracted from the longan peel using an alkaline extraction method under autoclave conditions. A dark brown alkaline lignin powder was obtained, with a yield of approximately 2.7% and a purity of 82.21%. The lignin particle size distribution ranged from 340 to 460 nm and had a granular shape. FTIR analysis confirmed the typical polyphenolic structure of lignin with guaiacyl enrichment and the presence of carbonyl groups. The antioxidant properties of alkaline lignin were investigated using DPPH and ABTS assays. The results showed that the lignin extract exhibited good antioxidant activity, with IC₅₀ values of 14.84 ± 0.15 and 7.31 ± 0.23 $\mu\text{g/mL}$, respectively. Moreover, alkaline lignin exhibited tyrosinase inhibitory activity of approximately 50% at a concentration of 1.52 $\mu\text{g/mL}$, corresponding to 2.46 ± 0.56 mg KAE/g extract in kojic acid equivalents. The cell cytotoxicity of lignin was investigated using the MTT method using the L929 fibroblast cell. The results demonstrated that cell viability significantly decreased, with an IC₅₀ of 19.41 $\mu\text{g/ml}$. This research indicated that alkaline lignin extract from longan peel possesses potent antioxidant activity and remarkable tyrosinase inhibition, suggesting its potential as a cosmetic ingredient in skincare formulations. However, it remains necessary to assess cytotoxicity at higher concentrations further.

Introduction:

Longan peel, which is the exocarp part of the seeds and a by-product of longan processing, poses challenges in biomass management. In Thailand, approximately two million tons of longan peel waste are generated annually, with over 80% originating from the northern region. Improper disposal of this waste can lead to decomposition, air pollution, and microbial contamination. Longan peel consists of the major lignocellulosic components, including cellulose, hemicellulose, and lignin. It is crucial to enhance or optimize its potential benefits, particularly those of lignin. Lignin is a naturally abundant biopolymer with a complex and heterogeneous structure that is synthesized from derivatives of three different alcohols, including *p*-coumaryl (H-unit), coniferyl (G-unit), and sinapyl (S-unit). Aromatic rings, methoxy groups, carbonyl groups, and aliphatic hydroxyl (-OH) are the main functional groups of lignin structure.¹ These characteristics are regarded as critical structures of lignin, as both its quantitative and qualitative properties are determined by its functional groups. For the industry, lignin is used as a reinforcing material because lignin is strong, durable, water-insoluble, and inelastic. When combined with other materials such as polymers or resins, it increases impact resistance, reduces the weight of the material, and is resistant to harsh environments.² Moreover, lignin is a biomedically active ingredient carrier for medication delivery systems. It has been studied for its potential to increase sensitivity to chemotherapy.³ In the cosmetics industry, lignin has attracted interest due to its biological

properties. It functions as an antioxidant, acting as a scavenger in biological systems. The antioxidant activity of lignin is mainly caused by the ortho-methoxyl substitution in aromatic rings and the existence of free phenolic hydroxyl groups.⁴ Lignin can also inhibit tyrosinase, the enzyme responsible for melanin synthesis, resulting in dark spots on the skin. Additionally, lignin exhibits anti-UV activity due to its unsaturated functional groups, which are capable of absorbing UV radiation.⁵ Therefore, the application of lignin in cosmetics is highly advantageous, as it possesses good biological properties and can be extracted naturally from agricultural waste products.

This work aimed to extract lignin from longan peel using alkaline extraction under autoclave conditions and to investigate the characteristics and biological properties of the extracted alkaline lignin. The antioxidant activity was examined using DPPH and ABTS radical scavenging assays. Tyrosinase inhibitory activity was evaluated in vitro using L-DOPA as a substrate. Cytotoxicity was determined using the MTT assay on L929 fibroblast cells to assess cell viability. The findings on the biological activities of alkaline lignin suggest promising opportunities for its utilization in lignin-based formulations designed for cosmetic and biomedical products. In particular, studies on longan peel-derived lignin could provide critical insights to advance its innovative applications in these fields.

Methodology:

Lignin extraction.

Longan peel was collected from the longan processing plant in Ban Hong district (Lamphun province, Thailand). It was treated with 40% sodium hydroxide solution with a solid-to-liquid ratio of 1:20 (w/v). The mixture was reacted under autoclave conditions (121°C, 15 psi) for 15 min and then filtered with nylon cloth using a vacuum pump to separate the solid residue. The obtained black liquor was acidified for lignin precipitation with concentrated sulfuric acid. The precipitate was separated by centrifuging at 1,000 rpm for 15 min and washed with 0.1 M hydrochloric acid until a colorless solution. The pH was adjusted to neutral by washing with distilled water. The extracted compound, termed alkaline lignin, was obtained and then dried at 65°C overnight and allowed to cool in a desiccator. The yield of alkaline lignin was evaluated by weighing.

Determination of alkaline lignin purity.

The purity of alkaline lignin was determined using Klason lignin extraction.⁶ Briefly, alkaline lignin was treated with 72% sulfuric acid and stirred at 20–30 °C for 2 h. The mixture was then diluted to 3% sulfuric acid, autoclaved at 121 °C for 1 h, and subsequently filtered. The resulting precipitate was oven-dried at 105 °C for 1 h and cooled in a desiccator to a constant weight. The insoluble lignin content was quantified after removal of residual inorganic material. To determine the ash content, the solid residue was ashed at 525 °C for 4 h. The insoluble lignin fraction was then calculated by subtracting the ash weight from the dried residue.

In addition, the soluble lignin content was determined according to TAPPI UM 250 (TAPPI Standards, 1985). The supernatant fraction was analyzed by measuring absorbance at 280 nm using a UV spectrophotometer. The soluble lignin concentration was calculated using the following equation:

$$\text{Soluble Lignin} = \frac{A}{110} \times \frac{\text{Dilution}}{\text{Sample weight}} \times 100$$

Where 110 is the absorptivity of soluble lignin expressed in $\text{Lg}^{-1}\text{cm}^{-1}$ and A is the absorbance at 280 nm.



Characterization of alkaline lignin.

The particle size distribution of lignin suspension (1%) was analyzed using Dynamic Light Scattering (DLS) using Zetasizer (Malvern Instruments, UK). The lignin morphology was determined using a scanning electron microscope (SEM) analysis. The lignin powder on the stub was coated with carbon tape and then coated with a thin layer of gold particles. The morphology of lignin was observed at various magnifications using a high-vacuum scanning electron microscope (SEM, Hitachi SU3800, Japan) with an acceleration voltage of 15 kV. The functional groups in the alkaline lignin structure were analyzed using Fourier transform infrared spectrophotometry (FTIR) (Bruker, InvenioS) in the ATR (Attenuated Total Reflectance) mode. The infrared spectra in the 400-4,000 cm^{-1} frequency range were used to measure the wavenumber.

Biological properties determination

Antioxidant activity assay.

The alkaline lignin suspension was prepared for evaluation of its antioxidant activity using DPPH and ABTS assays. For the DPPH assay, the lignin suspension was mixed with a DPPH reagent. The mixture solutions were vortexed and kept in the dark for 1 hour at ambient temperature. Then, the absorbance was measured at 515 nm by a spectrophotometric microplate reader. In the ABTS assay, the mixture of ABTS reagent and alkaline lignin solution was incubated in the dark at room temperature for 30 min and measured at 734 nm.

Tyrosinase inhibition.

The inhibitory activity of tyrosinase of alkaline lignin was tested using the dopachrome method and compared with a kojic acid standard. Tyrosinase (EC 1.14.18.1, SRL™, India) solution (100 units/mL) and L-3,4-dihydroxyphenylalanine (L-DOPA, 1 mg/mL) were prepared. A two-fold serial dilution was prepared for the alkaline lignin solution. 40 μL of each lignin sample, kojic acid, and tyrosinase enzyme were pipetted into a 96-well plate and incubated in the dark at 37 °C for 5 min. After that, L-DOPA was added and incubated in the dark at 37 °C for 20 min. The absorbance at 475 nm was measured.

Cell toxicity.

The L929 fibroblast cells (L929 mouse fibroblast, ATCC® CCL-1™) were cultured to obtain approximately 85-95% cell density. The cell cultures were prepared to achieve a density of 5.0×10^3 cells per well in a 96-well plate using 100 μL of RPMI 1640 complete media. The cells were cultured at 37 °C in a CO₂ incubator for 24 hr. The various concentrations of alkaline lignin solution (0-150 $\mu\text{g}/\text{mL}$) and the cell culture medium were added, and the mixture was incubated for 24 hr. After that, the cell culture medium was removed, and 100 μL of MTT solution (5 mg/mL) was added. The cells were then incubated for 4 h to induce formazan crystal formation. Then, 100 μL of DMSO was added to dissolve the crystals, to obtain a purple solution. The absorbances were measured at 550 nm. The intensity of the color produced is related to the number of living cells. The cell viability and the IC₅₀ value were calculated.

Statistical analysis.

The statistical analysis of the experimental data was performed using IBM SPSS Statistics 26 software. The significant difference for statistical comparison at the 95% level was considered. The experiment was carried out in triplicate.

Results and Discussion:

The alkaline extraction process using a sodium hydroxide solution is commonly employed for lignin extraction. The process solubilizes and extracts lignin from the biomass by penetrating and affecting the lignocellulosic structure. In this work, lignin was extracted from longan peels using alkaline extraction assisted with autoclave conditions. The alkaline lignin powder was obtained and was found to be 2.7% (w/w). These results correspond to those of Jiang et al. (2009)⁷, who reported that the lignin content ranged from 3.1 to 3.5 % (w/w) when extracted from longan peel by soaking in an alkaline solution for 2 h. The extracted lignin yield was markedly lower than the inherent lignin content in longan peel (about 20% w/w). The purity of alkaline lignin was determined to be 82.19%, comprising 4.61% acid-soluble lignin and 77.58% acid-insoluble (Klason) lignin. These results are consistent with previous reports, which typically indicate purities in the range of 75-80%, depending on the raw material and processing conditions.⁸ Moreover, lignin extraction from lignocellulosic materials is challenging, as lignin is covalently bound to both hemicellulose and cellulose. Under optimized or modified extraction strategies, higher purities of lignin have been reported. For example, a two-step alkaline fractionation applied to hardwood biomass yielded lignin with purities ranging from 80-90% ,⁹ while Dhara et al. (2023) achieved a maximum purity of 93.7% from *Saccharum ravannae* using KOH-based hydrothermal pretreatment optimized via response surface methodology (RSM).¹⁰ Moreover, the visual appearance of alkaline lignin from longan peel was a fine, dark brown, hard powder, as shown in Figure 1. The dark brown color resulted from the polymerization of lignin, which is made up of phenylpropyl and phenylethyl units joined by ether linkages and carbon-carbon bonds formed through oxidative polymerization reactions.

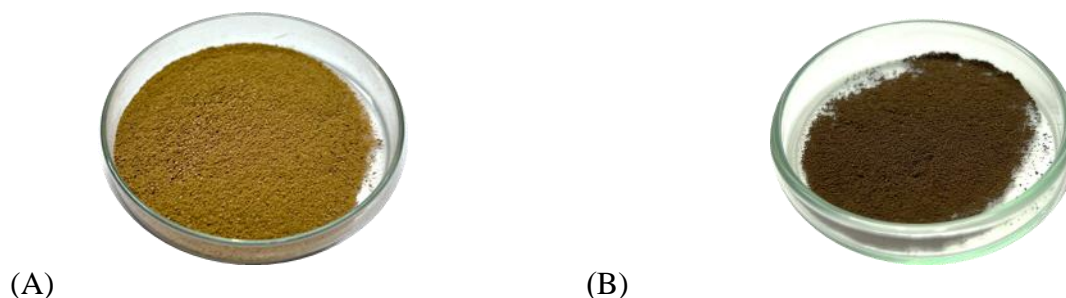
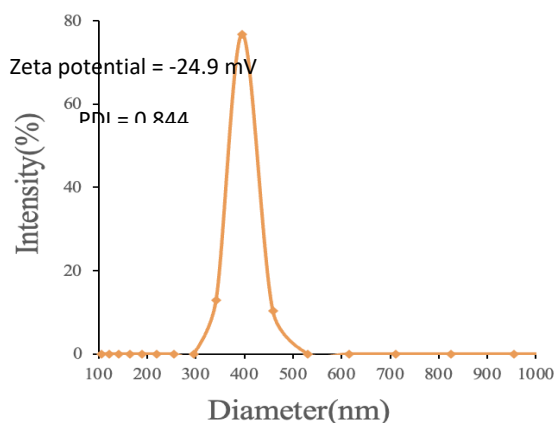


Figure 1.

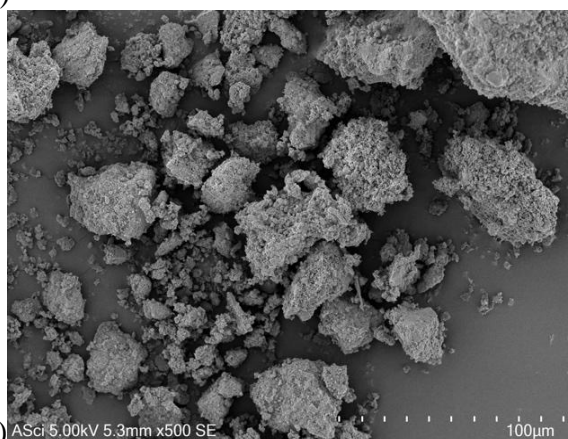
The characteristics of ground longan peel (A) and alkaline lignin powder (B)

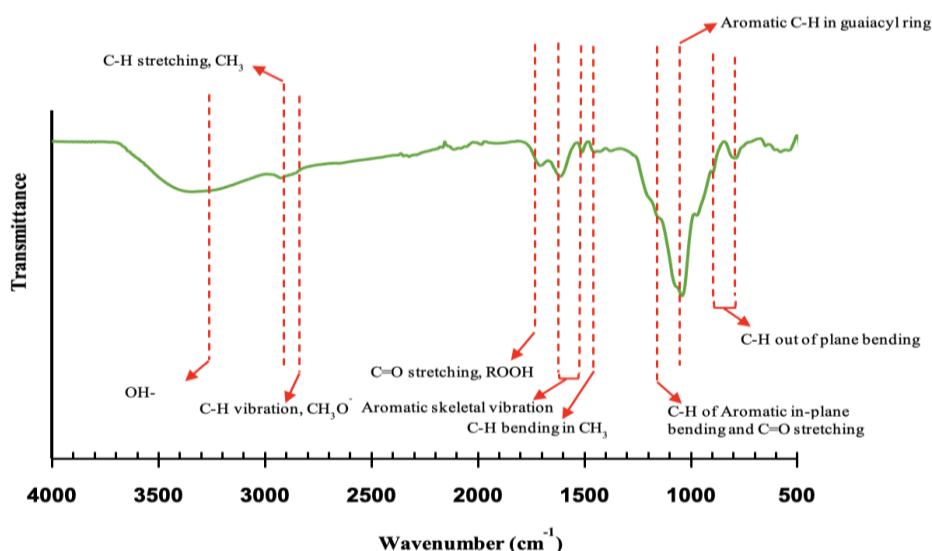
The physicochemical characteristics, such as particle size distribution and morphology, of alkaline lignin were analyzed. The particle size distribution was measured using DLS analysis and exhibited particle sizes in the range of 340-460nm, with an average particle size of 396 nm, as shown in Figure 2A. The alkaline lignin particles had a zeta potential value of -24.9 mV with a polydispersity index (PDI) value of 0.844. The results demonstrated that alkaline lignin exhibited moderately negative zeta potential values, indicating the presence of negatively charged functional groups on the particle surface and sufficient stability to remain dispersed in solution for a temporary period. The morphology of alkaline lignin was observed using SEM analysis and presented a granular shape, as shown in Figure 2B. Compared with corncob alkaline lignin, which exhibited relatively small particle sizes of 100-300 nm with a PDI below 1.7¹¹, Lignin nanoparticles derived from rice husk were spherical in shape, with a PDI of 0.257 ± 0.02 , an average size of 260 ± 10 nm, and a zeta potential of -35.2 ± 4.1 .¹² The infrared spectra of alkaline lignin are presented in Figure 2C. The FTIR spectrum exhibited a broad O-H stretching band at ~ 3400 cm^{-1} , aliphatic C-H stretching at 2930-2850

cm^{-1} , and a distinct carbonyl absorption near 1700 cm^{-1} . Strong aromatic skeletal vibrations at ~ 1600 and 1510 cm^{-1} confirmed the polyaromatic backbone, while the prominent band at $\sim 1270 \text{ cm}^{-1}$ was assigned to guaiacyl C-H bending. This feature indicates guaiacyl enrichment, consistent with the preferential degradation of syringyl units during alkaline pretreatment.¹³ Additional bands observed at $1220\text{-}1030 \text{ cm}^{-1}$ (C-O stretching in aryl-ether linkages and methoxy groups) and at $830\text{-}870 \text{ cm}^{-1}$ (aromatic C-H out-of-plane bending) further corroborated the typical lignin functionalities. These results are consistent with previous FTIR reports on bamboo lignin,¹⁴ indicating that alkaline lignin preserves the polyphenolic backbone while acquiring greater guaiacyl character and additional carbonyl groups.



(A)





(C)

Figure 2.

The physicochemical characteristics of alkaline lignin from longan peel (A) the particle size distribution, (B) the SEM image of alkaline lignin (5000×), and (C) the FTIR spectra of alkaline lignin

The antioxidant activities of the alkaline lignin from longan peel were measured by the radical scavenging activities of the DPPH and ABTS radicals, and the results are demonstrated in Figure 3. The DPPH scavenging capacity of alkali lignin exhibited strong antioxidant activity, with an IC₅₀ value of $14.84 \pm 0.15 \mu\text{g/mL}$. Comparison with vitamin E, a positive control commonly used as an ingredient in cosmetics, whose structure contains phenolic hydroxy groups, revealed that the antioxidant activity was not significantly different. Moreover, the alkali lignin extract was investigated for its antioxidant activity using the ABTS radical scavenging assay. The alkaline lignin extract exhibited an excellent antioxidant activity with an IC₅₀ value of $7.31 \pm 0.23 \mu\text{g/mL}$. It showed a significant difference when compared to the trolox standard, a modified vitamin E derivative, as shown in Table 1. According to industrial kraft and organosolv lignins, IC₅₀ values were significantly ranging from 3.47 to 5.16 $\mu\text{g/mL}$ in the ABTS assay, whereas those from the DPPH method ranged from 12.85 to 22.75 $\mu\text{g/mL}$.¹⁵ Comparison to corncob lignin showed IC₅₀ values of 170–260 $\mu\text{g/mL}$ in DPPH assay and 16–28 $\mu\text{g/mL}$ in ABTS assay.¹⁶ The results in this work revealed that the IC₅₀ value from the ABTS assay was lower than that from the DPPH assay, indicating a stronger scavenging capacity with both lipophilic and hydrophilic structures. This may be attributed to the higher reactivity of free radicals with the phenolic hydroxyl groups of lignin, as well as the nanoscale particle size (~396 nm), which provides a larger surface area and enhances the accessibility of reactive sites. These findings suggest that this lignin exhibits superior antioxidant potential, making it particularly suitable for applications in water-based cosmetic formulations, such as gels, toners, and serums, as well as cleansing oils, facial oils, or balms.

However, different lignin extraction processes result in variations in the properties of lignin. In previous studies, lignin extracted using deep eutectic solvents (DES) has been reported to exhibit even lower IC₅₀ values in both DPPH and ABTS assays, specifically 50 $\mu\text{g/mL}$ and 10 $\mu\text{g/mL}$, respectively. The DES preserves a higher content of phenolic hydroxyl groups and reduces condensation reactions that typically occur in harsh alkaline processes. Moreover, DES systems often facilitate partial depolymerization of lignin, generating smaller fragments with higher solubility and greater accessibility of active sites for radical

scavenging. Consequently, DES-derived lignin shows improved reactivity toward both polar and non-polar radicals.¹⁷ This suggests that integrating alkaline extraction with DES pretreatment could further enhance its potential for application in high-performance antioxidant formulations for cosmetics and pharmaceuticals.

Table 1.

Antioxidant activity and tyrosinase inhibition activity of alkaline lignin from logan peel

Samples	IC ₅₀ values (µg/mL)		
	Antioxidant activity		Tyrosinase inhibition activity
	DPPH	ABTS	
Alkaline lignin	14.84 ± 0.15 ^a	7.31 ± 0.23 ^b	1.52±0.21 ^a
Vitamin E	14.21 ± 1.23 ^a	-	-
Trolox	-	6.64 ± 0.42 ^a	-
Kojic acid	-	-	1.32±0.35 ^a

The inhibition of tyrosinase activity of alkaline lignin from longan peel was demonstrated in the IC₅₀ value of 1.52±21 µg/mL, which indicates no significant difference from kojic acid (1.32±35 µg/mL) (Table 1). Furthermore, kojic acid equivalent analysis indicated that alkaline lignin exhibited an activity corresponding to 2.46 ± 0.56 mg of kojic acid/g lignin sample. Compared with lignin extracted from corn stalks by the alkaline extraction method, which showed an IC₅₀ value of approximately 0.276 mg/mL.¹⁸ Thus, lignin from longan peel was found to display strong tyrosinase inhibitory activity.

The L929 fibroblast cells were treated with alkaline lignin at various concentrations (1.563–150 µg/mL). As shown in Figure 3A, cell viability was significantly reduced ($p < 0.05$), with an IC₅₀ value of 19.41 µg/mL. Furthermore, the morphology and distribution of L929 fibroblast cells (control and treated) observed under an inverted microscope at 20× magnification are presented in Figure 3B. The control cells displayed an elongated, slender morphology and were densely packed (Figure 3B(a)). In contrast, cells treated with 100 µg/mL alkaline lignin exhibited a shrunken morphology, with loosely distributed arrangements and the presence of formazan crystals (Figure 3B(b)). The results indicated that the extracted lignin exhibited cytotoxic effects at high concentrations, suggesting the need for caution in its applications. Nevertheless, the alkaline lignin demonstrated notable antioxidant activity and tyrosinase inhibitory effects, highlighting its potential as a functional ingredient in cosmetics.

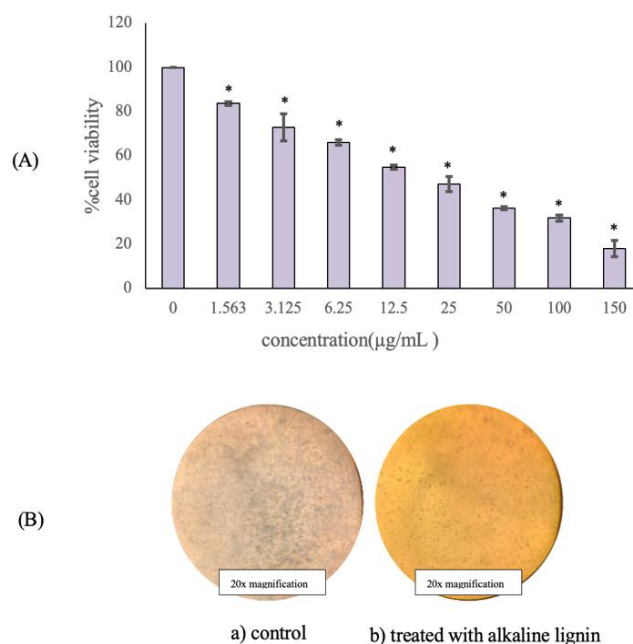


Figure 3.

The cell cytotoxicity of alkaline lignin on L929 fibroblast cells (A) cell viability after treatment with various concentrations of alkaline lignin solution after incubation for 24 h. (B) morphology and cell distribution under an inverted microscope: (a) control cells and (b) treated cells with 100.0 µg/mL alkaline lignin solution

The alkaline lignin extract from longan peel demonstrated pronounced biological activities, particularly in terms of antioxidant and tyrosinase inhibitory properties. Antioxidant capacity was confirmed by different assay systems, supporting the role of lignin as a phenolic-rich compound with radical scavenging and reducing abilities. Additionally, its ability to inhibit tyrosinase activity highlights its potential application as a natural skin-whitening or anti-pigmentation agent in cosmetic formulations. Nevertheless, cytotoxicity testing in fibroblast cells indicated a reduction in cell viability, suggesting that, despite its beneficial bioactivities, concerns remain regarding its safety at higher concentrations. These results indicated the dual nature of alkaline lignin as both a promising functional ingredient and a compound requiring further optimization, such as purification or testing in more relevant human skin cell models, to ensure its suitability for safe cosmetic applications.

Conclusion:

In this study, alkaline lignin was obtained from longan peel using an alkaline extraction assisted by an autoclave. The obtained alkaline lignin powder had a relatively low yield, was dark brown in color, and exhibited 82% purity. The size distribution of lignin particles was small in the nano-sized range. Its surface is negative with low dispersion stability. FTIR analysis confirmed the polyphenolic structure of lignin, with strong aromatic skeletal vibrations, guaiacyl signals, and new carbonyl groups formed during alkaline pretreatment. Alkaline lignin from longan peel exhibited potent antioxidant and tyrosinase inhibitory activities, supporting its potential as a natural bioactive ingredient for cosmetic applications. However, its cytotoxicity at higher concentrations raises safety concerns, indicating that further optimization is required. Future studies focusing on purification, structural modification, and evaluation in more relevant human skin cell models will be essential to ensure the safe and effective utilization of this material as a sustainable functional ingredient in cosmetics.



Acknowledgements:

The authors gratefully acknowledge the Department of Chemistry, Faculty of Science and Faculty of Medicine, Chiang Mai University, for providing the analytical instruments used in this study. The authors also appreciate the support of the Interdisciplinary Program of Biotechnology, Multidisciplinary and Interdisciplinary School, Chiang Mai University. This research was partially supported by Chiang Mai University, Chiang Mai, Thailand.

References:

1. Ralph J, Lapiere C, Boerjan W. *Curr Opin Biotechnol.* 2019; 56:240-249.
2. Zhang Z, Terrasson V, Guénin E. *Nanomaterials.* 2021; 11(5):1336.
3. Vukadinović A, Ognjanović M, Mijović M, Warren B, Erić S, Prijović Ž. *Pharmaceuticals.* 2025; 18(2):177.
4. Rangkadilok N, Sitthimonchai S, Worasuttayangkurn L, Mahidol C, Ruchirawat M, Satayavivad J. *Food Chem Toxicol.* 2007;45(2):328-336.
5. Antunes F, Mota IF, Fangueiro JF, Lopes G, Pintado M, Costa PS. *Int J Biol Macromol.* 2023; 234:123592.
6. Galiwango E, Abdel Rahman NS, Al-Marzouqi AH, Abu-Omar MM, Khaleel AA. *Chem Process Eng Res.* 2018; 57.
7. Jiang G, Prasad KN, Jiang Y, Yang B, Jia Y, Sun J. *Inno Food Sci Emerg Technol.* 2009; 10(4); 638-642.
8. Abolore R. S, Jaiswal S, Jaiswal A. K. *Industrial Crops and Products.* 2025; 235, 121696.
9. Tanis MH, Wallberg O, Galbe M, Al-Rudainy B. *Molecules.* 2023; 29(1), 98.
10. Dhara S, Samanta NS, Uppaluri R, Purkait MK. *Int J Biol Macromol.* 2023; 234, 123594.
11. Long J, Lu J, Chen L, Qiu X, Liu Q, Qin Y. *ACS Omega.* 2025; 10(7); 6210-6219.
12. Daassi R, Durand K, Rodrigue D, Stevanovic T. *Polymers.* 2023; 15(13), 2973.
13. Kadla JF, Kubo S, Venditti RA, Gilbert RD, Compere AL, Griffith WT. *Holzforschung.* 2002; 56(1), 37-44.
14. Liu J, Sun J, Wang S, Yu Y. *Int Wood Prod J.* 2019; 10(4), 146–153.
15. Michelin M, Liebentritt S, Vicente AA, Teixeira JA. *Int J Biol Macromol.* 2018;120(Pt A):159-169.
16. Gordobil O, Herrera R, Yahyaoui M, İlk S, Kaya M, Labidi J. *RSC Adv.* 2018; 8:24525-24533.
17. Morozova O, Vasil'eva I, Shumakovich G, Khlopova M, Chertkov V, Shestakova A, Yaropolov A. *Int. J. Mol. Sci.* 2024; 25(15):8277.
18. Wang R, Wang G, Xia Y, Sui W, Si C. *Int J Biol Macromol.* 2019; 128:107-113.



SSR-BASED MARKER-TRAIT ASSOCIATIONS FOR THE SELECTION OF DROUGHT-TOLERANT MAIZE S₁ GENOTYPES

Theerawut Wongwarat,^{1,*} Chaiyawat Nantachot,² Suriphat Thaitad³.

¹Khon Kaen Field Crops Research Center, 180, Sila, Mueang, Khon Kaen, Thailand

²Nakhon Sawan Field Crops Research Center, 146, Suksumran, Takfa, Thailand

³Field and Renewable Energy Crops Research Institute, 50, Chatuchak, Bangkok, Thailand

*e-mail: theerawut6949@gmail.com

Abstract:

The aim of this study was to evaluate the effectiveness of SSR markers in selecting drought-tolerant S₁ maize genotypes, with the goal of reducing the number of genotypes advanced to the S₂ generation for further breeding. Climate change has intensified drought condition, lead to reduced yields of field maize (*Zea mays* L.) and negatively affecting the domestic livestock feed production chain. Drought tolerance in maize is a complex quantitative trait influenced by both genetic and environmental factors. Although conventional breeding is effective, it is often time-consuming and resource-intensive. In this study, a total of one hundred and fifty S₁ genotypes derived from a cross between a drought-tolerant parent (Takfa 7) and a drought-susceptible parent (Ki 48) were genotyped using six SSR markers previously associated with drought-adaptive traits. These included umc1069 (glutathione-S-transferase 1), umc1139 (small kernel 501), umc1239 (trihelix transcription factor 43), umc1962 (pollen specific leucine rich repeat extensin 3) bnlg1079 (QTLs for vanillin and syrigaldehyde) and bnlg1526 (QTL for phosphorus utilization under deficit condition). Cluster analysis grouped the S₁ genotypes into distinct subpopulations, with two groups showing high frequencies of favorable drought-tolerance alleles. Based on cumulative marker profiles, seventy-three S₁ genotypes were selected as candidates for drought tolerance. The use of SSR-based marker-trait associations enabled the efficient identification of genotypes carrying favorable alleles, thereby reducing the number of genotypes advanced to the next generation. While this molecular approach shows promise, future studies incorporating phenotypic validation under drought condition will be essential to confirm the effectiveness of the selected genotypes. This combined strategy offers a robust pathway to accelerate the development of drought-resilient maize through marker-assisted selection.

Introduction:

Climate change has emerged as a major factor affecting feed maize production, particularly through reduced rainfall and increasing frequency of flash drought, which complicate drought prediction and management (Yuan et al., 2023)¹. Drought condition reduced soil moisture and cause rapid soil desiccation (Overperk and Udall, 2020)².

Drought stress critically maize development by disrupting male flower induction and reducing pollen viability. When drought persists during the development of female flowers, seed set is severely impaired (Herrero and Johnson, 198)³. These reproductive disruptions are major contributors to yield loss under water-deficit conditions.

Lunduka et al. (2017)⁴ defined drought-tolerant maize as varieties capable of retaining at least 30% of their yield potential during flowering and grain-filling stages under water-deficit conditions, availability. Globally, drought is estimated to reduce maize yields by approximately 15-20% annually, and this figure is expected to rise with ongoing climate change and more frequent drought episodes. The deployment of drought-tolerance hybrids remains a key strategy for mitigating these impacts. However, drought tolerance is a complex quantitative trait controlled by multiples genes and influenced by both shoot and root morphology (Polania et al., 2016)⁵. The expression of drought tolerance also varies with plant



development stage, genetic background and agroecological condition (Toscano et al., 2019)⁶, complicating accurate phenotypic selection. Conventional breeding, while effective, is often labour-intensive and time-consuming.

A fundamental understanding of the genetic basis of drought tolerance has been advanced through quantitative trait loci (QTL) mapping in bi-parental populations (Cattivelli et al., 2008)⁷. Linkage mapping has identified numerous QTLs associated with morphological traits such as flowering time and tassel size, as well as physiological traits such as abscisic acid metabolism and kernel starch content (Tuberosa et al., 2002; Almeida et al., 2013)^{8,9}.

Subsequent to linkage mapping, marker-trait association analysis based on linkage disequilibrium (LD) has been developed to enable the evaluation of multiple alleles within genetically diverse populations. Markers identified through association mapping are generally more transferable across genetic backgrounds and more suitable for marker-assisted selection (MAS), particularly for complex traits such as drought tolerance (Buckler and Thornsberry, 2002; Yu and Buckler, 2006; Sa et al., 2022)^{10,11,12}. MAS relies on markers that are tightly linked to target traits and have sufficiently high allele frequencies in breeding populations to ensure effective selection (Yu et al., 2005)¹³.

Simple sequence repeat (SSR) markers are highly polymorphic, co-dominant, genome-wide distributed, and reproducible, making them ideal for genetic diversity analysis and marker-trait association studies (Park et al., 2009)¹⁴. SSR-based association analysis has been extensively applied in various crops; however, limited studies have focused on identifying drought-tolerant genotypes in Thai maize germplasm, particularly using S₁ populations. Bridging this gap may facilitate the early-stage selection of promising genotypes and support the development of drought-resilient varieties. To our knowledge, this study represents the first attempt to apply SSR-based marker-trait association analysis in S₁ genotypes of Thai maize for drought tolerance. By identifying genotypes carrying drought-associated marker at the S₁ generation, this approach allows for the early elimination of genotypes lacking the desired alleles. When combined with phenotypic evaluation of key agronomic traits such as ear and kernel development, this method enables a significant reduction in the number of S₁ genotypes advanced to the S₂ generation. As a result, it enhances selection efficiency and reduces the resource requirement typically associated with traditional breeding pipelines.

Ilyas et al. (2023)¹⁵ reported significant associations between thirty-one SSR markers and seven physiochemical traits in maize under drought stress conditions using a mixed linear model (MLM) approach. For instance, specific markers such as umc1363 were associated with caffeic acid content, while bnlg1350 and bnlg1484 were linked to chlorogenic acid content. Other markers showed associated with gallic acid content, ferulic acid content, antioxidant activity (DPPH), leaf relative moisture content and total phenolic content. These findings highlight the potential of SSR markers to detect functional variation in metabolic traits under drought conditions and reinforce the importance of selecting markers with high allele frequencies for successful application in breeding programs.

The plant breeding using SSR markers often employs an additive inheritance model. In which genotypes are coded numerical based on their contribution to the desired phenotypic trait. These genotypes scores can then be summed across all maker loci and individuals with total scores exceeding 75% of the maximum possible score considered to carry a high proportion of favorable alleles (Chu et al., 2021)¹⁶. This scoring approach can be effectively applied during early-generation selection to reduce the number of genotypes advanced in breeding programs. Furthermore, the numerical coding of genotypes forms the basis for genomic selection model, which estimate the breeding values of individuals based on their DNA marker profiles (Medina et al., 2021)¹⁷



The objective of this study was to identify and select S₁ maize genotypes associated with drought tolerant using SSR markers. This approach aimed to reduce the number of S₁ genotypes advanced for selfing into S₂ generation, thereby enhancing the efficiency of subsequent breeding programs.

Methodology:

Plant materials and DNA extraction

A total of one hundred and fifty selfed S₁ genotypes of maize were developed from a cross between the female parent Takfa 7 (drought-tolerant) and the male parent Ki 48 (drought-susceptible). Leaf tissues were sampled from the uppermost fully expanded leaves of each genotype and immediately placed into screw-cap microcentrifuge tubes containing DNA extraction buffer.

The samples were ground using a bead mill homogenizer (Revvity, USA), followed by centrifugation to remove cellular debris. Genomic DNA was extracted using the DNAsure Plant Kit (TIANGEN, China), following the manufacturer's instructions. The quantity and purity of the extracted DNA were assessed using a Nano DOT microspectrophotometer (Hercuvan, UK). DNA samples were then diluted to a final concentration of 10 ng/μL.

PCR amplification

Polymerase chain reaction amplification (PCR) was performed in a total reaction volume of 10 μL using the AllTaq Master Mix and PCR Core Kits (QIAGEN, Germany). Each PCR mixture consisted of 4x AllTaq Master Mix, 0.5 μM of each primer, 1x Master Mix Trace and 15 ng of genomic DNA. The amplification program included an initial activation at 95°C for 2 minutes, followed by 35 cycles of denaturation at 95°C for 10 seconds, annealing at a temperature corresponding the melting temperature (T_m) of each primer pair from Table 1 for 30 seconds, and extension at 72°C for 20 seconds. A final extension was performed at 72°C for 10 minutes. PCR products were separated using the QIAxcel Advanced Electrophoresis System (QIAGEN, Germany) and fragment sizes were estimated performed using the association QIAxcel ScreenGel software.

Statistical analyzes

Table 1.
SSR markers used in this study.

Primer names	Forward	Reverse	T _m (°C)	References
umc1069	ATAAGTGGGGGAGGCG AGCTA	AGAGAATCCCCAAGCA AACAAAC	56	Dubey et al., 2009 ¹⁸
umc1139	TTTGTAATATGGCGCTC GAAAACT	GAAGACGCCTCCAAGA TGGATAC	58	
umc1962	ATAAGTGGGGGAGGCG AGCTA	GAGAACCAACCACCAA AGAAGTCC	60	
bnlg1079	CGTACGTCGTTGCTGT CTGT	CAGTACGTGCAGTCCC TCCT	58	Ilyas et al., 2023 ¹⁵
bnlg1526	ACGAGCGAGTGGAGAA TAGG	AGCCAGTACGTGGGG TC	60	
umc1239	ATCAACACACCTTTCGA TTTCTGG	CGGTGATTAGTCGATG AAGAGTGA	56	



Single Marker analysis (SMA)

A chi-square test (χ^2) was used to evaluate segregation distortion of marker genotypes in biparental S1 population. The test assessed whether the observed genotype frequencies significantly deviated from the expected Mendelian ratio of 1:2:1 for codominant markers, and whether segregation skewed toward either the female and male parent genotype.

Linkage Disequilibrium (LD)

Pairwise linkage disequilibrium (LD) between SSR markers was estimated using the squared correlation coefficient (r^2). All possible marker pairs were analyzed and the LD matrix was generated using the R programming language. A heatmap of pairwise LD values was visualized using the basic heatmap () function in R.

Genotypic analysis

Genotype data from SSR markers were scored in codominant form. Each genotype was numerically coded as AA = 3, AB = 1 and BB = 0 to reflect allele dosage and enhance score resolution for clustering purposes, as an alternative to the conventional 2 – 1 – 0 coding scheme. These numerical scores were used to assess genetic relationships among the one thousand and fifty S₁ genotypes using hierarchical cluster analysis. A dendrogram was constructed based on six SSR markers using Ward's method with squared Euclidean distance as the similarity measure.

For selection purposes, S₁ genotypes were considered potentially drought-tolerant if they met the following criteria: having AA genotypes at ≥ 2 loci, AB genotypes at ≥ 3 loci, BB genotypes at ≤ 2 loci and a total marker score of ≥ 9 . These criteria were established to ensure the presence of favorable homozygous alleles while maintaining genetic diversity through heterozygous loci and minimizing susceptibility-associated alleles.

Phenotypic validation under drought stress condition was not conducted in the present study, as the primary objective was to identify S₁ genotypes carrying favorable alleles associated with drought tolerance using SSR-based marker-trait association analysis. However, the selected genotypes will be advanced to the S₂ generation and evaluated under controlled drought stress conditions in field trials. This follow-up evaluation will allow for the validation of molecular selection results and confirm the drought tolerance performance of the identified genotypes in practical settings.

Results and Discussion:

Genotypic Segregation Analysis

Molecular markers are generally expected to segregate according to Mendelian inheritance, either as dominant or codominant markers. In this study, six SSR markers; umc1069, umc1139, umc1962, bnlg1079, bnlg1526 and umc1239 were analyzed in an S1 derived maize population comprising one hundred and fifty genotypes. Single marker analysis (SMA) using a chi-square (χ^2) test revealed that five markers (umc1069, umc1962, bnlg1079, bnlg1526 and umc1239) conformed to the expected 1:2:1 Mendelian segregation ratio ($P > 0.05$), indicating a good fit from Table 2. These markers were subsequently used in linkage disequilibrium (LD) analyses to evaluate the genetic linkage among loci.

In contrast, the marker umc1139 exhibited a significant deviation from Mendelian expectations, with observed genotype frequencies of 37 AA : 62 AB : 51 BB ($\chi^2 = 6.43$, $P < 0.05$). Notably, the heterozygous AB genotype was underrepresented, while the BB genotype was overrepresented. This significant segregation distortion (SD) suggests the occurrence of selection pressure within this specific genetic background. Several biological mechanisms may account for distortion including meiotic drive, gametophytic selection through processes such as pollen competition, pollen lethality and preferential fertilization (Taylor and Muona, 2003)¹⁹ and zygotic selection (Xu et al., 2013)²⁰. These findings underscore the evolutionary significance of SD and its potential implications for breeding outcomes.

Table 2.

Genotypic segregation of six SSR markers in S₁ maize population derived from a cross between Takfa 7 (drought-tolerant) and Ki 48 (drought-susceptible).

Genotypes		umc	umc	umc	bnlg	bnlg	umc
		1069	1139	1962	1079	1526	1239
		Ext. ¹	Obs. ²	Obs.	Obs.	Obs.	Obs.
Homozygous (tolerant):	AA	37.5	44	37	35	37	39
Heterozygous:	AB	70	63	62	77	79	75
Homozygous (susceptible):	BB	37.5	43	51	38	34	36
df			2	2	2	2	2
Chi-square value			4.56	7.52	0.22	0.54	0.88
P-value			0.10	0.02	0.89	0.76	0.94

¹Ext. = expect, ²Obs = observe

According to the MaizeGDB, umc1139 is located on chromosome 8 (bin. 8.01), within the small kernel 501 (smk501). Gene annotation indicates that this region encodes a RUBylation activation enzyme E1 subunit ZmECR1 (E1 C-TERMINAL RELATED 1), which plays a critical role in regulating kernel development. Furthermore, gene ontology (GO) analysis associated with nutrient reservoir activity (GO:0045735) and starch metabolic process (GO:0005982) identified 22 and 13 genes, respectively. Many of these genes including key starch biosynthetic enzymes such as Shrunken1 (Sh1), Shrunken2 (Sh2), starch synthase I (SSI) and Starch synthase IIa (SSIIa) were found to be downregulated in smk501 mutant kernels, consistent with the reduced starch accumulation observed compared with the wild type (Chen et al., 2021)²¹.

Linkage Disequilibrium (LD) Analysis

Linkage disequilibrium refers to the non-random association of alleles at different loci and is commonly measured using the squared correlation coefficient (r^2). An r^2 value close to 1 indicates strong linkage between markers, suggesting they are likely inherited together, whereas a value near 0 indicates linkage equilibrium (LE) or independent assortment. This parameter is widely used in molecular marker studies and in MAS to identify tightly linked markers and potential candidate genes (Zaykin et al., 2008)²².

LD analysis among the six SSR markers revealed varying degrees of association (Figure 1). The highest LD value ($r^2 = 0.72$) was observed between umc1962 and bnlg1079, indicating a strong linkage and suggesting that alleles at these loci are frequently co-inherited. Moderate to high LD was observed between bnlg1526 and bnlg1079 ($r^2 = 0.60$), while umc1239 and bnlg1526 showed a moderate LD ($r^2 = 0.50$). In contrast, umc1069 and umc1139 displayed very low LD values ($r^2 = 0.00 - 0.01$) with other markers, indicating complete LE and independent segregation from the other loci.

The marker umc1962, located on chromosome 10 (bin 10.03), is positioned in close proximity to several candidate genes, including abp4, ppo1 and nac1, which encode auxin-binding protein homolog 4 or condensing-2 complex subunit D3, polyphenol oxidase 1 and NaCl stress protein 1 or early drought-induced protein, respectively. These genes are involved in various stress-responsive pathway, such as auxin signaling, osmolyte biosynthesis, reactive oxygen species (ROS) detoxification and early abiotic stress response mechanisms that are essential for plant adaptation during developmental and stress-prone stages (Dubey et al., 2009)¹⁸. Previous studies have shown that markers associated with these functional genes influence key phenotypic traits under drought condition, including anthesis-silking interval (ASI), root system architecture, stay-green phenotype and grain yield (Khavkin and Coe, 1997)²³. The functional relevance of umc1962 is further supported by its

close positional relationship with pollen extension-like 3 (*pex3*), as reported in the MaizeGDB database. The *pex3* protein contains a highly conserved leucine-rich repeat (LRR) domain, which mediates ligand-specific interactions critical for pollen tube growth, a process tightly regulated during reproductive development (Stratford et al., 2001)²⁴. Given its proximity to multiple functional gene and its potential to exhibit strong LD with neighboring loci, *umc1962* may serve as a central or hub marker for simultaneously tracking multiple drought-related traits.

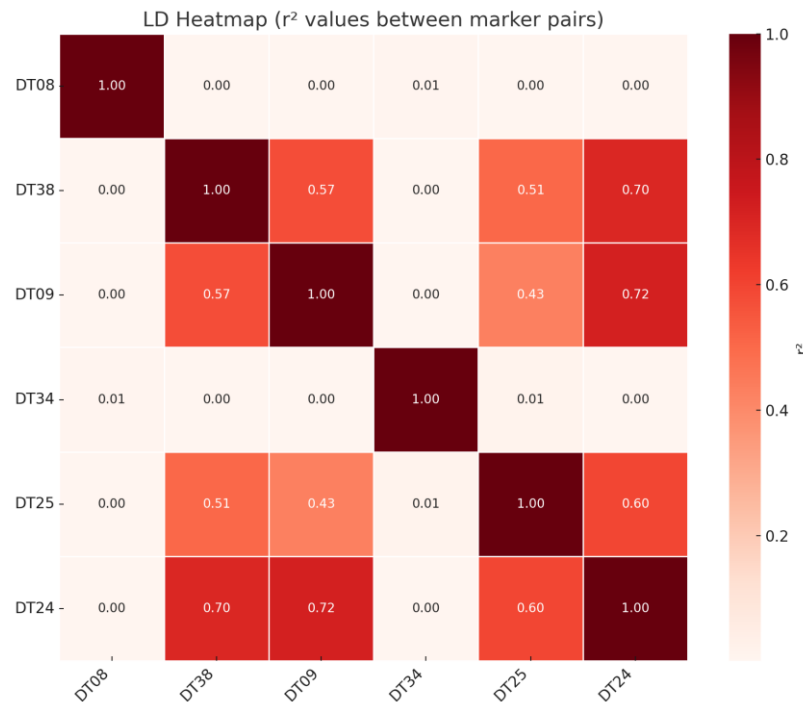


Figure 1.

Heatmap of pairwise linkage disequilibrium (LD) among six SSR markers based on r^2 values. Color intensity reflects the strength of LD, ranging from weak (light red) to strong (dark red). Values close to 1 indicate strong linkage, whereas values near 0 indicate linkage equilibrium.

Likewise, *bnlg1079*, also located on chromosome 10 (bin 10.03), has been associated with quantitative traits such as vanillin and syringaldehyde content, both of which are degradation products of lignin. Under drought conditions, enhanced lignin degradation in drought-susceptible genotypes can lead to compromised leaf structure integrity and increased water loss, ultimately resulting in reduced anthesis ASI performance and lower grain yield (Hu et al., 2021)²⁵.

The marker *bnlg1526*, located on chromosome 10 (bin 10.4), has been linked to quantitative trait loci (QTLs) for whole phosphorus use efficiency (WPUE) under phosphorus-deficient conditions. Since drought frequently disrupts soil phosphorus availability and nutrient dynamics, markers associated with WPUE under drought conditions are of particular interest for breeding programs (Chen et al., 2009)²⁶.

On the other hand, *umc1239*, located on 10 (bin 10.03) showed moderate LD with *bnlg1526* and was significantly associated with leaf relative moisture content (LRMC), suggesting the presence of putative gene affecting plant water status in this genomic region. According to MaizeGDB, *umc1239* is situated in close proximity to Trihelix- transcription factor 43 (*thx43*) (Ilyas et al., 2023¹⁵), which may play a regulatory role in leaf moisture

retention. LRMC is widely recognized as a reliable physiological indicator of plant water status, as it reflects the balance between water absorption into leaf tissues and water loss through transpiration (Zhang et al., 2012; Jin et al., 2017; Arshad et al., 2018)^{27;28;29}. Therefore, the identification of a marker closely linked to LRMC is of particular relevance for improving drought adaptation in maize. Several Trihelix proteins have been reported to reduce stomatal conductance and leaf transpiration, thereby improving water use efficiency and contributing to enhanced drought tolerance (Weng et al., 2012)³⁰. Given these findings, it is plausible that the significant association of umc1239 with LRMC observed in this study may be mediated through a regulatory mechanism involving nearby Trihelix TFs, particularly Thx43. This supports the potential use of umc1239 as a putative molecular marker in breeding programs targeting improved drought tolerance and water-use traits in maize.

In contrast, umc1069, located on chromosome 8 (bin 8.08), is positioned near the glutathione-S-transferase 1 (GST1). GST1 are key components in ROS-scavenging pathways and play an important role in detoxify ROS that accumulate under drought stress (Jha et al., 2011; Rong et al., 2014; Qi et al., 2018)^{31;32;33}. However, the r^2 value indicated no LD between umc1069 and other markers, which is consistent with its physical separation on a different chromosome.

Collectively, the strong LD observed among umc1239, umc1962, bnlg1079 and bnlg1526, all located within bin 10.03-10.04 on chromosome 10, indicates the presence of a genomic region potentially harboring multiple functional genes associated with drought-adaptive traits. Notably, bin 10.03 and 10.04 are separated by only ~ 1 cM (centimorgan), which is approximately equivalent to 1 Mb (megabase) in physical (Collins and Morton, 1998; Ulgen and Li, 2005). The tight genetic linkage among these markers, supported by LD values as high as $r^2 = 0.72$ suggest co-inheritance and underscores the feasibility of using one or more representative markers to simultaneously track favorable alleles for multiple traits. These findings highlight the potential of bin 10.03-10.4 as a breeding-relevant hotspot for MAS targeting complex drought-related traits such as ASI, stay-green phenotype, root system architecture and grain yield. The use of LD-informed marker from this region may significantly enhance selection efficiency and genetic gain in drought-resilient maize breeding programs. Conversely, umc1069 and umc1139, located on chromosome 8 exhibited complete LE with the other markers, consistent with Mendelian independent assortment due to their physical distance from the chromosome 10 region.

Previous studies have demonstrated that LD analysis using SSR and SNP markers is an effectively approach for identifying genomic regions associated with drought tolerance (Muthukumar et al., 2015). The detection of LD between molecular markers and target genes at a distance of approximately 10-15 cM, with an r^2 value of 0.2, suggests that these markers are located near genes regulating responses to drought stress. This underscores their potential for application in MAS, thereby enhancing the precision and efficiency of breeding programs (Jia et al., 2014)³⁴. In the study phenotypic evaluation revealed highly significant difference among genotypes for traits assessed ($P < 0.0001$), with most traits exhibiting moderate to high phenotypic and genotypic coefficient of variation. LD analysis further revealed that 32.92% of locus pairs had significant LD ($r^2 > 0.2$), indicating the present of potential useful marker-trait association for MAS. Notably, seven SSR markers were localized to chromosome regions previously report to be associated with drought tolerance traits. These markers represent promising candidates for use in drought-resilient development through MAS (Endre and Bantte, 2017)³⁵.

Cluster analysis of genotypes

The allelic status, AA, AB and BB, were numerically coded as AA = 2, AB = 1 and BB = 0 according to an additive genetic model (Freda et al., 2024). In this study, the scoring system

was modified to AA = 3, AB = 1, BB = 0 on order to enhance marker score resolution and increase the range of total score (0-18) across six SSR markers. In this context, The AA genotype represented the drought-tolerant allele inherited from the paternal line (Takfa 7), while the BB genotype indicated the presence of drought-susceptible alleles. This scoring scheme enabled the quantification of drought-related alleles and facilitated the assessment of genetic variability among the genotypes.

Four genotype clusters were identified based on hierarchical clustering (Figure 2)

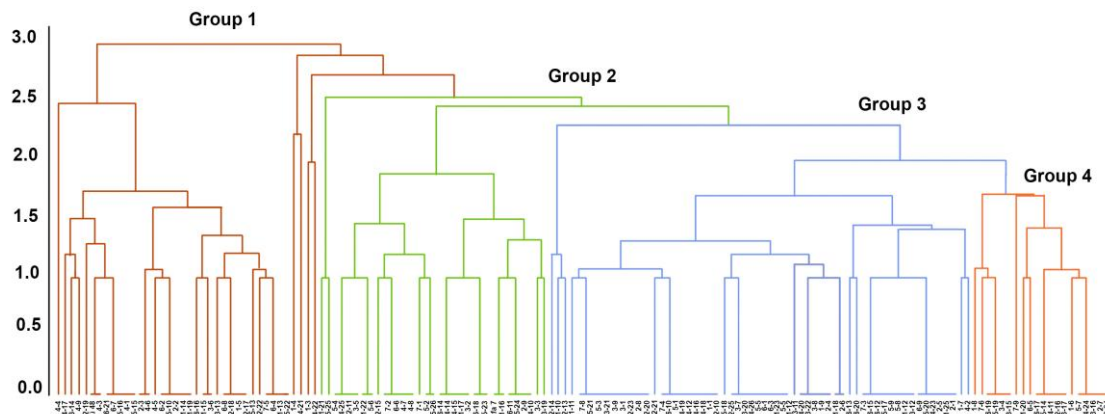


Figure 1.

Dendrogram of the one hundred and fifty S1 genotypes based on six drought-related molecular markers using Ward's method with squared Euclidean distance. The analysis classified the genotypes into four group; Group 1 (drought sensitive, including the susceptible parent Ki 48), Group 2 (drought tolerance, including the tolerant parent Takfa 7), Group 3 (intermediated drought tolerance) Group 4 (mixed genotypic profile). Candidate genotypes for future selection were primarily found in Groups 2 and 3.

Group 1 consisted of thirty-eight genotypes, most of which had 1-2 loci with the AA genotype, 1-2 loci with AB, and 2-6 loci with BB, resulting in total marker scores ranging from 0-8. This group included the drought-susceptible parent Ki 48, suggesting a genetic background associated with drought susceptible.

Group 2 consisted of twelve genotypes, characterized by 3-6 loci with AA, 1-2 loci with AB, and only 1 locus with BB, resulting in total scores of 13-18. This group contained the drought-tolerant parent Takfa 7, indicating genetic similarity to the drought-tolerant background.

Group 3 consisted of sixty-one genotypes, with 2-3 loci of AA, 1-6 loci of AB and 1-2 loci of BB, resulting in total scores ranging from 9-10, This group likely represents genotype with intermediate drought tolerance.

Group 4 consisted of thirty-nine genotypes, with 1 locus of AA, 4-6 loci of AB and 1-2 loci of BB, resulting in total scores of 4-7, This group displayed a mixed genotype composition with no clear indication of strong drought tolerance.

For selection purpose, genotypes were considered potentially drought-tolerant if they met the following criteria: AA \geq 2 loci, AB \geq 3 loci and BB \leq 2 loci and total marker scores \geq 9. Based on this classification, seventy-three candidate genotypes from group 2 and 3 were identified for self-pollination in the next generation (S₂), representing a 48.6% reduction in the total number of genotypes. In addition to molecular selection, candidate genotypes must also meet key agronomic performance criteria, which will further refine and reduce the number of genotypes advanced to the S₂ generation for the development of drought-tolerant maize.



Given the increasing vulnerability of tropical agriculture to drought events, the identification of drought-tolerant genotype through putative marker-assisted selection holds particular relevance for regions. The findings of this study contribute directly to breeding strategies aimed at developing maize genotypes adapted to tropical and semi-arid environments. The selected SSR markers and associated genotypes may also serve as a valuable resource for other drought-prone regions with similar agroecological conditions.

Conclusion:

To obtain S_1 maize genotypes with improved drought tolerance, SSR markers previously associated with drought-adaptive traits were employed for selection. Chi-square test confirmed Mendelian segregation in five markers (umc1069, umc1962, bnlgl1079, bnlgl1526 and umc1239), while umc1139 exhibited segregation distortion. Linkage disequilibrium analysis revealed moderate to moderate to high r^2 values among umc1962, bnlgl1079, bnlgl1526 and umc1239 on chromosome 10, indicating tight genetic linkage, whereas umc1069 and umc1139 on chromosome 8 exhibited independent segregation, consistent with linkage equilibrium. Cluster analysis grouped the genotypes based on marker profiles and identified seventy-three genotypes from group 2 and 3 were identified as candidates with favorable drought-tolerant profiles. These selected genotypes will be advanced for selfing into the S_2 for further drought-tolerant maize breeding.

Acknowledgements:

This research was financially supported by the National Science Research and Innovation Fund (NSRF) through the Department of Agriculture under the Fundamental Fund for the fiscal years 2025-2027.

References:

1. Yuan X, Yamiao W, Peng J, Peili W, Justin S. *Science*. 2023;380(6641):187-191.
2. Overperk JT, Udall B. *Proc Natl Acad Sci*. 2022;117(22):11856-11858.
3. Herrero MP, Johnson. *Crop Sci*. 1981;21:105-110.
4. Lunduka RW, Mateva KI, Magorokosho C, Manjeru P. *Clim Dev*. 2017;11:35-46.
5. Polania JA, Poschenrieder C, Beebe S, Rao LM. *Front Plant Sci*. 2016;7.
6. Toscano S, Ferrante A, Roman D. *Hortic*. 2019;5(1):6.
7. Cattivelli L, Rizza F, Badeck FW, Mazzucotelli E, Mastrageto AM, Francia E, Mare C, Tondelli A, Stanca. *Field Crops Res*. 2008;105(1):1-14.
8. Tuberosa RS, Salvi S, Sanguinelli MC, Landi P, Maccaferri M, Confi S. *Annals of Botany*, 2002;89:941-963.
9. Almeida GD, Makumbi D, Magorokosho S, Nair S, Borem A, Ribaut JM, Banziger M, Prasanna BM, Crossa J, Babu R. *Theor Appl Genet*. 2013;126:583-600.
10. Buckler ES, Thomsberry JM. *Curr Open Plant Biol*, 2002;5:107-111.
11. Yu J, Buckler E.S. *Curr Open Biotenhnol*. 2006;17:155-160.
12. Sa KJ, Park H, Fu Z, Jang SJ, Lee JK. *Plant Breed Biotechnol*. 2022;10:257-271.
13. Yu J, Arbelbide M, Bernardo R. *Theor Appl Genet*. 2005;110:1061-1067.
14. Park YL, Lee JK, Kim NS. *Mol*. 2009;14:4546-4569.
15. Ilyas MZ, Park H, Jang SJ, Cho J, Sa KJ, Lee JK. *Plants*. 2023;12(42):4092.
16. Chu Y, Bertioli D, Levinson CM, Stalker HT, Holbrook CC, Ozias-Akins P. *G3*. 2021;11(4):jkab066.
17. Medina CA, Kaur H, Ray I, Yi LX. *Cells*. 2021. 10(12):3372.
18. Dubey L, Prasana BM, Ramesh. *Indian J Genet*. 2009;69(4):344-351.
19. Taylor DR, Muona PK. *Genetica*. 2003;117:27-35.



20. Xu X, Li L, Dong X, Jin W, Melchinger AE and Chen S. *J Exp Bot.* 2013;64(4):1083-1096.
21. Chen Q, Zhang J, Wang J, Xie Y, Cui Y, Du X, Li L, Fu J, Liu Y, Wang J, Wang G, Gu R. *New Phytol.* 2021;230(6):2337-2354.
22. Zaykin DV, Pudovkin A, Weir BR. *Genetics.* 2008;180(1):533-545.
23. Khavkin E, Coe EH. *Theor Appl Genet.* 1997;95:343-352.
24. Stratford S, Bames W, Hohorst DL, Sagert JG, Cotter R, Golubiewski A, Shwalfer AM, McCormick S, Bedinger P. *Plant Mol Biol.* 2001;46:43-56.
25. Hu S, Wang M, Zhang X, Chen W, Song X, Fu X, Fang H, Xu J, Xiao Y, Li Y, Bai G, Li J, Yang X. *Plant Biotechnol J.* 2021;19(11):2129-2205.
26. Chen J, Xu L, Cai Y, Xu J. *Euphytica.* 2009;167:245-252.
27. Zhang Q, Li Q, Zhang G. *Spectrosc Int J.* 2012;27:93-105.
28. Jin X, Shi C, Yu CY, Yamada T, Sacks EJ. *Front Plant Sci.* 2017;8:1-8.
29. Arshad, M, Piskier D, Khurshid K, Ali A. *J Appl Remote Sens.* 2018;12:22203.
30. Weng H, Yoo CY, Gosney MJ, Hasegawa PM, Mickelbart MV. *Plos One.* 2012;7:e32925.
31. Jha B, Sharma A, Mishra. *Mol Biol Rep.* 2021;38:4823-4832.
32. Rong W, Qi L, Wang A, Ye X, Du L, Liang H, Xin Z, Zhang Z. *Plant Biotechnol J.* 2014;12:468-479.
33. Qi J, Song CP, Wang B, Zhou J, Kangasjarvi J, Zhu JK, Gong Z. 2018. *J Integr Plant Biol.* 2018;60(9):805-826.
34. Jia YH, Sun JL, Wang XW, Zhou ZL, He ZP, Pang BY, Wang LR, Wang XM. *J Integr Agric.* 2014;13(9):1845-1853.
35. Endre A, Bantle K. *Afr J Biotechnol.* 2014;16(13):631-642.



ENCAPSULATED FREEZE-DRIED LACTIC ACID BACTERIA MODULATE GUT MICROBIOTA, HEALTH, AND GROWTH OF *Penaeus monodon*

Narongchai Chupoon^{1*}, Nomchit Kaewthai Andrei¹, Sirinat Sriannual¹, and Thanikan Thorasin¹

¹Department of Food Innovation and Management, Faculty of Agro-Industry, Rajamangala University of Technology Srivijaya, Thung Yai District, Nakhon Si Thammarat 80240, Thailand

Abstract:

Black tiger shrimp (*Penaeus monodon*) is a high-value aquaculture species, yet its production is limited by recurrent disease outbreaks and growth constraints. This study evaluated dietary supplementation with freeze-dried encapsulated lactic acid bacteria (FEL) on growth, immunity, survival, and gut microbiota of *P. monodon* under hatchery and pond conditions. In the hatchery trial, shrimp fed 0.2–0.6% FEL showed significantly higher specific growth rate and enhanced immune responses, including total hemocyte count, phenoloxidase activity, and bacterial clearance, compared with the control. Survival after *Vibrio parahaemolyticus* (non-AHPND) challenge reached 100% in all FEL groups, versus $82.2 \pm 8.0\%$ in the control. In the pond validation trial, shrimp receiving 0.2% FEL attained significantly greater body weight after 40 days than the control. High-throughput 16S rRNA sequencing further revealed that FEL reduced the relative abundance of pathogenic *Photobacterium damsela* while enriching beneficial Roseobacter-group taxa such as *Phaeobacter inhibens* and *Ruegeria lacuscaerulensis*. Overall, FEL acted as both an immunostimulant and microbiota modulator, highlighting its potential as a functional feed additive for sustainable and biosecure *P. monodon* aquaculture.

Keywords: *Penaeus monodon*, lactic acid bacteria, microencapsulation, immunity, growth performance, gut microbiota

Introduction:

Aquaculture of *P. monodon* is a major sector in Asian aquaculture, contributing substantially to both the economy and food security. However, disease outbreaks, poor survival rates, and limited growth performance remain critical challenges for the sustainable production of this species [1,2]. In recent years, the application of probiotics, particularly lactic acid bacteria (LAB), has emerged as a promising strategy to enhance shrimp immunity, maintain gut microbiota balance, and improve growth performance [3–5]. Probiotics stimulate non-specific immune responses in shrimp by enhancing phagocytic activity, phenoloxidase (PO) activity, respiratory burst, and bacterial clearance, all of which contribute to disease resistance [6–9].

Dietary LAB supplementation has also been shown to improve intestinal microbial stability and nutrient utilization, thereby supporting higher survival and growth under both laboratory and field conditions [10–13]. Nevertheless, the efficacy of probiotics in aquaculture is strongly influenced by environmental stressors and feed processing. A major limitation of conventional probiotics is the low stability of live bacterial cells during feed manufacturing, storage, and passage through the gastrointestinal tract [14,15].

To overcome these limitations, encapsulation technology has been employed to protect viable bacterial cells and ensure controlled release and colonization in the shrimp gut [16–18]. Encapsulation with sodium alginate and calcium chloride is a widely used, simple, and non-toxic method for immobilizing LAB, producing microcapsules with high bacterial viability [16–19]. Freeze-drying (lyophilization) further improves stability, ensuring greater



survival and longer shelf life compared with non-encapsulated forms [16–20]. Encapsulated freeze-dried LAB have been shown to enhance growth and immunity in aquaculture species such as tilapia, carp, and Pacific white shrimp (*Litopenaeus vannamei*) [16–20]. However, their application in *P. monodon*, particularly under field conditions, remains limited.

Therefore, this study aimed to: (i) evaluate the effects of encapsulated FEL on growth, immune responses, and survival of *P. monodon* under hatchery conditions; (ii) characterize intestinal microbiota changes using NGS-based 16S rRNA profiling; and (iii) validate the practical application of FEL supplementation for improving shrimp growth and health in pond culture.

Methodology:

2.1 Shrimp husbandry and feeding protocol

Two independent cohorts of *Penaeus monodon* were used in this study: one cohort for the hatchery feeding and challenge trial (Phase 1), and a second cohort for the earthen-pond validation trial (Phase 2). Post-larvae (PL-5) were obtained from a certified specific pathogen-free hatchery in Ranod District, Songkhla Province, Thailand. Upon arrival, the shrimp were acclimatized and reared in nursery tanks at the Aquaculture Research Facility, Faculty of Science and Fisheries Technology, Trang Campus, Rajamangala University of Technology Srivijaya (RMUTSV), Thailand.

Rearing conditions were maintained under standard aquaculture practices, including continuous aeration and daily monitoring of water quality parameters. During the nursery phase (PL-5 to PL-30), shrimp were fed a commercial starter diet formulated for early juvenile shrimp (Phoca Starter P5–P30; Phoca Feed Co., Ltd., Thailand), containing approximately 40–42% crude protein, 4% crude lipid, 3% crude fiber, 13% ash, and 10% moisture. Feeding was provided to apparent satiation to support optimal growth prior to experimental trials.

2.2 Preparation of FEL

Encapsulated freeze-dried lactic acid bacteria (FEL) were prepared following Liu et al. [16] with modifications. Four strains *Lactobacillus acidophilus* TISTR 236, *L. plantarum* TISTR 542, *L. casei* TISTR 389, and *L. bulgaricus* TISTR 451 were separately produced by **batch fermentation** in MRS broth (37 °C, 50 rpm, 48 h). Cells from each strain were harvested (5,000 × g, 10 min, 4 °C), washed twice with sterile PBS (pH 7.2), and standardized to $\sim 1 \times 10^9$ CFU mL⁻¹ based on OD₆₀₀ calibration and plate counts. Equal volumes of each suspension were pooled to form a multi-strain inoculum, blended with sodium alginate, and extruded into 0.1 M 0.1 M calcium chloride under stirring (150 rpm) to form alginate cell beads. Beads were cross-linked for 30 min, rinsed with sterile water, and freeze-dried (CHRIST Delta 2-24 LSC, Germany). Encapsulation efficiency exceeded 89%, and mean bead diameter was 2.41 ± 0.07 mm (n = 10). FEL preparations were then incorporated into the experimental diets.

2.3 Experimental design

Phase 1 (hatchery screening): Juveniles (5.33 ± 0.03 g) were assigned to six FEL levels (0, 0.2, 0.4, 0.6, 0.8, 1.0% w/w). Each treatment had three replicate 100-L glass aquaria (hereafter referred to as tanks), with 15 shrimp per tank. Shrimp were fed five times daily (06:00–22:00) at 5–6% body weight for 50 days. The tank was considered the experimental unit (N = 3 per treatment).

Phase 2 (pond validation): The optimal FEL level (0.2%) was evaluated in two earthen ponds (1,600 m², 1.8 m depth), one per treatment (control vs FEL). Each pond was subdivided into three net cages (~200 shrimp per cage). At day 60 (initial weight 4.7 ± 0.2 g),

shrimp were reared for 40 days. At day 100, 10 shrimp per cage were sampled for growth and microbiota.

2.4 Challenge trials (Phase 1)

After 50 days of feeding, shrimp were acclimated for 10 days under hatchery conditions before challenge with *Vibrio parahaemolyticus*. The pathogen was cultured in TSB (1.5% NaCl, 30 °C, 18 h), washed, and adjusted to 2×10^7 CFU mL⁻¹. Shrimp were injected intramuscularly with 0.1 mL at the third abdominal segment, while controls received saline. Mortality was monitored twice daily for 15 days; however, no further deaths occurred beyond Day 9. Therefore, survival data are reported at the 9-day endpoint, and Kaplan–Meier survival curves were constructed following established protocols [3].

2.5 Immune response assays (Phase 1)

On day 9 post-challenge, hemolymph (~100 µL per shrimp) was sampled from three shrimp per **100-L glass aquarium (tank)** (n = 3 shrimp; N = 3 tanks per treatment). Unchallenged controls were sampled in parallel at the same time. For statistical analysis, values were averaged within each tank, and the tank mean was treated as one replicate. The immune parameters analyzed included total hemocyte count (THC), clearance ability (CA), and PO activity.

THC was determined by withdrawing hemolymph and mixing it 1:1 with anticoagulant solution (10 mM sodium citrate, 450 mM NaCl, pH 7.3). Hemocytes were counted in triplicate using a hemocytometer under a light microscope and expressed as cells mL⁻¹ [3,19].

CA was assessed by injecting shrimp intramuscularly with 100 µL of *V. parahaemolyticus* ($\sim 1 \times 10^5$ CFU mL⁻¹ in sterile saline). Hemolymph was collected at 0 h (baseline, N_i) and 3 h post-injection (N_t), serially diluted, and plated on TCBS agar. Colonies were enumerated after 24 h at 37 °C. CA was defined as the **percentage reduction in viable bacterial counts relative to baseline** and calculated as described by Liu et al. [11]:

$$CA (\%) = \frac{(N_i - N_t)}{N_i} \times 100 \quad (1)$$

where: N_i is the initial bacterial load (CFU/mL), and N_t is the bacterial load after time (CFU/mL⁻¹)

PO activity was measured by centrifuging hemolymph at $3,000 \times g$ for 10 min at 4 °C to obtain plasma. The assay was performed using 10 mM L-DOPA as substrate, and absorbance was recorded at 490 nm every minute for 10 min at 28 °C. Both basal and total (trypsin-activated) PO activities were determined following standard shrimp immune assay protocols [4,19]. Results were expressed as $\Delta A_{490} \text{ min}^{-1}$ for basal activity or $\Delta A_{490} \text{ min}^{-1} \text{ mg protein}^{-1}$ for total activity, and data were reported as mean \pm SE of tank means.

2.6 Growth performance (Phase 1)

Shrimp were fed the experimental diets for 50 days prior to the challenge test. Growth performance was evaluated based on tank-level mean weights (N = 3 per treatment). Specific growth rate (SGR) was calculated during the 9-day post-challenge period using the following equation:

$$SGR, \% \text{ day}^{-1} = \frac{(In Wt - In W0)}{t} \times 100 \quad (2)$$



where W_0 is the initial mean weight (g), W_t is the final mean weight (g), and t is the rearing period (days).

In Phase 2, shrimp were reared in earthen ponds for 40 days (days 60–100 of the culture period). Growth parameters were measured at the cage level (10 shrimp per cage, 3 cages per pond). With one pond per treatment, Phase 2 results are descriptive only.

2.7 Field trial methods (Phase 2)

In Phase 2, shrimp were reared in earthen ponds for 40 days (days 60–100 of the culture period). Fifty-day-old shrimp (initial mean weight = 4.7 ± 0.2 g, mean \pm SD) were transferred to two earthen ponds (1,600 m², 1.8 m depth) at the Faculty of Science and Fisheries Technology, RMUTSV, Trang Province, Thailand, and acclimated for 10 days. At day 60, one pond per treatment was used: a control pond receiving a standard diet and a treatment pond receiving the diet supplemented with 0.2% FEL. Each pond was subdivided into three net cages (4 \times 4 m; ~200 shrimp per cage), and growth parameters were measured at the cage level (10 shrimp per cage, 3 cages per pond). With one pond per treatment, Phase 2 results are presented descriptively only.

2.8 Analysis of microbial community composition

For pond-reared shrimp, the intestinal microbial community was profiled using 16S rRNA gene amplicon sequencing. Shrimp were reared in three replicate cages per dietary treatment (~200 individuals per cage). For each treatment, intestines from five shrimp per cage were pooled to obtain ~100 mg wet tissue, yielding three biological replicates per treatment (control and 0.2% FEL). All dissections were performed aseptically on ice. Composite intestinal samples were immediately placed in 2 mL screw-cap tubes containing zirconia/silica beads, snap-frozen in liquid nitrogen, and stored at -80 °C until DNA extraction.

DNA was extracted using the QIAamp Fast DNA Stool Mini Kit (Qiagen, Germany). The V3–V4 regions of the 16S rRNA gene were amplified by PCR with Illumina overhang adapter primers under the following conditions: 95 °C for 3 min; 25 cycles of 95 °C for 30 s, 55 °C for 30 s, and 72 °C for 30 s; followed by a final extension at 72 °C for 5 min. Amplicons were purified with AMPure XP, indexed using the Nextera XT Index Kit v2 (Illumina, USA), pooled at equimolar concentrations, spiked with 5% PhiX, and sequenced on an Illumina MiSeq platform using the **MiSeq Reagent Kit v3 (600-cycle), generating 2 \times 300 bp paired-end reads.**

2.9 Statistical Analysis

Phase 1 data were analyzed using a completely randomized design (CRD) with six FEL levels and three replicate tanks per treatment. The tank was considered the experimental unit, and values were averaged at the tank level prior to analysis. Differences among treatments were evaluated by one-way analysis of variance (ANOVA), and means were separated using Duncan's multiple range test (DMRT) at a significance level of $\alpha = 0.05$.

For Phase 2, growth and microbiota data were obtained from one pond per treatment, with three cages nested within each pond. Because pond-level replication was not available, results are presented descriptively as mean \pm standard deviation (SD) of cage means.

Results and Discussion:

Growth performance, immune responses, and survival of *P. monodon* under hatchery conditions

Viable LAB counts in FEL diets, confirmed after encapsulation and feed incorporation, ranged from 10^7 to 10^8 CFU g⁻¹, exceeding the recommended threshold of 10^6

CFU g⁻¹ for probiotic efficacy in aquafeeds [7,13]. These levels, consistent with the standardized inoculum (~10⁹ CFU mL⁻¹ per strain prior to pooling), indicate that dietary FEL supplementation significantly enhanced shrimp performance without compromising growth. Immune responses. FEL supplementation increased THC and CA in a dose-dependent manner, with peak values at 0.8–1.0% and significant effects from 0.4% onward (Table 1). PO activity also rose with FEL inclusion and plateaued at ≥0.8% (Figure 1), paralleling the improvements in THC and CA, and indicating coordinated activation of the prophenoloxidase system. These findings align with earlier reports that probiotics stimulate hemocyte proliferation and enhance bacterial clearance in shrimp [3,4,11,19]. FEL therefore acts as an effective immunostimulant, with maximal benefits at 0.8–1.0%.

Table 1.

Immune response parameters of *P. monodon* fed diets containing different levels of FEL supplementation (% w/w).

FEL supplementation (% w/w)	Total hemocyte count (10 ⁶ cells mL ⁻¹)	Clearance ability (%)
0.0	4.97 ± 0.09 ^d	2.67 ± 0.55 ^d
0.2	7.53 ± 0.32 ^c	4.37 ± 0.84 ^{cd}
0.4	8.80 ± 0.34 ^{bc}	13.97 ± 0.47 ^{bc}
0.6	10.00 ± 0.50 ^{ab}	15.30 ± 0.93 ^b
0.8	9.73 ± 0.41 ^{ab}	21.33 ± 0.58 ^a
1.0	10.10 ± 0.25 ^a	22.53 ± 0.66 ^a

Different superscript letters within the same column indicate significant differences among treatments ($p < 0.05$, Duncan's Multiple Range Test). Values are presented as mean ± SE of tank means (N = 3; 100-L glass aquaria with 15 shrimp per tank).

Survival rate

Following *V. parahaemolyticus* (non-AHPND) challenge, survival differed markedly among treatments (Figure 2). The control group exhibited a survival rate of 82.22 ± 8.02%, whereas all FEL-fed groups (0.2–1.0%) achieved 100.00 ± 0.00% survival. No additional mortality was observed beyond Day 9, confirming that FEL supplementation provided rapid and sustained protection. These findings support the role of probiotics in enhancing shrimp resistance to bacterial infection, consistent with previous studies highlighting the immunostimulatory and protective effects of dietary microbial supplements [4,7,9,13].

This study employed a non-AHPND strain of *V. parahaemolyticus*. Given that AHPND remains a serious challenge in shrimp aquaculture [2,6], further testing of FEL against virulent strains is required to establish its broader applicability [1–3,6].

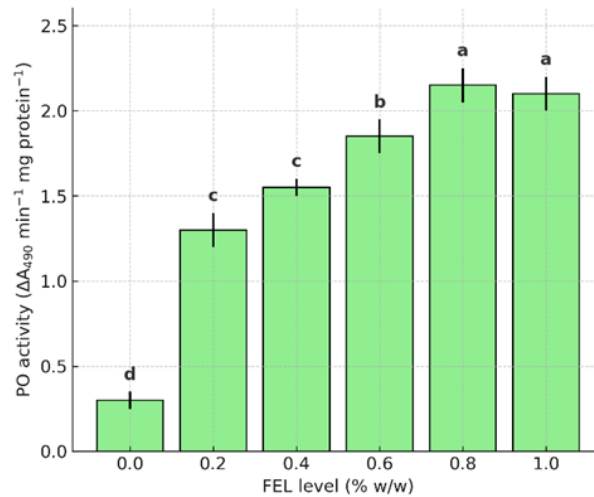


Figure 1.

PO activity of *P. monodon* after dietary supplementation with FEL. PO activity is expressed as $\Delta A_{490} \text{ min}^{-1} \text{ mg protein}^{-1}$. Bars represent mean \pm standard error (SE) ($n = 3$). Different letters indicate significant differences among treatments (DMRT, $p < 0.05$).

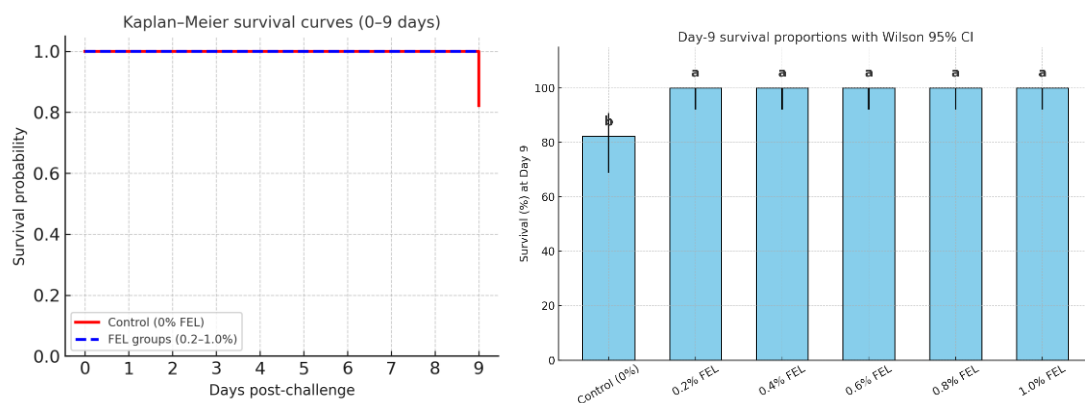


Figure 2.

Survival of *P. monodon* after *V. parahaemolyticus* challenge. (a) Kaplan–Meier curves (0–9 days). (b) Day-9 survival with Wilson 95% CI. Bars with different letters indicate significant differences (DMRT, $p < 0.05$). Replication: tank ($N = 3$; 15 shrimp/tank).

Growth performance

In parallel, SGR did not differ significantly among treatments during the challenge trial, indicating that FEL supplementation maintained growth while conferring immune and survival advantages. However, in the short feeding trial, shrimp fed 0.2–0.6% FEL showed significantly higher SGR and final weight than controls, whereas higher levels (0.8–1.0%) did not yield further gains (Table 2). This pattern suggests the existence of an optimal FEL range, consistent with earlier observations that excessive probiotic doses may reduce efficacy [7,9]. Similar growth-promoting effects of lactic acid bacteria through improved nutrient utilization and gut health have been reported in shrimp and fish [13,18]. Together, these findings demonstrate that FEL supplementation simultaneously enhanced immunity, survival, and growth performance under hatchery conditions, supporting its potential as a functional feed additive for *P. monodon*.

Table 2.

Growth performance of *P. monodon* fed diets supplemented with different levels of FEL (0–1.0% w/w) for 9 days.

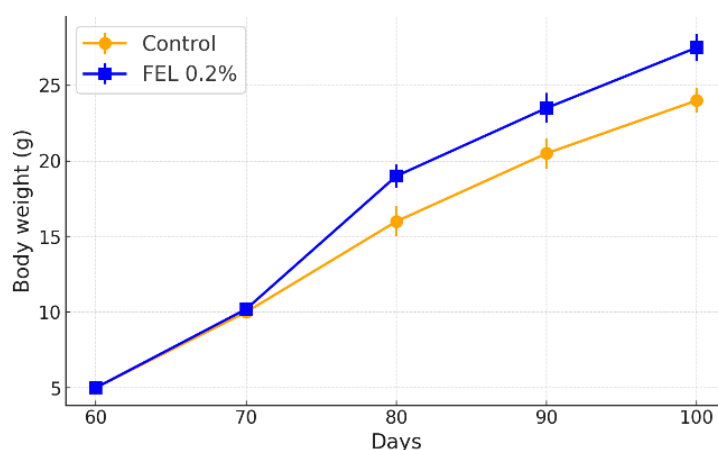
Parameter	Treatment						
	0%	0.2%	0.4%	0.6%	0.8%	1.0%	
Initial weight (g)	5.20	± 5.40	± 5.38	± 5.32	± 5.30	± 5.37	±
Final weight (g)	0.05	0.05	0.08	0.13	0.10	0.06	
SGR (% day ⁻¹)	1.33	± 1.94	± 1.92	± 1.89	± 1.84	± 1.79	±
	0.06 ^b	0.01 ^a	0.01 ^a	0.02 ^a	0.01 ^{ab}	0.02 ^b	

Different superscript letters within the same row indicate significant differences among treatments ($p < 0.05$, Duncan's Multiple Range Test). Values are presented as mean \pm SE of tank means ($n = 3$ aquaria per treatment).

The results confirmed that dietary FEL supplementation improved the growth performance of juvenile *P. monodon* within a 9-day feeding trial. Specifically, shrimp fed diets containing 0.2–0.6% FEL exhibited significantly higher SGR and final weight than the control group, whereas further increasing FEL levels (0.8–1.0%) did not provide additional improvement. This indicates that moderate supplementation levels are more effective for enhancing shrimp growth.

Growth Response of *P. monodon* to 0.2% FEL Supplementation under Pond Conditions

Dietary supplementation with 0.2% FEL was further evaluated under pond conditions to verify its practical effectiveness. **This trial was designed to confirm whether the growth-promoting effects observed in the hatchery could be reproduced under field culture conditions.**

**Figure 3.**

Growth performance of *P. monodon* during the Phase 2 pond trial. Shrimp were reared in two ponds (control vs. 0.2% FEL), each with three net cages (4 × 4 m; ~200 shrimp). At each time point, ten shrimp per cage were weighed to calculate cage means. Points show cage means ($n = 3$ per pond)

Shrimp fed with 0.2% FEL exhibited significantly higher body weight compared with the control group throughout the 40-day observation period (Figure 3). These results

demonstrate that FEL supplementation enhances somatic growth under field culture conditions, likely through improved nutrient assimilation and gut health. Comparable growth-promoting effects of probiotic supplementation in *P. monodon* and other shrimp species have been reported previously [7,9,13,18], supporting the consistency of the present findings with earlier research.

Modulation of intestinal microbiota by FEL supplementation

The intestinal microbiota is central to nutrient use, immunity, and disease resistance in shrimp [11,14]. Supplementation with 0.2% FEL significantly altered the gut community of *P. monodon*, as revealed by 16S rRNA sequencing. At the phylum level (Figure 3), FEL-fed shrimp showed increased Actinobacteria and Cyanobacteria, alongside a marked reduction in Proteobacteria, a group often associated with opportunistic pathogens. These shifts indicate that FEL promotes beneficial taxa while suppressing potential pathogens, thereby supporting a more balanced microbiota.

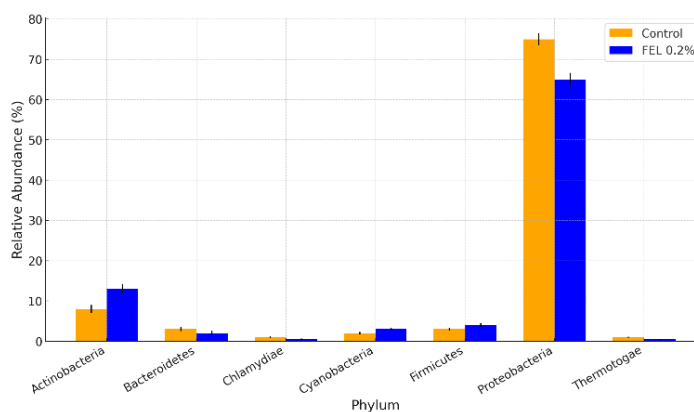


Figure 4.

Phylum-level intestinal microbiota of *P. monodon* fed 0.2% FEL and control.

Data are presented as mean \pm SD (n = 3).

At the species level (Figure 4), FEL-fed shrimp exhibited reduced abundance of *Photobacterium damsela* and enrichment of beneficial Roseobacter-group taxa, particularly *Phaeobacter inhibens* and *Ruegeria lacuscaerulensis*. Roseobacter members are known to produce antimicrobial metabolites that inhibit vibrios and support shrimp health [22]. Together with enhanced immune indices (THC, PO, clearance), these microbial shifts highlight the dual action of FEL in pathogen suppression and immune priming. The observed increase in Actinobacteria and decline in Proteobacteria parallel healthier gut profiles reported in earlier studies [11,14].

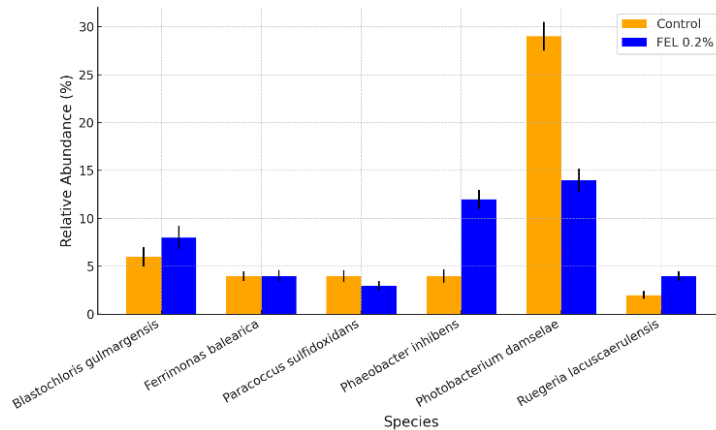


Figure 5.

Relative abundance of selected intestinal bacterial species in *P. monodon* fed 0.2% FEL and control. Data are presented as mean \pm SD (n = 3).

These findings suggest that FEL enhances shrimp survival by modulating gut microbiota and strengthening innate defenses, with encapsulation ensuring LAB viability and consistency with previous reports of healthier gut profiles [7,9–11,14,22].

Conclusion:

Dietary supplementation with FEL enhanced the health and performance of *P. monodon* under both hatchery and pond conditions. FEL (0.2–1.0%) improved immune responses, provided complete protection against *Vibrio parahaemolyticus*, and supported growth, with the strongest effects observed at 0.2%. Importantly, FEL also modulated the intestinal microbiota by reducing pathogenic *P. damsela* and enriching beneficial Roseobacter-group taxa, suggesting a dual role as both an immunostimulant and microbiota modulator. An effective range of 0.2–0.6% FEL therefore represents a practical balance between growth promotion and disease resistance. Collectively, these results highlight FEL as a promising functional feed additive that can reduce antibiotic dependence, enhance shrimp resilience, and promote sustainable and biosecure aquaculture. Limitations of this study include the use of a single pond per treatment, which reduced statistical robustness, and unresolved strain-specific roles and long-term stability under commercial conditions. Future research should address these gaps through replicated pond trials, strain-level tracking, and scalability assessments to confirm industry-wide applicability.

Acknowledgements:

The authors thank the National Research Council of Thailand (NRCT) for funding this study, and the Faculty of Agro-Industry, RMUTSV, for laboratory facilities and equipment. Appreciation is also extended to the Faculty of Science and Technology of Fisheries, for providing earthen ponds, and to the Office of Scientific Instrument and Testing, Prince of Songkla University, for NGS analysis support.

Ethical Approval

All experimental procedures involving animals were conducted in accordance with the guidelines for the care and use of laboratory animals of RMUTSV. The protocol was reviewed and approved by the Institutional Animal Care and Use Committee (IACUC) of RMUTSV. The experimental design and procedures were also endorsed by the funding review committee comprising expert reviewers.



Conflict of Interest

The authors declare no conflict of interest.

References:

1. Cai Y, Yuan W, Xu H, Cao Z, Wang S, Guo X, Zhang D. *Aquaculture*. 2023;565:739152.
2. Chai PC, Song YL, Huang SL. *Fish Shellfish Immunol*. 2016;54:602–610.
3. Chen YY, Yeh ST, Lee YC, Cheng W. *Aquac Rep*. 2021;21:100812.
4. Dawood MA, Koshio S, Esteban MA. *Rev Aquac*. 2018;10:950–974.
5. Farahmand A, Peighambardoust SH, Peighambardoust SJ, Valizadeh H. *LWT Food Sci Technol*. 2024;204:116459.
6. Holt CC, Bass D, Stentiford GD, van der Giezen M. *J Invertebr Pathol*. 2021;186:107387.
7. Hoseinifar SH, Ringø E, Shenavar Masouleh A, Doan HV. *Rev Fish Sci Aquac*. 2020;28:242–272.
8. Hoseinifar SH, Sun YZ, Zhou Z, Ringø E. *Rev Fish Sci Aquac*. 2022;30:163–190.
9. Kumar V, Roy S, Meena DK, Sarkar UK. *Rev Fish Sci Aquac*. 2020;28:1–20.
10. Li E, Xu C, Wang X, Wang S, Zhao Q, Zhang M, et al. *Rev Fish Sci Aquac*. 2018;26:381–399.
11. Liu H, Wang S, Cai Y, Guo X, Cao Z, Zhang D. *Fish Shellfish Immunol*. 2022;126:256–265.
12. Rajkumar M, Pandey PK, Aravind R, Vennila A, Bharti VS, Purushothaman CS. *Rev Aquac*. 2020;12:925–945.
13. Ringø E, Hoseinifar SH, Ghosh K, Doan HV, Beck BR, Song SK. *Front Microbiol*. 2018;9:1818.
14. Van Doan H, Hoseinifar SH, Ringø E. *Aquac Res*. 2021;52:1205–1221.
15. Wang H, Liu X, Lv Z, Chen Y, Zou Y. *Fish Shellfish Immunol*. 2021;119:36–45.
16. Wang Y, Gu Q, Zhou H, Wang Y. *Microorganisms*. 2020;8:1257.
17. Zhang Z, Xu H, Liu J, Xu Q, Yang N, Li D, Wang D. *Front Nutr*. 2022;9:872808.
18. Gao X, Zhou Y, Gu Q, Xu Y, Xu W. *Aquaculture*. 2021;545:737186.
19. Liu CH, Chiu CH, Wang SW, Cheng W. *Fish Shellfish Immunol*. 2018;72:543–550.
20. Soundarapandian P, Velmurugan B. *J Sci Ind Res*. 2008;67:62–66.
21. Xu T, Chen Y, Li E. *Fish Shellfish Immunol*. 2020;98:490–498.
22. Zokaeifar H, Balcázar JL, Saad CR, Kamarudin MS, Sijam K, Arshad A, Nejat N. *Aquaculture*. 2012;342–343:36–41.



EXPRESSION OF CHITINASE ENCODING GENE FROM *Serratia marcescens* MC_G07 AND TERMITICIDAL ACTIVITY AGAINST THE WOOD-FEEDING TERMITE *MICROcerotermes* sp.

Kittipong Chanworawit¹, Torphan Vitoonpanyakij,¹ Pinsurang Deevong^{1,*}

¹Department of Microbiology, Faculty of Science, Kasetsart University, 10900, Bangkok, Thailand

*e-mail: fsciprd@ku.ac.th

Abstract:

Termites (Isoptera) are insects that have the capacity to cause significant damage to wooden structures and materials. Chitinase, a chitinolytic enzyme that breaks down chitin, a major component of insect exoskeletons, is considered a promising tool for alternative biological control of pests including termites. The objectives of this study were to characterize the chitinase-encoding gene (*chi*) from the bacteria *Serratia marcescens* Mc_G07 obtained from termite guts and evaluate the ability of recombinant chitinase to enhance the mortality of wood-feeding termite *Microcerotermes* sp. The *chi* gene (~ 1,500-bp length) of *S. marcescens* Mc_G07 was amplified using polymerase chain reaction (PCR) and then cloned into the pGEM-T Easy vector. The positive clone was selected based on restriction analysis using the restriction enzyme *EcoRI*. The target gene was verified by DNA sequencing and subcloned into the expression vector pET-28a(+). The recombinant pET-28a(+)-*chi* was transformed into *Escherichia coli* BL21 (DE3) for protein expression and the expressed protein was purified using Ni-NTA affinity chromatography of His-tagged proteins. The purified recombinant chitinase had a specific activity of 234.52 mU/mg protein with a 15.52-fold purification and recovery yield of 70.02%. The 52-kDa recombinant chitinase exhibited strong termiticidal activity against *Microcerotermes* sp. with a lethal concentration 50 (LC₅₀) value of 440.10 ± 7.75 mU/treatment within 24 h. The results of this study provide insights for molecular biotechnological research and serve as a model for the development of bioinsecticides in the future.

Introduction:

Chitin is an insoluble homopolysaccharide polymer composed of β-1,4-linked N-acetyl-D-glucosamine (GlcNAc) ¹. It is a flexible polysaccharide that forms the exoskeletons of insects and is also found in fungal cell wall components and other structures like the peritrophic matrix (PM) in the insect digestive system ². Chitin is directly broken down into smaller units through the action of chitinases, which is called “chitinolysis”. Chitinase (EC 3.2.1.14) is a key enzyme involved in the natural degradation of the chitin biopolymer. It cleaves β-1,4 linkages of chitin to produce GlcNAc and chitooligomers ³. These enzymes are broadly classified into two main types, including endochitinases and exochitinases, based on their hydrolytic properties. The endochitinases randomly cleave chitin chains at internal sites to release chitin-oligosaccharides, while the exochitinases degrade chitin by cleaving glycosidic bonds at the non-reducing or reducing ends of the polysaccharide chain, releasing smaller units such as GlcNAc or chitobiose ⁴. Chitinases are classified into two main families, glycoside hydrolase family 18 and 19, based on amino acid sequences and domain structures ⁵. Chitinolytic bacteria are microorganisms capable of utilizing chitin as a nutrient source, with their enzymatic activity contributing to global carbon and nitrogen cycling and playing a role in the biological control of fungal and insect pests. Among them, *Serratia marcescens* has been extensively studied as a model chitin-degrading bacterium, producing chitinases with strong larvicidal activity against a variety of insects, including mosquitoes and other economically important pests ^{6,7}.



Termites (Isoptera) are terrestrial and social insects containing a chitinous shell. They play an important role as decomposers of lignocellulose, a complex carbohydrate found in wood and other plant-based materials⁸⁻¹⁰. Termites can cause significant wood damage in and around natural and human environments, weakening the structural integrity of buildings, which have significant financial losses, with global costs estimated at around \$40 billion annually¹¹. This damage is primarily attributed to subterranean wood-feeding termites, particularly those of the genera *Coptotermes* and *Microcerotermes*. Currently, chemical termiticides such as fipronil, imidacloprid, and bifenthrin are common ingredients that are designed to kill the termites¹². However, the chemicals used to control termites can be toxic to humans and pets if not handled and applied properly. One alternative way to reduce the use of chemical pesticides is biological control by hydrolytic enzymes such as chitinase. However, the effect of chitinase from *S. marcescens* on insecticidal activity against wood-feeding termites are still lacking. In the present study, the chitinase-encoding gene of *S. marcescens* isolated from the guts of the termite *Microcerotermes* sp. was successfully cloned, expressed, and purified. The recombinant chitinase was subsequently evaluated for its termiticidal activity against wood-feeding termites, *Microcerotermes* sp. These findings suggested that the recombinant chitinase may serve as a promising tool for the development of environmentally friendly strategies for green pest control in the future.

Methodology:

Bacterial strains and culture conditions

The chitinolytic bacteria *S. marcescens* Mc_G07 (accession number: OQ293916.1) was obtained from the guts of termite *Microcerotermes* sp. collected from the mango orchard in Nong Suea district, Pathum Thani province, Thailand by Chanworawit, et al.¹³. The plasmid pGEM-T Easy vector (Promega Corporation, Madison, WI, USA) and *Escherichia coli* DH5 α were used for gene cloning. The plasmid pET-28a (+) (Novagen, Darmstadt, Germany) and *Escherichia coli* BL21 (DE3) were used for protein expression. The bacterial strains were grown at 37°C on Luria Bertani (LB; HiMedia Laboratories Pvt. Ltd., Mumbai, India) medium pH 7.0.

Colloidal chitin preparation

To prepare colloidal chitin, 10% w/v chitin flakes (Tokyo Chemical Industry Co., Ltd., Tokyo, Japan) in concentrated HCl was incubated for 24 h. Subsequently, an equal volume of distilled water was added, and the mixture was allowed to stand. The chitin solution was then filtered through Whatman No. 1 filter paper, and the collected sediment was rinsed three times with distilled water before adjusting the pH to 7.0. The resulting colloidal chitin was stored at 4°C until use.

Molecular cloning of the chitinase (chi) gene from S. marcescens Mc_G07

Genomic DNA of *S. marcescens* Mc_G07 was extracted using the Genomic DNA Purification Kit (Thermo Scientific, Waltham, MA, USA) according to the manufacturer's instructions. Amplification of *chi* gene (~ 1,500 bp) was performed using the specific primer pair, *chi*_F (5'-GGCATATGTCCRMACGYAAAGCSGTTATTGG-3') and *chi*_R (5'-CCAAGCTTTCATTAYGCYASRCGGCCCACYTTCAGCC-3'), underlining indicates the *Nde*I and *Hind*III sites, respectively¹⁴. PCR conditions were as follows: initial denaturation at 94°C for 3 min; 25 cycles consisting of denaturation at 94°C for 40 sec, annealing at 52°C for 40 sec, and extension at 72°C for 90 sec; and final extension at 72°C for 10 min. The PCR product was analyzed by 1% agarose gel electrophoresis and purified using the TIANquick Midi Purification Kit (TIANGEN BIOTECH (Beijing) Co., Ltd, China). The purified *chi* gene was ligated to pGEM-T Easy vector and then transformed into *E. coli* DH5 α . The

transformant with a recombinant vector was selected using blue-white colony screening on LB agar supplemented with ampicillin (100 µg/mL), X-gal (40 µg/mL), and isopropyl thio-β-D-galactoside (IPTG; 0.5 mM). The randomly selected white colonies were used to extract recombinant DNA using the GF-1 Plasmid DNA Extraction Kit (Vivantis Technologies Sdn. Bhd., Selangor Darul Ehsan, Malaysia) and confirmed the insertion of *chi* gene using the restriction enzyme *EcoRI* (Thermo Scientific, Waltham, MA, USA). DNA sequencing was conducted by Macrogen (Seoul, Republic of Korea). The open reading frame (ORF) of *chi* gene was analyzed using ORF Finder and the nucleotide sequences were translated to deduce amino acids using ExPASy program. The amino acid sequence of recombinant chitinase was taxonomically identified using Protein BLAST (BLASTp). Then, three-dimensional (3D) structure was predicted using SWISS-MODEL server and multiple sequence alignment was generated using ESPript 3.0 program.

Protein expression and purification of recombinant chitinase

To express recombinant chitinase, the DNA fragments containing *chi* gene were subcloned into pET-28a (+) and then transformed into *E. coli* BL21 (DE3). In this step, the bacterial transformant with a recombinant pET-28a (+)-*chi* was incubated in LB broth containing kanamycin (25 µg/mL) at 37°C with shaking. After incubation for 6 h, the bacterial cells (OD₆₀₀ value of ~ 0.5) were added with IPTG (0.5 mM) for inducing protein expression. The cell pellet was collected by centrifugation at 8,000 rpm for 10 min and resuspended in lysis buffer (0.1 M Tris-HCl, pH 8.1, containing 0.3 M NaCl). Then, the bacterial cells were lysed on ice using an ultrasonicator, followed by centrifugation at 8,000 rpm for 15 min at 4°C to remove cell lysates. The expressed protein in crude protein extract was purified using His-tag purification kit (Zymo Research, Irvine, CA) according to the manufacturer's instructions. The purified recombinant protein was separated by sodium dodecyl sulfate-polyacrylamide gel electrophoresis (SDS-PAGE) and its chitinolytic activity was detected by zymography using 0.01% (v/v) glycol chitin (Sigma-Aldrich, St. Louis, MO, USA) as substrate. Briefly, protein samples were mixed with SDS-loading buffer (60 mM Tris-HCl pH 6.8, 14 mM 2-mercaptoethanol, 25% glycerol, 2% SDS, and 0.1% bromophenol blue) and boiled for 3 min. Acrylamide gel electrophoresis was performed at 120 V for 90 min in Tris-glycine buffer. The gel was then incubated in regeneration buffer (100 mM CH₃COONa and 1% Triton X-100) at 37°C for 3 h, followed by staining with 0.01% Calcofluor White M2R (Sigma-Aldrich, St. Louis, MO, USA). After washing with sterile distilled water, the gel was visualized under UV light (TFL-40 V High-Performance UV Transilluminator). In parallel, a replicate gel was stained with Coomassie blue for 30 min and destained until protein bands were clearly visible.

Determination of chitinase activity

Chitinase activity of the purified recombinant chitinase was determined by the 3,5-dinitrosalicylic acid (DNS) assay according to the method described by Miller¹⁵, using the chitin monomer GlcNAc (Sigma-Aldrich, St. Louis, MO, USA) as standard. The purified recombinant chitinase (100 µL) was mixed with 100 µL of 1% colloidal chitin in 50 mM phosphate buffer (pH 7.0) at 37°C for 30 min. Then, the reaction was stopped by 600 µL of DNS reagent, followed by heating in boiling water at 100°C for 10 min. The absorbance was measured at 540 nm using spectrophotometer. One unit of chitinase activity was determined as the amount of enzyme that released 1 µmol of reducing sugar per minute under the above assay conditions. Protein concentration of purified recombinant chitinase was determined by Lowry-Folin assay according to the method of Lowry, et al.¹⁶, using bovine serum albumin (BSA; Sigma-Aldrich, St. Louis, MO, USA) as a standard.

Termiticidal activity of recombinant chitinase

Termiticidal activity of purified recombinant chitinase was tested on the Thailand wood-feeding termite, *Microcerotermes* sp. The different concentrations of purified recombinant chitinase were used for the treatments. A sterile cellulose filter paper (2 × 2 cm; 0.05 gram) was treated with varying volumes of the purified enzyme in his-elution buffer until the required concentrations of 500, 250, and 125 mU per treatment were achieved. Following treatment, each paper was put into a sterile petri dish containing 10 worker termites. Each treatment was replicated three times and was kept at 28.0 ± 2.0°C with 65.0 ± 5.0% relative humidity in darkness. After incubation for 24 h, termite mortality was observed and the mortality percentage calculated using the following formula.

$$\text{Mortality percentage (\%)} = (\text{Number of dead termite} / \text{Number of total termite}) \times 100$$

The mortality percentage data were subjected to probit analysis to calculate lethal concentration (LC₅₀). The chemical termiticide fipronil (0.1% v/v) was used as a positive control and the his-elution buffer was used as a negative control (0 mU).

Animal use protocol

The animal use protocol in the current research was approved by the Kasetsart University Institutional Animal Care and Use Committee, Bangkok, Thailand (Approval ID. ACKU68-SCI-009) and was in accordance with the Guidelines of Animal Care and Use under the Ethical Review Board of the Office of National Research Council of Thailand for conducting scientific research.

Statistical analysis

All tests were performed at least in triplicate. The data were analyzed using GraphPad Prism version 9.0 software (La Jolla, CA, USA) and presented as standard deviation (S.D.) of the mean. Statistical significances were determined using one-way ANOVA followed by multiple comparisons test. The significance of differences between experimental variants were marked by asterisks $p < 0.05$ (*), $p < 0.01$ (**), or $p < 0.001$ (***).

Results and Discussion:

Molecular cloning of the chitinase (chi) gene from S. marcescens Mc_G07

The gene encoding chitinase (*chi* gene; 1,500-bp full length) from *S. marcescens* Mc_G07 (**Figure 1**) was successfully cloned into *E. coli* DH5 α . The *chi* gene harbored a complete open reading frame (ORF) encoding a protein of 499 amino acids. BLASTp analysis revealed that, the predicted protein shared 99.40% identity with a chitinase from *S. marcescens* (WP_156865799.1) and 99.20% identity with a glycosyl hydrolase family 18 chitinase from *S. marcescens* (WP_021505639.1). Structural modeling showed that, the three-dimensional (3D) structure of the recombinant chitinase from *S. marcescens* Mc_G07 exhibited 98.80% structural identity to the crystal structure of *S. marcescens* chitinase previously reported by Houston, et al.¹⁷. The Ramachandran plot revealed that, the majority of residues fell within the favored regions, indicating good stereochemical quality of the protein structure. Most residues were found to cluster around the regions corresponding to α -helices ($\Phi \approx -60^\circ$, $\Psi \approx -40^\circ$) and β -sheets ($\Phi \approx -120^\circ$, $\Psi \approx 120^\circ$), suggesting that the protein adopted a mixed secondary structure with significant contributions from both helices and sheets (**Figure 2**). Multiple sequence alignment based on the amino acid sequences of the recombinant chitinase are represented in **Figure 3**. Sequence and structural analysis of the chitinase insertion domain revealed two conserved motifs of the glycoside hydrolase family 18 (GH18), including the chitin-binding domain (SxGG) and the catalytic domain (DxDxE). Similarly,

the 1,572-bp full length gene (*PxChi52*) from *Paenibacillus xylanexedens* Z2-4 encoded 523 amino acid residues belonging to glycoside hydrolase family 18 (GH18) and the sequence analysis revealed two conserved motifs comprising the chitin-binding motif (SxGG) located in the fourth β -sheet, and the catalytic motif (DxDxE) located in the fifth β -sheet of the protein structure¹⁸.

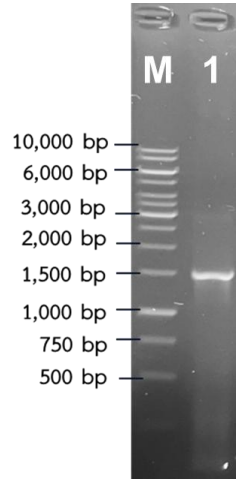


Figure 1.

Products of PCR amplification of the chitinase (*chi*) gene from *Serratia marcescens* Mc_G07. M: GeneRuler 1 kb DNA Ladder; and Lane 1: amplified *chi* gene

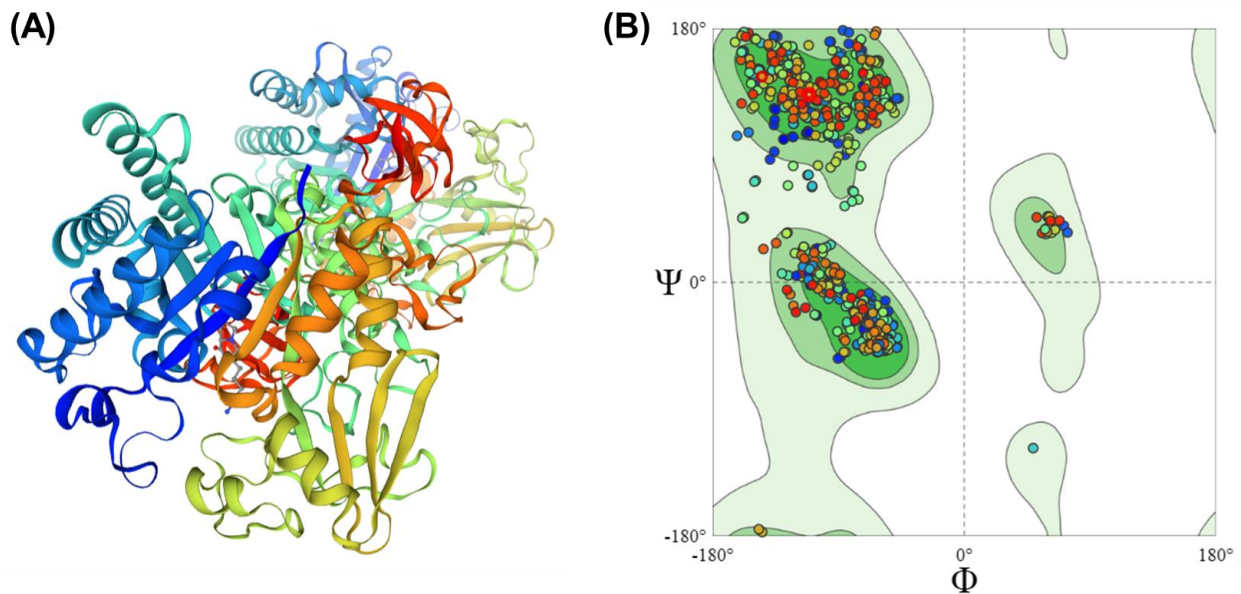
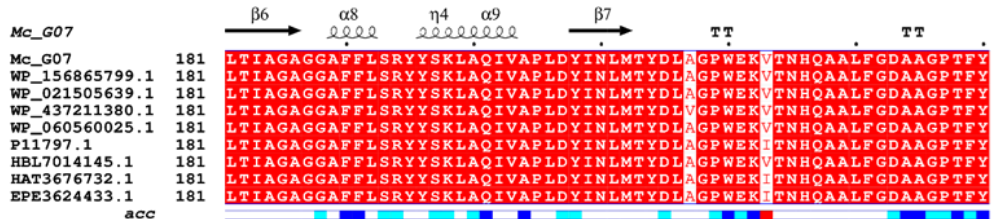
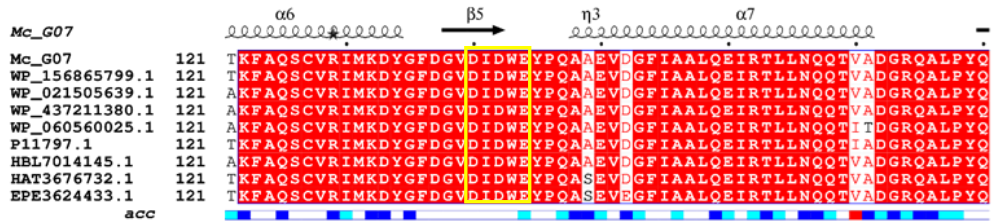
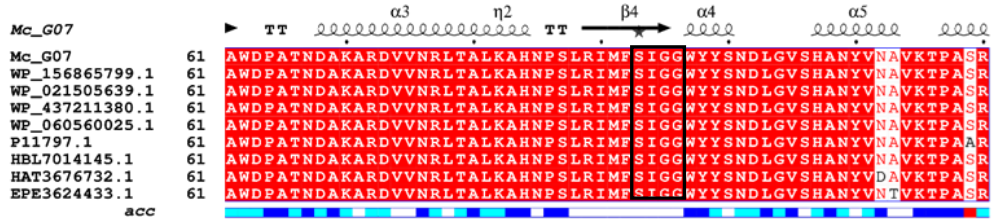
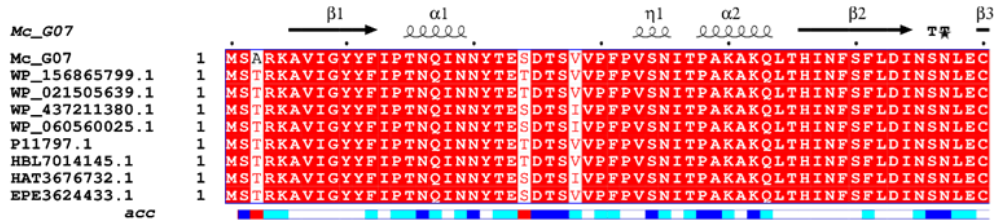


Figure 2.

Three-dimensional (3D) structure model (A) and Ramachandran plot (B) of the recombinant chitinase from *Serratia marcescens* Mc_G07



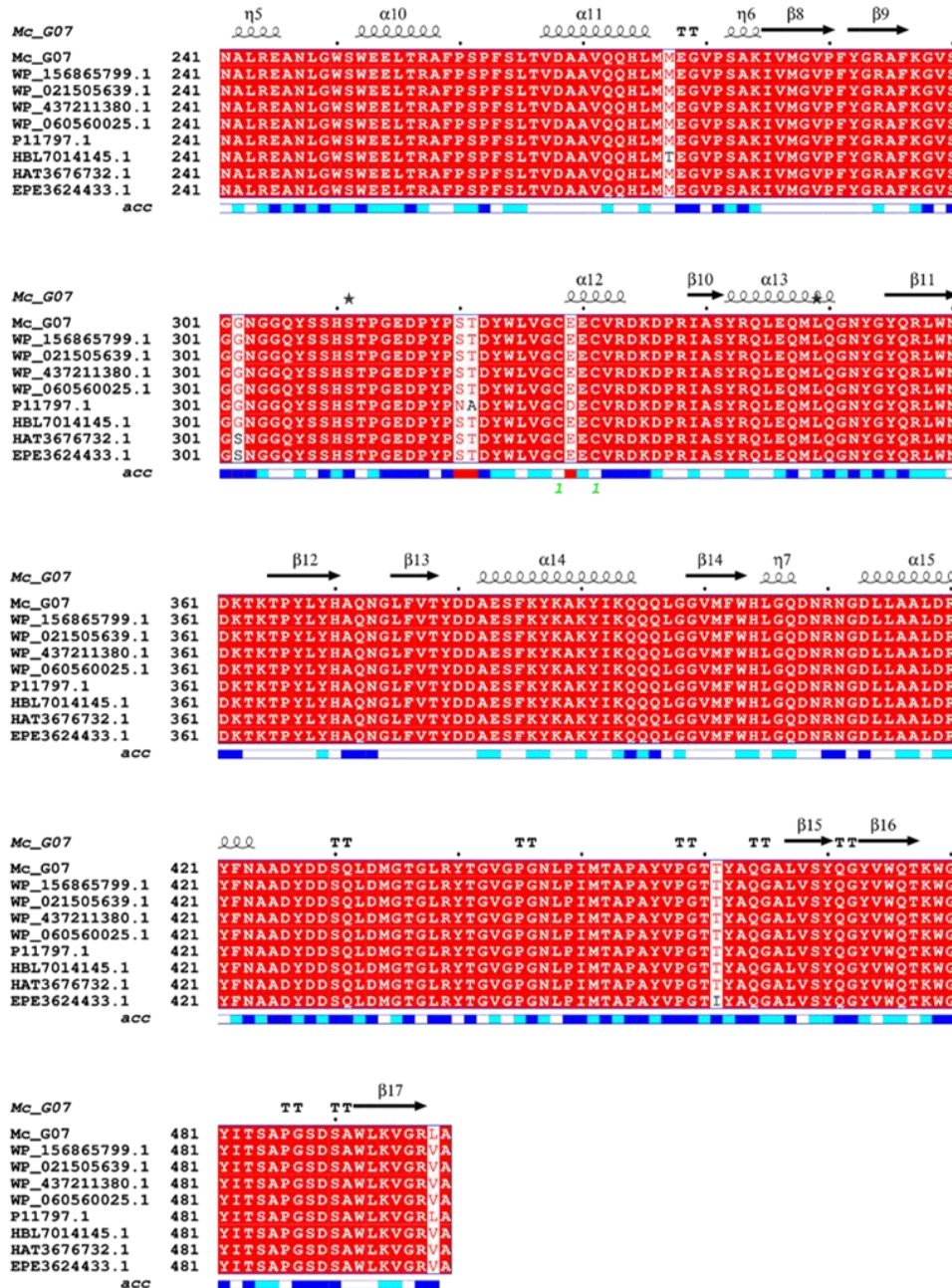


Figure 3.

Multiple amino-acid sequence alignment of the recombinant chitinase from *Serratia marcescens* Mc_G07 with other chitinases. The conserved motifs of chitin-binding domain (SxGG) and the catalytic domain (DxDxE) are labelled with black and yellow boxes around the sequences, respectively.

Protein expression and purification of recombinant chitinase

The recombinant vector (pGEM-T Easy-*chi*) was subcloned into pET-28a(+) to generate recombinant pET-28a(+)-*chi* and heterologous expressed in *E. coli* BL21 (DE3). The zymogram analysis with glycol chitin showed that, the purified recombinant chitinase had a molecular weight of approximately 52-kDa (**Figure 4**). This result is consistent with the active chitinase band from *S. marcescens* KCTC2172 previously reported by Gal, et al.¹⁹. In general, chitinases from *Serratia* spp. range from 22 to 60 kDa, as reported across various strains^{20,21}. The purified recombinant chitinase from *S. marcescens* Mc_G07 in the present

study exhibited a specific activity of 234.52 mU/mg protein with a 15.52-fold purification and a recovery yield of 70.02% towards colloidal chitin as the substrate (**Table 1**), which was comparable to other bacteria in the previous studies using *Paenibacillus chitinolyticus* UMBR 0002 (750.64 mU/mg protein with a 13.36-fold purification and 72.2% recovery yield)²², *Streptomyces alfaifa* ACCC 40021 (28.4 U/mg protein with a 3.7-fold purification and 71.9% recovery yield)²³, and *Paenibacillus xylanexedens* Z2-4 (16.0 U/mg protein with a 1.5-fold purification and 68.0% recovery yield)¹⁸.

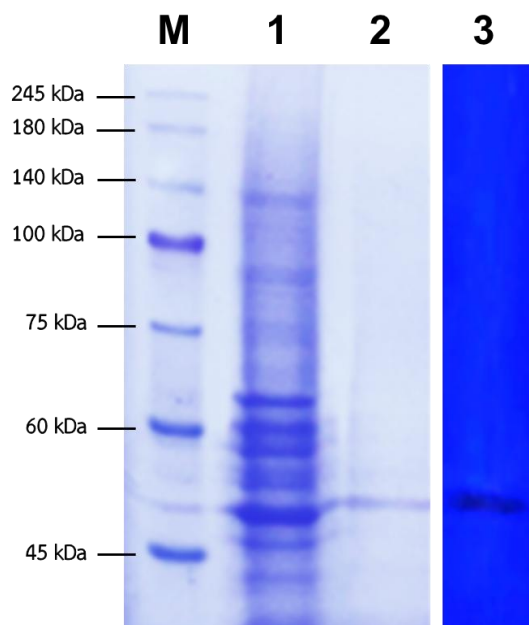


Figure 4.

Protein electrophoresis and zymography analysis on 12% SDS-PAGE gel of recombinant chitinase from *S. marcescens* Mc_G07. M: PM2600 ExcelBand™ 3-color High Range Protein Marker (SMOBIO, Republic of China); Lane 1: crude protein extract of *E. coli* BL21(DE3) including recombinant chitinase; Lane 2: purified recombinant chitinase from Ni-NTA affinity chromatography; and Lane 3: active band of purified recombinant chitinase on zymography analysis

Table 1.
Recombinant chitinase purified by Ni-NTA affinity chromatography

Purification step	Volume (mL)	Protein concentration (mg/mL)	Enzyme activity (mU/mL)	Specific activity (mU/mg protein)	Purification fold	Yield (%)
Crude enzyme	20	5.26	79.47	15.11	1	100
Ni-NTA affinity chromatography	2	2.38	558.16	234.52	15.52	70.02

Termiticidal activity of recombinant chitinase

The bioassay results demonstrated a dose-dependent increase in termite mortality upon treatments with purified recombinant chitinase. At the highest concentration (500 mU/treatment), chitinase induced the termite mortality to $56.67 \pm 15.28\%$, which was

significantly lower than the chemical pesticide fipronil ($96.67 \pm 5.77\%$ mortality), followed by the termite mortality at 250 mU/treatment ($23.33 \pm 5.77\%$), while the lowest chitinase concentration (125 mU/treatment) resulted in less than 10% mortality. The statistical analysis confirmed that, the termite mortality at higher chitinase concentrations (250–500 mU per treatment) was significantly different from the negative control ($p < 0.001$). Furthermore, the purified recombinant chitinase exhibited termiticidal activity with a lethal concentration 50 (LC_{50}) value of 440.10 ± 7.75 mU on the sterile cellulose filter paper (2×2 cm) within 24 h (**Figure 5**). Comparable to previous study of Hussin and Ab Majid ²⁴, the crude chitinase (0.0058 U/mL) from *Bacillus licheniformis* USMW10IK isolated from guts of the termite *Globitermes sulphureus* exhibited significant mortality to *G. sulphureus* at $61.11 \pm 5.56\%$ within 24 h, when compared with a negative control (without crude chitinase).

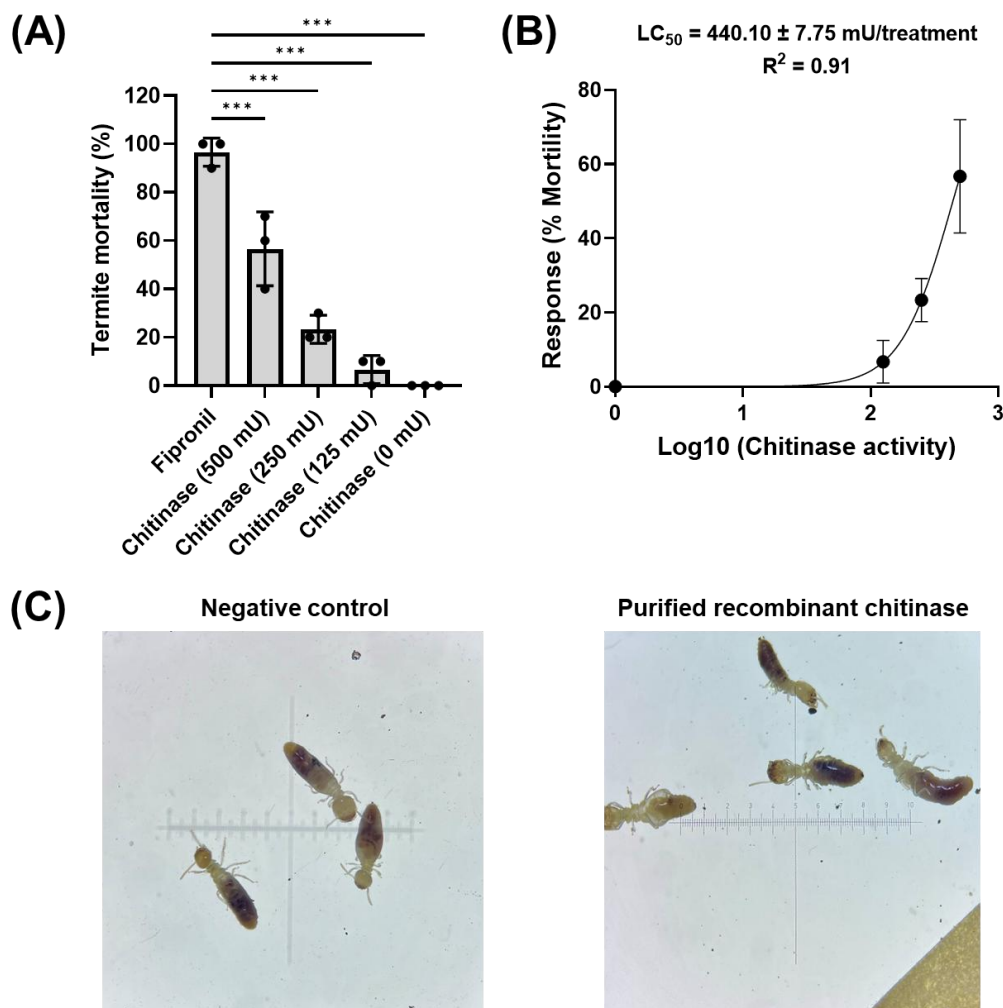


Figure 5.

Mortality percentage of *Microcerotermes* sp. after treatment with purified recombinant chitinase for 24 h (A); probit regression analysis of mortality (B); and physiological effects of purified recombinant chitinase on *Microcerotermes* sp. (C)

Conclusion:

The chitinase-encoding gene from *S. marcescens* Mc_G07 obtained from the termite guts was successfully cloned, expressed, and purified in this study. The purified recombinant chitinase with a molecular weight of approximately 52 kDa exhibited a specific activity of 234.52



mU/mg protein, along with high purification fold (15.52-fold) and recovery yield (70.02%). Moreover, the enzyme demonstrated significant termiticidal activity against the wood-feeding termite *Microcerotermes* sp., with an LC_{50} value of 440.10 ± 7.75 mU/treatment. These results highlight the potential of *S. marcescens* chitinase as an effective biopesticide and suggest its possible application as an environmentally friendly alternative to chemical pesticides for sustainable termite management.

Acknowledgements:

This research was partially funded by Undergraduate Research Matching Fund (URMF 2023), Faculty of Science, Kasetsart University. We thank Mr. Chinnaphat Meeto and Mr. Pachara Wangsoontorn for helping.

References:

1. Itoh T, Kimoto H. *Advances in experimental medicine and biology*. 2019; 1142:131-151.
2. Doucet D, Retnakaran A. Chapter Six - Insect chitin: metabolism, genomics and pest management advances in insect physiology. Edited by Dhadialla TS, vol. 43: Academic Press; 2012: 437-511.
3. Gonfa TG, Negessa AK, Bulto AO. *Heliyon*. 2023; 9(11):e21643.
4. Kidibule PE, Santos-Moriano P, Plou FJ, Fernández-Lobato M. *Biotechnology Reports*. 2020; 27:e00500.
5. Yan Q, Fong SS. *Bioresources and Bioprocessing*. 2015; 2(1):31.
6. Jupatanakul N, Pengon J, Selisana SMG, Choksawangkarn W, Jaito N, Saeung A, Bunyong R, Posayapisit N, Thammatinna K, Kalpongkul N *et al*. *Acta Tropica*. 2020; 212:105686.
7. Tao A, Wang T, Pang F, Zheng X, Ayra-Pardo C, Huang S, Xu R, Liu F, Li J, Wei Y *et al*. *AMB Express*. 2022; 12(1):100.
8. Chanworawit K, Deevong P. In *Proceedings of the 2nd National Conference Suvarnabhumi Institute of Technology*. 2024; 130-146.
9. Chanworawit K, Deevong P. *Trends in Sciences*. 2025; 22(11):10624.
10. Chanworawit K, Tomtong P, Chuglum P, Deevong P. *Agriculture and Natural Resources*. 2025; 59(4):590414.
11. Ahmad F, Fouad H, Liang SY, Hu Y, Mo JC. *Insect science*. 2021; 28(1):2-20.
12. Shi J, Merchant A, Zhou X. 2025; 16(2):208.
13. Chanworawit K, Wangsoonthorn P, Deevong P. *Bioscience, biotechnology, and biochemistry*. 2023; 87(9):1077-1091.
14. Danişmazoğlu M, Demir I, Sezen K, Muratoğlu H, Nalcacioglu R. *TURKISH JOURNAL OF BIOLOGY*. 2015; 39:78-87.
15. Miller GL. *Analytical Chemistry*. 1959; 31(3):426-428.
16. Lowry OH, Rosebrough NJ, Farr AL, Randall RJ. *The Journal of biological chemistry*. 1951; 193(1):265-275.
17. Houston DR, Synstad B, Eijsink VG, Stark MJ, Eggleston IM, van Aalten DM. *Journal of medicinal chemistry*. 2004; 47(23):5713-5720.
18. Zhang W, Ma J, Yan Q, Jiang Z, Yang S. *International Journal of Biological Macromolecules*. 2021; 182:1528-1536.
19. Gal SW, Choi JY, Kim CY, Cheong YH, Choi YJ, Lee SY, Bahk JD, Cho MJ. *FEMS microbiology letters*. 1998; 160(1):151-158.
20. Gal SW, Choi JY, Kim CY, Cheong YH, Choi YJ, Bahk JD, Lee SY, Cho MJ. *FEMS microbiology letters*. 1997; 151(2):197-204.



21. Song Y-S, Oh S, Han Y-S, Seo D-J, Park R-D, Jung W-J. Carbohydrate Polymers. 2013; 92(2):2276-2281.
22. Liu C, Shen N, Wu J, Jiang M, Shi S, Wang J, Wei Y, Yang L. PeerJ. 2020; 8:e8964.
23. Lv C, Gu T, Ma R, Yao W, Huang Y, Gu J, Zhao G. International Journal of Biological Macromolecules. 2021; 167:193-201.
24. Hussin NA, Ab Majid AH. Biocatalysis and Agricultural Biotechnology. 2020; 24:101548.



GENOME-BASED DISCOVERY OF NOVEL CYANOBACTERIAL NATURAL PRODUCTS DERIVED FROM *Gloeocapsa* sp. Strain BRSZ

Hari Winanda¹, Sasiprapa Samsri¹, Stephen B. Pointing², Hakuto Kageyama^{3,4}, and Rungaroon Waditee-Sirisattha^{1*}

¹Microbiology Department, Faculty of Science, Chulalongkorn University, Thailand

²Department of Biological Sciences, National University of Singapore, Singapore

³Graduate School of Environmental and Human Sciences, Meijo University, Japan

⁴Department of Chemistry, Faculty of Science and Technology, Meijo University, Japan

*e-mail: rungaroon.w@chula.ac.th

Abstract:

Extremophilic cyanobacteria are important microorganisms that having a great capacity for producing bioactive compounds (BACs). These BACs are produced through a set of enzymes that encoded by biosynthetic gene clusters (BGCs), either nonribosomal peptide synthetases (NRPS), polyketide synthases (PKS) or hybrids thereof, and ribosomally-synthesized and post translationally modified peptides (RiPPs). These BACs and BGCs can be predicted through genome mining approach to get putative BGCs and its BACs by using its genome sequencing data. *Gloeocapsa* sp. strain BRSZ, a thermophilic cyanobacterium, isolated from the Bo Khlueng hot spring (55 °C) comprised a total of 6,084,403 bp with a GC content 43.5%. Putative BGCs were divided into 6 categories with total 13 main putative BACs. These BACs may functionate as antibiotics, novel inhibitors, and bioactive compounds. Thus, this study revealed that *Gloeocapsa* sp. strain BRSZ is a potential source for biosynthesis of BACs.

1. Introduction:

Cyanobacteria are pivotal microorganisms and important as a primary producer on our planet. They are able to thrive in various habitats, ranging from terrestrial to aquatic habitats, fresh waters to sea water, and hot spring to cold arctic environments.¹ Some cyanobacteria are able to survive in extreme environments, known as extremophilic cyanobacteria due to its ability to endure extreme conditions. Extremophilic cyanobacteria are known to have a great capacity for producing bioactive compounds (BACs).² To date, around 260 families of BACs have been classified based on chemical structures and bioactivities which diverse to alkaloids, depsipeptides, lipopeptides, macrolides/lactones, peptides, terpenes, polysaccharides, lipids, polyketides, and others.³ These compounds exert various biological actions and functions such as cytotoxicity, neurotoxicity, hepatotoxicity, specific protease inhibition, enzyme inhibition, antiprotozoal, antifungal, antibacterial, antiviral, antioxidant, and anti-inflammatory activity.³

Cyanobacterial BACs are known to produce using a set of enzymes. These enzymes are encoded by biosynthetic gene clusters (BGCs), either nonribosomal peptide synthetases (NRPS), polyketide synthases (PKS) or hybrids thereof.⁴⁻⁶ Another BGC encoding ribosomally-synthesized and post translationally modified peptides, well-known as RiPPs, which are biosynthesized by post-ribosomal peptide synthesis (PRPS).⁷ Cyanobacterial genomes were found to comprise around 1-42 biosynthetic pathways for BACs. Ninety-five percents of BACs are present in chromosomes and remaining 5% in plasmids.⁸

Discovery of a wide range of cyanobacterial BACs are influenced by recent genome development such as genome mining. Through this method, that involves identifying the genes associated with secondary metabolites production which encoding the enzymes.⁹ With the rapid increase in the number of microbial genomes, it can be used through genome mining approach to get putative BGCs of another cyanobacterium and its putative BACs that combine with its genome sequencing data.



The aim of this study focused on putative BACs and its BGCs in thermophilic cyanobacterium *Gloeocapsa* sp. strain BRSZ,¹⁰ using genome mining approach and bioinformatic tools. We report here a variety of putative BACs in *Gloeocapsa* sp. strain BRSZ. Thus, this study revealed that *Gloeocapsa* sp. strain BRSZ is a potential source for biosynthesis of BACs.

2. Method:

2.1. Circular genome construction and genome mining for BGCs

The genome of *Gloeocapsa* sp. strain BRSZ were obtained as described previously¹⁰. Genomic data were annotated using Galaxy Prokka Pipeline (https://usegalaxy.eu/?tool_id=prokka) with default setting for bacteria. Artemis DNAPlotter was used for generating circular representing genome.¹¹ Putative secondary metabolite gene clusters (or BACs) were identified using antiSMASH version 7.1.0. Genomic data was analysed for clusters of genes involved in the biosynthesis of BACs. Each BGC was clarified manually using Minimum Information about a Biosynthetic Gene cluster (MIBiG) (mibig.secondarymetabolites.org/) to analyze structure of BGCs.

2.2. Putative BACs analysis in *Gloeocapsa* sp. strain BRSZ

AntiSMASH version 7.1.0 was used to predict BACs using default parameters. Domain analysis and annotation were executed and forward chemical structure of NRPSs and PKSs was predicted. Cluster Blast gene cluster comparative analysis and Secondary Metabolite Clusters of Orthologous Genes (smCOG) analysis were performed as secondary metabolism protein family analysis. Further, recovery and data interpretation were done by using GenBank output files of BACs predicted by antiSMASH.¹² Putative BACs were extracted from antiSMASH results singly to know the total secondary metabolite contains in *Gloeocapsa* sp. strain BRSZ. These secondary metabolites were analysed manually to know its function based on the references.

3. Results and Discussion:

Genome information of *Gloeocapsa* sp. strain BRSZ

The genome size of *Gloeocapsa* sp. strain BRSZ comprised a total of 6,084,403 bp with a GC content 43.5% (Figure 1). Rajneesh et al.¹³ found that cyanobacteria GC varied from 34 to 61.4%. *Gloeocapsa* sp. strain BRSZ is thermophilic cyanobacterium, originally isolated from the Bo Khlueng hot spring (55°C) showed a moderately high GC content which may correlate with thermal adaptation. Positive association was found in correlation between thermal adaptation and high GC content in prokaryotes growing in high temperatures as a response to heat mutagenesis.¹⁴

In most prokaryotes, the genome mostly contains protein-coding genes that clustered to be BGCs for BACs production.¹⁴ The number of BGCs and genome size showed a moderate positive significant as reported by Alam et al.¹⁵ that among 37 genomes of bacteria, they found that the smallest genome size, 4.689 Mbp, had 7 BGCs while the biggest genome size, 6.828 Mbp, was found 16 BGCs. In this study, *Gloeocapsa* sp. strain BRSZ genome is slightly large genome size is speculated having high abundance of BACs.

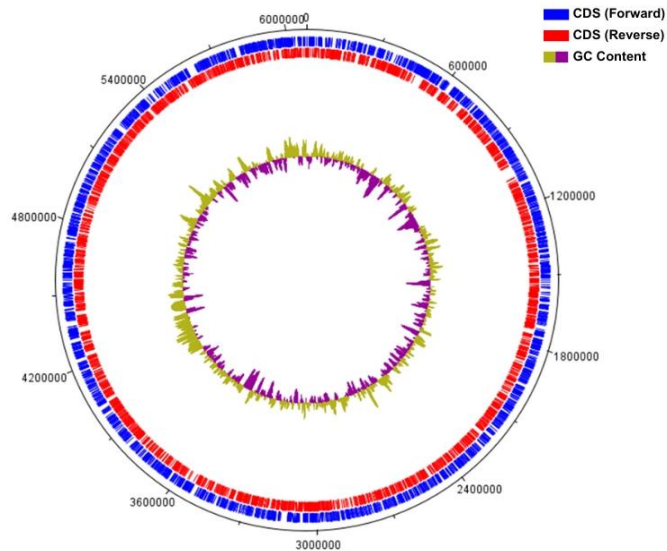


Figure 1.

The circular assembled genome of *Gloeocapsa* sp. strain BRSZ. Navy and red colours represent Coding DNA Sequence (CDS). This circular genome was constructed by Artemis DNAPlotter using whole genome sequencing data

Type of BGCs found in *Gloeocapsa* sp. strain BRSZ

The number of gene clusters for BACs were revealed with antiSMASH. These BACs were divided into 6 categories (NRP+Polyketide, NRP, NRP: Cyclic depsipeptide+polyketide: Modular type I polyketide, NRP: Cyclic depsipeptide, Polyketide+NRP: Cyclic depsipeptide, and NRP: Glycopeptide + Polyketide: Other polyketide + saccharide: Hybrid/tailoring saccharide). Among these BACs, the highest number was obtained from NRP+Polyketide (22 types), following by NRP (17 types). Meanwhile, the lowest was obtained from NRP: Cyclic depsipeptide, Polyketide+NRP: Cyclic depsipeptide (1 type) and NRP: Glycopeptide + Polyketide: Other polyketide + saccharide: Hybrid/tailoring saccharide (1 type) (Figure 2).

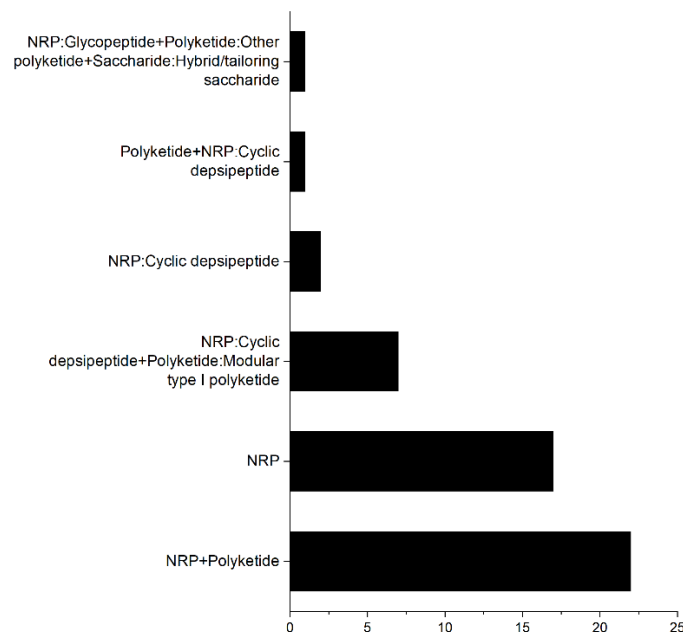


Figure 2.

BGCs type of BACs in *Gloeocapsa* sp. strain BRSZ. Constructed using OriginPro (<https://www.originlab.com/>) using BGCs data from antiSMASH results

Putative BACs and BGCs in *Gloeocapsa* sp. strain BRSZ

Using antiSMASH, 13 main putative BACs were classified in *Gloeocapsa* sp. strain BRSZ genome. Some of them contain sub-specific BACs, such as 12-epi-hapalindole J isonitrile/Ambiguine A/B/C/D/E/K/L/I/J isonitrile, Bartoloside 2/3/4/E/F/G/H/I/J/K, Fabclavine Ia/Ib/IIa/IIb, Minutissamide A/C/D, Nostopeptolide A1/A2/1052, and Puwainaphycin A/B/C/D/F, Scytocyclamide A/A2/B/B3/C (Figure 3). These BACs are function largely as antibiotic, inhibitor, anti-physiological diseases, and cytotoxic activity. As these secondary metabolites mostly encoded by NRP-PK that assumed having potent for pharmaceuticals and biological applications.

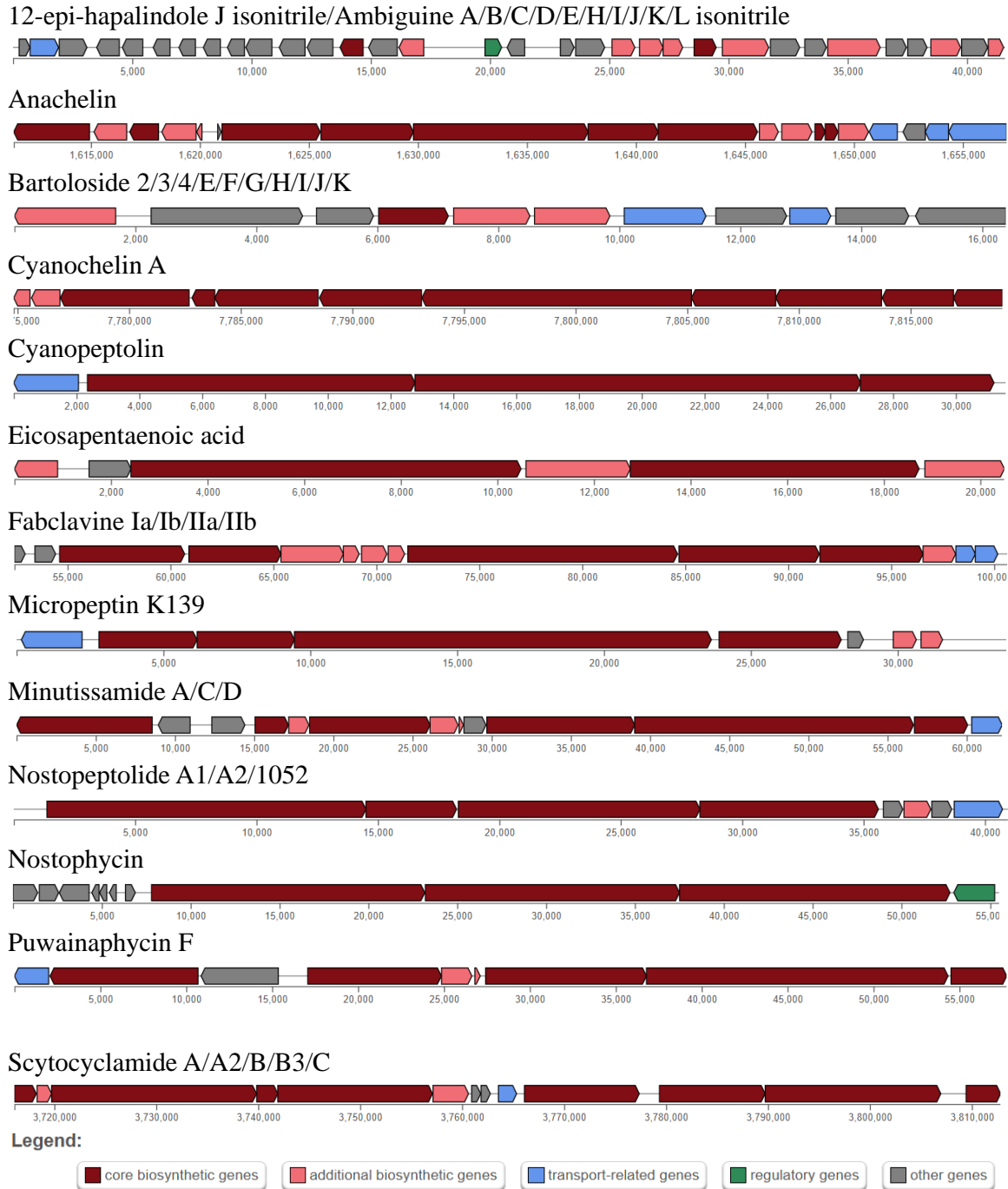


Figure 3.
Putative gene organizations of BACs in *Gloeocapsa* sp. strain BRSZ



Accumulating evidence has shown that 5-6% of cyanobacterial genomes dedicate for secondary metabolites production with 5 gene clusters per genome averagely, but some strains encoding up to 23 gene clusters with majority no known end-product.¹⁹ The total 13 main putative BACs found in *Gloeocapsa* sp. strain BRSZ is considerably a high abundance for production of BACs in a single microorganism compared to the mean. The high numbers of BACs in *Gloeocapsa* sp. strain BRSZ possibly resulted from genome size and environmental factors. The BACs in cyanobacteria can be affected by several factors, such as genome size, total gene numbers, and ecological niche as adaptation mechanisms.^{15,20}

Conclusion:

This study demonstrates *Gloeocapsa* sp. strain BRSZ as a potential novel BACs source for biotechnological and pharmaceutical applications. Genome mining approach revealed high abundance of BACs and BGCs in which there are 13 main putative BACs in genome of *Gloeocapsa* sp. strain BRSZ that produced largely through NRP+Polyketide set enzymes. These BACs may functionate as antibiotics, novel inhibitors, anti-physiological diseases, and cytotoxic activity. The total number of BACs assumed affecting by genome size, total genes, and ecological niche factors. The experimental validation for these putative BACs is highly recommended for better understanding of genes involved and environmental factors in induction, characteristic, and function of BACs.

References:

1. Chen M.Y., Teng W.K., Zhao L., Hu C.X., Zhou Y.K., Han B.P., Song L.R., Shu W.S. The ISME Journal. 2021;15(1): 211–227.
2. Drobac-Cik A., Dulic T., Stojanovic D., Svircev Z. Zbornik Matice Srpske Za Prirodne Nauke. 2007;112: 57–66.
3. Demay J., Bernard C., Reinhardt A., Marie, B. Marine Drugs. 2019;17(6):1-49.
4. Dittmann E., Gugger M., Sivonen K., Fewer D. P. Trends in Microbiology. 2015;23(10): 642–652.
5. Shah S., Akhter N., Auckloo B., Khan I., Lu Y., Wang K., Wu B., Guo Y.W. Marine Drugs. 2017;15(11):1-30.
6. Baunach M., Guljamow A., Miguel-Gordo M., Dittmann E. Natural Product Reports. 2024;41(3):347–369.
7. Arnison P. G., Bibb M. J., Bierbaum G., Bowers A. A., Bugni T. S., Bulaj G., Camarero J. A., Campopiano D. J., Challis G. L., Clardy J., Cotter P. D., Craik D. J., Dawson M., Dittmann E., Donadio S., Dorrestein P. C., Entian K.D., Fischbach M. A., Garavelli J. S., Van Der Donk W. A. Nat. Prod. Rep. 2013;30(1):108–160.
8. Popin R. V., Alvarenga D. O., Castelo-Branco R., Fewer D. P., Sivonen K. Frontiers in Microbiology. 2021;12:1-12.
9. Belknap K. C., Park C. J., Barth B. M., Andam C. P. Scientific Reports. 2020;10(1):1-9.
10. Aono T., Samsri S., Waditee-Sirisattha R., Kageyama H. Microbiology Resource Announcements. 2024;13(12):1-3.
11. Carver T., Thomson N., Bleasby A., Berriman M., Parkhill J. Bioinformatics. 2009;25(1):119–120.
12. Arulprakasam, K. R., & Dharumadurai, D. Microbial Pathogenesis. 2021;161:1-12.
13. Rajneesh, Pathak, J., Kannaujiya, V.K., Singh, S.P., & Sinha, R.P. 3 Biotech. 2017;7(3):1-14.
14. Hu E.Z., Lan X.R., Liu Z.L., Gao J., Niu D.K. BMC Genomics. 2022;23(1): 1-17.
15. Alam K., Islam Md. M., Li C., Sultana S., Zhong L., Shen Q., Yu G., Hao J., Zhang Y., Li R., Li A. Molecules. 2021;26(24):1-17.



16. Rath C. M., Scaglione J. B., Kittendorf J. D., Sherman D. H. In *Comprehensive Natural Products II*, Elsevier. 2010: 453-492.
17. Borsetto C., Amos G. C. A., Da Rocha U. N., Mitchell A. L., Finn R. D., Laidi R. F., Vallin C., Pearce D. A., Newsham K. K., Wellington E. M. H. *Microbiome*. 2019;7(1):1-11.
18. Khabthani S., Rolain J.M., Merhej, V. *Microorganisms*. 2021;9(11):1-17.
19. Dittmann E., Gugger M., Sivonen K., Fewer D. P. *Trends in Microbiology*. 2015;23(10):642–652.
20. Waditee-Sirisattha R., Kageyama H. In *cyanobacterial physiology*, Elsevier. 2022: 85-99.



EXPLORING CYANOBACTERIAL DIVERSITY FROM A NEUTRAL-ALKALINE HOT SPRING IN THAILAND AND THEIR PHOTOPROTECTIVE COMPOUND PRODUCTIONS

Chatchadarat Anantasophon,¹ Pawat Wangthaphan,¹ Tanawat Leknawin,¹ Sasiprapa Samsri,¹ Stephen B. Pointing,² Hakuto Kageyama^{3,4} and Rungaroon Waditee-Sirisattha^{1,*}

¹Department of Microbiology, Faculty of Science, Chulalongkorn University, Bangkok 10330, Thailand

²Department of Biological Sciences, National University of Singapore, Singapore 117557, Singapore

³Department of Chemistry, Faculty of Science and Technology, Meijo University, 1-501 Shiogamaguchi, Tenpaku-ku, Nagoya, Aichi 468-8502, Japan

⁴Graduate School of Environmental and Human Sciences, Meijo University, 1-501 Shiogamaguchi, Tenpaku-ku, Nagoya, Aichi 468-8502, Japan

*e-mail: Rungaroon.W@Chula.ac.th

Abstract:

Thermophilic cyanobacteria are prokaryotic photoautotrophic microorganisms that can grow at high temperatures. This study, the diversity of thermophilic cyanobacteria was explored in a neutral-alkaline Bo Khlung hot spring, Ratchaburi Province in central Thailand. To classify the taxonomy of the isolated strains, we used combination methods, including phenotypic, genotypic, and chemotaxonomic data. We discovered an interesting cyanobacterial strain with a morphological match to the genus *Stanieria*. Based on morphological features, this thermophilic cyanobacterium is a baeocyte producer. Moreover, its cell typically appeared to produce a dark blue-green pigment, implicating that the composition of chromophores is distinct. Molecular phylogenetic analysis of the 16S rRNA gene placed this strain with the closest similarity to *Stanieria cyanosphaera* (96% nucleotide identity). We therefore named this thermophilic cyanobacterium as *Stanieria* sp. strain Black (BL). HPLC and LC/MS analyses identified a UV-absorbing compound as porphyrin-334, produced by *Stanieria* sp. strain BL. Our results suggest that a thermally hot spring is a good bioresource for exploring novel extremophilic cyanobacteria.

Introduction:

Cyanobacteria is a group of the oldest microorganisms, having evolved over a long period of time. They are pivotal in the evolution of photosynthetic oxygen and maintaining the global carbon or nitrogen cycle. With their diverse morphological features, allow them to live freely or in symbiosis across many habitats. Microorganisms can adapt to almost any environmental condition. Recent studies have shown that microbial communities inhabit environments with extreme variations in temperature, pressure, and salinity, as well as combinations of these conditions. Such microorganisms, termed extremophiles, generate enzymes and biocatalysts that remain active and stable under harsh conditions.¹ They are abundant in extreme harsh conditions such as hot springs, glacial lakes in Antarctica, hypersaline environments, hot deserts, and many other unreceptive environments.²

Temperature is a key abiotic factor affecting species distribution, based on their optimum growth temperature. Thermophilic cyanobacteria are prokaryotic photoautotrophic microorganisms that can grow at temperatures between 45 and 73°C.³ A few thermophiles can grow at very high temperatures (above 80°C) they are known as hyperthermophiles. Hyperthermophiles were first discovered to inhabit the deep sea.⁴ But cyanobacterial species were reported in abundance with high environmental heterogeneity in high-temperature ecosystems such as hot springs. In these habitats, cyanobacteria often develop into structured mats that function as major primary producers. Some cyanobacterial species dominate hot



spring mats and serve as the main primary producers within these microbial communities. To date, various research groups have investigated the diversity of cyanobacterial taxa and the genomic adaptations that have evolved to tolerate high-temperature environments. Research combining classical morphology-based classification with modern molecular approaches has prompted a revision of cyanobacterial diversity, revealing many previously unrecognized taxa.⁵

This study aimed to explore the diversity of thermophilic cyanobacteria in a neutral-alkaline hot spring (Bo Khlueng hot spring, Ratchaburi). This hot spring is a part of neutral-alkaline hot springs across a 2100 km latitudinal gradient in Southeast Asia⁶ and contains sulfide-rich mineral water, traditionally thought to ease muscle aches, with a continuous flow throughout the year and temperatures ranging from 50 to 57°C. Moreover, Bo Khlueng hot springs represent a promising habitat for discovering distinctive bacterial and archaeal species. Approximately 80% of the prokaryotic sequences identified in this hot spring were previously uncharacterized.⁷ The discovery of numerous species within this hot spring presents significant challenges, yet it also holds the potential for uncovering novel and fascinating organisms.

Methodology:

Isolation and culturing of cyanobacteria

The cyanobacterial samples were collected from a thermally hot spring site (Bo Khlueng: 13.7368°N, 99.2395°E, Ratchaburi Province) in central Thailand in August 2022.⁸ The cyanobacterial strain was obtained and grown using established procedures. Cells were first serially diluted in BG11 medium, and individual cyanobacterial cells were subsequently isolated through micromanipulation.⁹ An individual cyanobacterial cell was isolated from the culture suspension using an inverted microscope equipped with a micromanipulator and sterile glass micro-capillaries (25-50 µm inner diameter). The isolated cell was then transferred into 500 µL of sterile BG11 medium for micromanipulation. The isolated culture was maintained under cool white fluorescent illumination at an intensity of 50 µmol photons m⁻²·s⁻¹. After around two weeks of incubation, when a dark blue-green culture appeared.⁸ It was then streaked onto BG11 agar plates to obtain single colonies. A distinct BL colony was subsequently confirmed as an axenic culture. Morphological identification was performed according to Bergey's manual.¹⁰ The cyanobacterial morphology was observed under a Nikon Upright Eclipse Ni-U microscope (Japan) at 100X magnification, using the NIS Elements D imaging system for documentation.

Extraction and analysis of UV-absorbing compound

The cyanobacterium *Stanieria* sp. strain BL was routinely cultured on BG11 agar plates and employed for the extraction of UV-absorbing compounds. The extraction was carried out according to a previously established protocol¹¹ with adjustments. In general, the precipitated cell fraction after centrifugation was weighed and measured for fresh weight. Methanol (90% v/v) was added to cyanobacterial pellets. The cell suspension was disrupted twice using a Vibra-Cell™ Ultrasonic Liquid Processor (VCX-130, Sonics, USA) with 30-s pulses followed by 10-s rests, totaling 10 min of sonication (counted as 5 min per session) or until the cells changed color from dark green to gray. After that, let it rest in a 4°C incubator overnight, then centrifuge at 12,000 rpm for 5 min. The supernatant was concentrated using a centrifugal vacuum concentrator (Eppendorf, Germany). The dried extract was then dissolved in 0.5 mL of Milli-Q water and 0.02 mL of chloroform, followed by centrifugation at 12,000 rpm for 5 min. The resulting supernatant was filtered through an Amicon Ultra-4 Ultracel-3K centrifugal unit (Merck, Germany) at 14,000 rpm for 30 min until most of the solution had passed through. The filtrate was subsequently analyzed using a BioMate 3S UV-Vis



spectrophotometer (Thermo Scientific, USA).⁸ High-performance liquid chromatography (HPLC) and liquid chromatography-mass spectrometry (LC-MS) analyses were carried out as previously described.¹¹

Genomic DNA preparation and 16s rRNA gene sequencing

Genomic DNA (gDNA) was extracted using the DNeasy® PowerLyzer® PowerSoil® kit (Qiagen, Germany) following the manufacturer's instructions, and its concentration was determined with a Nanodrop 2000 UV-Vis spectrophotometer (Thermo Fisher Scientific, USA). The cyanobacterial 16S rRNA gene was then amplified using primer pairs 5'-ACTGGAGCTTAACTCCGGGC-3' (forward) and 5'-AGATTTCGCTTACTCTTGCGAGCTTG-3' (reverse). PCR was carried out in a 25 µL reaction mixture comprising 50 ng of genomic DNA, 200 µM dNTPs, 1× Standard Taq Buffer, 0.2 µM of each primer, and 1 U of Taq DNA polymerase (New England Biolabs, USA).¹² The PCR amplification consisted of 30 cycles, beginning with an initial denaturation at 95°C for 10 min, followed by successive steps of annealing at 95°C for 30 s, at 60°C for 30 s, 68°C for 40 s, and with a final extension at 68°C for 3 min 20 s. The same primers at Macrogen, Inc. (Korea) were used to sequence the resulting PCR products.

Phylogenetic analysis

The 16S rRNA gene was employed for molecular phylogenetic analysis. Cyanobacterial sequences for this analysis were retrieved using a BLAST search of the KEGG database (<https://www.genome.jp/tools/blast/>). The phylogenetic analysis used a total of 100 taxa for the 16S rRNA gene. (Figure 2), *Gloeobacter kilaueensis* JS1 was used as the outgroup. The sequence alignment was generated using MUSCLE (Edgar, 2004), and a phylogenetic tree was subsequently inferred using the neighbor-joining approach method¹² with the analysis applied a General Time Reversible (GTR) model of sequence evolution with a discrete Gamma distribution across five categories (+G, parameter = 0.6957) was used, and 65.95% of sites were considered as evolutionarily invariant (+I). Branch support was assessed by showing the percentage of replicate trees (1,000 replicates) in which the corresponding taxa clustered together.¹³ The MEGA12 was used to perform analysis, including 100 nucleotide sequences comprising 1,548 positions in the final dataset and evolutionary analyses.¹⁴

Results and Discussion:

Cyanobacterial diversity obtained from Bo Khlueng hot spring

We have successfully isolated at least eight cyanobacterial strains previously.⁸ In this study, five of them were confirmed as axenic cultures. Therefore, they were used for morphological observation. All the enrichments were performed in the same culture medium recipe (BG11).¹⁵ As shown in Figures 1A-C, the morphologies of three cyanobacterial strains were observed as filaments, while one cyanobacterium was of the unicellular-colonial type (Figure 1D). The last one displayed its morphology as a unicellular type with large cells (approx. 10-20 µm in diameter) (Figure 1E). Due to its unique feature and rarely found in ecosystem, we emphasize studying this cyanobacterial strain. (Figure 1E). Initial morphological observations revealed that the strain showed single coccoid cells, generally spherical and attached to the substrate, with each cell measuring approximately 20 µm in diameter. The cells often formed aggregates connected to one another, surrounded by a thin, transparent sheath that facilitated surface attachment. These aggregates appeared dark blue-green and contained vegetative cells and baeocytes formed through multiple fission.¹⁶ This genus shows a distinctive reproductive mode, producing numerous small daughter cells (baeocytes) measuring approximately 1.5-4 µm in diameter, which subsequently attach to the substrate near the mother cell.¹⁷ Besides cell morphology, the dimensions of vegetative cells and baeocytes,

along with their reproductive characteristics, are key criteria typically used to considered in characterizing the genus *Stanieria*.¹⁶ Hereafter, we named this strain as *Stanieria* sp. strain Black (BL).

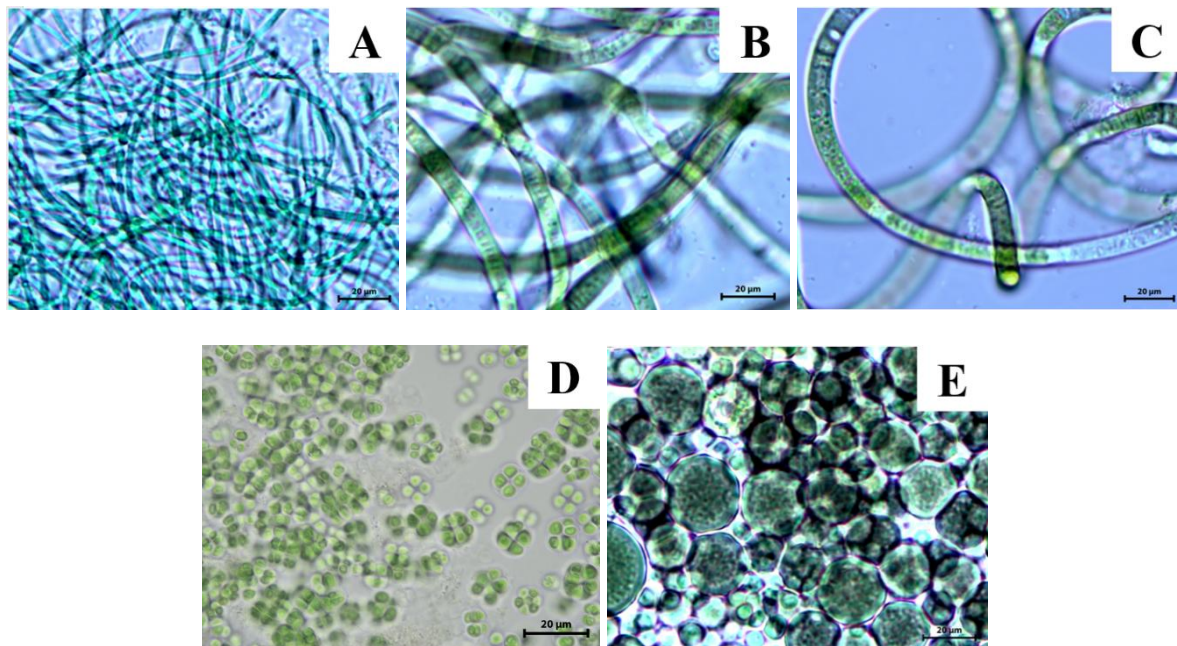


Figure 1.

Microphotographs of cyanobacterial diversity found in hot spring by using a light microscope. Filamentous cyanobacteria including (A), (B), (C), unicellular *Gloeocapsa* sp. strain BRSZ (D), and the cyanobacteria in this study *Stanieria* sp. strain BL (E).

Phylogenetic analysis

In this study, we could obtain the PCR product of the 16s rRNA gene of *Stanieria* sp. strain BL using a pair of specific primers. Nucleotide sequencing (1,216 bp) was used to align and compare across species to build the phylogenetic tree. The 16s rRNA phylogenetic tree was constructed from 100 sequences, with strain *Gloeobacter kilaueensis* JS1 used as the outgroup to root all trees. The cyanobacteria strain in this study, together with four taxa in the family Pleurocapsaceae, genus *Stanieria* (Figure 2). Genotypic affiliation of strains and phylogenetic placement represent at least two strains of *S. cyanosphaera* are nearest neighbor of the strain of BL in this study. The sequence similarity indicated that the cyanobacteria strain in this study was closest to the species *S. cyanosphaera*, including *Stanieria cyanosphaera* PCC 7437 (R0009) and *Stanieria cyanosphaera* PCC 7437 (R0032) with a similarity of 96%, as determined by the 16S rRNA gene. The sequence length of the cyanobacteria strain in this study is 1,216 nt. According to the phylogenetic tree, it is suggested that this cyanobacterium belongs to the genus *Stanieria*. Morphologically, *S. cyanosphaera* is similar in morphology to *Stanieria* sp. strain BL, which is single coccoid cells, generally spherical and attached to the substrate.¹⁶

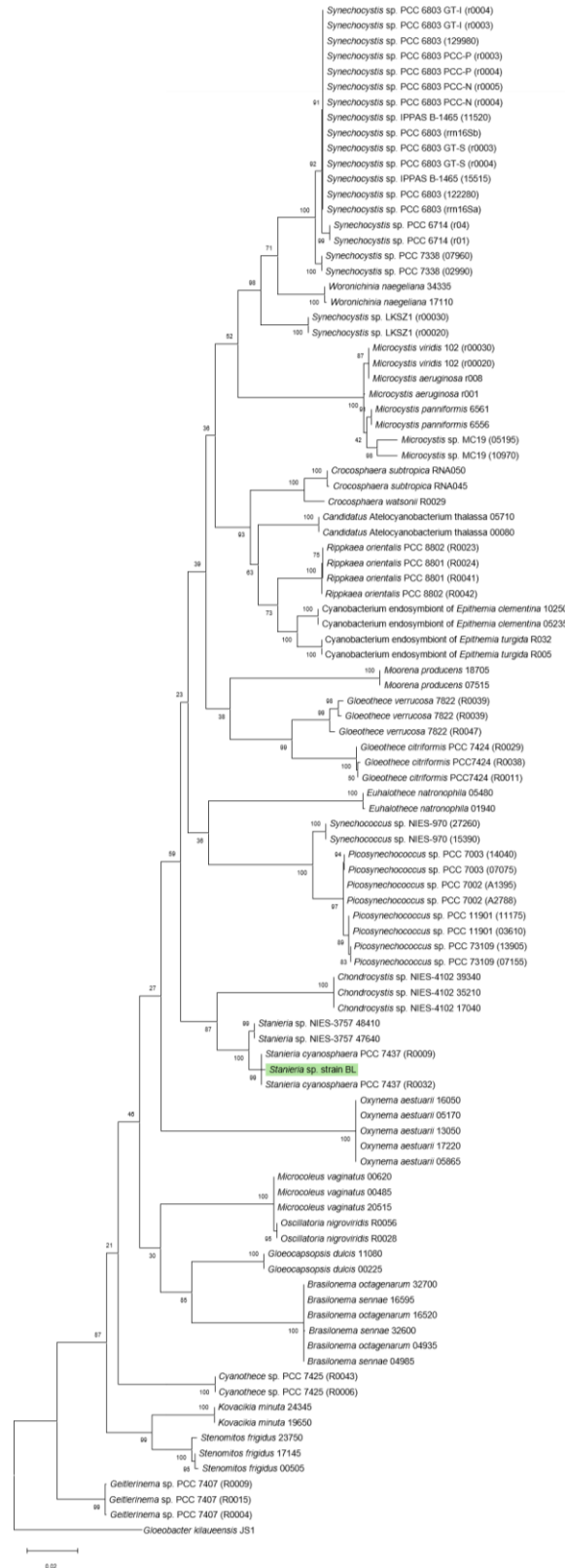


Figure 2.

Molecular phylogenetic analysis of 100 nucleotide sequences. The cyanobacteria *Stanieria* sp. strain BL, the green box, represents the strain identified in this study. Neighbor-joining tree constructed using 16S rRNA gene sequences with the GTR+G+I (general time reversible) model. The numerals indicate the confidence level from 1000 bootstrap replicates.

Stanieria sp. strain BL accumulates mycosporine-like amino acid

We investigated whether or not *Stanieria* sp. strain BL produces a natural sunscreen, particularly mycosporine-like amino acid (MAA). The UV absorption spectrum of the aqueous phase extracted from *Stanieria* sp. strain BL showed a single peak at around 334-336 nm (Figure 3A). Typically, a group of MAAs exhibit absorption spectra in a range of 310-362 nm.¹⁸ Further, the aqueous phase was subjected to HPLC and LC-MS analyses. HPLC analysis revealed a major peak with a retention time of 6.59 min (Figure 3B), with exactly the same as porphyra-334A few smaller, unknown peaks were also detected at 16.35, 17.09, and 19.85 min. Lastly, the fraction of retention time of 6.59 min was collected and subjected to LC-MS analysis. The fraction was found to exhibit m/z of 347 (Figure 3C), which corresponds to porphyra-334.¹⁹ Based on the same retention time and its mass, a UV-absorbing compound produced by *Stanieria* sp. strain BL is porphyra-334.

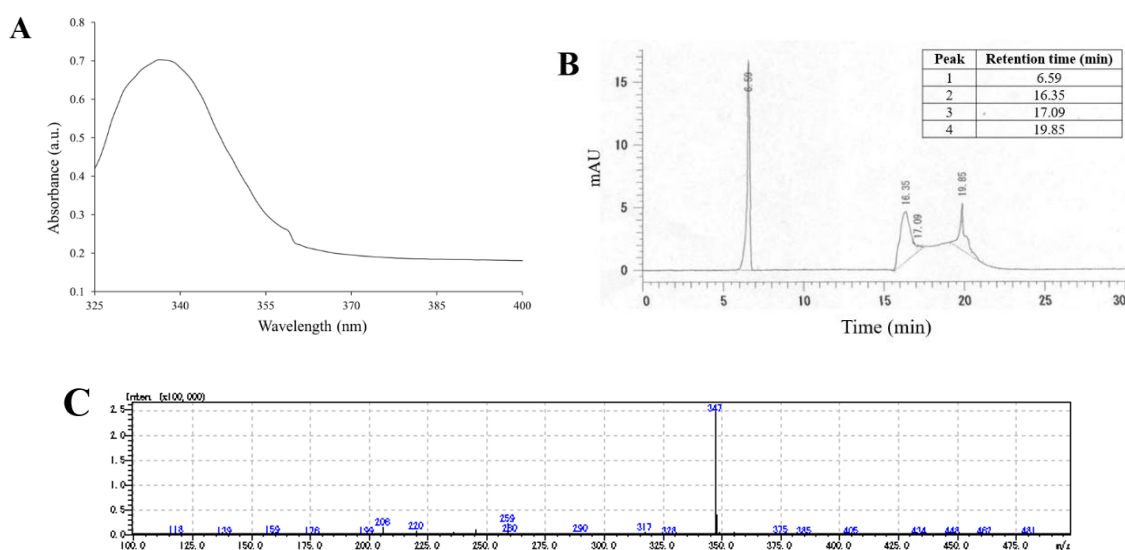


Figure 3.

UV absorption spectrum of the aqueous phase extracted from the cyanobacteria *Stanieria* sp. strain BL. (A), HPLC analysis (B), and LC/MS analysis (C) of UV-absorbing compound in *Stanieria* sp. strain BL.

Conclusion:

This study reported a novel cyanobacterial strain isolated from a hot spring in Thailand. Morphological and 16s rRNA identification revealed that the newly isolated strain belongs to the genus *Stanieria*. The 16S rRNA gene sequencing placed *Stanieria* sp. strain BL within a well-defined clade alongside known *Stanieria* species, closest related to the *Stanieria cyanosphaera* species, reinforcing its classification as part of this genus. In addition, HPLC and LC/MS analyses identify a UV-absorbing compound, i.e., MAA. MAA produced by *Stanieria* sp. strain BL was identified as porphyra-334. Furthermore, the findings suggest that further research into higher-level strains could confirm whether this strain is a new species.

References:

1. Bertus van den Burg. *Current Opinion in Microbiology*. 2003;6:213-218.
2. Mehetrea T.G, Zothanpuiab, Dekaa P, Carrirea W, Lalrokimia, Singhc B.P. *Cyanobacterial Lifestyle and its Applications in Biotechnology*. 2022;159-178.
3. Rasul F, You D, Jiang Y, Liu X, Daroch M. *Applied Microbiology and Biotechnology*. 2024;108-270.
4. Waditee-Sirisatthaa R, Kageyama H. *Cyanobacterial Physiology*. 2022;85-99.
5. Mehetrea Gajanan T, Zothanpuiab, Dekaa P, Carrirea W, Lalrokimia, Singhc Bhim P. *Cyanobacterial Lifestyle and its Applications in Biotechnology*. 2022; 159-178.
6. George C, Kortheerakul C, Khunthong N, Sharma C, Luo D, Chan KG, Daroch M, Hyde KD, Lee PKH, Goh KM, Waditee-Sirisattha R, Pointing SB. *Environmental Microbiome*. 2025;20(1):50.
7. Kanokratana P, Chanapan S, Pootanakit K, Eurwilaichitr L. J. *Basic Microbiol*. 2004;44(6):430-444.
8. Samsri S, Deprom T, Kortheerakul C, Sirisattha S, Pointing B. S, Kageyama H, Waditee-Sirisattha R. *Engineering Microbiology*. 2025;3.
9. Rippka R, Deruelles J, Waterbury J.B, Herdman M, Stanier R.Y, *Journal of General MicrobioLogy* 1979;111:1-61.
10. Herdman M, Castenholz R.W, Iteman I, Waterbury J.B, Rippka R. Subsection I: order “Chroococcales” Wettstein 1924, emend. Rippka, Deruelles, Waterbury, Herdman, Stanier 1979, in: Boone D.R, Castenholz, R.W. & Garrity, G.W. (Ed.), *Bergey’s manual of systematic bacteriology*. 2:1. The archaea, cyanobacteria and deeply branched bacteria, Springer-Verlag, New York, 2001;776.
11. Ngoennet S, Nishikawa Y, Hibino T, Waditee-Sirisattha R, Kageyama H. *Methods and Protocols*. 2018;1:46.
12. Saitou N, Nei M, *Molecular Biology and Evolution*. 1987;4(4):406-425.
13. Felsenstein J. *Evolution*. 1985;39:783-791.
14. Kumar S, Stecher G, Suleski M, Sanderford M, Sharma S, Tamura K. *Molecular Biology and Evolution* 2024;4:1-9.
15. Amarouche-Yala S, Benouadah A, Bentabet Abd El O, Lopez-Garcia P. *Extremophiles*. 2014;18:1035-1047.
16. Prihantini Betawati N, Sjamsuridzal W, Yokota A. *AIP Conference Proceedings*. 2016.
17. Yurista M, Prihantini. B. N, *AIP Conference Proceedings*. 2018.
18. Karsten U, Sawall T, Wiencke C, *Phycological Research*. 1998;46:271–279.
19. Choi S, Lee J.H, Oh S.W, Yu E, Kwon K, Jang, S.J, Shin D.S, Moh S.H, Lee J, *marine drugs*. 2023;21:121.



PHENOTYPIC VARIATION AND PLASTICITY OF ROOT HAIR TRAITS IN AUSTRALIAN DURUM WHEAT (*Triticum turgidum* subsp. *Durum*) UNDER PHOSPHORUS DEFICIENCY

Sukrita Majak,¹ Samir Alahmad,² Lee Thomas Hickey,² Alexander Bucksch,^{3,4} Patompong Johns Saengwilai^{1,*}

¹ Department of Biology, Faculty of Science, Mahidol University, 10400 Thailand

² Queensland Alliance for Agriculture and Food Innovation, The University of Queensland, St Lucia, Brisbane, QLD 4072, Australia

³ School of Plant Sciences, The University of Arizona, AZ, 85721 USA

⁴ Bio5 Institute, The University of Arizona, AZ, 85721 USA

*e-mail: patompong.sae@mahidol.edu

Abstract:

Durum wheat (*Triticum durum* L.) is an important cereal crop in arid and semi-arid regions. However, its yields can be greatly reduced under phosphorus (P) deficiency. Root hairs play an important role in the uptake of water and nutrients by expanding root surface areas, which could mitigate stresses. The phenotypic diversity and plasticity of root hair traits in durum wheat, despite their importance for nutrient uptake, are still largely unexplored. This study evaluated root hair length (RHL), root hair density (RHD), and root hair diameter in twelve parental genotypes, including two Australian cultivars and ten ICARDA founder lines, under P-sufficient (0.2 mM) and P-deficient (0 mM) hydroponic conditions. Significant genotypic variation was observed for RHL and RHD responses to P availability, while RH diameter remained stable. Under P deficiency, DBA Aurora showed a 16.34% reduction in RHL. Among ICARDA lines, Fastoz03B had the largest decrease in RHL by 65.73%, while Outrob4 increased RHL by 44.41%. Plasticity analysis revealed diverse patterns, such as Fastoz07 had high plasticity, while DBA Aurora had low plasticity in RHL. These findings demonstrate diversity in root hair phenotypes and plasticity, providing potential targets for breeding durum wheat with improved P-use efficiency in P-deficient environments.

Introduction:

Durum wheat (*Triticum durum* L.) is an important staple crop in many arid and semi-arid regions of the world. It also plays an important role in agriculture and food production, as it is a key ingredient in pasta and bread [1]. However, its production is increasingly challenged by both biotic and abiotic stresses, among which phosphorus (P) deficiency is a major limiting factor. These challenges are further intensified by climate change and the ongoing degradation of agricultural soils [2]. P is an essential macronutrient required for plant growth and development at all stages, as it plays a key role in many metabolic processes, including the synthesis of DNA and RNA [3]. In wheat, P deficiency has been associated with stunted growth, chlorosis, delayed flowering, and disruptions in physiological and biochemical functions, ultimately leading to reduced yield [4]. Severe phosphorus deficiency has been reported to cause wheat yield reductions of up to 57% compared with P-sufficient conditions [5]. To mitigate P deficiency, phosphorus fertilizers are widely used in many areas. However, this solution is not a long-term and sustainable solution, as costs tend to be high as P demand increases in each area, and this increases the risk of eutrophication of surface waters [6]. Therefore, it is essential to explore sustainable strategies that maintain crop productivity while minimizing environmental impact. One of the strategies is the development of plant breeding programs targeting P-efficient traits.

Root hairs are lateral extensions of epidermal cells that contribute to increasing the root surface for water and nutrient uptake, since root hairs can cover up to 90% of the root



surface, facilitating intimate contact with the soil [7-9]. This enlarged surface is particularly critical for the efficient uptake of relatively immobile nutrients, such as P, which often exist in limited availability within the soil solution and are predominantly taken up through the root surface in direct contact with the soil [10, 11]. Under P-deficient conditions, it has been reported that up to 90% of total P uptake by plants can occur through root hairs. Furthermore, root systems possessing root hairs have been shown to absorb approximately 78% more P compared to those lacking root hairs [12–14]. Due to their direct and crucial function in nutrient acquisition under P-limited conditions, studying root hair traits will be useful for future plant breeding.

Previous studies have already linked root hair traits to improved P uptake efficiency, enhanced grain yield, and better water relations, highlighting their potential as breeding targets [15–17]. For example, the expression of the *TaRSL4* gene has been positively correlated with increased RHL in both diploid and allotetraploid wheat. Interestingly, it has been reported that under nutrient-poor conditions, the overexpression of the *TaRSL4-A* homologue led to enhanced RHL and contributed to increased shoot fresh biomass [18]. This gene also shows higher expression under water-deficient conditions, suggesting a dual role in adaptation to multiple stresses. While traits such as RHL and RHD have been extensively studied for their contributions to nutrient and water uptake, research on RH diameter remains limited. This trait may represent a novel adaptive characteristic for coping with nutrient-deficient environments but its relevance for breeding nutrient-efficient wheat has not been thoroughly investigated. To begin addressing this knowledge gap, we evaluated 12 parental genotypes of durum wheat, many of which are part of or related to the broader NAM population previously characterized for other root traits (e.g., [19, 20]). This specific set of genotypes was selected to characterize the range of variation in root hair morphology and phenotypic plasticity in response to P availability. While high plasticity is generally desirable for adaptation to fluctuating environments, understanding the inherent plasticity of these diverse lines is crucial for identifying genotypes with optimal root hair strategies and for informing future genetic studies. This detailed phenotypic characterization provides a robust foundation for subsequent, more complex genetic analyses aimed at gene discovery.

Methodology:

Plant material

A total of 12 parental lines were evaluated for RHL, RHD, and RH diameter under P-deficient and P-sufficient conditions. These included two Australian cultivars, DBA Aurora and Jandaro, known for their superior grain quality, and ten founder lines from the International Center for Agricultural Research in the Dry Areas (ICARDA) in Morocco, including Fastoz02, Fastoz03B, Fastoz06, Fastoz07, Fastoz08, Fastoz10, Outrob4, Fadda98, Fastoz01, and Fastoz03A, which were selected for their drought tolerance and disease resistance [19].

Plant growth conditions

Plants were grown under controlled laboratory conditions at Mahidol University's Salaya Campus. Seeds were surface-sterilized in 10% sodium hypochlorite (NaClO) for 5 minutes, followed by 5–6 rinses with distilled water. All seeds were pre-germinated for 3 days at 25°C in roll-up paper under natural light. Subsequently, five uniformly germinated seeds per line were transferred to new roll-ups and grown for 14 days at 25°C under continuous light. This growth regime was adapted from speed breeding protocols, which utilize extended photoperiods to accelerate plant growth and development, especially in long-day crops, including wheat [21]. In this study, it was applied to facilitate precise early-stage phenotyping of root hair traits within a short 14-day growth period. The roll-ups were placed upright in



plastic containers containing 2 L of nutrient solution. A 20% Hoagland solution, modified for optimal wheat growth according to [22], was used. In the P-sufficient condition, phosphorus was supplied normally (0.2 mM); in the P-deficient treatment, phosphorus was omitted. The pH of the solution was adjusted to 5.5 using HCl and KOH.

Plant sampling and measurement

Two weeks after transplanting, when plants reached the early tillering stage, five healthy seedlings per genotype were harvested for analysis. Roots were preserved in 70% ethanol for root hair analysis [23]. Root hairs were stained using a 0.1% (w/v) Toluidine Blue solution, rinsed with distilled water, and imaged under a light compound microscope (ZEISS Primo Star) equipped with a digital camera. Images were captured from the middle region of the root, where root hairs were fully developed. For each root segment, the five longest root hairs were measured to determine RHL. RHD was assessed by counting the number of root hairs within a 1 mm region at two separate points along the root. For the RH diameter, five root hairs were selected as representative, and the proximal, middle, and distal parts of the root hairs were measured. All measurements were conducted using ImageJ software.

Plasticity of root hair

In this study, root phenotypic plasticity was defined as the response of root hair growth, including length, density, and diameter, to a P deficiency condition compared with the P sufficiency conditions according to the equation below [24]

Statistical analysis

Statistical calculations are performed in © R 4.0.4 statistical software (R core team 2020). The Shapiro-Wilk normality test was used to determine normal distribution, t-test, two-way ANOVA (p-value), and a least significant difference (LSD) was selected to be used in the data analysis.

Results and Discussion:

Phenotypic variation of RH traits under P-sufficient and P-deficient conditions

Under P-deficient conditions, an average value of RHD of the parental lines significantly decreased from 34.38 ± 1.08 to 28.27 ± 0.96 hair/mm, representing a 17.78% reduction compared to the P-sufficient condition (Figure 2B). In contrast, RHL and RH diameter showed no significant overall difference between the two P conditions. However, a significant genotype x condition interaction was found for RHL ($p < 0.05$), indicating that the effect of P-deficiency on RHL is dependent on the specific genotype. For example, DBA Aurora exhibited a reduction in RHL by 16.34% under P deficiency, while Jandaroi showed no change. Among the ICARDA founder lines, significant differences in RHL between P treatments were observed in four genotypes, including Fastoz03B, Fastoz07, Fastoz10, and Outrob4. Fastoz03B and Fastoz10 had longer RHL under P-sufficient conditions, with Fastoz03B showing the largest reduction among all genotypes (65.73%) under P deficiency. Conversely, Fastoz07 and Outrob4 had longer RHL under P-deficient conditions, with Outrob4 increasing by 44.41% (Figure 3A). In terms of RHD, DBA Aurora again showed the strongest reduction (36.75%), and significant declines were also observed in Fastoz03B, Fastoz06, and Fadda98 which Fastoz03B had the largest RHD reduction (15.33%) (Figure 3B). For RH diameter, on the other hand, no significant differences were observed in any of the parental lines between P-sufficient and P-deficient conditions (Figure 3C).

The parental lines exhibited phenotypic variation in root hair traits under P deficiency. These results are consistent with those reported in other crop species. Interestingly, our study revealed that most parental durum wheat genotypes reduced RHL and RHD under P

deficiency. These findings diverge from those reported in rice [25], barley [26,27], and spring wheat, where RHL increased under low-P conditions [28]. Increased RHL and RHD could enhance P acquisition, primarily due to an increase in root surface area. This can be attributed to several factors, including increased rhizosheath formation, which allows for better root particle retention and improved water, nutrient, and P uptake [29–31]. Interestingly, in our study, most parental lines showed reduced RHD and no difference in RH diameter under P deficiency. Plants employ diverse strategies to cope with nutrient stress, beyond just root hair modifications, such as enhancing rhizosphere acidification or altering overall root system architecture [31]. However, the metabolic cost of soil exploration is also an important consideration for plants under P deficiency. Developing and maintaining extensive root structures, including dense root hairs, requires substantial carbon allocation [10,32]. Therefore, plants might strategically regulate root hair number and size to avoid excessive metabolic expenditure and to minimize self-competition for P, thereby optimizing P acquisition efficiency under limiting conditions [33]. This suggests a reduction or lack of increase in RHD and diameter under P deficiency in some genotypes, potentially reflecting different strategies for adaptation under nutrient-limited conditions. ICARDA founder lines are known to be drought-tolerant but most of them had shorter RHL in P deficiency. While long and dense root hairs could be beneficial for nutrient uptake, they also increase the root surface area and its contact with the soil which could be detrimental under drought [34]. Balancing adaptation strategies or being “plastic” play important roles in surviving among different stresses.

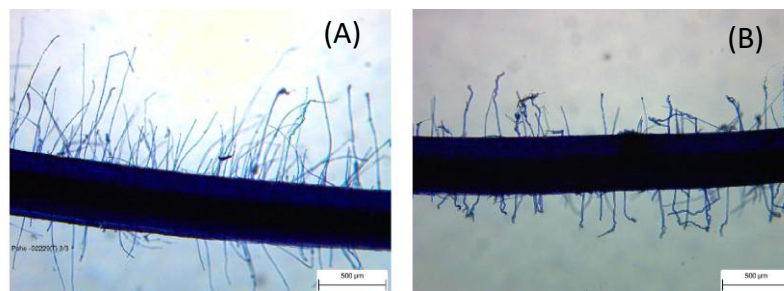


Figure 1.

Phenotypic variation of root hair traits in Australian durum wheat under P-deficient conditions. Representative images of dense root hair (A) and less root hair (B)

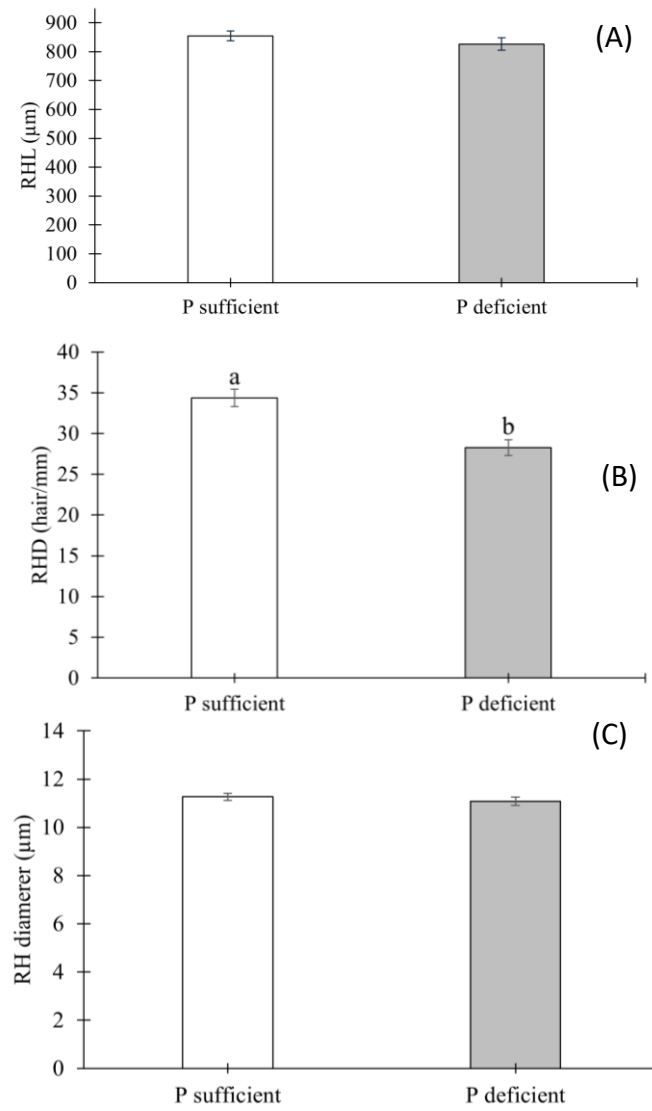


Figure 2.

Root hair traits under P-sufficient and P-deficient conditions for: (A) RHL, (B) RHD, and (C) RH diameter, t-test ($p < 0.05$)

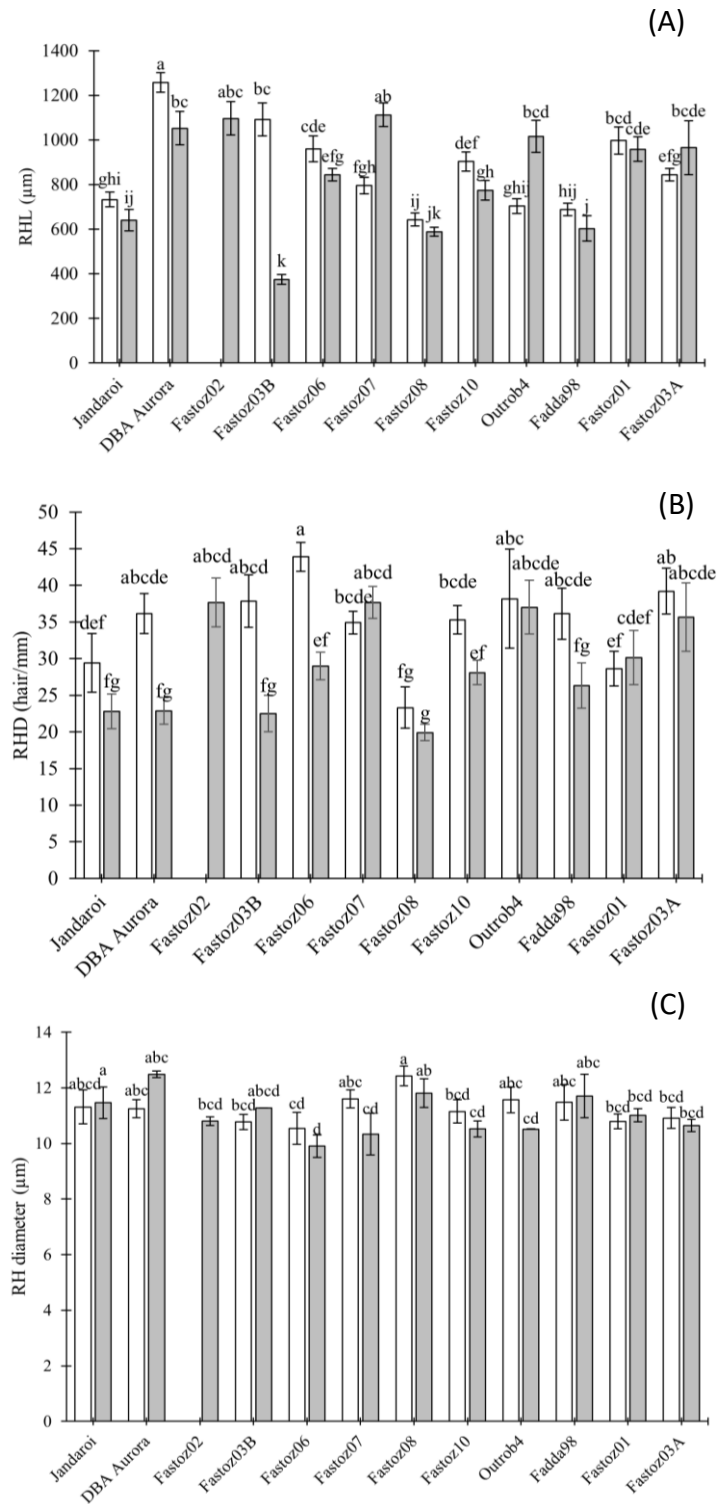


Figure 3.

RHL (A), RHD (B), and RH diameter (C) of twelve parental genotypes. Values are means \pm SE, where lines labelled with/or sharing the same letters are not significantly different according to the least significant difference (LSD) test ($P \leq 0.05$). The white bars displayed the value of the P-sufficient condition, and the grey bars displayed the value of the P-deficient condition. Fastoz02 (P-sufficient) was excluded due to seed contamination issues.

Phenotypic plasticity of RH traits in parental lines

Root plasticity was described as the ability of plant roots to modify their growth and development in response to changing environmental conditions [35]. In this work, plasticity was used to assess the relative change in traits under P-deficient conditions compared with the P-sufficient control. A positive plasticity value indicates a reduction in RHL, RHD, or RH diameter under P deficiency, whereas a negative value reflects an increase in these traits.

Across the parental genotypes, only a few lines showed significant plastic responses in RHL under P deficiency, highlighting that not all genotypes respond equally to nutrient stress. For RHL plasticity, among these, Outrob4 and Fastoz07 exhibited high negative plasticity values. This adaptive response is likely to enhance P acquisition by expanding the root surface area, facilitating greater nutrient uptake. Conversely, Fastoz03B displayed significantly high positive plasticity value, with a marked reduction in RHL under P deficiency. Additionally, DBA Aurora and Fastoz10 displayed a low positive plastic value response. Such a response may limit nutrient acquisition and suggest a less advantageous adaptation under low-phosphorus environments. (Figure 4A). For RHD plasticity, DBA Aurora, Fastoz06, Fadda98, and Fastoz03B show high positive plasticity values (Figure 4B). However, for RH Diameter plasticity, no genotypes showed a statistically significant plastic response (Figure 4C). Additionally, Fastoz03B exhibited the widest range in both RHL and RHD plasticity, indicating high variability in response to P availability.

The phenotypic plasticity of root hair traits is a crucial adaptive mechanism for plants, especially for immobile organisms facing heterogeneous nutrient availability in soil [35]. Our findings highlight the diverse utility of this plasticity, demonstrating that some responses are highly beneficial while others can be harmful. For instance, Fastoz07 and Outrob4 exhibited high, beneficial RHL plasticity, an adaptive response that helps plants efficiently acquire immobile nutrients like P by expanding the soil volume accessible for depletion [36]. In contrast, Fastoz03B also displayed high plasticity, but its response may be detrimental to the P acquisition efficiency of the plant due to short root hair. Meanwhile, DBA Aurora and Fastoz10 exhibited low RHL plasticity, indicating a minimal plastic response to P availability, which could limit their adaptive capacity in fluctuating environments where dynamic changes are required for efficient resource capture. For RHD, although an increase under P deficiency is generally considered advantageous, our results highlight that plasticity involves trade-offs. Maintaining dense root hairs requires substantial carbon allocation, and downregulation of RHD or RH diameter may represent a strategic adjustment to reduce metabolic costs and avoid self-competition for P [10, 32–33, 36]. Collectively, our results suggest that plasticity is not always beneficial. The adaptive value depends on the environment and direction of the plastic response and whether it enhances nutrient acquisition efficiency under phosphorus deficiency. In this case, adaptive plasticity in traits like RHL appears to provide an efficient strategy for P acquisition, which supports the idea that plants regulate their root traits by weighing the trade-off between metabolic cost and nutrient gain.

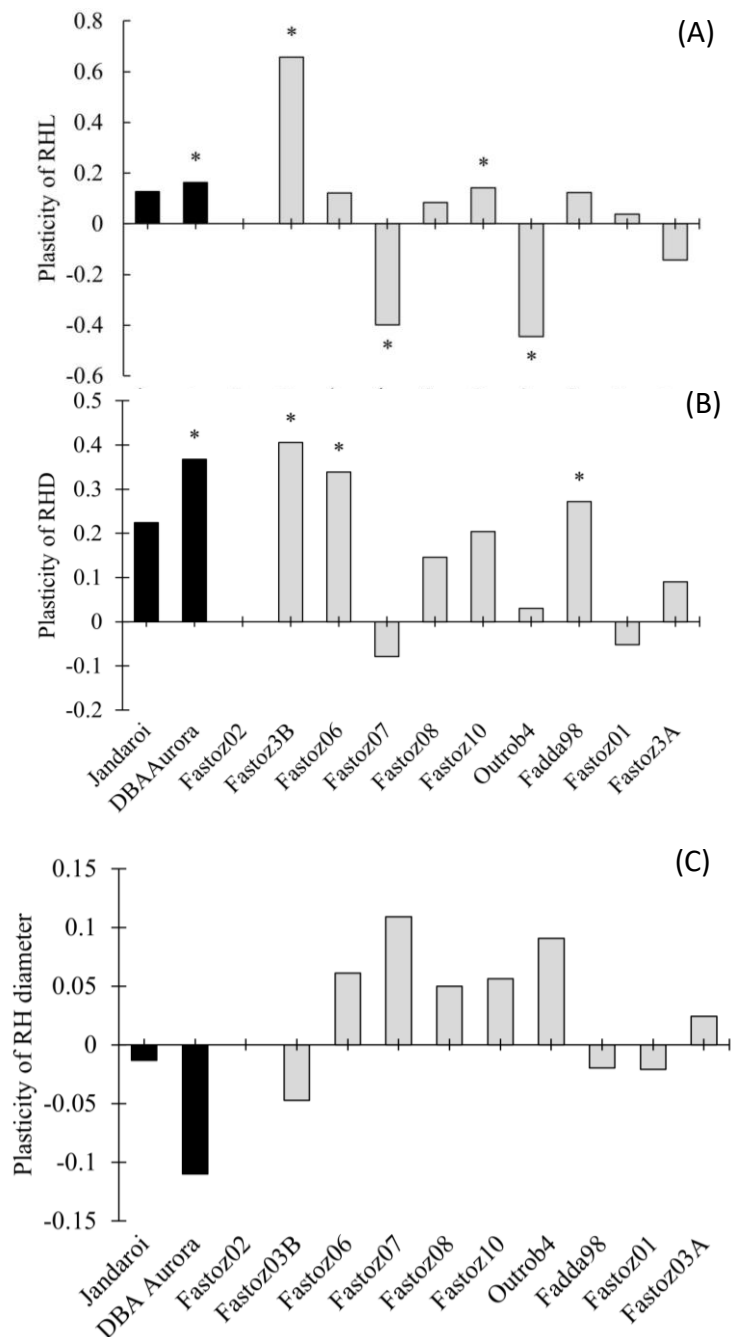


Figure 4.

Phenotypic plasticity of RHL (A), phenotypic plasticity of RHD (B), and phenotypic plasticity of RH diameter (C) in twelve parental genotypes. The black bars displayed the value of Australian cultivars, and the grey bars displayed the value of ICARDA lines. An asterisk (*) above a bar indicates a statistically significant plastic response ($p < 0.05$).

Fastoz02 (P-sufficient) was excluded due to seed contamination issues.

Conclusion:

Parental lines of the Australian durum wheat showed diverse responses in root hair traits under different P conditions. Unlike the commonly reported trend of increased RHL and RHD under P deficiency, several genotypes in this study showed reductions in RHD and no change in RH diameter, indicating alternative strategies for P acquisition. The Australian

cultivars, DBA Aurora and Jandaroi, known for high grain quality but sensitive to crown rot, displayed distinct patterns of plasticity, with DBA Aurora showing a substantial reduction in RHD under P deficiency. In contrast, ICARDA founder lines, originally developed for drought and heat adaptation and tolerance to soil-borne diseases, expressed significant plasticity in RHL, consistent with their broader stress tolerance. This genetic variation represents a promising resource for breeding new durum wheat varieties with improved phosphorus-use efficiency and resilience to multiple environmental challenges.

Acknowledgements:

This research is supported by the Faculty of Graduate Studies, Mahidol University.

References:

1. Grosse-Heilmann M, Cristiano E, Deidda R, Viola F. Vol. 17, Resources, Environment and Sustainability. Elsevier B.V.; 2024.
2. Alewell C, Ringeval B, Ballabio C, Robinson DA, Panagos P, Borrelli P. *Nat Commun.* 2020 Sep 11;11(1):4546.
3. Khan F, Siddique AB, Shabala S, Zhou M, Zhao C. *Plants.* 2023 Aug 3;12(15):2861.
4. Xu H, Hassan MA, Sun D, Wu Z, Jiang G, Liu B, et al. *Front Plant Sci.* 2022 Feb 11;13.
5. Ortiz-Monasterio JI, Pena RJ, Pfeiffer WH, Hede AH. *Proc 5th Int Triticale Symp, Radzików, Poland.* 2002 Jun 30–Jul 5;1–6.
6. Ros MBH, Koopmans GF, van Groenigen KJ, Abalos D, Oenema O, Vos HMJ, et al. *Sci Rep.* 2020 Dec 1;10(1).
7. Bates TR, Lynch JP. *Plant Soil.* 2001;236(2):243–50.
8. Duddek P, Ahmed MA, Javaux M, Vanderborght J, Lovric G, King A, et al. *New Phytologist.* 2023 Dec 31;240(6):2484–97.
9. Xiao S, Liu L, Zhang Y, Sun H, Zhang K, Bai Z, et al. *J Agron Crop Sci.* 2020 Dec 13;206(6):679–93.
10. Vance CP, Uhde-Stone C, Allan DL. Vol. 157, *New Phytologist.* 2003. p. 423–47.
11. Lynch JP. *Plant Physiol.* 2011;156(3):1041–9.
12. Barley KP, Rovira AD. *Commun Soil Sci Plant Anal.* 1970 Sep 11;1(5):287–92.
13. Brown LK, George TS, Thompson JA, Wright G, Lyon J, Dupuy L, et al. *Ann Bot.* 2012;110(2):319–28.
14. Raghothama KG. In 2005. p. 353–78.
15. Delhaize E, Rathjen TM, Cavanagh CR. *J Exp Bot.* 2015 Aug;66(15):4527–36.
16. Horn R, Wingen LU, Snape JW, Dolan L. *J Exp Bot.* 2016 Aug;67(15):4535–43.
17. Singh Gahoonia T, Care D, Nielsen NE. Vol. 191, *Plant and Soil.* Kluwer Academic Publishers; 1997.
18. Maqbool S, Saeed F, Raza A, Rasheed A, He Z. *Plants.* 2022 Aug 29;11(17):2235.
19. Alahmad S, El Hassouni K, Bassi FM, Dinglasan E, Youssef C, Quarry G, et al. *Front Plant Sci.* 2019 Apr 10;10.
20. van der Bom FJT, Williams A, Raymond NS, Alahmad S, Hickey LT, Singh V, et al. *Plant Soil.* 2024 Jul 1;500(1–2):69–89.
21. Watson A, Ghosh S, Williams MJ, Cuddy WS, Simmonds J, Rey MD, et al. *Nat Plants.* 2018 Jan 1;4(1):23–9.
22. Guo Y, Kong F mei, Xu Y feng, Zhao Y, Liang X, Wang Y ying, et al. *Theoretical and Applied Genetics.* 2012 Mar 17;124(5):851–65.
23. Okano N, Goto R, Kato T, Saisho D, Kato K, Miura H, et al. *Plant Soil.* 2020 Jul 23;452(1–2):171–84.



24. Sandhu N, Raman KA, Torres RO, Audebert A, Dardou A, Kumar A, et al. *Plant Physiol.* 2016 Aug 2;171(4):2562–76.
25. Vejchasarn P, Lynch JP, Brown KM. *Rice.* 2016 Dec 13;9(1):29.
26. Brown LK, George TS, Thompson JA, Wright G, Lyon J, Dupuy L, et al. *Ann Bot.* 2012 Jul 1;110(2):319–28.
27. Xie Y, Rathinasabapathi B, Schaffer B, Mylavarapu R, Liu G. *Agronomy.* 2020 Oct 13;10(10):1556.
28. Wang YS, Jensen LS, Magid J. *Plant Soil Environ.* 2016 Dec 31;62(12):540–6.
29. Haling RE, Brown LK, Bengough AG, Young IM, Hallett PD, White PJ, et al. *J Exp Bot.* 2013 Sep;64(12):3711–21.
30. Basirat M, Mousavi SM, Abbaszadeh S, Ebrahimi M, Zarebanadkouki M. *Plant Soil.* 2019 Dec 29;445(1–2):565–75.
31. Lyu Y, Tang H, Li H, Zhang F, Rengel Z, Whalley WR, et al. *Front Plant Sci.* 2016 Dec 21;7.
32. Lynch JP, Ho MD. *Plant and Soil.* 2005. p. 45–56.
33. Ma Z, Bielenberg DG, Brown KM, Lynch JP. *Plant Cell Environ.* 2001 Apr;24(4):459–67.
34. Duddek P, Ahmed MA, Javaux M, Vanderborght J, Lovric G, King A, et al. *New Phytologist.* 2023 Dec 31;240(6):2484–97.
35. Yetgin A. *Ecological Frontiers.* 2024 Feb;44(1):112–9.
36. Zhu J, Zhang C, Lynch JP. *Functional Plant Biology.* 2010;37(4):313.



UNVEILING THE QUANTITATIVE LANDSCAPE OF GINGEROL AND ITS DERIVATIVES IN THAI GINGER (*Zingiber officinale* Roscoe)

Kronsirinut Rothjanawan¹, Nattakanwadee Khumpirapang², Alisa Kongthong³, Pimprapa Chaijak^{3,*}

¹ Department of Computer Engineering, Faculty of Engineering, Princess of Naradhiwas University, Naradhiwat 96000, Thailand

² Department of Pharmaceutical Chemistry and Pharmacognosy, Faculty of Pharmaceutical Science, Naresuan University, Phitsanulok 65000, Thailand

³ Department of Biological Science, Faculty of Science and Digital Innovation, Thaksin University, Phatthalung 93210, Thailand

*e-mail: pimprapa.c@tsu.ac.th

Abstract:

The ginger rhizome is consumed worldwide as a spice and medicine owing to its sensory and bioactive compounds, which are mainly phenolic compounds known as gingerols. Among these, 6-gingerol is a major pharmaceutical component in the ginger rhizome. This study aimed to profile six major gingerol-related metabolites (6-gingerol, 8-gingerol, 10-gingerol, 6-shogaol, 8-shogaol, and 10-shogaol) in ginger samples collected from various regions across Thailand using HPLC. The analysis of total gingerols and total shogaols revealed significant variation in metabolite concentrations among the samples, largely influenced by regional growth conditions. Notably, the Naradhiwat extract contained the highest level of total gingerols (6-gingerol, 8-gingerol, and 10-gingerol), followed by the Phitsanulok extract. In contrast, the concentration of 8-shogaol displayed minimal variation across regions, suggesting limited sensitivity to environmental factors compared to other analogues. These findings contribute to a better understanding of the chemical diversity of Thai ginger and provide a basis for its potential applications in nutraceutical and pharmaceutical industries.

Introduction:

Ginger (*Zingiber officinale* Roscoe) is widely recognized for its characteristic pungency and extensive use in traditional medicine. Numerous studies have documented its therapeutic potential, including anti-inflammatory [1], antioxidant [2], and cardioprotective properties that support cardiovascular and circulatory functions [3]. Additional reported bioactivities comprise analgesic and antipyretic effects [4], anticancer potential [5] and antimicrobial actions [6].

In fresh ginger rhizome, the distinctive sensory characteristics and therapeutic effects are primarily associated with gingerols, a class of O-methoxyphenyl alkyl ketones [7-8]. These compounds vary structurally according to the length of their alkyl side chains with 6-gingerol, 8-gingerol, and 10-gingerol identified as the predominant constituents [9].

During the drying process, gingerols undergo thermal dehydration to form shogaols, primarily through the elimination of a hydroxyl group and an adjacent hydrogen atom from the alkyl side chain. This transformation typically occurs at approximately 120 °C over a period of 6 hr. This structural transformation introduces an alkene fraction, resulting in metabolites that are not only more pungent but also frequently reported to possess enhanced biological activities [10-13].

Several investigations have examined the distribution of gingerols and their derivatives (6-gingerol, 8-gingerol, 10-gingerol, 6-shogaol, 8-shogaol, and 10-shogaol) in ginger cultivated across different regions, including Jamaica [14], Cuba [15], Malaysia [16], Hawaii [17], Guinea [18] and China [18]. A more comprehensive analyzed 80 fresh ginger samples from China, India, Malaysia, Thailand and Vietnam, demonstrating that the relative composition of gingerols and shogaols could serve as a metabolite “fingerprint” to

differentiate samples according to their geographical origin [19]. However, limited data are available regarding the gingerol and shogaol content of Thai ginger cultivated in different regions of Thailand.

Among the phenolic compounds in ginger certain molecules such as gingerols (GNs), enhance its nutraceutical potential. Gingerols possess chemical structures associated with antioxidant activity and have been investigated for their role in cancer prevention [20]. Ginger also contains various phytochemicals including 4-gingerol, 6-gingerol, 8-gingerol, 10-gingerol and 12-gingerol, and shogaols such as 6-shogaol, 8-shogaol and 10-shogaol [21].

This study aimed to characterize the gingerol and shogaol content in dried Thai ginger samples, providing baseline data on the variation of these bioactive compounds across different cultivation regions.

Methodology:

1. Sample collection and preparation

The 8-month-old ginger rhizomes (Figure 1) were collected from the various regions of Thailand such as Northern (Phitsanulok province), Eastern (Trat province), Northeastern (Si Sa Ket province) and Southern (Narathiwat province).



Figure 1.

The 8-month-old ginger rhizomes used in this experiment.

The rhizome samples were cut into small pieces and dried at approximately 50 °C for 72 hr or until completely dry (Figure 2A). The samples were ground into powder before being used in the next section (Figure 2B).



Figure 2.

The dried ginger rhizome samples (2A) and dried ginger rhizome powder (2B).

2. Extraction

Approximately 12.50 g of powdered ginger sample was suspended in 875 mL of 90% ethanol and the extraction was carried out at 60 °C for 30 min, repeated 3 times to ensure maximum yield of the crude extract. The crude extract was then evaporated under a vacuum using a

rotary evaporator at 50 °C . The dried extracts (Figure 3) were kept at 4 °C until the next section. The extract yield was calculated according to Eq. (1).



Figure 3.
The dried extract of ginger rhizome.

$$\text{Extract yield (\%)} = (W_{\text{crude}} / W_{\text{sample}}) \times 100 \quad (1)$$

Where W_{crude} is the weight of crude extract (g) and W_{sample} is the weight of initial sample (g)

3. Gingerol profiling

Total gingerols such as 6- gingerol, 8- gingerol, and 10-gingerol and shogaols such as 6-shogaol, 8-shogaol, and 10-shogaol were quantified using an HPLC system equipped with a vacuum degasser, quaternary pump, column compartment, photodiode array detector, and autosampler (Young In Chromass, South Korea). Separation was performed on a Luna C18 column (150 × 4.6 mm, 5 μm) with a C18 guard column (10 × 4.6 mm, 5 μm) using a water–acetonitrile gradient over 30 min. Five μL sample was injected into a column. The separation was performed by using a flow rate of 1 mL/min at 30 °C, and the products were detected at A282.

4. Statistic analysis

All experiments were performed in triplicate. Statistical analysis was conducted using SPSS software (SPSS Inc., United States).

Results and Discussion:

The extract yield of the ginger rhizome was evaluated and calculated after the extraction process. The highest extract yield (18.88±0.01%) was obtained from the sample collected in Narathiwat province, followed by those from Trat (13.72±0.00%), Si Sa Ket (11.61±0.00%), and Phitsanulok (8.23±0.02%) provinces, respectively (Figure 4).

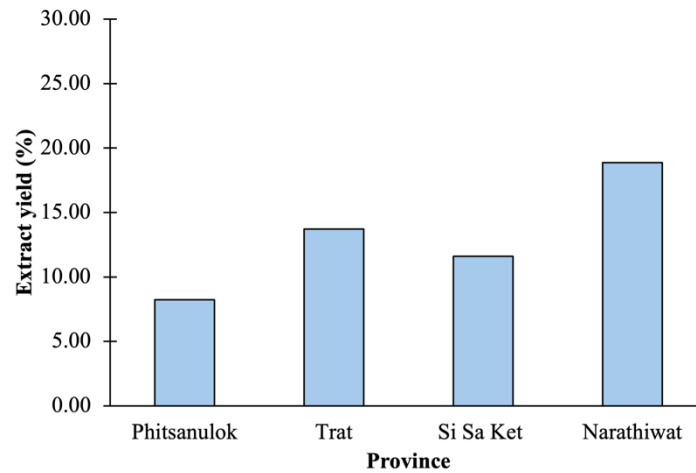


Figure 4.

The extract yields of various rhizome.

A 50 µg/mL of gingerol standards (6-gingerol (6G), 8-gingerol (8G), 10-gingerol (10G), 6-shogaol (6SH), 8-shogaol (8SH) and 10-shogaol (10SH)) was injected into the HPLC under the same conditions used for the extracted samples to establish the gingerol profile. Figure 5 shows the resulting HPLC chromatogram of the standards.

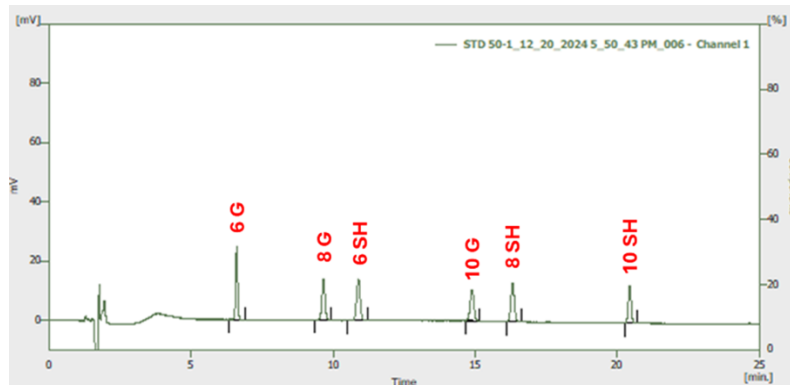


Figure 5.

The HPLC chromatogram of the gingerol standards.

A 10 mg/mL concentration of each sample was injected into the HPLC system. The chromatograms for each sample are displayed in Figure 6-9.

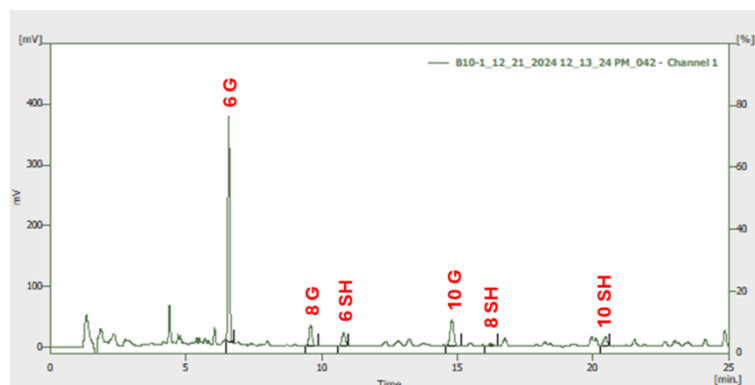


Figure 6.

The HPLC chromatogram of extracted rhizome ginger from Trat province.

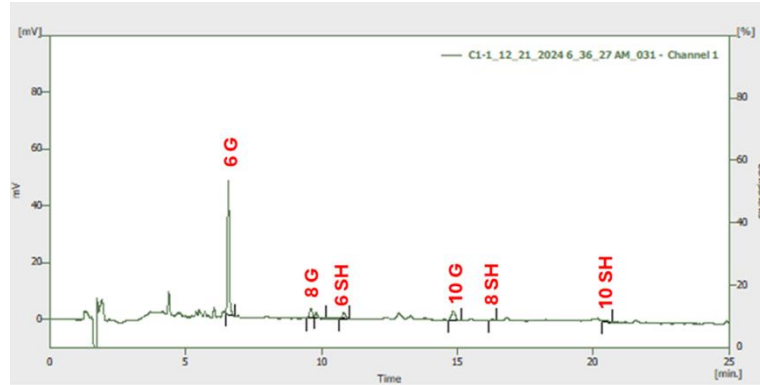


Figure 7.

The HPLC chromatogram of extracted rhizome ginger from Si Sa Ket province.

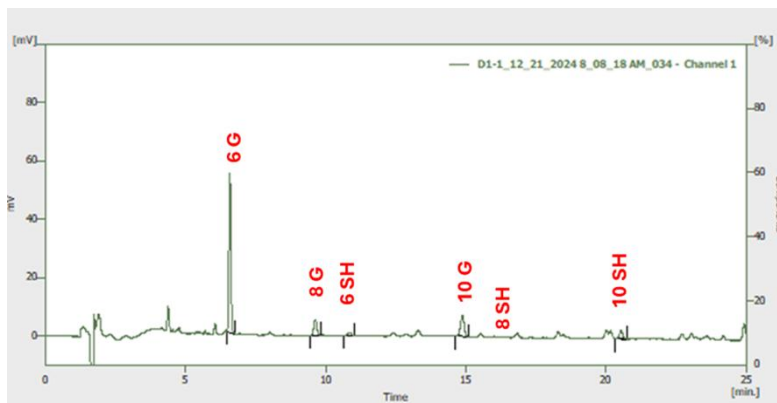


Figure 8.

The HPLC chromatogram of extracted rhizome ginger from Phitsanulok province.

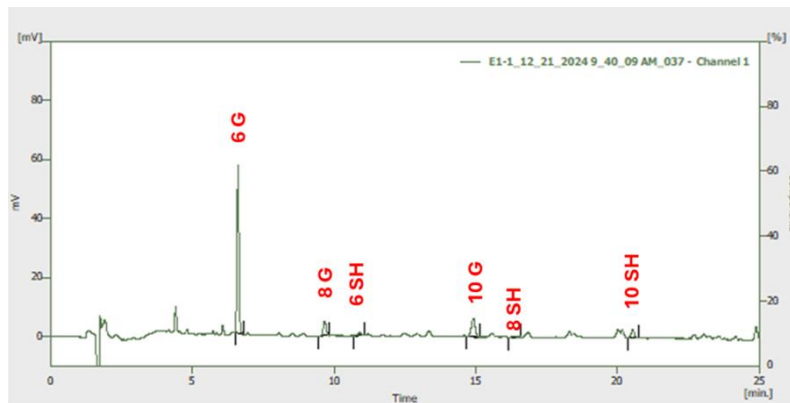


Figure 9.

The HPLC chromatogram of extracted rhizome ginger from Narathiwat province.

Table 1.

The contents of gingerols and shogaols in the extracted ginger rhizomes (p-value < 0.025).

Total gingerols/ Total shogaols	Areas (Province)			
	Trat (% w/w ± SD)	Si Sa Ket (% w/w ± SD)	Phitsanulok (% w/w ± SD)	Narathiwat (% w/w ± SD)
6-gingerol	6.94±0.09	9.74±0.51	10.91±0.02	11.94±0.13
8-gingerol	1.28±0.03	1.30±0.01	0.18±0.01	0.17±0.00
10-gingerol	1.96±0.03	1.57±0.01	3.17±0.03	2.80±0.05
6-shogaol	0.78±0.00	0.74±0.01	0.05±0.00	0.05±0.00
8-shogaol	0.13±0.00	0.10±0.00	N.D.	N.D.
10-shogaol	0.76±0.01	0.44±0.01	1.18±0.03	1.22±0.07
Total gingerols	10.19±0.13	12.62±0.51	14.27±0.04	14.91±0.16
Total shogaols	1.67±0.01	1.28±0.02	1.23±0.03	1.27±0.07

Across the 4 Thailand growing areas analyzed, 6-gingerol was the predominant metabolite in all extracts, followed by 10-gingerol. Total shogaols were an order of magnitude lower than total gingerols. On an extract-weight basis, total gingerols were highest in Narathiwat (14.91 % w/w), closely followed by Phitsanulok (14.27 %), whereas Trat showed the highest total shogaols (1.67 % w/w). Notably, 8-shogaol was not detected in the Phitsanulok and Narathiwat samples under our HPLC conditions. These province-level differences in both absolute levels and relative profiles (gingerols vs. shogaols) align with the well-documented influence of geographical origin and postharvest/processing conditions on ginger's pungent phenolics [22].

Large multi-origin surveys using HPLC-DAD/chemometrics (e.g., 80 fresh samples from China, India, Malaysia, Thailand, and Vietnam) demonstrated that the relative composition of 6- gingerol, 8-gingerol, 10-gingerol, and their dehydration products (shogaols) can fingerprint origin [22]. Our data show province-specific patterns like higher proportions of 6-gingerol and 10-gingerol with very low 6-shogaol in Phitsanulok and Narathiwat provinces that are consistent with origin-linked compositional signatures reported previously, although our values are expressed on an extract basis rather than raw tissue.

Comparisons with studies reporting concentrations in raw herb must be made cautiously because extraction solvents, drying regimes and the reporting basis (mg/g dry herb vs. % of extract) vary widely. For example, LC-PDA quantification in raw dried ginger reported approximately 9.30, 1.60, 2.30, and 2.30 mg/g (0.93, 0.16, 0.23, 0.23 % w/w) for 6-gingerol, 8-gingerol, 10-gingerol, and 6-shogaol that are lower than ours due to being measured per raw herb. Similarly, a capsule study quantified 2.15% w/w of 6-gingerol, 0.72% w/w of 8-gingerol, 1.78% w/w of 10-gingerol, and 0.37% w/w of 6-shogaol in commercial extract [23-24].

Our low shogaol levels and non-detects for 8-shogaol in 2 provinces likely reflect the mild drying protocol (approximately 50 °C) and extraction conditions used. Thermal studies show that gingerols dehydrate to shogaols during heating with shogaol formation increasing sharply at ≥100–130 °C and with longer times and oven or hot-air drying can specifically boost 6-shogaol, 8-shogaol and 10-shogaol. Therefore, the higher shogaol totals in Trat province may indicate subtle differences in pre-analytical handling (such as slightly higher effective temperatures, longer drying and storage times) or inherent varietal differences [25-



27]. Finally, our province-level variance is directionally consistent with prior origin-discrimination work that attributes compositional shifts to genotype, agro-climate, soil and postharvest handling.

Conclusion:

This study demonstrated that the concentrations of gingerol- and shogaol-related metabolites in Thai ginger vary considerably depending on the growing region. The highest levels of total gingerols were observed in samples from Narathiwat province followed by Phitsanulok province, highlighting the influence of regional growth conditions on metabolite accumulation. In contrast, 8-shogaol showed little regional variation, suggesting lower sensitivity to environmental factors compared to other analogues. Overall, these results provide important insights into the chemical diversity of Thai ginger and highlight its potential as a valuable source for nutraceutical and pharmaceutical applications.

Acknowledgements:

This research was supported by the Unit for the Management and Administration of Area-Based Development Funds (PMU).

References:

1. Grzanna R, Lindmark L, Frondoza CG. *J Med Food*. 2005; 8:125-132.
2. Siddaraju MN, Dharmesh SM. *Mol Nutr Food Res*. 2007; 51:324-332.
3. Ghayur MN, Gilani AH. 2005. *J Cardiovasc Pharmacol*. 2005; 45:74-80.
4. Ojewole JAO. *Phytother Res*. 2006; 20:764-772.
5. Prasad S, Tyagi AK. 2015. *Gastroenterol Res Pract*. 2015; 2015:142979.
6. Panpatil VV, Tattari S, Kota N, Nimgulkar C, Polasa K. 2013; 2:143-148.
7. Raghuvver KG, Govindarajan VS. *J Food Qual*. 1979; 2:41-54.
8. Kumara M, Shylajab M, Nazeem P, Babu T. *J Dev Drugs*. 2017; 6:1-6.
9. Yudthavorasit S, Wongravee K, Leepipatpiboon N. *Food Chem*. 2014; 158:101-111.
10. Ghasemzadeh A, Jaafar HZe, Baghdadi A, Tayebi-Meigooni A. *Molecules*. 2018; 23:1646.
11. Huang TC, Chung CG, Wang HY, Law CL, Chen HH. *Dry Technol*. 2011; 29:1884-1889.
12. Wohlmuth H, Leach DN, Smith MK, Myers SP. *J Agric Food Chem*. 2005; 53:5772-5778.
13. Jung MY, Lee MK, Park HJ, Oh EB, Shin JY, Park JS, Jung SY, Oh JH, Choi DS. *Food Sci. Biotechnol*. 2017; 27:687-693.
14. Salmon CAN, Bauley-Shaw YA, Hibbert S, Green C, Smith AM, Williams LAD. *Food Chem*. 2012; 131:1517-1522.
15. Pino JA, Marbot R, Rosado A, Batista A. *J Essent Oil Res*. 2004; 16:186-188.
16. Abd Malek SN, Ibrahim H, Sok Lai H, Guan Serm L, Kam Seng C, Ali NAM. *Malays J Sci*. 2005; 24:26687-26699.
17. Jolad SD, Lantz RC, Solyom AM, Chen GJ, Bates RB, Timmermann BN. *Phytochemistry*. 2004; 65:1937-1954.
18. Toure A, Xiaoming Z. *J Agron*. 2007; 6:350.
19. Yudthavorasit S, Wongravee K, Leepipatpiboon N. *Food Chem*. 2014; 158:101-111.
20. Mao QQ, Xu XY, Cao SY, Gen RY, Corke H, Li HB. *Foods*. 2019; 8:185.
21. Jesudoss VAS, Santiago SVA, Venkatachalam K, Subramanian P. *Gastrointestinal Tissue*. 2017; 1:287-297.
22. Yudthavorasit S, Wongravee K, Leepipatpiboon N. *Food Chem*. 2014; 158:101-111.



23. Lee S, Khoo C, Halstead CW, Huynh T, Bensoussan A. *J AOAC Int.* 2007; 90:1219-1226.
24. Zick SM, Djuric Z, Ruffin MT, Litzinger AJ, Normolle DP, Feng MR, Brenner DE. *Cancer Epidemiol Biomarkers Prev.* 2008:1930-1936.
25. Jung MY, Lee MK, Park HJ, Oh EB, Shin JY, Park S, Jung SY, Oh JH, Choi DS. *Food Sci Biotechnol.* 2017; 27:697-693.
26. Ghasemzadeh A, Jaafar HZE, Baghdadi A, Tayebi-Meigooni A. *Molecules.* 2018; 23:1646.
27. Ho SC, Su MS. *Int J Food Prop.* 2016; 19:1884-1898.



CHARACTERIZATION OF MULTI-STRESS TOLERANT PGPR FROM ORCHARD SOILS IN CHANTHABURI PROVINCE, THAILAND

Jirapat Chanthamalee^{1,*}, Winyou Puckdee¹, Chewa Thassana²

¹Department of Biology, Faculty of Science and Technology, Rambhai Barni Rajabhat University, Muang, Chanthaburi, 22000, Thailand

²Department of Physics and General Science, Faculty of Science and Technology, Rambhai Barni Rajabhat University, Muang, Chanthaburi, 22000, Thailand

*e-mail: jirapat.c@rbru.ac.th

Abstract:

Abiotic stresses are considered major factors in the reduction of plant yield and quality worldwide. Plant growth-promoting rhizobacteria (PGPR) have emerged as a sustainable alternative due to enhancing plant stress resilience. However, only a few studies have evaluated abiotic stress of PGPR strains from orchard soils which represent unique reservoirs of stress-adapted microbes. This study aimed to characterize nineteen PGPR isolates from orchard soils in Chanthaburi for their tolerance to various abiotic stresses and to identify elite candidates for bioinoculant development. They were screened for tolerance to salinity (7% NaCl), alkalinity (pH 12), acidity (pH 4), high temperature (45–50 °C), and drought stress simulated with PEG 6000. Collectively, sixteen isolates were found to withstand drought conditions, while eight PGPR isolates exhibited tolerance to alkaline pH levels, suggesting a high degree of adaptability. Among them, the MuD01-2 isolate exhibited multi-stress tolerance by showing robust growth at high NaCl concentrations, drought, and temperatures up to 50 °C. While NaD01-2 and ThD02-2 isolates demonstrated significant tolerance to acidic and alkaline environments, respectively. This research successfully identified PGPR with distinct and complementary stress-tolerant profiles. MuD01-2 stands out as a prime candidate for developing bioinoculants to promote sustainability and resilience in orchard management under changing climatic conditions.

Introduction:

Global warming and climate change are predicted to increase the frequency and intensity of abiotic stresses including drought, salinity, heat, and soil pH extremes [1]. This phenomenon threatens global agriculture and is responsible for an estimated 60–80% reduction in crop productivity [2]. Soil salinity is a global issue and results in a reduction of crop yields by approximately 18-21% of the world's cultivated land [2, 3]. This figure is expected to exceed 50% by 2050 [4]. These challenges correspond to the fact that Thailand is highly vulnerable to climate change impacts, particularly severe in durian and mangosteen orchards in eastern Thailand. This region, a major production hub for tropical fruits, faces increasing risks from fluctuations in rainfall, extreme heat, and climate variability. These problems lead to plant diseases and insect pests, resulting in low yields and low quality of products (e.g., large-sized durians with damaged texture, thick durian peel) [5, 6].

Plant growth-promoting rhizobacteria (PGPR) play an important role in sustainable agriculture by enhancing plant growth and stress tolerance [7]. These beneficial soil microbes may help plants to thrive under abiotic stress by improving stress tolerance through multiple mechanisms, including the production of phytohormones such as indole-3-acetic acid, improved nutrient uptake, and modulation of plant stress responses [7, 8]. Elite PGPR isolates with multi-stress tolerance are valuable for mitigating the adverse effects of abiotic factors on crop productivity, plant physiology, metabolism, and overall growth [4].

Despite extensive studies on PGPR in annual crops, the systematic characterization of multi-stress tolerant strains from the eastern orchard soils of Thailand remains limited. These complex ecosystems have been exposed to fluctuating moisture, temperature extremes,



salinity, and pH shifts. This has led to the selection of elite, stress-resilient strains from the under-explored microbial reservoirs [5, 9]. The nineteen isolates selected for this study have been previously characterized; all are known to produce catalase, while eight produce oxidase. Additionally, all 19 isolates produced exopolysaccharides (EPS) under simulated drought stress, with isolate MuD01-2 identified as the highest producer ($45.02 \pm 1.15\%$) [10]. Therefore, the present study aimed to assess the growth performance of these nineteen PGPR isolates from Chanthaburi's tropical fruit orchards under various abiotic stresses, including drought, high salinity, high temperature, and acidity, and to identify those with multi-stress tolerance. The selected strains will be used to develop targeted bioinoculants to support sustainable orchard management under climate change scenarios.

Methodology:

Source of PGPR isolates

A total of nineteen PGPR isolates in this study were selected from 85 isolates. They were previously obtained from the rhizosphere soils of major fruit orchards in Chanthaburi, Thailand. Based on a preliminary screening of *in vitro* osmotic stress tolerance, these nineteen PGPR isolates cultured in Tryptic Soy Broth (TSB) with 15% (w/v) polyethylene glycol (PEG 6000) exhibited an optical density at 600 nm (OD_{600}) greater than 0.20, which means they showed drought tolerance [10].

Screening for abiotic stress tolerance

A total of nineteen PGPR isolates from orchard soils were screened for salt, alkaline, and elevated temperature tolerance. The isolates were tested for their ability to tolerate salinity and alkalinity by streaking the bacterial isolates onto tryptic soy agar (TSA) supplemented with 7% (w/v) NaCl or adjusted to pH 12, respectively, and incubated at 28 °C for 24 h. Heat tolerance was assessed by streaking isolates on standard TSA plates and incubating at 45 °C and 50 °C for 24 h [11]. The bacterial growth was evaluated based on the most vigorous colony development under each condition [12]. Only isolates exhibiting good growth were selected for further quantitative assessment.

Quantitative assessment of abiotic stress tolerance

A total of nineteen PGPR isolates were tested for tolerance to acidic pH (pH 4) and drought stress (326 g of PEG 6000 per 1 L of media creates an osmotic pressure of -1.2 MPa). Only PGPR isolates exhibiting growth in the screening stage were quantitatively evaluated for tolerance to salinity (7% w/v NaCl), alkaline pH (pH 12), and elevated temperatures (45 °C and 50 °C). Bacterial inocula were prepared by suspending 24-hour-old cultures in sterile 0.85% (w/v) NaCl to a turbidity equivalent to the 0.5 McFarland standard (approximately 1.5×10^8 CFU mL⁻¹). A 100- μ L aliquot was then inoculated into 10 mL of TSB modified according to the respective stress condition. Cultures were incubated at 150 rpm for 24 h at 28 °C for salinity and alkaline tests, and at 45 °C and 50 °C for high-temperature tests. Bacterial growth was determined by measuring OD_{600} , and isolates were classified as stress-tolerant if the final OD_{600} was ≥ 0.10 [13].

Results and Discussion:

Screening for abiotic stress tolerance

Effect of salinity, alkalinity, and high-temperature stress on growth of PGPR isolates

A preliminary qualitative screening for abiotic stress tolerance of nineteen PGPR isolates obtained from orchard soils indicated significant phenotypic diversity in their tolerance to salinity, alkalinity, and high temperature (Table 1). Under high salinity (7% NaCl), five isolates demonstrated tolerance, with MuD01-2 showing moderate growth (Figure 1b),

whereas the remaining isolates exhibited slight growth. Under alkaline conditions (pH 12), eleven isolates maintained growth, with ten of these showing excellent and consistent growth on the tested media, indicating high resistance to salinity stress. This suggested a widespread occurrence of alkaliphilic adaptation among PGPR derived from orchard environments. The prevalence of thermotolerance was notably low: only KID02-6 and MuD01-2 were capable of growth at 45 °C, and MuD01-2 was the only isolate that demonstrated the ability to grow at both 45 °C and 50 °C (Figures 1 c–d). From this, only PGPR isolates exhibiting good growth under these stressful conditions will be chosen for further quantitative assessment.

Table 1.
PGPR isolates showing various abiotic stress tolerance.

PGPR isolates	Abiotic stress condition			
	Salinity (7% NaCl)	Alkalinity (pH 12)	High temperature (45 °C)	High temperature (50 °C)
KaD01-2	-	++	-	-
KaD02-1	-	-	-	-
KID01-2	-	-	-	-
KID02-6	+	+++	++	-
KhD02-1	-	+++	-	-
ThD01-4	-	-	-	-
ThD02-2	-	+++	-	-
NaD01-2	-	-	-	-
NaD02-1	+	+++	-	-
LaD02-2	-	+++	-	-
PoD01-2	-	-	-	-
PoD02-4	-	+++	-	-
MaD01-7	+	+++	-	-
MaD02-7	+	-	-	-
MuD01-2	++	-	+++	+++
MuD02-5	-	+++	-	-
SoD01-1	-	+++	-	-
SoD02-3	-	-	-	-
LaD01-2	-	+++	-	-

Note: Growth was visually assessed after 24 h. Symbols indicate the level of growth as follows:

- (+++): Excellent and consistent growth
- (++) : Moderate growth
- (+) : Low or slight growth
- (-) : No growth

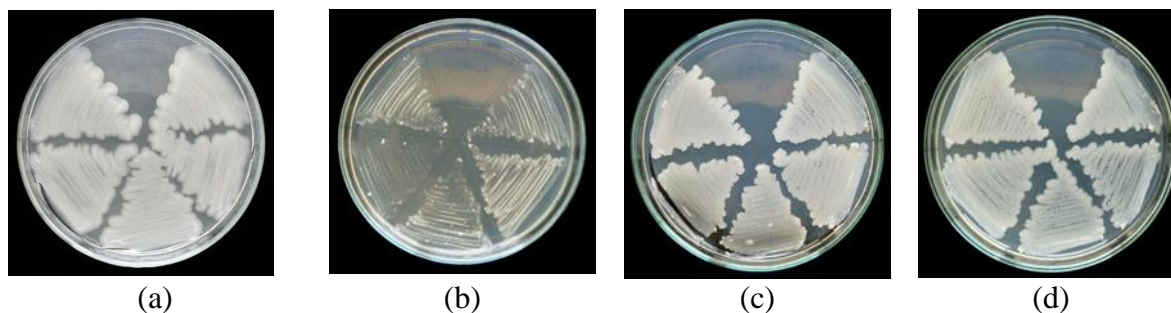


Figure 1.

Qualitative assessment of abiotic stress tolerance of isolate MuD01-2 on Tryptic Soy Agar (TSA). Representative colony morphologies are shown under: (a) control conditions (28 °C), (b) salinity stress (7% w/v NaCl), (c) elevated temperature (45 °C), and (d) extreme temperature (50 °C).

This study revealed the phenotypic diversity in the tolerance of nineteen orchard-derived PGPR to abiotic stresses including salinity, alkalinity and temperature extremes which are consistent with other findings. Even among isolates from similar environments, they often observe that stress tolerance is not uniformly distributed. This variability arises from the distinct mechanisms through which different PGPR strains interact with plants and their environments [3, 4, 14]. The isolation of these PGPR isolates from the dry rhizosphere of orchard soils [10] is consistent with other research focused on sourcing microbes from abiotic-stressed regions, where microbial communities have evolved mechanisms to thrive under harsh environmental conditions [15]. Studies have shown that stress tolerance in PGPR is commonly associated with the production of phytohormones such as indole-3-acetic acid (IAA), ACC deaminase, exopolysaccharides, and compatible solutes, which collectively enhance plant stress adaptation [4, 15]. One important finding is that isolate MuD01-2 is a special strain combining multiple stress resistances, able to thrive at extreme temperatures (50 °C) and high salinities (7% NaCl). This is consistent with studies showing that elite strains with a variety of stress tolerances are ideal candidates for abiotic stress mitigation in the fields where stressors often co-occur [16, 17].

Effect of acidic and drought stress on growth of PGPR isolates

This study revealed the limitation of acid tolerance among orchard-derived PGPR strains since only NaD01-2 exhibited robust growth at pH 4 ($OD_{600} = 0.709 \pm 0.010$), as shown in Figure 2. This observation aligns with previous studies demonstrating that acidic pH significantly limits the survival and persistence of *Rhizobium* and other rhizobacteria in soil, underscoring acid stress as a stringent selective barrier [18-19]. Soil pH is a critical factor affecting microbial community composition, with studies showing that pH variations can lead to significant changes in the diversity of PGPR in the rhizosphere [20]. For instance, certain PGPR strains, such as *Burkholderia* sp., demonstrate increased phosphorus solubilization and organic acid production at lower pH levels, which is beneficial for nutrient availability in acidic soils [21].

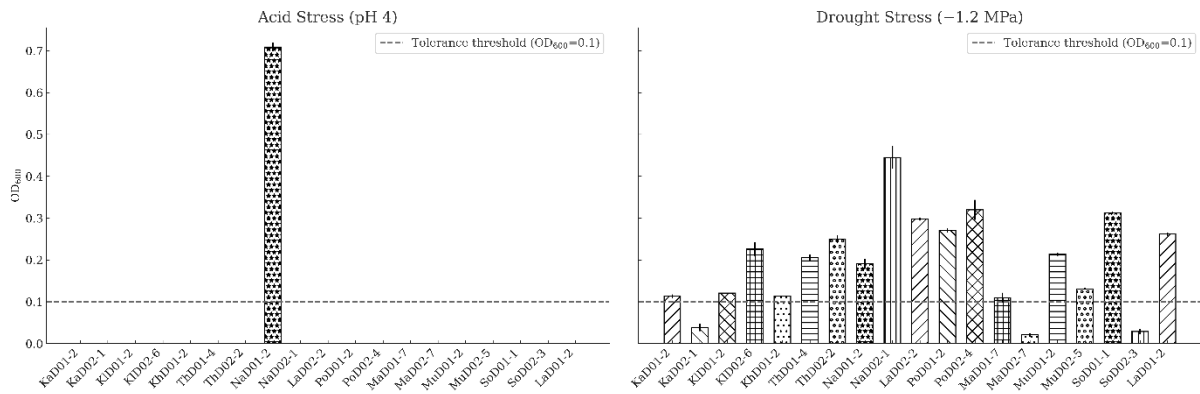


Figure 2.

Growth of nineteen PGPR isolates under acidic (pH 4) and drought stress, as determined by optical density readings at 600 nm (OD₆₀₀).

In contrast, Figure 2 showed that PGPR from orchard soils could effectively mitigate drought stress (−1.2 MPa), as demonstrated by sixteen isolates that surpassed the tolerance threshold (OD₆₀₀ = 0.1). Strains such as NaD02-1 (OD₆₀₀ = 0.445 ± 0.027), PoD02-4 (0.320 ± 0.024), and SoD01-1 (0.312 ± 0.003) displayed particularly vigorous growth. These findings are in agreement with recent literature that PGPR exhibit greater tolerance to drought compared to acidic conditions through several key mechanisms, including osmolyte accumulation, phytohormones production, improved nutrient uptake, and enhanced root architecture [7, 14]. The findings of this study have suggested that drought-adapted PGPR are dominant in orchard soils. This is likely because of natural selection for these common types of microbes under the dry conditions within orchards over a long period of time.

Stress tolerance characteristics of selected orchard-derived PGPR isolates

Growth responses of selected orchard-derived PGPR isolates exhibiting good growth from the screening procedure were used for quantitative assessment under salt, temperature, and alkaline stress, as shown in Figure 3. Under 7% NaCl (Fig. 3a), only isolate MuD01-2 (OD₆₀₀ = 0.504), surpassed the tolerance threshold while all other isolates exhibited negligible growth (OD₆₀₀ < 0.1), indicating limited halotolerance. Thermotolerance was more restricted (Fig. 3 b): only MuD01-2 sustained substantial growth at elevated temperatures, reaching OD₆₀₀ equal to 0.732 at 45 °C and 0.287 at 50 °C.

In contrast, eight dominant strains exhibiting high tolerance to alkaline conditions (pH 12; Fig. 3c), with OD₆₀₀ values exceeding 0.1 in several cases, indicating robust alkaliphilic adaptation. This prevalence of alkalinity tolerance among the tested PGPR suggested that orchard soils may select for strains capable of thriving in high-pH environments. The pH of orchard soils significantly influences the selection and diversity of plant growth-promoting rhizobacteria (PGPR) strains, which in turn affects soil health and plant growth. Collectively, these results highlight isolate-specific resilience to abiotic stress, consistent with reported that PGPR mechanisms involving osmotic adjustment, ion homeostasis, and antioxidant defense [22].

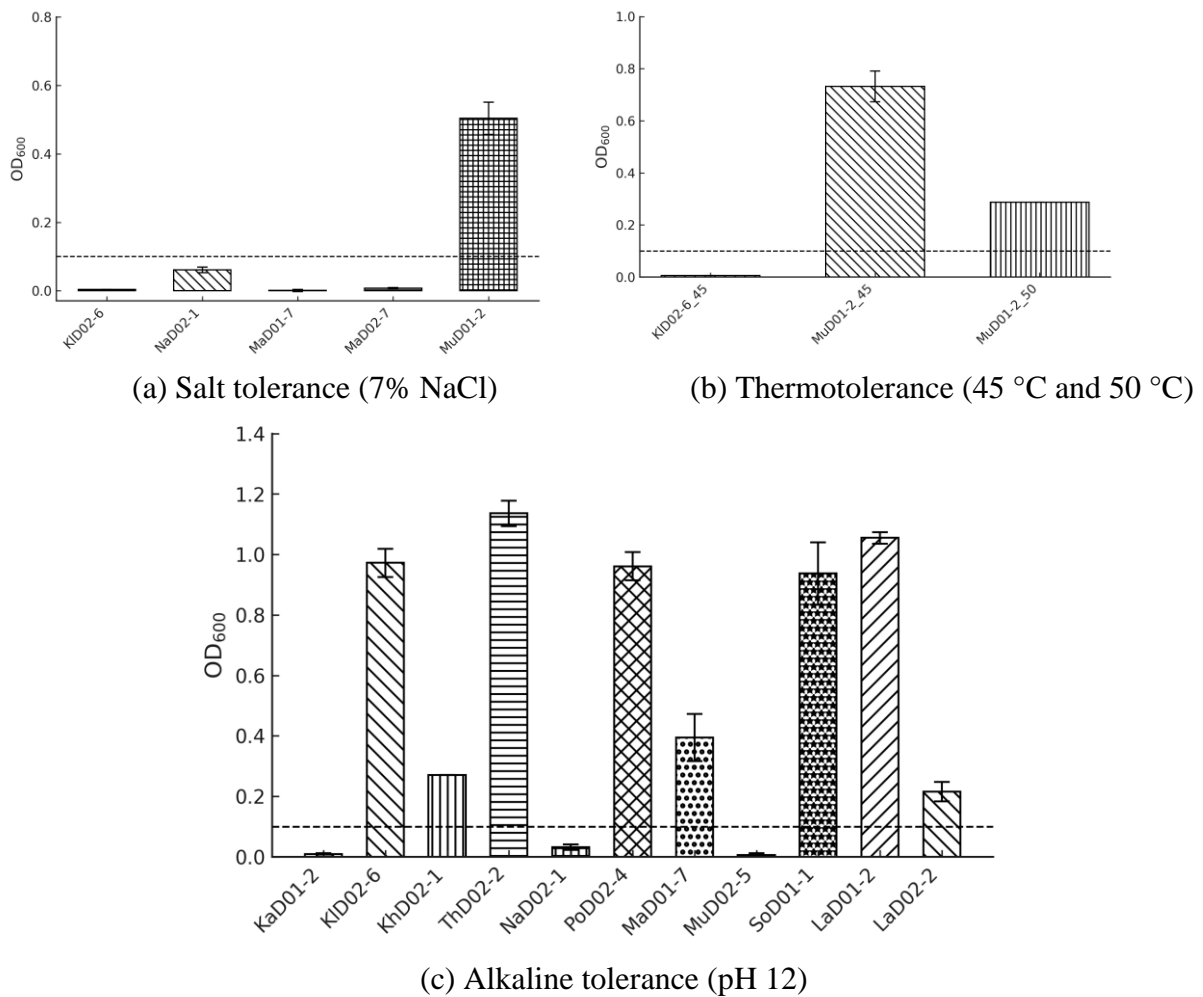


Figure 3.

A comparison of the stress tolerance characteristics for the selected PGPR isolates. It displays their tolerance to salt (a), high temperature (b), and alkalinity (c), as measured by growth (OD₆₀₀). The dashed line represents the tolerance threshold (OD₆₀₀ = 0.1), and the error bars indicate the standard deviation (n=3).

Multi-stress tolerance profiles of the three dominant PGPR isolates

To visualize the comparative performance of PGPR isolates across all tested abiotic stresses, a radar plot was constructed using OD₆₀₀ values from quantitative assays. The profiles of abiotic stress tolerance showed in Figure 4 revealed distinct survival strategies among the elite PGPR isolates. Two isolates like ThDo2-2 exhibited significant tolerance under alkaline conditions (pH 12) while NaD01-2 was uniquely adapted to acidic stress (pH 4). Whereas MuD01-2 was identified as a multi-stress tolerant which demonstrated moderate-to-high tolerance across multiple stress types, including high salinity (7% NaCl), drought, and extreme heat (45 °C and 50 °C). Radar plot visualization highlights the broader tolerance range of MuD01-2 compared to stress-specific adaptation in other isolates.

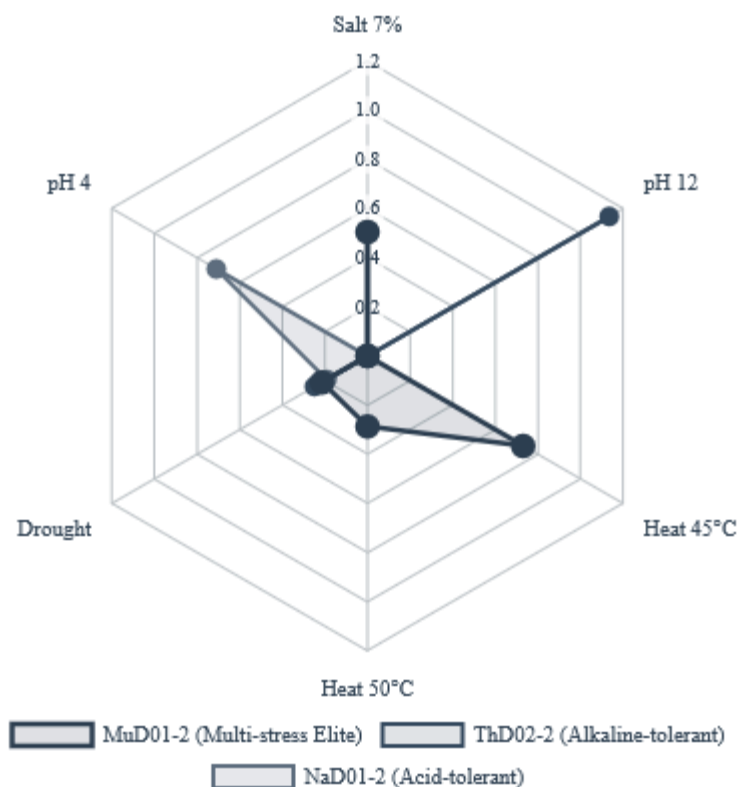


Figure 4.

Multi-stress tolerance profiles of the three dominant PGPR isolates based on OD₆₀₀ values under six abiotic stress conditions: salinity (7% NaCl), alkalinity (pH 12), acidity (pH 4), drought (15% PEG), heat at 45 °C, and heat at 50 °C.

The remarkable drought tolerance of MuD01-2 is supported by previous work documenting its high production of exopolysaccharides (EPS), a trait linked to rhizosphere moisture retention [10]. In the present study, additional beneficial functions of MuD01-2 like ammonia and siderophore production were also observed (data not shown). The research conducted concerning a broad stress-tolerance MuD01-2 orchard-derived PGPR aligns with a prior investigation, which successfully identified five out of 64 bacterial strains isolated from the rhizosphere of *Miscanthus sinensis* as proficient PGPR, notably including *Enterococcus mundtii* and *Pseudomonas qingdaonensis*, both of which exhibited remarkable tolerance to salt stress and demonstrated enhanced plant growth-promoting characteristics, such as the production of indole-3-acetic acid (IAA) and salicylic acid [8]. As a result, the combination of a multi-stress-tolerant profile, documented EPS production, and key PGP traits highlights MuD01-2 as an effective strain for bioinoculant development and potential successful application in the complex and fluctuating stress conditions of orchard ecosystems.

Conclusion:

This study identified elite PGPR from orchard soils with distinct and complementary abiotic stress tolerance profiles, providing candidate strains for targeted deployment in stress-prone perennial fruit systems. Specialists such as ThD02-2, and NaD01-2 address specific constraints (alkalinity, acidity), while MuD01-2 offers broad adaptability across multiple stresses. Supported by both prior and current findings, MuD01-2 stands out as a prime candidate for climate-smart orchard management. Future work should prioritize in planta validation, optimized formulation, and integration into microbial consortia to deliver sustainable yield stability in high-value perennial crops under variable climatic conditions.



Acknowledgements:

This research was funded by the Research Fund of Rambhai Barni Rajabhat University for the fiscal year 2025. AI tools were utilized to assist with the writing and review of the English language content.

References

1. Suman B, Triveni S, Latha PC, Srilatha M, Rani CVD. *J Res PJTSAU*. 2018;46:31-40.
2. Karnwal A, Shrivastava S, Al-Tawaha ARMS, Kumar G, Kumar A, Kumar A. *J Plant Growth Regul*. 2024;43:2955-71.
3. Kelbessa BG, Dubey M, Catara V, Ghadamgahi F, Ortiz R, Vetukuri RR. *CABI Rev*. 2023;2023:1.
4. Sonowal T, Gupta N, Kumar S, Rustagi S, Rai AK, Singh S, et al. *J App Biol Biotech*. 2024;12:41-47.
5. Lilavanichakul A, Pathak TB. *Clim Serv*. 2024;34:100475.
6. Apiratikorn S, Sdoodee S, Lerslerwong L, Rongsawat S. *Kasetsart J (Nat Sci)*. 2012;46:1-9.
7. Chattaraj S, Samantaray A, Ganguly A, Thatoi H. *Discov Appl Sci*. 2025;7:68.
8. Injamum-Ul-Hoque M, Imran M, Zainurin N, Shaffique S, Kang SM, Ahsan SM, et al. *Sustainability*. 2024;16:9263.
9. Nghia NK, Dalma KE, Haydee KM, Xa LT, Morton LW, Tecimen HB, et al. *Front Soil Sci*. 2025;5:1610343.
10. Chanthamalee J, Puckdee W. *J Sci Technol Innov Kalasin Univ*. 2024;3:25-35.
11. Benaissa A, Djebbar R, Abderrahmani A. *Adv Horti Sci*. 2018;32:525-534.
12. Suman B, Triveni S, Latha PC, Srilatha M, Rani CVD. *J Res PJTSAU*. 2018;46:31-40.
13. Kumar GP, Ahmed SKMH, Desai S, Amalraj ELD, Rasul A. *Int J Bacteriol*. 2014;2014:195946.
14. Getahun A, Muleta D, Assefa F, Kiros S. *Int J Microbiol*. 2020;2020:8897998.
15. Akhreim AA, Jadhav AU, Gaballa MF, Ahire KD, Abid AADM, Sulaiman G, et al. *Pak J Life Soc Sci*. 2024;22:14202-14223.
16. Shultana R, Kee Zuan AT, Yusop MR, Saud HM. *PLoS ONE*. 2020;15:e0238537.
17. Tafaroji SH, Abtahi SA, Jafarinia M, Ebadi M. *Front Microbiol*. 2025;16:1551310.
18. Keneni A, Assefa F, Prabu PC. *J Agr Sci Tech*. 2010;12:365-376.
19. Yermenko L, Czopek K, Staniak M, Marenych M, Hanhur V. *Biomolecules*. 2025;15:118.
20. Moura RL, Monteiro DA, Fonseca E da S, Balieiro F de C, Cesário FV, Rachid CTC da C. *Microbiol Res*. 2024;15:314-325.
21. Fitriatin BN, Fauziah DA, Hindersah R, Simarmata T. *KnE Life Sci*. 2022;7:115-121.
22. Waheed A, Zhuo L, Wang M, Hailiang X, Tong Z, Wang C, et al. *Plant Stress*. 2024;14:100652.



EFFECT OF SKIM MILK SUPPLEMENTATION ON THE PRODUCTION OF AIR-DRIED LACTIC ACID BACTERIAL STARTER CULTURE IMMOBILIZED ON CORN HUSK AND ITS ANTAGONISTIC ACTIVITY AGAINST *Aspergillus flavus*

Possawee Boonyong,¹ Cheewanun Dachoupan Sirisomboon,^{1,*}

¹Department of Microbiology, Faculty of Science, Chulalongkorn University, Bangkok 10330, Thailand

*e-mail: cheewanun.d@chula.ac.th

Abstract:

The present study aimed to investigate the effects of skim milk supplementation on immobilized lactic acid bacterial starter cultures on corn husk, to evaluate their antagonistic activity against fungal growth, and to establish optimal rehydration conditions. The immobilized *Lactobacillus paracasei* AN3 on ground corn husk, with and without skim milk addition, was subjected to air drying at 45°C for 6 h. The effect of adding skim milk at different concentrations (0, 0.5, 1, and 2% w/v) to the cultured medium before air drying on the production of air-dried *L. paracasei* AN3 starter culture was evaluated. Skim milk supplementation increased the surface tension of the cultured media, and the SEM image showed the formation of a rough surface on the corn husk due to matrix deposition. The addition of 2% skim milk resulted in the highest survival rate of air-dried *L. paracasei* AN3 (66.02%) on ground corn husk after air drying. Skim milk supplementation did not affect the antagonistic activity of *L. paracasei* AN3 against *Aspergillus flavus* M3T8R4G3. Rehydration conditions for air-dried *L. paracasei* AN3 with 2% skim milk were investigated. Tap water without sucrose supplementation at ambient temperature and 30°C yielded the highest bacterial viability (8.53 and 8.57 log CFU/mL, respectively) and recovery rates (100.93% and 94.09%, respectively). The findings indicate that air drying represents a promising alternative for producing lactic acid bacterial starter cultures. Future studies should focus on evaluating the long-term stability of the starter culture during storage and its application.

Introduction:

Aflatoxins are highly toxic secondary metabolites produced by *Aspergillus* species and are classified as Group 1 human carcinogens by the International Agency for Research on Cancer (IARC).¹ These mycotoxins are strongly associated with liver cancer in humans and livestock and are frequently detected in feed materials such as corn silage.² Aflatoxin contamination in livestock feed reduces animal productivity and leads to the presence of aflatoxin derivatives, such as aflatoxin M1, in animal-derived products, thereby posing health risks to consumers.³ Lactic acid bacteria (LAB) play a crucial role in silage fermentation by reducing the pH and inhibiting the growth of undesirable microorganisms, particularly spoilage fungi.^{4, 5} Some LAB strains also exhibit antagonistic effects through competition for nutrients and space.⁶ In addition, several LAB have demonstrated mycotoxin-binding capacity, which may contribute to the reduction of aflatoxin levels in contaminated silage.⁷

Several researchers have demonstrated dehydration methods for producing dried LAB starter cultures, particularly freeze drying and spray drying, which can achieve a high survival rate after dehydration.⁸ However, these methods are associated with high production costs. In addition, heat exposure during spray drying has been reported to cause significant cellular damage or death in LAB.⁹ Cell immobilization is a strategy for enhancing bacterial survival during dehydration, for example, by immobilizing LAB on a fiber matrix before freeze drying.¹⁰ Several studies have demonstrated that microbial immobilization improves the stability of viable cells and ensures the retention of their functional properties upon dehydration.^{11, 12, 13} Moreover, the addition of a cell protectant, such as skim milk, can

stabilize the bacterial cell structures, especially the cell membrane, and preserve enzyme activity, which can also enhance cell viability.¹⁴ While freeze-drying and spray-drying remain the most effective techniques, alternative low-cost approaches such as air drying remain underexplored.

In our previous study, *Lactobacillus paracasei* AN3 isolated from the corn silage showed antagonistic activity against *Aspergillus flavus* M3T8R4G3 and aflatoxin production *in vitro* and in corn silage.¹⁵ Lactic acid bacterium corn steep liquor-molasses (LCM) medium was developed as a suitable medium for lactic acid bacteria. Therefore, the present study aimed to: (i) investigate the effects of skim milk supplementation at different concentrations on immobilized starter cultures on corn husk, (ii) evaluate their antagonistic activity against fungal growth, and (iii) establish optimal rehydration conditions for the air-dried lactic acid bacterial starter cultures.

Methodology:

Microorganisms

L. paracasei AN3 and *A. flavus* M3T8R4G3 used in this study were deposited at the Culture Collection Unit, Department of Microbiology, Faculty of Science, Chulalongkorn University. A single colony of *L. paracasei* AN3 was initially activated in 5 mL of De Man–Rogosa–Sharpe (MRS) broth (Difco™, BD, USA) and incubated at 30°C for 24 hours. This culture was then transferred into fresh MRS broth at a 5% (v/v) inoculum, followed by incubation at 30°C for 14 h to reach the mid-log phase. Afterward, the cells were harvested and washed twice with Lactic acid bacterium corn steep liquor-molasses (LCM) broth, adjusted to pH 5, and inoculated with 5% (v/v) inoculum into the same LCM medium. The culture was incubated at 30°C for 10 h to allow the cells to reach the mid-log phase. A spore suspension of *A. flavus* M3T8R4G3 was activated on Potato Dextrose Agar (PDA) (Difco™, BD, USA) and incubated at 25 °C for 7 days in the dark

Air drying of the lactic acid bacterium

Preparation of cultured medium

The mid-log phase *L. paracasei* AN3 in LCM medium was evaluated for the effect of various skim milk concentrations. Skim milk (Difco™, BD, USA) was prepared at 5%, 10%, and 20% (w/v) in deionized water and sterilized by autoclaving at 115°C for 15 min. A 10 mL skim milk solution of each concentration was added to 90 mL of cultured LCM medium containing mid-log phase *L. paracasei* AN3 to achieve final skim milk concentrations of 0% (using deionized water as control), 0.5%, 1%, and 2% (w/v). The medium was then allowed to stand for 20 min to facilitate the interaction.

The surface tension (mN/m) of the cultured LCM medium was measured using the Du Noüy ring method, calibrated with deionized water, as described by Faisal et al.¹⁶ to evaluate the reduction of surfactant activity prior to immobilization. All pretreated LCM media were centrifuged at 5,000 rpm for 10 min. The supernatant was then filtered through a sterile 0.20 µm nylon syringe filter. The cell-free supernatant was used to determine the surface tension using the K6 force tensiometer (KRÜSS GmbH, Germany).

Air drying process

The method of air drying was carried out with modifications based on Tchamani Piame et al.¹⁷ Ground corn husk (particle size less than 1.6 mm) was sterilized by autoclaving at 121°C for 45 min, followed by air-drying at 60°C for 24 h. The bacterial culture in LCM medium, supplemented with different concentrations of skim milk, was mixed with sterile ground corn husk at a ratio of 100 mL of culture medium to 20 g of ground corn husk. The mixture was poured into an aluminium tray (20.5 x 20.5 cm) and air-dried at 45°C for 6 h using a food



dehydrator (GE-BLACK12, Spring Green Evolution Co., Ltd, Thailand). Samples were collected every 1 h. For viable count, 1 g of the sample was suspended in 99 mL of 0.1% peptone solution (HiMedia™, India) and sonicated for 15 min before planting on MRS agar, subsequently incubated at 30°C for 48 h to determine viability and survival rate (%). For moisture content (MC), 2 g of the sample was dried at 135°C for 2 h according to AOAC 930.15.

The immobilization of air-dried *L. paracasei* AN3 on ground corn husk was examined using a scanning electron microscope (JSM-IT500HR, JEOL Ltd, Japan). Prior to imaging, samples were sputter-coated with gold and observed under an accelerating voltage of 10 kV. SEM analysis was used to confirm bacterial adhesion and to characterize the surface morphology of the corn husk matrix.

Evaluation of the antagonistic activity of air-dried lactic acid bacteria

Preparation of microbial suspensions

Each 1 g of air-dried *L. paracasei* AN3 was suspended in 99 mL of 0.1% peptone solution and sonicated for 15 min. The suspension was used to inoculate MRS broth at a 5% inoculum and incubated at 30°C for 24 h. This culture was then transferred to fresh MRS broth with a 5% inoculum and incubated at 30°C for 14 h to reach the mid-log phase. The single colony of fresh *L. paracasei* AN3 was activated and reached the mid-log phase in MRS, as mentioned above. The mid-log *L. paracasei* AN3 in MRS broth was washed twice with Phosphate-buffered saline (PBS; 137 mM NaCl, 2.7 mM KCl, 10 mM Na₂HPO₄, 1.8 mM KH₂PO₄, pH 7.2) by centrifugation at 5,000 rpm for 10 min. The cell concentration was adjusted to 10⁶ cells/mL using a hemacytometer. A 7-day-old spore of *A. flavus* M3T8R4G3 was collected and suspended in 0.85% NaCl solution with 1% Tween 80. The spore suspension was adjusted to 10⁶ spores/mL using a hemacytometer.

Dual cultivation of lactic acid bacterium and pathogenic fungus

The dual culture assay was performed according to Pantelides et al.¹⁸ A 10 µL of both the cell suspension obtained from the dried starter culture and fresh cells was individually streaked in a straight line. Fungal spore suspension was then inoculated onto the same MRS agar plate at a distance of 2.5 cm from the bacterial streak. Control plates were inoculated separately with the spore suspension and PBS lacking antagonistic microorganisms. All plates were incubated at 25°C in the dark for 7 days. The diameter of the fungal colony was measured and calculated for the inhibition (%).

Optimization of rehydration conditions of air-dried lactic acid bacterial starter culture

Optimization of rehydration solution

Rehydration conditions were optimized according to the procedure described by de Valdez et al.¹⁹ with adaptations for this study. One gram of air-dried starter culture was rehydrated in 100 mL of different solutions, including 0.1% peptone (as a control) and tap water supplemented with 0%, 5%, or 10% (w/v) sucrose, obtained as pure fine sugar (Mitr Phol Sugar Corp., Ltd., Thailand). Each rehydrated starter culture was sonicated for 15 min and incubated at 30°C. Samples were collected every 3 h over 24 h to determine cell viability using the drop plate method on MRS agar, which was incubated at 30°C for 48 h. The recovery rate (%) was determined using the following equation: Recovery rate (%) = $(V_F - V_I) / V_I \times 100\%$, where V_F is the final viability of LAB (log CFU/mL), and V_I is the initial viability of LAB (log CFU/mL).



Optimization of rehydration temperature and incubation time

The selected rehydration solution was used to optimize rehydration temperature and incubation time, as it yielded the highest recovery rate in the preliminary evaluation of rehydration solutions. One gram of the air-dried starter culture was rehydrated in 100 mL of tap water and subjected to sonication for 15 min. The rehydrated culture was then incubated at ambient temperature, 30°C and 37°C. Samples were collected every 3 h over a 36 h period to assess cell viability and recovery rate (%) as described above.

Statistical analysis

The resulting data were obtained in triplicate and analyzed using one-way ANOVA in SPSS version 28.0. Tukey's post-hoc test was employed to declare statistical significance ($p < 0.05$).

Results and Discussion:

The effect of skim milk on the air-dried lactic acid bacterial starter culture

The addition of skim milk to the *L. paracasei* AN3 cultured LCM medium demonstrated significant changes during the mid-log growth phase. Surface tension measurements revealed that supplementation with 2% skim milk resulted in the highest surface tension value of 35.30 ± 0.55 mN/m, which was statistically significantly different from 0% and 0.5% skim milk concentrations ($p = 0.001$ and $p = 0.005$, respectively), but not significantly different from 1% skim milk ($p > 0.05$) (**Figure 1A**). The viability of *L. paracasei* AN3 during air-drying at 45°C demonstrated a rapid decline across all skim milk concentrations after 3 hours. At 6 hours, the viable cell counts ranged from 5.42 to 6.12 log CFU/g (**Figure 1B**). Concurrently, moisture content progressively decreased across all treatments, reaching a final range of 9.42-9.59% at 6 hours (**Figure 1C**). Survival rate analysis of *L. paracasei* AN3 after 6 hours of air-drying at 45°C revealed survival rates between 59.26-66.02%, with the highest survival rate observed at 2% skim milk concentration. However, statistical analysis indicated no significant differences in survival rates among different skim milk concentrations ($p > 0.05$) (**Figure 1D**). These results revealed that increasing the skim milk concentration can promote the surface tension of the media and slightly enhance the survival rate. The LAB culture media are mostly supplemented with Tween 80 (polysorbate 80), including MRS and LCM medium, which supports LAB growth by improving membrane properties and nutrient uptake.^{20, 21} Casein in skim milk can interact with Tween 80, resulting in a physical change of micelle structure and influence surface tension.^{22, 23} The moisture content of the starter culture progressively declined during air drying but, the drying rate was slower when skim milk was present, particularly at the later stages (3–5 h). This reduction is attributed to the protein network structure in skim milk, which binds water molecules, forms a protective matrix around cells and the corn husk surface, and gradually releases free water during dehydration. In agreement with Zheng et al.,²⁴ the presence of skim milk prolonged moisture content retention, slowed drying, and enhanced LAB protection. Moreover, protein-type protectants increase bound water in the starter culture, slow the drying rate, and help preserve cell components, resulting in stable cell viability after drying.²⁵ Several studies have suggested that skim milk enhances microbial survival after dehydration, mainly through milk proteins and calcium ions that coat cells and stabilize membranes, whereas lactose alone provides little protection.^{14, 24}

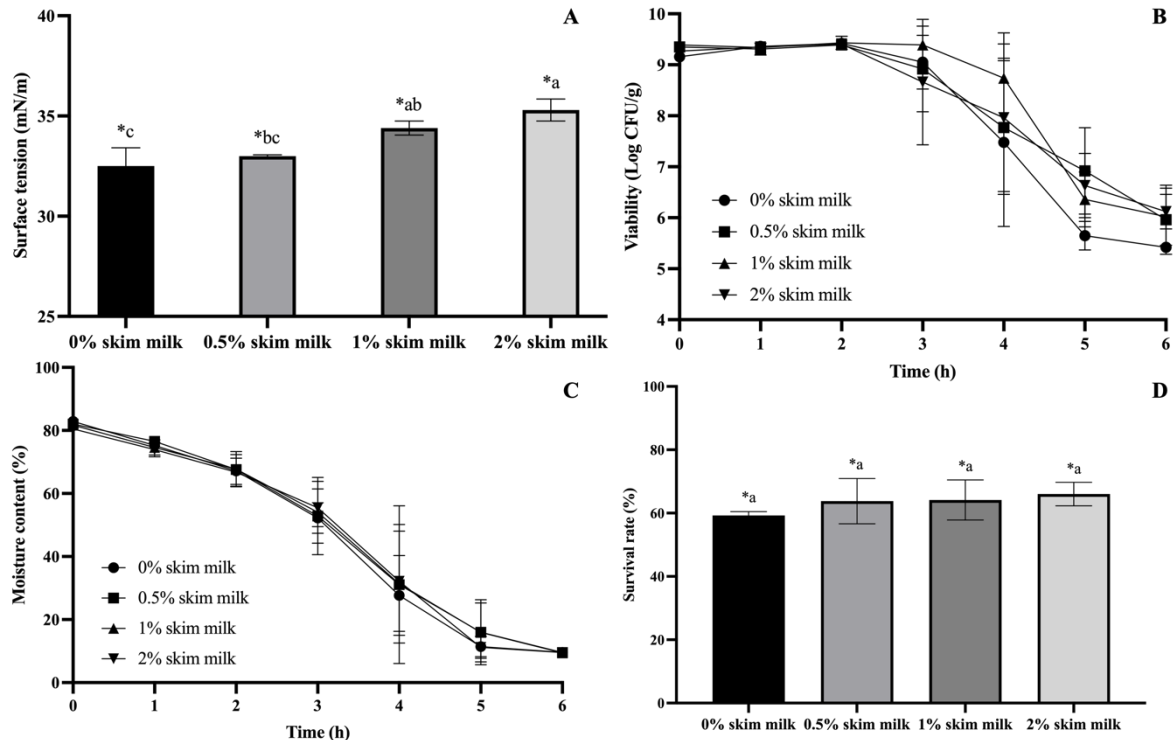


Figure 1.

Effect of skim milk addition at different concentration on the air drying of *L. paracasei* AN3 starter culture; (A) surface tension of cultured LCM medium with different skim milk concentrations, (B) viable count of starter culture during air drying at 45°C for 6 h, (C) moisture content of starter culture during air drying at 45°C for 6 h, and (D) survival rate of air-dried starter culture at 6 h. The bar graph represents mean±SD, n=3, and *different superscript letters represent significant difference declared by Tukey's post-hoc test ($p < 0.05$).

Figure 2 shows the scanning electron microscope (SEM) images of immobilized *L. paracasei* AN3 on ground corn husk with and without skim milk. Bacterial cells were clearly observed attached to the corn husk surface. The presence of skim milk resulted in the formation of an extracellular-like matrix covering the corn husk, which generated a rougher surface (**Figure 2B-2D**). This matrix likely promoted bacterial immobilization by enhancing cell-surface interaction, in agreement with previous studies reporting that protective or carrier-derived matrices improve bacterial adhesion and stability during immobilization.²⁶

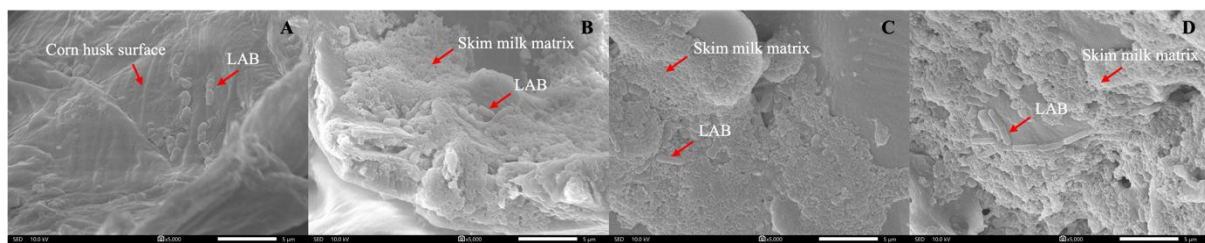


Figure 2.

Scanning electron microscope (SEM) images of immobilized *L. paracasei* AN3 on ground corn husk with the addition of skim milk at different concentrations; (A) 0% skim milk, (B) 0.5% skim milk, (C) 1% skim milk, and (D) 2% skim milk.

The evaluation of the antagonistic activity of air-dried lactic acid bacteria against *A. flavus*

Figure 3A and 3B illustrate the antagonistic activity of air-dried *L. paracasei* AN3 starter culture against *A. flavus* M3T8R4G3. The colony diameter of *A. flavus* M3T8R4G3 in the control was 75.11 ± 0.77 mm, whereas the dual cultures with fresh and air-dried *L. paracasei* AN3 at all skim milk concentrations significantly reduced the fungal colony diameter ($p < 0.001$) to 58.22-59.89 mm, corresponding to the inhibition of 20.27-22.49%, with no significant difference between the two forms ($p > 0.05$). The findings indicated that the air-drying method with skim milk supplementation has no effect on the antagonistic activity of *L. paracasei* AN3. This result is consistent with Han et al., who reported that yeast cells retained their antagonistic activity against pathogenic fungi after freeze drying.²⁷

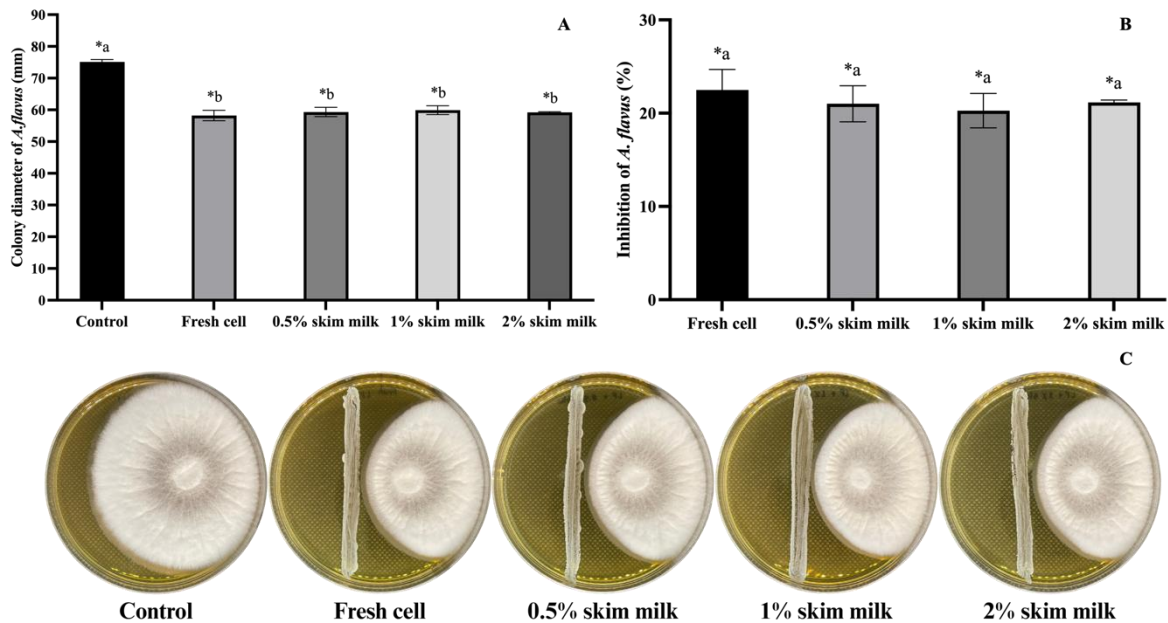


Figure 3.

The growth of *A. flavus* M3T8R4G3 with and without dual culturing with *L. paracasei* AN3 (A). The inhibition of *A. flavus* M3T8R4G3 by fresh and air-dried *L. paracasei* AN3 (B). The dual culture plate of *A. flavus* M3T8R4G3 on MRS agar (C). The bar graph represents mean \pm SD, $n = 3$, and *different superscript letters represent significant difference declared by Tukey's post-hoc test ($p < 0.05$).

The optimization of rehydration conditions of air-dried lactic acid bacterial starter culture

Figure 4A and 4B present the viable counts of rehydrated air-dried *L. paracasei* AN3 with 2% skim milk in different rehydration solutions at 30°C. Immediately after rehydration, all treatments show approximately 4 log CFU/mL, and the viable counts increased slightly during the first 6 h. After 24 h of incubation, the viable counts reached 6.53-7.07 log CFU/mL, with tap water (no sucrose supplementation) providing the highest count (7.07 ± 0.05 log CFU/mL). The recovery rates at 24 h were in the range of 55.07-66.64% and there was no significant difference between the rehydration solutions ($p > 0.05$). These results demonstrate that the air-dried starter culture powder contained sufficient nutrients to support *L. paracasei* AN3 growth after rehydration. On the other hand, higher sucrose supplementation tended to reduce the recovery rate, possibly due to osmotic imbalance.²⁸

In addition, the effects of rehydration temperature (ambient temperature, 30°C, and 37°C) and incubation time on the viability of air-dried *L. paracasei* AN3 with 2% skim milk in tap water without sucrose supplement are shown in **Figure 4C and 4D**. Initially, all treatments yield a viable count of approximately 4 log CFU/mL. At 37°C, the viable count

rapidly increased between 6 and 21 h, but then stabilized without exceeding 8 log CFU/mL throughout the incubation. In contrast, the ambient temperature and 30°C promoted a more gradual increase after 6 h, reaching significantly higher final count at 36 h (8.53 ± 0.02 and 8.57 ± 0.05 log CFU/mL, respectively). The corresponding recovery rates were 100.93 ± 2.48 and $94.09 \pm 3.63\%$, respectively, both significantly higher than 37°C ($p < 0.001$ and $p = 0.002$, respectively), while no significant difference was observed between ambient temperature and 30°C ($p > 0.05$). The findings indicate that temperature was a critical factor influencing rehydration performance, with temperatures close to ambient levels (28–30°C) providing the highest survival and recovery of *L. paracasei* AN3.

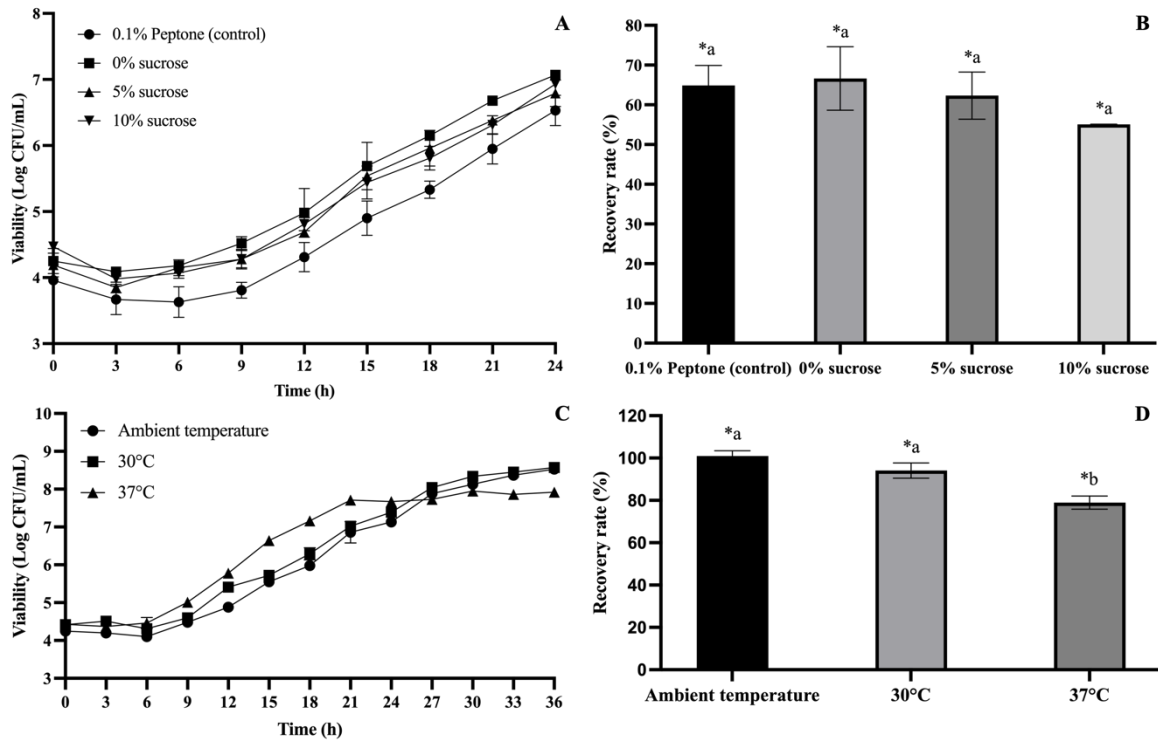


Figure 4.

The viability of rehydrated starter culture in various rehydration solutions incubated at 30°C (A). The recovery rate of rehydrated starter culture in various rehydration solutions at 24 h of incubation at 30°C (B). The viability of rehydrated starter culture in tap water incubated at different temperatures (C). The recovery rate of rehydrated starter culture in tap water at 36 h of incubation at different temperatures (D). The bar graph represents mean \pm SD, $n=3$, and *different superscript letters represent significant difference declaring by Tukey's post-hoc test ($p < 0.05$).

Conclusion:

This study demonstrated that skim milk supplementation enhanced surface properties by increasing surface tension and forming a matrix on corn husk, thereby improving bacterial adhesion. The addition of 2% skim milk provided the highest survival rate of *L. paracasei* AN3 (66.02%) on ground corn husk after air drying. The air drying method with skim milk maintained the antagonistic activity of *L. paracasei* AN3 against *A. flavus* M3T8R4G3. Moreover, rehydration of air-dried starter culture in tap water without sucrose supplementation at ambient temperature and 30°C resulted in the highest bacterial viability (8.53 and 8.57 log CFU/mL, respectively) and recovery rates (100.93 and 94.09%, respectively). Air drying appears to be a feasible alternative for producing lactic acid



bacterial starter cultures. Future studies should assess both storage stability and functional performance in practical applications.

Acknowledgements:

This research is supported by the 90th Anniversary of Chulalongkorn University Scholarship under the Ratchadapisek Somphot Endowment Fund.

References:

1. Gemede HF. *Toxins*, 2025;17.
2. Ogunade IM, Martinez-Tupia C, Queiroz OCM, Jiang Y, Drouin P, Wu F, Vyas D, Adesogan AT. *J. Dairy Sci.* 2018;101:4034-4059.
3. Jiang Y, Ogunade IM, Vyas D, Adesogan AT. *Toxins*. 2021;13.
4. Kim D, Lee KD, Choi KC. *AIMS Agric. Food.* 2021;6:216-234.
5. Li J, Wang W, Chen S, Shao T, Tao X, Yuan X. *Toxins*. 2021;13.
6. Siedler S, Balti R, Neves AR. *Curr. Opin. Biotechnol.* 2019;56:138-146.
7. Zhang L, Zhang C, Song M, Dang D, Zhao J, Zhang L, Fu T. *Anim. Feed Sci. Technol.* 2023;304:115724.
8. Buahom J, Siripornadulsil S, Sukon P, Sooksawat T, Siripornadulsil W. *Vet. World.* 2023;16:1849-1865.
9. Moreira MTC, Martins E, Perrone IT, de Freitas R, Queiroz LS, de Carvalho AF. *Compr. Rev. Food Sci. Food Saf.* 2021;20:3267-3283.
10. Jagannath A, Raju PS, Bawa AS. *LWT - Food Sci. Technol.* 2010;43:1197-1203.
11. Kandyliis, P, Manousi, ME, Bekatorou, A, Koutinas, AA. *LWT – Food Sci. Technol.* 2010; 43:1485-1493.
12. Fijałkowski, K, Peitler, D, Rakoczy, R, Żywicka, A. *LWT – Food Sci. Technol.* 2016;68:322-328.
13. Dimitrellou, D, Kandyliis, P, Kourkoutas, Y. *LWT – Food Sci. Technol.* 2016;69:468-473.
14. Liu J, Xie S, Xu M, Jiang X, Wang Q, Zhao H, Zhang B. *Microorganisms*. 2024;12.
15. Rungchaiwattanukul T, Chareonpornwattana S, Sirisomboon CD. *Agric. Nat. Resour.* 2022;56:673–686.
16. Faisal ZG, Mahdi MS, Alobaidi KH. *Int. J. Microbiol.* 2023;2023:1571991.
17. Tchamani Piame, L, Kaktcham, PM, Foko Kouam, EM, Fotso Techeu, UD, Ngouenam, RJ, Zambou Ngoufack, F. *J. Agric. Food Res.* 2024;15:100942.
18. Pantelides IS, Christou O, Tsolakidou M-D, Tsaltas D, Ioannou N. *Biol. Control.* 2015;88:46-53.
19. de Valdez, GF, de Giori, GS, de Ruiz Holgado, AP, Oliver, G. *Appl. Environ. Microbiol.* 1985;50:1339-1341.
20. Reitermayer D, Kafka TA, Lenz CA, Vogel RF. *BMC Microbiol.* 2018;18:72.
21. Zaręba D, Ziarno M. *Acta Biochim. Pol.* 2024;71.
22. Ion Titapiccolo G, Corredig M, Alexander M. *J. Dairy Sci.* 2010;93:506-514.
23. Ho TM, Tanzil A, Bhandari BR, Bansal N. *Food Bioproc. Tech.* 2023;16:1781-1793.
24. Zheng, X, Fu, N, Duan, M, Woo, MW, Selomulya, C, Chen, XD. *Food Res. Int.* 2015;76:478-488.
25. Chen, B, Liang, Z, Lin, X, Li, W, Lin, X, He, Z. *LWT.* 2022;163:113511.
26. Mamun AA, Masniyom P, Maneesri J. *Sains Malays.* 2021;50:2229-2240.
27. Han P, Ni L, Wei Y, Jiang S, Xu F, Wang H, Shao X. *Biol. Control.* 2021;161:104707.
28. Papadimitriou K, Alegría Á, Bron PA, de Angelis M, Gobbetti M, Kleerebezem M, Lemos JA, Linares DM, Ross P, Stanton C, Turrone F, van Sinderen D, Varmanen P, Ventura M, Zúñiga M, Tsakalidou E, Kok J. *Microbiol. Mol. Biol. Rev.* 2016;80:837-890.



BIOELECTRICITY FROM PALM OIL MILL EFFLUENT: THE ROLE OF THE PENTOSE PHOSPHATE PATHWAY IN *Choricystis parasitica* SW-03

Alisa Kongthong, Thanopon Yooyen, Pimprapa Chaijak*

Department of Biological Science, Faculty of Science and Digital Innovation, Thaksin University, Phatthalung 93210, Thailand

*e-mail: pimprapa.c@tsu.ac.th, chaijak.pimprapa@gmail.com

Abstract:

Palm oil mill effluent (POME) is a major environmental concern in Thailand due to its large volume and high organic load, which pose serious risks to ecosystems and human health if discharged untreated. This study investigates the potential of the heterotrophic microalga *Choricystis parasitica* SW-03 for simultaneous POME bioremediation and bioelectricity generation using microbial fuel cell (MFC) technology. The system achieved a maximum open-circuit voltage (OCV) of 0.863 ± 0.032 V, with corresponding volumetric current and power densities of 137.17 ± 3.69 mA/m³ and 18.82 ± 1.00 mW/m³, respectively. Although the maximal biomass concentration (0.03 ± 0.00 g/L) and yield (0.002 ± 0.000 g/L/day) were relatively low, the cells exhibited chlorophyll a (0.38 ± 0.01 µg/mL) and chlorophyll b (0.28 ± 0.01 µg/mL), indicating active photosynthetic and heterotrophic metabolism. These findings suggest that the pentose phosphate pathway in *C. parasitica* SW-03 plays a key role in channeling POME-derived organic matter toward both energy metabolism and electron transfer. This work highlights the dual role of heterotrophic microalgae in bioelectricity generation and wastewater valorization, offering a sustainable strategy for POME management.

Introduction:

Water is a fundamental bio-resource that underpins a wide range of industrial sectors, including pharmaceuticals, food production, agriculture, petrochemicals, and beverages [1]. However, the direct discharge of contaminated wastewater from industrial and agricultural activities poses a serious environmental risk due to its complex composition of pollutants. Wastewater often contains a broad spectrum of chemical constituents, some of which may occur at concentrations that are highly toxic to living organisms. In addition, it typically exhibits elevated levels of organic and inorganic nutrients, as reflected by high chemical oxygen demand (COD) and biological oxygen demand (BOD) values. Excessive discharges of nitrogen (N) and phosphorus (P) further exacerbate eutrophication in aquatic ecosystems, leading to adverse outcomes such as algal blooms, hypoxia, secondary solid waste accumulation, and the release of malodorous gaseous emissions [2–3].

Palm oil mill effluent (POME) is the principal liquid biomass generated during crude palm oil (CPO) production, particularly in the sterilization, extraction, and clarification stages [4]. It represents the largest waste stream produced in palm oil processing and is a major contributor to environmental pollution [5]. The production of one ton of CPO requires approximately 5.0-7.5 tons of water, of which more than half is discharged as wastewater [6]. Furthermore, each ton of CPO processing is reported to generate approximately 2.5 m³ of POME [7]. POME is typically characterized as a dark brown colloidal suspension composed of both organic and inorganic constituents [8-9]. Although non-toxic, it is acidic (pH 4.0-5.0) and exhibits extremely high concentrations of BOD (10,250-43,750 mg/L) and COD (15,000-100,000 mg/L), underscoring its high pollution potential if discharged untreated [10-11]. The management of POME therefore poses persistent challenges to the palm oil industry, particularly in relation to safe disposal [12]. Its highly polluting nature also imposes both technical and economic burdens on wastewater treatment systems [13]. With the global demand for palm oil projected to increase, the corresponding generation of POME is likewise

expected to rise [9]. Consequently, the development and adoption of effective strategies for treatment, valorization, and resource recovery from POME are of critical environmental and industrial importance.

Microalgae represent a diverse group of unicellular microorganisms, including blue-green algae, eukaryotic protists, and prokaryotic cyanobacteria. They possess a range of advantageous traits that make them highly valuable for numerous biotechnological applications. Microalgae utilize photosynthesis to convert light, carbon dioxide (CO₂), water and nutrients into biochemical energy to sustain cellular growth and development [14]. Their biomass is primarily composed of lipids, proteins, and carbohydrates with the proportions varying across species and growth conditions [15]. Owing to their remarkable adaptability, microalgae can thrive in a wide range of environmental conditions and can be cultivated in both open pond systems and closed photobioreactors [16-17]. Previous study indicated that microalgae can utilize the organic carbon through pentose phosphate pathway under anaerobic digestion [18].

Microbial fuel cell (MFC) is the innovative technology that can convert the organic matter in the wastewater into electrical energy through the microbial mechanism without combustion process [19]. Microalgae-based microbial fuel cells simultaneously enable waste utilization, energy generation and resource recovery. Their high current density results from efficient electron transfer by the anodic biofilm and the photosynthetic activity of microalgae in the cathode chamber [20].

This study investigates the potential of heterotrophic microalgae to generate electricity in microbial fuel cells via the pentose phosphate pathway using POME as a substrate. Finally, the microalgae biomass was analyzed.

Methodology:

1. Microalgae

The heterotrophic microalgae *Choricystis parasitica* SW-03 was obtained from the Faculty of Science and Digital Innovation, Thaksin University, Thailand. The microalgae was cultured in BG-11 medium (Himedia, India) at room temperature (approximately 30 °C) under continuous light for 7 days before use.

2. POME

The POME was collected from a palm oil extraction factory in Trang province, Southern Thailand. The sample was collected in a plastic bottle, kept in an icebox and immediately sent to the Faculty of Science and Digital Innovation, Thaksin University.

The wastewater was filtered through sterile medical gauze (MedCare, Thailand) 2-3 times to remove contaminated sediment. The filtered wastewater was sterilized at 121 °C for 15 mins in the autoclave (Hirayama, Japan) to remove contaminating microbes. The sterilized wastewater was stored at -25 °C in a freezer (Hitachi, Japan) until it was used to preserve its properties.

3. MFC operation

The membrane-less microalgae-based MFC was constructed using a sterile 1-L working volume plastic bottle (SRG plastic, Thailand) as the MFC chamber. The bottle lid was wrapped with parafilm (Bemis, United States) to prevent the release of oxygen gas into the system. The 4 cm² aluminum and copper plates (RS Pro, Thailand) were used as electrodes. A 0.5 mm copper wire (RS Pro, Thailand) was used to link the electrodes. 500 g of volcanic rock was used to separate the electrodes. The schematic of the membrane-less microalgae-based MFC used in this experiment is shown in Figure 1.

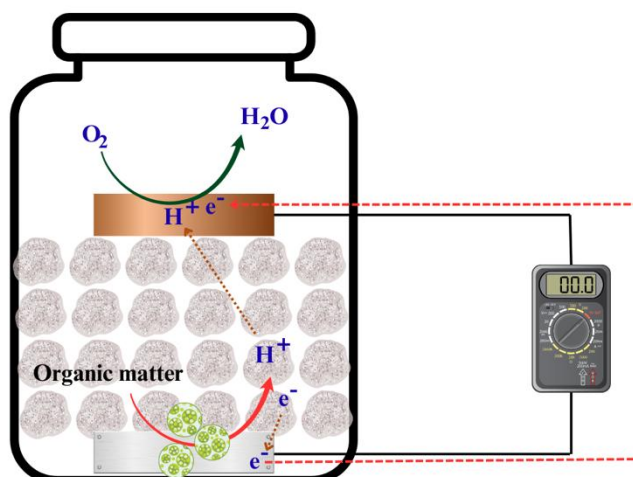


Figure 1.

The schematic of the membrane-less microalgae-based MFC.

For this operation, 100 mL of 7 day-old microalgae SW-03 was mixed with 900 mL of sterile POME. The resulting mixture was then added to the MFC chamber. The open circuit voltage (OCV) was tracked every 12 hrs for 14 days. After the system reached a stationary phase, the closed circuit voltage (CCV) was measured with a 1000 Ω external load connected. The electrochemical properties were then calculated using the provided equations.

4. Electrochemical properties

The electrochemical properties were calculated under Ohm's Law.

$$I = V / R \quad (1)$$

$$P = I \times V \quad (2)$$

$$CD = I / A \quad (3)$$

$$PD = P / A \quad (4)$$

$$R_{int} = (V_s \times R_L / V_o) - R_L \quad (5)$$

Where I is the current (A), V is the CCV (V), R is the external load (Ω), P is the power (W), CD is the current density (A/m^3 or A/m^2), A is the working volume (m^3) or electrode area (m^2), PD is the power density (W/m^3 or W/m^2), R_{int} is the internal resistance (Ω), V_s is the OCV (V), V_o is the CCV (V) and R_L is the external load (Ω).

The normalized energy recovery (NER) was analyzed to described the MFC energy production by considering the treatment capacity and conversion of organic compounds to energy follows the provided equation.

$$NER_v = (P \times t) / V \quad (6)$$

$$NER_{COD} = (P \times t) / (V \times \Delta COD) \quad (7)$$

Where NER_v is the normalized energy recovery per wastewater volume (Wh/m^3), P is the power (W), t is the operating time (h), V is the working volume (m^3) NER_{COD} is the normalized energy recovery per chemical oxygen demand ($Wh/kgCOD$), ΔCOD is the change of chemical oxygen demand ($kgCOD$).



5. Biomass analysis

The biomass concentration was determined every 24 hrs for 14 days using UV-Vis spectrophotometry at a wavelength of 680 nm and calculated according to the following equation.

$$Y = 0.4076 \times OD_{680} - 0.0052 \quad (8)$$

Where Y is the biomass concentration (g/L) and OD_{680} is the absorbance value at a wavelength of 680 nm. The biomass yield (g/L/day) was calculated as a equation (9).

$$\text{Biomass yield} = (C_{mt} - C_{m0}) / t \quad (9)$$

Where C_{mt} is the initial biomass concentration (g/L), C_{m0} is the biomass concentration at t day (g/L) and t is the culture time (day).

Microalgae cells were collected from the wastewater after the treatment system by centrifugation at 12,000 rpm for 10 mins using a bench-top microcentrifuge (Biosan Laboratories Inc, United States). The cell pellet was collected and washed 2-3 times with sterile reverse osmosis water. Following, 1 mL of 70% ethanol was added to 1 g of the cell pellet for pigment extraction. The mixture was then vortexed and incubated for 10 mins.

The microalgae pigments were analyzed using the Lichtenthaler and Wellburn equations with measurements taken at wavelengths of 663, 645 and 630 nm.

$$\text{ChloA} = (11.64A_{663} - 2.16A_{645} + 0.10A_{630})v / l \times V \quad (10)$$

$$\text{ChloB} = (-3.94A_{663} + 20.97A_{645} + 3.66A_{630})v / l \times V \quad (11)$$

Where A_{663} , A_{645} and A_{630} is the absorbance values at 663, 645 and 630 nm. ChloA is the chlorophyll a concentration ($\mu\text{g/mL}$), ChloB is the chlorophyll b concentration ($\mu\text{g/mL}$), v is the ethanol volume (mL), l is the spectrophotometric length (cm), and V is the sample volume (mL).

Results and Discussion:

In MFC systems, the pentose phosphate pathway (PPP) plays a crucial role in enabling microorganisms to effectively metabolize complex organic waste, such as palm oil mill effluent (POME). Running parallel to glycolysis, the PPP is central to two key functions: the production of nicotinamide adenine dinucleotide phosphate (NADPH), which provides the reducing power essential for the biosynthesis of cellular components and the generation of five-carbon sugars, which are fundamental for nucleotide synthesis [21]. By supplying the building blocks and reducing agents needed for growth, the PPP ensures the sustained proliferation and metabolic activity of the microbe. This process enhances the microbial capacity to degrade the organic compounds within POME and convert them into energy. This metabolic flexibility is critical for maintaining robust microbial activity and optimizing electricity generation in MFCs treating industrial wastewater [22].

In this study, the membrane-less MFC achieved a maximum OCV of 0.863 ± 0.032 V (863 ± 32 mV) during the stationary phase (Figure 2), where the corresponding volumetric current density (CD) and power density (PD) were 137.17 ± 3.69 mA/m³ and 18.82 ± 1.00 mW/m³, respectively (Table 1).

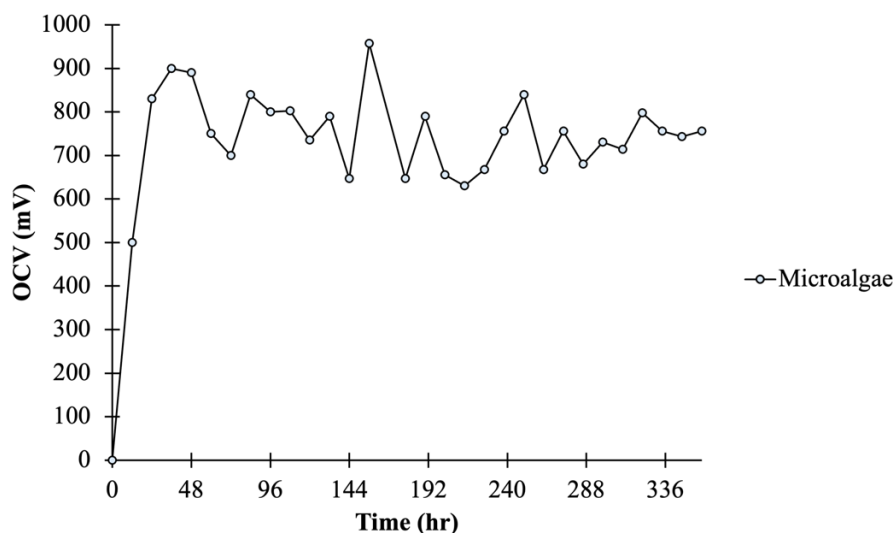


Figure 2.

The open circuit voltage of the membrane-less MFC integrated with microalgae *C. parasitica* sw-03

Table 1.

The electrochemical properties of the membrane-less MFC integrated with microalgae *C. parasitica* sw-03

Electrochemical properties	Values
I (mA)	0.14±0.00
P (mW)	0.02±0.00
CD (mA/m ²)	342.92±9.21
CD (mA/m ³)	137.17±3.69
PD (mW/m ²)	47.06±2.51
PD (mW/m ³)	18.82±1.00
R _{int} (Ω)	5301.11±405.41
NER _v (Wh/m ³)	6.74±0.36
NER _{COD} (Wh/kgCOD)	4.49±0.24

The maximal biomass concentration was 0.03 ± 0.00 g/L (Figure 3), and the maximal biomass yield was 0.002 ± 0.000 g/L/day (Figure 4).

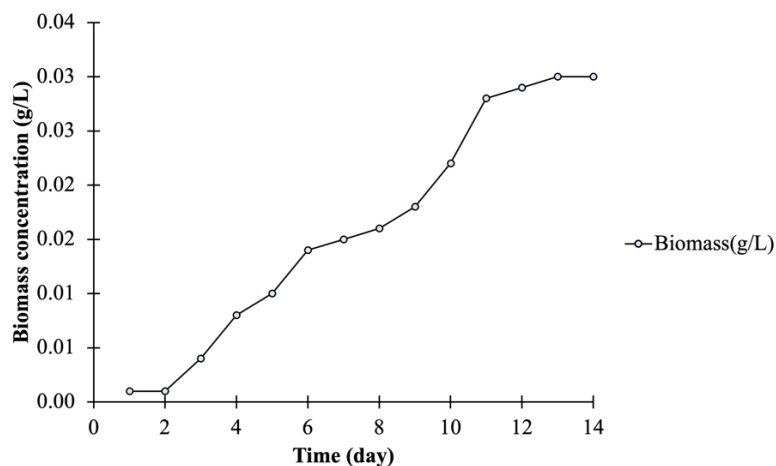


Figure 3.

The biomass concentration (g/L) of the microalgae *C. parasitica* SW-03 in POME.

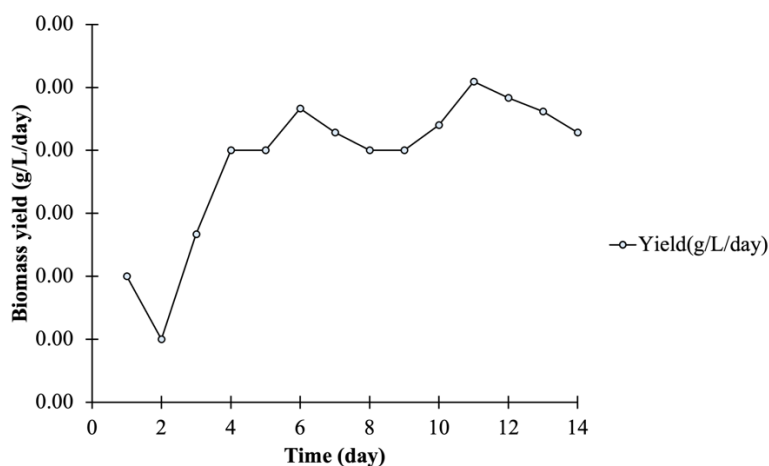


Figure 4.

The biomass yield (g/L/day) of the microalgae *C. parasitica* SW-03 in POME.

Following electricity generation, the concentrations of chlorophyll A and chlorophyll B were determined to be $0.38 \pm 0.01 \mu\text{g/mL}$ and $0.28 \pm 0.01 \mu\text{g/mL}$, respectively.

In contrast, a system utilizing *Desmodesmus subspicatus* co-cultured with bacteria and operated with synthetic wastewater achieved a maximum OCV of 560 mV [23]. The lower voltage in this co-culture system compared with *C. parasitica* may be attributed to differences in substrate composition as synthetic wastewater provides more readily degradable organics than the complex, recalcitrant compounds present in POME. Moreover, the monoculture of *C. parasitica* demonstrates the feasibility of electricity generation directly from untreated POME without requiring bacterial partners, while the co-culture approach highlights the potential synergistic benefits of microbial consortia in improving bioelectrochemical performance.

These findings suggest that heterotrophic microalgae such as *C. parasitica* can serve as effective biocatalysts for direct conversion of industrial wastewater into electricity. At the same time, co-culture strategies integrating microalgae with bacteria could further enhance system efficiency. Future studies should explore mixed-culture systems with *C. parasitica* to exploit both the pentose phosphate pathway and bacterial metabolism, thereby optimizing energy recovery and wastewater treatment from POME. The comparison of electricity generation in microalgae-based MFC was showed in Table 2.

Table 2.
Comparison of electricity generation in microalgae-based MFC.

Microalgae	Wastewater	Maximal PD (mW/m ²)	Reference
<i>Choricystis parasitica</i> SW-03	POME	47.06±2.51	This study
<i>Chlorella vulgaris</i>	Anaerobic sludge	110.89	[24]
<i>Chlorella vulgaris</i>	Anaerobic sludge	12.60	[25]
<i>Spirulina platensis</i>	Tapioca wastewater	14.47	[26]
<i>Synechococcus</i> sp.	Kitchen wastewater	42.50	[27]
<i>Haematococcus lacustris</i>	Anaerobic sludge	33.76	[28]

In MFCs, NADPH and NADH act as key intracellular electron carriers, which can ultimately contribute to extracellular electron transfer (EET) either through direct mechanisms or via secreted redox mediators [29]. Therefore, an enhanced PPP flux in *C. parasitica* under POME conditions likely supports the redirection of metabolic resources toward bioelectricity generation rather than biomass accumulation.

Moreover, heterotrophic microalgae such as *C. parasitica* may inherently exhibit low biomass yields when grown on non-optimized or inhibitory substrates, particularly under oxygen-limited or anaerobic conditions common in closed MFC environments [30].

Conclusion:

The membrane-less MFC demonstrated its potential as a sustainable bioelectrochemical platform by achieving a maximum OCV of 0.863 ± 0.032 V with corresponding volumetric current and power densities of 137.17 ± 3.69 mA/m³ and 18.82 ± 1.00 mW/m³, respectively. Although the maximal biomass concentration (0.03 ± 0.00 g/L) and yield (0.002 ± 0.000 g/L/day) were relatively low, the presence of chlorophyll A (0.38 ± 0.01 µg/mL) and chlorophyll B (0.28 ± 0.01 µg/mL) confirmed the persistence of heterotrophic metabolism following electricity generation. These findings highlight the feasibility of integrating microalgal growth and electricity production in membrane-less MFCs, offering a cost-effective and environmentally friendly strategy for simultaneous bioenergy recovery and biomass utilization. Further optimization of operational parameters and scaling approaches could enhance system performance, advancing its applicability in wastewater treatment and renewable energy production.

Acknowledgements:

This work was supported by Thailand Science Research and Inno Office of National Higher Education Science Research and Innovation Policy Council, Thaksin University (research project grant) Fiscal Year 2024.

References:

1. Morsetto P, Mooren CE, Munaretto S. *Circ Econ Sustain.* 2022; 2:1463-1477.
2. Chen M, Chang L, Zhang J, Guo F, Vymazal J, He Q, Chen Y. *Environ Sci Ecotechnol.* 2020; 4:100063.
3. Wang C, Luo D, Zhang X, Huang R, Cao Y, Liu G, Zhang Y, Wang H. *Environ Sci Ecotechnol.* 2022; 10:100167.
4. Low SS, Bong KX, Mubashir M, Cheng CK, Lam MK, Lim JW, Ho YC, Lee KT, Munawaroh HSH, Show PL. *Sustainability.* 2021; 13:3247.
5. Hasanudin U. *Asian J Environ Biotechnol.* 2018; 2:52-62.
6. Ni F, Peng X, He J, Yu L, Zhao J, Luan Z. *Chem Eng J.* 2012; 213:195-202.



7. Zulfahmi I, Kandi RN, Huslina F, Rahmawati L, Muliari M, Sumon KA, Rahman MM. *Environ Technol Innov.* 2021; 21:101260.
8. Hossain MS, Omar F, Asis AJ, Bachmann RT, Sarker MZI, Ab Kadir MO. *J Clean Prod.* 2019; 219:86-98.
9. Lim KS, Sethu V, Selvarajoo A. *Mater Today Proc.* 2022, 48:871-887.
10. Muhamad NAS, Mokhtar NM, Lau WJ, Ismail AF, Naim R. *J Water Process Eng.* 2022; 49:102969.
11. Soo PL, Bashir MJK, Wong LP. *J Environ Manag.* 2022; 320:115750.
12. Mohammad S, Baidurah S, Kobayashi T, Ismail N, Leh CP. *Processes.* 2021; 9:739.
13. Adeleke AO, Al-Gheethi AA, Daud Z. *Chemosphere.* 2017; 174:232-242.
14. Cheah WY, Show PL, Chang JS, Ling TC, Juan JC. *Bioresour Technol.* 2015; 184:190-201.
15. Cheng SY, Show PL, Lau BF, Chang JS, Ling TC. *Trends Biotechnol.* 2019; 37:1255-1268.
16. Francisco EC, Neves DB, Jacob-Lopes E, Franco TT. *J Chem Technol Biotechnol.* 2010; 85:395-403.
17. Handler RM, Canter CE, Kalnes TN, Lupton FS, Kholiquv O, Shonnard DR, Blowers P. *Algal.* 2012; 1:83-92.
18. Su Y. *Sci Total Environ.* 2021; 762:144590.
19. Rabaey K, Verstraete W. *Trends Biotechnol.* 2005; 23:291-298.
20. Rusanowska P, Debowski M, Zielinski M. *Energies.* 2025; 18:963.
21. Qiao J, Yu Z, Zhou H, Wang W, Wu H, Ye J. *IJMS.* 2025; 26:610
22. Wang H, Feng C. *Bioresour Technol.* 2020; 296:122340.
23. Ribeiro VR, Osorio HDD, Ulrich AC, Rizzetti TM, Barrios AS, Schneider RDCS, Benitez LB. *J Water Proc Eng.* 2022; 48:102882.
24. Li M, Zhou M, Luo J, Tan C, Tian X, Su P, Gu T. *Bioresour Technol.* 2019; 280:95-103.
25. Bazdar E, Roshandel R, Yaghmaei S, Mardanpour MM. *Bioresour Technol.* 2018; 261:350-360.
26. Hadiyanto H, Christwardana M, Costa DC. *Energy Sour. Part A Recover Util Environ Eff.* 2023; 45:3409-3420.
27. Mohamed SN, Hiranman PA, Muthukumar K, Jayabalan T. *Bioresour Technol.* 2020; 295:122226.
28. Ahirwar A, Khan MJ, Khandelwal P, Singh G, Harish H, Vinayak V, Ghangrekar MM. *Sci Rep.* 2025; 15:30196.
29. Rabaey K, Verstraete W. *Trend. Biotechnol.* 2005; 23:291-298.
30. Moreno-Garrido I. *Sci. World J.* 2008; 8:866-880.



ISOLATION AND CHARACTERIZATION OF FUNGI FROM ORGANIC RICE CULTIVATION SOIL FOR ENHANCING RICE SEED GERMINATION

Anuruk Seeka,¹ Gregorius Nico Adi Setiawan,² Manato Nishikawa,³ Nuttapon Pombubpa^{1,*}

¹Department of Microbiology, Faculty of Science, Chulalongkorn University, Bangkok, Thailand

²Plant Pathology/Phytopathology, Wageningen University & Research, Wageningen, Gelderland, Netherlands

³Department of Biotechnology, Graduate School of Engineering, The University of Osaka, Osaka, Japan

*Corresponding author: E-mail: Nuttapon.Po@chula.ac.th

Abstract:

Rice (*Oryza sativa* L.) seed germination is a critical determinant of yield stability under variable environmental conditions. Seed biopriming with beneficial fungi offers a sustainable approach to enhance seed vigor and early seedling establishment. This study isolated and screened fungal strains from rice rhizosphere soils under three fertilizers: pure fermented chitin waste (FCW), FCW combined with organic fertilizer (OFC), and FCW combined with chemical fertilizer (CFC), to evaluate their potential for promoting germination and gibberellic acid production, as GA₃ leads to breaking seed dormancy and stimulating germination. A total fungal isolate of 37 sporogenous isolates were recovered using soil dilution plating on PDA medium. Seven isolates (FCW201, FCW205, OFC202, OFC305, OFC405, OFC408, and CFC212) have significantly higher germination percentage (90–95%) compared with the control (88.33%) by using one-way ANOVA and Tukey's post hoc test ($p = 0.025, 0.011, 0.011, 0.001, 0.018, 0.018, \text{ and } 0.0005$, respectively, ($p < 0.05$)). Among these, CFC212 showed the highest germination rate (95%) while six isolates (CFC401, OFC405, OFC305, OFC202, OFC408, and CFC212) produced potentially 3.7–23.7 times higher gibberellic acid compounds absorbance values at 254 nm than the reference strains *Fusarium oxysporum* and the control. These results demonstrate that organic-chitin amendments enrich the functional potential of beneficial fungal communities for seed biopriming to improve germination in sustainable rice production.

Introduction:

Rice (*Oryza sativa* L.) is one of the world's most important staple crops, providing food for nearly half of the global population.¹ In recent years, climate change and environmental changes have intensified challenges in agricultural production, particularly with limited domestic resources, as time, temperature, relative humidity, and stress conditions can significantly influence the properties of germinated rice. Therefore, the germination stage of rice is the most sensitive period before the rice plant undergoes transformation. Currently, dry direct seeding (DDS) technology, which involves sowing non-germinated rice seeds into shallow soil layers (1–2 cm) and then irrigating to initiate germination, has become widely adopted. However, DDS often results in poor germination and uneven seedling emergence due to factors such as high calcium or lignin content in the seed coat, which restricts water absorption by the embryo.²

Enhancing seed vigor and germination is therefore critical for stabilizing and improving rice yield. Seed priming is an effective pre-sowing treatment that regulates the hydration process under controlled temperature and moisture conditions to activate metabolic processes, bringing the seed closer to the point of germination and promoting faster, more uniform, and stress-tolerant germination.² This low-cost and low-risk approach enhances seedling establishment by reducing lag time, repairing cellular damage, and accumulating



germination-promoting metabolites during seed imbibition. Various priming methods, including hydropriming, osmopriming, nutrient priming, and chemical priming, have been successfully applied to improve rice performance under diverse environmental stresses.³ In rice, the demand for seed priming is increasingly evident, particularly in attending to agronomic implications for productivity gains under stressful environments. The rice seeds are treated to improve seed vigor, germination percentage, and plant establishment before sowing in the seedbed, transplanting seedlings, or in the fields.⁴

Recently, seed biopriming, which exploits beneficial plant-microorganism interactions, provides an eco-friendly alternative to chemical seed treatments by enhancing plant growth, nutrient uptake, and stress tolerance, while reducing dependency on fertilizers and pesticides. Plant growth-promoting fungi (PGPF) have been recognized for their benefits to plant development and have been extensively studied by researchers worldwide. PGPF has stimulated growth-promoting effects in various host plants, including maize, pea, chickpea, cucumber, and rice. Moreover, PGPF was found in agricultural soil where fermented chitin fertilizer was applied, which enriches the soil by supplying accessible nitrogen and carbon sources that stimulate beneficial fungal growth. Previous research showed that these potential PGPF support a balanced microbial community and enhance soil health. Additionally, the deacetylated form of chitosan suppresses pathogenic fungi by disrupting their cell membranes and walls, thereby reducing disease incidence.^{5,6}

PGPF can improve seed germination and crop development through organic matter decomposition, enhanced mineral absorption, promoting dormancy breaking and seedling vigor, and hormone production (particularly gibberellic acid).^{7, 8, 9} Gibberellic acid induces the amylase biosynthesis in rice endosperm for converting starch into soluble sugars, leading to breaking dormancy and stimulating the secretion of hydrolytic enzymes to weaken the seed coat and promote seed germination.¹⁰ These properties make gibberellic acid a valuable tool in agriculture. Examples of PGPF include *Fusarium oxysporum*¹¹, *Trichoderma harzianum*¹², and *Penicillium citrinum*¹³. Despite the availability of agricultural products aimed at disease suppression or root growth enhancement, few target the improvement of rice seed germination.

Therefore, this study aims to isolate fungal strains from organically cultivated rice soils and their ability to promote seed germination in the “Pathum Thani 1” rice variety. Additionally, the effects of selected fungi on germination rate and seedling physiological traits will be assessed. We hypothesize that fungi isolated from organic rice soil can enhance rice seed germination compared to untreated controls. The findings of this investigation provide new insights into harnessing certain rice seed germination-promoting fungal species for sustainable rice cultivation.

Methodology:

Soil collection

Bulk soil samples from rice plant cultivation in a greenhouse with controlled temperature and humidity at the Department of Botany, Faculty of Science, Chulalongkorn University, were collected by uprooting rice and were gently shaken to remove excess or loose soil into labeled sterile conical centrifuge tubes containing 17 mL of sterile distilled water containing 0.1% (v/v) Tween 80.⁸ Twelve samples including four samples of bulk soil obtained from rice grown with fermented chitin waste fertilizers (FCW), four samples of bulk soil obtained from rice grown with mixed fertilizers between fermented chitin waste fertilizers and chemical fertilizers (CFC), and four samples of bulk soil obtained from rice grown with mixed fertilizers between fermented chitin waste fertilizers and organic fertilizers (OFC). All bulk soils were from Setiawan et al.¹⁴ and stored in the refrigerator (4 °C).

Fungal isolation

Fungal strains were isolated from rice bulk soil following the method of Tarroum et al⁸, with minor modifications. Soil samples were serially diluted (10^{-1} – 10^{-6}) with 9 mL of sterile distilled water containing 0.1% (v/v) Tween 80 in glass test tubes. Then, a 0.1 mL aliquot from each dilution was spread onto potato dextrose agar (PDA) plates supplemented with tetracycline at 45 mg/L to inhibit bacterial growth. Plates were incubated at room temperature for 5–9 days in duplicate. Distinct fungal colonies were sub-cultured onto fresh PDA plates and purified through repeated single-spore transfers on PDA containing tetracycline for 7 days at room temperature.

Germination promotion and Pathogenicity test of fungal strains

To examine fungal colonization in rice seeds and consider the adverse effect on inhibiting rice seed germination, rice seeds were surface sterilized with a 1% sodium hypochlorite solution for 10 minutes, washed three times with sterile water, and then left to dry on sterile filter paper in a flow cabinet. The 10-day-old fungal isolates were cultured on PDA, which promotes rapid sporulation and supports diverse fungi. The cultures were then flooded with sterile saline water, and the spores were harvested by filtration using sterile filter paper. The spore suspensions were prepared and adjusted to 1×10^6 spores/mL using a hemocytometer.¹ Then, each rice seed was inoculated with 20 μ L of each fungal suspension in petri dishes (20 grains per plate) containing filter paper that had absorbed sterile distilled water, 2 mL, and was incubated for 7 days at room temperature. The number of non-germinated and normal seedlings was recorded and calculated as the percentage of seed germination as the percentage (%) $GP = 100 \times N/n$, where N is the number of normal seedlings and n is the total number of tested seeds in different treatments by inoculation with fungal isolates, which was determined the initial seedlings from observation on both the appearance of the apical between growth-promoting and pathogenic isolates. Each treatment (20 seeds) was repeated three times for each isolate.¹ Fungal strains with a higher and equal germination percentage than the control are subcultured onto a PDA plate for further studies. This will prioritize strains showing strong germination rate and exclude weak or inhibitory isolates for further characterization. Data from germination percentage (GP) calculation were collected at least three times, and the data expresses the results as the mean \pm standard deviation (SD). Data was subjected to statistical analysis by one-way analysis of variance (ANOVA) with a significance level of $p < 0.05$, followed by a post hoc Tukey's test to compare mean values.¹¹ For each comparison of differences in the control group and test group, a p-value of < 0.05 (+) was considered statistically significant, while a p-value of > 0.05 (–) was considered not statistically significant.⁶

Screening test of fungal strains for gibberellic acid (GA) production

To screen fungal strains that enhance rice seed germination through examination of the potential of gibberellic acid production. Gibberellic acid production of fungal isolates was determined by measuring the wavelength absorbance. Fungal isolates were cultured on a sterile Czapek's liquid medium (sucrose 30.00 g/L, NaNO_3 3.00 g/L; K_2HPO_4 1.00 g/L, $\text{MgSO}_4 \cdot 7\text{H}_2\text{O}$ 0.50 g/L, KCl 0.50 g/L, FeSO_4 0.01 g/L, and 1000 ml distilled water at pH (at 25°C) 6.8 ± 0.2) with tetracycline 45 mg/L. Fungal liquid cultures were incubated at 30 °C for 7 days at 200 rpm. Culture solutions (10 mL) were mixed with 0.5 mL of zinc acetate solution (1 M) in a centrifuge tube and shaken for 3 min. This mixture was then supplemented by 0.5 ml of potassium ferrocyanide solution (1 M) and centrifuged for 15 min. 2.5 ml of supernatant was transferred to a flask containing 8 ml of absolute ethanol and 90 ml of HCl (30%). Suspensions were incubated at 20 ± 2 °C in a water bath for 12 hours, and the absorbance was read at 254 nm on a UV-vis spectrophotometer against water as a blank

control at least once. For the control, 35 mL of HCl solution (5%) was taken in a flask, and the volume was adjusted to 100 mL with 65 mL of distilled water. The absorbance values were reported as a fold-change comparison (FC): $\text{Fold Change} = (\text{Value in Experimental Sample}) / (\text{Value in Control Sample})$. Fungal strains with a high absorbance value of gibberellic acid were sub-cultured into a PDA plate for further studies.¹¹

Results and Discussion:

66 fungal isolates were obtained, including 12 fungal isolates from rice soil samples under pure fermented chitin waste fertilizers (FCW) treatment, 26 fungal isolates from rice soil samples under mixed fertilizers between FCW fertilizers and organic fertilizers (OFC) treatment, and 28 fungal isolates from rice soil samples under mixed fertilizers between FCW fertilizers and chemical fertilizers (CFC) treatment. From these isolates, only 37 different morphological fungal strains produced spores (sporogenous fungi) under normal conditions (25-30 °C, 90% humidity, 12-hour light period). Seven sporogenous fungal isolates were obtained from a rice soil sample under treatment with pure fermented chitin waste fertilizers (FCW) (Figure 1). Twelve sporogenous fungal isolates were obtained from rice soil samples under mixed fertilizers, including both FCW fertilizers and organic fertilizers (OFC), treatment (Figure 2). Eighteen sporogenous fungal isolates were obtained from rice soil samples under mixed fertilizers, including both FCW fertilizers and chemical fertilizers (CFC) treatment (Figure 3).

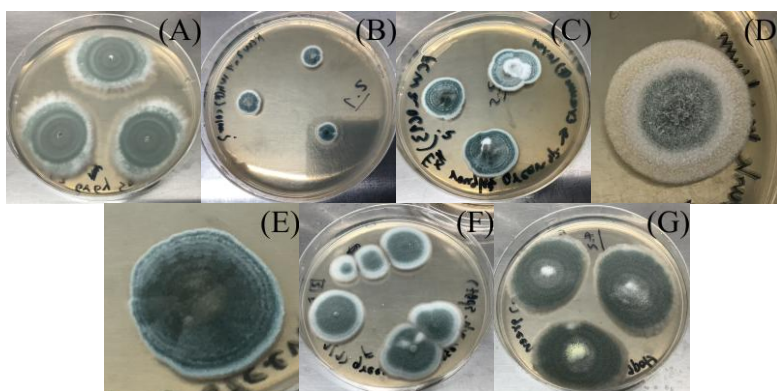


Figure 1.

Colonies of sporogenous fungal isolates from rice soil sample under the pure fermented chitin waste fertilizers (FCW) treatment (A: FCW101, B: FCW201, C: FCW205, D: FCW206, E: FCW301, F: FCW402, and G: FCW405)

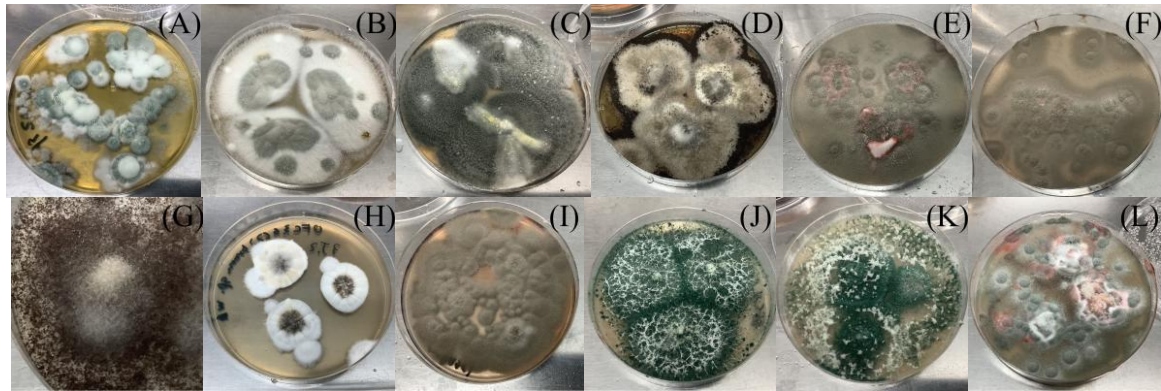


Figure 2.

Colonies of sporogenous fungal isolates from rice bulk sample under the mixed fertilizers between FCW fertilizers and organic fertilizers (OFC) treatment (A: OFC201, B: OFC202, C: OFC305, D: OFC306, E: OFC307, F: OFC308, G: OFC309, H: OFC310, I: OFC401, J: OFC402, K: OFC405, and L: OFC408)

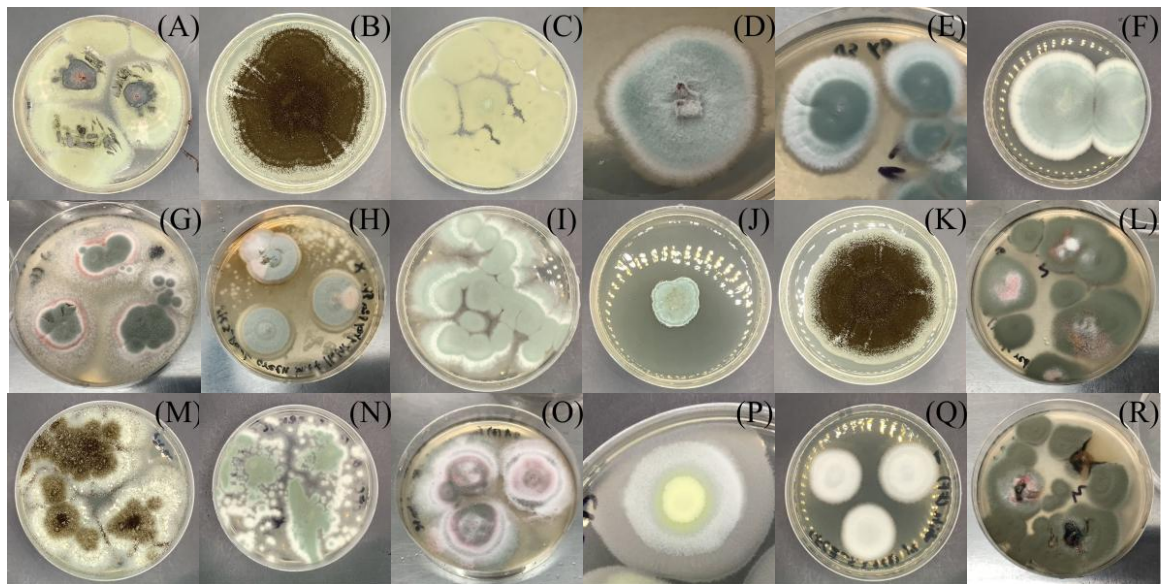


Figure 3.

Colonies of sporogenous fungal isolates from rice bulk sample with obtained the mixed fertilizers between FCW fertilizers and chemical fertilizers (CFC) treatment (A: CFC201, B: CFC203, C: CFC204, D: CFC205, E: CFC206, F: CFC207, G: CFC209, H: CFC302, I: CFC401, J: CFC304, K: CFC305, L: CFC403, M: CFC404, N: CFC211, O: CFC212, P: CFC213, Q: CFC306, and R: CFC216)

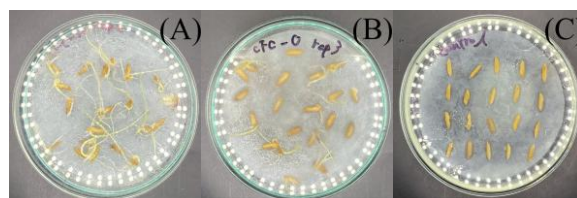


Figure 4.

Physiological feature of rice seed germination on a glass petri plate (treatment with fully germinated seed (20 seeds: CFC212 rep2 (A)), Treatment with rarely germinated seed (13 seeds: OFC305 rep3 (B)), and Treatment with non-germinated seed (C))

Germination promotion and pathogenicity tests of all 37 sporogenous fungal isolates, analyzed using the one-way ANOVA followed by Tukey's post-hoc comparisons, revealed significant differences in germination percentage compared with the control. Germination performance was evaluated based on the emergence of the apical shoot and primary root (first rooting) (Figures 4A–C). Seven isolates (FCW201, FCW205, OFC202, OFC305, OFC405, OFC408, and CFC212) exhibited notably higher germination percentages (91.67%, 91.67%, 91.67%, 91.67%, 90%, 90%, and 95%, respectively) than the control (88.33%) follow as Figure 5. Among them, CFC212 demonstrated the highest germination rate (95%) (Figure 5), indicating strong seed germination–promoting activity. The analysis yielded a high F-statistic and a highly significant p-value ($p = 0.0005$), confirming that these isolates significantly enhanced germination. Furthermore, OFC305 showed a significant increase ($p = 0.001$), followed by FCW205, OFC202, OFC405, and OFC408 ($p = 0.011, 0.011, 0.018, \text{ and } 0.018$, respectively), while FCW201 also exhibited a potentially significant effect ($p = 0.025$). Post-hoc analysis indicated that the most pronounced enhancement occurred in CFC212, followed by FCW201, FCW205, OFC202, and OFC305, all of which differed significantly from the control at the 95% confidence level ($p < 0.05$).

Five fungal isolates (OFC201, OFC307, OFC402, CFC401, and CFC403) recorded equal numbers of average germinated seeds comparable to the control (Figure 5), exhibited a slight increase in the relative germination percentage compared to 88.33% of the control. However, one-way ANOVA followed by Tukey's post-hoc test indicated that these differences were not statistically significant ($p > 0.05$). In contrast, twenty-five isolates (CFC201, CFC203, CFC204, CFC205, CFC206, CFC207, CFC209, CFC211, CFC213, CFC216, CFC302, CFC304, CFC305, CFC306, CFC404, OFC306, OFC308, OFC309, OFC310, OFC401, FCW101, FCW206, FCW301, FCW402, and FCW404) exhibited lower germination percentages (76.67–86.67%) and reduced germination rates, which displayed limited germination-promoting ability or may indicate inhibitory effects (Figure 5).



Figure 5.
Comparison of the germination percentage (GP) of each sporogenous fungal isolate

Figure 6 shows that the crude gibberellin compounds produced by the selected fungal isolates exhibited markedly higher absorbance values at 254 nm compared with *Fusarium oxysporum* and the control. Relative absorbance as a proxy for crude gibberellin compounds concentration to the control ($A_{(254)} = 0.564$), *F. oxysporum* showed a 108% increase ($A_{(254)} = 1.172$), while the six fungal isolates (OFC202, OFC305, OFC405, OFC408, CFC401, and

CFC212) produced between 3.7-fold to 23.7-fold higher absorbance values. Among them, CFC401 exhibited the highest crude gibberellin compounds production, with an absorbance value approximately 24 times greater than the control and 11 times higher than *F. oxysporum*. followed by OFC405 and OFC305 followed with ~12-fold and 9-fold increases, respectively, whereas OFC202, OFC408, and CFC212 produced 3.7 to 6-fold higher absorbance. In contrast, the remaining isolates (FCW201, FCW205, OFC201, OFC308, OFC402, and CFC403) produced lower crude gibberellin compounds production than *Fusarium oxysporum* and the control. These observations suggest that all six isolates synthesized substantially greater amounts of crude gibberellin compounds, strongly supporting the hypothesis that they possess higher gibberellin biosynthetic capacity than *F. oxysporum* and the control, although statistical confirmation of significance was not possible due to the lack of replicate measurements.

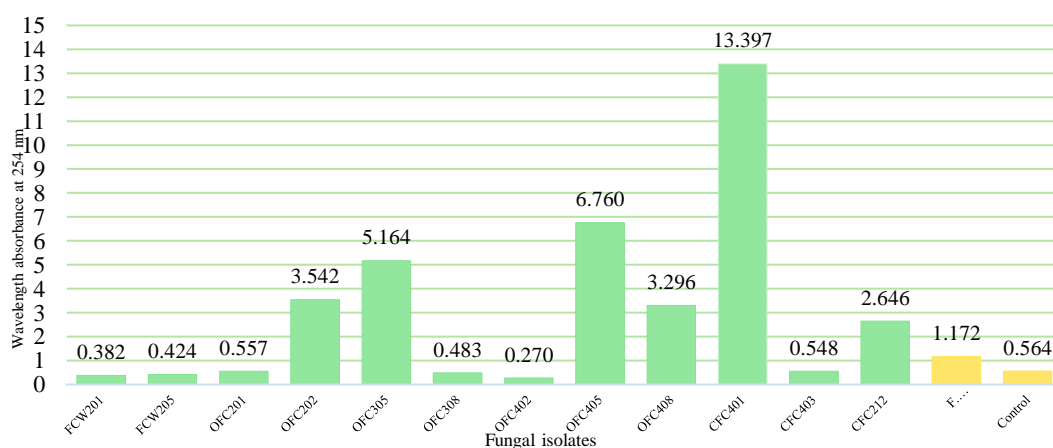


Figure 6.

The gibberellic acid wavelength absorbance value of each sporogenous fungal isolate

From result found that the 37 sporogenous fungal isolates recovered from rice rhizosphere soils, seven strains (FCW201, FCW205, OFC202, OFC305, OFC405, OFC408, and CFC212) significantly enhanced rice seed germination relative to the control. Among these, CFC212 exhibited the highest germination rate (95%), exceeding the control (88.33%), which was highly significant to be a beneficial fungus for enhancing rice seed germination ($p = 0.0005$). Isolate OFC305 also showed strong stimulatory activity ($p = 0.001$), followed by FCW205, OFC202, OFC405, and OFC408 ($p = 0.011$ – 0.018). These results highlight their strong potential as beneficial fungi for improving rice seed germination.

The germination-promoting effects of selected isolates are likely associated with the biosynthesis of bioactive metabolites especially, gibberellic acids (GA_3), known to stimulate the mobilization of seed reserves, promote cell elongation, and enhance embryo development. Previous studies have demonstrated that *Fusarium*, *Aspergillus*, and *Penicillium* species improve seed germination through GA_3 compounds production that stimulate seed metabolism. Similarly, six of the selected isolates (CFC401, OFC405, OFC305, OFC202, OFC408, and CFC212) produced notably higher quantities of gibberellin-like compounds than *Fusarium oxysporum*, a known GA_3 producer. This suggests that these isolates may promote early seedling growth through the synthesis of gibberellic acids (GA_3). Particularly CFC401 and OFC405, suggesting that they may serve as promising alternatives for biofertilizer development. The high germination percentage of CFC212 corresponds to its strong gibberellin production capacity, supporting a positive correlation between



phytohormone biosynthesis and seed germination stimulation. Moreover, fungal isolates OFC305, OFC405, and FCW205 may similarly enhance seed vigor by influencing endogenous hormone balance, water uptake, and hydrolytic enzyme activity in rice seeds. Collectively, these findings highlight CFC401, OFC405, and CFC212 as promising plant growth-promoting fungi (PGPF) for rice biopriming applications.

The distribution of these beneficial fungal isolates from each fertilizer treatment (FCW, OFC, and CFC) supports the influence of soil management on microbial community dynamics.¹⁴ Interestingly, most of the high gibberellin-producing isolates (four of six fungal isolates, 66.67%) originated from soils of OFC (organic + FCW) treatment. This suggests that mixed chitin-based or organic compounds inputs may favor enrichment of plant-beneficial fungi over neutral or pathogenic taxa. Comparable findings have been reported in rhizosphere community studies where FCW, in combination with organic or chemical fertilizers, enhanced fungal richness and increased the abundance of beneficial genera such as *Penicillium*, *Talaromyces*, and *Cladosporium*.¹⁴ Such selective enrichment is consistent with the concept that organic amendments can shape microbial communities toward functional groups with plant growth-promoting traits.

Overall, this study indicates that only a subset of sporogenous fungi exhibit plant growth-promoting potential, likely mediated by gibberellin compounds biosynthesis and related signaling pathways. The strong positive performance of fungal isolates CFC212, OFC305, and FCW205 indicates their potential as effective biopriming agents to enhance rice seed vigor and early seedling establishment. However, isolates that reduced germination may produce inhibitory metabolites or induce stress-related responses, warranting further investigation. The results underscore the importance of strain-specific evaluation when developing microbial inoculants for seed treatment and sustainable crop production. Future work should focus on field trials to assess the efficacy of biopriming under natural conditions and on developing practical biopriming formulations that can enhance rice seed germination and early seedling vigor, offering a sustainable alternative to synthetic hormones and chemical fertilizers.

Conclusion:

Fertilizer regime influenced fungal diversity and function: although all treatments yielded 37 sporogenous isolates, only a few promoted rice seed germination. This study identified seven sporogenous fungal isolates that significantly enhanced rice seed germination, with CFC212 exhibiting the strongest promotive effect. The results indicate that the germination-enhancing activity is likely linked to gibberellin (GA₃) biosynthesis, as several isolates produced higher levels of gibberellin-like compounds than *Fusarium oxysporum*. Most beneficial isolates originated from soils treated with mixed organic and chitin-based fertilizers, suggesting that such inputs promote plant growth-promoting fungal communities. Among the isolates, CFC212, OFC305, and FCW205 showed the greatest potential as biopriming agents for improving rice seed vigor. These findings highlight the value of strain-specific screening for developing sustainable microbial inoculants as eco-friendly alternatives to synthetic hormones and chemical fertilizers.

Acknowledgements:

This research project is supported by the scholarship from the Department of Microbiology, Faculty of Science, Chulalongkorn University.

References:

1. Jiang, H.; Wu, N.; Jin, S.; Ahmed, T.; Wang, H.; Li, B.; Wu, X.; Bao, Y.; Liu, F.; Zhang, J.-Z. Identification of rice seed-derived *Fusarium* spp. and development of

- LAMP assay against *Fusarium fujikuroi*. *Pathogens* **2021**, *10* (1), 1. DOI: 10.3390/pathogens10010001.
2. Hou, D.; Bi, J.; Ma, L.; Zhang, K.; Li, D.; Rehmani, M. I. A.; Tan, J.; Bi, Q.; Wei, Y.; Liu, G.; et al. Effects of soil moisture content on germination and physiological characteristics of rice seeds with different specific gravity. *Agronomy* **2022**, *12* (2), 500. DOI: 10.3390/agronomy12020500.
 3. Zhang, K.; Khan, M. N.; Luo, T.; Bi, J.; Hu, L.; Luo, L. Seed priming with gibberellic acid and ethephon improved rice germination under drought stress via reducing oxidative and cellular damage. *Journal of Soil Science and Plant Nutrition* **2024**, *24* (2), 2679-2693. DOI: 10.1007/s42729-024-01691-3.
 4. Ramya, S.; Kour, B.; Sudheer, K.; Kumar, M. B. A.; Ramakrishnan, B. Seed priming alters the microbial community composition in seedlings of rice (*Oryza sativa* L.). *Journal of Plant Growth Regulation* **2024**. DOI: 10.1007/s00344-024-11534-1.
 5. Sharp, R. G. A review of the applications of chitin and its derivatives in agriculture to modify plant-microbial interactions and improve crop yields. *Agronomy* **2013**, *3* (4), 757-793. DOI: 10.3390/agronomy3040757.
 6. Xu, S.; Li, F.; Gao, J.; Zhou, X.; Li, M.; Li, L.; Hui, C.; Zhang, S.; Liu, K.; Kong, W.; et al. Low GHG emissions and less nitrogen use in mushroom-based protein production from chitin-containing waste and cottonseed hull with two phase SSF. *Industrial Crops and Products* **2023**, *201*, 116970. DOI: 10.1016/j.indcrop.2023.116970.
 7. Metwally, R. A.; Abdelhameed, R. E.; Soliman, S. A.; Al-Badwy, A. H. Potential use of beneficial fungal microorganisms and C-phycoyanin extract for enhancing seed germination, seedling growth and biochemical traits of *Solanum lycopersicum* L. *BMC Microbiology* **2022**, *22* (1), 108. DOI: 10.1186/s12866-022-02509-x.
 8. Tarroum, M.; Ben Romdhane, W.; Ali, A. A. M.; Al-Qurainy, F.; Al-Doss, A.; Fki, L.; Hassairi, A. Harnessing the rhizosphere of the halophyte grass *Aeluropus litoralis* for halophilic plant-growth-promoting fungi and evaluation of their biostimulant activities. *Plants* **2021**, *10* (4), 784. DOI: 10.3390/plants10040784.
 9. Cardarelli, M.; Woo, S. L.; Roupael, Y.; Colla, G. Seed treatments with microorganisms can have a biostimulant effect by influencing germination and seedling growth of crops. *Plants* **2022**, *11* (3), 259. DOI: 10.3390/plants11030259.
 10. Fu, D.; Wu, W.; Mustafa, G.; Yang, Y.; Yang, P. Molecular mechanisms of rice seed germination. *New Crops* **2025**, *2*, 100051. DOI: 10.1016/j.ncrops.2024.100051.
 11. Ben Rhouma, M.; Kriaa, M.; Ben Nasr, Y.; Mellouli, L.; Kammoun, R. A new endophytic *Fusarium oxysporum* gibberellic acid: optimization of production using combined strategies of experimental designs and potency on tomato growth under stress condition. *Biomed Res Int* **2020**, *2020*, 4587148. DOI: 10.1155/2020/4587148.
 12. Rawat, L.; Singh, Y.; Shukla, N.; Kumar, J. Seed biopriming with salinity tolerant isolates of *Trichoderma harzianum* alleviates salt stress in rice: Growth, physiological and biochemical characteristics. *Journal of Plant Pathology* **2012**, *94*, 353-365.
 13. Khan, S. A.; Hamayun, M.; Yoon, H.; Kim, H.-Y.; Suh, S.-J.; Hwang, S.-K.; Kim, J.-M.; Lee, I.-J.; Choo, Y.-S.; Yoon, U.-H.; et al. Plant growth promotion and *Penicillium citrinum*. *BMC Microbiology* **2008**, *8* (1), 231. DOI: 10.1186/1471-2180-8-231.
 14. Setiawan, G. N. A.; Kojonna, T.; Chadchawan, S.; Chantarachot, T.; Pombubpa, N. The investigation of 'PHATUMTHANI 1' rice rhizosphere-fungal composition under commercial organic fertilizer and chemical fertilizer treatments. In The 49th International Congress on Science, Technology and Technology-based Innovation (STT 49), Faculty of Science, Prince of Songkla University, Hatyai campus; 2024.



IDENTIFICATION AND FUNCTIONAL CHARACTERIZATION OF SMALL HEAT SHOCK PROTEINS IN SHRIMP IMMUNE RESPONSES TO *Ecytonucleospora hepatopenaei* (EHP) INFECTION

Pithiwat Maiket,¹ Nutthapon Sangklai,¹ Anchalee Tassanakajon^{1,*}

¹Center of Excellence for Molecular Biology and Genomics of Shrimp, Department of Biochemistry, Faculty of Science, Chulalongkorn University, Bangkok, Thailand

*e-mail: Anchalee.K@chula.ac.th

Abstract:

Small heat shock proteins (sHSPs) are ATP-independent chaperones synthesized by cells in response to various stresses, including pathogen infection, to maintain cellular and protein homeostasis. sHSPs range in size from 10 to 40 kDa, yet their biological functions in shrimp immunity remain poorly understood. In this study, we identified *sHSP* genes in the *Litopenaeus vannamei* genome, including *LvHSP10*, *LvHSP21*, and *LvHSP22*. These *sHSPs* were expressed in all examined tissues and were strongly induced by microsporidian *Ecytonucleospora hepatopenaei* (EHP) infection. Notably, *LvHSP10* expression increased more than 20-fold upon EHP challenge. Silencing *LvHSP10* led to a dramatic rise in EHP load, approximately 100-fold higher than the *dsGFP* control at 9- and 11 days post-cohabitation, and was accompanied by up-regulation of antimicrobial peptides (*LvALF1*, *LvPEN3*, *LvLyz-c*). Conversely, suppression of *LvHSP10* down-regulated several immune-related genes, including *Toll*, *JAK/STAT*, and components of the prophenoloxidase cascade. Collectively, these findings indicate that *LvHSP10* may play a crucial role in the shrimp immune response to EHP by modulating the expression of both antimicrobial peptides and components of immune signaling pathways.

Introduction:

Heat shock proteins (HSPs) are a highly conserved family of molecular chaperones that play a vital role in maintaining cellular homeostasis and regulating immune responses across a wide range of organisms, including crustaceans^{1,2}. In the shrimp's immune system, HSPs act as key regulators, mediating the balance between protein synthesis and degradation, particularly under stressful conditions such as oxidative stress, changes in temperature or salinity and microbial infections³⁻⁵. Previous studies have demonstrated that various HSPs respond to viral, bacterial, and microsporidian infections, highlighting their crucial role as a first line of defense during pathogen invasion⁶.

Small heat shock proteins (sHSPs), with molecular weights typically ranging from 10 to 40 kDa, are a major family of HSPs that function as ATP-independent chaperones, preventing the irreversible aggregation of denatured proteins⁷⁻⁹. Research has shown that sHSPs, such as *SpHSP40*, *MrHSP37*, *PmHSP21*, and *PcHSP21*, are directly involved in the immune response in various shrimp species¹⁰⁻¹³. Specifically, *Litopenaeus vannamei* heat shock protein 10 (*LvHSP10*) has been shown to be significantly upregulated following infection with *Vibrio parahaemolyticus* and the white spot syndrome virus (WSSV), suggesting a key function in antiviral and antibacterial immunity¹⁴. However, the specific role of *LvsHSPs* against microsporidian infection remains largely unknown.

Ecytonucleospora hepatopenaei (EHP) is an obligate intracellular microsporidian parasite that has become a major threat to the global shrimp aquaculture industry^{15,16}. EHP primarily targets the hepatopancreas of shrimp, causing a disease known as hepatopancreatic microsporidiosis (HPM)¹⁷. Although EHP infection does not typically cause mass mortality, it leads to severe economic losses due to significant growth retardation, size variation, and increased susceptibility to other diseases. Shrimp, like other invertebrates, lack an adaptive immune system and rely mainly on their effective innate immune system to combat

pathogens. This response involves both cellular and humoral immunity, including the activation of pattern recognition receptors (PRRs), the prophenoloxidase (proPO) system, and the production of antimicrobial peptides (AMPs)^{18–20}. The ability of EHP to evade or suppress this host immune response is a critical factor in its successful proliferation^{21–23}.

Given the importance of HSPs in mediating stress and immune responses, and the limited understanding of the host-pathogen interaction in EHP-infected shrimp, this study aims to investigate the potential role of sHSPs in *L. vannamei* immunity against EHP. First, we identified sHSPs, including *LvHSP10*, *LvHSP21*, and *LvHSP22*, from the *L. vannamei* genome database. Then, we investigated the tissue distribution of these sHSPs in various shrimp tissues via semi-quantitative RT-PCR. The temporal expression pattern of *LvHSP10*, *LvHSP21*, and *LvHSP22* following EHP cohabitation was determined using quantitative RT-PCR. Furthermore, RNA interference (RNAi) was employed to silence the *LvHSP10*, allowing us to evaluate its impact on EHP infection and the expression of the immune-related genes. This research provides insights into the intricate innate immunity of shrimp and could contribute to the development of novel strategies for controlling EHP in aquaculture.

Methodology:

1. Analysis of *LvsHSPs* expression in shrimp tissues by semi-quantitative RT-PCR

To investigate the specific expression of *LvHSP10* (accession number: MF062460.1), *LvHSP21* (accession number: XM_070125649.1) and *LvHSP22* (accession number: XM_027373023.2) in various shrimp tissues, total RNA from different shrimp tissues including hemocytes, gills, hepatopancreas, heart, intestine, muscle, eyestalk, and stomach were extracted using a FavorPrep Blood/Cultured Cell Total RNA Mini Kit (Favorgen, Taiwan) according to the manufacturer's instruction and reverse transcribed to first-stranded cDNA using Maxime™ RT PreMix Kit (Intron, Korea). The gene expression was analyzed by semi-quantitative RT-PCR using the elongation factor 1 α (*LvEF1 α*) as an internal control. All amplified products were separated by agarose gel electrophoresis and visualized by UV-transillumination.

2. Temporal gene expression analysis of sHSPs after EHP challenge by qRT-PCR

To investigate the expression of *LvHSP10*, *LvHSP21* and *LvHSP22* during EHP infection, sixty specific pathogen-free (SPF) *L. vannamei* were separated into thirty shrimps in the control group and thirty shrimps in the infected group. EHP-infected shrimps were prepared by cohabitation method described previously²⁴. The shrimps were reared together with 15–20 EHP-positive shrimps. Hemocytes were collected from each group (n=5) at 1-, 7-, 9-, 11-, 13-, and 15 days post cohabitation. The total RNA from the hemocyte was extracted and used for cDNA synthesis. The mRNA expression of *LvHSP10*, *LvHSP21* and *LvHSP22* were investigated using Luna Universal qPCR Master Mix (New England Biolabs, USA) and CFX96 Touch® Real-time PCR Detection System (Bio-Rad, USA) with qPCR gene-specific primers, the *LvEF1 α* was used as an internal control (Supplementary Table 1). The qPCR conditions were as follows: one cycle at 95 °C for 2 min, followed by 40 cycles consisting of 5 s at 95 °C and 30 s at 60 °C. The GraphPad Prism 9 software was used for the statistical analyses. In this experiment, a two-tailed unpaired Student's t-test was used to compare the differences between the two groups.

3. Suppression of *LvHSP10* by RNA interference and the effect on EHP infection

3.1. dsRNA synthesis

To prepare specific dsRNA for gene-knockdown, the PCR products of *LvHSP10* were amplified using gene-specific primers flanked with T7 promoter sequence (Supplementary Table 1). The gene fragments of *LvHSP10* and the control *GFP* were synthesized using T7



RiboMAX Express RNAi System kit (Promega, USA) according to the manufacturer's protocol. The quality of dsRNA was verified after annealing by gel electrophoresis with UV visualization and quantified using NanoDrop™ 2000 spectrophotometer (Thermo Scientific, USA).

3.2. Gene expression analysis in *LvHSP10* silenced shrimp

To silence *LvHSP10* by dsRNA, each shrimp was double injected at the third abdominal segment with 1.5 µg/g shrimp of *dsLvHSP10*, or *dsGFP*, the second injection was carried out after 24 hours following the first injection. Then, shrimps were reared together with 15-20 EHP-positive shrimps. EHP-infected shrimps were prepared by cohabitation. Hemolymph was collected from each group (n=5) at 1-, 7-, 9-, and 11 days after dsRNA double injection. Shrimp hemocytes were collected for total RNA extraction and first-strand cDNA was synthesized. The cDNA samples were used to investigate *LvHSP10* suppression efficiency via qRT-PCR using forward and reverse primers (Supplementary Table 1). The expression was calculated relative to the *dsGFP* injected group. The GraphPad Prism 9 software was used for the statistical analyses. In this experiment, a two-tailed unpaired Student's t-test was used to compare the differences between the two groups.

3.3. EHP copy number detection by absolute qRT-PCR

To investigate the effect of gene-silencing on EHP copy numbers, absolute qRT-PCR was performed using small subunit ribosomal RNA gene (SSU rRNA) (accession number: FJ496359.1) forward and reverse primers (Supplementary Table 1). Genomic DNA was extracted from the hepatopancreas using the FavorPrep™ Tissue Genomic DNA Extraction Mini Kit (Favorgen, Taiwan). The five individual gDNA (10 ng) from each time point was used in absolute qRT-PCR by Luna® Universal qPCR Master Mix (NEB, USA) following the user's manual. The qPCR conditions were as follows: one cycle at 95 °C for 2 min, followed by 40 cycles consisting of 5 s at 95 °C and 30 s at 60 °C. The Ct value of each sample was used to calculate the copy number from the SSU rRNA standard curve. The GraphPad Prism 9 software was used for the statistical analyses. In this experiment, a two-tailed unpaired Student's t-test was used to compare the differences between the two groups.

3.4. Effect of *LvHSP10*-silencing on immune-related pathways associated with EHP infection

The expression of immune-related genes, including Toll, JAK/STAT signaling pathway, proPO-activating cascade, and antimicrobial peptides (AMPs), was investigated in *LvHSP10*-silenced shrimp during EHP infection. The mRNA expression of representative genes in Toll, JAK/STAT signaling pathways, included *LvTLR2*, *LvMyD88*, *LvDorsal*, *LvDOME*, *LvJAK*, and *LvSTAT*. Moreover, the proPO-activating cascade, including *LvLGBP*, *LvproPO1*, *LvproPO2*, and antimicrobial peptides (AMPs), including *LvALF1*, *LvPEN3*, and *LvLyz-c*, was investigated using Luna Universal qPCR Master Mix (New England Biolabs, USA) and CFX96 Touch® Real-time PCR Detection System (Bio-Rad, USA) with qPCR gene-specific primers (Supplementary Table 1). The qPCR conditions were as follows: one cycle at 95 °C for 2 min, followed by 40 cycles consisting of 5 s at 95 °C and 30 s at 60 °C. The *LvEF1α* was used as an internal control. The expression was calculated relative to the *dsGFP* injected group. The GraphPad Prism 9 software was used for the statistical analyses. In this experiment, a two-tailed unpaired Student's t-test was used to compare the differences between the two groups.

Results and Discussion:

The small heat shock proteins (sHSPs) are a group of proteins with a monomer range of ~ 10-40 kDa. These sHSPs are essential in preventing aggregation of nonnative proteins by

binding them in stable complexes²⁵. From the *L. vannamei* genome, three sHSPs, including *LvHSP10* (accession number: MF062460.1), *LvHSP21* (accession number: XM_070125649.1), and *LvHSP22* (accession number: XM_027373023.2) were identified. Tissue specific expression revealed that *LvHSP10*, *LvHSP21*, and *LvHSP22* were expressed in all examined tissues, including hepatopancreas, muscle, hemocytes, intestine, gills, eyestalk, heart, and stomach (Figure 1). Similar to the previous work, sHSPs are mostly expressed in several tissues to maintain cell homeostasis by preventing the formation of protein aggregates that can disrupt cellular processes and lead to cell death^{26,27}. These results indicate that sHSPs may play a key role in maintaining cellular health in different tissues, which is crucial for survival and stress adaptation.

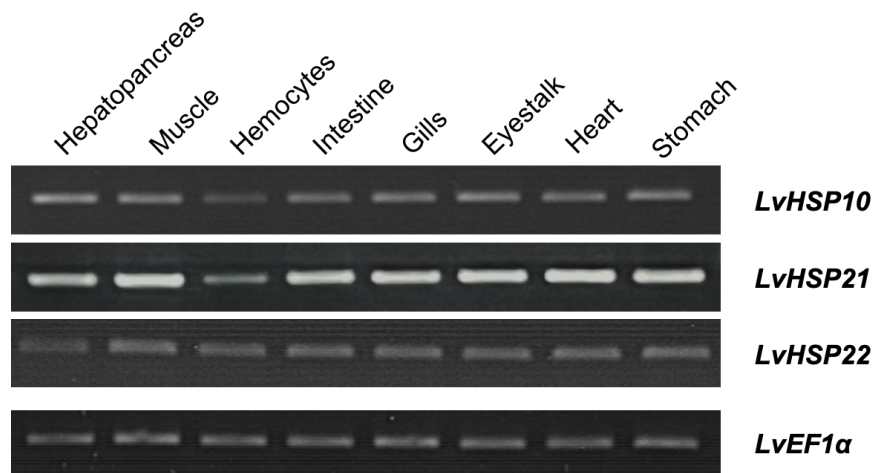


Figure 1.

Tissue specific expression of of small heat shock protein genes.

The expression level of *LvHSP10*, *LvHSP21*, and *LvHSP22* was analyzed using semi-quantitative RT-PCR. *LvEF1α* was used as an internal control.

The expression level of *LvHSP10*, *LvHSP21*, and *LvHSP22* during the EHP infection was further investigated. It was found that the expression of *LvHSP21* was up-regulated at 7 days post cohabitation (dpc) and down-regulated at 9- and 11 dpc (Figure 2B). Whereas, the expression level of *LvHSP22* was significantly decreased throughout the day, except at 15 dpc, which was upregulated (Figure 2C). A recent study has indicated that sHSPs may exert either inhibitory or promotive effects on pathogenic processes and infection²⁸. Importantly, *LvHSP10* expression significantly increased over 20-fold at 7 dpc (Figure 2A). Hence, it is possible that sHSPs might play a crucial role during EHP infection.

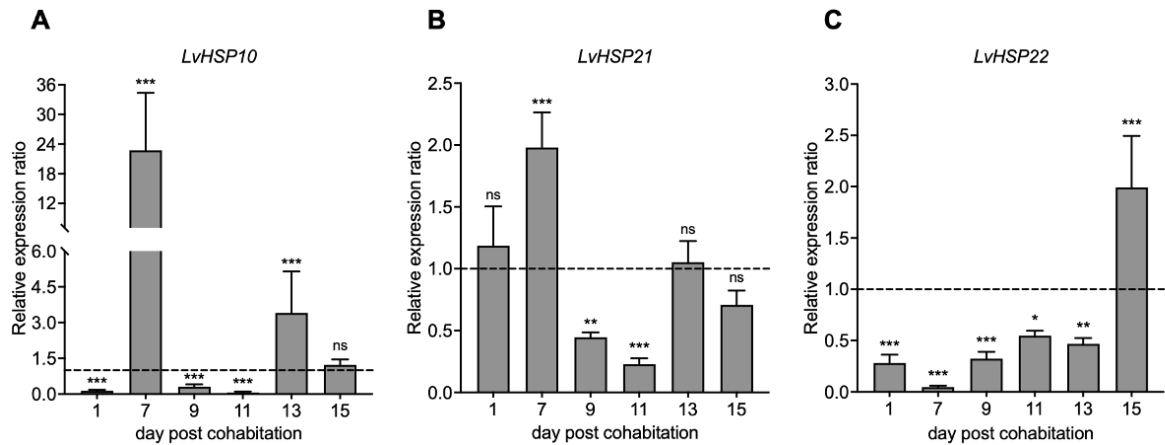


Figure 2.

The expression pattern of sHSPs during EHP infection.

(A) *LvHSP10*, (B) *LvHSP21*, (C) *LvHSP22*. The expression of sHSPs was analyzed using quantitative RT-PCR (qRT-PCR). Each data point was normalized to the expression of the *LvEF1 α* gene and calculated relative to the expression level in the non-infected (represents in dashed line).

Previous studies have demonstrated that sHSPs could act as a chaperone to refold proteins during pathogenic infections²⁹. Hence, we further investigated the role of *LvHSP10* by knocking down *LvHSP10* expression during EHP infection. Silencing *LvHSP10* with RNAi resulted in decreased levels of *LvHSP10* until 11 dpc (Figure 3A). Importantly, silencing *LvHSP10* led to a dramatic rise in EHP load, approximately 100-fold higher than the *dsGFP* control at 9- and 11 dpc (Figure 3B). In accordance with previous work, *Scylla paramamosain* HSP20-silenced cells promoted apoptosis by suppressing the function of Apoptosis Inhibitor 5 (API5), leading to a significant increase in the viral copy number within the host³⁰. These results imply the important role of *LvHSP10* in combating EHP infection.

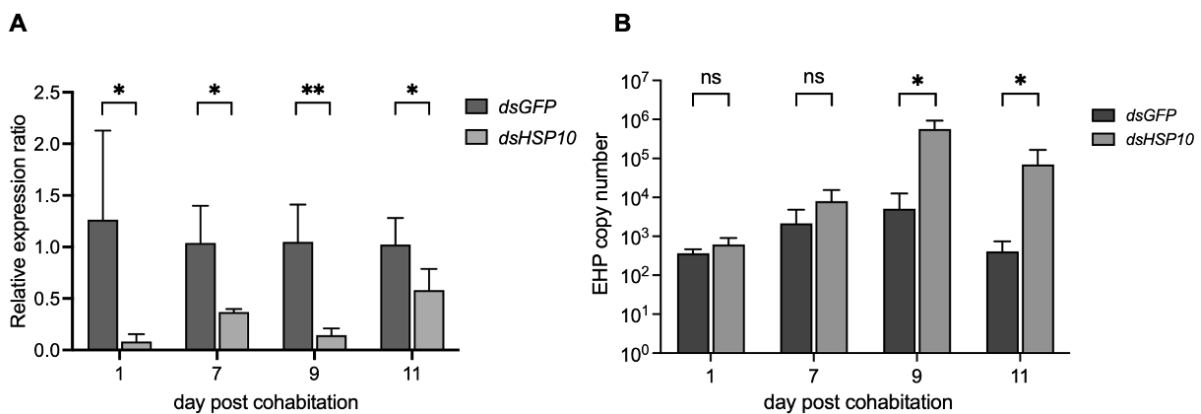


Figure 3.

Effect of *LvHSP10* suppression by RNAi (A) Expression level of *LvHSP10* (B) EHP copy numbers. The mRNA expression level of *LvHSP10* was quantified by qRT-PCR. EHP copy numbers were analyzed using absolute qPCR, compared with the *SSU* rRNA gene of EHP.

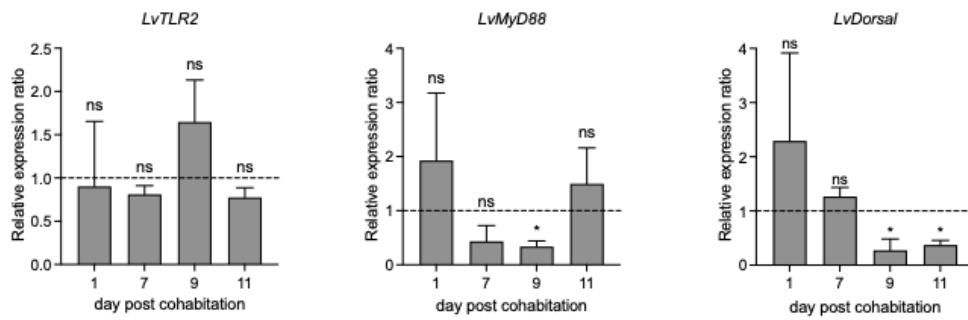
The *GFP* dsRNA-treated shrimp were used as a control. All the data were analyzed by



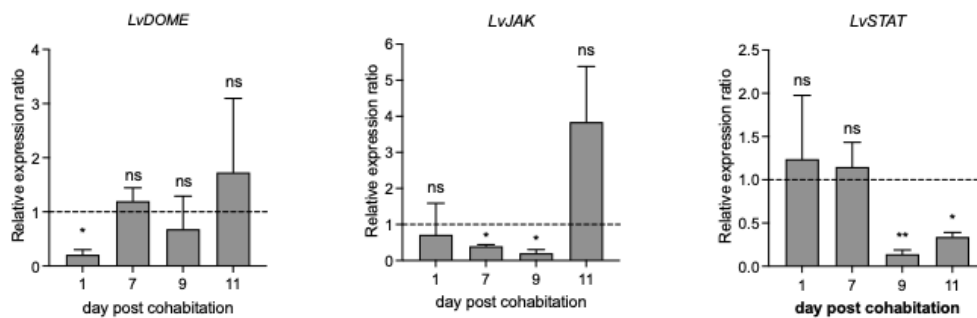
Student's T-test with * indicating statistically significant differences ($P < 0.033$); bars with ** indicate highly statistically significant ($P < 0.002$).

Previous studies have shown that stress-related proteins, *LvPrx4* and *LvHSP70*, bind to the immune receptor to activate the signaling pathway and produce the antimicrobial peptide (AMPs) ^{31,32}. Here, we investigated the effect of *LvHSP10* knockdown on the immune-related pathways, including Toll, JAK/STAT, proPO-activating cascade, and the expression of AMPs. Here, we found that expression levels of several genes in the immune-related pathway were downregulated after HSP10 was silenced, including Toll and JAK/STAT. The expression of effector genes, *LvMyD88* and *LvJAK*, as well as transcription factors, *LvDorsal* and *LvSTAT*, was mostly down-regulated at 9- and 11 dpc (Figure 4A and 4B). These results highlighted the correlation of HSP10 and the immune-related pathway during the EHP infection. In addition, the expression of components of the prophenoloxidase cascade, *LvLGBP*, *LvproPO1*, and *LvproPO2*, was decreased after HSP10-silencing (Figure 4C). A recent work on the role of the prophenoloxidase cascade suggests that the proPO system has a crucial role in reducing EHP infectivity and works in coordination with other humoral and cellular responses to defend against EHP infection ³³. On the contrary, suppression of *LvHSP10* resulted in the upregulation of *LvPEN3*, *LvLyz-c*, and *LvALF1* at 7- and 11 dpc (Figure 4D). This might be correlated with the higher EHP copy number in the *LvHSP10*-silenced group; the increased production of AMPs is employed to counteract the higher EHP infection. In previous studies revealed that AMPs such as *LvALF1*, *LvLyz-c*, and *LvPEN3* were upregulated at the late stage of EHP infection. Moreover, recombinant *LvLyz-c* exhibited chitinase activity to digest the EHP endospore, which reduced the spore germination ³⁴. These results suggest that *LvHSP10* may play an important role in defense against EHP infection.

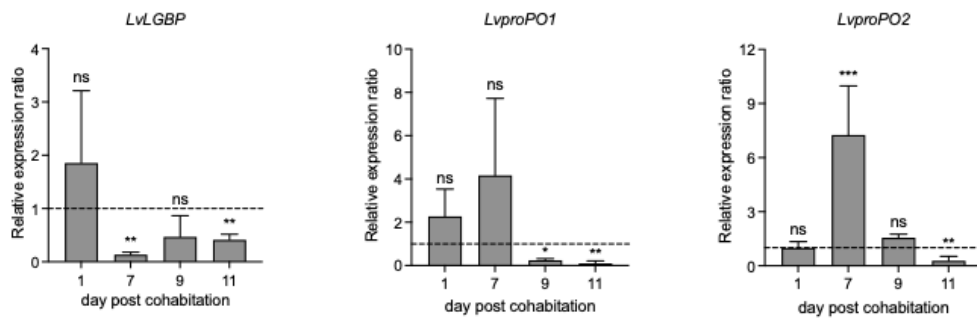
A. Toll signaling pathway



B. JAK/STAT signaling pathway



C. proPO-activating cascade



D. Antimicrobial peptides

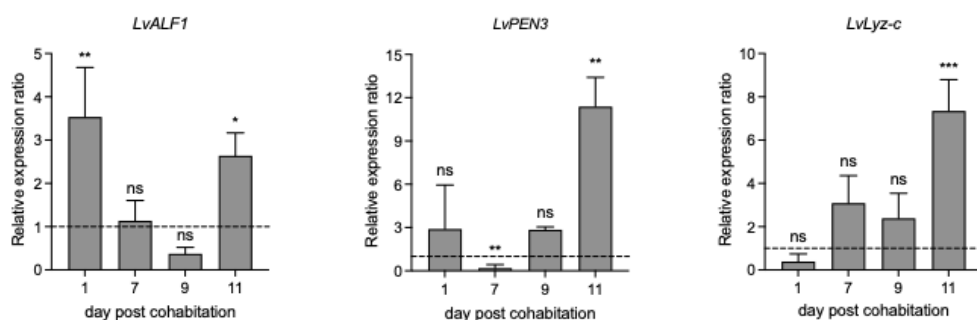


Figure 4.

Expression analysis of immune-related genes in hemocytes of *LvHSP10*-silenced and EHP-infected shrimp. Each data point was normalized to the expression of the *LvEF1 α* gene and calculated relative to the expression level in the non-infected shrimp (represents in dashed line).

Conclusion:

In conclusion, our study provides valuable insights into the role of small heat shock proteins (sHSPs) in *Litopenaeus vannamei*, particularly during EHP infection. We identified three sHSPs, including *LvHSP10*, *LvHSP21*, and *LvHSP22*, and demonstrated their widespread tissue distribution, indicating their significance in maintaining cellular homeostasis across various tissues. Notably, *LvHSP10* showed a significant upregulation in response to EHP infection, and its silencing resulted in increased EHP load and downregulated of the key immune pathways, indicating that HSP10 may function as a crucial molecular chaperone in the shrimp's immune defense. These findings underscore the potential of sHSPs, especially HSP10, as targets for enhancing disease resistance in shrimp aquaculture, and their contribution to a better understanding of the molecular mechanisms underlying host-pathogen interactions in crustaceans.

Acknowledgements:

The authors thank the Marine Shrimp Broodstock Research Center II (MSBRC-2), Charoen Pokphand Foods PCL, for providing the experimental animals.

References:

1. Kumar V, Roy S, Behera BK, Das BK Life. 2022;12:1777.
2. Roberts RJ, Agius C, Saliba C, Bossier P, Sung YY. J Fish Dis. 2010;33:789-801.
3. Zügel U, Kaufmann SHE. Clin Microbiol Rev. 1999.
4. Barna J, Csermely P, Vellai T. CMLS. 2018;75:2897–2916.
5. Morimoto RI. Genes Dev. 2008;22:1427–1438.
6. Yik Sung Y. J Mar Sci Res Dev. 2013;4.
7. Bepperling A, Alte F, Kriehuber T, Braun N, Weinkauff S, Groll M, Haslbeck M, Buchner J. PNAS. 2012;109: 20407–20412.
8. Junprung W, Supungul P, Tassanakajon A. Dev Comp Immunol. 2021;115: 103875.
9. Feder ME, Hofmann GE. Annu Rev Physiol. 1999;61:243-82.
10. Cheng CH, Ma HL, Feng J, Su YL, Deng YQ, Chen XL, Guo ZX. IJA. 2018;70.
11. Arockiaraj J, Vanaraja P, Easwvaran S, Singh A, Othman RY, Bhassu S. Mol Biol Rep. 2012;39:6671–6682.
12. Huang PY, Kang ST, Chen WY, Hsu TC, Lo CF, Liu KF, Chen LL. Fish Shellfish Immunol. 2008;25:250–257.
13. Dai LS, Kausar S, Gul I, Zhou HL, Abbas MN, Deng MJ. Dev Comp Immunol. 2020;111:103755.
14. Wang MQ, Wang BJ, Jiang KY, Liu M, Han SY, Wang L. Invertebr Surviv J. 2017;14:404–413.
15. Kumar V, Das BK, Dhar S, Bisai K, Pande GS, Zheng X, Parida SN, Adhikari A, Jana AK. BMC Microbiol. 2024;24:1–13.
16. Kim JH, Lee C, Jeon HJ, Kim BK, Lee NK, Choi SK, Han JE. Aquacult. 2022;547:737525.
17. Chaijarasphong T, Munkongwongsiri N, Stentiford GD, Aldama-Cano DJ, Thansa K, Flegel TW, Sritunyalucksana K, Itsathitphaisarn O. J Invertebr Pathol. 2021;186:107458.
18. Wang XW, Wang JX. Fish Shellfish Immunol. 2013;34:981-9.
19. Amparyup P, Charoensapsri W, Tassanakajon A. Fish Shellfish Immunol. 2013;34:990-1001.
20. Patnaik BB, Baliarsingh S, Sarkar A, Hameed AS, Lee YS, Jo YH, Han YS, Mohanty J Rev Aquac. 2024;16:190–233.
21. Haridevamuthu B, Sudhakaran G, Rajagopal R, Alfarhan A, Arshad A, Arockiaraj J

- Acta Parasitol. 2025;70:1–18.
22. Zhang L, Zhang S, Qiao Y, Cao X, Cheng J, Meng Q, Shen H. Int. J Mol Sci. 2023;24:16738.
 23. Sangklai N, Udomphonphaibun T, Keawpanya K, Watson PR, Coudray N, Koliopoulos MA, Thepmanee O, Dhar AK, Ekiert DC, Bhabha G, Tassanakajon A. bioRxiv. 2025:2025-07.
 24. Salachan PV, Jaroenlak P, Thitamadee S, Itsathitphaisarn O, Sritunyalucksana K. BMC Vet Res. 2016;13:9.
 25. Haslbeck M, Franzmann T, Weinfurtner D, Buchner J Nat Struct Mol Biol. 2005;12:842–846.
 26. Sejerkilde M, Sørensen JG, Loeschcke V. J Insect Physiol. 2003;49:719-26.
 27. Treweek TM, Meehan S, Ecroyd H, Carver JA. Cell Mol Life Sci. 2014;72:429–451.
 28. Bakthisaran R, Tangirala R, Rao CM. Biochim Biophys Acta. 2015;1854:291-319.
 29. Dev R. J Pure Appl Microbiol, 2021;15.
 30. Hu H, Deng N, Zhao X, Yi C, Wei W, Gong Y. Front Microbiol. 2023;14:1323382.
 31. Ran XQ, Gao L, Yan M, Kang CJ. Front Immunol. 2022;13:907183.
 32. Junprung W, Supungul P, Sangklai N, Tassanakajon A. J Immunol. 2022;209:582-92.
 33. Sukonthamarn P, Wongvises P, Sangklai N, Jaroenlak P, Tassanakajon A. Fish Shellfish Immunol. 2024;154:109925.
 34. Sangklai N, Supungul P, Jaroenlak P, Tassanakajon A. PLoS Pathog. 2024;20:e1012199.

Supplementary Table 1.
Primers used in this study

Primer name	Sequence (5'→3')	Purpose
<i>LvEF1α-F</i>	CTTGATTGCCACACTGCTCAC	qRT-PCR
<i>LvEF1α-R</i>	TCTCCACGCACATAGGCTTG	qRT-PCR
<i>SSU rRNA-F</i>	ATTAGACACCGCTGTAGTTC	qRT-PCR
<i>SSU rRNA-R</i>	GTTATTGCCTTCTCCCTC	qRT-PCR
<i>LvHSP10-F</i>	TGGCTGGTGCTCTGAAGAGG	qRT-PCR
<i>LvHSP10-R</i>	GATTGTGGTGCCGGCTTCAG	qRT-PCR
<i>LvHSP21-F</i>	CACGAGGAGAAGTCTGACAAC	qRT-PCR
<i>LvHSP21-R</i>	GAGAGCGAGGACTTGATGAG	qRT-PCR
<i>LvHSP22-F</i>	GAGGACAACCAGTGCTACAA	qRT-PCR
<i>LvHSP22-R</i>	CACCACGTCGAACCTCAC	qRT-PCR
<i>LvTLR2-F</i>	TCCTTGATATCCGTGGGAAC	qRT-PCR
<i>LvTLR2-R</i>	CCTCCGTCACGTCTATCAG	qRT-PCR
<i>LvMyD88-F</i>	GTGCACCAGAGTCATTGTAG	qRT-PCR
<i>LvMyD88-R</i>	GGGAGTGGCAGAACTTATC	qRT-PCR
<i>LvDorsal-F</i>	TCACTGTTGACCCACCTTAC	qRT-PCR
<i>LvDorsal-R</i>	GGAAAGGGTCCACTCTAATC	qRT-PCR
<i>LvDOME-F</i>	TCAGACAGGAGGTCTCATAC	qRT-PCR
<i>LvDOME-R</i>	GTACCAGTGTGAAGCCTTAC	qRT-PCR
<i>LvJAK-F</i>	TACCCTGGTCTACGCTATAC	qRT-PCR
<i>LvJAK-R</i>	TGAGACGGTAGTACCCATTC	qRT-PCR
<i>LvSTAT-F</i>	CCAGTGCTTGAACACTGAAC	qRT-PCR
<i>LvSTAT-R</i>	GGCTTTGAATGTGGGATAGG	qRT-PCR

Primer name	Sequence (5'→3')	Purpose
<i>LvLGBP-F</i>	AACCCTTGGGCGGCTGGATC	qRT-PCR
<i>LvLGBP-R</i>	CCCTCGCGTTCCAGAAGTCG	qRT-PCR
<i>LvproPO1-F</i>	AACTCCATTCCGTCCGTCTG	qRT-PCR
<i>LvproPO1-R</i>	GGCTTCGTCTGGTTAGGAT	qRT-PCR
<i>LvproPO2-F</i>	CTCAGCGTGAAGTGGCCTTA	qRT-PCR
<i>LvproPO2-R</i>	CCTGCTCAGTGTACGGTCT	qRT-PCR
<i>LvALF1-F</i>	GTCCTCCGTGATGAGATTACTCTG	qRT-PCR
<i>LvALF1-R</i>	TTACTTCAATGGCAGGATGTGG	qRT-PCR
<i>LvPEN3-F</i>	CACCCTTCGTGAGACCTTTG	qRT-PCR
<i>LvPEN3-R</i>	AATATCCCTTTCCACGTGAC	qRT-PCR
<i>LvLyz-c-F</i>	CCCATGTTCCGATCTGATGTC	qRT-PCR
<i>LvLyz-c-R</i>	CACCTTGCTGTTGTAAGCCACC	qRT-PCR
<i>dsHSP10-F</i>	AAAGGCTGAGGCTCTGAC	RNAi
<i>dsHSP10-R</i>	CCTCAAGGGTGACCTTTGTG	RNAi
<i>dsRNA-HSP10-T7-F</i>	GGATCCTAATACGACTCACTATAGGAAA GGCTGAGGCTCTGAC	RNAi
<i>dsRNA-HSP10-T7-R</i>	GGATCCTAATACGACTCACTATAGGCCTC AAGGGTGACCTTTGTG	RNAi
<i>dsRNA-GFP-F</i>	GGTGAGCAAGGGCGAGGA	RNAi
<i>dsRNA-GFP-R</i>	ACTTGTACAGCTCGTCCA	RNAi
<i>dsRNA-GFP-T7-F</i>	TAATACGACTCACTATAGGATGGTGAGC AAGGGCGAGGA	RNAi
<i>dsRNA-GFP-T7-R</i>	TAATACGACTCACTATAGGTTACTTGTAC AGCTCGTCCA	RNAi



IDENTIFICATION OF SIGNALING PATHWAYS CONTROLLING ANTIMICROBIAL PEPTIDE GENE EXPRESSION IN BLACK TIGER SHRIMP

Penaeus monodon

Chayanit Khunrit^{1,2,3}, Thapanan Jatuyosporn^{2,3}, Anchalee Tassanakajon³ and Kuakarun Krusong^{2,*}

¹ Program in Biotechnology, Faculty of Science, Chulalongkorn University, Bangkok, 10330, Thailand

² Center of Excellence in Structural and Computational Biology, Department of Biochemistry, Faculty of Science, Chulalongkorn University, Bangkok 10330, Thailand

³ Center of Excellence for Molecular Biology and Genomics of Shrimp, Department of Biochemistry, Faculty of Science, Chulalongkorn University, Bangkok 10330, Thailand

*e-mail: Kuakarun.k@chula.ac.th

Abstract:

Black tiger shrimp (*Penaeus monodon*) farming in Thailand has faced increasing impacts from infectious diseases over the past few decades, causing significant economic losses. Improving disease resistance requires a deeper understanding of the shrimp's innate immune system. A key part of this defense involves antimicrobial peptides (AMPs), such as penaeidins and anti-lipopolysaccharide factors (ALFs), which help protect against bacteria, fungi, and viruses. However, the regulatory mechanisms that link immune signaling pathways to AMP expression remain unclear. This study focuses on two AMP genes, *ALFPm3* and *PenPm5*, the latter of which includes two isoforms (*PenPm5.1* and *PenPm5.2*). Using a luciferase reporter assay, we examined whether these genes are transcriptionally regulated through the Toll signaling pathway via the transcription factor *PmDorsal*. The results showed a significant increase in luciferase activity when *PmDorsal* was co-expressed, suggesting that *PmDorsal* binds to the promoter regions of both genes. These findings indicate that *PenPm5* and *ALFPm3* are transcriptionally regulated via the Toll pathway, providing new insights into the immune response mechanisms of *P. monodon*. This knowledge may contribute to the development of strategies to enhance shrimp immunity and reduce disease-related losses in aquaculture.

Introduction:

The black tiger shrimp (*Penaeus monodon*) is an economically important aquatic species, widely farmed and exported by many countries, including Thailand, Vietnam, Indonesia, and India. Despite its commercial significance, shrimp production has been declining globally due to outbreaks of infectious diseases caused by viruses, bacteria and fungi. These pathogens have a significant impact on shrimp health and production, posing major challenges for the aquaculture industry.

Shrimp rely on their innate immune system as the first line of defense against invading microbes, since they lack adaptive immunity. To combat pathogen infections, antimicrobial peptides (AMPs) play a crucial role in eliminating infections caused by bacteria, viruses, and fungi. Previous studies have shown that various types of AMPs have been reported in black tiger shrimp, including penaeidins and anti-lipopolysaccharide factors (ALFs), each of which demonstrates activity against different pathogens. For example, penaeidins exhibit antibacterial activity against Gram-positive bacteria and fungal infections¹. In contrast, ALFs have demonstrated effectiveness against both Gram-positive and Gram-negative bacteria, as well as fungi².

The production of AMPs is usually initiated by recognizing pathogen-associated molecular patterns (PAMPs) such as lipopolysaccharides (LPS), peptidoglycans (PGN), and β -1,3-glucans. These PAMPs interact with pattern recognition proteins (PRPs) to initiate



specific intracellular signaling cascades, In shrimp, the Toll, IMD (immune deficiency), and JAK-STAT pathways have been reported to regulate the production of several AMPs^{3,4}.

The Toll pathway primarily responds to Lys-type PGNs found in Gram-positive bacteria and possibly responds to β -1,3-glucans from fungi. The activation of this pathway involves Spätzle, the extracellular ligand that interacts with several Toll receptors and triggers the nuclear translocation of the transcription factor Dorsal, allowing it to translocate into the nucleus and bind to the promoter region of specific AMPs, controlling transcription.^{5,6}

A previous study suggested that Dorsal possibly regulates the expression of penaeidin⁷. However, certain AMPs, such as ALFs, may be regulated by alternative regulatory mechanisms, as evidenced by differential expression patterns observed following transcription factor knockdown⁶. However, the direct evidence connecting specific transcription factors to certain AMP genes remains limited in shrimp.

Previous studies have also revealed crosstalk between the Toll and IMD pathways. For example, in black tiger shrimp, silencing Toll signaling has been observed to increase IMD expression and vice versa, suggesting a coordinated immune response. Moreover, AMP genes such as *ALFPm3* are regulated by both Toll and IMD pathways^{8,9}. Despite these insights, the precise molecular interactions between transcription factors and AMP gene promoters in *Penaeus monodon* remain to be fully elucidated. This study aims to investigate the binding capabilities of key transcription factors to promoters of two AMP genes (*ALFPm3* and *PenPm5*, including *PenPm5.1* and *PenPm5.2* isoforms). Understanding these regulatory mechanisms will advance our knowledge of shrimp immune responses and may inform strategies to enhance disease resistance in shrimp aquaculture.

Methodology:

1. Construction of Recombinant Plasmids for AMP Promoter Analysis

To investigate the regulatory activity of AMP gene promoters, recombinant plasmids were constructed using promoter regions of *ALFPm3* and *PenaeidinPm5*. In this study, two AMP genes (*ALFPm3* and *PenPm5*) were investigated. *PenPm5* includes two isoforms, *PenPm5.1* and *PenPm5.2*, which were defined based on sequence differences within the promoter region identified from genomic DNA and confirmed by sequencing. Genomic DNA was extracted from the gill of *Penaeus monodon*, as gill tissue provides high yield and quality for promoter cloning, while hemocyte RNA was used for ORF cloning of *PmDorsal* due to its high expression in immune-related cells. Specific primers targeting the promoter regions of AMP genes were designed and used to amplify the desired fragments via polymerase chain reaction (PCR). The primer sequences are shown in Table 1. The PCR products were digested with restriction enzymes and ligated into the pGL3-Basic luciferase reporter vector (Promega). Then, the recombinant plasmids were transformed into *Escherichia coli* TOP10 using the heat shock transformation method. Transformed colonies were selected on LB agar containing ampicillin as a selective marker. After that, the plasmids were isolated from the overnight cultures. To confirm the insertion of the promoter fragment, the constructs were digested with restriction enzymes and verified by Sanger DNA sequencing to ensure the accurate sequence of promoter regions.

Table 1.
Summary of primers in this study

Name	Sequence (5'-3')	Enzyme	Position
<i>PmDorsal</i> -F	GGATCCATGGCTGACCCAATGTTTG	<i>Bam</i> HI	
<i>PmDorsal</i> -R	CTCGAGGTGTTTGGATGTGAGCTG	<i>Xho</i> I	
ALF <i>Pm3</i> -F	GTACGCTAGCGAAAGGGCAGTGGATTTCCC	<i>Nhe</i> I	-567 to -590
ALF <i>Pm3</i> -R	GATCAAGCTTCACGCATCTTCTGCAAGG	<i>Hind</i> III	+1 to +25
Pen <i>Pm5</i> -F	CTAGGCTAGCGGAAGGGAACGATAAACTATGC	<i>Nhe</i> I	-574 to -598
Pen <i>Pm5</i> -R	TTACAAGCTTACCAGGAAGACCAGGCAGAC	<i>Hind</i> III	+1 to +25

Note: Underline indicates restriction enzyme recognition site; the position of translation start site ATG is defined as +1; Product size of *PmDorsal* is 2,055 bp, Product size of ALF*Pm3* is 597 bp, Product size of Pen*Pm5* is 630 bp

2. Construction of Recombinant Plasmids for Transcription Factor Expression

A recombinant plasmid was constructed for the expression of the transcription factor *PmDorsal* (accession no. MG775232.1). Total RNA was extracted from hemocytes of *Penaeus monodon* and reverse-transcribed into cDNA using reverse transcriptase. The open reading frame (ORF) of *PmDorsal* was amplified using gene-specific primers. The PCR products were digested with restriction enzymes and cloned into the pc.DNA3.1(+)-C-Myc expression vector. The primer sequences are shown in Table 1. The resulting plasmids were transformed into *E. coli* TOP10 cells by the heat shock method. Colonies were selected using ampicillin resistance, followed by plasmid extraction and restriction enzyme digestion. The inserts were verified through DNA sequencing to confirm their accuracy.

3. Luciferase Reporter Assay to Evaluate Promoter–Transcription Factor Interaction

A dual-luciferase reporter assay was performed to evaluate the interaction between the promoter region of AMPs and the transcription factor *PmDorsal*. The pGL3 vector containing promoter regions of ALF*Pm3* (pGL3_ALF*Pm3*) or Penaeidin*Pm5* (pGL3_Pen*Pm5*) was co-transfected into HEK293T (human embryonic kidney 293T) cells along with the pRL-TK plasmid (containing Renilla luciferase as an internal control) and the *PmDorsal* expression plasmid (pc.DNA3.1 _DI). Each well was transfected with 50 ng of the pGL3 construct, 1,000 ng of pc.DNA3.1 construct, and 10 ng of pRL-TK. Transfection was carried out in 24-well plates using Lipofectamine™ RNAiMAX Transfection Reagent (Thermo Fisher Scientific), following the protocol provided in the Dual-Glo® Luciferase Assay System manual (Promega). After 72 hours, both firefly and Renilla luciferase activities were measured by chemiluminescence using a spectrophotometer. Luminescence was recorded using the endpoint mode with a 1000 ms integration time to ensure optimal signal detection. The luminescence ratio (Firefly/Renilla) was calculated to assess the transcriptional activity of each promoter in response to *PmDorsal*. Each condition was tested in triplicate, and the assay was performed on three independent replicates to ensure reproducibility. Statistical analysis was performed using one-way ANOVA followed by Turkey's multiple range test, and differences were considered statistically significant at $P < 0.001$.

Results and Discussion:

To determine whether the Toll signaling pathway mediates the transcription of ALF*Pm3* and Pen*Pm5*, a dual-luciferase reporter assay was conducted. The coding sequence of *PmDorsal* was cloned into the pc.DNA3.1(+)-C-Myc vector, whereas the putative promoter regions of ALF*Pm3* and Pen*Pm5* (including isoforms Pen*Pm5*.1 and Pen*Pm5*.2) were inserted upstream

of the luciferase reporter gene in pGL3. The plasmid pc.DNA3.1_Dl denotes pc.DNA3.1(+)-C-Myc containing the *PmDorsal* ORF. All experiments were performed in HEK293T cells for consistency. In future experiments, *PmDorsal* expression in HEK293T cells will be verified by anti-Myc Western blot prior to luciferase measurement. HEK293T cells were chosen as a heterologous system due to their high transfection efficiency, although species-specific differences may limit direct extrapolation to shrimp immune mechanisms.

Co-transfection of HEK293T cells with the respective constructs revealed that *PmDorsal* markedly enhanced luciferase activity driven by the ALFPm3 and PenPm5.1 promoters, showing approximately 6.3-fold and 2.8-fold increases, respectively, compared with controls (No plasmid, pc.DNA3.1, pGL3, pc.DNA3.1_Dl, pGL3_ALFPm3 and pGL3_PenPm5.1) ($P < 0.001$) (Fig. 1A and Fig. 1B). For PenPm5.2, luciferase activity increased by about 1.4-fold ($P < 0.001$) relative to controls (No plasmid, pc.DNA3.1, pGL3, and pc.DNA3.1_Dl), although the difference was not significant compared with pGL3_PenPm5.2 (Fig. 1C). These findings provide strong evidence that *PmDorsal*, a key transcription factor in the Toll pathway, directly regulates the transcription of ALFPm3 and PenPm5 in *P. monodon*. The robust activation of the ALFPm3 promoter suggests high responsiveness to *PmDorsal*, whereas the moderate and weaker responses of PenPm5.1 and PenPm5.2 indicate isoform-specific regulatory control.

These findings are consistent with previous work showing that Toll pathway components are essential regulators of antimicrobial peptides (AMPs) in shrimp and other invertebrate animals^{10, 11}. For example, Kamsaeng et al. reported that the ALFPm3 promoter in *P. monodon* contains a Rel/NF- κ B motif at -280/-270 that is critical for promoter activity.⁹ Similarly, Ding et al. demonstrated in *M. japonicus* that Toll3 is crucial for initiating immune responses against bacterial infection, such as *S. aureus*, by activating Dorsal. Further study revealed that Evolutionarily conserved signaling intermediate in Toll pathways (ECSIT) serves as an essential mediator linking Toll3 to Dorsal, enabling the transcriptional activation of ALFs. This provides mechanistic insight into how Toll–Dorsal signaling orchestrates AMP expression in shrimp¹². Li et al. also showed that Toll4 in *L. vannamei* activates Dorsal to induce ALFs and lysozyme, thereby restricting WSSV infection.¹³

Beyond ALFs, RNAi studies provide complementary evidence for the functional importance of the Toll–Dorsal axis. Although direct knockdown of *PmDorsal* in *P. monodon* has not yet been reported, several studies indicate that manipulation of upstream elements alters *PmDorsal* expression and AMP output. For instance, depletion of *PmAP2- β* , which control signaling pathway via clathrin coated mediated endocytosis, markedly enhanced the transcription of Toll related genes including *PmSpätzle*, *MyD88*, and *PmDorsal* during yellow head virus infection, accompanied by strong upregulation of AMPs such as ALFPm3.¹⁴ Likewise, silencing *PmDOME* or *PmSTAT* under WSSV challenge significantly modulated immune gene expression; although *PmDorsal* mRNA itself showed limited changes, suppression of these signaling components produced distinct patterns of AMP induction and other immune responses.¹⁵ Taken together, these data support the view that *PmDorsal* acts as a downstream effector in the Toll pathway, with its regulatory capacity shaped by upstream receptor/adaptor molecules.

Additionally, our results reveal *PmDorsal* regulation of PenPm5, a member of the penaeidin family, which possesses antimicrobial and antifungal activities^{11, 16}. The strong induction of the PenPm5.1 promoter and the moderate effect on PenPm5.2 suggest isoform-specific promoter architectures. This observation is consistent with studies showing that penaeidin isoforms display tissue-specific and infection stage–dependent expression patterns, underscoring functional diversification within this AMP family.

The observed differences in promoter activation among *ALFPm3*, *PenPm5.1*, and *PenPm5.2* likely reflect variations in promoter architecture, chromatin accessibility, co-activators, and post-translational modifications of *PmDorsal*. Future work employing promoter mutagenesis and *in vivo* knockdown of *PmDorsal* will be essential to map direct binding sites and determine their physiological relevance.

These findings demonstrated that *PmDorsal* could potentially bind to the *ALFPm3* and *PenPm5* promoters, acting as a potent activator, thereby supporting the hypothesis that their transcription is regulated via the Toll signaling pathway.

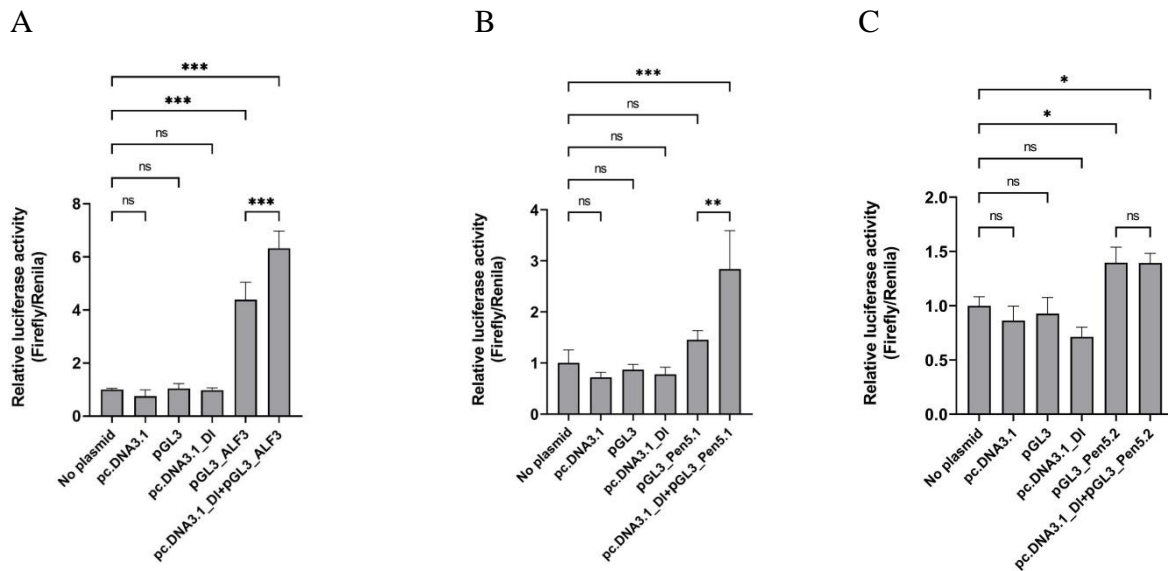


Figure 7.

PmDorsal activates *ALFPm3* and *PenPm5* promoters via the Toll signaling pathway.

Dual-luciferase reporter assays were performed in HEK293T cells to assess *PmDorsal*-mediated transcriptional activation of the *ALFPm3*, *PenPm5.1*, and *PenPm5.2* promoters. The coding sequence of *PmDorsal* was cloned into pc.DNA3.1(+)-C-Myc, and the promoter regions of the target genes were inserted upstream of a firefly luciferase reporter in the pGL3 vector. A Renilla luciferase plasmid was co-transfected as an internal control. Firefly luciferase activity was measured 72 h post-transfection and normalized to Renilla luciferase activity using the Dual-Luciferase Reporter Assay System (Promega). Data are expressed as the mean \pm SD of normalized luciferase activities from three independent experiments ($n = 3$). Asterisks indicate significant differences of mean values calculated by one-way ANOVA (*, $p < 0.05$; **, $p < 0.01$; ***, $p < 0.001$).

(A) Activation of the *ALFPm3* promoter by *PmDorsal* showing a ~6.3-fold increase in luciferase activity compared with controls.

(B) Activation of the *PenPm5.1* promoter by *PmDorsal* showing a ~2.8-fold increase relative to controls.

(C) Modest activation of the *PenPm5.2* promoter by *PmDorsal* (~1.4-fold), indicating isoform-specific regulation.



Conclusion:

In summary, this study demonstrates that *PmDorsal* functions as a key transcriptional regulator of *ALFPm3* and *PenPm5* via the Toll signaling pathway. The differential activation of *PenPm5* isoforms highlights isoform-specific promoter regulation, while the strong activation of *ALFPm3* confirms its high responsiveness to Dorsal. Combined with evidence from knockdown studies of upstream Toll pathway components, our results underscore the essential role of the Toll–Dorsal axis in modulating AMP expression and innate immune responses. These findings provide a mechanistic basis for understanding shrimp immunity and suggest potential strategies for enhancing disease resistance in aquaculture through selective breeding or immune modulation.

Acknowledgements:

We acknowledge Chulalongkorn University for supporting, the 90th Anniversary of Chulalongkorn University Fund, Center of Excellence in Structural and Computational Biology (to K.K.) and Center of Excellence for Molecular Biology and Genomics of Shrimp (to A.T.).

References:

1. Tassanakajon, A., et al. *Fish Shellfish Immunol*, 2013. **34**(4): p. 954-67.
2. Somboonwiwat, K., et al. *Dev Comp Immunol*, 2005. **29**(10): p. 841-51.
3. Iwanaga, S. and L.L. Bok. *Journal of Biochemistry and Molecular Biology*, 2005. **38**(2): p. 128-150.
4. Janeway, C.A. and R. Medzhitov. *Annual Review of Immunology*, 2002. **20**(1): p. 197-216.
5. Arts, J.A.J., et al. *Fish & Shellfish Immunology*, 2007. **23**(3): p. 504-513.
6. Wang, P.-H., et al. *Developmental & Comparative Immunology*, 2012. **36**(2): p. 359-371.
7. Li, F., et al. *Developmental & Comparative Immunology*, 2010. **34**(8): p. 874-883.
8. Arayamethakorn, S., et al. *Developmental & Comparative Immunology*, 2017. **67**: p. 18-29.
9. Kamsaeng, P., Tassanakajon A., and Somboonwiwat K. *Scientific Reports*, 2017. **7**(1): p. 12694.
10. Wang, P.H., et al. *Cell Mol Immunol*, 2013. **10**(5): p. 423-36.
11. Tassanakajon, A., Somboonwiwat K., and Amparyup P. *Dev Comp Immunol*, 2015. **48**(2): p. 324-41.
12. Ding, D., et al. *Frontiers in Immunology*, 2022. **Volume 13 - 2022**.
13. Li, H., et al. *PLOS Pathogens*, 2018. **14**(9): p. e1007109.
14. Jatuyosporn, T., et al. *Sci Rep*, 2021. **11**(1): p. 10534.
15. Laohawutthichai, P., et al. *Sci Rep*, 2023. **13**(1): p. 9852.
16. Destoumieux, D., et al. *J Cell Sci*, 2000. **113** (Pt 3): p. 461-9.



THE EFFICACY OF IN STRAW DILUTION METHOD ON SURVIVAL RATES OF VITRIFIED BOVINE EMBRYOS

Chanyada Angchuan¹, Traimat Boonthai², Rangsun Parnpai^{1*}

¹Embryo Technology and Stem Cell Research Center, School of Biotechnology Institute of Agricultural Technology, Suranaree University of Technology, Nakorn Ratchasima 30000, Thailand

²Department of Aquatic Science, Faculty of Science, Burapha University, Chon Buri 20130, Thailand

*Corresponding author: rangsun@g.sut.ac.th

Abstract:

Cryopreservation of bovine embryos is a key technology for facilitating genetic improvement and reproductive efficiency in cattle. Vitrification has largely replaced conventional slow freezing because of its higher survival and developmental rates; however, its practical use in the field is limited by the need for laboratory-based warming procedures. To address this challenge, in-straw warming methods have been developed to simplify embryo handling and reduce reliance on laboratory infrastructure. This study aimed to evaluate the efficiency of an in-straw warming protocol using different sucrose concentrations for vitrified in vitro-produced (IVP) bovine blastocysts under field conditions. A total of 500 blastocysts were randomly allocated into five groups (n = 100 each): fresh control, conventional warming, and vitrification followed by in-straw dilution with 0.2 M, 0.3 M, or 0.4 M sucrose. Embryo survival and development were assessed based on re-expansion at 2 h and 24 h, and full expansion and hatching at 48 h post-warming. The fresh control group exhibited the highest survival and developmental rates, with 100.00% re-expansion at 2 h, 93.33% at 24 h, 82.61% full expansion, and 72.87% hatching. Among vitrified groups, in-straw warming with 0.2 M sucrose achieved the most favorable outcomes, with 89.88% re-expansion at 2 h, 78.99% at 24 h, 65.96% full expansion, and 44.91% hatching at 48 h. These results were significantly higher than those of conventional warming (79.29%, 55.09%, 46.75%, and 32.70%, respectively) and closer to the fresh control group. In contrast, embryos treated with 0.3 M or 0.4 M sucrose displayed reduced survival, particularly the 0.4 M group, which showed only 3.42% hatching at 48 h. In conclusion, in-straw warming with 0.2 M sucrose provides an effective, practical, and field-adaptable alternative to conventional warming methods. This protocol minimizes the need for specialized laboratory equipment while maintaining embryo viability and developmental potential. The adoption of this approach may enhance the efficiency and accessibility of bovine embryo transfer programs, particularly in settings with limited infrastructure.

Keywords: Bovine, *In vitro* embryo production, Vitrification, In straw dilution

Introduction:

Vitrification has become a widely adopted cryopreservation technique due to its rapid cooling rate, simplicity, and high embryo survival [1]. This technique prevents ice crystal formation, which can otherwise damage cellular structures. Vitrification of bovine embryos produced through in vitro fertilization (IVF) has shown to be superior to traditional slow freezing, especially regarding post-thaw developmental rates and viability. Studies report that vitrified bovine embryos achieve higher survival and improved developmental competence, ultimately supporting greater success in assisted reproductive programs [2].

Despite its clear advantages, the widespread adoption of vitrification in field applications remains limited. Conventional warming protocols are highly dependent on controlled laboratory environments, requiring precise temperature management, specialized



media, and experienced personnel to perform stepwise dilution and embryo evaluation prior to transfer [3]. Such requirements hinder practical use in rural or resource-limited areas, where laboratory infrastructure may be inadequate.

To solve these limitations, researchers have developed simplified alternatives, such as in-straw warming. This technique offers a promising solution by incorporating thawing and dilution within a single straw, reducing handling steps and potential contamination [4]. Despite its simplicity, the effectiveness of this method can vary based on sucrose concentration.

This study aimed to investigate the effects of in-straw warming and dilution on vitrified bovine embryos and to determine the optimal concentration of sucrose in the warming solution for in-straw dilution and assess its impact on embryo survival. This research seeks to provide practical insights into improving cryopreservation techniques for use in field conditions, ultimately contributing to more efficient and effective reproductive strategies in the livestock industry.

The objectives of this study were:

- (1) To determine the survival and developmental potential of vitrified *in vitro* produced bovine embryos thawed using in-straw dilution at various sucrose concentrations (0.2, 0.3, and 0.4 M);
- (2) To compare embryo viability following in-straw dilution with conventional thawing and fresh controls;
- (3) To identify the optimal sucrose concentration that maximizes embryo survival.

Ethical number : COA. SUT-IACUC-038/2024

Methodology:

2.1 Embryo Production

Bovine oocytes were collected from slaughterhouse ovaries and matured in *in vitro* maturation (IVM) medium for 23 hours. Then the matured oocytes were fertilized with frozen Wagyu semen at concentration 2 million sperms/ml and cultured in *in vitro* fertilization (IVF) medium before incubating under humidified atmosphere of 5% CO₂ and 5% O₂ at 38.5 °C for 10 hours. After that fertilized oocytes were cultured in *in vitro* culture (IVC) medium (CR1aa medium) under 5% CO₂ and 5% O₂ at 38.5 °C. All embryos were evaluated morphologically and classified as Grade 1 or 2 before vitrification. A total of 500 blastocysts were used in this study, divided equally among five experimental groups (n = 100 per group). For vitrification, the blastocysts were washed with base medium (BM) containing TCM199 HEPES supplemented with 20% (v/v) FBS. Then, the blastocysts were incubated at 25°C in an equilibration solution (ES) consisting of BM supplemented with 7.5% (v/v) ethylene glycol (EG) and 7.5% (v/v) dimethyl sulfoxide (DMSO) for 3 min. After that, the blastocysts were subsequently submerged in vitrification solution consisting of BM supplemented with 15% DMSO, 15% EG, and 0.5 M sucrose for 1 min then placed on Cryotop® (Kitazato BioPharma, Fujinomiya, Japan) and quickly immersed in liquid nitrogen. This vitrification protocol associates sucrose and high cryoprotectant concentration for fast dehydration.

2.2 In-Straw Thawing Procedure

Embryos were thawed using a pre-filled 0.25 ml straw containing sucrose solutions (0.2, 0.3, 0.4 M) layered above dilution medium. The Cryotop was inserted into the first column (5 min), shaken to mix with the second column (20 sec), inverted (3.20 min), and finally warmed horizontally (1.40 min). Embryos remained enclosed within the straw throughout the process, avoiding direct exposure to the environment. The procedure required only a portable water bath and no Petri dishes or laminar flow hood, thus reducing the risk of contamination



and making it suitable for on-farm use. Each sucrose concentration group consisted of $n = 100$ (grade 1 and grade 2 embryos.)

The sucrose concentrations (0.2, 0.3, and 0.4 M) were chosen based on prior reports in bovine and porcine embryos demonstrating effective osmotic balance within this range [5,6]. Preliminary laboratory tests confirmed that concentrations exceeding 0.4 M induced excessive dehydration and blastocoel collapse, leading to reduced embryo survival.

2.3 Conventional Thawing Procedure

The conventional warming method involved transferring vitrified embryos from Cryotop into a stepwise sucrose dilution in petri dishes at 38.5°C. Embryos were sequentially transferred through 0.5 M, 0.25 M, and 0.0 M sucrose solutions at 3-minute intervals before washing in CR1aa + 5% FBS. This group also consisted of $n = 100$ (grade 1 and grade 2 embryos.)

2.4 Assessment and statistical analysis

Post-thaw embryos were cultured in CR1aa + 5% FBS for 24 and 48 hours. Survival was determined based on morphological expansion. A fresh control group of $n = 100$ embryos was included. All data were analyzed using one-way analysis of variance (ANOVA) to compare outcomes among the five groups: fresh control, conventional warming, and in-straw dilution with 0.2 M, 0.3 M, and 0.4 M sucrose. When a significant main effect was detected ($p < 0.05$), Tukey's post hoc test was applied for pairwise comparisons. Data were expressed as mean \pm standard deviation (SD), and statistical analysis was performed using GraphPad Prism (Version 5.01)

Results and Discussion:

The survival and developmental outcomes of bovine blastocysts following vitrification and warming are summarized in Table 1. Clear differences were observed among the five treatment groups in terms of re-expansion, full expansion, and hatching rates.

At 2 h post-warming, fresh control embryos exhibited complete re-expansion (100.00 \pm 0.00%), which was significantly higher ($p < 0.05$) than all vitrified groups. Among vitrified treatments, the 0.2 M sucrose group showed the highest re-expansion (89.88 \pm 3.91%), significantly exceeding conventional warming (79.29 \pm 4.12%) and 0.4 M sucrose (68.91 \pm 5.32%). The 0.3 M group (84.11 \pm 3.78%) displayed intermediate values, differing from both 0.2 M and 0.4 M ($p < 0.05$). These results indicate that moderate sucrose concentrations support a smoother osmotic transition during cryoprotectant removal, reducing membrane damage [4].

At 24 h, fresh control embryos maintained high viability (93.33 \pm 2.91%), whereas survival declined across vitrified groups. The 0.2 M sucrose group (78.99 \pm 3.65%) again outperformed conventional warming (55.09 \pm 4.12%) and higher sucrose concentrations ($p < 0.05$). The 0.3 M (58.85 \pm 4.03%) and 0.4 M (38.49 \pm 5.07%) groups exhibited reduced re-expansion, suggesting that elevated sucrose levels may impose osmotic stress that disrupts embryonic membranes.

At 48 h, the 0.2 M sucrose group maintained superior full expansion (65.96 \pm 3.78%) and hatching rates (44.91 \pm 3.56%), significantly higher ($p < 0.05$) than conventional warming (46.75 \pm 3.92% and 32.70 \pm 3.41%, respectively) and much greater than the 0.3 M and 0.4 M groups. Fresh controls showed the highest hatching (72.87 \pm 3.33%), but the 0.2 M group did not differ statistically from this level ($p > 0.05$), indicating near-equivalent developmental potential.

The negative impact of high sucrose concentrations (> 0.3 M) can be attributed to increased osmotic pressure leading to rapid dehydration and collapse of the blastocoel cavity. Such stress may compromise cytoskeletal organization, impair mitochondrial activity, and

enhance reactive oxygen species (ROS) production, thereby reducing ATP generation and cell viability [1,6]. In contrast, a moderate osmotic gradient, as achieved with 0.2 M sucrose, allows controlled rehydration and minimizes mechanical damage during warming. Previous studies support these findings, demonstrating that in-straw dilution simplifies the vitrification-to-transfer process and reduces the need for laboratory infrastructure while maintaining embryo viability [3,7,8]. This approach also minimizes contamination risk by keeping embryos enclosed in the straw throughout the warming process.

Taken together, these results indicate that in-straw warming with 0.2 M sucrose yields survival and developmental rates most comparable to fresh embryos, significantly outperforming conventional warming and higher sucrose concentrations. The findings validate this approach as a reliable, field-adaptable alternative, supporting the broader application of embryo vitrification in commercial cattle breeding programs.

Table 1.

Effect of warming protocols on re-expansion and hatching rates of in vitro-derived cattle embryos. (n = 100 per group).

Protocol	No. blastocyst	No. (%) re-expanded blastocysts at 2 h	No. (%) re-expanded blastocysts at 24 h	No. (%) Full-expanded blastocysts at 48 h	No. (%) hatching/ed blastocysts at 48 h
Fresh control	100	100 (100 ± 0) ^a	93 (93.33 ± 2.759) ^a	82 (82.61 ± 3.519) ^a	70 (72.87 ± 4.894) ^a
Conventional warming	100	79 (79.29 ± 3.925) ^{bc}	58 (55.09 ± 3.945) ^b	48 (46.75 ± 3.284) ^b	31 (32.70 ± 2.847) ^b
0.2 M one-step dilution	100	88 (89.88 ± 2.805) ^b	80 (78.99 ± 4.024) ^c	62 (65.96 ± 4.007) ^c	46 (44.91 ± 2.865) ^c
0.3 M one-step dilution	100	83 (84.11 ± 2.717) ^b	61 (58.85 ± 3.510) ^b	40 (40.15 ± 4.203) ^b	29 (26.74 ± 4.760) ^b
0.4 M one-step dilution	100	71 (68.91 ± 3.097) ^c	38 (38.49 ± 3.513) ^d	16 (11.97 ± 3.847) ^d	5 (3.420 ± 1.737) ^d

Conclusion:

In-straw dilution using 0.2 M sucrose proved to be an efficient, reliable, and field-adaptable approach for warming vitrified bovine embryos. The method produced post-warming survival and developmental outcomes comparable to those of fresh embryos while minimizing handling and contamination risk. Its simplicity allows practical implementation in field conditions without requiring advanced laboratory facilities.



Although the current study focused on *in vitro* survival and developmental competence, further investigation is required to evaluate the *in vivo* performance of embryos warmed using this technique. Future studies should assess pregnancy establishment and calving rates following embryo transfer to confirm the real-world applicability of the protocol under field conditions.

Acknowledgements:

This work was supported by One Research, One Graduate, Suranaree University of Technology (SUT). The authors thank the Embryo and Stem Cell Technology Research Center, SUT, and the Saraburi slaughterhouse for their cooperation.

References:

1. Kuwayama, M., Vajta, G., Kato, O., & Leibo, S. P. (2005). Highly efficient vitrification method for cryopreservation of human oocytes. *Reproductive Biomedicine Online*, 11(3), 300–308.
2. Rizos, D., Ward, F., Duffy, P., Boland, M. P., & Lonergan, P. (2002). Consequences of bovine oocyte maturation, fertilization or early embryo development *in vitro* versus *in vivo*: Implications for blastocyst yield and blastocyst quality. *Molecular Reproduction and Development*, 61(2), 234–248.
3. Vajta G, Holm P, Kuwayama M, Booth PJ, Jacobsen H, Greve T, Callesen H. Open pulled straw (OPS) vitrification: a new way to reduce cryoinjuries of bovine ova and embryos. *Mol Reprod Dev.* 1998;51:53–58. doi: 10.1002/(SICI)1098-2795(199809)51:1<#x0003c;53::AID-MRD6<#x0003e;3.0.CO;2-V.
4. Caamaño, J. N., Gómez, E., Trigal, B., Muñoz, M., Carrocera, S., Martín, D., & Díez, C. 2015. Survival of vitrified *in vitro*-produced bovine embryos after a one-step warming in-straw cryoprotectant dilution procedure. *Theriogenology*, 83.5: 881-890.
5. Saito, N., Imai, K., and Tomizawa, M. 1994. Effect of sugars-addition on the survival of vitrified bovine blastocysts produced *in vitro*. *Theriogenology*. 41.5: 1053-1060.
6. Dhali, A., Manik, R. S., Das, S. K., Singla, S. K., & Palta, P. (2000). Vitrification of buffalo (*Bubalus bubalis*) oocytes. *Theriogenology*, 53(6), 1295–1303.
7. Stachecki, J. J., Garrisi, J., Sabino, S., Caetano, J. P. J., Wiemer, K. E. and Cohen, J. 2008. A new safe, simple and successful vitrification method for bovine and human blastocysts. *Reprod. BioMed. Online*. 17: 360-367.
8. Oliveira, C. R., Lavorato, V. B. F., Rodrigues, B. A., Ferreira, V. J., Sales, A. D., Pires, P. A. A., ...& Seneda, M. M. (2020). In-straw warming protocol improves survival of vitrified embryos and allows direct transfer in cattle. *Cryobiology*, 97, 95-101.



PROCESS OPTIMIZATION OF LIQUEFACTION IN ENZYMATIC HYDROLYSIS OF WASTE BREAD USING RESPONSE SURFACE METHODOLOGY

Hsu Yadanar Htun¹, Natta Laohakunjit^{1*}, Nattapon Kaisangsri², Apiradee Uthairatanakij³, PUNCHIRA Vongsawasdi⁴, Ratchadaporn Kaprasob², Orrapun Selamassakul²

¹Division of Biochemical Technology, School of Bioresources and Technology, King Mongkut's University of Technology Thonburi, Bangkok, Thailand

²Pilot Plant Development and Training Institute, King Mongkut's University of Technology Thonburi, Bangkok, Thailand

³Division of Postharvest Technology, School of Bioresources and Technology, King Mongkut's University of Technology Thonburi, Bangkok, Thailand

⁴Department of Microbiology, Faculty of Science, King Mongkut's University of Technology Thonburi, Bangkok, Thailand

*e-mail: nutta.lao@kmutt.ac.th

Abstract:

Enzymatic hydrolysis is an eco-friendly and efficient approach for converting starchy waste into fermentable sugars. Expired bread is a rich source of carbohydrates that can be valorized as a renewable raw material in creating functional products, rather than being discarded as waste. In the enzymatic hydrolysis of starch-rich substrates such as waste bread, liquefaction is a crucial first step that directly influences the efficiency of the subsequent saccharification process. In this study, the liquefaction step was optimized using a response surface technique with Box-Behnken Design to determine the best conditions for fungal α -amylase activity prior to saccharification by examining the combined effects of enzyme concentrations (X_1), temperature (X_2), and pH (X_3). There were three center points out of a total of 15 experimental runs. The highest concentrations of total sugar (459.29 g. L⁻¹) and reducing sugar (331.57 g. L⁻¹) were obtained at 3% enzyme concentration, temperature 45–50°C and pH 5–6. The highest dextrose equivalent (44.21%) was also observed at 3% enzyme concentration, temperature 50°C and pH 5. Thus, the optimal liquefaction conditions were 3% enzyme concentration, temperature 50°C and pH 5–6. This study revealed that effective liquefaction optimization is essential for efficient hydrolysis and sustainable utilization of waste bread.

Keywords: enzymatic hydrolysis, liquefaction, fungal α -amylase, RSM, waste bread

Introduction:

Food loss and waste (FLW) has become a critical global issue, posing threats to food security, economic stability, and environmental sustainability. The Food and Agriculture Organization (FAO) has estimated that approximately one-third of food produced for human consumption, about 1.3 billion tons annually, is lost or wasted worldwide (FAO, 2013). Among the various food products, bread is the most widely consumed food worldwide and it is also one of the most wasted bakery products due to its short shelf-life, rapid spoilage and overproduction in bakeries and retailers. Every year, large volumes of unsold or expired bread were discarded globally, leading to economic losses and environmental burdens associated with food waste management (Dymchenko et al., 2023). However, the main composition of the bakery waste was mainly starch and bread waste was a by-product of overproduction and food disposal. Therefore, it can serve as an interesting raw material for the production of sugar-rich ingredients such as glucose syrup at minimal cost (Rosa-Sibakov et al., 2022). Current methods of addressing bakery waste involved incineration, utilization as animal feed, or biofuel production, but efficient recycling back to food industry was rare (Dymchenko et al., 2023).



Enzymatic hydrolysis is the most applied method to convert starch-rich substrates into fermentable sugars. In conventional glucose syrup production, starch derived mainly from wheat, corn and potato undergoes three sequential stages: gelatinization (dissolution of starch granules to form a viscous suspension), liquefaction (partial hydrolysis of starch) and saccharification (further hydrolysis to yield glucose and maltose) (Olsen, 1995). In enzymatic hydrolysis, liquefaction is a critical first step, during which α -amylase hydrolyzes internal α -1,4-glycosidic bonds to produce soluble dextrin and oligosaccharides and reduce the viscosity of the gelatinized starch slurry. The efficiency of liquefaction strongly influenced the performance of subsequent saccharification, while oligosaccharides were further hydrolyzed into fermentable sugars using glucoamylase, both in term of reaction rate and final sugar yield (Sigüenza-Andrés et al., 2022; Pele et al., 2021).

Therefore, optimizing liquefaction parameters are essential to maximize sugar release and ensure consistent process performance. The efficiency of hydrolysis is strongly influenced by factors such as temperature, pH, enzyme concentration, and reaction time, yet conventional one-factor-at-time (OFAT) approaches often fail to capture the interactive effects among these variables. To address these limitations, statistical methods such as Response Surface Methodology (RSM) were commonly applied. RSM enables simultaneous assessment of multiple factors and their interactions while minimizing the number of experimental trails required (Chen & Chen, 2025).

Sigüenza-Andrés et al. (2022) applied RSM to optimize simultaneous hydrolysis (liquefaction and saccharification) of bread waste using α -amylase and glucoamylase, resulting in high-glucose slurries under optimal pH and temperature conditions. Furthermore, Pele et al. (2021) showed how RSM-driven liquefaction optimization of starchy substrates, such as breadfruit starch, can successfully improve reducing sugar yields. However, the specific optimization of liquefaction stage for bread waste is less explored. Therefore, the objectives of this study were mainly to optimize the liquefaction step in enzymatic hydrolysis of waste bread using Response Surface Methodology, and to maximize the liquefaction efficiency— assessed by dextrose equivalent, concentration of total sugar and reducing sugar, and thereby improved the effectiveness and yield of the subsequent saccharification step.

Methodology:

Sample preparation

Leftover white bread (free of mold) was directly collected from the company (after shelf life, returns from shops). The bread was cut into small, uniform dice to ensure consistent drying. The chopped bread was dried in a drying oven at 100 °C for 3 hours. These slices were then mashed and sieved through a 40-mesh sieve to obtain the fine powder. To ensure sterility, the powder was packed in the aluminum foil bag, autoclaved at 121 °C and stored in a refrigerator until further use.

Enzymes

Fungal α -amylase (SBE-03FA) derived from *Aspergillus oryzae* (CAS No. 900-90-2; EC 3.2.1.1.), with an enzymatic activity of 100,000 U/g in powder form, was purchased from Sunson Industry Group Co., Ltd. and used as the hydrolytic enzyme in this study.

Proximate analysis of dried bread powder

The proximate composition of the bread powder, including moisture, crude protein, crude fat, crude fiber, ash and total carbohydrates, was determined according to standard procedures described by the Association of Official Analytical Chemists (AOAC, 2012). All measurements were conducted in triplicate, and results were expressed on a dry weight basis (dwb).

Experimental design and optimization of liquefaction step

Response Surface Methodology (RSM) using a Box-Behnken Design (BBD), generated by Minitab 17 version, was applied to optimize the process conditions of liquefaction step and to investigate the combined effects of variables influencing dextrose equivalent values (Table 1). Three factors were varied at three levels: enzyme concentration (X_1), temperature (X_2), and pH (X_3). There were three center points and 15 runs in the intended matrix (Table 1). The range of the pH and temperature were chosen following the enzyme technical sheets provided by the supplier. The substrate-to-water ratio was fixed at 1:10 w/v (15g of dried bread powder to 150 mL of DI water), and the reaction time was maintained at 3 hours for all experiments.

Table 1
Factors and levels for Box-Behnken Design (BBD)

Factors	Symbol	Factor level		
		Low (-1)	Medium (0)	High (1)
Enzyme concentration% (w/w)	Enz. Conc. %	1	3	5
Temperature (°C)	Temp.	45	50	55
pH	pH	4	5	6

Liquefaction of bread powder using fungal α -amylase

For each treatment, 15g of pre-treated bread powder was mixed with 150 mL of DI water in a 250 mL PYREX flask. The mixture was gelatinized at 90 °C for 30 mins in a water bath to disrupt starch granules. After gelatinization, the flasks were cooled to 45 °C. The pH of each mixture was then adjusted to the designated value using 0.1 M HCl and 0.1 M NaOH solutions. Following pH adjustment, the fungal α -amylase (SBE-03FA, 100,000 U/g; CAS No. 900-90-2; EC 3.2.1.1) was added in specific amounts corresponding to the desired concentrations. The slurries were immediately incubated in a water bath shaker for 3 hours at the designated temperatures. After 3 hours, the reaction mixtures were heated in a water bath at 95 °C for 20 mins to inactivate the enzyme activity. The slurries were then centrifuged at 10,000 rcf for 20 mins to separate the solids. The resulting supernatants were filtered three times through Whatman no. 1 filter paper using a vacuum filtration system to ensure clarity. The clear filtrates were then concentrated using a rotary evaporator at 50 °C until the final volume reached approximately 20 mL. The concentrated samples were stored at -4 °C for further analysis.

Determination of Total sugar concentration

According to Dubois et al. (1956), 1 mL of the sample was mixed with 1 mL of 5 % Phenol. After that, 5 mL of concentrated H₂SO₄ was added and the mixture was shaken using vortex. The reaction stands at room temperature for 20 mins. The absorbance of the sample was measured using a UV-Vis spectrophotometer at a wavelength of 490 nm.

Determination of Reducing sugar concentration

The DNS method was used to analyze reducing sugars. The clarified supernatant was transferred into a test tube in volume of up to 1 mL, followed by the addition of 1 mL of DNS reagent. The mixture was thoroughly shaken and then heated in a boiling water bath at 95°C for 10 mins. After heating, the test tube was cooled in ice water. Subsequently, 5 mL of DI



water was added, and the mixture was shaken again using vortex before measuring the absorbance at 540 nm using UV-VIS spectrophotometer (Miller, 1959). Glucose was used as a standard.

Dextrose equivalent (DE)

Dextrose equivalent (DE) was determined by reducing sugar evaluation using 3,5-Dinitrosalicylic acid (DNS) method as described by Miller (1959). According to Shariff et al. (2009), DE was calculated as follows:

$$DE = \frac{\text{reducing sugar expressed as glucose (g)}}{\text{dry solid weight (g)}} \times 100\%$$

Total soluble solids (%TSS)

% TSS was determined using a refractometer. A drop of the clear supernatant was placed on the refractometer, and the refractive index was measured.

Statistical analysis

All tests were performed in triplicates and statistical analysis of all experiment data was conducted using test of significance and analysis of variance (ANOVA) in IBM SPSS version 20. Additionally, RSM was employed to optimize the process conditions, and the three-dimensional response surface plot of the experimental model was generated using Statistica 7 program.

Results and Discussion:

Proximate composition of the dried bread powder

The proximate composition of the bread powder was summarized in Table 2. The moisture content was relatively low (0.63%), indicating that the drying process was effective in reducing water activity. The carbohydrate content represented the major component (77.34%), followed by protein (15.05%) and fat (4.56%). The ash and fiber contents were comparatively low (1.34% and 1.08%). These values confirmed that bread powder can serve as a carbohydrate-rich substrate for hydrolysis.

Table 2
Proximate composition of the dried bread powder

%Moisture	%Crude Protein	%Crude Fat	%Ash	%Crude Fiber	%Total Carbohydrate
0.63±0.03	15.05±0.13	4.56±0.06	1.34 ±0.13	1.08±0.08	77.34±0.21

All values are reported as mean ± standard deviation from triplicate determination.

Determination of total sugar concentration (TS_c), reducing sugar concentration (RS_c), dextrose equivalent (DE) and total soluble solids (% TSS)

The combined effects of enzyme concentration % (w/w), incubation temperature, and pH were significant interaction on total sugar concentration, reducing sugar concentration, dextrose equivalent and %TSS during the liquefaction of bread waste (Table 3). Total sugar concentration varied between 312.48 and 459.29 g. L⁻¹, while reducing sugar concentration ranged from 175.57 to 331.57 g. L⁻¹. Correspondingly, the DE values increased with hydrolysis, ranging from 23.41 to 44.21%, indicating a progressive conversion of starch into shorter chain dextrans and fermentable sugars. The maximum total sugar concentration (459.29 g. L⁻¹) was achieved at 3% enzyme concentration (w/w), 45 °C and pH 6, but the

highest reducing sugar concentration (331.57 g. L⁻¹) was obtained under 3% enzyme concentration, 50 °C and pH 5. The highest DE (44.21%) was also observed at 3% enzyme concentration, 50 °C and pH 5. The optimum total soluble solids value (50.5 %) was recorded at 5% enzyme concentration, incubation temperature 50 °C and pH 6. In addition, higher enzyme concentrations (3–5%) and moderate temperatures (45°C–50°C) favored greater starch hydrolysis, as reflected in higher TS_c, RS_c and DE values. Fungal α -amylase, the enzyme used in this study, is not thermostable like bacterial α -amylases. It generally exhibited good catalytic performance at moderate temperatures but tends to lose activity once the temperature exceeds above 60 °C (Balakrishnan et al., 2021). With respect to pH, a lower pH value (pH 4) resulted in reduced sugar concentrations, while pH 5-6 produced higher concentrations of sugar. A similar trend was reported by Abidin and Hassan (2023) who conducted their enzymatic hydrolysis at pH 6, achieving maximum sugar yield at 50 °C with 6.0% enzyme concentration (w/v) and reaction time 180 mins. These findings highlight the importance of optimizing each parameter during enzymatic hydrolysis to maximize sugar recovery from bread waste while preserving enzyme functionality.

Table 3

Box-Behnken design and responses for the study of optimum conditions in the liquefaction step

Run	Experimental Factors			Responses			
	E ^a	T ^b	pH	TS _c ^c	RS _c ^d	DE ^e	%TSS ^f
1	1	45	5	380.74	251.90	33.59	37.4
2	5	45	5	347.59	259.57	34.61	45.3
3	1	55	5	367.62	258.57	34.48	38.7
4	5	55	5	312.48	262.57	35.01	47.3
5	1	50	4	321.70	215.90	28.79	36.0
6	5	50	4	334.47	230.57	30.74	43.4
7	1	50	6	385.00	298.90	39.85	41.9
8	5	50	6	431.81	321.23	42.83	50.5
9	3	45	4	315.14	175.57	23.41	44.8
10	3	55	4	351.67	234.90	31.32	39.6
11	3	45	6	459.29	299.90	39.99	48.0
12	3	55	6	399.54	280.57	37.41	40.4
13	3	50	5	428.18	321.23	42.83	45.5
14	3	50	5	425.46	318.57	42.48	45.7
15	3	50	5	443.33	331.57	44.21	45.9

^a Enzyme concentration % (w/w); ^b Incubation temperature (°C); ^c Total sugar Concentration (g. L⁻¹); ^d Reducing sugar concentration (g. L⁻¹); ^e Dextrose equivalent (%), ^f Total soluble solids (%)

Optimization of the Liquefaction Step of Waste Bread Hydrolysis

The efficiency of liquefaction step was evaluated in terms of dextrose equivalent (DE), as this parameter directly reflects the extent of starch hydrolysis. This response was used to construct second-order polynomial models via multiple regression analysis. The model demonstrated great significance ($p \leq 0.05$) and has less variation around the mean R² value of

0.990. This indicated that 99.0% of the variability in DE values could be explained by this quadratic model. The adequacy of the quadratic model in predicting the maximum dextrose equivalent value of the liquefaction step was assessed in Table 4. As shown in Table 4, the model p- and F- values were 0.000 and 53.853, respectively, suggesting that the model was highly significant. Among the tested variables, the linear term for the pH showed a p-value less than 0.05, indicating it plays a critical role in liquefaction step to obtain the highest DE. In contrast, enzyme concentration % (w/w) and temperature (°C) did not exhibit statistically significant effects at the linear level ($p > 0.05$). When selecting two variables for the construction of 3-D surface plot, priority was given to those with the most influence on the response (DE). Since pH was the most significant factor, it was selected as one variable. When comparing enzyme concentration % and temperature (°C), the linear coefficient of temperature was slightly higher than that of the enzyme concentration. In addition, both the interaction and quadratic terms for temperature contributed more significantly to the model. In the second-order regression equation, enzyme concentration exhibited the least influence on the response which indicated by its relatively small regression coefficient and higher p-value. Therefore, temperature was selected alongside pH to visualize and interpret the response surfaces more effectively. For the construction of the surface plot, enzyme concentration was held constant at its center level. Temperature and pH, which showed greater effects on the response, were selected as the independent variables and plotted on the X and Y axes to better visualize their interactive effects on dextrose equivalent.

Table 4
Regression coefficient and analysis of variance of the model obtained by RSM

Source	Regression coefficients	Significant (p-value)
Model	43.173	0.0000
A-Enzyme concentration %	0.810	0.074
B-Temperature (°C)	0.827	0.070
C-pH	5.728	0.000
AB	-0.122	0.819
AC	0.257	0.634
BC	-2.623	0.004
A ²	-3.115	0.002
B ²	-5.635	0.000
C ²	-4.505	0.000
Validation of the model		
R ²	0.990	
Adjusted R ²	0.971	
p-value	0.000	
F-value	53.853	

Based on the BBD design, the results were fitted to a second-order polynomial model, represented by the following equation:

Dextrose equivalent (DE) = 43.173+ 0.827B+5.728C–2.623BC–5.635 B²–4.505C²,
when A = 0

In the above equation, A denotes % enzyme concentration (w/w), B represents incubation temperature (°C) and C indicates pH.

3D surface plot generated for dextrose equivalent clearly illustrated the interactive effects of temperature and pH with the enzyme concentration fixed at the center point (3 % w/w) (Figure 1). In this plot, an increasing trend in the response value was observed with the elevation of pH. The result indicated that elevated pH levels within the studied range promoted enzyme activity, resulting in the maximum DE. However, according to the second-order regression equation, the quadratic term of pH (C^2) exhibited a negative effect, suggesting that beyond the optimum level, further increases in pH may lead to a decline in response value. In contrast, the effect of temperature showed a less consistent trend across the

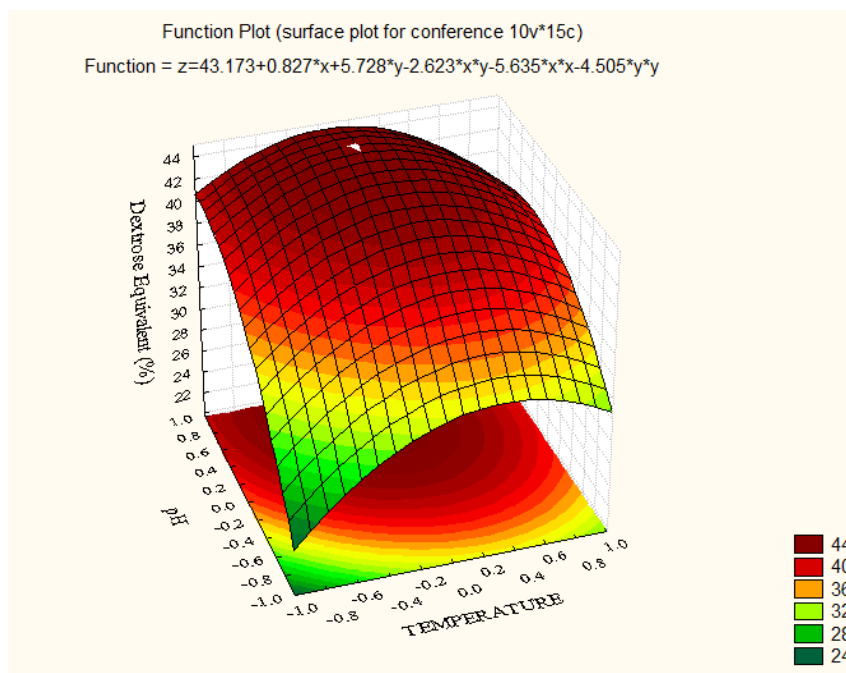


Figure 1

3D response surface plot showing the effects of pH and temperature, with enzyme concentration fixed at center point

plot. Although the clear increase or decrease was not observed across the full temperature range, the surface profile showed that moderate temperature favored the maximum DE. According to Balakrishnan et al. (2021), fungal α -amylase performed efficiently under moderate temperatures but rapidly lost activity when the temperature exceeded 60°C. Indeed, the highest DE (44.21%) and the maximum reducing sugar concentration (331.57 g. L⁻¹) were achieved at 3% enzyme concentration, incubation temperature 50 °C and pH 5. These results confirm that moderate temperature levels were optimal for maximizing sugar release and conversion in liquefaction step using fungal α -amylase. According to the surface trends and experimental data, the optimal conditions for liquefaction stage were defined as at 3% enzyme concentration (w/w), incubation temperature 50 °C and pH 5–6. To validate the regression model, a confirmation experiment was performed at the predicted optimal conditions (3% enzyme concentration, 50°C and pH 6). The experimental DE obtained (44.38 %) was in close agreement with the model predicted DE value (44.396 %), with less than 0.04% error. This agreement confirmed that the RSM model was reliable and accurate for predicting DE value under the selected conditions.



Conclusion:

The enzymatic liquefaction of leftover bread using fungal α -amylase effectively converted the carbohydrate-rich substrate (waste bread) into fermentable sugars under designated conditions. The highest concentrations of total sugar (459.29 g. L⁻¹) and reducing sugar (331.57 g. L⁻¹) were obtained at 3% enzyme concentration (w/w), incubation temperature 45–50 °C and pH 5–6. The highest dextrose equivalent (44.21%) was observed at 3% enzyme concentration, 50 °C and pH 5. Surface plot analysis further confirmed that increasing pH led to a consistent increase in the response up to a peak point, while moderate temperatures produced higher concentration compared to extreme conditions. The optimal liquefaction conditions were identified as 3 % enzyme concentration, temperature 50 °C and pH 5–6.

Acknowledgements:

Deepest thanks are extended to the German Academic Exchange Service (DAAD) for their generous support through the EU Mobility Programme for Myanmar (EMPM) scholarship. Special appreciation goes to my advisor, Assoc. Prof. Dr. Natta Laohakunjit, for her valuable guidance and support. I also would like to express my sincere gratitude to the Agricultural and Food Processing Laboratory at King Mongkut's University of Technology Thonburi for providing essential facilities, insightful advice, and encouragement throughout this work.

References:

1. Abidin ZZ, Hassan SR. Kinetic studies of enzymatic hydrolysis pre-treatment of waste bread under preliminary conditions. *Journal of Engineering and Science Research*. 2023;7(3):09-14.
2. AOAC International. *Official Methods of Analysis of AOAC International* (19th ed.). Gaithersburg, MD, USA: AOAC International. 2012.
3. Balakrishnan M, Jeevarathinam G, Kumar SK, Muniraj I, Uthandi S. Optimization and scale-up of α -amylase production by *Aspergillus oryzae* using solid-state fermentation of edible oil cakes. *BMC biotechnology*. 2021;21(1):33.
4. Chen HY, Chen C. Importance of Using Modern Regression Analysis for Response Surface Models in Science and Technology. *Applied Sciences*. 2025;15(13):7206.
5. DuBois M, Gilles KA, Hamilton JK, Rebers PA, Smith F. Colorimetric method for determination of sugars and related substances. *Analytical chemistry*. 1956; 28(3):350-356.
6. Dymchenko A, Gersl M, Gregor T. Trends in bread waste utilization. *Food Science & Technology*. 2023; 132:93-102.
7. Food and Agriculture Organization of the United Nations. *Food Wastage Footprint: Impacts on Natural Resources: Summary Report*. FAO, Rome. 2013.
8. Miller GL. Use of dinitrosalicylic acid reagent for determination of reducing sugar. *Analytical chemistry*. 1959;31(3):426-8.
9. Olsen H. Enzymatic production of glucose syrups. In *Handbook of starch hydrolysis products and their derivatives*. Springer. 1995;26-64.
10. Pele GI, Bolade MK, Enujiugha, VN, Sanni DM, Ogunsua AO. Optimization of the liquefaction steps of breadfruit starch hydrolysis by alpha-amylase using a statistical approach. *IRESPUB Journal of Agriculture, Food & Nutrition*. 2021;1(2).
11. Rosa-Sibakov N, Sorsamäki L, Immonen M, Nihtilä H, Maina NH, Siika-aho M, Katina K, Nordlund E. Functionality and economic feasibility of enzymatically hydrolyzed waste bread as a sugar replacer in wheat bread making. *Journal of Food Processing and Preservation*. 2022;46(3): e16378.



12. Shariffa YN, Karim AA, Fazilah A, Zaidul IS. Enzymatic hydrolysis of granular native and mildly heat-treated tapioca and sweet potato starches at sub-gelatinization temperature. *Food hydrocolloids*. 2009;23(2):434-40.
13. Sigüenza-Andrés T, Pando V, Gómez M, Rodríguez-Nogales JM. Optimization of a Simultaneous Enzymatic Hydrolysis to Obtain a High-Glucose Slurry from Bread Waste. *Foods*. 2022;11(12):1793.



DEVELOPMENT AND CHARACTERIZATION OF CELLULOSE ACETATE/CHITOSAN FILMS INCORPORATED WITH *Piper betel* EXTRACT FOR ANTIMICROBIAL FOOD PACKAGING

Prapot Kumhang¹, Piyarat Khanthawaro², Nichapat Takiaw¹, Thanaporn Srichomphu¹, Songsirin Ruengvisesh^{1,2} *

¹Department of Microbiology, Faculty of Science, King Mongkut's University of Technology Thonburi, Bangkok, 10140, Thailand

²Food Safety Center, Institute for Scientific and Technological Research and Services, King Mongkut's University of Technology Thonburi, Bangkok, 10140, Thailand

*email: songsirin.rue@kmutt.ac.th

Abstract:

This study investigated the development of chitosan/cellulose acetate (CS/CA) composite films incorporated with Piper betel leaf extract (PBE) for potential food packaging applications. The films were prepared by optimizing the cellulose acetate (CA) concentration to achieve a balance between mechanical strength, transparency, and flexibility. The optimal formulation, 1% chitosan and 0.12% cellulose acetate, was selected for incorporating varying concentrations of PBE (0%, 1%, 1.5%, and 2%). The films were characterized for thickness, light transmittance, tensile strength, extensibility, color, and antimicrobial activity. Results indicated that increasing the concentration of PBE enhanced the antimicrobial properties, with films containing 1% PBE exhibiting significant inhibition against *Salmonella* Newport (16.09 ± 0.30 mm), *Salmonella* Typhimurium (17.21 ± 0.51 mm), and *Listeria innocua* (18.14 ± 0.49 mm). The 1% PBE formulation achieved the best balance of mechanical strength (34.43 ± 1.99 MPa), extensibility (1.66 ± 0.28 mm), and moderate transparency ($27.70 \pm 2.0\%$ transmittance), making it a promising candidate for food packaging applications. Although higher PBE concentrations (1.5% and 2%) further improved antimicrobial activity, they reduced film transparency and whiteness. Overall, the developed CS/CA-PBE films may provide a sustainable and active packaging solution, offering enhanced food safety and extended shelf life, which contributes to the growing demand for eco-friendly alternatives in the food industry.

Introduction:

The growing demand for sustainable and functional food packaging has driven the development of biodegradable films with enhanced mechanical, optical, and antimicrobial properties. Chitosan (CS), a natural polysaccharide derived from chitin, is widely recognized for its film-forming ability, biodegradability, and inherent antimicrobial activity. However, its mechanical limitations and sensitivity to moisture often require blending with other polymers. Cellulose acetate (CA), a semi-synthetic derivative of cellulose, offers complementary properties such as improved film strength and transparency, making it a suitable co-polymer for chitosan-based films.

To further enhance the functionality of CS/CA films, natural plant extracts rich in bioactive compounds have gained attention. Unlike other plant extracts previously incorporated into chitosan-based films, *Piper betel* leaf extract (PBE) offers a distinctive profile of bioactive compounds, particularly hydroxychavicol and eugenol, which exhibit potent antimicrobial and antioxidant properties. Its notably high phenolic content enhances the film's functional performance, especially in microbial inhibition. Moreover, *P. betel* holds deep cultural significance in Southeast Asia, where it has been traditionally used for medicinal and preservative purposes. This cultural relevance, combined with its potent bioactivity, positions PBE as a unique and sustainable additive for developing active packaging materials that align with both scientific innovation and regional heritage.



Therefore, incorporating PBE into biopolymer matrices not only introduces active functionality but also aligns with clean-label and eco-friendly packaging trends. This study aims to optimize the formulation of chitosan/cellulose acetate films with varying concentrations of *P. betel* leaf extract (PBE) and evaluate their physical, optical, mechanical, and antimicrobial properties. The goal is to identify a balanced composition suitable for active food packaging applications, particularly for products sensitive to microbial contamination and light exposure.

Methodology:

Preparation of chitosan/cellulose acetate films

A CS solution was prepared by dissolving 1.2 g of CS in 2% (v/v) acetic acid (100 mL) under magnetic stirring at 1200 rpm for 1 hour at room temperature, until complete dissolution was achieved. Separately, CA (0.144, 0.216, and 0.288 g) was dissolved in acetone (20 mL) under identical conditions. The two solutions were then blended to obtain composite CS/CA film-forming solutions with final polymer concentrations of 1% (w/v) CS and 0.12%, 0.18%, or 0.24% (w/v) CA, respectively.

Preparation of Piper betel leaf extract

Fresh *P. betel* leaves were washed with distilled water, dried in a hot air oven at 55°C for 24 hours, then ground into a fine powder. The powder was extracted with 95% (w/v) ethanol at a ratio of 1:5, sealed, and kept at room temperature for 72 h with occasional stirring. The mixture was filtered sequentially through cotton wool and Whatman No.1 filter paper. Ethanol was removed using a rotary vacuum evaporator at 55°C to yield a crude extract, which was stored at 2–4°C in amber containers until use.

Preparation of chitosan/cellulose acetate films combined with piper betel extract

CS/CA films were characterized to determine the optimal condition, and 1% CS/0.12% CA was selected for combining with PBE. For the active films, PBE was incorporated into the optimized 1%CS/0.12%CA solution at concentrations of 1%, 1.5%, and 2% (w/v). The mixtures were stirred for an additional 1 h until homogeneous. Then, 6 ml of film solutions were added to a 90 mm × 15 mm Petri dish and dried at room temperature for 48 h. After drying, the active films were removed from the Petri dishes and placed in a desiccator at 50% RH for 48 h. The 1% CS/0.12% CA film without PBE was also prepared as a control.

Film thickness analysis

Film samples (1.5 cm × 3 cm) were cut and measured for thickness using a digital micrometer with a precision of 0.01 mm. Measurements were taken at three different positions on each film, repeated five times, and the mean thickness was calculated.

Light transmittance analysis of films

The light transmittance of the films was measured using a spectrophotometer at a wavelength of 600 nm. Film samples (1.5 cm × 3 cm) were cut and mounted on paper supports of the same dimensions as the cuvette holder. The film-mounted paper was placed in the spectrophotometer, and transmittance values were recorded. A blank cuvette (without film) was used as the reference. Each measurement was performed in triplicate.

Mechanical properties of films

The mechanical properties of the films were evaluated in terms of tensile strength and extensibility using a texture analyzer equipped with an A/TG probe. Film samples (1 cm × 5



cm) were clamped between the two grips of the instrument and stretched at a crosshead speed of 0.0833 cm/s until breakage. Each test was performed 5 times ($n = 5$).

Color analysis of films

The color of the films was analyzed using a colorimeter, which provided values of lightness (L^*), red–green (a^*), and yellow–blue (b^*). The instrument was calibrated using a light trap standard prior to measurement. Film samples were placed on the reflectance port of the colorimeter, and readings were recorded via the connected computer. Measurements were taken at three different points of each sample and repeated three times. The color difference (ΔE) and whiteness index (WI) were calculated using the following equations:

$$\Delta E = \sqrt{(L^* - L)^2 + (a^* - a)^2 + (b^* - b)^2}$$

$$WI = 100 - \left((100 - L^*)^2 + (a^*)^2 + (b^*)^2 \right)^{0.5}$$

Where:

L^* = lightness of the sample (0 = black, 100 = white)

a^* = red (+) to green (-) coordinate

b^* = yellow (+) to blue (-) coordinate

L, a, b = reference values (typically standard white plate)

ΔE = overall color difference between the sample and the reference

WI = whiteness index, representing the degree of whiteness of the film

Antimicrobial Activity Test

The antimicrobial activity of the films was evaluated against *Salmonella* Typhimurium, *Salmonella* Newport, and *Listeria innocua* using the agar disk diffusion method. Each bacterial strain (approximately 10^5 CFU/ml) was swabbed uniformly onto Mueller–Hinton agar plates. Film samples were cut into circular discs (6 mm diameter) and aseptically placed on the inoculated agar surface. The plates were incubated at 37 °C for 24 h. The diameters of the clear inhibition zones were measured using a digital vernier caliper and expressed as mm \pm SD. All tests were performed in triplicate.

Statistical analysis

Statistical analysis was performed using IBM SPSS Statistics software (Version 21). One-way analysis of variance (ANOVA) was applied to determine significant differences among treatments at a confidence level of $p < 0.05$. Duncan's multiple range test was subsequently used to identify significant differences between mean values.

Results and Discussion:

Optimization of cellulose acetate concentration

To determine the optimal CA concentration for the composite CS/CA films, 1%CS was blended with CA at 0.12%, 0.18%, and 0.24% without PBE. The film thickness, optical properties, and mechanical performance were analyzed, as summarized in Table 1.

Film thickness

The thickness of composite films increased with higher CA concentrations, particularly at 0.18% and 0.24%, indicating a positive correlation between total polymer content and film density. This trend suggested that increased CA contributed to a more compact matrix during solvent evaporation, resulting in thicker films. The semi-hydrophobic nature of CA might also promote tighter polymer aggregation, enhancing structural integrity. These findings align with Bahmid *et al.* (2021) (1), who reported that higher solid content in film-forming



solutions leads to increased film thickness due to reduced solvent loss and enhanced polymer packing.

Optical properties

Light transmittance (%T) decreased progressively with increasing CA concentrations, reflecting a transition from transparent to more opaque films. The highest transmittance was observed at the lowest CA level (0.12%), making it suitable for packaging applications that require product visibility. Conversely, films with 0.24% CA exhibited significantly reduced transmittance, likely due to increased light scattering and absorption within the denser polymer matrix. This behavior is also consistent with that of Romão *et al.* (2022) (2) and Bahmid *et al.* (2021) (1), who noted that polymer-rich films tended to exhibit lower transparency due to their internal microstructural complexity. The ability to modulate light transmission is particularly relevant for packaging light-sensitive foods, such as oils or pigments, where reduced exposure can help preserve product quality.

Mechanical strength

The tensile strength of the chitosan–cellulose acetate (CS–CA) films decreased significantly with increasing CA concentration, from 54.45 ± 4.16 MPa at 0.12% CA to 34.27 ± 5.43 MPa at 0.24% CA. This reduction suggested that while the initial addition of CA contributed to a more compact polymeric structure, excessive CA incorporation may have disrupted the hydrogen bonding network between CS and CA, leading to weaker intermolecular interactions and lower load-bearing capacity. Similar trends have been observed in other CS–CA and cellulose-based composites, where an optimal blend ratio improved strength, but higher CA levels reduced compatibility and cohesion within the film matrix (3)

In contrast, extensibility did not show significant differences among treatments, with values ranging from 0.82 ± 0.19 to 0.87 ± 0.15 mm across all CA concentrations. This stability indicated that CA addition influenced the rigidity and transparency of the films more strongly than their stretchability. Comparable findings have been reported in other cellulose–chitosan systems, where mechanical strength was sensitive to composition changes, but extensibility remained relatively constant, likely due to the plasticizing effect of chitosan that balanced stiffness and flexibility (Cazón *et al.*, 2018)

Together, these results suggested that higher CA levels compromised the film's strength without significantly enhancing or impairing its ability to deform under stress, indicating a need for compositional optimization to maximize both tensile and functional performance.

Optimal formulation

Among the tested formulations, the 0.12% CA formulation was selected as optimal because it produced films with the highest tensile strength and transparency, which are key indicators of film quality. Although extensibility did not differ significantly among formulations, this concentration maintained a good balance between strength and flexibility. In contrast, higher CA concentrations (0.18–0.24%) reduced tensile strength and transparency, suggesting phase disruption in the polymer matrix. Therefore, 0.12% CA provided the most desirable combination of mechanical strength, clarity, and structural stability.

Table 1.

Thickness, light transmittance, tensile strength, and extensibility of the composite films (1%CS+ varying concentrations of CA)

Cellulose acetate concentration (w/v)	Thickness (mm)	%Transmittance	Tensile strength (MPa)	Extensibility (mm)
0.12%CA	0.017±0.007 ^b	56.40±0.54 ^a	54.45±4.16 ^a	0.87±0.15 ^a
0.18%CA	0.028±0.007 ^a	45.50±3.02 ^b	50.29±3.02 ^b	0.88±0.06 ^a
0.24%CA	0.030±0.003 ^a	36.30±1.10 ^c	34.27±5.43 ^c	0.82±0.19 ^a

Different letters within columns indicate a significant difference ($p < 0.05$).

Characterization of CS/CA films containing PBE

According to CA optimization, 1%CS/0.12%CA was selected for developing an active film containing PBE. The film thickness, optical properties, mechanical performance, and color of 1%CS/0.12%CA film containing 0%, 1%, 1.5% and 2%PBE were analyzed and reported in Table 2.

Film thickness

The thickness of the composite films increased significantly with higher concentrations of PBE. The control film (0%PBE) exhibited the lowest thickness, while the film with 2%PBE showed the highest value. This increase could be attributed to the higher total solid content in the film-forming solution, which promoted denser material deposition during drying. Bahmid *et al.* (2021) (1), also reported that increasing the concentration of bioactive extracts or polymers enhanced film thickness due to increased solution viscosity and particle aggregation.

Optical properties

Film transparency, expressed as light transmittance (%T), decreased significantly with increasing extract concentration. The control film showed the highest transparency (~56%), while films with 1.5% and 2% extract exhibited the lowest values (~16% and ~14%, respectively). This reduction in %T is likely due to the darker pigments in PBE and the denser internal structure caused by polymer–phenolic interactions, which enhance light scattering within the matrix. Similar observations were reported by Romão *et al.* (2022) (2) and Bahmid *et al.* (2021) (1), who demonstrated that incorporating plant-derived extracts reduced transparency due to the presence of phenolic compounds and chromophores. For food packaging applications, films with moderate transparency are desirable when product visibility is required, whereas low-transmittance films are beneficial for protecting light-sensitive products.

Mechanical properties

The tensile strength of the films exhibited a nonlinear trend. Among CS/CA+PBE films, the highest tensile strength (34.43±1.99 MPa) was recorded at 1% PBE, suggesting optimal polymer–extract interactions that reinforced the film's structural integrity. At higher PBE concentrations (1.5% and 2%), tensile strength decreased, likely due to excessive aggregation of phenolic compounds, which weakened the molecular network. These findings are consistent with Siripatrawan & Harte (2010) (4), who reported that moderate levels of phenolic-rich extracts enhanced hydrogen bonding between chitosan and phenolic compounds, while excessive addition led to structural discontinuities and reduced strength.

Extensibility increased progressively with higher PBE concentrations, reaching its maximum at 1.5% and 2% PBE. The higher flexibility observed at elevated extract levels could be attributed to the plasticizing effect of phenolic compounds, which reduced intermolecular forces within the polymer matrix. However, films with excessive flexibility exhibited reduced tensile strength, indicating a trade-off between strength and elasticity.

Table 2.

Thickness, light transmittance, tensile strength, and extensibility of the active films (1%CS/0.12%CA + varying concentrations of PBE)

PBE concentration (w/v)	Thickness (mm)	% Transmittance	Tensile strength (MPa)	Extensibility (mm)
0%	0.017±0.007 ^c	56.40±0.54 ^a	54.45±4.16 ^a	0.87±0.15 ^b
1%	0.048±0.002 ^c	27.70±2.00 ^b	34.43±1.99 ^b	1.66±0.28 ^b
1.5%	0.058±0.002 ^b	16.90±1.30 ^c	22.75±1.25 ^c	2.55±0.83 ^a
2%	0.073±0.006 ^a	14.80±1.40 ^c	12.28±0.70 ^d	2.63±0.67 ^a

Different letters within columns indicate a significant difference ($p < 0.05$).

Color properties of active CS/CA films containing PBE extract

Composite 1%CS/0.12%CA films incorporated with different concentrations of PBE are shown in Figure 1. The color parameters (L^* , a^* , b^* , ΔE , and WI) of the active films are presented in Table 3. A significant reduction ($p < 0.05$) in lightness (L^*) was observed as the PBE concentration increased from 0% to 2%, with values decreasing from 36.77 ± 0.48 for the control film to 16.04 ± 0.30 at 2% PBE. A higher L^* value indicated greater lightness and transparency, suggesting that the addition of PBE contributed to the darkening of the films. This darkening effect could be attributed to the presence of natural pigments such as chlorophyll, tannins, and polyphenols in the extract, which absorbed more light and reduced film transparency (4).

For chromaticity, the a^* and b^* values were also affected by PBE concentration. The control film exhibited nearly neutral color values ($a^* = -0.02$, $b^* = -0.37$), reflecting its transparent and slightly greenish-white appearance. Films with 1% PBE showed the highest positive a^* (2.26) and b^* (6.48) values, indicating a shift toward red and yellow hues. However, at higher PBE concentrations (1.5% and 2%), both a^* and b^* values decreased sharply, suggesting that excessive pigment deposition from the extract suppressed these tones, resulting in a darker green-brown film. This effect is consistent with previous findings, where increased phenolic and chlorophyll content masked lighter tones and enhanced overall opacity (5).

The overall color difference (ΔE) decreased with higher extract concentrations, from 0.41 ± 0.46 in the control to 0.24 ± 0.30 at 2% PBE. A lower ΔE indicated a more uniform color appearance due to better dispersion of pigments at higher extract levels. Similarly, the Whiteness Index (WI) decreased significantly from 36.77 ± 0.48 (control) to 16.03 ± 0.30 (2% PBE), confirming the loss of whiteness and increased film opacity. This reduction in WI is linked to both light absorption by pigments and the denser microstructure of films containing higher amounts of extract, which enhances light scattering and lowers reflectance (6).

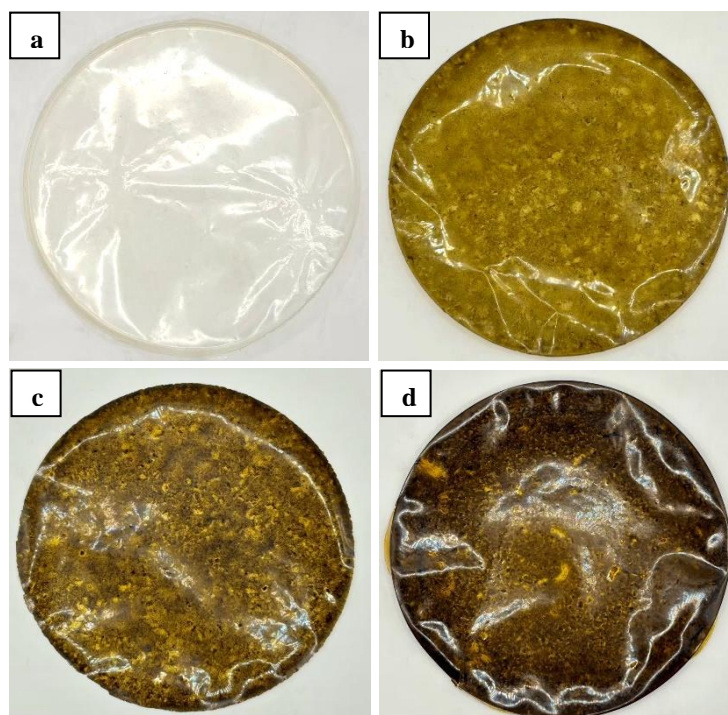


Figure 1.

Composite films of a) 1%CS/0.12%CA, b) 1%CS/0.12%CA+1%PBE, c) 1%CS/0.12%CA+1.5%PBE, and d) 1%CS/0.12%CA+2%PBE

Table 3.

Color analysis of active films (1%CS/10.12%CA + varying concentrations of PBE)

%PBE	L*	a*	b*	ΔE	WI
0%	36.77±0.48 ^a	-0.02±0.02 ^c	-0.37±0.09 ^c	0.41±0.46 ^a	36.77±0.48 ^a
1%	26.05±0.45 ^b	2.26±0.13 ^a	6.48±0.46 ^a	0.51±0.60 ^a	25.73±0.41 ^b
1.5%	23.29±0.36 ^c	2.08±0.06 ^a	3.03±0.03 ^b	0.52±0.37 ^a	23.21±0.36 ^c
2%	16.04±0.30 ^d	1.07±0.03 ^b	0.17±0.02 ^a	0.24±0.30 ^a	16.03±0.30 ^d

Different letters within columns indicate a significant difference ($p < 0.05$).

L* = lightness of the sample (0 = black, 100 = white)

a* = red (+) to green (-) coordinate

b* = yellow (+) to blue (-) coordinate

L, a, b = reference values (typically standard white plate)

ΔE = overall color difference between the sample and the reference

WI = whiteness index, representing the degree of whiteness of the film

Antimicrobial activity

The study investigated the antimicrobial activity of 1%CS/0.12%CA film with varying concentrations of PBE against *S. Newport*, *S. Typhimurium*, and *L. innocua*. As shown in the provided table, the film without PBE exhibited no inhibition zone against the tested bacteria. This is because, while chitosan has inherent antimicrobial properties, its effectiveness is limited in a solid film format without an acidic environment to release its active compounds. Additionally, cellulose acetate itself has no antimicrobial properties. However, the addition of PBE significantly enhanced the film's antimicrobial activity, as evidenced by the formation of inhibition zones. Overall, the antimicrobial effect was dose-dependent, indicating that the inhibition zone size increased with the concentration of the PBE in the film.

The potent antimicrobial activity of the films containing PBE could be attributed to the bioactive compounds present in the extract, such as eugenol, hydroxychavicol, phenolics, and flavonoids. These compounds work by damaging bacterial cell membranes, leading to the loss of ion balance and disrupting essential metabolic processes, such as protein and nucleic acid synthesis. This prevented the bacteria from multiplying and growing. Furthermore, incorporating the PBE into the film's polymer matrix helped to stabilize the active compounds and provided a sustained release of antimicrobial agents onto the film's surface. This prolonged release mechanism enhances the long-term effectiveness of the films against microbial contamination. These results are also consistent with previous research, which also highlighted the high antimicrobial potential of betel leaf components, particularly against *Salmonella* and *Listeria* species (7, 8). Therefore, the development of these PBE-infused films represents a promising approach for creating active food packaging that can reduce contamination risks and extend the shelf life of food products.

Table 4.
Antimicrobial activity of CS/CA and CS/CA+PBE films

Film	Inhibition zone (mm)		
	<i>S. Newport</i>	<i>S. Typhimurium</i>	<i>L. innocua</i>
1%CS/0.12%CA	n/a	n/a	n/a
1%CS/0.12%CA+1%PBE	16.09±0.30 ^c	17.21±0.51 ^b	18.14±0.49 ^c
1%CS/0.12%CA+1.5%PBE	19.46±0.58 ^b	20.21±0.63 ^a	20.53±0.28 ^b
1%CS/0.12%CA+2%PBE	21.04±0.23 ^a	21.14±0.19 ^a	23.02±0.45 ^a

Different letters within columns indicate a significant difference ($p < 0.05$).

Based on the combined results from the physical, colorimetric, and antimicrobial analyses, the CS/CA film containing 1% PBE (1%CS/0.12%CA+1%PBE) emerges as the most balanced and promising formulation for food packaging applications. This film demonstrated significantly enhanced tensile strength (1685.34 g), moderate extensibility, and acceptable transparency (27.70%), making it mechanically robust yet visually suitable for packaging that requires partial product visibility. Color analysis revealed that while the film darkened slightly ($L^* = 26.05$), it retained a natural tone with moderate whiteness ($WI = 25.73$) and controlled color variation ($\Delta E = 10.72$), which supports aesthetic acceptability. Importantly, antimicrobial testing showed effective inhibition against all tested pathogens, with zones ranging from 16.09 to 18.14 mm, confirming its active functionality. Although higher PBE concentrations (1.5% and 2%) improved antimicrobial efficacy further, they also led to reduced transparency and whiteness, which may limit consumer appeal. Therefore, the 1% PBE formulation may offer an optimal compromise between mechanical strength, antimicrobial activity, and visual quality—making it well-suited for further development as a biodegradable active food packaging film.

Conclusion:

This study demonstrated that incorporating PBE into CS/CA films significantly enhanced their functional properties for food packaging applications. Among the tested formulations, the film containing 1% PBE (1%CS/0.12%CA+1%PBE) exhibited the most favorable balance of mechanical strength, moderate transparency, acceptable whiteness, and effective antimicrobial activity against *S. Newport*, *S. Typhimurium*, and *L. innocua*. While higher extract concentrations improved antimicrobial efficacy, they also led to reduced visual clarity and whiteness, which may limit consumer acceptance. Therefore, the 1% PBE formulation is recommended for further development as an active biodegradable packaging material,



offering both protective functionality and aesthetic suitability for light-sensitive food products.

Acknowledgements:

This research was financially supported by the Faculty of Science, King Mongkut's University of Technology.

References:

1. Bahmid NA, Dekker M, Fogliano V, Heising. *J. Food Packaging Shelf.* 2021;30:100753. <https://doi.org/10.1016/j.fpsl.2021.100753>.
2. Romão S, Bettencourt A, Ribeiro IA. *Polymers.* 2022;14:4968. <https://doi.org/10.3390/polym14224968>.
3. Zhou H, Tong H, Lu J, Cheng Y, Qian F, Tao Y, et al. *Carbohydr Polym.* 2021;270:118381. <https://doi.org/10.1016/j.carbpol.2021.118381>.
4. Siripatrawan U, Harte BR. *Food Hydrocoll.* 2010;24:770–5. <https://doi.org/10.1016/j.foodhyd.2010.04.003>.
5. Nxumalo KA, Fawole OA, Aremu AO. *Processes.* 2024;12:23. <https://doi.org/10.3390/pr12010023>.
6. Wang L, Auty M, Kerry J. *J. Food Eng.* 2010;96:199–207. <https://doi.org/10.1016/j.jfoodeng.2009.07.025>.
7. Nayaka N, Sasadara MMV, Sanjaya DA, Yuda P, Dewi N, Cahyaningsih E, et al. *Molecules.* 2021;26:2321. <https://doi.org/10.3390/molecules26082321>.
8. Ruengvisesh S, Wenbap P, Damrongsaktrakul P, Santiakachai S, Kasemsukwimol W, Chitvittaya S, et al. *J. Microbiol. Biotechnol.* 2023;33:771–9. <https://doi.org/10.4014/jmb.2212.12052>.



DISCREPANCIES OF ANTIMICROBIAL RESISTANT GENOTYPES AND PHENOTYPES IN FOODBORNE BACTERIA *Vibrio parahaemolyticus* FROM AQUATIC BIRD FECES IN THAILAND

Wijitra Khaosoong¹, Yuki Matsumoto², Shota Nakamura², Tetsuya Iida^{3,4}, Carla N. Mavian⁵, Chonchanok Muangnapoh^{1*}

¹Department of Microbiology, Faculty of Science, Chulalongkorn University, Bangkok, Thailand

²Department of Infection Metagenomics, Bioinformatics Center, Research Institute for Microbial Diseases (RIMD), The University of Osaka, Suita, Osaka 565-0871, Japan

³Department of Bacterial Infections, Research Institute for Microbial Diseases (RIMD), The University of Osaka, Suita, Osaka 565-0871, Japan

⁴Center for Infectious Disease Education and Research, The University of Osaka, Suita, Osaka 565-0871, Japan

⁵Emerging Pathogens Institute, Department of Pathology, College of Medicine, University of Florida, Gainesville, Florida, USA

*e-mail: chonchanok.m@chula.ac.th

Abstract:

Vibrio parahaemolyticus is a foodborne pathogen associated with seafood and marine environments, but it has also been detected in wildlife and environmental reservoirs. In this study, we isolated and characterized antimicrobial resistance (AMR) of *V. parahaemolyticus* from aquatic bird feces in Thailand. Antimicrobial susceptibility testing of confirmed *V. parahaemolyticus* isolates were performed by the Kirby–Bauer disc diffusion method, and whole-genome sequencing (WGS) was used to characterize AMR determinants. A total of 12 *V. parahaemolyticus* were isolated from 33.3% (5/15) of the collected samples. All isolates were resistant to streptomycin, while resistance to ampicillin (8/12; 66.7%) and gentamicin (2/12; 16.7%) was also observed. In contrast, WGS revealed no known streptomycin- or gentamicin-resistance genes, suggesting possible involvement of chromosomal mutations or uncharacterized mechanisms. On the other hand, β -lactamase genes (*bla*_{CARB}) were identified in all isolates, and the quinolone resistance gene of the *qnrVC* family (*qnrVC6*) was detected in one isolate (8.3%). Notably, *qnrVC6* was located on the chromosome and associated with mobile genetic elements. Our findings suggest that aquatic birds may act as carriers of AMR *V. parahaemolyticus*. The phenotype–genotype discrepancies warrant further investigation and highlight the importance of One Health-based surveillance integrating wildlife, environment, and foodborne pathogens.

Introduction:

Vibrio parahaemolyticus is a Gram-negative bacterium commonly found in marine and estuarine environments. This microorganism is a foodborne pathogen that causes human food poisoning, primarily through the consumption of raw or undercooked contaminated seafood. It is a leading cause of acute gastroenteritis worldwide, often presenting with self-limited watery diarrhea, abdominal pain, nausea, and vomiting.²¹ *V. parahaemolyticus* was first described by Fujino during a 1950 shirasu food poisoning outbreak in Japan.²⁴ In Thailand, the Department of Disease Control has reported that *V. parahaemolyticus* is the leading causative agent of human gastroenteritis, accounting for 50–60% of reported cases, with the incidence increasing every year.

Several studies have reported pathogenic *V. parahaemolyticus* not only in clinical samples but also in seafood and environmental reservoirs.⁴ Although aquatic birds are not natural hosts of *V. parahaemolyticus*, they can act as carriers of potentially pathogenic *Vibrio* species by feeding on marine animals harboring this bacterium.^{8,10,19,20} The role of birds as



carriers and transmission of infectious diseases is well established due to their mobility, diverse diet, and frequent interaction with human activities such as aquaculture and tourism, thereby posing a potential risk of pathogen dissemination, including *Vibrio* species, to humans.^{8,15} Within the intestinal environments, pathogenic bacteria such as *Vibrio* species are exposed to stressors that promote genetic adaptation through horizontal gene transfer (HGT), which can reshape their genome by acquiring new genetic elements, resulting in enhanced virulence or antibiotic resistance.^{22,31}

AMR poses a major global challenge for healthcare and the economy.²⁵ It arises from the overuse of antimicrobial agents in medical, agriculture, and aquaculture, which drives bacteria to develop drug resistance mechanisms.⁵ *V. parahaemolyticus* has been reported to exhibit varying AMR profiles across different samples and geographical regions.⁷ Additionally, AMR genes are one of the critical issues that have been previously reported to disseminate among bacterial populations and potentially transmitted and affect humans through various pathways.^{9,18} AMR genes can spread through HGT or phage-mediated transmission from resistant to sensitive pathogens, either in plasmids or chromosomes.¹¹

Many studies have reported that *V. parahaemolyticus* from environmental and clinical isolates shows AMR to ampicillin, penicillin, and tetracycline.⁷ However, strains harboring AMR genes do not always exhibit an antimicrobial-resistant phenotype accordingly. Assana (2024) reported that *V. parahaemolyticus* isolated from seawater at Bang Pu recreational center, Samut Prakan, Thailand, harbored AMR genes on their chromosomes, conferring resistance to beta-lactams (*bla_{CARB}*), trimethoprim (*dfrA31*), quinolones (*qnrC* and *qnrS5*), and fosfomycin (*fos*). Despite this, some isolates did not exhibit the corresponding resistant phenotypes. However, research on *V. parahaemolyticus* in aquatic birds remains limited, particularly in antimicrobial profiling.

In this study, we aimed to isolate *V. parahaemolyticus* from aquatic bird feces collected at Bang Pu Recreation Center, Samut Prakarn Province, Thailand, and determine their AMR profiles by phenotypic and genotypic analyses. The outcomes of this study will provide a better understanding of the potential role of aquatic birds as reservoirs and disseminators of AMR *V. parahaemolyticus* in the marine ecosystems.

Methodology:

Sample collection and bacterial isolation

Fecal samples were collected from aquatic birds at Bang Pu recreational center, Samut Prakan, Thailand, on 16th January 2025. Aquatic bird feces were swabbed from the ground using sterile cotton swabs and directly streaked onto a selective medium, thiosulfate citrate bile salt sucrose (TCBS) (Difco™, USA) agar. The same swabs were then resuspended in 8 mL of alkaline peptone water (APW) supplemented with 3% w/v of sodium chloride (APW+3% NaCl). Both the TCBS agar plates and the APW+3% NaCl enrichment broths were incubated at 37°C for 18 to 24 hours, within 5 hours after transfer to the laboratory at the Department of Microbiology, Chulalongkorn University, Bangkok. Subsequently, bacterial cultures from the APW+3% NaCl enrichment broths were sub-cultured onto TCBS agar and incubated at 37°C for 18 to 24 hours.

Identification of V. parahaemolyticus strains

Primary identification using selective media

One to three suspected green colonies of *V. parahaemolyticus* from both the direct TCBS plates and the TCBS plates enriched by APW+3% NaCl were selected based on the different colony morphology. In total, three to five colonies were collected for each fecal sample. The selected colonies were then sub-cultured onto CHROMagar™ *Vibrio* (CHROMagar, France) for primary identification of *V. parahaemolyticus* strains. Suspected mauve colonies on



CHROMagar™ *Vibrio*, which have green colonies on TCBS agar, were selected for further confirmation of *V. parahaemolyticus*.

Species-specific identification by Polymerase Chain Reaction (PCR)

All suspected *V. parahaemolyticus* isolates from aquatic bird feces were confirmed by PCR using species-specific primers targeting the lecithin-dependent hemolysin (*ldh*) gene of *V. parahaemolyticus* (Table 1). Genomic DNA (gDNA) was extracted from the isolates using the PureLink™ Genomic DNA Mini Kit (Invitrogen, USA) according to the manufacturer's instructions and was used as the template for PCR. The PCR protocol was adapted from a previously published study.¹⁴ Subsequently, PCR products were analyzed by electrophoresis on a 1% agarose gel and visualized under UV light. Confirmed *V. parahaemolyticus* isolates were preserved in tryptic soy broth (TSB) (HiMedia, India) supplemented with 3% (w/v) NaCl (TSB+3% NaCl) and 30% (v/v) glycerol and stored at -80°C for further analysis.

Table 1.
Species-specific gene primers used for the identification of isolates

Species	Gene	Primer sequence (5' – 3')	Amplicon size (bp)	Reference
<i>V. parahaemolyticus</i>	<i>ldh</i>	F: AAAGCGGATTATGCAGAAGCACTG R: GCTACTTTCTAGCATTTTCTCTGC	450	Joshi et al., 2014

Whole genome sequencing (WGS)

Genomic DNA from *V. parahaemolyticus* isolates obtained from aquatic bird feces was sequenced using an Illumina MiSeq sequencer, and genomes were assembled using minimap2 by the Research Institute for Microbial Diseases, Osaka University, Osaka, Japan. Assembly files of all isolates were obtained for AMR gene detection.

Antimicrobial resistance analysis

Antimicrobial susceptibility testing (AST) by the Kirby–Bauer disc diffusion

The purified *V. parahaemolyticus* isolates were cultured onto tryptic soy agar (TSA) (HiMedia, India) supplemented with 3% (w/v) NaCl (TSA+3% NaCl), followed by inoculation into Mueller-Hinton broth (MHB) (HiMedia, India) supplemented with 3% w/v of sodium chloride (MHB+3% NaCl), to achieve log-phase growth. The bacterial suspensions were then inoculated in 0.85% w/v of sodium chloride and adjusted to a concentration of 0.5 McFarland turbidity standard (approximately 1.5×10^8 CFU/mL). Each bacterial suspension was swabbed onto the Mueller-Hinton agar (MHA) (HiMedia, India) supplemented with 3% w/v of sodium chloride (MHA+3% NaCl) using a sterile cotton swab. Eleven antimicrobial discs were used to test against *Vibrio* spp., including ampicillin (10 µg), amoxicillin-clavulanic (20/10 µg), cefotaxime (30 µg), imipenem (10 µg), chloramphenicol (30 µg), gentamicin (10 µg), streptomycin (10 µg), ciprofloxacin (5 µg), sulfamethoxazole-trimethoprim (23.75/1.25 µg), erythromycin (15 µg), and tetracycline (30 µg), representing 7 different classes of antimicrobial agents. The discs were then placed onto the agar and incubated at 37°C for 18 to 24 hours. After incubation, the diameters of the inhibition zones around the antimicrobial discs were measured to determine antimicrobial susceptibility according to the Clinical and Laboratory Standards Institute (CLSI) M45 guideline.

Antimicrobial resistance (AMR) gene detection

The assembled genomes of all *V. parahaemolyticus* isolates were screened for AMR genes using ResFinder v4.7.2 (<http://genepi.food.dtu.dk/resfinder>) with a minimum 90% identity threshold. In addition, mobile genetic elements (MGEs) associated with AMR genes were characterized using VRprofile2 (<https://tool2-mml.sjtu.edu.cn/VRprofile/>).

Results and Discussion:

Twelve suspected *V. parahaemolyticus* isolates were recovered from aquatic bird feces samples with a detection rate of 33.3% (5/15). Colony morphology on TCBS agar and CHROMagar™ *Vibrio* revealed that all 12 suspected *V. parahaemolyticus* isolates exhibited green colonies on TCBS agar and mauve colonies on CHROMagar™ *Vibrio* (Figure 1).

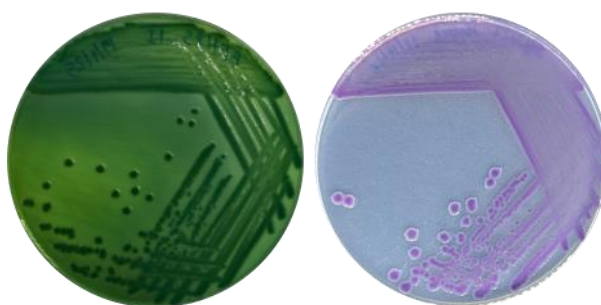


Figure 1.

Examples of colony morphologies of suspected *V. parahaemolyticus* on TCBS agar (left) and CHROMagar™ *Vibrio* (right)

All suspected *V. parahaemolyticus* isolates (n=12) were confirmed by species-specific genes using specific oligonucleotide primers. Detection of the *ldh* gene was performed by a single PCR assay. As a result, all suspected isolates were confirmed to be *V. parahaemolyticus* (Figure 2). Agarose gel electrophoresis revealed a specific 450 bp amplicon of the *V. parahaemolyticus* *ldh* gene at the same position as the reference *V. parahaemolyticus* strain. The 12 confirmed *V. parahaemolyticus* isolates were further examined for the AMR analysis.

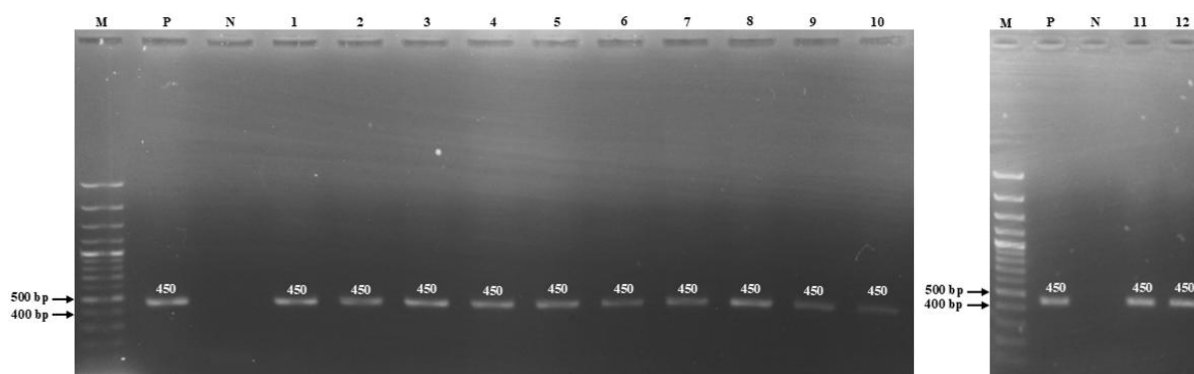


Figure 2.

Gel electrophoresis of PCR products of *V. parahaemolyticus* species-specific gene *ldh*. The 1% gel electrophoresis showed DNA bands of the expected sizes of *ldh*, which were 450 bp.

Lane M: 100 bp DNA marker (Thermo Scientific, USA), Lane P: positive control (*V. parahaemolyticus* BG26), Lane N: negative control (deionized water), Lane 1-12: PCR products of suspected 12 *V. parahaemolyticus* isolates

The confirmed *V. parahaemolyticus* isolates exhibited phenotypic AMR to streptomycin (100%), ampicillin (8/12; 66.7%), and gentamycin (2/12; 16.7%). These AMR profiles were consistent with those reported by Changsen et al. (2023) and Siriphap et al. (2024), who found high resistance to ampicillin and streptomycin in *V. parahaemolyticus* isolates in Thailand. On the other hand, all isolates were susceptible to amoxicillin-clavulanic (100%), tetracycline (100%), sulfamethoxazole-trimethoprim (100%), ciprofloxacin (100%), chloramphenicol (100%), imipenem (100%), and cefotaxime (11/12; 91.7%), respectively (Table 2 and Figure 3).

Antibiotics with a high level of intermediate resistance were erythromycin (100%) and gentamicin (6/12; 50%) (Figure 3). This should be concerning, as bacteria can develop and adapt to full resistance under selective pressure in the environment, potentially contaminating seafood and ecosystems, and posing health risks to humans through seafood consumption as well as to aquatic ecosystems. In this study, *V. parahaemolyticus* isolates showed AMR to at least 1 antibiotic, with most isolates resistant to 2 antibiotics (10/12; 83.3%) (Table 2).

Table 2.
AMR profile of *V. parahaemolyticus* isolates (n=12)

Antibiotics	No. (%) of AMR Profiles		
	Susceptible (S)	Intermediate (I)	Resistant (R)
β-lactams			
Ampicillin (AM)	3 (25)	1 (8.3)	8 (66.7)
Amoxicillin-clavulanic (AMC)	12 (100)	0 (0)	0 (0)
Cefotaxime (CTX)	11 (91.7)	1 (8.3)	0 (0)
Imipenem (IPM)	12 (100)	0 (0)	0 (0)
Phenicol			
Chloramphenicol (C)	12 (100)	0 (0)	0 (0)
Aminoglycosides			
Gentamicin (GEN)	4 (33.3)	6 (50)	2 (16.7)
Streptomycin (STR)	0 (0)	0 (0)	12 (100)
Quinolones			
Ciprofloxacin (CIP)	12 (100)	0 (0)	0 (0)
Folate			
Sulfamethoxazole-Trimethoprim (SXT)	12 (100)	0 (0)	0 (0)
Macrolides			
Erythromycin (ERY)	0 (0)	12 (100)	0 (0)
Tetracyclines			
Tetracycline (TET)	12 (100)	0 (0)	0 (0)
Number of Resistance Isolates			
1	2 (16.7)		
2	10 (83.3)		

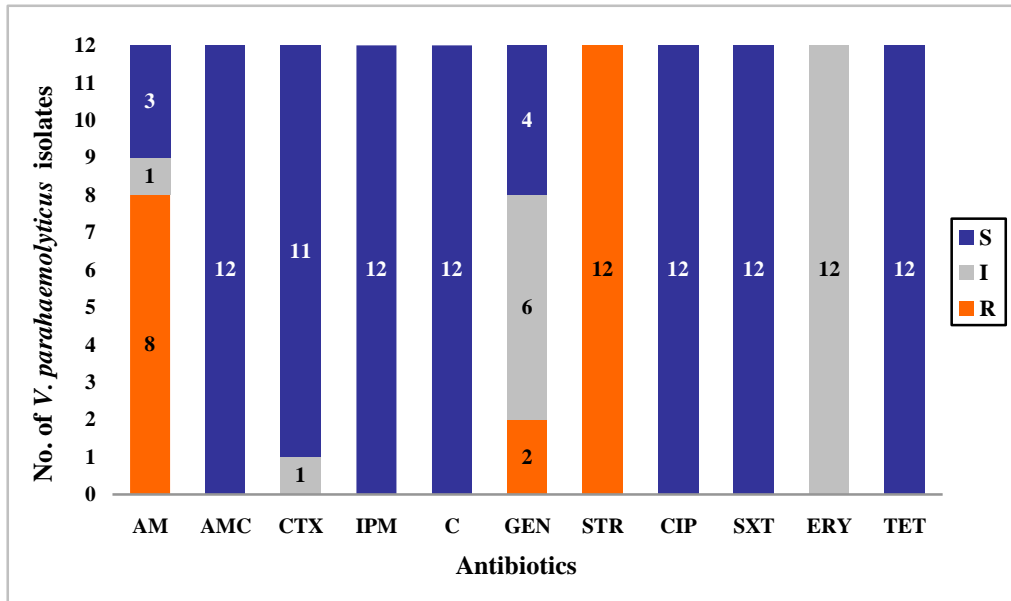


Figure 3.

Proportion of antimicrobial-resistant *V. parahaemolyticus* isolates from aquatic bird feces against each tested antimicrobial

In addition, AMR gene detection by ResFinder analysis revealed that 12 *V. parahaemolyticus* isolates harbored 2 AMR genes. Among these, the *bla_{CARB}* gene was detected in all isolates (12/12; 100%), whereas the *qnrVC6* gene was detected only in CUBF112 (1/12; 8.3%) (Figure 4). All 12 isolates carried the *bla_{CARB}* gene with different subtypes of the *CARB* genes, which encode a β -lactamase conferring resistance to ampicillin, piperacillin, and amoxicillin, commonly used antibiotics for bacterial infections.³ In contrast, the quinolone resistance gene, *qnrVC6*, associated with ciprofloxacin resistance, showed the highest sequence identity in the ResFinder database with resistance genes located on the plasmids of *V. parahaemolyticus* pVP1 (98.5%). Ciprofloxacin is a broad-spectrum antibiotic commonly used to treat various bacterial infections.

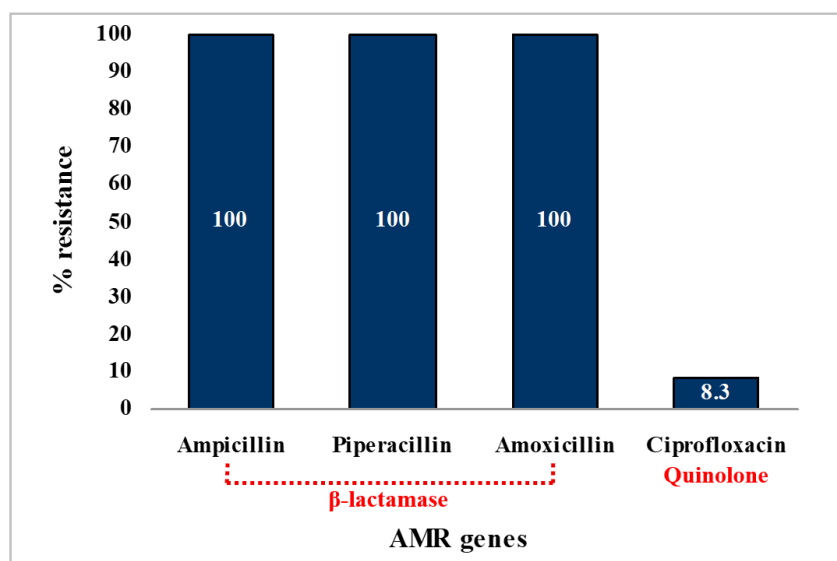


Figure 4.

AMR genes of 12 *V. parahaemolyticus* isolates from aquatic bird feces by using ResFinder

VRprofile2 analysis was used for investigating the position of AMR genes and the genetic elements associated with them that are present in bacterial genomics. The result revealed that all AMR genes were located on the chromosome, indicating a stable genetic basis for resistance, making these genes unlikely to be lost, suggesting that the resistance genes are integrated into the bacterial genome rather than being carried on plasmids or other MGEs^{16,32}. However, despite the chromosomal presence of AMR genes, isolate CUBF112 showed an association between AMR genes and MGEs, which are genetic elements capable of transferring between bacteria through HGT, thereby facilitating the spread of resistance across different bacterial populations.^{13,27} Furthermore, possession of the MGEs-associated *qnrVC6* in the isolate CUBF112 was located on a genomic island (GI) that overlaps with an integron region (Table 3).

Table 3.

AMR genes position and the associated mobile genetic elements (MGEs)

Isolates	AMR			MGE		
	Contig	Replicon	AMR genes	ARG associated MGE	MGE coords	Size (bp)
CUBF112	2	Chromosome	<i>qnrVC6</i>	GI	753595..919669	166,074
				Integron	754719..909357	154,638

WGS analysis demonstrated that the *qnrVC6* gene cassette of isolate CUBF112 (Figure 5) was located on a GI overlapping with an integron region and was flanked by hypothetical genes. The integron region was identified by the presence of the XerD integrase gene. Several insertion sequences, including ISVpa3, ISAb01, ISSham2, and ISVvu4, were classified as transposons. Additionally, a leucine efflux protein, part of an efflux pump system, was detected. The toxin CcdB, belonging to a Toxin-Antitoxin system, was also present, along with a virulent protein.

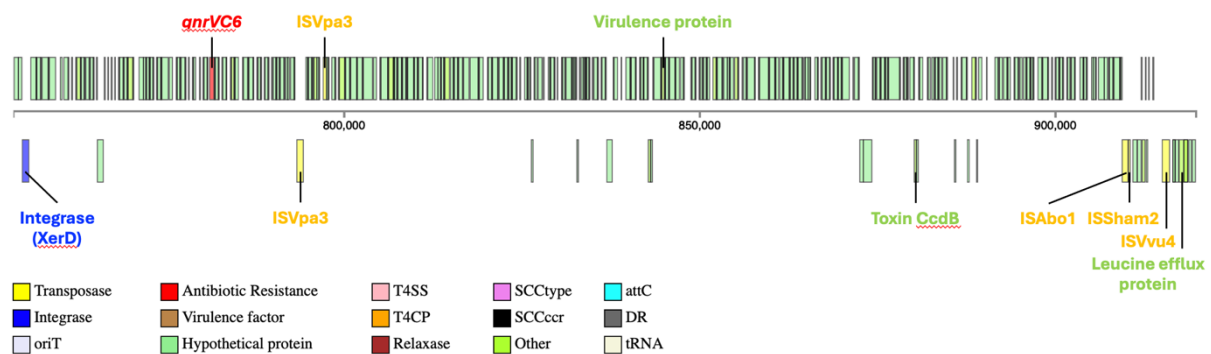


Figure 5.

The *qnrVC6* gene cassette in *V. parahaemolyticus* CUBF112 on a GI overlapped with an integron region

A comparative analysis of phenotypic and genotypic AMR profiles (Table 4) revealed consistent results in 8 of 12 *V. parahaemolyticus* isolates, in which resistance to ampicillin correlated with the presence of the *bla_{CARB}* gene in their genome. These findings were consistent with Changsen et al. (2023), who reported that all ampicillin-resistant *V. parahaemolyticus* isolates from seafood in Thailand also carried the *bla_{CARB}* gene. Interestingly, some isolates in our study harbored the *bla_{CARB}* gene, but did not exhibit an ampicillin resistance phenotype. Yan et al. (2020) also reported this incidence and suggested that point mutations in the *bla_{CARB}* gene and/or insufficient gene expression may be

responsible for the lack of a full resistance phenotype. However, discrepancies were also observed in other antibiotics, indicating discordance between resistance phenotypes and the corresponding resistance gene profiles. In this study, AST revealed that all isolates exhibited phenotypic resistance to streptomycin (12/12; 100%), while resistance to gentamicin (2/12; 16.7%) was also observed. However, WGS revealed that no known streptomycin- or gentamicin-resistance genes were detected, suggesting the involvement of alternative mechanisms regulating the expression of AMR phenotypes. In contrast, the quinolone resistance gene of the *qnrVC* family (*qnrVC6*) was detected in one isolate (1/12; 8.3%); however, neither gene expresses resistant phenotypes. This discrepancy could be because genes are not always expressed, meaning resistance might not be observed despite the presence of resistance genes. Gene expression can be influenced by factors such as gene regulation, limitations in gene detection, and environmental pressures. Additionally, phenotypic resistance may be observed in the absence of identifiable genetic resistance mechanisms, which could result from alternative resistance mechanisms and methodological limitations in the interpretation of results.^{23,29}

Similar discrepancies between AMR genotypes and phenotypes have been increasingly reported in *V. parahaemolyticus*.^{2,12,17,30} For instance, Assana (2024) reported that *V. parahaemolyticus* isolated from seawater in Thailand, which harbours quinolone resistance genes (*qnrC* and *qnrS5*) on the chromosome, was unable to express quinolone-resistant phenotypes. It is plausible that AMR genes may express low levels of resistance proteins that are not enough for resistance phenotypes, and/or they may act as silent genes expressed only under specific conditions.⁶

Table 4.

A comparative analysis of phenotypic and genotypic AMR profiles of *V. parahaemolyticus* isolates from aquatic bird feces

Isolates	AMR phenotype			AMR genotype	
	AM	STR	GEN	<i>bla_{CARB}</i>	<i>qnrVC6</i>
CUBF74	+	+	-	+	-
CUBF96	-	+	-	+	-
CUBF97	-	+	-	+	-
CUBF104	-	+	+	+	-
CUBF106	+	+	-	+	-
CUBF108	+	+	-	+	-
CUBF111	+	+	-	+	-
CUBF112	+	+	-	+	+
CUBF115	+	+	-	+	-
CUBF117	+	+	-	+	-
CUBF123	-	+	+	+	-
CUBF124	+	+	-	+	-

+ indicates the presence of an AMR phenotype or genotype

- indicates the absence of an AMR phenotype or genotype

Conclusion:

V. parahaemolyticus were isolated from aquatic bird feces in Thailand, and their AMR profiles were determined. All isolates exhibited phenotypic resistance to streptomycin, while resistance to ampicillin and gentamicin was also observed in some isolates. In contrast, genotypic analysis showed no detection of streptomycin- or gentamicin-resistance genes. On the other hand, the quinolone resistance gene *qnrVC6* was detected without expression of a quinolone-resistant phenotype. AMR gene analysis also indicated that *qnrVC6* was located on



the chromosome and associated with MGEs. Our findings suggest that aquatic birds may act as carriers of AMR *V. parahaemolyticus*; however, further studies are required to investigate the molecular mechanisms underlying discrepancies between AMR phenotypes and genotypes in this organism.

Acknowledgements:

This study was supported by the Grant for the U.S.-Japan Cooperative Medical Sciences Program (USJCMSP) Collaborative Awards, 2023.

References:

1. Assana C. Chula ETD. 2024;11505.
2. Bourdonnais E, Briet A, Brauge T, Debuiche S, Helsen N, Granier, SA, Midelet G. Microbiol Spectr. 2024;12:e00175-24.
3. Bush K, Bradford PA. Cold Spring Harb Perspect Med. 2016;6:a025247.
4. Changsen C, Likhitrattanasrisal S, Lunha K, Chumpol W, Jiemsup S, Prachumwat A, Kongkasuriyachai D, Ingsriswang S, Chaturongakul S, Lamalee A, Yongkiettrakul S, Buates S. PeerJ. 2023;11:e15283.
5. Darby EM, Trampari E, Siasat P, Gaya MS, Alav I, Webber MA, Blair JMA. Nat Rev Microbiol. 2023;21:280–295.
6. Deekshit VK, Srikumar S. J Appl Microbiol. 2022;133:2902–2914.
7. Elmahdi S, DaSilva LV, Parveen S. Food Microbiol. 2016;57:128–134.
8. Fernández-Delgado M, Sanz V, Giner S, Suárez P, Contreras M, Michelangeli F, García-Amado MA. J Wildl Dis. 2016;52:621–626.
9. Fernández-Trapote E, Oliveira M, Cobo-Díaz JF, Alvarez-Ordóñez A. Microb Biotechnol. 2024;17:e14530.
10. Fu S, Hao J, Yang Q, Lan R, Wang Y, Ye S, Liu Y, Li R. Sci Rep. 2019;9:16303.
11. Igbinsola EO, Beshiru A, Igbinsola IH, Ogofure AG, Uwhuba KE. Front Microbiol. 2021;12:632266.
12. Jeamsripong S, Khant W, Chuanchuen R. FEMS Microbiol Ecol. 2020;96:fiaa081.
13. Jian Z, Zeng L, Xu T, Sun S, Yan S, Yang L, Huang Y, Jia J, Dou T. J Basic Microbiol. 2021;61:1049-1070.
14. Joshi J, Srisala J, Truong VH, Chen IT, Nuangsaeng B, Suthienkul O, Lo CF, Flegel TW, Sritunyalucksana K, Thitamadee S. Aquaculture. 2014;428–429:297–302.
15. Kobuszevska A, Wysok B. Animals. 2024;14:968.
16. Lehtinen S, Huisman JS, Bonhoeffer S. bioRxiv. 2021.
17. Lou Y, Liu H, Zhang Z, Pan Y, Zhao Y. Food Control. 2016;59:207–211.
18. Martak D, Henriot CP, Hocquet D. Infect Dis Now. 2024;54:104895.
19. Miyasaka J, Yahiro S, Arahira Y, Tokunaga H, Katsuki K, Hara-Kudo Y. Epidemiol Infect. 2006;134:780–785.
20. Muangnapoh C, Tamboon E, Supha N, Toyting J, Chitrak A, Kitkumthorn N, Ekcharyawat P, Iida T, Suthienkul O. Microbiol Spectr. 2022;10:e00886-22.
21. Ndraha N, Wong HC, Hsiao HI. Compr Rev Food Sci Food Saf. 2020;19:1187-1217.
22. Nyholm SV, McFall-Ngai MJ. Appl Environ Microbiol. 2003;69:3932–3937.
23. Schwan CL, Lomonaco S, Bastos LM, Cook PW, Maher J, Trinetta V, Bhullar M, Phebus RK, Gragg S, Kastner J, Vipham JL. Front Microbiol. 2021;12.
24. Shinoda S. Biocontrol Sci. 2011;16:129–137.



25. Silva IP, Carneiro CDS, Saraiva MAF, Oliveira T ASD, Sousa OVD, Evangelista-Barreto NS. *Mar Pollut Bull.* 2018;131:757–762.
26. Siriphap A, Prapasawat W, Borthong J, Tanomsridachchai W, Muangnapoh C, Suthienkul O, Chonsin K. *FEMS Microbiol Lett.* 2024;371:fnad134.
27. Wang Y, Batra A, Schulenburg H, Dagan T. *Philos Trans R Soc Lond B Biol Sci.* 2022;377:20200467.
28. Yan W, Ji L, Xu D, Chen L, Wu X. *PLoS ONE.* 2020;15:e0240143.
29. Yee R, Dien Bard J, Simner PJ. *J Clin Microbiol.* 2021;59.
30. Yu Y, Tang M, Wang Y, Liao M, Wang C, Rong X, Li B, Ge J, Gao Y, Dong X, Zhang Z. *Ecotoxicol Environ Saf.* 2023;252:114615.
31. Zheng L, Zhu LW, Jing J, Guan JY, Lu GJ, Xie LH, Ji X, Chu D, Sun Y, Chen P, Guo XJ. *Front Vet Sci.* 2021;8:638820.
32. Zongo PD, Cabanel N, Royer G, Depardieu F, Hartmann A, Naas T, Glaser P, Rosinski-Chupin I. *Nat Commun.* 2024;15:4093.



IMPACT OF BACTERIOPHAGE CONTAMINATION FROM SILAGE ON YOGURT FERMENTATION

Noppakorn Thadasawate¹, Jeeranan Kamchai¹, Suratsa Nuansakun¹, Punyawee Dulyayangkul², Thanyaporn Srimahaeak^{1,*}

¹Department of Biotechnology, Faculty of Engineering and Industrial Technology, Silpakorn University, Nakhon Pathom 73000, Thailand

²Laboratory of Biotechnology, Chulabhorn Research Institute, Bangkok 10210, Thailand

*e-mail: srimahaeak_t@su.ac.th

Abstract:

Silage is a common fermented feed used in dairy cattle diets and is considered a possible source of bacteriophages that can contaminate raw milk and disrupt yogurt fermentation. This study investigated phage contamination in silage samples collected from small-scale dairy farms in Ratchaburi, Thailand, across three seasons (2024–2025). No phages were detected in summer, while silage samples from the rainy and dry seasons showed concentrations of 4.8×10^3 and 2.5×10^5 PFU/g, respectively, from which 36 and 31 phage isolates were picked and purified. Host range analysis revealed that the commercial starter culture *Lactobacillus delbrueckii* spp. *bulgaricus* YB01 was susceptible to all rainy-season phages, whereas none of the dry-season phages infected this strain. Bacteriophages were grouped into five infectivity levels based on Efficiency of Plating (EOP) values ranging from 0.01 to 4.39. Representative phages from each group were selected for yogurt fermentation tests. Phage contamination delayed fermentation, increasing the final pH from 4.29 to 4.52 and loosening the yogurt's texture. These findings highlight the seasonal impact of silage-derived phages on yogurt quality and emphasize the need for monitoring phage contamination in dairy production.

Introduction:

Silage is widely used in dairy cattle farming because it provides essential nutrients and beneficial microorganisms. Its fermentation is mainly driven by lactic acid bacteria (LAB)¹. Common facultative heterofermentative LAB, such as *Lactobacillus plantarum*, *Lactobacillus casei*, *Enterococcus faecium*, and *Pediococcus* spp., are frequently applied as inoculants^{1,2}. However, fermentation can fail due to microbial contamination from bacteria, fungi, or bacteriophages. Bacteriophages (phages) infect bacterial cells, replicate within them, and cause lysis. While phages are sometimes used as biological agents against pathogens, they also threaten industrial fermentation processes^{3–5}. Phages found in silage are one of the hidden factors that pose a potential contamination risk during the fermentation process.

In yogurt fermentation, the main starter cultures are *Streptococcus thermophilus* and *Lactobacillus delbrueckii* subsp. *bulgaricus*. However, phage infections targeting these cultures are a leading cause of fermentation failure. Phage-induced lysis disrupts acid production, which reduces yield and quality and results in substantial economic losses. As in silage fermentation, phages have long been regarded as a critical challenge in dairy fermentations that must be carefully controlled^{5–8}.

In Thailand, there is still limited information on phage contamination in fermented milk products, particularly in relation to possible sources within dairy farm environments. Environmental factors surrounding farms are often linked to phage occurrence, and silage has been identified as a potential reservoir. These phages may enter dairy production systems and interfere with milk fermentation. This study therefore focuses on bacteriophages present in silage from dairy farm environments in Thailand and investigates their potential impact on yogurt fermentation.



Methodology:

Bacterial Strain and Growth Conditions

The reference strains *Lactobacillus delbrueckii* subsp. *bulgaricus* (TBRC1339, TBRC5031, and TISTR892) and *Streptococcus thermophilus* (TBRC4654 and TISTR894) were obtained from the Thailand Bioresource Research Center (TBRC) and the Thailand Institute of Scientific and Technological Research (TISTR) for use as host-indicator strains in phage detection. In addition, three *L. bulgaricus* and twelve *S. thermophilus* strains were isolated from commercial yogurt products in Thailand for use in comparative analysis.

Lactobacillus strains were cultured in Lactobacilli MRS broth (HiMedia, India) and *Streptococcus* strains in M17 broth (HiMedia, India). Prior to use, all strains were streaked onto appropriate agar media and subsequently propagated in broth. Bacterial cultures were incubated anaerobically at 37 °C for 24–48 hours.

Phage Isolation, Purification, and Propagation

Silage samples were collected from dairy farms in Photharam, Ratchaburi, Thailand. Each 3 g sample was extracted with 30 mL of MRS or M17 broth (depending on the host strain) supplemented with 5 mM CaCl₂, followed by centrifugation (10,000 × g, 15 min, 4 °C) and filtration through a 0.45 μm membrane. For initial screening, phages were detected using the spotting technique and double agar layer methods⁹. Briefly, 100 μL of overnight bacterial culture was mixed with 5 mL of molten MRS or M17 agar (0.5% agar) and overlaid onto MRS plates. After solidification, 10 μL of filtered samples were spotted onto the lawn and plates were incubated anaerobically at 37 °C for 2 days before plaque observation. Samples showing plaques were further processed for phage isolation using the double agar layer method. In this step, 100 μL of contaminated samples were mixed with 100 μL of overnight bacterial culture and 5 mL of molten MRS or M17 agar, overlaid onto plates, and incubated anaerobically at 37 °C for 2 days.

Phage purification and propagation were performed as described by Imklin et al.⁹. Briefly, single plaques were picked and purified three times using the agar overlay method to obtain uniform plaques, then suspended in sterile SM buffer. Purified phages were propagated on host lawns, after which the overlay agar was scraped and eluted with 2 mL of SM buffer. The suspension was centrifuged (10,000 × g, 15 min, 4 °C) and filtered through a 0.22 μm membrane. Phage concentrations were determined using the spotting technique as described, and stocks were prepared at titers of 10⁹–10¹⁰ plaque-forming units per milliliter (PFU/mL). Filtered phage samples were stored at 4 °C until use.

Host Range and Efficiency of Plating (EOP)

Host range and Efficiency of Plating (EOP) The host range of isolated phages was evaluated against fifteen bacterial strains—three *L. bulgaricus* and twelve *S. thermophilus* isolates using the spot assay method adapted from Imklin et al.⁹. Briefly, 10 μL of phage suspension (10⁸ PFU/mL) was spotted onto soft agar lawns of each overnight bacterial strain and incubated at 37 °C for 24 - 48 hours.

Phage infectivity was evaluated by calculating the efficiency of plating (EOP) using the agar overlay method, with EOP determined by dividing the phage titer on each test strain by that on the reference host strain (*L. bulgaricus* TBRC1339). Phages were classified as follows: >1.00, highly efficient/strongly virulent; 1.00–0.50, moderately efficient/moderately virulent; 0.50–0.10, low efficient/weakly virulent; 0.10–0.001, inefficient/poorly virulent; and <0.001, non-infective/inactive. Strains producing no plaques were considered non-susceptible (-). Representative phages from each EOP category were selected for subsequent yogurt fermentation experiments.



Yogurt Fermentation

Yogurt fermentation was conducted to simulate phage contamination during yogurt production adapted from Sun et al.¹⁰. Yogurt was prepared using starter cultures of *L. bulgaricus* YB01 and *S. thermophilus* YB02. Bacterial strains were freshly grown overnight and sub-cultured until reaching a concentration of 10^8 CFU/mL. Cultures were centrifuged at $10,000 \times g$ for 10 min at 4 °C, the supernatant was discarded, and the cells were washed with 0.85% NaCl solution. The cells were centrifuged again, the supernatant removed, and the same volume of milk was added to obtain milk starter cultures at 10^8 CFU/mL.

For samples with bacteriophage contamination, phages were added at a final concentration of 10^7 PFU/mL to the prepared milk with starter cultures and mixed thoroughly. All treatments were performed in triplicate. The yogurt fermentation in this study was carried out with set yogurt, with phage-free samples serving as controls. Yogurt prepared with starter cultures was incubated at 37 °C for 16 hours. After fermentation, the color, aroma, and pH of the resulting yogurt were evaluated.

Sensory analysis

Sensory evaluation of yogurt samples was performed immediately after fermentation. Both phage-infected and control (phage-free) yogurts were assessed. The assessment was conducted by five people (age 20 – 25 years old).

The evaluation focused on two attributes: texture and aroma. Texture was assessed by visual observation and consistency, which categorized as dense/creamy, soft-bodied, or semi-fluid. Aroma was evaluated by direct sniffing of freshly opened samples and described qualitatively as sour and acidic (typical yogurt-like), sour and sweet, or sour but milk-like.

Statistical Analysis

All data are presented as mean \pm standard deviation (Mean \pm SD). Comparisons between two groups were performed using unpaired two-tail Student's t-test ($p < 0.05$). Data analysis and graph generation were carried out using Microsoft Excel.

Results and Discussion:

Screening and characterization of phages in silage samples

In this study, silage samples were collected from small-scale dairy farms in Photharam, Ratchaburi, Thailand, across three seasons: summer (March–June 2024), rainy (July–October 2024), and dry (November 2024–February 2025). The results showed that no phages were detected in silage samples during the summer. This absence may be due to either phage levels being below the detection limit or the lack of contamination at the time of sampling. In contrast, phage contamination rose during the rainy season (4.8×10^3 PFU/g) and further increased during the dry season (2.5×10^5 PFU/g). In addition, *L. bulgaricus* TBRC1339 was found as the most suitable host for phage isolation in this study, as this strain was susceptible to phage infection in all silage samples. The higher phage concentration observed in the dry season suggests that factors such as temperature, and humidity may create favorable conditions for phage proliferation¹¹. As phage research in Thailand remains limited, direct comparisons with other local studies are not yet possible. Nevertheless, previous studies conducted in other countries have also reported seasonal variation in phage abundance^{12–15}.

Phage isolates obtained from the rainy and dry seasons were randomly selected for host range analysis (36 and 31 isolates, respectively). The results revealed that all phages from the rainy season were capable of infecting only a single strain, *L. bulgaricus* YB01—a commercial starter culture strain—aside from their propagation host. In contrast, phages isolated during the dry season did not infect any of the bacterial strains tested. These findings suggest that seasonal variation may influence both the diversity and host specificity phages in

the farm environments. Moreover, since *L. bulgaricus* YB01 is a starter culture isolated from a commercial yogurt product, phages from the rainy season could potentially affect yogurt fermentation if contamination occurs during industrial processing.

The lytic ability of bacteriophages isolated during the rainy and dry seasons was evaluated against other bacterial strains using the spot assay. Three *L. bulgaricus* strains and twelve *S. thermophilus* strains were tested. The results showed that all 36 phage isolates obtained during the rainy season were able to lyse only one non-host strain, *L. bulgaricus* YB01. In contrast, phages isolated during the dry season were unable to infect any additional host strains. These findings indicate that, although the rainy-season phages were primarily specific to *L. bulgaricus* TBRC1339 (the original host strain), they were also capable of infecting *L. bulgaricus* YB01, a strain isolated from yogurt. This suggests a partial expansion of the host range of these phages.

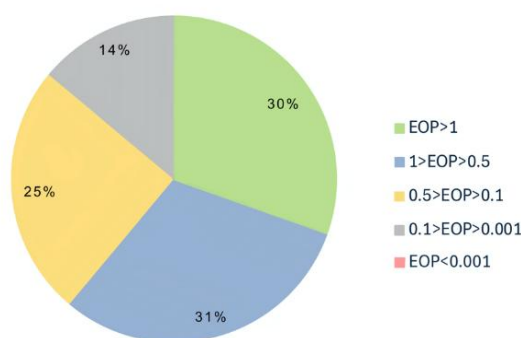


Figure 1.

Diversity and efficiency of plating (EOP) of phage isolates from silage samples collected during the rainy season of 2024.

The EOP values of phages from the rainy season against *L. bulgaricus* YB01 ranged from 0.006 to 4.389, indicating the effective diversity among the isolates (Table 1, Figure 1). Of the 36 phages tested, 11 or 30.5% were highly efficient (EOP >1.00), another 11 or 30.5% were moderately efficient (EOP 0.50–1.00), 9 or 25% were weakly efficient (EOP 0.01–0.50) and 5 or 14% were inefficient or poorly virulent (EOP 0.001–0.01). This distribution suggests that phages from the rainy season exhibit a broad spectrum of infectivity, with some isolates capable of strongly infecting the starter strain, while others show limited or negligible activity. Such variation in virulence may influence the extent to which phage contamination affects yogurt fermentation.

Table 1.

Efficiency of Plating (EOP) values of phage isolates from silage samples collected during the rainy season of 2024.

Phage	JulS_1	JulS_2	JulS_3	JulS_4	JulS_5	JulS_6	JulS_7	JulS_8	JulS_9	JulS_10	JulS_11	JulS_12
EO	0.00	0.22	1.09	0.16	0.49	1.42	0.55	0.71	0.10	1.36	4.38	1.71
P	6	9	5	9	0	5	9	6	2	7	9	1
Phage	JulS_13	JulS_14	JulS_15	JulS_16	JulS_17	JulS_18	JulS_19	JulS_20	JulS_21	JulS_22	JulS_23	JulS_24
EO	0.08	0.30	0.31	0.52	0.11	0.27	0.93	0.77	2.03	0.40	2.63	0.50
P	8	8	0	7	2	5	1	4	0	0	3	0
Phage	JulS_25	JulS_26	JulS_27	JulS_28	JulS_29	JulS_30	JulS_31	JulS_32	JulS_33	JulS_34	JulS_35	JulS_36
EO	0.04	0.66	0.06	0.95	1.34	0.05	1.58	0.67	2.25	0.52	0.57	2.90
P	0	7	7	2	5	5	3	5	0	4	4	5

Simulation of phage contamination during yogurt fermentation

To simulate phage contamination during yogurt production, 20% of phages from each EOP group except the inactive group (EOP < 0.001) were randomly selected. *L. bulgaricus* YB01 and *S. thermophilus* YB02 were used as the starter culture, with phage-free samples serving as the control. Phage-inoculated samples exhibited changes in several yogurt characteristics, whereas the color remained unchanged (Table 2). The most pronounced change was observed in texture: yogurt containing phages was noticeably softer and less firm compared with the dense and creamy texture of the control samples, except for the sample inoculated with JulS1_3, which exhibited a texture similar to the control. The pH of the JulS1_3-inoculated samples was slightly higher, while the aroma remained largely comparable to that of the control. This suggests that, although JulS1_3 belonged to the highly efficient group (EOP > 1.00), it may not have effectively interfered with yogurt formation—possibly due to host–phage interaction dynamics, strain-specific resistance, or reduced phage activity during fermentation^{7,16–18}. In contrast, phages from the moderately efficient group (0.50 < EOP < 1.00) appeared to have a greater impact on yogurt quality. Yogurt from this group exhibited softer and more liquid-like textures, along with a milkier aroma compared with the control. Notably, the pH of samples inoculated with JulS1_8 and JulS1_19 was significantly higher than that of the control ($p < 0.05$).

Table 2.

Characteristics of yogurt in control and phage-contaminated groups, including texture, aroma, and pH values (Mean \pm SD).

Group (EOP)	Phage	Texture	Aroma	pH (Mean \pm SD)
	Control	Dense and creamy	Sour and acidic	4.29 \pm 0.02*
EOP > 1.00	JulS1_3	Dense	Sour and sweet	4.34 \pm 0.02*
	JulS1_11	Soft-bodied	Sour but milk-like	4.51 \pm 0.06*
	JulS1_23	Soft-bodied	Sour and sweet	4.36 \pm 0.03
1.00 > EOP > 0.50	JulS1_8	Semi-fluid	Sour but milk-like	4.52 \pm 0.06*
	JulS1_19	Semi-fluid	Sour but milk-like	4.49 \pm 0.03*
	JulS1_34	Semi-fluid	Sour but milk-like	4.35 \pm 0.08
0.50 > EOP > 0.10	JulS1_4	Soft-bodied	Sour and sweet	4.39 \pm 0.01*
	JulS1_5	Soft-bodied	Sour but milk-like	4.37 \pm 0.04
0.10 > EOP > 0.001	JulS1_27	Soft-bodied	Sour and acidic	4.40 \pm 0.02*

* indicates a significant difference compared with the control (phage-free group) at $p < 0.05$.

Not only the highly and moderately efficient groups, but also the low-efficiency group (0.50 > EOP > 0.10) and the poorly efficient group (0.01 > EOP > 0.001) were found to affect yogurt formation. In particular, inoculation with JulS1_4 and JulS1_27 (representing the weakly and poorly efficient groups, respectively) resulted in a significant increase in pH and produced yogurt with a softer texture, although the aroma remained unchanged. These results suggests that even phages with relatively low infectivity can impair the activity of starter cultures, reducing their ability to metabolize sugars and produce acids as well as exopolysaccharides (EPS) ^{4,7}. Moreover, changes in aroma were observed across all groups, with the appearance of an off-flavor that detracts from one of the key quality characteristics of yogurt ^{16,18–20}.

Altogether, the results demonstrate that the contamination of phages in silage exhibit clear seasonal variation, with higher concentrations in the rainy and dry seasons and absence in summer. Rainy-season phages were capable of infecting the commercial starter strain *L. bulgaricus* YB01, whereas dry-season phages showed little to no infectivity, suggesting that environmental factors such as temperature and humidity may influence both phage abundance and host specificity ^{11,14,21}. Efficiency of Plating (EOP) analysis revealed considerable diversity among isolates, and even phages with low infectivity were able to impair yogurt fermentation, resulting in softer texture and slightly elevated pH. Moderately efficient phages produced more pronounced effects, including altered aroma, indicating that phage activity can disrupt acid production and exopolysaccharide (EPS) synthesis by starter cultures ^{16,17,19,22}.

Bacteriophages are known to infect starter cultures in many fermented dairy products, reducing bacterial activity responsible for converting sugars into amino acids, organic acids, and aromatic compounds—key contributors to product quality ^{4,7}. In this study, the observed changes in yogurt texture may have resulted from reduced EPS or lactic acid production. This effect is likely due to the infection of *L. bulgaricus* YB01 by the inoculated phages, which decreased its activity. Since *L. bulgaricus* plays a crucial role in metabolite production that stimulates the growth of *S. thermophilus*, its reduction subsequently limited the growth and activity of both starter culture strains, leading to lower production of key fermentation by-products ^{7,16,17,23}.



Although silage samples were collected from only three small-scale dairy farms, these findings still highlight the potential for environmental phages to enter dairy processing when proper hygiene and handling are not maintained during milking and transportation. Despite advancements in phage control, including phage-resistant starter cultures, rotation of starter strains, and heat treatment, phage contamination can still occur sporadically in industrial settings^{7,8,24}. Therefore, awareness and proactive management of phage contamination should be emphasized at all stages, from farm-level practices to industrial production, to maintain product quality.

Conclusion:

This study demonstrated the seasonal occurrence of bacteriophage contamination in silage from small-scale dairy farms in Ratchaburi, Thailand, with a notable absence during the summer and higher incidence in the rainy season. Phages isolated were capable of infecting commercial yogurt starter strains, particularly *L. bulgaricus* YB01. Efficiency of plating (EOP) analysis identified varying infectivity levels, with EOP values ranging from 0.01 to 4.39. Selected phages from each infectivity group were further tested in yogurt fermentation, where their presence led to increased final pH (up to 4.52±0.06) and a loose texture compared to the control (pH 4.29±0.02). These findings suggest that phage contamination from silage can significantly impair yogurt fermentation performance and quality, emphasizing the importance of monitoring phages in the dairy production chain.

Acknowledgements:

This work was supported by the Research, Innovation, and Creativity Fund, Silpakorn University. The authors also gratefully acknowledge the Department of Biotechnology, Faculty of Engineering and Industrial Technology, Silpakorn University, for providing technical support and guidance.

References:

1. Sáenz JS, Rios-Galicia B, Rehkugler B, Seifert J. Dynamic Development of Viral and Bacterial Diversity during Grass Silage Preservation. *Viruses*. 2023;15(4). doi:10.3390/v15040951
2. Doi K, Zhang Y, Nishizaki Y, Umeda A, Ohmomo S, Ogata S. A comparative study and phage typing of silage-making *Lactobacillus* bacteriophages. *J Biosci Bioeng*. 2003;95(5):518-525. doi:10.1016/s1389-1723(03)80054-3
3. Wang Y, Gao Y, Wang X, et al. Insights into the phage community structure and potential function in silage fermentation. *J Environ Manage*. 2024;358. doi:10.1016/j.jenvman.2024.120837
4. Połaska M, Sokołowska B. Review bacteriophages—a new hope or a huge problem in the food industry. *AIMS Microbiol*. 2019;5(4):324-347. doi:10.3934/microbiol.2019.4.324
5. O'sullivan L, Bolton D, McAuliffe O, Coffey A. Bacteriophages in Food Applications: From Foe to Friend. *Annu Rev Food Sci Technol*. 2019;10. doi:10.1146/annurev-food-032818-121747
6. Fernández L, Escobedo S, Gutiérrez D, et al. Bacteriophages in the dairy environment: From enemies to allies. *Antibiotics*. 2017;6(4):1-14. doi:10.3390/antibiotics6040027
7. Giraffa G, Zago M, Carminati D. Lactic acid bacteria bacteriophages in dairy products: problems and solutions. In: Poltronieri P, ed. *Microbiology in Dairy Processing: Challenges and Opportunities*. 1st ed. John Wiley & Sons Ltd and the Institute of Food Technologists; 2018. www.ebi.ac.uk/



8. Panezai N, Mandokhail K, Panezai M, Muhammad DG, Panezai M. Strategies Used to Control Bacteriophages Contamination in Dairy Food and Industry. *Pak Euro Journal of Medical and Life Sciences*. 2021;4. doi:10.31580/pjmls.v4iSpecialIs.1866
9. Imklin N, Patikae P, Poomirut P, Arunvipas P, Nasanit R, Sajapitak S. Isolation of bacteriophages specific to bovine mastitis-causing bacteria and characterization of their lytic activity in pasteurized milk. *Vet World*. 2024;17(1):207-215. doi:10.14202/vetworld.2024.207-215
10. Sun MC, Hu LY, Yu SQ, et al. Effect of reuterin addition before and after fermentation on yogurt quality. *J Dairy Sci*. Published online September 2025. doi:10.3168/jds.2025-26792
11. Liao Y Te, Lavenburg VM, Lennon M, Salvador A, Hsu AL, Wu VCH. The effects of environmental factors on the prevalence and diversity of bacteriophages lytic against the top six non-O157 Shiga toxin-producing *Escherichia coli* on an organic farm. *J Food Saf*. 2023;43(2). doi:10.1111/jfs.12865
12. Cai L, Xu B, Li H, Xu Y, Wei W, Zhang R. Spatiotemporal Shift of T4-Like Phage Community Structure in the Three Largest Estuaries of China. *Microbiol Spectr*. 2023;11(2). doi:10.1128/spectrum.05203-22
13. Maurice CF, Bouvier T, Comte J, Guillemette F, del Giorgio PA. Seasonal variations of phage life strategies and bacterial physiological states in three northern temperate lakes. *Environ Microbiol*. 2010;12(3):628-641. doi:10.1111/j.1462-2920.2009.02103.x
14. Sandaa RA, Larsen A. Seasonal variations in virus-host populations in Norwegian coastal waters: Focusing on the cyanophage community infecting marine *Synechococcus* spp. *Appl Environ Microbiol*. 2006;72(7):4610-4618. doi:10.1128/AEM.00168-06
15. Williamson SJ, Houchin LA, McDaniel L, Paul JH. Seasonal variation in lysogeny as depicted by prophage induction in Tampa Bay, Florida. *Appl Environ Microbiol*. 2002;68(9):4307-4314. doi:10.1128/AEM.68.9.4307-4314.2002
16. Kiliç AO, Pavlova SI, Ma WG, Tao L. Analysis of *Lactobacillus* Phages and Bacteriocins in American Dairy Products and Characterization of a Phage Isolated from Yogurt. *Appl Environ Microbiol*. 1996;62(6):2111-2116. <https://journals.asm.org/journal/aem>
17. Yahya HMA, Naeima MHY. Detection and characterization of bacteriophages attacking dairy *Streptococcus thermophilus* starter cultures. *Afr J Microbiol Res*. 2014;8(27):2598-2603. doi:10.5897/ajmr12.2201
18. Benbadis L, Faelen M, Slos P, Fazel A, Mercenier A. Characterization and comparison of virulent bacteriophages of *Streptococcus thermophilus* isolated from yogurt*. *Biochimie*. 1990;(72):855-862.
19. Kang SS, Kim MK, Kim YJ. Comprehensive evaluation of microbiological and physicochemical properties of commercial drinking yogurts in Korea. *Food Sci Anim Resour*. 2019;39(5):820-830. doi:10.5851/kosfa.2019.e72
20. Arab M, Yousefi M, Khanniri E, Azari M, Ghasemzadeh-Mohammadi V, Mollakhalili-Meybodi N. A comprehensive review on yogurt syneresis: effect of processing conditions and added additives. *J Food Sci Technol. Springer*. 2023;60(6):1656-1665. doi:10.1007/s13197-022-05403-6
21. Jiang SC, Paul JH. Inter-Research Science Center Seasonal and diel abundance of viruses and occurrence of lysogeny/bacteriocinogeny in the. *Mar Ecol Prog Ser*. 1994;104(1):163-172.
22. Saritaş S, Mondragon Portocarrero A del C, Miranda JM, Witkowska AM, Karav S. Functional Yogurt: Types and Health Benefits. *Applied Sciences (Switzerland). Multidisciplinary Digital Publishing Institute (MDPI)*. 2024;14(24). doi:10.3390/app142411798



23. Madera C, Monjardín C, Suárez JE. Milk contamination and resistance to processing conditions determine the fate of *Lactococcus lactis* bacteriophages in dairies. *Appl Environ Microbiol.* 2004;70(12):7365-7371. doi:10.1128/AEM.70.12.7365-7371.2004
24. Ma C, Chen Z, Gong G, Huang L, Li S, Ma A. Starter culture design to overcome phage infection during yogurt fermentation. *Food Sci Biotechnol.* 2015;24(2):521-527. doi:10.1007/s10068-015-0068-1



CHARACTERIZATION AND SCREENING OF FLAVOR-PRODUCING non-*Saccharomyces* YEASTS FOR FERMENTATION APPLICATIONS

Manutsanun Boonyanuwat¹ Thamonwan Tassanaset¹ Jirasin Koonthongkaew^{1, *}

¹Department of Microbiology, Faculty of Sciences, Chulalongkorn University, Thailand

*e-mail: Jirasin.K@chula.ac.th

Abstract:

The fermentation of alcoholic beverages, such as beer, wine, and distilled spirits, has undergone continuous evolution, both in terms of production processes and the improvement of product aroma and flavor. A key factor influencing beverage quality is yeast, particularly non-*Saccharomyces* yeasts, which contribute to expanding the diversity and uniqueness of flavors and aromas. Non-*Saccharomyces* yeasts were isolated from natural sources, including pineapple fruit, mango leaves, and kale leaves, as well as two sugar factories in Thailand: The Thai Multi-Sugar Industry and the Ratchaburi Sugar Factory. Researchers have suggested that non-*Saccharomyces* yeasts can produce aroma compounds distinct from those generated by *Saccharomyces*, which play a crucial role in contributing to the flavor and aroma of beverages within the same category. The results of the study indicated that *Candida sake* JK315 and JK316 exhibited good fermentation efficiency, as demonstrated by accumulated net CO₂ loss of 1.093±0.387 and 1.243±0.583 g, respectively, which were greater than *S. cerevisiae*, 0.713±0.235 g. Their results revealed the trend in production of primary aroma compounds, tolerance to ethanol concentrations up to 16% v/v, and the ability to grow within a pH range of 2–10. These non-*Saccharomyces* yeasts show promising potential for enhancing alcoholic beverage fermentation and can be used in combination with *S. cerevisiae* to increase aroma diversity. Furthermore, they are amenable to scale-up for assessing fermentation yields and exploring their applications in commercial production.

Introduction:

Alcoholic beverages have been known and associated with humanity for many centuries, and they continue to remain highly popular at present. Alcoholic beverages are not only consumed at social gatherings or celebratory occasions, but they also serve as symbols that reflect the history, culture, and beliefs of people in various regions around the world.^[1] Traditional alcoholic fermentation originated from the natural fermentation processes of microorganisms, particularly yeasts, which are commonly found in vegetables, fruits, and cereals. Different regions around the world employ various raw materials for alcoholic fermentation, resulting in beverages with distinctive flavors and aromas that reflect local uniqueness and diversity. Examples of such raw materials include grapes, berries, apples, corn, and barley.^[2]

The aroma and flavor profiles of alcoholic beverages are not only influenced by the raw materials but are also strongly affected by the microorganisms involved in the fermentation process.^[3] Yeasts are among the most widely used microorganisms in alcoholic fermentation due to their high capacity for sugar utilization and ethanol production. In addition, yeasts are capable of synthesizing a wide range of flavor compounds, such as isoamyl acetate (banana, pear), ethyl acetate (fruity), β-phenylethyl alcohol (floral, honey), ethyl hexanoate (apple, fruity), and 3-methyl-1-butanol (whiskey, malt, burnt notes).^[4]

In the modern alcoholic beverage industry, fermentation is predominantly carried out using a single yeast strain, *Saccharomyces cerevisiae*. This yeast is favored because it can withstand the harsh environmental conditions encountered during fermentation, including the high sugar concentrations present at the initial stage and the elevated ethanol levels accumulated toward the end of the process. Moreover, its rapid growth rate reduces the risk of contamination in the fermenting medium, thereby ensuring consistent product quality



across production batches.^[5] *S. cerevisiae* is classified as a microorganism within the group of Generally Recognized as Safe (GRAS), indicating its safety for use in food applications. Moreover, it is a Crabtree-positive yeast, capable of producing ethanol even under aerobic conditions when exposed to high sugar concentrations.^[6, 7]

Although *S. cerevisiae* possesses several advantages for the alcoholic beverage industry, one significant limitation is that the alcoholic beverages currently produced tend to exhibit reduced flavor diversity. Non-*Saccharomyces* yeasts have gained increasing attention, particularly when revisiting traditional alcoholic beverages that are characterized by greater flavor complexity due to natural fermentations involving multiple yeast species, commonly found on the surface or flesh of fruits and vegetables. Non-*Saccharomyces* yeasts are notable for their capacity to generate diverse flavor compounds; however, their ethanol production efficiency is generally lower than that of *S. cerevisiae*. Consequently, a common practice in modern production is to employ non-*Saccharomyces* yeasts during the initial fermentation stage to enhance flavor complexity, followed by the introduction of rapidly growing *S. cerevisiae* in the subsequent stage to increase ethanol yield.^[8, 9] Therefore, in this study, the researcher aimed to isolate yeasts from various sources to identify the yeast isolate suitable for further application in industrial-scale fermentation processes, considering their ability to produce flavor compounds, growth performance, and tolerance to fermentation conditions.

Methodology:

Isolation and screening of non-Saccharomyces yeast

The yeast used in this research was isolated from natural sources, including pineapple fruit, mango leaves, kale leaves, and two sugar factories in Thailand are the Thai Multi-Sugar Industry and the Ratchaburi Sugar Factory. Pineapple, mango leaves, and kale leaves were coarsely ground and mixed with sterile distilled water. A sterile inoculating loop was used to transfer liquid samples from each source and streak them onto YPD agar plates (yeast extract, 10 g/L; peptone, 20 g/L; glucose, 20 g/L; agar, 20 g/L). The plates were then incubated at 30°C for 24 h. After the incubation period, the morphological characteristics of the colonies were observed. Distinct single colonies were selected and streaked onto new YPD agar plates, which were then incubated at 30 °C for 24 h. The procedure was repeated three times. Once pure single yeast colonies were obtained, microscopic examination was performed to study their morphological characteristics.

Preliminary identification of the isolated yeast

The isolated yeast was identified using biochemical testing by the API 32C Kit (bioMérieux) to examine the ability of each isolate to assimilate different sugar sources. Yeast colonies were reactivated in liquid YPD medium and incubated at 30 °C while shaking at 200 rpm for 24 h. The cultures were then diluted in API C Medium to achieve a cell density of 2×10^7 – 5×10^7 cells/mL and filled into each well of the API 32C strip. The strips were incubated at 30 °C for 24 h, and the results were analyzed by comparing the numerical profiles with the APIWEB™ database.

Fermentation test

The fermentation performance of each yeast isolate was evaluated based on its ability to utilize sugar. Yeast colonies were reactivated in 5 mL of liquid YNB medium (yeast nitrogen base 6.7 g/L, peptone 20 g/L, glucose 20 g/L) with shaking at 200 rpm for 24 h. Cells were collected by centrifugation at 7,000 rpm at room temperature for 3 min. The cell pellets were washed twice with sterile distilled water and then resuspended in sterile distilled water. The optical density (OD) of the yeast suspension was measured at 600 nm, and the initial cell concentration was adjusted to an OD₆₀₀ of 0.1 per mL. The resuspended cells were inoculated



into YNB medium supplemented with 25% glucose at a volume of 1,220 mL and incubated in the dark at room temperature. The weight of the tube was recorded over 14 days and compared to the weight on the first day to calculate the fermentation capacity based on the accumulation of CO₂ in the fermentation medium.

Primary sensory screening

After 14 days of fermentation, the fermentation broth was centrifuged at 8,000 rpm and 4 °C for 10 min to remove the cells. The broth was then evaluated for its aroma by trained sensory panelists as a preliminary assessment to guide the selection of yeast isolate with the potential to produce desirable aroma compounds for the beverage industry.

Characterization of yeast growth by growth phenotype determination

Each isolated yeast colony was reactivated in SD medium (yeast nitrogen base without amino acids and ammonium sulfate 1.7 g/L, glucose 20 g/L, ammonium sulfate 2.5 g/L) and incubated at 30 °C with shaking at 200 rpm for 48 h. The initial cell concentration was then adjusted to an optical density (OD₆₀₀) of 0.1 per mL in 50 mL of SD medium in 250 mL flasks, which were incubated at 30 °C with shaking at 200 rpm for 36 hours. The OD₆₀₀ was recorded every 4 h, and the data were plotted to monitor the growth of the yeast over time.

Assessment of yeast tolerance to alcohol and pH

Each isolated yeast colony was reactivated in SD broth and incubated at 30°C with shaking at 200 rpm for 48 hours. A 5% (v/v) yeast suspension was then inoculated into 5 mL of SD broth containing ethanol at concentrations of 8, 10, 12, 14, and 16% (v/v) and incubated at 30 °C with shaking at 200 rpm for 48 h. Similarly, to assess pH tolerance, a 5% (v/v) yeast suspension was inoculated into 5 mL of SD broth adjusted to pH values of 2, 4, 6, 8, and 10. The optical density at 600 nm (OD₆₀₀) was measured for both experiments to evaluate the growth ability of yeast under conditions of high ethanol concentrations and varying pH values.

Results and Discussion:

A total of six yeast isolates were isolated from pineapple fruit (JK303), mango leaves (JK310), kale leaves (JK308), the Thai Multi-Sugar Industry (JK313, JK316), and the Ratchaburi Sugar Factory (JK315). Morphological characterization under a microscope and species identification using the API 32C test kit were performed, and the results are presented in **Table 1**. The experimental results revealed that yeast isolated JK303 was identified as *Kloeckera apislaticulata*, JK308 as *Rhodotorula glutinis*, and JK313, JK315, and JK316 as *Candida sake*, all of which belong to the non-*Saccharomyces* group.

Table 1.

Morphological characteristics of yeast colonies isolated from various sources and species identification performed using the API 32C kit, with results compared to the APIWEB™ database.

Sample code	Isolation Source	Colony Morphology	Species Identification (API 32C test kit)
JK303	Pineapple fruit	Round, glossy colonies with smooth surface and entire margin, creamy-white	<i>Kloeckera apislaticulata</i>

Sample code	Isolation Source	Colony Morphology	Species Identification (API 32C test kit)
JK308	Kale leaves	Round, glossy colonies with smooth surface, dark pink	<i>Rhodotorula glutinis</i>
JK310	Mango leaves	Round, glossy colonies with smooth surface and fimbriate margin, creamy-white	<i>Cryptococcus humicola</i>
JK313	Multi-Sugar Industry	Round, glossy colonies with smooth surface and entire margin, creamy-white	<i>Candida sake</i>
JK315	Ratchaburi Sugar Factory	Round, glossy colonies with smooth surface and entire margin, creamy-white	<i>Candida sake</i>
JK316	Multi-Sugar Industry	Round, glossy colonies with smooth surface and entire margin, creamy-white	<i>Candida sake</i>

The amount of carbon generated in the culture medium throughout the fermentation process originates from the utilization of glucose by yeast as a carbon source, in which the carbon is metabolically converted into carbon dioxide gas. This gas gradually accumulates in the medium and subsequently diffuses into the atmosphere, leading to a progressive reduction in the weight of the fermentation vessel. Therefore, periodic weighing provides a preliminary method for evaluating the fermentative efficiency of the yeast isolate.^[10] The results of the fermentation performance of the non-*Saccharomyces* yeast, compared with the control *S. cerevisiae*, which is commonly employed in the commercial production of alcoholic beverages such as beer and wine, are presented in **Figure 1**. The results indicated that during the first 3–5 days, the *S. cerevisiae* exhibited the highest accumulated net CO₂ loss compared to the non-*Saccharomyces* yeasts, consistent with the general ability of this yeast isolate to efficiently and rapidly utilize sugar. On day 14, the accumulated net CO₂ loss reached a maximum of 0.713 g. Between days 6 and 11, the non-*Saccharomyces* yeasts showed higher accumulated net CO₂ loss than the *S. cerevisiae*. On day 14, the accumulated net CO₂ loss of isolated JK303, JK308, JK310, JK313, JK315, and JK316 was 0.740±0.111, 0.703±0.327, 1.010±0.300, 1.200±0.522, 1.093±0.387, and 1.243±0.583 g, respectively, in contrast to *S. cerevisiae*, which showed 0.713±0.235 g. Therefore, the yeast isolated exhibiting the highest fermentation performance was JK316, followed by JK313. The isolate with the lowest fermentation capacity, showing values comparable to the control, was JK308.

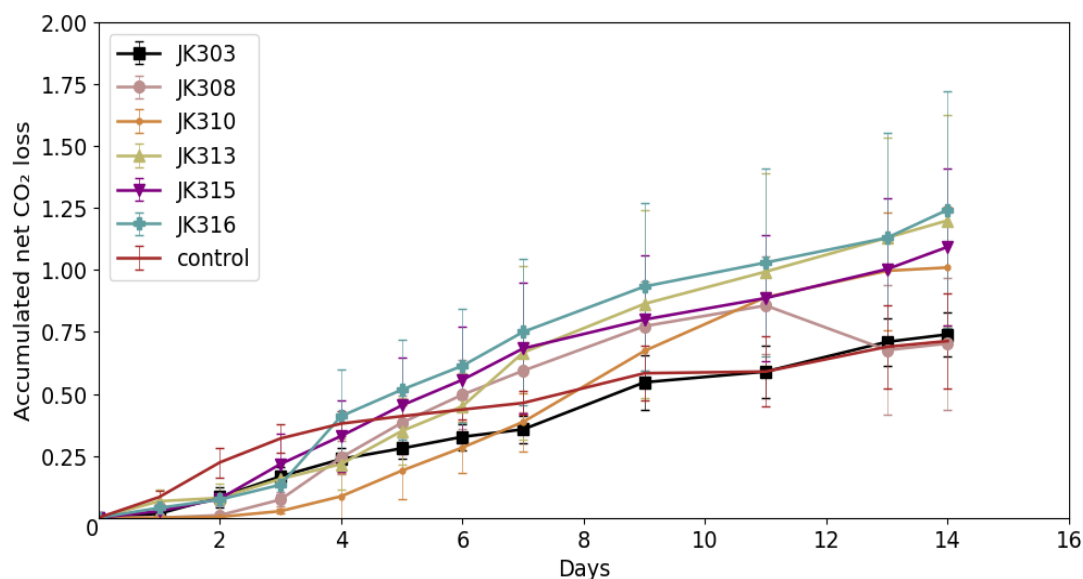


Figure 1.

Fermentation performance of different non-*Saccharomyces* yeasts isolates compared with the control *S. cerevisiae* (Fermentis Ale yeast).

Preliminary aroma assessment of each yeast isolate was conducted using primary sensory screening, in which trained sensory panelists provided initial descriptions presented in **Table 2**. Isolated JK315, which produced aromas of tofu, chestnut, rounded, and Japanese salad dressing, and isolated JK316, which produced aromas of slight vinegar, lemon, rounded, and lightly chicken soaked in alcohol, were suggested to have potential suitability for application in the beverage industry.

Table 2.

Preliminary descriptions of the aromas produced by each yeast strain as evaluated by sensory panelists.

Sample code	Preliminary aroma description
Control	Astringent, alcoholic, rounded, mushroom-like, vegetal, green-like, and slightly musty
JK303	Yeasty, reishi mushroom, earthy, woody, peanut-like, and mushroom-like
JK308	Strong alcohol, chicken soaked in alcohol
JK310	Strong alcohol, goji berry, clean aroma
JK313	Chicken soaked in alcohol, mushroom-like, vinegar, white wine, and steak sauce
JK315	Tofu, chestnut, rounded, Japanese salad dressing
JK316	Slight vinegar, lemon, rounded, lightly chicken soaked in alcohol

Isolated JK315 and JK316, which exhibited favorable fermentation performance and desirable aroma characteristics for alcoholic beverages, were subsequently subjected to growth characterization using the growth phenotype determination method. The results of this experiment are presented in **Figure 2**. Therefore, the growth profile revealed that isolated JK315 exhibited a logarithmic phase between 8 and 16 hours, with the highest optical density at 600 nm (OD_{600}). The isolated strain JK316 exhibited a log phase between 8 and 12 hours and reached a maximum OD_{600} of 7.517 ± 0.764 per mL, which was lower than that of JK315, with a maximum OD_{600} of 10.717 ± 2.106 per mL. The control strain (*S. cerevisiae*) also displayed a log phase between 8 and 12 hours but reached the lowest maximum OD_{600} of



4.407 ± 0.297 per mL. Based on cell density in the suspension as determined by OD₆₀₀ measurements, JK315 demonstrated the best overall growth performance. The experimental results indicate that the yeast growth profile affects the timing of secondary metabolite production during the stationary phase. Studying the aroma and flavor compounds produced by yeast in long-term fermentation allows for the accumulation of various metabolites at different growth stages, which may influence the resulting aroma and flavor.^[11]

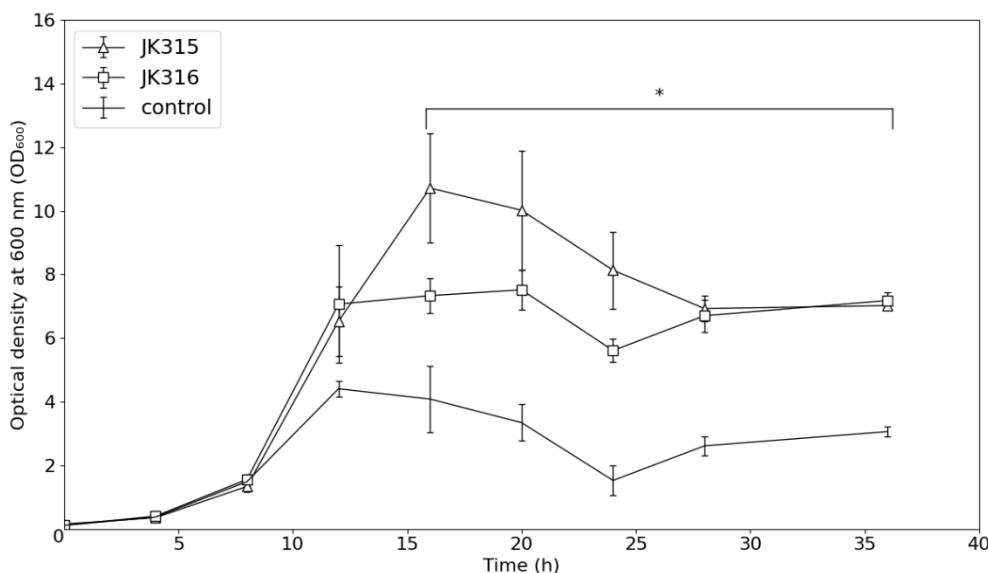


Figure 2.

Growth profiles of the non-*Saccharomyces* yeast isolates JK315 and JK316 compared with the control strain *S. cerevisiae* (Fermentis Ale yeast). The asterisk (*) indicates a statistically significant difference at $p < 0.05$ verified by Student's T-Test.

The growth ability of the non-*Saccharomyces* yeast isolates JK315 and JK316 in culture media containing ethanol at concentrations of 8, 10, 12, 14, and 16% (v/v) is presented in **Table 3**. Their tolerance to different pH conditions, with pH values of 2, 4, 6, 8, and 10, is shown in **Table 4**. Based on the results of both experiments, isolates JK315 and JK316 exhibited growth across all tested ethanol concentrations and pH values. Notably, those pH ranges and ethanol concentrations were found in the fermentation of alcoholic beverages.^[12, 13]

Table 3.

The ethanol tolerance of non-*Saccharomyces* yeasts was determined by comparing OD₆₀₀ values at 0 and 48 hours.

Sample code	Concentration of ethanol (% v/v)				
	8	10	12	14	16
Control	1.468±0.051	0.241±0.050	0.007±0.007	-	-
JK315	0.735±0.025	0.148±0.043	0.063±0.026	0.028±0.033	0.069±0.089
JK316	0.420±0.016	0.115±0.123	0.027±0.018	0.023±0.007	0.030±0.030

Note: ‘-’ indicates the difference in OD₆₀₀ between the value at 0 hours and at 48 hours, where the OD₆₀₀ at 48 hours is lower than that at 0 hours.

**Table 4.**

pH tolerance of non-*Saccharomyces* yeast was determined by comparing OD₆₀₀ values at 0 and 48 hours.

Sample code	Acid–base value				
	pH2	pH4	pH6	pH8	pH10
Control	0.063±0.018	4.088±1.016	2.932±0.114	5.394±1.123	2.636±1.456
JK315	2.756±0.590	7.005±0.673	5.307±0.298	6.901±2.804	6.819±3.016
JK316	2.469±0.193	9.931±1.707	6.636±0.712	6.634±3.711	5.806±2.736

Conclusion:

The results indicate that non-*Saccharomyces* yeast strains JK315 and JK316, identified as *Candida sake*, were preliminarily confirmed to produce aroma compounds with the potential to improve the taste and aroma of alcoholic beverages, similar to previous studies that have reported that *Candida sake* is one of the promising strains for modifying the taste and composition of beverages, including reducing the alcohol content, especially of wine.^[14] Moreover, these isolates exhibited favorable fermentation performance, growth, and stress tolerance under fermentation conditions compared to *S. cerevisiae*, a commonly used yeast species in alcoholic beverage production. Further studies can be conducted to confirm the production of potent flavor compounds from isolate JK316 by quantifying the key flavor compounds using GC-MS analysis, along with an investigation into the mechanism of production of these potent flavor compounds. Afterward, these newly isolated *C. sake* strains could be further applied to diversify the flavor and aroma of fermentation beverages through the co-fermentation technique with *S. cerevisiae*.

Acknowledgements

The author would like to thank Ms. Thamonwan Tassanaset, who served as the primary researcher for this study, as well as Dr. Jirasin Koonthongkaew and Dr. Supapid Eknikom for their valuable guidance and support, which made the completion of this research and full paper possible.

References:

- Núñez-Caraballo A, Grumezescu AM, Holban AM. *Process Sustain Beverages*. 2019; 2:37–72.
- Lee CH, Ahn J, Son HS. *J Ethn Foods*. 2024; 11(1):39.
- Qiu S, Zhang Y, Li M, Chen W, Zhao H. *Food Res Int*. 2022; 157:111391.
- Carrau F, Boido E, Dellacassa E. *Fungal Genet Biol*. 2017; 2:569–597.
- Goold HD, Kroukamp H, Bauer FF. *Microb Biotechnol*. 2017;10(2):264–278.
- Parapouli M, Vasileiadis A, Afendra AS, Hatziloukas E. *AIMS Microbiol*. 2020;6(1):1–31.
- Chai KF, Desa MNM, Chong GH, Ayob MK, Chin NL. *Curr Opin Food Sci*. 2022; 47:100881.
- Wang X, Liu P, Zhang J, Li Y, Xu Y. *J Food Compos Anal*. 2023; 124:105660.
- Qin T, Liu Y, Yang Q, Sun H, Zhao Y. *J Fungi (Basel)*. 2021; 12:667821.
- Guadalupe-Daqui M, Fernández-López J, Ramírez-Casillas J, Rodríguez-Casillas E. *J Ind Microbiol Biotechnol*. 2023; 50(1):1–12.
- Dartora B, et al. *Food Res Int*. 2023; 174:113569.
- Chen A, et al. *Fermentation*. 2024; 10(7):364.
- Liu X, et al. *J Food Sci*. 2015; 80(4): M800–M808.
- Gschaedler A. *Curr Opin Food Sci*. 2017; 13:73–77.



ISOLATION AND CHARACTERIZATION OF *Chlorella* sp. AARLG049N MUTANTS WITH HIGH PROTEIN AND LOW CHLOROPHYLL CONTENT

Kitkarn Veeraphisitt,¹ and Niyom Kamlangdee^{2*}

¹Department of Microbiology, Faculty of Science, King Mongkut's University of Technology Thonburi, Bangkok, Thailand

*e-mail: niyom.kam@kmutt.ac.th

Abstract:

In the current food and pharmaceutical industries, there is interest in microalgae due to the rising demand from health-conscious consumers for supplements. These consumers want products with increased protein and antioxidant properties. Microalgae possess these desired qualities and low-cost resources. Microalgae biomass can be utilized as a coloring in food. However, Limitation is consumer non-acceptance, primarily to green color. The objective of this research was to develop *Chlorella* sp. strain with higher protein and low chlorophyll content. The random mutagenesis with Ethyl methane sulfonate (EMS) was used to induce mutations. EMS affects the targeted cells specifically converting (GC) pairs to (AT). Treated with 300 mM EMS, colonies were analyzed after 168 hours on BG-11 agar under 4400 lumen (LM) of fluorescent light. Colonies with a light green color were identified as Mutant 01. The protein content in wildtype and mutant 01 isolates was $38.83 \pm 0.86\%$ and $41.44 \pm 1.20\%$ DW. The chlorophyll in the Mutant01 strain was reduced by $4.33 \mu\text{g/ml}$ compared to the original strain. These results indicated that the successful genetic modification of *Chlorella* sp. has the potential to increase protein content and reduce chlorophyll, which will be useful as an ingredient in the future development of new healthy food.

Keywords: Ethyl methane sulfonate, *Chlorella* sp, Phenotype, Mutant, chlorophyll

Introduction:

At present, they find that the population is paying more attention and has more needs regarding physical health, especially among teenagers, adults, or the elderly. This can be done in the form of exercise, eating clean food, or another way is taking dietary supplements that include protein promotion or help with vitamins that will be received.

Microalgae are single-celled green algae. It is recognized as a sustainable biological resource for the future, one of which is *Chlorella* algae. This is because of the ability of algae. Just being in a suitable environment can be able to reproduce and grow rapidly. Because it is well adapted. The cost of cultivation is relatively low. In addition, the advantages of microalgae are rich in vitamins, minerals, high protein, essential fatty acids, pigments¹ including being able to fight free radicals or the immune system in the body.² In the European Union, if microalga used as food must comply with Regulation (EU) 2015/2283 on novel foods, they have been used for a long time.³ This data from the Web of Science database, there are 416 studies on microalgae in the field of food science and technology. These studies show that research on the application of *Chlorella* in food technology is ongoing.⁴

In the food industry, microalgae are widely used in two ways as a coloring agent and as a nutritional enhancer. The *Chlorella* chlorophyll pigment, which is found in relatively high concentrations in microalgae, will result in a deep green color, and affect sensory perception with a greenish-smelling taste. The thick cell walls of algae also affect the utilization and processing of nutrients.⁵

Despite the health and well-being benefits, *Chlorella* has low sensory acceptability in food products. To improve the sensory properties, one alternative is to reduce or eliminate the problematic chlorophyll pigment. to promote better taste.⁶ This can be achieved by reducing



chlorophyll content using heterotrophic culture stress.⁷ The development of microalgae will be random mutagenesis using a substance like Ethyl methane sulfonate, which is a preferable option because mutation is not considered as the (GMO) principle. This method was chosen because the mutation promotes target cells to have abnormal gene pairing and stimulates the production of metabolites. There is no gene editing or modification, just to improve the properties.⁸ Therefore, the main objective of this research was to develop *Chlorella* sp. AARLG049N strain that has a higher protein content and lower chlorophyll content by using random mutagenesis with Ethyl methane sulfonate (EMS). This will make it more reasonable for future applications in the nutritional and food industries.

Methodology:

Preparation of Chlorella sp. AARLG049N

The *Chlorella* sp. AARLG049N strain was obtained from the Faculty of Science, Chiang Mai University. The culture was re-streaked for purity and freshness. The inoculum was transferred to BG-11 flasks, containing 1.5 g/L Sodium Nitrate, 0.040 g/L Dipotassium Hydrogen Phosphate, 0.075 g/L Magnesium Sulfate, 0.036g/L Calcium Chloride, 0.020 g/L Sodium Carbonate, 0.006 g/L Citric Acid, 0.006 g/L Ferric Citrate, 0.001 g/L Disodium EDTA and add stock trace metal mixA5 1 ml/L comprising 2.86g/L Boric Acid, 1.81 g/L Manganese Chloride, 0.222 g/L Zinc Sulfate, 0.39g/L Sodium Molybdate, 0.079 g/L Copper Sulfate, 0.0494 g/L Cobalt Nitrate.⁹ The cultures were divided into 500-ml flasks, each containing 300 ml of the medium. The culture was incubated at 24:0 hrs of a light cycle with a fluorescent light intensity of 4400 lumens (LM), and the temperature of $28 \pm 2^\circ\text{C}$.

Random Mutagenesis and Selection of Chlorophyll-Deficient Mutants

Chlorella sp. AARLG049N. Cells (1×10^6 cells ml^{-1}) were transferred to 50 ml centrifuge tubes with a working volume of 20 ml. They were then concentrated 10-fold by centrifugation (3,000 g, 10 min). The concentrated cell was treated with 300 mM Ethyl methane sulfonate (EMS, Merck, USA) for 1 h in the dark.¹⁰ After 1 h, 5% sodium thiosulfate was added to stop the EMS reaction, and the cells were pelleted by centrifugation at 3,000 g for 10 minutes and washed three times with sterile distilled water. Cells were incubated in the dark for 24 hours to prevent photoreactivation of DNA damage. The isolation of mutant cells was performed by plating on BG-11 agar using serial dilutions and incubating at 26°C for 168 hours under light conditions at 4400 LM. The light green color of mutants was selected by visual observation under a light microscope. These mutant colonies were subcultured several times on BG-11 agar and subsequently transferred to liquid medium. This strain was named Mutant01.

Erlenmeyer Flask Experiment

A comparative study was conducted to assess the growth efficiency of the Wildtype and Mutant01 strains. Both strains were cultivated under controlled light conditions at 4400 lumen (LM) with 24:0 light cycle. The experiment was performed in 500-ml Erlenmeyer flasks with a final working volume of 300 ml using BG-11 medium and maintained at a temperature of $28 \pm 2^\circ\text{C}$ for 7 days.

Sampling and Growth Assessment

Samples were collected from each medium ratio and concentration. These samples were used to analyze growth parameters, including optical density (OD) at 750 nm, measured using a UV-Vis spectrophotometer, and light microscopy at 400x magnification.

Chlorophyll content determination

To determine chlorophyll content, twenty milliliters of cultured algae were extracted from each sample and centrifuged for 2,500 g for 15 min at (HERMLE Labortechnik GmbH, Wehingen, Germany). Chlorophyll extraction, The chlorophyll was the extracted using methanol, and the cells were sonicated for 10 min. After 10 min, the supernatant was centrifuged, and the remaining biomass was re-extracted until colorless. The absorbance values of the extracted solution were recorded at 663, 645, and 470 nm using a Genesys 10S UV-Vis spectrophotometer (Thermo Scientific, Massachusetts, USA). The final chlorophyll content was then calculated using the following equation:^{11,12}

$$\text{Chl a } (\mu\text{g/ml}) = (12.7 \times A_{663}) - (2.69 \times A_{645}).$$

$$\text{Chl b } (\mu\text{g/ml}) = (22.9 \times A_{645}) - (4.68 \times A_{663}).$$

$$\text{Total chlorophyll } (\mu\text{g/ml}) = \text{Chl a} + \text{Chl b}.$$

Protein Analysis

Protein content was determined using CHN composition analysis using a dry-weighed cell sample loaded onto a CHN Analyzer for analysis (Leco Corporation, Saint Joseph, Michigan USA). The final protein content was calculated by multiplying the measured percentage of nitrogen by a conversion factor 6.25.

Results and Discussion:

Results of the study on growth efficiency Wildtype compared to Mutant01 Strain

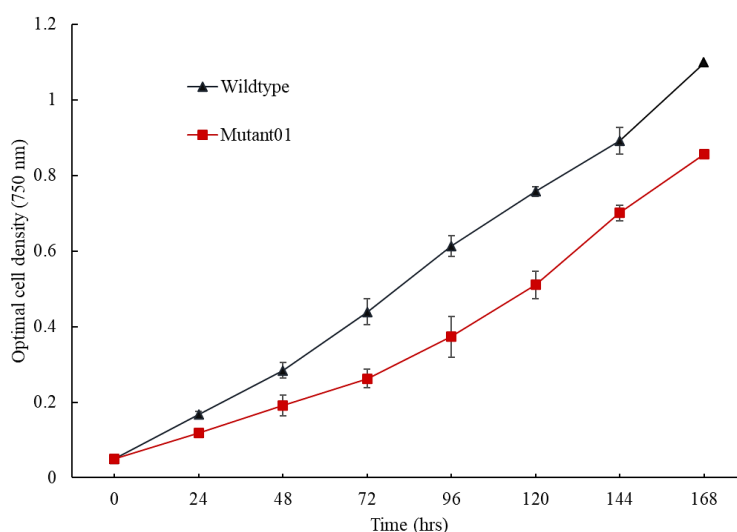


Figure 1.

Shows the growth rate of *Chlorella* sp. AARLG049N in liquid BG-11 medium under autotrophic conditions at a light intensity of 4400 lumen for 168 hours.

The growth study was conducted to compare the performance of the Wildtype and Mutant01 strains under a light intensity of 4400 LM with aeration. Before the experiment, the algal cells of both strains were adjusted to the same initial concentration, with an OD of 0.050 at 750 nm, in 300 ml of liquid BG-11 medium. Growth data were then collected simultaneously from 0 to 168 hours using a spectrophotometer at an absorbance of 750 nm. As shown in Figure 1, the number of algal cells in both strains at 0-48 hours showed a slight increase. At 48 hours, the wildtype strain had increased to 0.284 ± 0.001 , and the mutant01 strain had

increased to 0.191 ± 0.001 . At 96 hours, a clear difference was observed among strains. Wildtype strains increased to 0.612 ± 0.03 , while Mutant01 strains only reached 0.373 ± 0.02 . At the final incubation time at 168 hours, the wildtype strain increased to 1.098 ± 0.03 , while mutant01 strains reached 0.857 ± 0.02 . The data show that between 0 and 48 hours, there was a slight increase in growth as the cells were adapting. Normally, algal cells can grow under suitable conditions, with sufficient temperature, light, or nutrients. This stage is known as the adaptation phase.¹³ At 168 hours, both strains were in the logarithmic phase of exponential cell growth. However, a key finding emerged: despite starting with the same cell count, the mutant strain grew at a slower rate than the wild-type strain. This result demonstrates the impact of mutations, as mutagens affect the cells' photosynthetic systems. This results in photosensitivity of the cells and stunted growth, as the medium doesn't provide an alternative carbon source. This may support the data of previous research the mutant strains were tested under light and dark conditions, with glucose as an additional energy source.¹⁴ It was found that mutant strains grew as well as the wildtype strains under light conditions. However, when the glucose in the liquid medium was insufficient, the mutant strains also showed a reduced growth rate. Therefore, the mutations, along with defective pigmentation (reduced chlorophyll production), likely led to slower growth performance.

Chlorophyll pigment composition of Wildtype and Mutant01 strains

Table 1.

Chlorophyll pigment profiles of wildtype and mutant strains of *Chlorella* sp. AARLG049N grown under 4400 lumen light conditions, measured in microalgae $\mu\text{g/ml}$. Each displayed value is the average of three replicates.

Isolate	Chl a ($\mu\text{g/ml}$)	Chl b ($\mu\text{g/ml}$)	Total chlorophyll ($\mu\text{g/ml}$)
Wildtype	10.71 ± 0.39	9.24 ± 0.78	19.95 ± 1.17
Mutant01	8.640 ± 0.81	6.98 ± 0.58	15.62 ± 1.38

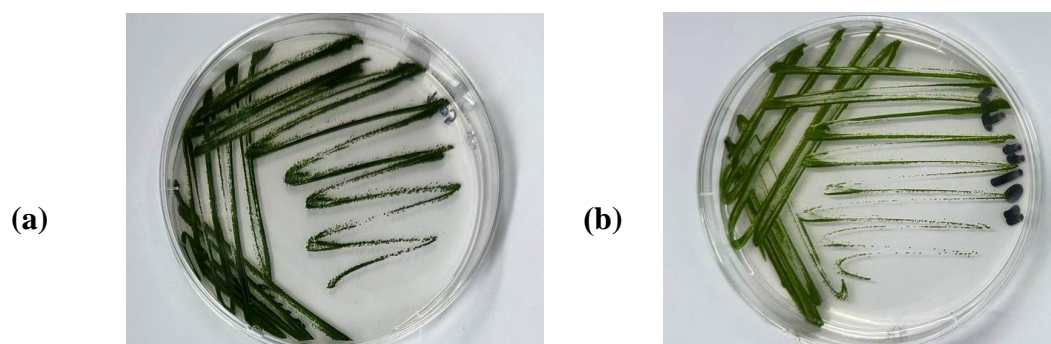


Figure 2.

Phenotypic differences observed between the wildtype strain (a) and the Mutant01 strain (b).

Samples were grown on BG-11 agar medium under continuous light for 7 days at a light intensity of 4400 lumen.

A chlorophyll-deficient mutant of *Chlorella* sp. AARLG049N was developed by treating with 300 mM Ethyl methane sulfonate mutagen by selecting on BG-11 agar and colonies with the light green phenotype. After selection, the mutant colonies were cultured repeatedly to evaluate the color of the non-reversible colonies and named Mutant01.

They were then cultured in liquid medium for chlorophyll content analysis. From Figures 2a and 2b, the results clearly show the color difference between the Wildtype (Figure

2a) and Mutant01 (Figure 2b) colonies, with the mutant appearing noticeably paler. The amount of pigment observed has a lighter chlorophyll character. And when analyzing the data from Table 1, the Wildtype strain had a combined ratio of Chl a and Chl b at 19.95 ± 1.17 $\mu\text{g/ml}$. In the Mutant01 strain, the total chlorophyll content was found at 15.62 ± 1.38 $\mu\text{g/ml}$, which represents a reduction of 4.33 $\mu\text{g/ml}$ in total chlorophyll, confirming that the mutagenesis was successful in producing a strain with the desired paler appearance.

The mutagen EMS primarily causes genetic mutations by promoting faulty pairing, changing GC base pairs to AT. Evidence from reports also suggests that EMS can cause insertions or deletions of base pairs, particularly at the N-7 position of guanine, which can lead to chromosomal damage.¹⁵ Previously reported, plant greening and photosynthesis, synthesized from Glutamyl-tRNAGlu, found that chlorophyll synthesis was inhibited, possibly due to the downregulation of genes encoding CAO of Mutant01 strain.^{16,17} Impaired Protein Transport. The reduced chlorophyll content may also be caused by a Light-Harvesting Complex Protein (LHCP) translocation defect. The mutation in the Mutant01 strain is suspected to be in a homologous gene, which affects the transport protein ARSA. This impairment in protein import activity, potentially due to faulty TOC34 synthesis, leads to the pale green phenotype.¹⁸

Cell morphology of Chlorella sp. AARLG049N Wildtype compared to Mutant01 strain.

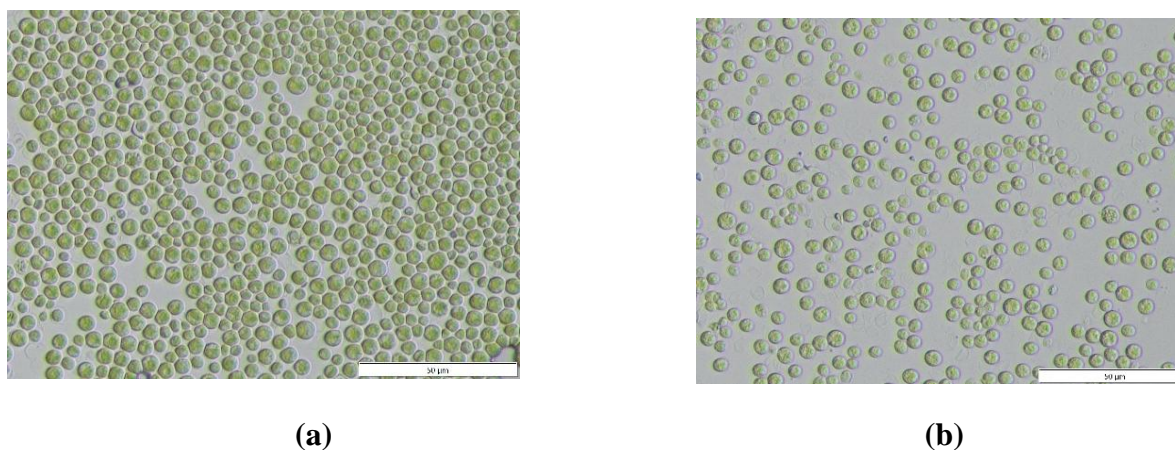


Figure 3.

Cell morphology of *Chlorella* sp. AARLG049N algae of the wildtype (a) and mutant01 (b) at 400x magnification grown in BG-11 liquid medium under autotrophic conditions.

As a result, the image shown in Figure 3 presents microscopic images (400x magnification) of Wildtype and Mutant01 *Chlorella* sp. AARLG049N cells after 168 hours of cultivation in liquid BG-11 medium. The images highlight key morphological differences between the two strains at the cellular level. The wildtype strain exhibits green cells, with chloroplasts clearly visible, which are green in color due to their high chlorophyll. Cells of both strains alternate in size, appearing small and large. This is because cells in the early stages of cell division appear small, or this could be due to the environment. When cells are in a healthy state, they are larger and have different shapes. In contrast, the Mutant01 strain (b) has a noticeably different appearance. Cellular components are clearer and hollower, and the chloroplast content is reduced due to the reduction of green coloration from chlorophyll. This data is consistent with (Figure 2), which shows a light green phenotype. A mutation inserted into the cytosol homologous gene of ARSA1 results in reduced chloroplast size and chlorophyll content.¹⁹ Impaired photosynthesis efficiency. Defective chloroplast formation reduces the efficiency of photosynthesis because chloroplasts are fewer and smaller, which may be why

the mutant strain grows more slowly than the normal strain under light alone and without any other carbon source.

Protein content Wildtype compared to Mutant01 strain.

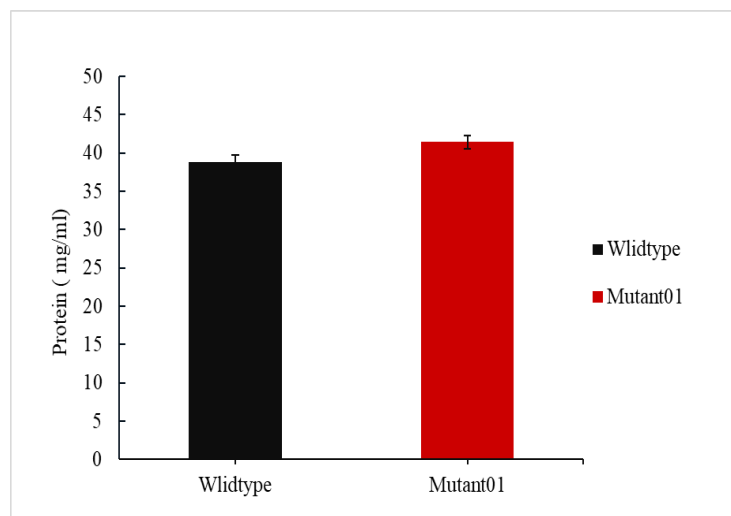


Figure 4.

Protein composition of wildtype and mutant01 strains of *Chlorella* sp. AARLG049N. Data are shown as the mean \pm standard deviation of three replicates.

For the analysis of intracellular protein content, measurements were made after the end of the culture experiment of both algae strains. The cells that were adjusted to the initial concentration were cultured at the same concentration for 168 hours. Protein content was determined using a CHN-Analyzer, with the final value calculated by multiplying the intracellular nitrogen accumulation by a conversion factor of 6.25. The results showed that the Mutant01 strain had a higher protein content than the Wildtype strain. Specifically, the Wildtype strain had a protein accumulation of $38.83 \pm 0.86\%$ DW, while the Mutant01 strain accumulated $41.44 \pm 1.20\%$ DW. Alternatively, when cells are genetically damaged or in an unsuitable environment caused by EMS, the cells may develop protective mechanisms to prevent them from entering cell death mode. This causes the accelerated production of certain proteins to repair the damaged areas, adapt to new conditions, or prevent further damage. The increased production of proteins is not simply the use of parts that cannot produce chlorophyll, but rather the cells' own stress response, stimulating the synthesis of proteins essential for survival in higher-than-normal amounts. When the total protein content was measured, it was higher than that of the wild-type strain. This is consistent with data suggesting that a decrease in chlorophyll levels may be due to a problem with light-dependent photosynthesis. However, when this system is unable to function normally, a process of photon conversion to biomass accumulation occurs.²⁰ Previous reports also support that mutant algal cells grown under light conditions accumulated as much as 48% protein, compared to the wildtype strain, which could accumulate only 35.3% protein.¹⁴ After mutation, photosynthetic capacity may be altered. It was found that higher light intensity, while affecting chlorophyll production, promoted higher protein production.²¹

In conclusion, this study successfully developed the Mutant01 strain of *Chlorella* sp. AARLG049N through ethyl methane sulfonate (EMS) mutagenesis, demonstrating that it's possible to improve the sensory qualities of the algae. The research confirmed that the mutant strain achieved the key objectives of the study, showing an increase in protein content while simultaneously having a significant decrease in chlorophyll content. This directly addresses



the issue of unacceptable color and taste that often limits the use of *Chlorella* in food products.

Acknowledgement:

We would like to thank Assist. Dr. Jiraporn Pakkao from the Department of Biology, Faculty of Science, Chiang Mai University, for kindly providing the *Chlorella* strain in this study.

References:

1. Abdel-Rahman Mohamed A, El-Kholy SS, Dahran N, El Bohy KM, Moustafa GG, Saber TM, Metwally MMM, Gaber RA, Alqahtani LS, Mostafa-Hedeab G, El-Shetry ES. Erratum in: *Gene*. 2022;839:146749.
2. Yu Z, Geisler K, Leontidou T, Young REB, Vonlanthen SE, Purton S, Abell C, Smith AG. *Algal Res*. 2021;56
3. Lafarga T, Fernández-Sevilla JM, González-López C., Ación-Fernández FG. *Food Res Int*. 2020; 137:109356.
4. Zheng X, Chen L, Yin L, Rao H, Zheng H, Xun C, Hao J. *Heliyon*. 2024;10:2-11.
5. Takeda H. *Phytochem*. 1993; 34:1053-1055.
6. Lucas BF, Morais MG, De Santos TD, and Costa JAV. *LWT*. 2018;90:270-276.
7. Caporgno MP, Böcker L, Müssner C, Christina Müssner, Stirnemann E, Haberkorn I, Adelman H, Handschin S, Windhab EJ, Mathys A. *Innov. Food Sci*. 2020;59:102275.
8. Zimny T, Sowa S, Tyczewska A, and Twardowski T. *N. Biotechnol*. 2019;51:49-56.
9. Moghazy RM. *Water SA*. 2019;45(1):20-28
10. Spencer-Lopes MM, Forster BP, Jankuloski L. *Manual on mutation breeding*. 2018; xvii + 299.
11. Daniel IA. *Plant Physiology*. 1949;24(1):1-15.
12. Porra RJ, Thompson WA, Kriedemann PE. *Biochimica et Biophysica Acta (BBA)*. 1989;975(3):384-394.
13. Guerrero L, Omil F, Mendez R, Lema JM. *Water Research*. 1999;33:3281-3290.
14. Schüler L, Greque de Morais E, Trovão M, Machado A, Carvalho B, Carneiro M, Maia I, Soares M, Duarte P, Barros A, Pereira H, Silva J and Varela J. *Front. Bioeng. Biotechnol*. 2020;8:469.
15. Sega GA. *Mutat Res*. 1984;134(2-3):113-42.
16. Sun D, Wu S, Li X, Ge B, Zhou C, Yan X, Ruan R, Cheng P. *Marine Drugs*. 2024; 22(2):65.
17. Biswal AK, Pattanayak GK, Ruhil K et al. *Physiol Mol Biol Plants*. 2024;30:1–16.
18. Ziehe D, Dünschede B, Schünemann D. *Photosynth Res*. 2018;138(3):303-313.
19. Formighieri C, Cazzaniga S, Kuras R, Bassi R. *Plant J*. 2013;73(5):850-61.
20. Dall'Osto L, Cazzaniga S, Guardini Z et al. *Biotechnol Biofuels*. 2019;12:221.
21. Ogbonda KH, Aminigo RE, Abu GO. *Bioresource Technology*. 2007;98:2207-2211.



ISOLATION, MORPHOLOGICAL IDENTIFICATION, AND GROWTH OF THRAUSTOCHYTRID ISOLATED FROM MANGROVE HABITATS IN THE GULF OF THAILAND

Sasiwimol Duangvichai,¹ Niyom Kamlangdee,^{2,*} Kaliyamoorthy Kalidasan³

^{1,2}Department of Microbiology, Faculty of Science, King Mongkut's University of Technology Thonburi, Bangkok, Thailand

³Department of Marine Science, Faculty of Science, Chulalongkorn University, Bangkok, Thailand

*e-mail: niyom.kam@kmutt.ac.th

Abstract:

Thraustochytrids are microorganisms used for industrial purposes, particularly in pharmaceuticals and supplements, due to their ability to produce high levels of fatty acids. It can also be cultivated and purified more easily than extracted from marine fish or other microorganisms. This study aimed to isolate thraustochytrids from fallen leaves in mangrove habitats in the Gulf of Thailand to study their growth and biomass accumulation. Six strains of thraustochytrid were isolated from Wat Khun Samut Chin Temple, Samut Prakan Province, Thailand. Morphological observation showed that the characteristics of the isolated strains were exactly like those in previous research. After 120 hours of cultivation, the dry weight of the six isolates ranged from 0.81 to 1.36 g/L, with WK3 producing the highest biomass yield and reaching an OD of 3.863. Based on these results, WK1 and WK3, which had the highest growth rate, were selected to culture with different glucose concentrations (0.3-8% w/v) to observe their ability to grow. The WK3 isolate achieved the highest growth at 4% glucose, reaching an OD of 8.0. This study suggests that thraustochytrid strains, particularly WK3, have the potential to develop increased biomass production or essential fatty acids in the future.

Keywords: biomass production, fatty acids, mangrove habitats, Thraustochytrids

Introduction:

Polyunsaturated Fatty Acids (PUFAs), or Omega-3 fatty acids, especially DHA (Docosahexaenoic Acid), EPA (Eicosapentaenoic Acid), and ALA (Alpha-Linolenic Acid). These are essential nutrients that provide several health benefits, they improve brain cell function, reduce blood pressure, and prevent Alzheimer's disease. Normally, these fatty acids cannot be synthesized by the human body on their own. However, consuming marine fish has an impact on the marine ecosystem and has high production costs, and the product quality of the fish oil obtained depends on many factors.^{1,2}

In addition, the demand for squalane has increased dramatically, as it is the most prominent component along with polyunsaturated fatty acids in the skin and is often used as a moisturizer. The antioxidant and moisturizing properties in various skincare products can help reduce serum cholesterol levels.³ It strengthens and enhances the immune response to the vaccine and inhibits the spread of tumors. However, squalane is extracted from the liver of an endangered deep-sea shark, and the extraction is also at risk of heavy metal contamination and the limitation of unpleasant odors and tastes, making it difficult to produce enough to meet human industrial demand.²

Thraustochytrids are another option to reduce the use of marine resources and reduce the risk of marine toxic contamination.² because thraustochytrid microorganisms are found in mangrove forests that can produce polyunsaturated fatty acids. Thraustochytrids also have a high ability to produce non-toxic squalene^{2,3} because thraustochytrids can grow heterotrophically when exposed to organic carbon sources and can accumulate triacylglycerol



up to 50-80% dry weight. In many studies, it has been reported that thraustochytrids can accumulate high levels of DHA, and some strains accumulate squalene up to 171 mg/g dry weight and 0.9 g/L, which can be used as an alternative to squalene production.⁴ The species found in the mouth of the Gulf of Thailand has not been studied. Therefore, this study aimed to isolate thraustochytrid from mangrove habitats in the Gulf of Thailand to study the production and accumulation of biomass (fatty acids and squalene) for creating a profile in the database for further study.

Methodology:

Sample collection

Fallen mangrove leaves were collected from the two locations of Wat Khun Samut Chin Temple (WK) and Pom Phra Chulachomkiao (P) mangrove habitats. Collect leaf samples in sterile plastic bags and store at 4 °C until further processed. The leaf samples were washed with sterile natural seawater (30 psu) to reduce the risk of contamination before being placed the leaf samples onto modified GYP agar plates containing glucose (10 g/L), yeast extract (1.25 g/L), peptone (1.25 g/L), agar (10 g/L) and natural seawater 30 psu salinity (80% v/v) at pH 7.2 with the addition of antibiotic mixture (300 µg/L Penicillin-Streptomycin, Thermo Fisher Scientific, MA, USA) agents to prevent bacterial contamination and incubated at 28 °C for 48 hours until colonization appeared.⁵

Isolation of Thraustochytrids

The colonies were examined under light microscopes with a 40× objective lens for their colony morphological structure. Thraustochytrid colonies were selected and sub-cultured onto fresh GYP agar plates until pure isolates were obtained. To ensure purity, the selected colonies were repeatedly transferred and purified in salty medium (seawater) several times to obtain pure cultures, so both the colony isolation under aseptic conditions and salt medium will help reduce contamination of yeast and other eukaryotic microorganisms. The pure isolates were maintained on agar plates and sub-cultured every 7 days.

Morphological Identification of Thraustochytrids

Pure colonies of thraustochytrid strains were sub-cultured using a sterilized inoculating loop, streaked onto GYP agar plates, and incubated at 28 °C for 48 hours. The colonies appearing on GYP agar plates were transferred to GYP broth and incubated at 28 °C for 48 hours. Cell suspensions of thraustochytrid strains were transferred to the slide chamber. These were examined under the light microscope for morphological characteristics of thraustochytrid strains, such as the presence of ectoplasmic net, zoospores, amoeboid cells, vegetative cells, zoospores and zoosporangia.⁶

Growth behavior observation of Thraustochytrids

Pure colonies of thraustochytrid were cultured and inoculated into GYP broth and incubated at 28 °C for 48 hours in the incubator shaker at 150 rpm. After incubated the optical density was adjusted to 0.5 with sterile GYP broth and 3% (v/v) of inoculum transferred to GYP broth containing glucose (3 g/L), yeast extract (1.25 g/L), peptone (1.25 g/L) and natural seawater 30 psu salinity (80% v/v) at pH 7.2 in a 100 mL Erlenmeyer flask and incubated at 28 °C for 48 hours in the incubator shaker at 150 rpm. The growth of thraustochytrid strains was plotted by the optical density (OD) at 600 nm for up to 120 hours. The growth behavior of thraustochytrid strains was performed in triplicate for each isolate.⁵

Growth behavior of Thraustochytrids in the different glucose concentrations

The growth behavior of thraustochytrid isolates in 250 mL Erlenmeyer flask containing 100 mL of GYP broth adjusted to glucose concentrations at (0.3, 2, 4, 6, and 8%, w/v); yeast extract (1.25 g/L), peptone (1.25 g/L) and natural seawater 30 psu salinity (80% v/v) at pH 7.2, obtained for each of thraustochytrid isolates were inoculated with 3% (v/v) and incubated at 28 °C for 120 hours in the incubator shaker at 150 rpm.^{5,7} The growth of thraustochytrid strains was monitored by measuring the optical density (OD) at 600 nm for up to 120 hours. The growth behavior of thraustochytrid strains at different times at 0 to 120 hours, is performed in triplicate of each isolate.

Biomass determination

All thraustochytrid cells in the Erlenmeyer flask were transferred to the centrifuge tube and harvested by centrifugation at 8000 rpm for 5 min at 4 °C using a 50 mL centrifuge tube. The cell pellet was washed twice with sterile distilled water to remove the medium from the pellet. The pellet cells were freeze-dried overnight and weighed until constant. Biomass production was expressed in milligrams per 100 mL of growth medium.^{5,8} The biomass was stored at -20 °C before further studies.

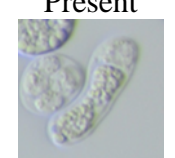
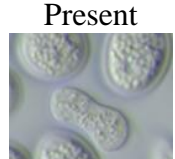
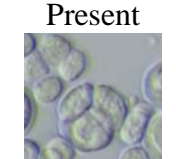
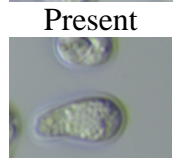
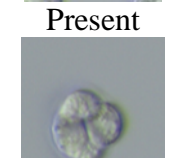
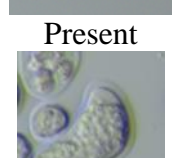
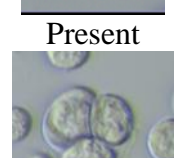
Results and Discussion:

Morphological and identification of thraustochytrids

The thraustochytrid strains were isolated from two locations in the Gulf of Thailand, namely Wat Khun Samut Chin Temple (WK) and Pom Phra Chulachomklao (P) mangrove habitats in Samut Prakan Province. Six isolates were obtained from Wat Khun Samut Chin Temple (WK). A Total of six isolates were recovered, and their morphological characteristics are shown in **Table 1**. The environmental parameters at the sample site included a seawater temperature of approximately 30 °C, a salinity of 30 psu, and a pH value of about 7.

All thraustochytrid isolates were found in creamy white colony, and the thraustochytrid cells were examined under a light microscope at 60× magnification to determine cell shape and size. The cells range from 10-20 µm. **Figure 1**. The colony and cellular morphology observed in this study were consistent with previous reports of thraustochytrids isolated from Andaman mangrove habitats⁵ and mangrove habitats in Thailand.⁹ In this study, morphological identification including the presence of ectoplasmic network, zoospores, zoosporangium, amoeboid cells and vegetative cells were used as a preliminary approach for identification, following previous studies.^{6,9}

Table 1.
Morphological features of the isolated thraustochytrids

Isolate	Mangrove Habitats	Colony Morphology	Ectoplasmic Network	Cell Wall	Amoeboid Cell	Binary Cell Division	Shape and Size of Vegetative cells
WK1	WK	Large Circular colonies, creamy white, raised with an entire margin	Present (unclear)	Thin	Present 	Present 	Globose 10-20 μm diam
WK2	WK	Large Circular colonies, creamy white, raised with an entire margin	Present (unclear)	Thin	Present 	Present 	Globose 10-20 μm diam
WK3	WK	Large Circular colonies, creamy white, raised with an entire margin	Present (unclear)	Thin	Present 	Present 	Globose 10-20 μm diam
WK4	WK	Small Circular colonies, creamy white, raised with an entire margin	Present (unclear)	Thin	Present 	Present 	Globose 10-20 μm diam
WK5	WK	Small Circular colonies, creamy white, raised with an entire margin	Present (unclear)	Thin	Present 	Present 	Globose 10-20 μm diam
WK6	WK	Small Circular colonies, creamy white, raised with an entire margin	Present (unclear)	Thin	Present 	Present 	Globose 10-20 μm diam

WK - Wat Khun Samut Chin Temple mangrove habitat.

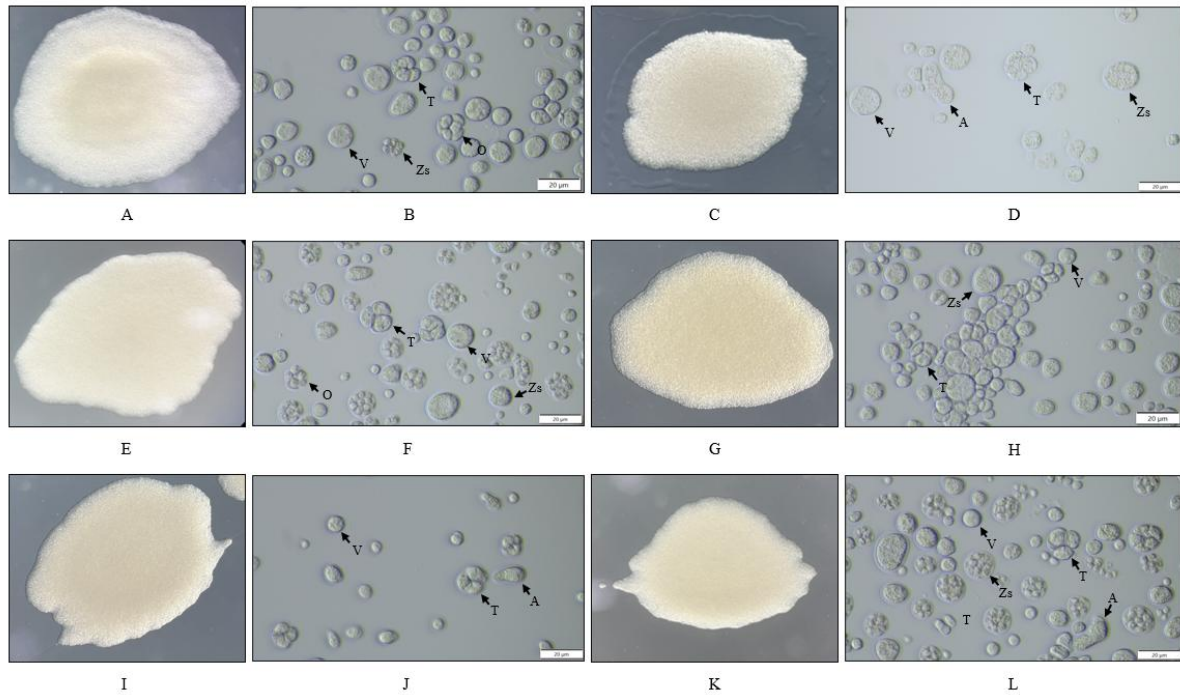


Figure 1.

Thraustochytrid colonies and cells, WK1 (A-B), WK2 (C-D), WK3 (E-F), WK4 (G-H), WK5 (I-J) and WK6 (K-L). (scale bar = 20 µm), (A) Amoeboid cell (O) Octad (T) Tetrad (V) Vegetative cell (Zs) Zoosporangium that contains zoospores

Growth behavior observation of Thraustochytrids

The six thraustochytrid strains were cultured in 100 mL of GYP broth with an incubator shaker at 150 rpm at 28 °C for 5 days. Thraustochytrid growth was measured in optical density at 600 nm. Growth of all isolates was detected at 12 h of incubation, all strains showed significant growth during 24 to 60 h, and slight decline at 72 h. The cell death was observed from 96 h onwards, isolated WK3 showed the highest growth, reaching an OD of 3.863 **Figure 2**. Growth is usually dependent on the strain or species and the carbon source. Over time, the limited nutrients available will decrease, allowing the cells to use fewer nutrients for cell division.⁵ and the results of this study are similar to previous research.^{5,7}

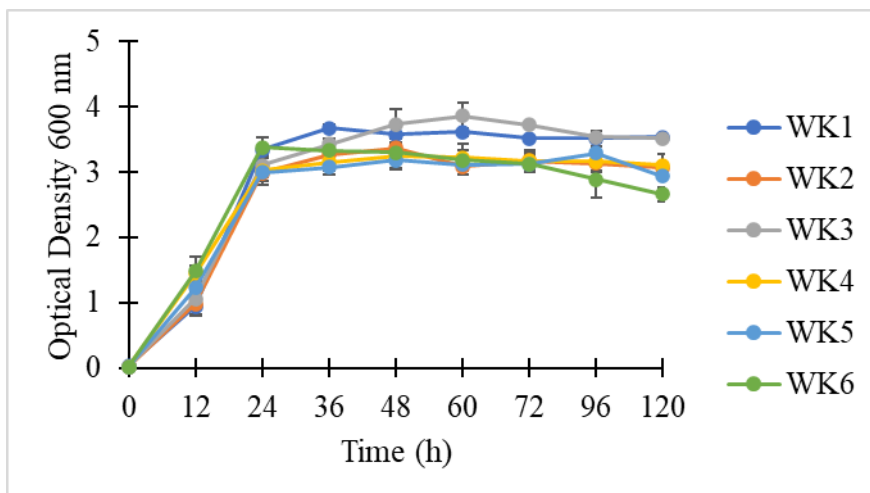


Figure 2.

Growth behavior of thraustochytrid isolates. (0.3% w/v of glucose)

Biomass production of thraustochytrids

All thraustochytrid strains were cultured in 100 mL of GYP broth using an incubator shaker at 150 rpm, 28 °C for 120 hours. Biomass production ranged from 0.81 g/L to 1.36 g/L dry cell weight, The highest biomass value was obtained from strain WK3, which showed a similar value to strain WK1. **Figure 3.**

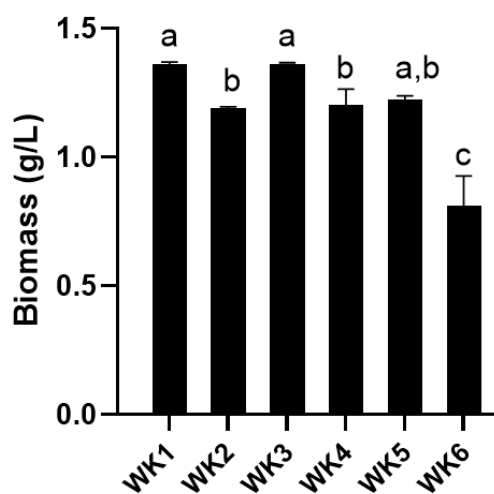


Figure 3.

Biomass production of thraustochytrids after culturing for 5 days. Values are represented as mean \pm standard deviation (n=3). Different compact letters indicate statistically significant differences at the $p < 0.05$, analyzed by ANOVA analysis and comparisons with Tukey's HSD at the $p < 0.05$ level of significance.

Growth behavior of Thraustochytrids in the different glucose concentrations

The two highest growth thraustochytrid strains were selected from the previous studies and cultured in 100 mL of GYP broth with different glucose concentrations at (0.3, 2, 4, 6, and 8%, w/v). Thraustochytrid growth was measured at optical density (OD 600) nm. Growth of

both isolates was detected at 12 h of incubation, all strains showed significant growth from 24 h to 60 h and maintained their growth up to 120 h in some isolates.

The highest biomass accumulation of WK1 was observed at 4% (w/v) glucose with an OD₆₀₀ of 3.35 at 48 h, after which the growth slightly declined. At 0.3% and 2% (w/v) glucose, cell density reached moderate OD values ranging from 2.0 to 3.14 before stabilizing, and at 6% and 8% (w/v), glucose inhibition of growth, possibly due to osmotic stress or excessive glucose concentration, therefore, the resulting OD value is lower **Figure 4a**.

In addition, the highest biomass accumulation of WK3 was observed at 4% (w/v) glucose with an OD₆₀₀ of 8.0 at 120 h, which was more than that of WK1, and all concentrations maintained their growth up to 120 h without a decline. These results show that WK3 has a higher nutrient capacity and stress tolerance compared to WK1 and also indicate that WK3 has a better ability to adapt and grow **Figure 4b**.

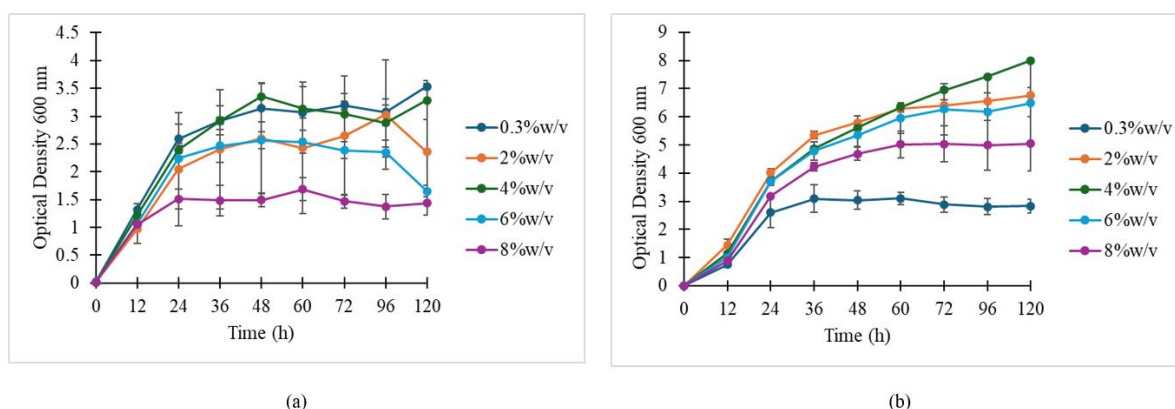


Figure 4.

Growth behavior of thraustochytrid isolates in different glucose concentrations
(a) WK1 and (b) WK3

Thraustochytrids that are fed in conditions where the culture medium is limited, especially the nitrogen source, are used up and depleted after 24 to 36 hours, and because there is still a large source of carbon or glucose in the medium, the thraustochytrid will continue to absorb the carbon source, but cannot divide the cell due to lack of nitrogen, and as a result, the cell will convert the carbon or glucose source into the lipid accumulated within the cells.¹⁰ The biomass was stored at -20 °C before freeze-drying for weight analysis and use for further fatty acid analysis.

Conclusion:

In conclusion, six isolates of thraustochytrids could produce biomass, depending on the type of species. In this study, WK3 exhibited the highest biomass yield and the best growth with a biomass value of 1.36 g/L dry cell weight, with a maximum OD of 3.863. Based on initial results, WK1 and WK3 showed the two highest growth rates; these were selected for further evaluation in a medium containing different glucose concentrations (0.3-8% w/v), which revealed that glucose concentrations from 0.3% to 4% supported better growth than higher concentrations. Especially, WK3 achieved the highest growth at 4% glucose, with an optical density at OD 8.0. This study showed a characteristic of heterotrophic growth of thraustochytrid, which requires less carbon source for growth compared to other microorganisms. Molecular identification using 18S rRNA gene sequencing provides more accurate species-level classification. However, since the main objective of this study was to isolate thraustochytrids and evaluate their growth and biomass, morphological identification



was considered sufficient. Molecular approaches such as 18S rRNA sequencing will be incorporated in future work to confirm the taxonomy of these isolates.

Acknowledgements:

The research project was supported by Assistant Professor Dr.Niyom Kamlangdee, Dr. Kaliyamoorthy Kalidasan, and Scientific members, who provided valuable guidance and knowledge. The researcher feels deeply grateful for their kindness and would like to thank all the members here.

References:

1. Shahidi F, and Ambigaipalan P. *Annual Review of Food Science and Technology*. 2018; 9:345-381.
2. Patel A, Liefeldt S, Rova U, Christakopoulos, P., Matsakas, L. *Sci Rep*. 2020;10,1992.
3. Patel, A., Bettiga, M., Rova, U., Christakopoulos, P., Matsakas, L. *Trends in Biotechnology*. 2022;40(10):1261-1273.
4. Nakasawa A, Matsuura H, Kose R, Kato S, Honda D, Inouye I, Kaya K, Watanabe MM. *Bioresource Technology*. 2012; 109:287-291.
5. Kalidasan K, Vinithkumar NV, Peter DM, Dharani G, Dufossé L. *Marine Drugs*. 2021;19(10):571.
6. Yokoyama R, Salleh B, Honda D. *Mycoscience*. 2007; 48:329-341.
7. Arifiles KHV, Alcantara JCO, Cordero PRF, Batoon JAL, Galura FS, Leano E, Gina RD. *Mycosphere*. 2011;2(5):521-531.
8. Kamlangdee N and Fan KW. *Songklanakarin J. Sci. Technol*. 2003;25(5):643-650.
9. Unagul P, Suetrong S, Preedanon S, Klaysuban A, Gundool W, Suriyachadkun C, and Sakayaroj J. *Botanica Marina*. 2017;60(4):363-379.
10. Burja AM, Radianingtyas H, Windust A., and Barrow CJ. *Applied Microbiology and Biotechnology*. 2006; 72:1161-1169.



INFLUENCE OF ETHANOL DESOLVATION RATIO ON LUTEIN ENCAPSULATION IN WHEY PROTEIN ISOLATE PARTICLES

Peerapong Wongthahan, Araya Chaorungrit, Panadda Nonthanum*

Faculty of Technology, Khon Kaen University, Khon Kaen, 40002, Thailand

*e-mail: panano@kku.ac.th

Abstract:

This study examined the influence of ethanol as a desolvating agent on the characteristics of lutein-loaded whey protein isolate (WPI) particles prepared via desolvation. Particles were synthesized with different ethanol to WPI dispersion ratios (0.25x, 0.50x, and 0.75x). Morphological and size analyses (SEM, DLS) revealed a direct correlation between increased ethanol ratios and larger particle sizes, ranging from 246.3 nm to 852.4 nm. Encapsulation efficiency (EE) reached its maximum at 88.51% when an ethanol ratio of 0.50x was employed. In-vitro digestion assays demonstrated that formulations prepared with lower ethanol ratios facilitated more substantial lutein release. Notably, the 0.50x ethanol formulation, exhibiting the highest EE, also provided enhanced storage stability, effectively mitigating lutein degradation across various storage temperatures. These results highlight the significance of precisely modulating the ethanol desolvation ratio for optimizing WPI-based encapsulation systems.

Introduction:

Lutein is a lipophilic bioactive carotenoid essential for human health, which the body cannot synthesize. Notably abundant in dark green leafy vegetables, various fruits, and egg yolks, its consistent dietary consumption has been associated with positive ocular health outcomes, particularly in preventing age-related macular degeneration and cataracts [1]. However, lutein exhibits low stability, undergoing rapid degradation when exposed to light, oxygen, or heat [2]. Furthermore, its limited water solubility restricts absorption within the gastrointestinal tract, thereby diminishing its bioaccessibility. Consequently, encapsulation techniques have been extensively investigated to enhance lutein's bioavailability, solubility, and stability. The desolvation technique is a widely employed method for encapsulating bioactive compounds, prized for its procedural simplicity, high reproducibility, and ease of preparation. In this process, a desolvating agent (e.g., acetone or ethanol) is gradually introduced into an aqueous protein solution under constant agitation. This induces protein dehydration and a subsequent conformational change, facilitating nanoparticle formation [3]. Whey protein isolates (WPI) are prominent milk-derived proteins frequently used as coating materials due to their water solubility, cost-effectiveness, nutrient density, and GRAS status [4]. The characteristics and size of the polymeric particles formed are governed by several preparation parameters, including protein concentration, pH, ionic strength, crosslinking agent concentration, agitation speed, and the amount of desolvating agent [5]. This study aimed to investigate how the amount of ethanol, utilized as a desolvating agent, influenced various characteristics of lutein encapsulated in WPI samples, including its encapsulation efficiency, morphology, particle size, in-vitro digestibility, and stability across different storage temperatures.

Methodology:

Materials

Whey protein isolate (WPI) containing 92.79% protein was supplied by Mullins Whey (Wisconsin, USA). Lutein (FloraGLO, a 20% solution in safflower oil) was generously provided by Thai Food and Chemicals (Bangkok, Thailand). Lutein (>95% purity), pepsin, and pancreatin were purchased from Sigma-Aldrich (St. Louis, MO, USA). Chloroform was acquired from Thermo Fisher Scientific (Massachusetts, USA). Sodium hydroxide (NaOH)



was obtained from Ajax Finechem (Massachusetts, USA). Absolute ethanol and hydrochloric acid (HCl) were supplied by Merck (New Jersey, USA).

Encapsulation of Lutein in WPI Particles

Whey protein isolate (WPI) was prepared as a 1% (w/v) dispersion in deionized water and left to hydrate overnight. For the lutein solution, lutein was dissolved in absolute ethanol and subjected to sonication at 37 kHz for 15 minutes in an ultrasonic water bath (EASY 30 H, Elma, Germany). The prepared ethanol solution containing lutein was added dropwise to the WPI dispersion (20 mL), with the total volume of the added solution ranging from 0.25 to 0.75 times the volume of the WPI dispersion (designated 0.25x–0.75x), while continuously stirring at 500 rpm on a magnetic stirrer (IKA C-MAG HS7, North Carolina, USA). In all samples, the final lutein content in the combined dispersion was 5 mg. The combined lutein and WPI solution was transferred to an aluminum pan and subsequently dried. A vacuum oven (Fisher Scientific Isotemp 281, New Hampshire, USA) operated at 40°C and 30 mmHg was utilized for 4 hours to achieve drying. Dried samples were kept in aluminum bags prior to analysis.

Determination of Encapsulation Efficiency (EE)

Dried samples (0.1% w/v) were dispersed in absolute ethanol, stirred for 30 minutes to extract surface lutein, and centrifuged (10,000 rpm, 15 min). Lutein concentration in the supernatant was then determined from its absorbance at 446 nm, using a standard curve of lutein in ethanol [6]. Encapsulation efficiency (EE) was calculated with the following equation:

$$EE (\%) = \frac{w_1 - w_2}{w_1} \times 100$$

where EE is encapsulation efficiency; w_1 and w_2 represent the total theoretical lutein used in preparation and the amount of lutein on the surface of particles, respectively

Determination of Particle Size

Dried lutein-loaded WPI samples were dispersed in deionized water at 0.05% (w/v) concentration. The particle sizes were subsequently determined using the dynamic light scattering (DLS) method in a NanoPlus particle size analyzer (Particulate Systems, GA, USA).

Morphological Characterization

Sample morphology was characterized by scanning electron microscopy (SEM) using a Carl Zeiss EVO HD unit (Oberkochen, Germany) operating at 10 kV. Prior to imaging, particle surfaces were gold-coated with a Cressington 108Auto sputtering coater (Redding, Canada).

In-vitro Digestion Study

The experiment was conducted following the methodology outlined by Sotomayor-Gerding et al., 2016 [7]. Concisely, a 0.15 mg/ml dispersion of the sample in deionized water was combined with an equal volume of simulated salivary fluid containing mucin and salts. The pH of the mixture was adjusted to 6.8 with 0.5 M NaOH, followed by incubation at 37°C for 10 minutes with continuous agitation at 100 rpm in a Gallenkamp Environmental Shaker (Model 10X400, UK). Simulated gastric fluid (SGF) preparation involved dissolving 2 g of NaCl and 7 mL of HCl in 1 liter of water, followed by pH adjustment to 1.2 using 1 M HCl. The mixture from the oral phase was blended with the SGF in equal volumes (1:1, v/v), and

the pH was finely adjusted to 1.5 with 0.5 M NaOH. Pepsin (3 mg) was added, and the sample was incubated at 37°C for 2 hours with continuous shaking. The simulated intestinal fluid (SIF) containing 6.8 g/L K₂HPO₄ was combined with the gastric digest at a 1:3 ratio (v/v) along with pancreatin at 4 mg/mL. The mixture was adjusted to pH 7.0 using 0.2 N NaOH, followed by a further incubation at 37°C for 3 hours. Samples were withdrawn from the shaker incubator at hourly intervals. The digested samples were further centrifuged at 4000 rpm for 40 minutes. The micellar phase (5 mL), hypothesized to contain bioavailable lutein, was isolated and subjected to liquid-liquid extraction by vortexing with 5 mL of chloroform. Following centrifugation, the absorbance of the chloroform layer was measured at 452 nm using a GENESYS 6 UV/Vis spectrophotometer (Thermo Scientific, USA). The measured absorbance enabled the calculation of lutein concentration via a standard curve prepared with lutein in chloroform. The amount of lutein released was calculated using the following equation:

$$\text{Lutein released (\%)} = \frac{C_{\text{middle phase}}}{C_{\text{raw digesta}}} \times 100$$

where $C_{\text{middle phase}}$ and $C_{\text{raw digesta}}$ are lutein concentrations in the micelle fraction and the raw digesta, respectively.

Lutein Stability during Storage

Samples were sealed in aluminum foil bags and stored in the dark at 4, 25, and 40 °C. Entrapment efficiencies were evaluated at 5, 10, and 15 days.

Statistical Analysis

All experimental data were conducted in triplicate and presented as mean values with standard deviation. Statistical evaluation of encapsulation efficiency and particle size data was performed using one-way analysis of variance (ANOVA) through SPSS Statistics 16 software (SPSS Inc., Chicago, IL, USA). Significant differences among means were determined using Duncan's multiple range test at $p < 0.05$.

Results and Discussion

Morphology and particle sizes

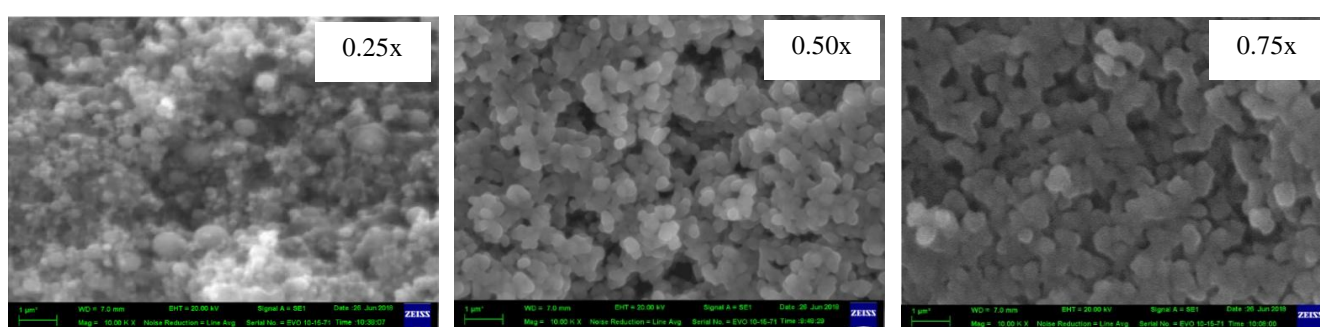
The morphology of lutein-loaded whey protein isolate (WPI) particles, prepared using incremental ratios of ethanol (0.25x to 0.75x) as a desolvating agent, was examined via scanning electron microscopy (SEM) (**Figure 1**). SEM images revealed an increase in particle size corresponding to higher ethanol ratios. This finding was quantitatively supported by dynamic light scattering (DLS) data, which demonstrated a direct correlation between the ethanol desolvating agent ratio and particle hydrodynamic diameter (**Table 1**). Particle sizes for the lutein-loaded WPI formulations were determined to be within the range of 246.3-852.4 nm. These findings align with previous research by Feng et al., 2022 [8], which reported the increase in WPI protein aggregation when higher concentrations of ethanol were introduced. Ethanol induces the molecular unfolding of native WPI, which subsequently leads to aggregation. This aggregation is driven by the formation of disulfide bonds, intramolecular hydrogen bonds, and enhanced hydrophobic interactions [9].

Table 1.

Mean particle sizes and lutein encapsulation efficiency of lutein-loaded WPI samples prepared with various ethanol/WPI dispersion ratios (0.25x–0.75x).

Ethanol/WPI dispersion ratios	Mean particle sizes (nm)	Encapsulation efficiency (%)
0.25x	246.3±3.97 ^c	79.26±1.25 ^c
0.5x	432.2±1.64 ^b	88.51±0.76 ^a
0.75x	852.4±6.94 ^a	84.73±1.16 ^b

Means with different superscripts are significantly different ($p < 0.05$) in their respective column

**Figure 1.**

Morphology of lutein-loaded WPI particles at different ethanol/WPI dispersion ratios (0.25x–0.75x), as observed by scanning electron microscopy (SEM) at 10,000× magnification.

Encapsulation efficiency

Milk proteins bind hydrophobic molecules through several mechanisms, primarily involving hydrophobic interactions, van der Waals attractions, and hydrogen bonds [10]. In this study, the encapsulation efficiency (EE) of lutein, prepared at varying ethanol/whey protein isolate (WPI) dispersion ratios (0.25x–0.75x), demonstrated values ranging from 79.26% to 88.51% (**Table 1**). Notably, the highest lutein EE ($p < 0.05$) was attained with an ethanol ratio of 0.50x. This enhanced EE at moderate ethanol ratio can be attributed to the partial unfolding of WPI, which likely exposes additional hydrophobic sites, thereby strengthening the hydrophobic interactions between WPI and lutein. Conversely, at a higher ethanol ratio (0.75x), excessive protein unfolding may lead to WPI self-aggregation rather than effective binding with lutein, ultimately resulting in a reduction in encapsulation efficiency.

In-vitro digestion study

The release profiles of lutein encapsulated within WPI, under sequential simulated gastric and intestinal digestion, are presented in **Figure 2**. A clear trend indicated that lutein release increased as the ethanol ratio applied during particle formation decreased. Although particle size does not directly govern encapsulation efficiency, it plays a critical role in the controlled release of active pharmaceutical ingredients. This is attributed to the increased surface area-to-volume ratio in smaller particles, which enhances the accessibility for enzymes or the surrounding release medium, leading to a more pronounced release compared to larger particles [11].

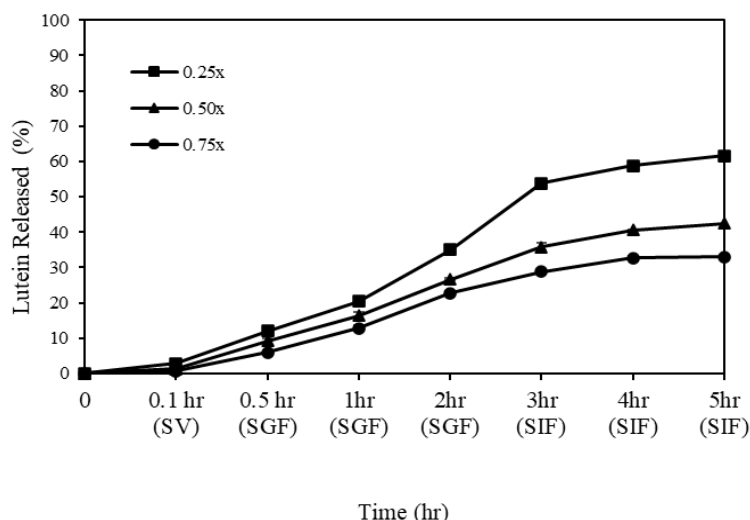


Figure 2.

Release profiles of lutein entrapped with WPI prepared at different ethanol/WPI dispersion ratios (0.25x–0.75x), under in-vitro digestion stages; SV (simulated saliva fluid), SGF (simulated gastric fluid), and SIF (simulated intestinal fluid).

Stability at different storage temperatures

Figure 3 illustrates that lutein content declined with increasing storage temperature and duration. Notably, lutein encapsulated in WPI prepared with an ethanol ratio of 0.50x exhibited the highest stability, surpassing formulations prepared with 0.25x and 0.75x ethanol ratios. This enhanced stability observed in samples with higher encapsulation efficiency (EE) values suggests superior protection of lutein against degradation from light and oxygen, likely conferred by the encapsulating WPI matrix.

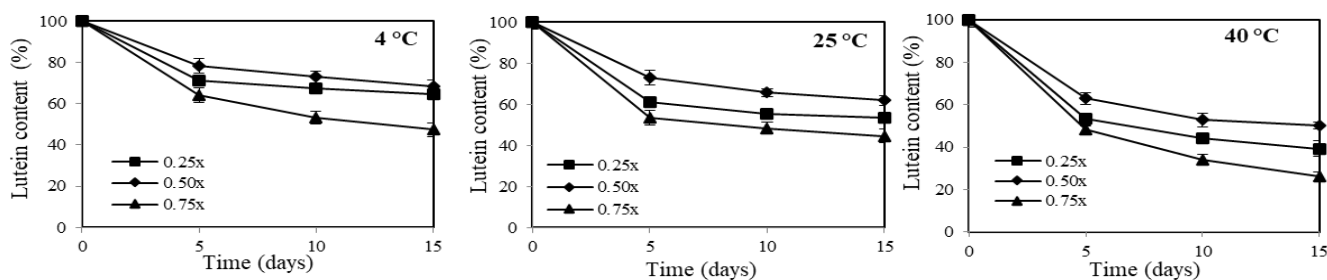


Figure 3.

Stability of lutein encapsulated in WPI particles, prepared with varying ethanol/WPI dispersion ratios (0.25x–0.75x), under different storage temperatures (4, 25, and 40 °C).

Conclusion:

This study demonstrates that the ratio of ethanol used as a desolvating agent significantly influences the properties of lutein-loaded whey protein isolate (WPI) particles. Increasing the ethanol concentration resulted in larger particle sizes which may be attributed to enhanced unfolding and aggregation of WPI. An optimal ethanol ratio of 0.50x yielded the highest encapsulation efficiency (EE). In-vitro digestion analyses revealed that smaller particles, formed at lower ethanol concentrations, promoted greater lutein release. Moreover, the highest EE, achieved at the 0.50x ethanol ratio, was associated with improved lutein stability during storage, suggesting effective protection by the WPI matrix. These findings underscore



the critical role of precise ethanol control in optimizing the encapsulation and delivery of lutein.

References:

1. Steiner BM, McClements DJ, Davidov-Pardo G. Trends Food Sci Technol. 2018;82:71-81.
2. Teo A, Lee SJ, Goh KKT, Wolber FM. Food Chem. 2017;221:1269-1276.
3. Mohammadian M, Waly MI, Moghadam M, Emam-Djomeh Z, Salami M, Moosavi-Movahedi AA. Food Sci Human Wellness. 2020;9:199-213.
4. Ye Q, Woo MW, Selomulya C. Food Chem. 2019;280:255-261.
5. Sailaja AK, Amareshwar P. Asian J Pharm Clin Res. 2012;5(2):132-134.
6. Qv XY, Zeng ZP, Jiang JG. Food Hydrocoll. 2011;25:1596-1603.
7. Sotomayor-Gerding D, Oomah BD, Acevedo F, Morales E, Bustamante M, Shene C, Rubilar M. Food Chem. 2016;199:463-470.
9. Feng Y, Yuan D, Kong B, Sun F, Wang M, Wang H, Liu Q. Curr Res Food Sci. 2022;5:1386-1394.
9. Feng Y, Ma X, Kong B, Chen Q, Liu Q. Food Hydrocoll. 2021;111:106379.|
10. Jiang Y, Fan Y, Yokoyama W, Zhang Y, Zhao L. Food Chem. 2016;200:91-97.
11. Mehta N, Kumar P, Verma AK, Umaraw P, Kumar Y, Malav OP, Sazili AQ, Domínguez R, Lorenzo JM. Appl. Sci. 2022;12:1424.

SMART IMAGING SOLUTIONS FOR LIFE SCIENCE RESEARCH



FV4000

Confocal Laser Scanning Microscope

- **Next-Generation SiVIR™ Detector:**
 - Extremely Low Noise
 - Wider Dynamic Range with Linearity
 - Higher Detection Efficiency in a Broader Range with Stability
- **Software and Laser Power Monitoring with Compensation**
- **Enhanced super resolution up to 120 nm**

VS200

SLIDEVIEW - Slide Scanner

- **5 imaging modes:** BF, FL, PH, DF and Simple POL
- High-Resolution Scanning by **60X, 100X** with **automatic oil immersion**
- Centralized image storage via **Net Image Server (NIS)** - access anytime, anywhere



APX100

Digital Imaging System

- **High-speed autofocus** for effortless image capture
- Smart navigator **auto-detects samples**
- **Images are organized and easy to find**
- **5 imaging modes:** BF, FL, PH and GC

CM30

Incubation Monitoring System

- **Remotely monitor cell cultures 24/7**
- Provides **quantitative data** about the health of cells in the incubator
- **Reduces sample damage** caused by temperature changes and contamination





“LEADER IN SMART TECHNOLOGY”

f isciencetech

02-509-1623, 089-446-9111

email : info@isciencetech.com
website : www.isciencetech.com



revvity



Bead Ruptor Elite is advanced and easy to use bead mill homogenizer

PCRBIO SYSTEMS
simplifying research



We are the PCR experts

minipcr bio



Making science accessible to everyone everywhere

INFUSION TECH



Realize prompt and accurate molecular diagnostic



Department of Microbiology
Faculty of Science
Chulalongkorn University

Microbiology and Microbial Technology

Ph.D. & M.Sc. PROGRAMS

Why us?

- ✓ Best Program in Microbiology in Thailand!
- ✓ Thailand's Oldest and Most Prominent School of Science
- ✓ Intensive and Advanced Courses
- ✓ Exchange Opportunities Overseas
- ✓ Cutting Edge Research for Future Applications



Advancing the world of MICROBIOLOGY

JOIN US NOW!
Admission 2026

FB: microbiologysciencechula
Call: (+66) 2 2185070-71

SCAN ME





Chula
Chulalongkorn University



Proceedings Book



More information

Tel: +66 81 701 8345, +66 94 251 2103
Email: tsb2025thailand@gmail.com
Website: www.tsb2025.org

Organized by

Department of Microbiology, Faculty of Science, Chulalongkorn University
The Institute of Biotechnology and Genetic Engineering of Chulalongkorn University
Thai Society of Biotechnology